



University of HUDDERSFIELD

University of Huddersfield Repository

Pashley, Joe

Development of a Fused Metrology Method for Detailed Analysis of Worn Hip Implant Bearing Components

Original Citation

Pashley, Joe (2022) Development of a Fused Metrology Method for Detailed Analysis of Worn Hip Implant Bearing Components. Doctoral thesis, University of Huddersfield.

This version is available at <http://eprints.hud.ac.uk/id/eprint/35728/>

The University Repository is a digital collection of the research output of the University, available on Open Access. Copyright and Moral Rights for the items on this site are retained by the individual author and/or other copyright owners. Users may access full items free of charge; copies of full text items generally can be reproduced, displayed or performed and given to third parties in any format or medium for personal research or study, educational or not-for-profit purposes without prior permission or charge, provided:

- The authors, title and full bibliographic details is credited in any copy;
- A hyperlink and/or URL is included for the original metadata page; and
- The content is not changed in any way.

For more information, including our policy and submission procedure, please contact the Repository Team at: E.mailbox@hud.ac.uk.

<http://eprints.hud.ac.uk/>



**Development of a Fused Metrology Method for Detailed
Analysis of Worn Hip Implant Bearing Components**

Joe Pashley

A thesis submitted to the University of Huddersfield in partial fulfilment of the
requirements for the degree of Doctor of Philosophy

January 2022

Copyright Statement

The author of this thesis (including any appendices and/ or schedules to this thesis) owns any copyright in it (the "Copyright") and s/he has given The University of Huddersfield the right to use such Copyright for any administrative, promotional, educational and/or teaching.

Copies of this thesis, either in full or in extracts, may be made only in accordance with the regulations of the University Details of these regulations may be obtained from the Librarian. Details of these regulations may be obtained from the Librarian. This page must form part of any such copies made.

The ownership of any patents, designs, trademarks and any and all other intellectual property rights except for the Copyright (the "Intellectual Property Rights") and any reproductions of copyright works, for example graphs and tables ("Reproductions"), which may be described in this thesis, may not be owned by the author and may be owned by third Such Intellectual Property Rights and Reproductions cannot and must not be made available for use without permission of the owner(s) of the relevant Intellectual Property Rights and/or Reproductions.

Declarations

I declare that this thesis has been composed solely by myself and that it has not been submitted, in whole or in part, in any previous application for a degree. Except where states otherwise by reference or acknowledgment, the work presented is entirely my own.

Abstract

Due to the prevalence of aseptic loosening induced by wear particles, a common focus of hip implant experimental studies is the wear performance of the implant. Coordinate measurement machines (CMM) are commonly used for volumetric wear measurements. Allowing a wear map of the bearing surface to be created, and the size and location of wear areas to be analysed. To understand wear mechanisms and tribological behaviour on a surface scale, areal surface measurements are used.

Most manufacturing companies engaged in orthopaedic manufacture have access to high quality CMMs and surface metrology systems. In fact, these are required for compliance with company and international quality standards. However, they do not in general have the ability to combine outputs of these systems in a fused data context to allow them to investigate tribological/wear behaviour.

There is therefore the opportunity to develop an advanced fixture system specifically designed to combine CMM and surface measurement data together for detailed hip implant bearing analysis. Allowing for high accuracy positional targeting of surface measurements anywhere on a worn bearing surface. Such a fixture system with data fusion capability will improve future hip implant surface measurement studies, ensuring the most critical surface topography data is captured easily and quickly. This fixture system also aims to stitch surface measurements through wear areas, this currently has never been achieved and would be a novel step forward in analysis of worn hip implant components.

A motorised fixture was developed, utilising custom designed brackets and two precision rotary stages, allowing for measurement access to the entire bearing surface. The size of the fixture is minimal, 271 x 155 x 93 mm (LWH), ensuring it is compatible with the majority of surface metrology instruments. The software for the fixture system was developed on MATLAB, this software allows for: wear map creation from CMM data; selection of surface measurement locations in relation to the wear map; and control of the fixture. Once developed, the fixture system underwent thorough testing using CMM measurement, allowing the positional error of the fixture to be calculated.

The fixture system was utilised to measure a range of retrieved large MoM femoral heads. Of the ten femoral heads, two showed clear wear areas, with wear volumes of 3.5 mm³ and 3.0 mm³. A series of surface measurements were taken on the worn femoral heads, with the corresponding CMM wear maps used as positional reference. The surface within the wear area roughened for both femoral heads, increasing from 32 to 138 nm (Sa), and 11 to 119 nm (Sa).

Surface topography mapping showed that the area of roughening did not closely match the shape of the CMM defined wear area. The area of roughening could extend out of the wear area or be contained to a very small portion of the wear area. Stitches of surface measurements through the wear area were completed, highlighting crucial stages, including the boundary regions. Allowing for a deeper understanding of the tribological mechanisms occurring.

Through the successful development of the fixture system, a novel surface measurement method for worn hip implant bearings has been created, facilitating accurate data fusion of CMM and surface measurement datasets. Newly developed surface analysis tools such as surface topography mapping and stitching through the wear area allows the worn bearing surface to be studied at a level of detail previously unattainable.

This method will allow for better judgment of hip implant performance and can be utilised for both in-vitro and in-vivo testing for all material types. Alternatively, the fixture system can also be useful for quality inspection of newly manufactured components. As the development cost of the fixture was kept minimal, redevelopment across industry or research environments is achievable.

Contents

Abstract.....	3
Contents.....	4
List of Figures.....	8
List of Tables.....	13
List of Acronyms	14
Acknowledgements.....	15
Publications.....	15
Chapter 1: Introduction.....	16
1.1 Current Issue.....	17
1.2 Aim.....	17
1.3 Objectives.....	18
1.4 Overview of Chapters.....	18
Chapter 2: Literature Review	19
2.1 Total Hip Replacement.....	19
2.1.1 Joints	19
2.1.2 Anatomy of the Hip Joint	20
2.1.3 Degenerative Joint Disease	22
2.1.4 Joint Replacement.....	23
2.1.5 The History of Hip Replacement	24
2.1.6 The Modern Hip Implant Design	26
2.1.7 Total Hip Replacement Surgical Procedure	27
2.1.8 Current Trends of Hip Implant Design	28
2.1.9 Failure of Hip Implants.....	34
2.1.10 Biotribology of Hip Implants	40
2.1.11 Chapter Summary	51
2.2 Metrology for Hip Implants.....	52
2.2.1 Measurement Applications.....	52
2.2.2 Coordinate Measuring Machines.....	57
2.2.3 Wear Measurement Methods	61
2.2.4 Comparing Gravimetric and Volumetric Wear Measurement Methods	68
2.2.5 Surface Metrology.....	70
2.2.6 Chapter Summary	85
2.3 Surface Metrology Studies on Worn Hip Implant Bearings	86
2.3.1 Changing Surface Topography within Wear Areas	86
2.3.2 Roughening or Smoothing of the Surface Within the Wear Area.....	93

2.3.3	Linking Surface Topography and Implant Wear Rates.....	95
2.3.4	Chapter Summary	97
2.4	Wear Map Positional Targeting of Surface Measurements.....	98
2.4.1	Spherical Coordinates	98
2.4.2	Metrology Data Fusion.....	98
2.4.3	Wear Map Targeted Surface Measurements.....	99
2.4.4	Surface Measurement Limitations for Acetabular Cups.....	100
2.4.5	Fixturing to Support Wear Map Targeted Surface Measurements	101
2.4.6	Modern Measurement Instruments	105
2.4.7	RedLux OrthoLux.....	107
2.4.8	Chapter Summary	108
2.5	Gaps in Knowledge from Literature Review	109
Chapter 3: Comparison of the RedLux Optical CMM to an Analogue Probe CMM.....		110
3.1	Introduction	110
3.2	Methodology.....	113
3.2.1	CMM Performance Specifications.....	113
3.2.2	Cohort	113
3.2.3	Fixture Setup	114
3.2.4	CMM Qualification	115
3.2.5	Scanning Strategy.....	116
3.2.6	Data Analysis.....	117
3.3	Results.....	118
3.3.1	Metal Femoral Head	119
3.3.2	Polymer Acetabular Liner.....	120
3.3.3	Ceramic Acetabular Liner	121
3.3.4	Wear Maps.....	122
3.4	Discussion.....	126
3.4.1	Radius Comparison to Tolerance Bands	126
3.4.2	Measurement Time.....	126
3.4.3	CMM Fixture Setup	127
3.4.4	RedLux Wear Depth Measurement	127
3.4.5	RedLux Analysis Software	128
3.4.6	Further Work.....	128
3.5	Chapter Summary	129
Chapter 4: Development of the Custom Fixture System.....		130
4.1	Design Requirements Checklist.....	130
4.2	Required Positional Uncertainty of the Fixture System.....	133
4.2.1	Accuracy, Uncertainty, and Error for Metrology	133

4.2.2	Calculating the Target Positional Uncertainty	134
4.3	Hardware Development.....	139
4.3.1	Initial Designs	139
4.3.2	Rotary Stages Selection.....	142
4.3.3	3D Printed Prototype	143
4.3.4	Final Design Overview.....	145
4.3.5	Design Features.....	148
4.3.6	Material Choice	159
4.3.7	Manufacturing and Assembly	160
4.4	Software Development	162
4.4.1	CMM Analysis.....	163
4.4.2	Selecting Surface Measurement Locations.....	166
4.4.3	Control of the Fixture System	170
4.5	Method Flowchart	175
4.6	Chapter Summary	176
	Chapter 5: Testing of the Custom Fixture System	177
5.1	Statistics	177
5.2	Testing Phases.....	178
5.3	Phase 1 – Initial Measurement Testing.....	179
5.3.1	Method.....	179
5.3.2	CMM Angular Measurement Repeatability	182
5.3.3	Angular Measurement Error Caused by Inconsistent Probing	184
5.3.4	Phase 1 Positional Error Testing Results Summary.....	186
5.4	Phase 2 – Improved Method Testing	188
5.4.1	Method Improvements.....	188
5.4.2	Angular Measurement Repeatability of the CMM	191
5.4.3	Angular Measurement Error Caused by Inconsistent Probing	193
5.4.4	Positional Repeatability of the Fixture.....	198
5.4.5	Positional Error of the Fixture.....	200
5.5	Phase 3 – Error Compensation.....	206
5.5.1	Error Compensation Adjustment	206
5.5.2	Post Error Compensation Testing	209
5.6	Calculating the Combined Positional Error of the Fixture System.....	214
5.6.1	Azimuth Rotation Error	214
5.6.2	Elevation Rotation Error.....	214
5.6.3	Combining Azimuth and Elevation Positional Error	215
5.6.4	Positional Error from Azimuth Alignment Error.....	217
5.7	Testing with the Surface Metrology Instrument.....	221

5.7.1	Re-locating Features Test.....	221
5.7.2	Stitching Test.....	222
5.8	Chapter Summary	223
Chapter 6: Analysis of Retrieved Metal-on-Metal Bearings		224
6.1	Cohort	224
6.2	Methodology for Wear Assessment	224
6.2.1	Summary	224
6.2.2	CMM.....	225
6.2.3	Surface Measurement.....	227
6.2.4	Custom Fixture System	228
6.3	Hypothesis.....	232
6.3.1	Wear	232
6.3.2	Surface Topography	232
6.4	Results.....	233
6.4.1	CMM Measurement.....	233
6.4.2	Unworn Surface	236
6.4.3	Wear Area Surface	240
6.5	Discussion.....	258
6.5.1	Stages Through the Wear Area	258
6.5.2	Surface Pattern Groups.....	262
6.5.3	MoM Wear Mechanism Theory	268
6.6	Chapter Summary	272
Chapter 7: Project Conclusions		274
7.1	Attainment of Aim and Objectives.....	274
7.2	Major Conclusions.....	275
7.3	Benefits of the Custom Fixture System.....	276
7.4	Novel Contributions	279
7.5	Limitations of the Work	280
7.6	Potential Improvements to the Custom Fixture System.....	281
7.7	Future Work.....	282
References.....		284
Appendix.....		293
	Metrology Definitions	293
	RedLux and Zeiss Full CMM Measurement Results	294
	Phase 1 Measurement Testing of the Custom Fixture System	295
	Repeatability Testing.....	295
	Positional Uncertainty Testing	297
	Retrieved MoM Wear Maps	301

Unworn Area Surface Measurements	306
Wear Surface Measurements – Femoral Head 135.....	316
Surface Measurements – Femoral Head 294	321

List of Figures

Figure 1: Comparison of synovial and solid joints.....	19
Figure 2: Features of a synovial joint	19
Figure 3: The hip joint	20
Figure 4: Surrounding the hip joint	21
Figure 5: Posterior view of the gluteus maximus muscle	21
Figure 6: Osteoarthritis of the hip joint	22
Figure 7: Radiograph of total hip replacement and total knee replacement.....	23
Figure 8: Number of joint replacement procedures in the UK between 2003 and 2017	23
Figure 9: Charnley metal femoral stem and acetabular cup components	25
Figure 10: Components of a hip implant.....	26
Figure 11: Comparison of THR approaches.....	27
Figure 12: Comparison of cemented and uncemented fixation designs.....	29
Figure 13: Fixation type by year of primary hip replacement in the UK	29
Figure 14: Comparison of bearing material combinations.....	30
Figure 15: Percentage of each bearing material combination for cemented hip replacements in the UK.....	32
Figure 16: Percentage of each bearing material combination for uncemented hip replacements in the UK.....	32
Figure 17: Percentage of each bearing material combination for uncemented hip replacements in the UK.....	33
Figure 18: Comparison of femoral head sizes	34
Figure 19: Failure factors for hip implant surgery.....	35
Figure 20: Radiograph images of aseptic loosening.....	36
Figure 21: Soft tissue damage from an adverse reaction to metal wear debris	37
Figure 22: Radiograph of dislocated hip implant	38
Figure 23: Comparison of macro and micro tribology factors of the hip implant.....	40
Figure 24: Comparison of large and small bearings	41
Figure 25: Steep cup inclination angle causing edge loading.....	42
Figure 26: Micro-separation causing the head to slide towards the edge of the cup.....	42
Figure 27: The effect of cup inclination angle on the size and location of wear areas	43
Figure 28: Location of expected third body wear damage on the acetabular cup	44
Figure 29: Comparison of lubrication regimes and their relationship with the Stribeck curve for a MoM bearing	46
Figure 30: The Stribeck curve with different bearing material combinations.....	46
Figure 31: Apparent (A) and real (B) area of contact between surfaces.....	47
Figure 32: Wearing of the hip implant bearing	48
Figure 33: Profile showing typical scratch and associated parameters to describe scratches.....	49
Figure 34: SEM images of scratches on the surface of CoCr femoral heads	49
Figure 35: Diametrical clearance diagram	52
Figure 36: Example quality inspection measurement strategy	53
Figure 37: Experimental study types.....	55
Figure 38: CMMs	57
Figure 39: Touch trigger probe system	58
Figure 40: Analogue probe system	59
Figure 41: Probe offset during CMM measurement	60
Figure 42: CMM measurement of acetabular liners	60
Figure 43: Gravimetric measurement method	61
Figure 44: Fluid uptake during simulator testing on UHMWPE acetabular cups	61
Figure 45: Volumetric measurement of a femoral head.....	62
Figure 46: Reconstructing pre-wear geometry for retrieval studies.....	63

Figure 47: Polar scan strategy, each scan line emanates from the pole to the equator of the component	64
Figure 48: Square scan strategy, highlighting the resultant edge effects	65
Figure 49: Measurement error caused by insufficient measurement points	67
Figure 50: Stedman diagram showing the typical measurement capabilities of measurement instrument groups	70
Figure 51: Example of a profile type surface measurement	71
Figure 52: Example areal optical surface measurement of a retrieved CoCr femoral head.	72
Figure 53: Areal and profile surface measurements of a retrieved CoCr femoral head compared	72
Figure 54: Profile surface measurement split into waveforms	73
Figure 55: Relationships between S-filter, L-filter, F-operator and SF and SL surfaces.....	74
Figure 56: Scale limited surface filtering using a Gaussian filter.....	74
Figure 57: Michelson Interferometer	75
Figure 58: Coherence scanning interferometry	76
Figure 59: Focus variation surface measurement.....	77
Figure 60: Areal height parameters	80
Figure 61: Areal surface measurements with identical Sq values but varying Ssk values.....	81
Figure 62: Areal surface measurements with identical Sq values but varying Spd and Spc values	81
Figure 63: Areal surface measurements with identical Sq values but varying Sdq and Sdr values.	82
Figure 64: Developed interfacial area ratio (Sdr).....	83
Figure 65: Texture direction (Std)	84
Figure 66: Wear map of a retrieved MoM femoral head.....	86
Figure 67: Types of wear damage for MoM hip implant bearings	87
Figure 68: Surface measurement images of retrieved MoM resurfacing components	88
Figure 69: SEM images of types of MoM bearing wear	89
Figure 70: SEM images of retrieved MoP femoral heads.....	90
Figure 71: Surface measurements of retrieved MoP components	90
Figure 72: AFM images of a ceramic head	91
Figure 73: SEM images showing surface damage within the wear area of retrieved CoC implant.	92
Figure 74: Changing surface topography of a MoP bearing.....	93
Figure 75: Wear rates of the polymer pin against the metal counterface roughness under wet testing conditions	95
Figure 76: The wear of the polythene socket (k) plotted against the mean skewness (Rsk) for each femoral head	96
Figure 77: The wear factor of the polymer liners against the roughness of the femoral heads	96
Figure 78: Spherical coordinates of a femoral head	98
Figure 79: CMM wear map of retrieved femoral head	99
Figure 80: Surface measurement limitations for acetabular cups	100
Figure 81: Surface measurement of femoral head	101
Figure 82: Basic tilt fixture	102
Figure 83: Manual translation and rotation stages.....	103
Figure 84: Motorised fixture with digital control.....	104
Figure 85: Bruker-Alicon uCMM.....	106
Figure 86: Data fusion of focus variation surface measurements using the Bruker Alicona uCMM [173].	106
Figure 87: RedLux OrthoLux.....	107
Figure 88: RedLux Optical CMM, measurement of femoral head and acetabular liner.....	110
Figure 89: Comparison of Optical and Analogue Probe CMM	111
Figure 90: Measurement cohort	113
Figure 91: Fixturing setups.....	114
Figure 92: Comparison of scanning strategies	116
Figure 93: CMM analysis with CATIA	117
Figure 94: Box and whisker plots for metal femoral head measurement results	119
Figure 95: Box and whisker plots for polymer acetabular liner measurement results	120
Figure 96: Box and whisker plots for ceramic acetabular liner measurement results.....	122
Figure 97: Metal femoral head wear maps.....	123
Figure 98: Polymer acetabular liner wear maps	124
Figure 99: Ceramic acetabular liner wear maps	125
Figure 100: Alternative fixture setup for acetabular liners.....	127
Figure 101: Diagram of scratch measurement on the Zeiss and RedLux	127

Figure 102: Stitching of surface measurements through the wear area of a femoral head	134
Figure 103: Relationship of bearing size with required elevation angle adjustment.....	135
Figure 104: Distance along the surface between two measurements in a stitch series	136
Figure 105: Calculation of the change in elevation angle between stitch measurements	137
Figure 106: Calculating the target positional uncertainty for the custom fixture system	138
Figure 107: Height limit of surface metrology instrument.....	139
Figure 108: Concept design of fixture system, Design 1	140
Figure 109: Concept design of fixture system, Design 2	141
Figure 110: Standa 8MR174-11 Motorized Rotation Stage	142
Figure 111: Concept design of fixture system, Design 3	143
Figure 112: 3D printed prototype of the fixture system using the Standa rotary stages.....	144
Figure 113: Exploded assembly view of the final fixture system design.....	145
Figure 114: Rendered CAD images of the final fixture system design	146
Figure 115: Fixture system in use with the Taylor Hobson Talysurf CCI	147
Figure 116: Close up image of the fixture in use with the Taylor Hobson Talysurf CCI.....	147
Figure 117: Alignment pockets on the fixture	148
Figure 118: Azimuth alignment error between CMM and surface measurement	149
Figure 119: Retrieved femoral head with a visual reference mark on the underside of the component.....	150
Figure 120: Using fixturing alignment to minimise the effect of rotational azimuth error.....	151
Figure 121: Coregistration slide component.....	151
Figure 122: Laser mount with coregistration slide attached	152
Figure 123: Reference mark from the coregistration slide located using the CCI sensor output	152
Figure 124: Top view of laser mount component	153
Figure 125: Top wireframe view of the laser mount to coregistration slide interface	154
Figure 126: Femoral head spherical centre is too low compared to the elevation rotary axis	155
Figure 127: The elevation angle is altered to approximately 80 degrees	156
Figure 128: Z adjust stage mounted below the azimuth rotary stage	156
Figure 129: Working principle of the z-screw taper.....	157
Figure 130: Mounted laser measurement sensor working principle	158
Figure 131: Manufacturing Images	160
Figure 132: CMM measurement of the middle bracket to set the elevation rotary stage origin position	161
Figure 133: CMM Measurement tab	163
Figure 134: Selecting unworn area data for an improved calculation of the component radius and volume parameters. ..	164
Figure 135: Overview of the coding used to generate a wear map from CMM data for femoral heads	165
Figure 136: App versions.....	165
Figure 137: Select Surface Measurement Locations tab.....	166
Figure 138: Opening a new figure and allowing data to be selected by the cursor	167
Figure 139: Selecting the start and end points of the stitch.	168
Figure 140: Collecting the start and end stitch coordinates	168
Figure 141: Calculating the stitch coordinates and storing them in the 'DATA POINTS' table	169
Figure 142: Control fixture tab.....	170
Figure 143: Standa MATLAB functions linking the rotary stages to the app.....	171
Figure 144: Start-up of the rotary stages	172
Figure 145: Sending the rotary stages to their home/origin positions using the 'command_move' function	172
Figure 146: Stopping both rotary stages using the 'command_sstp' function	172
Figure 147: Origin positions of both the azimuth and elevation rotary stages.....	173
Figure 148: Control of the rotary stages, moving the azimuth rotary stage to a custom position	174
Figure 149: The empirical rule diagram	177
Figure 150: Zeiss PRISMO Access CMM	179
Figure 151: CMM measurement of the square artefact	180
Figure 152: Pre-measurement procedure	181
Figure 153: Five-point plane probing strategy.....	182
Figure 154: Measurement of angular deviation between planes using Calypso	182
Figure 155: Box and whisker plot of the azimuth measurements and elevation measurements.....	183
Figure 156: Inconsistent probing diagram	185

Figure 157: Median error values from the 10 repeated measurements	186
Figure 158: Comparison of probing strategies.....	189
Figure 159: 25 mm gauge block attached to the fixture using glue.....	190
Figure 160: Lowest scan point on the gauge block	190
Figure 161: Measurement scanning strategy	191
Figure 162: Resultant measurement points from the scanning strategy	191
Figure 163: Box and whisker plots of CNC repeated measurements from phase 2 testing	193
Figure 164: Box and whisker plots of the median values from the inconsistent probing testing	196
Figure 165: Comparing the measurement error created by inconsistent probing from phase 1 and phase 2 testing	196
Figure 166: Scatter plot of azimuth measurements during phase 2 positional error testing	202
Figure 167: Scatter plot of elevation measurements during phase 2 positional error testing	205
Figure 168: Phase 2 testing results for the elevation rotary stage	206
Figure 169: Error compensation code for elevation rotary stage	207
Figure 170: The predicted elevation positional error results post error compensation	207
Figure 171: The predicted azimuth positional error results post error compensation	208
Figure 172: Azimuth positional error testing post error compensation adjustment	211
Figure 173: Elevation positional error testing post error compensation adjustment	213
Figure 174: Calculation of the combined positional error	215
Figure 175: Haversine formula	216
Figure 176: Roughness guide	218
Figure 177: CCI measurement of the roughness guide.....	218
Figure 178: Relocating the same feature using the CCI sensor and fixturing system	221
Figure 179: Stitch of three surface measurements.....	222
Figure 180: Zeiss Prismo Access CMM	225
Figure 181: CMM Polar Measurement Strategy	226
Figure 182: CMM analysis with CATIA, method steps	227
Figure 183: Taylor Hobson Talysurf CCI MP measuring a femoral head with the custom fixture system	227
Figure 184: Surface measurement analysis stages	228
Figure 185: Custom fixture system	229
Figure 186: Unworn measurement locations	230
Figure 187: Wear scar measurement locations	231
Figure 188: Previous surface measurement studies, SEM images	233
Figure 189: Clear wear area femoral heads	234
Figure 190: Minimal wear area femoral heads	235
Figure 191: Femoral head 109 wear map, unworn component	235
Figure 192: Median Sa Values of each component, 25 measurements, wear scars excluded from measurement area.....	237
Figure 193: Median Sa Values of each component, 20 measurements on the main bearing, 5 measurements on the rim .	238
Figure 194: Median Sdr Values of each component, 25 measurements, wear scars excluded from measurement area	238
Figure 195: Median Ssk Values of each component, 25 measurements, wear scars excluded from measurement area	239
Figure 196: Grouped measurement locations on the wear maps of worn femoral heads	240
Figure 197: Stitch measurement locations displayed on the wear map.....	241
Figure 198: The median Sa values in both the unworn/rim area and the central wear area	243
Figure 199: The median Sa values in each of the location groups	244
Figure 200: Median Sdr Values by Location Group	245
Figure 201: Median Ssk Values by Location Group	246
Figure 202: Sa overlay plots of grouped measurements on femoral heads 135 and 294	247
Figure 203: Sdr overlay plots of grouped measurements on femoral heads 135 and 294	248
Figure 204: Ssk overlay plots of grouped measurements on femoral heads 135 and 294	248
Figure 205: Sa overlay plots of stitch measurements on femoral heads 135 and 294	249
Figure 206: Sa Scatter plots of a selected stitch line through the wear area.....	250
Figure 207: Sa scatter plots of all stitch lines.....	251
Figure 208: Sdr overlay plots of stitch measurements on femoral heads 135 and 294	252
Figure 209: Sdr scatter plots of all stitch lines	252
Figure 210: Ssk overlay plots of stitch measurements on femoral heads 135 and 294	253
Figure 211: Ssk scatter plots of all stitch lines	253

Figure 212: Surface topography maps	254
Figure 213: The median Sa values in both the unworn area and the main roughening area	255
Figure 214: Median Sa values in surface topography areas	256
Figure 215: Median Sdr values in surface topography areas	256
Figure 216: Median Ssk values in surface topography areas	257
Figure 217: Pristine Condition	262
Figure 218: Multi-directional Light Scratches	263
Figure 219: Groups of Peaks	264
Figure 220: Pitting Holes	265
Figure 221: High Roughness Uni-directional Scratches	266
Figure 222: Destroyed Surface Uni-directional Scratches	267
Figure 223: Pristine Metal Femoral Head Surface	268
Figure 224: Contact area at the bearing interface and the possible resultant lubrication regimes.....	269
Figure 225: Roughened wear area from retrieval femoral head 135	270
Figure 226: Roughened wear area from retrieval femoral head 294	270
Figure 227: Roughening to smoothing cycle.....	271
Figure 228: Outwards spread of the wear area	271
Figure 229: Comparison of fixture methods	276
Figure 230: Advanced surface analysis tools	277
Figure 231: Quality inspection of femoral heads	278
Figure 232: Box and whisker plots for the repeatability testing of the fixture at the home position	295
Figure 233: Box and whisker plots for the repeatability testing of the fixture at the random position	296
Figure 234: Scatter plot of the angular error at each azimuth position during uncertainty testing	298
Figure 235: Scatter plot of the angular error at each elevation position during uncertainty testing	300
Figure 236: Box and whisker plot containing the angular error values from the azimuth and elevation testing	300
Figure 237: Femoral Head 135 Wear Map	301
Figure 238: Femoral Head 294 Wear Map	301
Figure 239: Femoral Head 213 Wear Map	302
Figure 240: Femoral Head 608 Wear Map	302
Figure 241: Femoral Head 082 Wear Map	303
Figure 242: Femoral Head 109 Wear Map	303
Figure 243: Femoral Head 131 Wear Map	304
Figure 244: Femoral Head 162 Wear Map	304
Figure 245: Femoral Head 550 Wear Map	305
Figure 246: Femoral Head 618 Wear Map	305

List of Tables

Table 1: Typical wear rates of different bearings reported in clinical studies	31
Table 2: COF values for different bearing material combinations	47
Table 3: Wear measurement results for retrieved MoM hip bearing components	50
Table 4: Wear measurement results for retrieved MoM hip bearing components	50
Table 5: Manufacturing tolerance requirements set as part of ISO 7206 for hip replacement components	54
Table 6: Deviation analysis between perfect 50 mm hemisphere and meshes with different mesh spacing parameters	65
Table 7: Volumetric uncertainty budget contributions	66
Table 8: Example specifications for a CSI instrument	78
Table 9: Typical performance of a modern coherence scanning interferometer Bruker Contour GT-X	79
Table 10: CMM Performance Specifications	113
Table 11: Comparison of Zeiss CMM and RedLux CMM	118
Table 12: Radius tolerance bands for each component measured	126
Table 13: Repeated measurements at the origin position	183
Table 14: CNC repeated measurement set at Az 10, El 0	191
Table 15: CNC repeated measurement set at Az 0, El 10	192
Table 16: 5 separate measurements at the azimuth origin position	194
Table 17: 5 separate measurements at the elevation origin position	194
Table 18: Phase 2 repeatability measurements for the azimuth rotary stage	198
Table 19: Phase 2 repeatability measurements at the elevation position	199
Table 20: Phase 2 azimuth positional error measurements	200
Table 21: Phase 2 elevation positional error testing	203
Table 22: Phase 3 azimuth positional error testing	209
Table 23: Phase 3 elevation positional error testing	211
Table 24: Resulting angles from the azimuth alignment error testing	219
Table 25: CMM measurement results	233
Table 26: Median surface parameter values for each component from the 25 unworn area surface measurements	236
Table 27: Grouped measurements	242
Table 28: Metrology ISO definitions set by VIM:2008	293
Table 29: RedLux and Zeiss full CMM measurement results	294
Table 30: Repeatability test of the fixture at origin position results	295
Table 31: Repeatability test of the fixture at random position	296
Table 32: Angular positional error from varying azimuth rotary stage	297
Table 33: Angular positional error from varying elevation rotary stage	299
Table 34: Femoral Head 135, Unworn Area Surface Measurements	306
Table 35: Femoral Head 294, Unworn Area Surface Measurements	307
Table 36: Femoral Head 213, Unworn Area Surface Measurements	308
Table 37: Femoral Head 608, Unworn Area Surface Measurements	309
Table 38: Femoral Head 082, Unworn Area Surface Measurements	310
Table 39: Femoral Head 109, Unworn Area Surface Measurements	311
Table 40: Femoral Head 131, Unworn Area Surface Measurements	312
Table 41: Femoral Head 162, Unworn Area Surface Measurements	313
Table 42: Femoral Head 550, Unworn Area Surface Measurements	314
Table 43: Femoral Head 618, Unworn Area Surface Measurements	315
Table 44: Component 135, Grouped Measurements, Full Surface Measurement Results	316
Table 45: Component 135, Stitched Measurements, Full Surface Measurement Results	317
Table 46: Component 294, Full Surface Measurement Results, Grouped Measurements	321
Table 47: Component 294, Full Surface Measurement Results, Stitch Measurements	322

List of Acronyms

CMM	Coordinate Measurement Machine
THR	Total Hip Replacement
MoM	Metal on Metal
MoP	Metal on Polymer
CoP	Ceramic on Polymer
CoC	Ceramic on Ceramic
CSI	Coherence Scanning Interferometry

Acknowledgements

I would like to express the deepest thanks and appreciation to Professor Liam Blunt, Dr Paul Bills and Dr Radu Racasan. This thesis would not have been achieved without their guidance and support. I would also like to thank my fellow PhD students from the Future Metrology Hub for all their support.

Finally, I would like to thank the staff at DePuy Synthes for allowing for me to attend a six-month placement at their workplace, learning about orthopaedics and using the RedLux CMM system.

Publications

Two journal articles are planned for publication in 2022, the first journal article focusses on the results obtained from measurement of MoM retrievals using the newly developed method from this project. The second journal article, co-authored by staff from DePuy Synthes Leeds, will focus on the comparison of the RedLux optical CMM to a more typical analogue probe CMM.

Chapter 1: Introduction

Hip replacement, sometimes referred to as hip arthroplasty, is the replacement of the natural hip joint with an artificial implant. The leading cause for hip replacement is osteoarthritis, osteoarthritis damages the cartilage of the hip joint, leading to abnormal stresses and discomfort [1]. The prevalence of younger patients undertaking joint replacement has risen significantly, with the strongest increase in patients aged 45 – 55 [2]. Currently patients can expect a hip replacement implant to last around 25 years in 58% of cases before revision is needed [3]. Therefore, implants need to last longer to meet the demands of younger more active patients.

Aseptic loosening is the most common cause of revision worldwide, and the most well studied factor causing aseptic loosening is periprosthetic osteolysis (bone loss around the implant) induced by the presence of wear particles [4-6]. As implant wear rates increase, the risk of osteolysis and aseptic loosening increases [6, 7], therefore manufacturers must keep implant wear rates as low as possible. Most wear debris is generated at the bearing interface, from the femoral head and acetabular cup components [8]. Patient, surgical practice, and implant design factors all play a role in the tribological performance of the implants bearing interface. The ideal bearing would run in a full-fluid lubrication mode, ensuring a low friction and low wear environment [9].

Metrology is a crucial tool for the orthopaedics industry, particularly for quality inspection of new components and experimental studies of new designs or retrieval implants [10-12]. Due to the prevalence of aseptic loosening induced by wear particles a common metrology focus is the wear performance of the implant [12]. Coordinate measurement machines (CMMs) are commonly used for volumetric wear measurements, this allows a wear map of the bearing surface to be created, and the size and location of wear areas to be analysed [13]. To understand wear mechanisms and tribological behaviour at a micro/nano scale, areal surface measurements can be used. Coherence scanning interferometry (CSI) is currently one of the most common methods for areal surface measurement of orthopaedic implants due to its flexibility and broad application for measurement [14]. CSI can be used to measure smooth surfaces, under 50 nm, which is crucial for measurement of metal or ceramic bearing surfaces [15].

The surface topography of a hip implant bearing will change within its wear area due to the wear mechanisms occurring. This has been proven for all popular bearing material combinations [16-24]. Therefore, it is vital when taking surface measurements on worn bearings that measurements are positionally targeted both within and outside the wear area, to allow for a comprehensive analysis of the entire component. Previous surface measurement studies may have been improved with more accurate positional targeting of surface measurements. Many studies declare that surface

measurements have been 'targeted' within wear areas but there is no information on the accuracy of this positional targeting, or the fixtures used to achieve this. A small change in position of where surface measurements are taken with the wear area can lead to a dramatic change in surface measurement results.

To improve wear analysis studies, CMM wear maps can be used as positional reference for targeting surface measurements. It is important that the targeting of surface measurements is done so with high positional accuracy. If positional accuracy is poor, then surface measurement data may not capture the most critical surface topography and lead to misleading results. To positionally target surface measurements the implant must be manoeuvred using a fixture (holding device). A common theme among scientific studies is a lack of information on the fixture utilised and no real consideration of the positional accuracy of the fixture.

1.1 Current Issue

Most manufacturing companies engaged in orthopaedic manufacture have access to high quality CMMs and surface metrology systems. In fact, these are required for compliance with company and international quality standards [10, 25]. However, they do not in general have the ability to combine outputs of these systems in a fused data context to allow them to investigate tribological/wear behaviour. Commercially available fixtures are currently inadequate and associated control software is not specific for hip implant wear map positional targeting.

1.2 Aim

The primary aim of the project is to develop an advanced fixture system designed to combine CMM and surface measurement data together for detailed hip implant bearing analysis. Allowing for high accuracy positional targeting of surface measurements anywhere on a worn bearing surface. Such a fixture must:

- Be relatively low cost.
- Facilitate high accuracy positional control.
- Must be easily compatible with CMM and surface metrology instruments.
- Facilitate data fusion of captured data.

Such a fixture system with data fusion capability will improve future hip implant surface measurement studies, ensuring the most critical surface topography data is captured easily and quickly. This fixture system also aims to stitch surface measurements through wear areas, this currently has never been achieved and would be a novel step forward in analysis of worn hip implant components. To test the

capabilities of this developed fixture system, a study will be undertaken on a cohort of retrieved MoM femoral heads.

1.3 Objectives

- Design and manufacture the fixture system hardware.
- Develop the fixture system software.
- Test the custom fixture system and calculate the resultant positional error.
- Use the custom fixture system to analyse a range of MoM retrieval femoral heads.

1.4 Overview of Chapters

Chapter 2 – Literature Review

A detailed review into total hip replacement, metrology used for hip implant analysis, previous surface metrology studies on worn hip implant bearings, and the process of wear map targeted surface measurements.

Chapter 3 – Comparison of the RedLux Optical CMM to an Analogue Probe CMM

A comparison study of the RedLux optical CMM with a traditional Zeiss analogue probe CMM. There is currently limited literature comparing the CMMs and it would be beneficial to compare their effectiveness for measurement of hip implant bearings.

Chapter 4 – Development of the Custom Fixture System

This chapter details the development process of the custom fixture system including both the hardware and software development.

Chapter 5 – Testing of the Custom Fixture System

At this stage the custom fixture system has been created, to test its effectiveness it is measured using a CMM whilst the fixture is driven to different positions replicating the positional adjustment of a hip implant bearing component. This allows for a calculation of the positional error of the fixture system.

Chapter 6 – Analysis of Retrieved Metal-on-Metal Bearings

To showcase the effectiveness of the newly developed fixture system a cohort of retrieved metal on metal femoral heads are analysed. This allows the benefits of the fixture system to be seen and the novel surface analysis tools utilised.

Chapter 2: Literature Review

2.1 Total Hip Replacement

2.1.1 Joints

The site where two skeletal elements come together are termed joints. There are two general categories of joints, synovial joints and solid joints. In synovial joints the skeletal elements are separated by a narrow articular cavity, whereas in solid joints there is no cavity, the components are held together by connective tissue [1], figure 1.

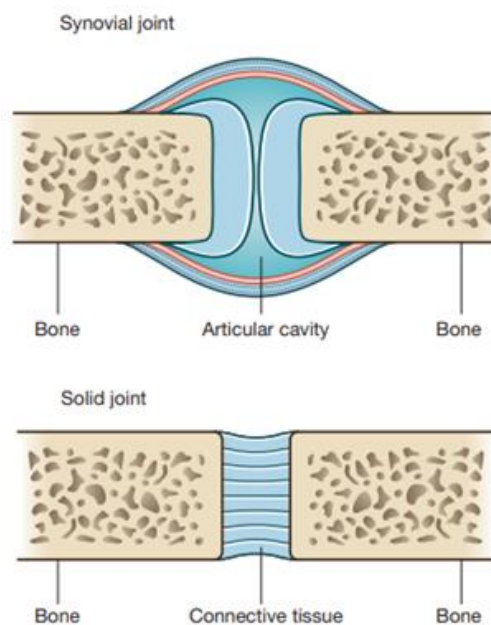


Figure 1: Comparison of synovial and solid joints [1].

2.1.1.1 Synovial Joints

Synovial joints have a layer of cartilage, usually hyaline cartilage, which covers the articulating surfaces of the skeletal elements, this prevents the bony surfaces contacting each other. The joint capsule is an important

feature, this consists of an inner synovial membrane and an outer fibrous membrane. The synovial membrane attaches at the interface between the cartilage and bone. The synovial membrane encloses the articular cavity and produces synovial fluid which lubricates the articulating surfaces. Synovial membranes can also occur outside of the joint as either synovial bursae or tendon sheaths. The fibrous membrane surrounds the joint and ensures stability, parts of the fibrous membrane may thicken to form ligaments. Outside of the capsule, ligaments surround the joint providing strength and reinforcement [1], figure 2.

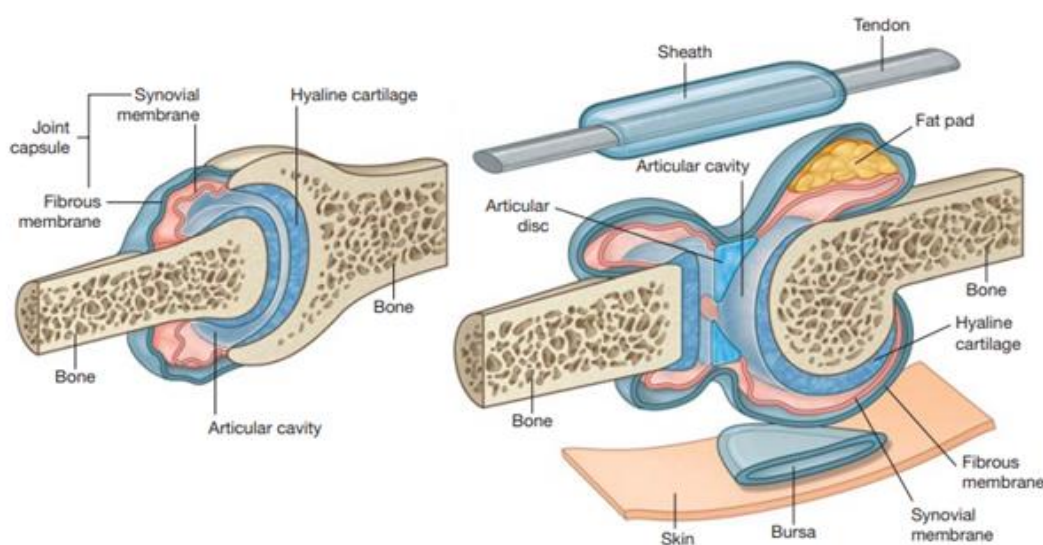


Figure 2: Features of a synovial joint [1].

2.1.2 Anatomy of the Hip Joint

The hip joint is a form of synovial joint located at the head of the femur and the acetabulum of the pelvic bone, figure 3(A). The joint is a multi-axial ball and socket joint, this allows for movement around multiple axis: flexion, extension, abduction, adduction, circumduction and medial/lateral rotation [1, 26]. The articulating surfaces of this joint are the spherical head of the femur, often described as the ‘femoral head’, and the lunate surface of the acetabulum of the pelvic bone. The acetabulum surrounds the femoral head providing joint stability, the lunate surface of both the acetabulum and femoral head is covered by hyaline cartilage, figure 3(B).

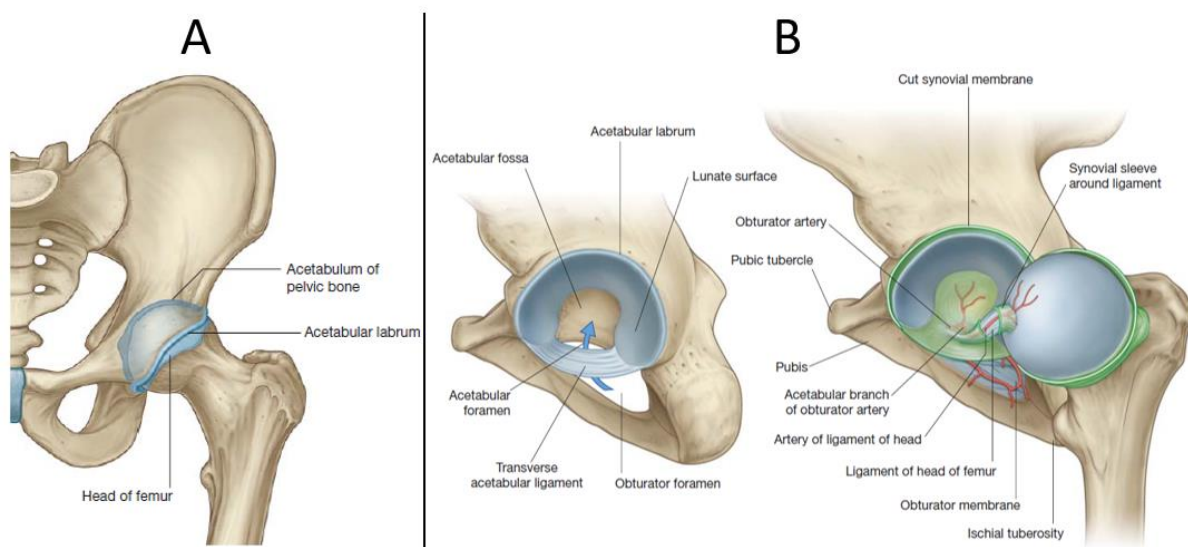


Figure 3: The hip joint. A: Anterior view of the hip joint [1]. B: Detailed view of the acetabular and femoral head. Note the femoral head has been removed from the acetabulum to reveal the ligament [1].

Connective tissue attaches to the fovea on the femoral head, the other end attaches to the acetabular fossa, the transverse acetabular ligament and the margins of the acetabular notch. This tissue carries a small branch of the obturator artery, which helps supply blood to the femoral head. The synovial membrane, figure 4(A), surrounds the joint providing lubrication, attaching to the margins of the articular surfaces. The fibrous membrane encloses the joint, providing stability, this fibrous membrane is much thicker and stronger compared to the synovial membrane [1]. Reinforcing the fibrous membrane are three ligaments, the iliofemoral ligament, the pubofemoral ligament and the ischiofemoral ligament, these ligaments provide further stability to the joint. The iliofemoral and pubofemoral ligaments support the anterior aspect of the fibrous membrane whereas the ischiofemoral ligament supports the posterior aspect of the fibrous membrane. The fibres that build up the ligaments are spiralled around the hip joint, so as the joint is extended they become taut. This further stabilises the joint and reduces the muscle energy required to maintain a standing position [1], figure 4(B).

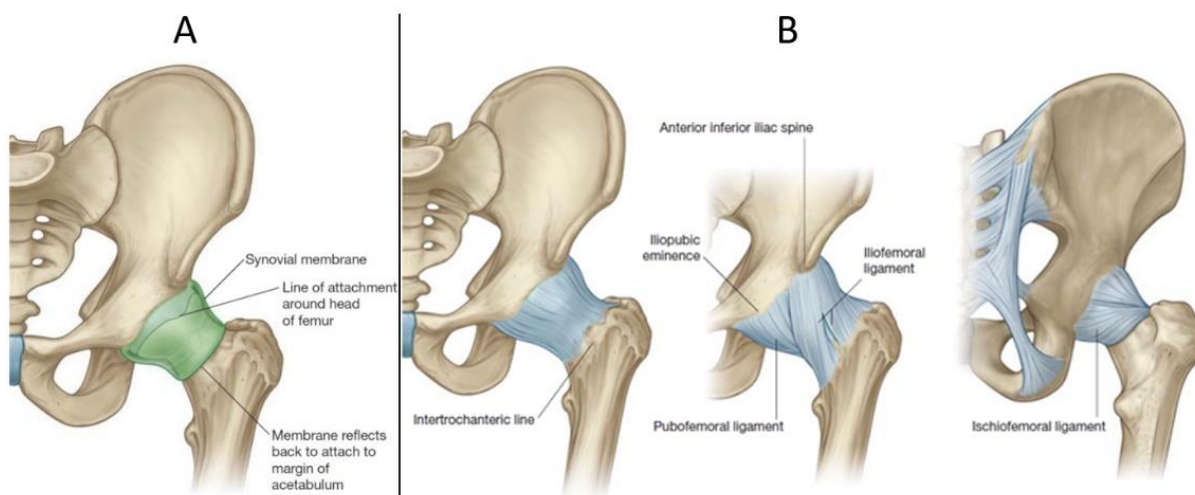


Figure 4: Surrounding the hip joint. A: Synovial membrane of the hip joint [1]. B: Fibrous membrane of the joint (left). Anterior view of the Iliofemoral and pubofemoral ligaments (centre). Posterior view of the ischiofemoral ligament (right) [1].

Muscles in the gluteal region provide movement for the hip joint, the muscles are used to abduct, extend, and laterally rotate the femur relative to the pelvic bone, figure 5. The gluteus minimus, gluteus medius and gluteus maximus are large muscles that abduct and extend the hip. The gluteus maximus is the largest muscle out of the three and overlies the other muscles. Deeper, smaller muscles are used to rotate the femur at the hip joint, these include: the piriformis, obturator internus, gemellus superior, gemellus inferior, and quadratus femoris [1].

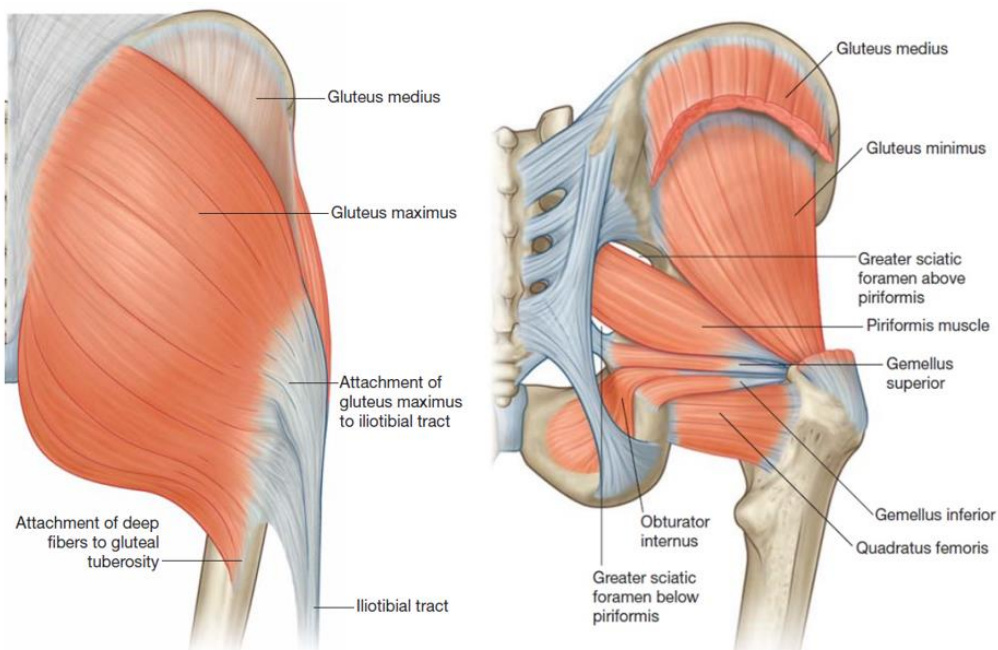


Figure 5: Posterior view of the gluteus maximus muscle (left). Posterior view of the deeper muscle group (right) [1].

2.1.3 Degenerative Joint Disease

Degenerative joint disease is more commonly known as osteoarthritis and typically presents in older patients and results from wear and tear during natural aging. As the patient ages, there is a decrease in water and proteoglycan content within the cartilage. The cartilage becomes more fragile and susceptible to wear, as the cartilage wears, the bone underneath the cartilage becomes fissured and thickens. The synovial fluid which usually provides lubrication for the joint is forced into small cracks in the bone which produces large cysts. Bony nodules, known as osteophytes, are formed on the bone, figure 6. This alters the shape of the joint, creating non-conformal bearing surfaces, leading to abnormal stresses and further discomfort [1]. As well as physical examination, the diagnosis of osteoarthritis can be achieved through imaging tests. Evidence of narrowing in the joint space, changes in the bone and presence of bony spurs indicates osteoarthritis [27].

The wider term arthritis embodies other joint related conditions, such as rheumatoid arthritis. In the UK more than 10 million people have arthritis, osteoarthritis makes up the majority of cases, affecting approximately 9 million people [28]. In the United States, osteoarthritis accounts for up to one-quarter of primary health care visits [1]. There is currently no known cure for arthritis, usually physical therapy is undertaken, and anti-inflammatory drugs are prescribed for patients. For severe cases, joint replacement is needed to relieve the patients pain and restore joint mobility [1, 28].

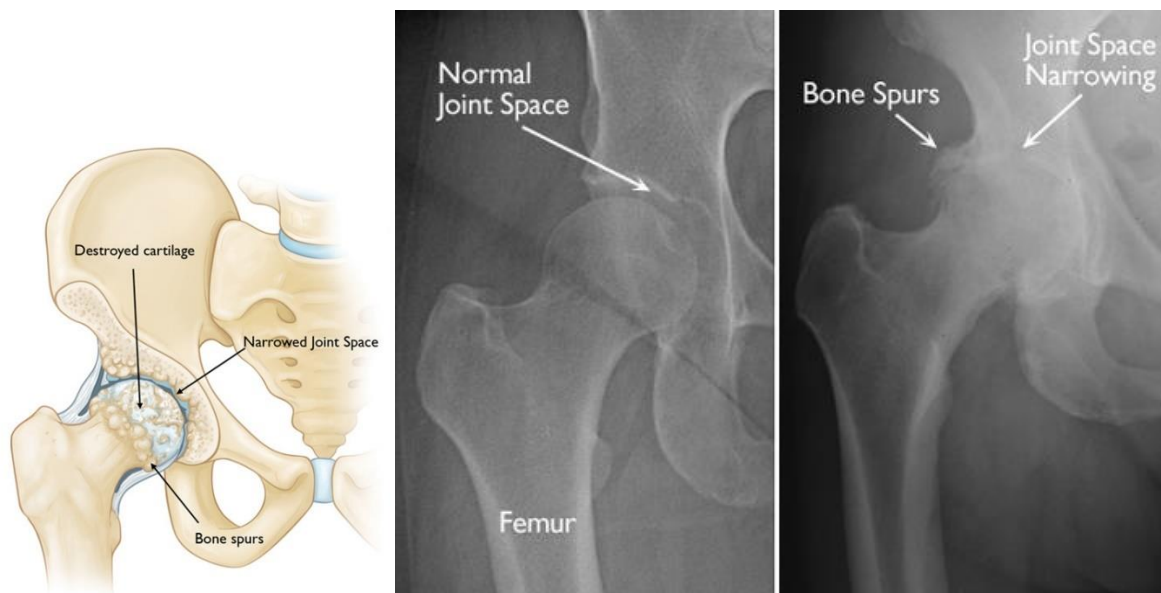


Figure 6: Osteoarthritis of the hip joint [27]. A: Diagram of hip osteoarthritis. B: Radiograph comparison of a healthy hip joint (left) and an arthritic hip joint (right).

2.1.4 Joint Replacement

Joint replacement is the replacement of a damaged joint with an artificial implant, figure 7 [28]. The larger weight-bearing joints, hips and knees, account for most joint replacement surgeries, however, ankles, shoulders, and elbows can also be replaced. According to National Joint Registry (NJR) data, hip and knee replacement surgeries account for approximately 98% of all joint replacement surgeries in the UK. Between 2003 and 2017 there were 992,090 primary total hip replacements and 1,087,611 knee replacements [4], figure 8.

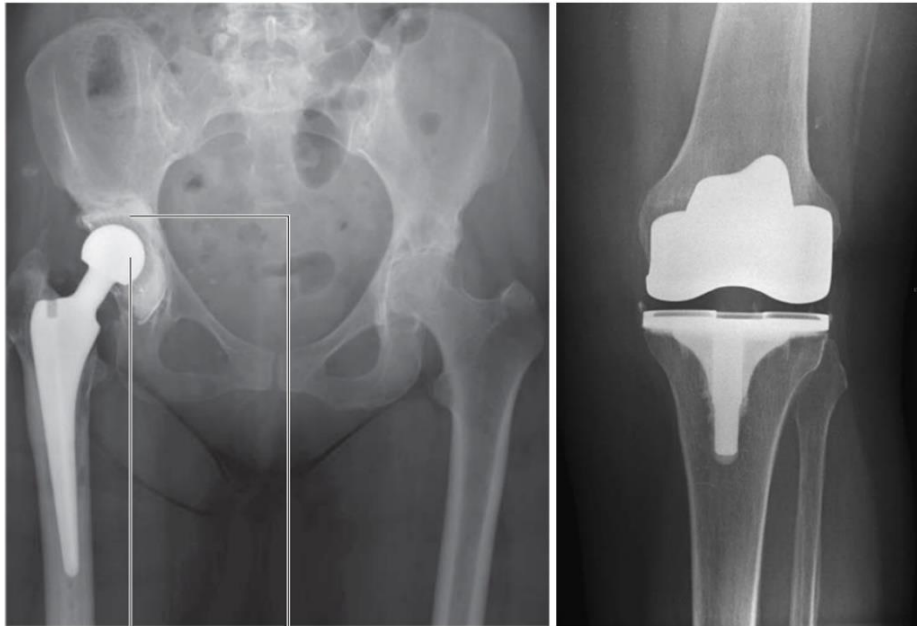


Figure 7: Radiograph of total hip replacement (left) and total knee replacement (right) [1].

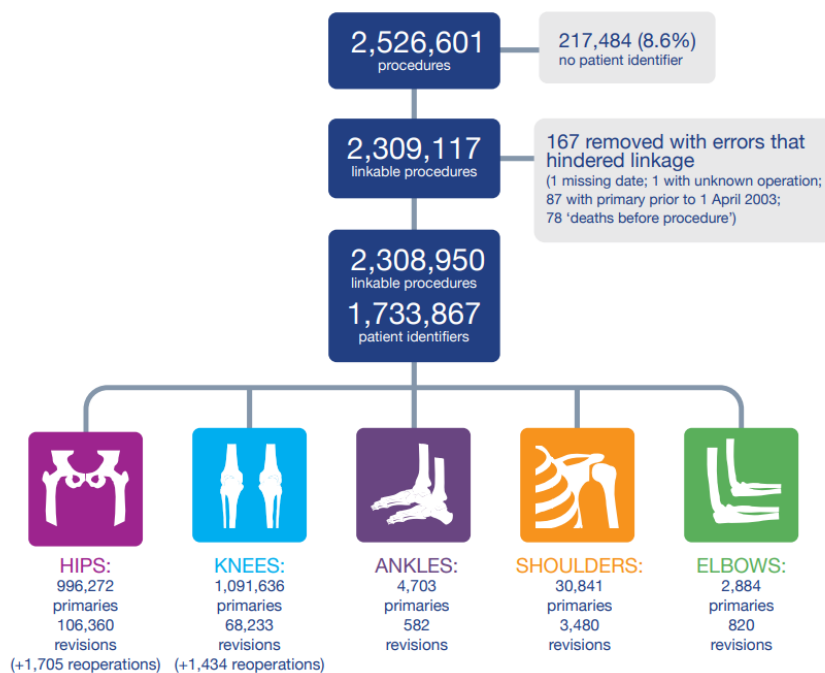


Figure 8: Number of joint replacement procedures in the UK between 2003 and 2017 [4].

According to NJR data osteoarthritis was given as a documented indication in 91.9% of primary hip replacement surgeries and the sole reason in 88.8% primary hip replacement surgeries. Osteoarthritis was given as a documented indication in 97.3% of primary knee replacements and the sole reason in 96.2% of primary knee replacements [4]. Other than osteoarthritis, hip fractures are the second most common reason for joint replacement. Hip fractures are cracks or breaks in the femur, typically at the head of the femur, usually caused by a fall. This is more common in older patients due to their reduced mobility and balance, and their increased likelihood of osteoporosis. Osteoporosis is a condition in which the bone quality is normal, but the quantity of bone is deficient, this weakens the bone and increases the likelihood of the bone breaking [1, 29, 30].

The demand for joint replacement is increasing. The percent increase in total annual primary total hip replacement in the United States is projected to be a 284% rise between 2019 to 2040. Primary total hip replacement is projected to increase for both females and males, in all age groups [31].

The prevalence of younger patients undertaking joint replacement surgery has risen significantly. It is projected that by the year 2030, 52% of primary total hip replacements and 55% of total knee replacements will be implanted in patients younger than 65, with the strongest increase in patients aged 45-55 [2]. The age of the patient is a major factor for the implant's performance outcomes. NJR data indicates younger patients have a much higher revision risk compared to elderly patients. For example, a hip replacement in male patients under the age of 55, the revision estimate is nearly 16% at 14 years compared to just 2.5% in male patients over 75 [4]. This is likely due to the more active lifestyle of younger patients, increasing the performance demand on the implant.

2.1.5 The History of Hip Replacement

The earliest recorded attempts of hip replacement occurred in Germany in 1891, with Professor Themistockles Gluck using ivory to replace a patient's femoral head. In the late 19th and early 20th century, experiments took place involving placing tissue at the hip joint bearing interface for arthritic patients [32]. Although Gluck's joint replacements were successful in the short term, all ultimately failed because of chronic infection. This pioneering work was dismissed during his lifetime and remains largely unrecognised [33].

In 1925, the American surgeon Marius Smith-Petersen created the first mould arthroplasty. This design consisted of a hollow glass hemisphere which fitted over the patient's arthritic femoral head, thus providing a new smooth bearing surface. This design failed due to the brittleness of the material, failing to withstand the forces applied through the joint. Marius Smith-Peterson later used Vitallium

alloy to create the first total hip replacement, fitting the implant using bolts and screws. This new design and surgical method significantly increased the repair success for broken hips, which at one time was considered an unresolvable fracture [32, 34].

The British surgeon George McKee designed the first metal on metal prosthesis in 1953, he used a one-piece cobalt-chrome socket as the new acetabulum in combination with a modified Thompson stem. This design had a good survival rate for the time, with an estimated 28-year survival rate of 74% [32]. Many other scientists were crucial for this period of joint replacement innovation between the 1700s and 1950s [35].

The British surgeon Sir John Charnley is considered the father of the modern total hip arthroplasty. His design was developed in the early 1960s, consisting of two main components: a one-piece metal femoral stem/head and an ultra-high molecular weight polyethylene acetabular component, with the use of acrylic bone cement to fixate the components in place, figure 9. Charnley advocated for the femoral head size to be small as he theorised this would reduce the amount of wear [32, 36]. Studies suggest the Charnley implant has a survival curve of approximately 85% after 25 years [37]. The Charnley design is similar to designs in use today, with the main difference being the modularity of modern femoral head components, which can be removed from the femoral stem.



Figure 9: Charnley metal femoral stem and acetabular cup components [38].

2.1.6 The Modern Hip Implant Design

The modern hip implant usually consists of either three or four main components, figure 10:

Femoral Stem – The damaged head of the femur is removed during surgery, to replace the damaged head a metal stem (usually made of Ti alloys) is pressed into the hollowed-out centre of the femur. This stem can be either cemented in place using polymethyl methacrylate (PMMA) cement or designed to be fixated without.

Femoral Head – A metal (often a Cobalt Chrome alloy) or ceramic ball (usually made of Alumina) is fixed to the top of the femoral stem through a taper connection, this ball replaces the damaged head of the femur. The reason for a separate stem and head is so the surgeon can select the appropriate head size for the specific patient or even change the head size during surgery.

Acetabular Cup – The damaged acetabulum of the pelvic bone is reamed out during surgery and replaced with either a polymer (UHMWPE), ceramic (Alumina) or metal (CoCr alloy) cup which is pressed into the acetabulum. Screws or bone cement can be used to fixate the cup.

Acetabular Liner – A liner may also be used depending on the design of the implant, uncemented fixation designs will use a liner and a metal shell (usually Ti). The metal shell is pressed into the acetabulum and the polymer or ceramic liner will then be pressed into the shell. The femoral head will rotate within the acetabular cup/liner, replicating the natural movement of the head of the femur within the acetabulum of the pelvis.

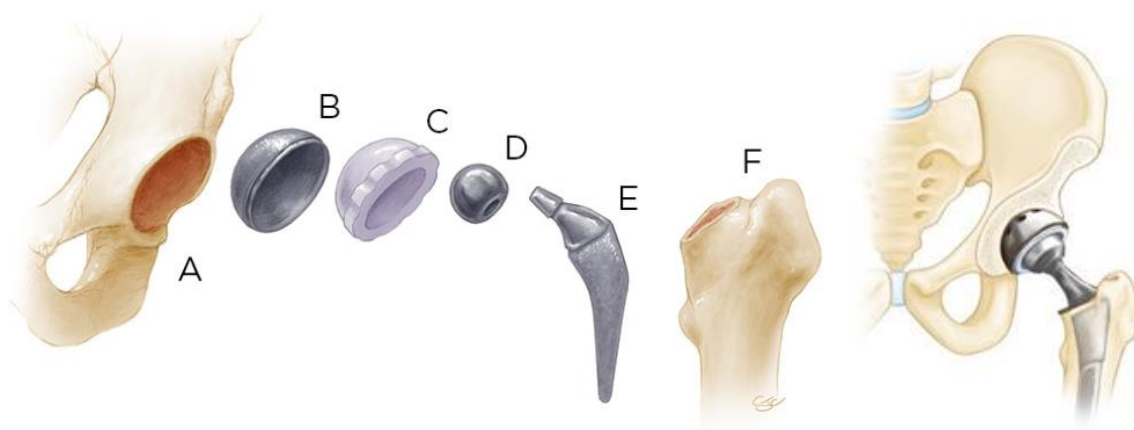


Figure 10: Components of a hip implant. The acetabulum of the pelvic bone (A), acetabular cup/shell (B), acetabular liner (C), femoral head (D), femoral stem (E), the femur bone (F) [39, 40].

2.1.7 Total Hip Replacement Surgical Procedure

2.1.7.1 Surgical Approaches

There are three common approaches to hip replacement surgery: direct anterior, direct lateral and posterior, figure 11. Each approach has unique advantages and disadvantages, usually the surgical approach chosen is based upon the surgeons preference using their training and experience [41, 42].

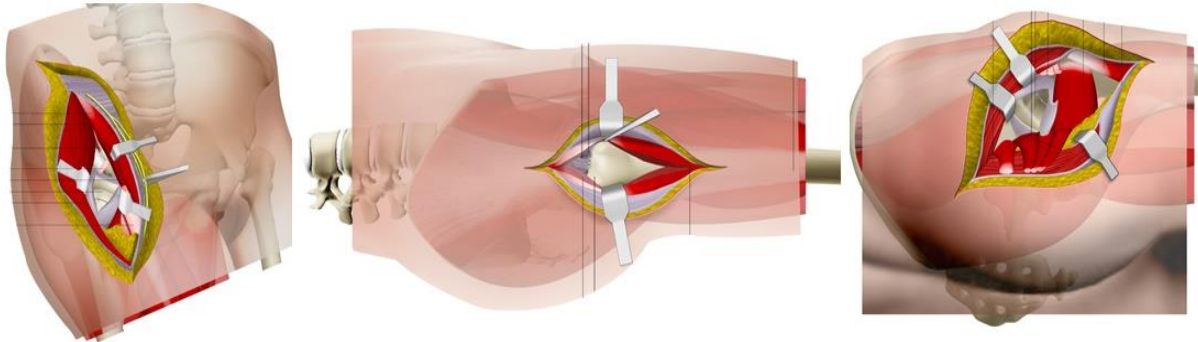


Figure 11: Comparison of THR approaches. Direct anterior (left), direct lateral (centre) and posterior (right) [42].

2.1.7.2 Procedure Overview

The exact surgical procedure will vary depending on the patient's needs, the surgeons training, and the surgical approach selected, but a general outline is as follows [43]:

- The patient's vital signs are checked before surgery begins; a mark is made on the hip which is to be replaced.
- General anaesthesia or local anaesthesia is administered to the patient, the type of anaesthesia is decided well before surgery begins.
- The surgeon makes an incision at their preferred surgical approach, cutting through muscle and soft tissue to expose the hip joint.
- The head of the femur is dislocated from the acetabulum of the pelvis.
- The head of the femur is cut off using a bone saw.
- A hemispheric reamer is used to shape the acetabulum, preparing it for the acetabular cup to be implanted.
- The acetabular cup is pressed into the acetabulum, this may be done with bone cement or screws.
- Depending on the type of design a liner may now be pressed within the acetabular cup.
- The femur bone is hollowed out using a femoral rasp preparing for the femoral stem.
- The femoral stem is pressed within the femur bone, bone cement may or may not be used.
- A trial femoral head is placed on the femoral stem and the joint is tested for its mobility.
- The actual femoral head is placed on the femoral stem and the joint is again tested for its mobility, the chance of dislocation and correct leg length is achieved.
- Radiographs are taken of the joint to ensure proper positioning of the implant has been achieved.
- The cut muscle and soft tissue are repaired, and the skin incision is stitched together.

2.1.8 Current Trends of Hip Implant Design

There are a wide range of hip implant designs available for surgeons to select for their patients. Often the choice for which design becomes popular is driven by registry data [4]. Registry data is available from many countries and is useful to track the failure rates of implants, it also collects data recording patient and surgeon specific factors that can influence failure rates. Failure rates can in some cases be misleading, for example if a specific design is used for mainly younger patients, this will likely have higher failure rates due to the increased activity and could not be a design related factor [4]. The main design factors of a hip implant are covered in this section.

2.1.8.1 Fixation Type

The fixation type of a hip implant describes how the implant is fixated into the bone, this can be done either with or without bone cement, figure 12.

Cemented implants are fixated into position using Polymethyl methacrylate (PMMA) cement. In this case the cavities are charged with cement (sometimes under pressure) and the implants are pressed into the prefilled cavities

Uncemented implants are surface engineered to encourage bony integration between the component and the patient's bone. Either bony on-growth or in-growth is encouraged depending on the surface. On-growth surfaces are created through grit blasting or plasma spraying hydroxyapatite (HA), creating a textured surface onto which bone can grow. In-growth surfaces are created using sintered beads, fiber mesh and porous metals, creating microscopic pores for bone to grow into [44]. The latest implants can be additively manufactured giving a surface engineered for bony ingrowth [45].

The implant can also be fixated with cement only at the femoral stem and without cement at the acetabulum, this is called hybrid fixation [46]. The reverse of this is also possible, with cement at the acetabulum and without cement at the femoral stem, this is called reverse-hybrid fixation [47].

Resurfacing is a type of hip replacement usually targeted at younger more active patients, particularly athletes. Resurfacing consists of reshaping the femoral head and covering it with a CoCr metal cap, the damaged acetabulum of the pelvic bone is fully replaced. Higher failure rates for this type of implant have led to their use being extremely rare and not normally recommended [4, 48].

Data from the UK, figure 13, shows cemented fixation accounted for the majority of surgeries in the early 2000s, 56.1% in 2004. However, this has decreased to now only approximately 28.2% in 2017. The use of uncemented and hybrid fixation has increased, with uncemented accounting for approximately 37.8% and hybrid accounting for approximately 30.3% of surgeries in the UK. Hybrid fixation is the fastest growing type of fixation in the past decade [4].



Figure 12: Comparison of cemented and uncemented fixation designs. Cemented design (left) [49] and uncemented design (right) [50]. Note the textured surface finish of the uncemented design.

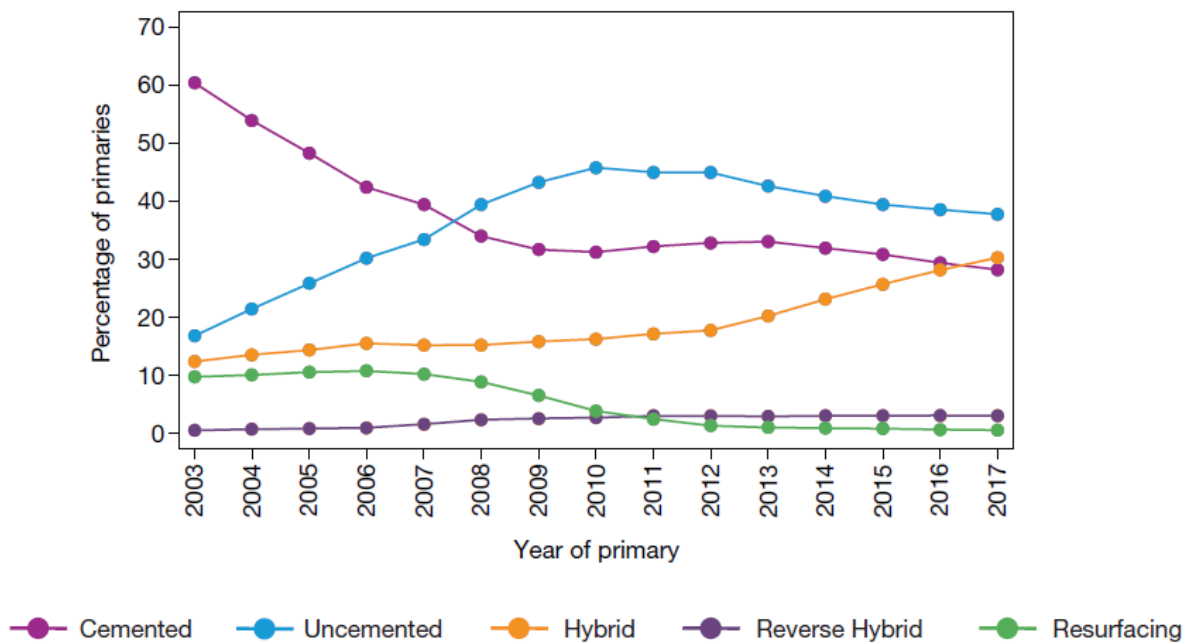


Figure 13: Fixation type by year of primary hip replacement in the UK [4].

2.1.8.2 Bearing Material

The ideal bearing materials have a low coefficient of friction, low roughness, high surface hardness, with low ductility and good scratch resistance, generation of wear particles should be as low as possible. Surfaces exposed to tissue need to be non-cytotoxic, biocompatible and bioinert. The bearing materials chosen will play a crucial role on the tribological performance of the implant, the common materials in use are grouped into three categories: polymers, metals and ceramics [51, 52].

The most popular bearing material combinations are: Metal-on-Polymer (MoP), Metal-on-Metal (MoM), Ceramic-on-Ceramic (CoC) and Ceramic-on-Polymer (CoP), figure 14. If a metal/ceramic head and cup are used in combination this is referred to as a 'hard on hard' bearing combination, whereas if a polymer cup/liner is used with a metal/ceramic head this is referred to as a 'hard on soft' bearing combination.

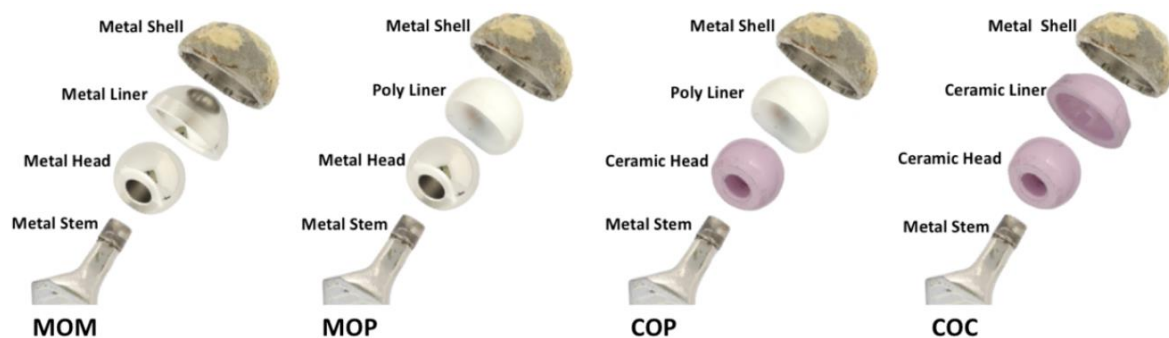


Figure 14: Comparison of bearing material combinations [53].

Ultra-high molecular weight polyethylene (UHMWPE) is the traditional polymer material utilised for hip implants and was first used in the Charnley design. The properties of UHMWPE have been further improved over time leading to highly cross-linked polyethylene (HXPLE) [9, 54, 55]. HXPLE has shown good outcomes compared to conventional UHMWPE with wear rates reduced up to 80% [9, 56, 57]. The latest developments in the use of polymers include antioxidant doped polyethylene and 2-methacryloyloxyethyl phosphorylcholine (PMPC) but long term clinical results for either are not yet available [51].

In terms of bearing materials, there are three metal alloys used for hip implants: CoCrMo, CoCr and stainless steel, CoCrMo is the most widely used metal alloy. The amount of carbon content is critical to the wear resistance of the metal. With high carbon content alloys (> 0.15%) exhibiting a wear reduction of 64-94% compared to low carbon content alloys (< 0.08%) [9, 58, 59].

Alumina-zirconia composites are the most popular ceramic in use, manufactured under the trade name BIOLOX Delta. Earlier ceramic materials such as alumina (Al_2O_3) and zirconia (ZrO_2) have been abandoned due to issues with their brittleness. BIOLOX delta is an alumina matrix composite which

combines the excellent tribological behaviour of alumina with the good mechanical/toughness properties of yttria-stabilised zirconia [9, 51, 60]

The MoP combination is the most common and traditional choice following on from the Charnley design, with successful performance from long term registry data. Over time polyethylene (PE) debris can be generated and initiate osteolysis causing the implant to loosen and ultimately fail, this is referred to as aseptic loosening [7, 51].

Metal on metal bearings became popular in the early 2000s with the primary aim to reduce wear rates, improve the range of movement and lower dislocation rates. However large head MoM implants reported issues with local bone and tissue necrosis and metallosis, leading to very high failure rates, 2-3x higher than non-MoM bearings, these implants are no longer favoured for use [4, 51, 61, 62].

Ceramic on ceramic bearings are biologically relatively inert and have lower wear rates than MoP or MoM bearings [51, 63]. The current main issues with CoC include squeaking noises, stripe wear and potential chipping of the implant during insertion [51, 64]. The CoP bearing is designed to keep the advantage of the softer less rigid PE cup and utilise the benefits of the ceramic head [51].

When comparing wear debris production by bearing type, hard-on-soft bearings have higher wear rates compared to hard-on-hard bearings. It is ideal to keep wear rates as low as possible to ensure implant longevity, however the relationship between lower wear rates and lower failure rates is not always evident. For example, MoP bearings are currently one of the most popular choices with good survival rates, despite having the highest wear rates of the bearing material combinations, table 1.

Table 1: Typical wear rates of different bearings reported in clinical studies [9].

Head/cup	h_{clin} ($\mu\text{m}/\text{Mc}$)	V_{clin} (mm^3/Mc)
MoP	50-500 (50)	10-500 (80)
CoP	30-150	15-50
MoM (RI)	1-50	0.1-25
MoM (SS)	0.1-1	0.05-4
MoM _{RHR} (RI + SS)	0.2-10	0.2-2.9
MoM _{RHR} (ADT)	1.5-46	0.2-95
CoC	0.01-1	0.005-2

RI: Running-In; SS: Steady state; ADT: Adverse tissue reaction; 1 Mc: 10^6 cycles.

Registry data from the UK shows that the MoP bearing combination accounts for the majority of cemented surgeries, decreasing only slightly from 91.3% in 2004 to 81.6% in 2017. CoP has increased in popularity in recent years, accounting for 18.1% of cemented surgeries in 2017 [4], figure 15.

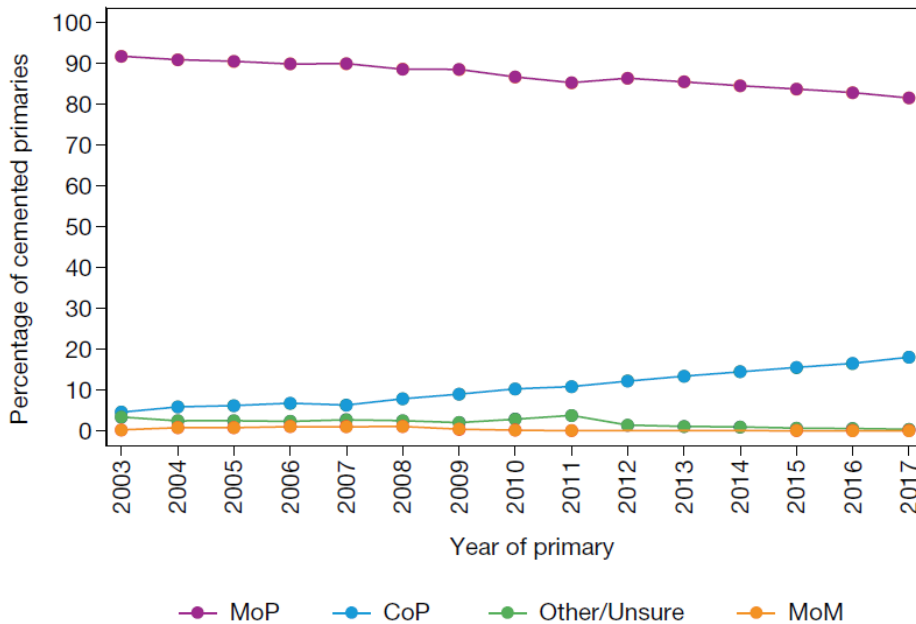


Figure 15: Percentage of each bearing material combination for cemented hip replacements in the UK [4].

For uncemented implants MoP is also the most popular choice but with a much smaller majority, accounting for 41.8% of uncemented surgeries in 2017. CoP is increasing in popularity, accounting for 37.8% of uncemented surgeries in 2017. The use of CoC has decreased since 2011 and the use of MoM implants has ceased since their decline in 2007 [4], figure 16.

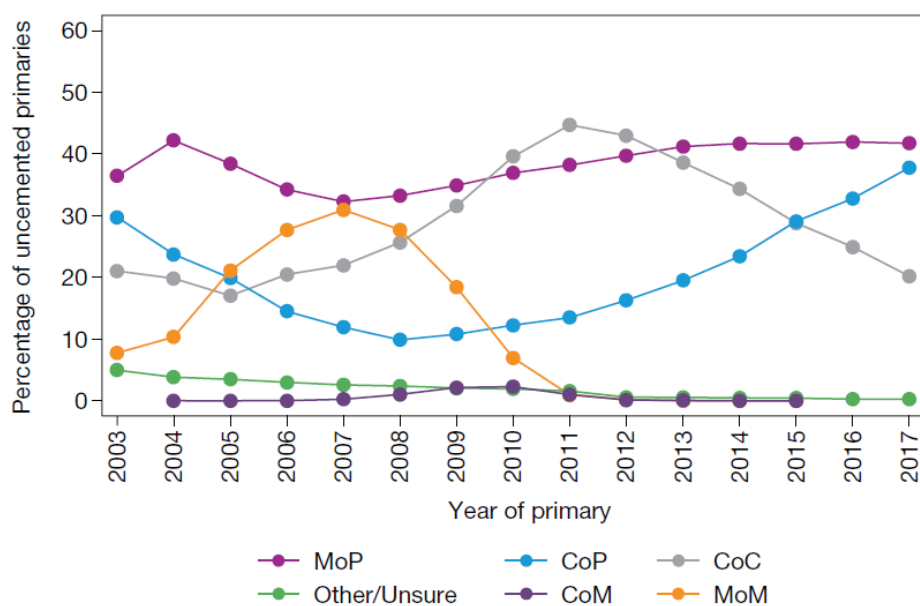


Figure 16: Percentage of each bearing material combination for uncemented hip replacements in the UK [4].

For hybrid implants MoP is again the most popular choice, accounting for 53.8% of hybrid surgeries and again CoP is increasing in popularity in recent years, accounting for 41.3% of hybrid surgeries in 2017 [4], figure 17.

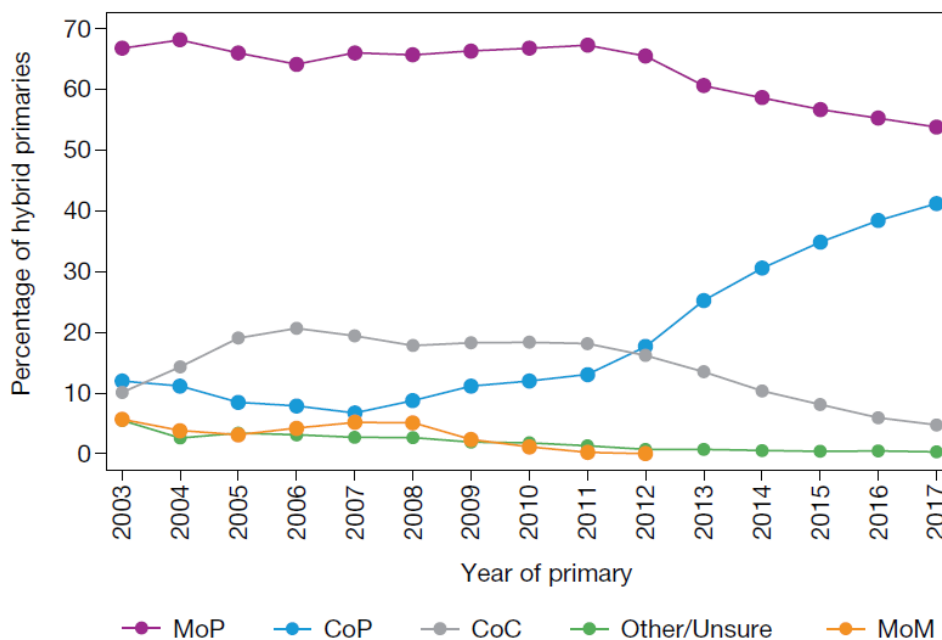


Figure 17: Percentage of each bearing material combination for uncemented hip replacements in the UK [5].

2.1.8.3 Femoral Head Size

The femoral head size of implants can vary considerably, the most common femoral head sizes are 28 and 32 mm, but common sizes can vary from 22.25 mm to 44 mm, uncemented MoM implants could even be as large as 54 mm, figure 18. Generally cemented implants tend to have a smaller femoral head size compared to uncemented, but sizes will vary from patient to patient [4].

Larger sized heads are designed to provide a more conformal fit, promote lubrication and prevent dislocation. In theory, larger heads should reduce wear rates due to the reduction in contact pressure and increased amount of lubrication. However, a larger femoral head size also increases the bearing contact area and reduces the diametrical clearance which can lead to more wear debris production when edge loading is present. Smaller sized heads have a greater risk of dislocation, they also reduce the contact area between bearing surfaces which can result in lower wear rates compared to poor performing large heads. However small heads are known to increase contact pressure, dispersing lubrication and potentially have increased wear rates compared to well performing large heads. Therefore, further research is still required to determine the desirable femoral head size to limit wear debris production [9, 65-67].

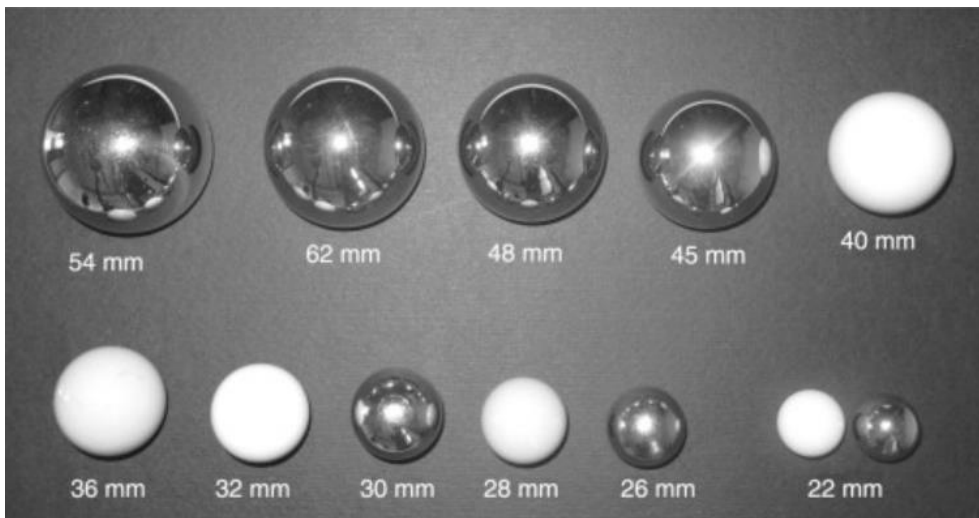


Figure 18: Comparison of femoral head sizes [68].

Registry data from the UK provides a mixed picture with respect to femoral head size and performance. The largest head sizes in cemented MoP/CoP and uncemented MoP appear to have higher failure rates, particularly for the largest sizes (36 mm for cemented fixation and >36 mm with hybrid and uncemented fixation). The exception to this pattern, is the CoC bearing, larger heads actually tend to have lower failure rates [4].

2.1.9 Failure of Hip Implants

2.1.9.1 Implant Lifetime

Ideally an implant will last as long as possible, restoring patient's joint mobility and relieving their pain. However, as patients generally become younger, this requires implants to last much longer than previously expected, and with more demanding performance expectations. Currently patients can expect a hip replacement to last 15-20 years in around 75% of cases and last 25 years in 58% of cases before revision may be needed [3]. The risk of further revision increases after the initial revision surgery [69]. According to UK registry data the risk of multiple revisions is increased if the primary implant needs revising early, with 11.66% of hips revised within the first year since primary needing re-revision within three years [4]. Therefore, it is crucial primary implants last as long as possible to stop this cycle of revision.

2.1.9.2 Failure Factors

There are a wide range of factors that can lead to an implant failing prematurely, these factors can be grouped into three main categories: patient, surgical practice, and implant design, figure 19. Patient factors include: the patients age, body mass index, natural hip anatomy and level of activity after surgery. Registry data has shown that younger patients have higher revision rates and this is likely due to their increased level of activity compared to older patients [4]. The weight of a patient is also critical, heavier patients put greater stresses through their implants. Patients who lose weight after surgery have better clinical outcomes [70]. Surgical factors include: the surgeons experience, the surgeon's technique, adequate equipment, these factors play a role in the likelihood of a successful surgery. Implant design factors describe the previously discussed design choices: fixation type, material choice and femoral head size. A successful design can have a huge effect on the rate of failure, for example, the revision rate for uncemented MoM bearings is 19.06%-22.21% at 14 years, whereas for cemented CoP they are 3.77% [4].

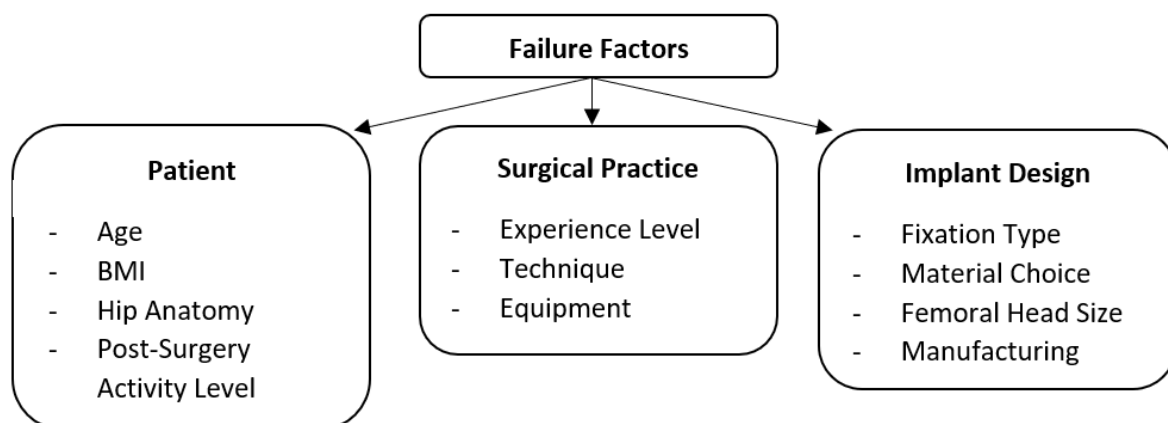


Figure 19: Failure factors for hip implant surgery.

2.1.9.3 Failure Modes

Aseptic Loosening

Periprosthetic bone resorption resulting in loosening of the implant, otherwise known as aseptic loosening, is regarded as the most common cause of revision worldwide [5, 6], figure 20. Aseptic loosening and other related failure factors (wear, lysis, soft tissue reaction) account for the majority of causes for revision surgery in the UK, but the exact amount is unclear due to changes in the reporting technique [4]. In Sweden aseptic loosening is the primary reason for more than 70% of revision surgeries [71]. Aseptic loosening is a multifactorial event and is probably the result of a combination of several events [6].

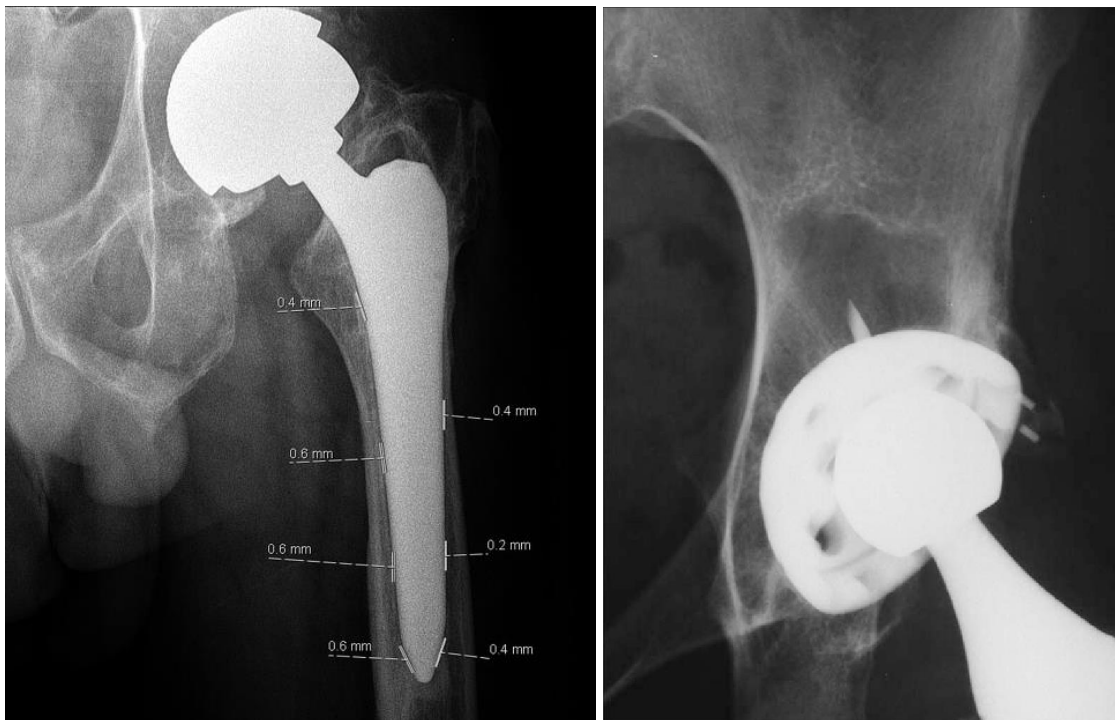


Figure 20: Radiograph images of aseptic loosening. Left: Bone resorption around the femoral stem, with distance markers to indicate the amount of bone loss [72]. Right: Bone resorption around the acetabular cup [73].

Wear Particles

The most well studied factor leading to aseptic loosening is periprosthetic osteolysis induced by the presence of wear particles. As implant wear rates increase, the risk of osteolysis and aseptic loosening also increases [6, 7]. It is therefore a critical aim for manufacturers to keep wear rates of implants as low as possible. The majority of wear debris is generated primarily at the bearing interface, but wear debris can also be produced at non-articulating surfaces or from bone cement [8]. Depending on the materials used in the implant, the morphology of the generated wear debris will vary, and therefore so will the bodily induced reaction [6]. It is also important to consider that patient genetic factors play an important role in how the body will react [6, 74].

Metal Wear Particles

MoM hip implants have been used in over 60,000 patients in England and Wales since 2003 (when registry data first began to record) in the US the figure is closer to a million [4, 75]. With lower in-vitro wear rates demonstrated by MoM bearings this would suggest a well performing implant, in practice this has not been the case [76, 77]. Revision rates are much higher in MoM implants compared to other material types across both fixation types, for this reason the use of MoM implants has now virtually ceased [4, 75].

MoM bearings produce only metal wear debris from the bearing interface, whereas MoP implants will produce primarily polymer wear debris, the body reacts differently to these two materials. It is likely that the size of particles is of major importance to the severity of the macrophage induced inflammatory response [74]. Metal debris is smaller in size (0.015 - 0.025 μm), compared to polymer debris (0.1-0.5 μm). Consequently, for similar volumes of polymer and metal wear debris, the number of metal particles will be approximately 100x greater than the number of polymer particles [67, 78-81]. Within the wear debris metal ions are released, these ions seep into local tissue causing adverse immune system reaction and consequent soft tissue destruction [75, 82, 83], figure 21. Apart from the direct adverse periprosthetic effects of these particles, the 10 – 1000 fold increase in blood Co, Cr and Mo concentrations may have systematic effects [67, 75, 84-86].

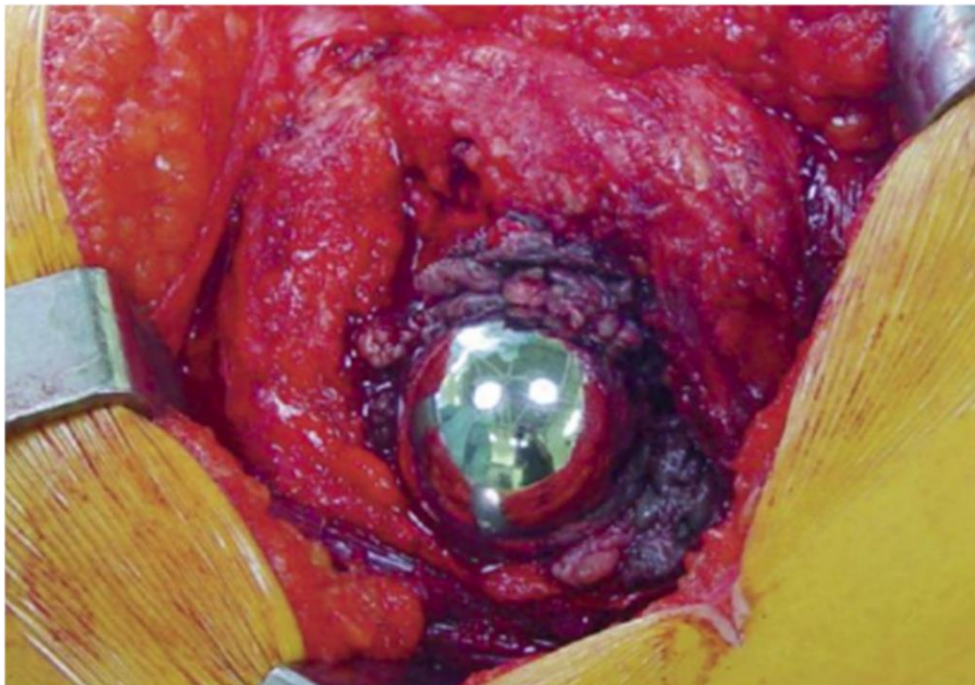


Figure 21: Soft tissue damage from an adverse reaction to metal wear debris. The damaged tissue appears darker compared to healthy tissue, and is concentrated surrounding the femoral head of the implant [83].

Micromotion

Micromotion, sometimes referred to as fretting motion, describes small movements between a prosthesis (whether cemented or uncemented) and the surrounding bone, that are not detected by conventional radiographic methods [6, 87]. Micromotion affects implant stability and may open the interface to joint fluid and wear particles leading to aseptic loosening [6, 88]. Surgical technique is important to prevent micromotion, if malalignment occurs then the risk of micromotion increases, it is also equally important that patients follow strict exercise and physical therapy recommendations to ensure good stability [6].

Stress Shielding

When a hip implant is used to replace a joint, this leads to new loading conditions in the bone surrounding the implant. Sometimes the bone surrounding specific areas of the implant will have reduced mechanical loading compared to pre-implant levels. When the bone is not experiencing enough mechanical loading it will begin reducing in density, weakening the bone strength. It is theorised that stress shielding may facilitate aseptic loosening by further exposing the bone to wear particles [6, 89-91].

Dislocation

Dislocation occurs when the femoral head is forced out of the acetabular cup, figure 22, dislocation is the stated reason for approximately 17% of revisions in the UK [4]. The majority of dislocations occur soon after surgery when damaged muscles are still rebuilding [92-94].



Figure 22: Radiograph of dislocated hip implant [95].

Surgical factors related to dislocation include: component positioning, failure to restore leg length or offset, the abductor mechanism and capsule insufficiency [94]. Dislocation is also more likely to occur with a posterior surgical approach compared to a direct anterior or lateral approach [42]. Patient factors related to dislocation include: the patients natural pelvic inclination and obliquity, the activity level of the patients post-surgery, and whether they rebuild muscle through suggested physical therapy exercises [92, 93]. The most significant implant design factor related to dislocation is the size of the femoral head, a larger femoral head size significantly reduces the chance of dislocation [65, 66].

Infection

A hip implant may become infected during surgery, or potentially weeks to years after the surgery, infection is usually caused by bacteria entering the surgical wound [96]. Infection is the stated reason for approximately 14% of revisions in the UK [4]. To reduce the risk of infection during surgery all implants and medical equipment must be sterile, antibiotics are also taken by the patient before and after surgery [96]. Evidence also suggest that the chance of infection is reduced with the use of ceramic implants and increased with the use of metal implants [4, 97]. Whether revision surgery is required depends on the level of infection, in some cases just the skin and soft tissue around the joint is infected and antibiotics can stop the infection. If the infection goes beyond the superficial tissue, surgery will be required [96].

Periprosthetic Fracture

Periprosthetic fractures describe fractures of the bone around implant prosthesis, these fractures can occur either during surgery or post-surgery [98]. The incidence of periprosthetic fractures overall appears to be increasing due to increasing patient longevity, more demanding activity levels and increasing rate of revision surgeries [92, 99, 100]. The incidence of periprosthetic fracture is greater during revision surgery compared to primary surgery, and greater for uncemented implants compared to cemented [98-100]. Patients with advanced age and osteoporosis are also more likely to develop these periprosthetic fractures [98-100].

Implant Fracture

Implant fracture describes the fracture of the prosthesis, not to be confused with periprosthetic fracture where the bone around the implant is fractured. The most likely place for a hip implant fracture is at the femoral stem and at the site of stress concentrations, there is also an increased risk of fracture for ceramic components [101]. The likelihood of hip implant fracture is rare, estimated at 304 fractures per 100,000 implants, a fracture will require revision surgery [101].

Unexplained Hip Pain

Unexplained hip pain is one of the leading revision reasons, stated as the reason for approximately 17% of revisions in the UK [4]. Although the hip pain is unexplained, it is likely that previously mentioned failure modes contribute to the pain, specifically aseptic loosening and infection [92]. Other common reasons for unexplained hip pain, could be increased stress concentration in the thigh from the implant, abductor tendinitis or impingement of the implant [92].

2.1.10 Biotribology of Hip Implants

In this section the tribological factors of the hip implant bearing will be discussed in more detail, these factors will be split into macro and micro scale, figure 23. Macro scale will cover factors considering the full size of the components, whereas micro scale will cover factors related to the surface topography of the components. It is important to note that the factors covered in this section are closely interlinked and contribute to each other. The key factors of tribological interaction are friction, lubrication, and wear, these will be considered for each section covered.

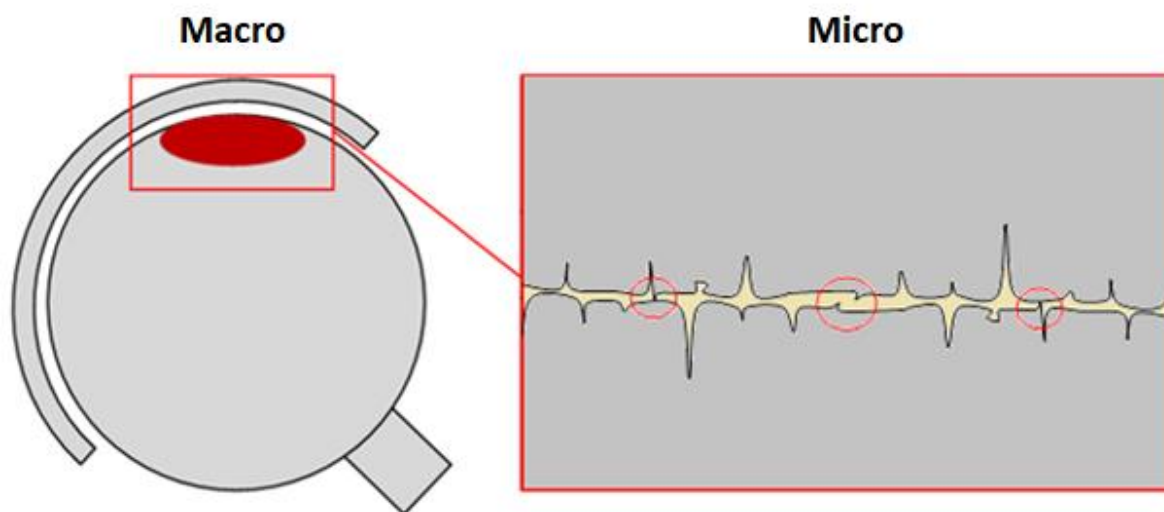


Figure 23: Comparison of macro and micro tribology factors of the hip implant.

2.1.10.1 Macro Scale Factors

Conformity of the Bearing

The hip joint is considered a conformal spherical joint where the head and cup have the same nominal radius. In reality a small clearance is required between the head and the cup, this clearance can range from approximately 20 – 400 microns, the higher the clearance, the less conformal the surfaces. A conformal bearing will have a larger contact area whereas a less conformal bearing will have a smaller contact area [9], figure 24.

The contact pressure is lower for more conformal bearings compared to less conformal bearings [9]. This reduction in contact pressure can result in an increase in lubrication presence, lower friction, and reduced wear [9, 67, 102], however in practice the performance of more conformal large MoM bearings has been poor. The more conformal bearings also decrease the distance between the edge of the contact area and the rim of the cup, increasing the risk of edge loading [103]. The more conformal bearings require a tighter manufacturing tolerance to achieve, evidence suggests for some large MoM implants this manufacturing tolerance may have been missed, leading to poor tribological performance and increased wear rates [104].

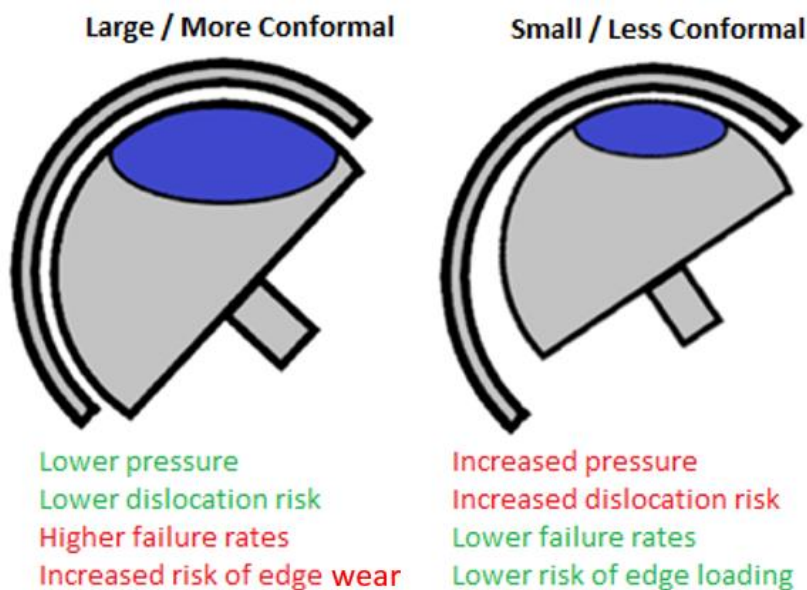


Figure 24: Comparison of large and small bearings. Area of possible bearing contact is indicated in blue.

Contact Pressure from Material Selection

For hard on soft bearings the polymer cup is more elastic than the metal head, therefore as the head is pressed into the cup during usage, the cup can 'creep to conformance' i.e. change shape resulting in a larger contact area and less contact pressure. For hard on hard bearings both materials are much more rigid, therefore the contact area is smaller and results in a larger contact pressure [9].

When implants of equal size are compared, the contact width is four times larger for MoP bearings compared to MoM bearings. The resulting contact pressure is tenfold higher on MoM bearings compared to MoP bearings [9]. An increase in pressure can result in the potential reduction of lubrication, increased friction, and consequent increased wear.

Cup Inclination Angle, Edge Loading and Micro-separation

High wear rates for MoM implants have been associated with high (> 55 degrees) cup inclination angles [105], figure 25. These high inclination implants exhibit deep wear areas suggesting the presence of edge loading. Edge loading occurs when the contact of the head-cup extends over the cup rim, resulting in a large local increase in contact pressure, disrupting the lubricant supply and creating a high wear scenario [9]. Micro-separation, figure 26, is the lateral sliding of the head to the edge of the cup during gait, this results in edge loading. This is more likely to occur when there is joint laxity [105]. In one study a high cup inclination angle (> 60°) resulted in a 9x increase in wear rates, high cup inclination angle and micro-separation resulted in a 17x increase in wear rates [105]. Edge wear is also common in MoP bearings, however evidence suggests that edge loading in MoP bearings does not accelerate overall wear rates [106].

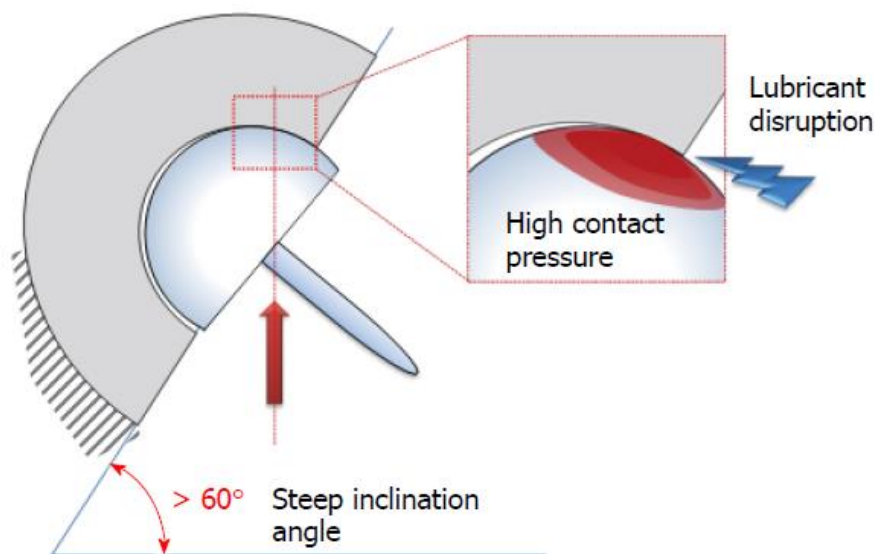


Figure 25: Steep cup inclination angle causing edge loading [9].

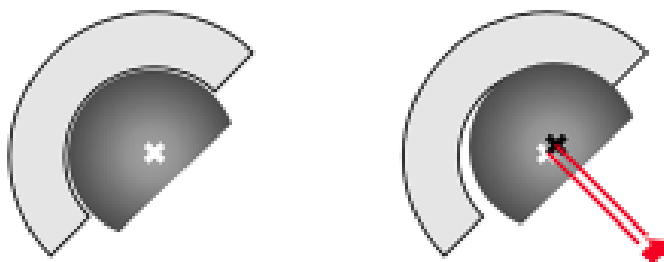


Figure 26: Micro-separation causing the head to slide towards the edge of the cup [107].

Wear Area Location

For hard-on-soft bearings the majority of wear will be from the acetabular component. For hard-on-hard bearings the amount of wear is estimated to be approximately evenly split between the two components [108, 109], however retrieval studies have shown this is not always the case and both the femoral head or acetabular cup can exhibit the majority of the bearing wear [13, 110].

The wear area on both bearing surfaces is unlikely to be at the pole of the component due to the natural inclination of the hip joint, figure 27. Howie, 2005 [17], measured retrieval femoral heads and found the maximum wear area ranged from 40° to 84° degrees elevation (mean 57°; SD 11.3). It is not stated whether the elevation angle is measured upwards from the rim or downwards from the pole, although the author contends that it is more likely it has been measured upwards from the rim. Therefore, if the elevation angles were measured downwards from the pole the values would result in a mean value of 33°, and a range of 6° - 50°. Throughout this project the elevation angle is measured downwards from the pole, figure 27.

For the acetabular cup, the location of the maximum wear area depends on the implanted inclination angle. As the inclination angle becomes steeper the expected wear area moves away from the pole and closer to the edge of the component [105], figure 27. The wear area is also likely to reduce in size as the inclination angle becomes steeper, hence reducing contact area, reducing lubrication presence and increasing wear [105].

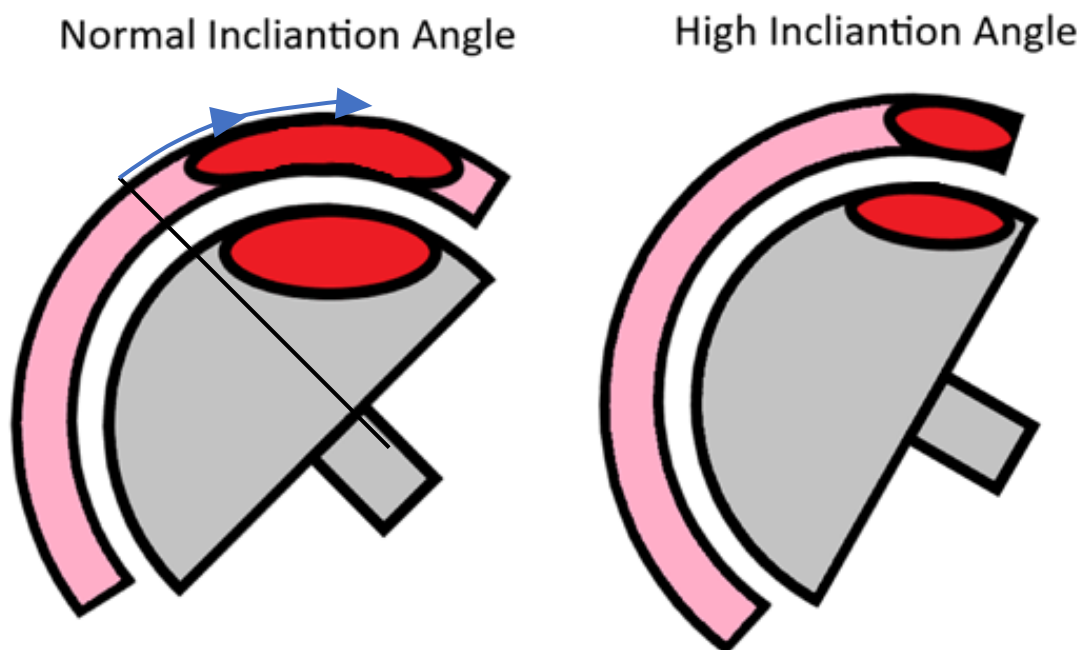


Figure 27: The effect of cup inclination angle on the size and location of wear areas. Note the larger and more centralised wear area on the normal inclination angle cup compared to the smaller and closer to the edge wear area on the high inclination angle cup. The elevation direction is indicated by the blue arrows.

Lundberg, 2006, used computational modelling to estimate the most likely location of third body wearing to occur on the acetabular cup. The locations for third body wear were consistently concentrated on the supero-lateral aspect of the acetabular cup surface [111], figure 28. This also matches the wear area location from experimental data of retrieval studies [17].

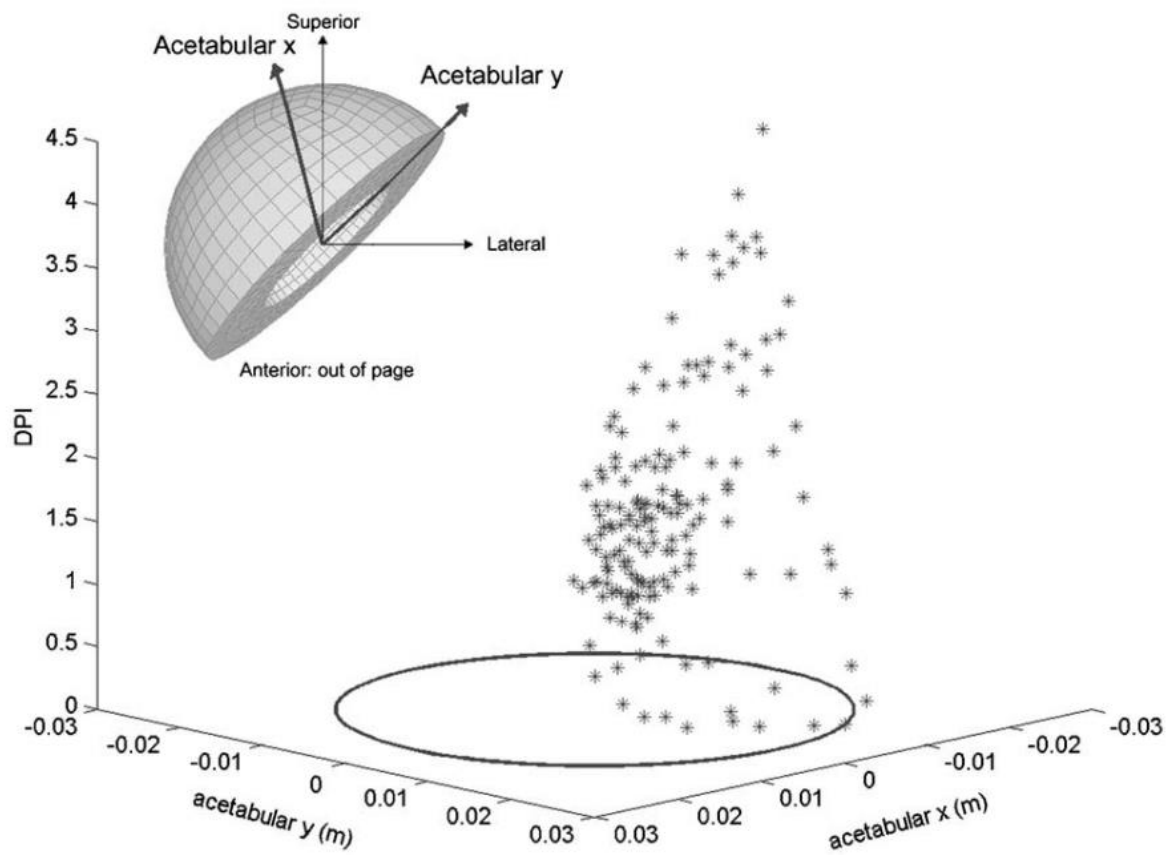


Figure 28: Location of expected third body wear damage on the acetabular cup [111]. DPI is a measure of wear damage, as the value increases the amount of damage from wear increases.

2.1.10.2 Micro Scale Factors

Lubrication

Lubrication ensures surface asperities are separated and reduces the number of surface asperity interactions [9]. The body uses a natural secreted lubricant, synovial fluid. Post hip replacement synovial fluids are typically lower in viscosity but evidence suggests this is still adequate to allow for good performance in the majority of artificial bearings [112]. There are three lubrication regimes possible at the hip cup interface: boundary, mixed and fluid film (hydrodynamic). In boundary conditions the loading between the surfaces is largely carried by the asperities in contact. In this case asperities can plastically deform and break away generating wear particles and associated debris. In mixed conditions the loading is carried between the surface asperities in contact and the fluid hydrodynamic pressure. In fluid film conditions the surfaces are completely separated, the loading is carried by the hydrodynamic pressure of the lubricant [9].

The Stribeck curve plots the coefficient of friction against the Sommerfeld parameter, figures 29, 30. The Sommerfeld parameter is proportional to the dynamic viscosity of the lubricant, to the sliding speed and to the inverse of the load magnitude. As the Sommerfeld parameter increases so does the thickness of the lubricant and the distance between the bearing surfaces [9]. Ideally lubrication should be present between the surfaces as this prevents the surface asperities contacting, thus limiting the production of wear debris, and lowering the friction between the surfaces. The most ideal lubrication point is just as fluid film lubrication is achieved, as shown on the Stribeck curve, this is where the coefficient of friction is lowest. It has been shown that conormal bearings are more likely to perform in the fluid film regime due to the lower contact pressure achieved [9]. Low surface roughness increases the distance between surface asperities, also increasing the chance of a fluid film regime [9]. Under realistic loads and in the presence of synovial fluid, MoP hip joints articulate in the mixed film or boundary lubrication regime. Hard-on-hard bearings primarily work in the fluid film and mixed film lubrication regime; however, with increasing femoral head size (>28 mm), a shift toward full fluid film (hydrodynamic) lubrication can be observed as well [67, 113].

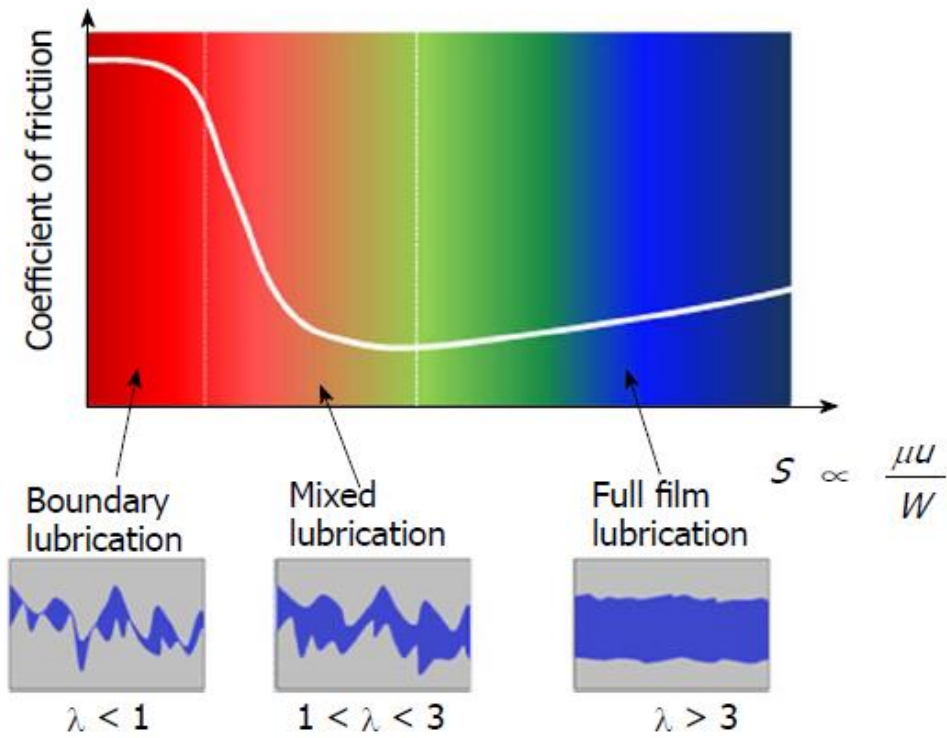


Figure 29: Comparison of lubrication regimes and their relationship with the Stribeck curve for a MoM bearing [9].

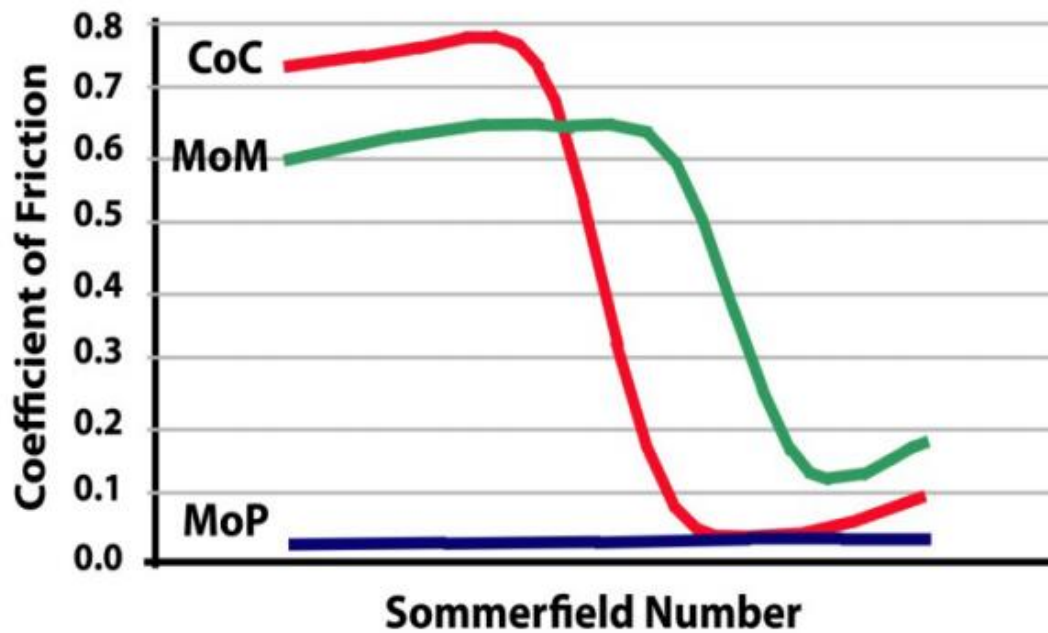


Figure 30: The Stribeck curve with different bearing material combinations. Note how the MoP bearing has much lower friction in boundary lubrication conditions compared to the hard-on-hard bearings [67, 113, 114].

Friction

Friction is the resistance restraining relative motion of two surfaces, the major contribution to friction is the interaction between surface asperities, figure 31.

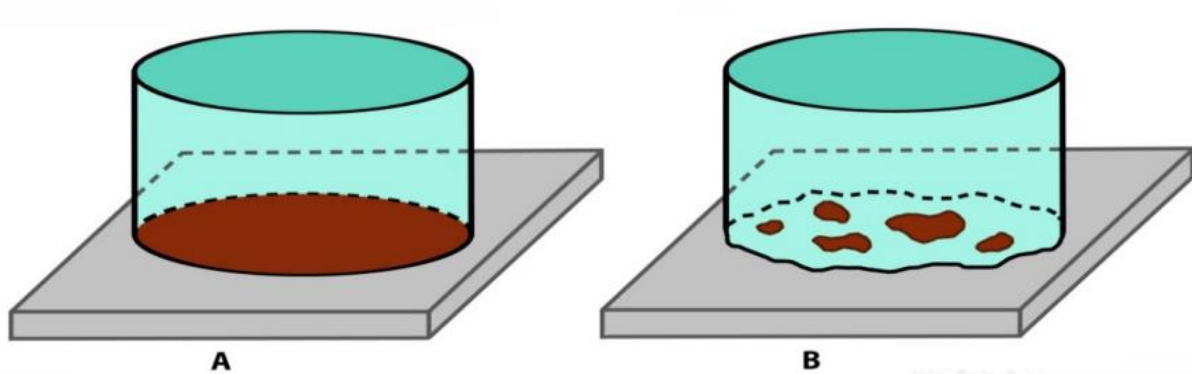


Figure 31: Apparent (A) and real (B) area of contact between surfaces [114].

The coefficient of friction can vary largely with the system conditions, such as the geometry of the bearing, materials in use and the amount of loading [9]. As previously discussed COF (coefficient of friction) is lowest when the bearing interface is entering the full-fluid lubrication regime. When comparing the COF values by bearing material type studies show that the highest COFs were found in MoM bearings (0.096 – 0.12). Whereas the lowest COF values were demonstrated in CoC bearings (0.04-0.056). MoP and CoP bearings showed similar levels of COF (0.056-0.064) [9, 115, 116], table 2. The larger more conformal bearings were shown to promote lubrication and therefore lower the COF [115]. As the load applied to the implant increased, a representation of the weight or activity levels of the patient, the COF also increased [116].

Table 2: COF values for different bearing material combinations [9, 115, 116].

Head/cup	COF 25% Bovine serum	COF 100% Bovine serum
MoP	0.062 (+ 0.008)	0.064 (\pm 0.01)
CoP	0.056 (+ 0.01)	0.06 (\pm 0.012)
MoM	0.12 (\pm 0.02)	0.096 (\pm 0.012)
MoM _{RHR}	0.098 (\pm 0.02)	0.079 (\pm 0.011)
CoC	0.04 (+ 0.007)	0.056 (\pm 0.01)

Wear

Wear is the most clinically important factor for the study of hip implant bearings as it has been previously discussed that increased wear rates directly relate to the failure of the implant. The multi-axial rotational movement of the femoral head within the acetabular cup allows the joint to function, but as this movement occurs wear debris can be generated. When the bearing is in boundary lubrication mode, the contact is between surface asperities, when movement occurs, asperities can be detached by abrasive or adhesive mechanisms leading to the production of wear debris. To prevent excessive wear, it is crucial to have a fluid film lubrication regime, as this prevents the asperities from contacting.

If the implant is a hard on soft bearing, the majority of wear debris will be from abrasive wear, this is where the hard material removes the soft acetabular component by abrasive mechanisms, figure 32. For hard on hard implants adhesive wear is more likely, this is when local welding of asperities occurs and then the debris is removed during movement, figure 32 [9]. As asperities detach, they can remain trapped in between the bearing surfaces. Any loose debris in between the bearing surfaces is called third body debris, trapped third body debris will likely further increase the amount of wear occurring [117]. Third body debris poses a greater risk when the hardness of the material is greater, ceramic materials are the hardest, followed by metals and finally polymers [118].

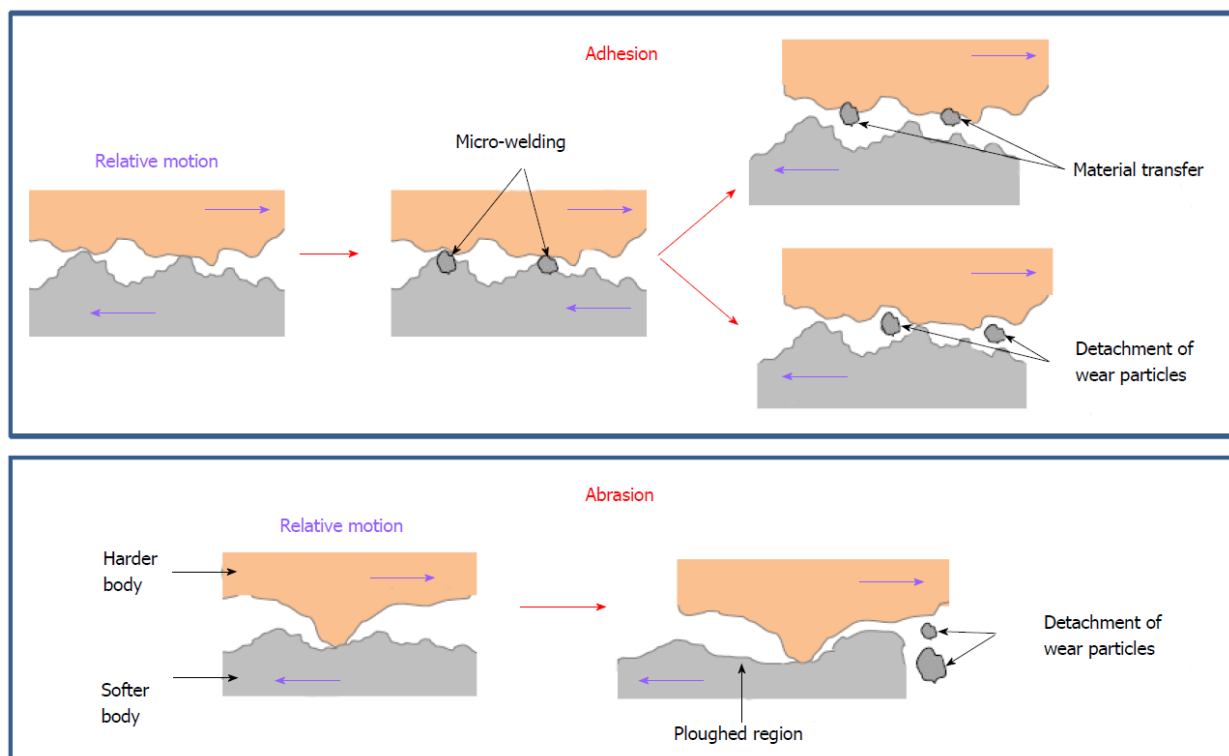


Figure 32: Wearing of the hip implant bearing. Adhesive wear (top), abrasive wear (bottom) [9].

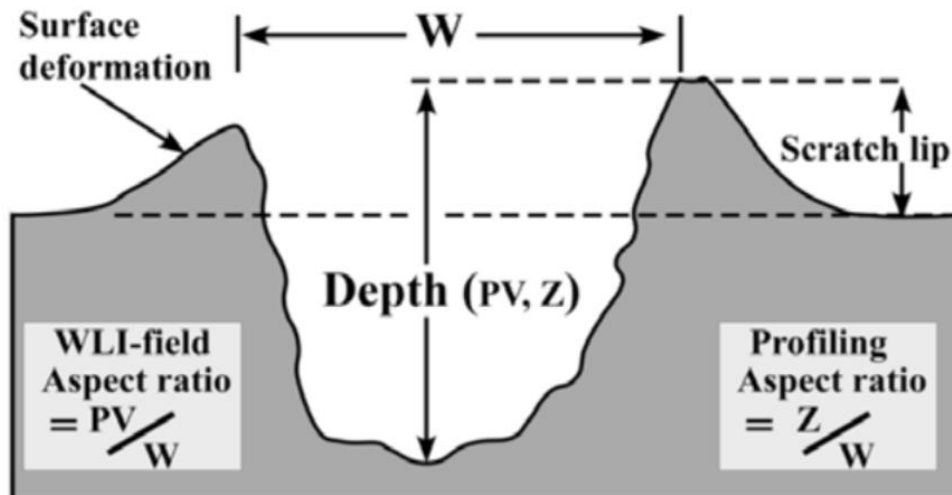


Figure 33: Profile showing typical scratch and associated parameters to describe scratches [118]. Note the scratch lip generated at the sides of the scratch, these peaks of the scratch lip are now at risk to be removed as wear debris.

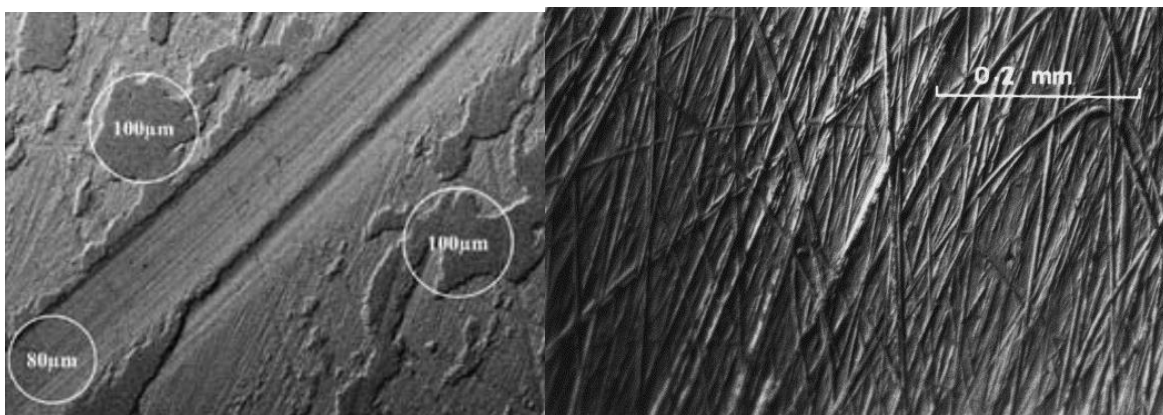


Figure 34: SEM images of scratches on the surface of CoCr femoral heads. Left: Scratch created by an 80- μm wide alumina wear debris [118]. Right: A heavily scratched area on the surface of an explanted MoP femoral head [18].

The surface finish of the bearing surfaces will play an important role in the wear performance of the implant. If the surface roughness of the bearing material is lower, this increases the distance between surface asperities, promoting lubrication, reducing friction and reducing wear [9]. Therefore, bearing surfaces should be manufactured as smooth as possible. Following manufacture, the polymer bearing surfaces are the roughest of the popular material types, with an R_a range of 0.1 – 0.2 μm . Metal bearing surfaces range from 0.01 – 0.05 μm and ceramic surfaces range from 0.001 – 0.005 μm [9].

To prevent wear from occurring surface asperities should be as small as possible and they need to be separated by a fluid film lubrication regime. The macro and micro tribological factors previously discussed will play a role understanding whether this is achieved.

The Case of MoM Wear

A study by Bills [13] measured six retrieval MoM bearing pairs, the level of wear measured ranged from 21.78 to 556.25 mm³ for each bearing pair, this shows the wide range of wear scenarios present in retrieved components, table 3. The wear was split between the femoral head and acetabular cup; however, either component was shown to exhibit the majority of the bearing wear. The mean wear volume for the femoral heads was 23.98 mm³ and 32.57 mm³ for the acetabular cup, however each bearing pair varied greatly in its wear distribution between the femoral head or acetabular cup, and the amount of bearing wear overall varied greatly.

Table 3: Wear measurement results for retrieved MoM hip bearing components, Bills [13].

Component ID	Radius unworn (mm)	Radial clearance unworn (mm)	Max wear depth (μm)	Wear volume (mm ³)	Overall wear volume (mm ³)
Cup 19	21.087	0.170	60.0	11.24	34.40
Head 19	20.917		56.5	23.16	
Cup 35	25.083	0.091	30.0	42.63	58.23
Head 35	24.992		27.9	15.60	
Cup 57	26.780	0.820	428.2	84.11	556.25
Head 57	25.960		528.5	472.14	
Cup 64	24.014	0.097	11.1	20.55	21.78
Head 64	23.917		3.0	1.23	
Cup 89	24.027	0.135	30.4	44.26	82.08
Head 89	23.892		36.8	37.82	

A study by Gascoyne [110] measured 24 retrieval large MoM bearing pairs, table 4, the volume loss ranged from 0.15 – 338.20 mm³, with a median value of 2.19 mm³ for the femoral heads. For the acetabular cups the volume loss ranged from 0.07-139.72 mm³, with a median value of 0.52 mm³. The vast majority of components exhibited low wear ≤ 3mm³. On average femoral heads showed slightly increased wear amounts compared to the acetabular liners, but this was not always the case.

Table 4: Wear measurement results for retrieved MoM hip bearing components, measured by Gascoyne [110].

Sample ID	Time (y)	Damage Score Total	Head Taper Goldberg Score	Head Wear (mm ³)	Liner Wear (mm ³)	Head Taper Damage (mm ³)	Liner Taper Damage (mm ³)	Total Metal	
								Volume (mm ³)	Rate (mm ³ /y)
2046	4.5	14	2	0.838	0.148	7.10	0.00	8.09	1.79
2082	5.3	20	3	2.396	0.474	1.70	0.18	4.75	0.89
2101	5.3	18	4	2.362	0.819	2.42	0.00	5.60	1.05
2159	3.5	16	2	4.707	2.356	0.48	0.00	7.54	2.17
2160	8.8	5	2	149.832	–	0.53	–	150.36	17.08
2219	8.8	17	3	0.706	0.359	1.21	0.00	2.28	0.26
2221	5.0	17	2	8.734	8.933	0.39	0.00	18.06	3.59
2232	3.1	17	4	18.266	11.444	3.85	0.00	33.56	10.73
2257	6.2	19	2	1.346	0.066	0.21	0.22	1.84	0.30
2309	4.2	12	2	0.151	0.517	0.29	4.28	5.24	1.26
2395	6.4	11	3	0.335	0.226	5.67	2.28	8.51	1.32
2451	4.1	17	3	5.47	43.386	0.72	1.62	51.19	12.48
2629	8.5	13	4	1.689	2.046	0.77	0.00	4.51	0.53
2645	5.6	21	3	2.012	0.818	0.87	0.58	4.28	0.77
2683	6.0	20	2	9.849	0.318	0.71	0.00	10.88	1.82
2708	6.0	20	2	0.806	0.151	0.25	0.00	1.21	0.20
2710	5.6	6	2	1.01	0.323	4.91	0.00	6.24	1.12
2718	7.3	14	3	3.019	1.109	8.21	0.00	12.34	1.68
2722	7.2	20	4	338.199	139.719	9.32	0.00	487.24	68.05
2738	8.5	12	3	15.39	10.246	2.11	3.26	31.01	3.63
2767	7.0	17	4	1.157	0.181	5.40	0.00	6.74	0.96
2770	9.0	17	2	1.228	0.111	0.41	0.00	1.75	0.19
2795	6.7	20	2	1.331	0.126	23.18	0.00	24.64	3.70
2874	7.3	19	2	8.756	7.151	0.03	0.00	15.94	2.17
Median	6.1	17	2.5	2.19	0.52	1.04	0.00	7.81	1.50
Range	3.1-9.0	5-21	2-4	0.15-338.20	0.07-139.72	0.03-23.18	0.00-4.28	1.21-487.24	0.19-68.05

MoM implants have stricter manufacturing tolerances compared to MoP implants [10, 11]. A study concluded that some MoM implants were manufactured outside of their specified bearing radius

tolerance, this could lead to poor tribological performance and increased wear rates [104]. This is one theory to further explain why MoM bearings had such poor performance in practice. As previously discussed large head MoM implants reported issues with local bone and tissue necrosis and metallosis, leading to very high failure rates, 2-3x higher than non-MoM bearings [4, 51, 61, 62].

2.1.11 Chapter Summary

The hip joint is a multi-axial ball and socket joint located at the head of the femur and the acetabulum of the pelvic bone [1]. Osteoarthritis damages the cartilage of the hip joint, forming bony spurs on the joint surface and narrowing the joint space, leading to abnormal stresses and discomfort [1]. Typically, osteoarthritis presents in older patients, and is a documented indication in 91.9% of primary hip replacement surgeries [4].

Hip replacement is the replacement of the damaged hip joint with an artificial implant. The modern hip implant design has three main components: the femoral stem, the femoral head, and the acetabular liner. The prevalence of younger patients undertaking joint replacement surgery has risen significantly, with the strongest increase in patients aged 45-55 [2]. Therefore, implants need to last longer, with increased performance demands, due to younger, more active patients.

Currently patients can expect a hip replacement to last 25 years in around 58% of cases before revision is needed [3]. Once revision surgery is required, the likelihood of another revision in the future increases, therefore primary implants need to last as long as possible [4, 69]. Aseptic loosening is the most common cause of revision worldwide [4-6], and the most well studied factor causing aseptic loosening is periprosthetic osteolysis induced by the presence of wear particles. As implant wear rates increase, the risk of osteolysis and aseptic loosening increases [6, 7], therefore manufacturers must keep implant wear rates as low as possible.

The majority of wear debris is generated at the bearing interface [8], for hard-on-soft bearings the majority of the wear will be from the polymer acetabular liner, whereas for hard-on-hard bearings, the majority of wear can come from either component [13, 110]. Although MoM implants have demonstrated lower wear rates [76, 77], in many instances the aggressive biological reaction to metal wear debris leads to poor performance and high revision rates [4, 75, 82, 83]. Patient, surgical practice, and implant design factors all play a role in the tribological performance of the bearing interface. With the ideal bearing running in full-fluid lubrication mode, ensuring a low friction, and low wear environment.

2.2 Metrology for Hip Implants

2.2.1 Measurement Applications

In this chapter the most common measurement procedures applied to hip implant bearings are discussed. Highlighting the critical importance of metrology for both manufacturing quality assessment and experimental wear studies.

2.2.1.1 Manufacturing Quality Inspection

Once a hip implant has been manufactured the components need to be measured according to agreed standards to ensure the desired levels of geometrical tolerancing have been achieved.

Geometrical Measurement

Geometrical measurements of bearing surfaces are vital to check that the diameter and sphericity of newly manufactured components are within their specified tolerances. The femoral head and acetabular cup are manufactured to be conformal with a small difference in diameter to allow the femoral head to fit within the acetabular cup, resulting in a small diametrical clearance in-between the head and the cup, figure 35. The amount of diametrical clearance will vary by implant design, generally small clearances are favoured as low diametrical clearance is designed to promote lubrication presence and reduce wear rates. However, if the clearance is too small this can increase the chance of edge loading occurring, actually increasing wear. Some implant designs can have a diametrical clearance as low as 20 microns [9].

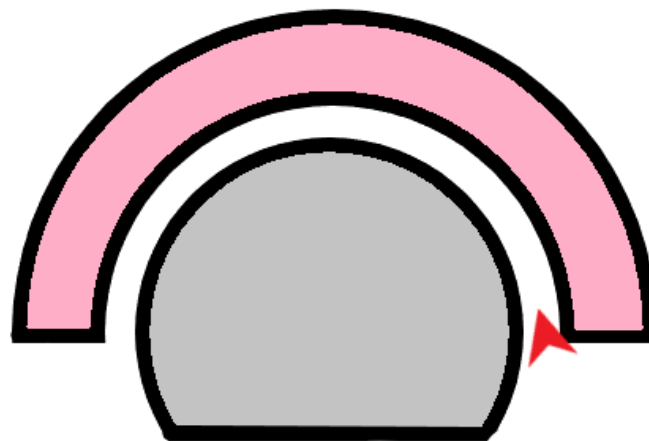


Figure 35: Diametrical clearance diagram. The red arrow indicates the small gap between the femoral head and acetabular cup, known as the diametrical clearance.

To measure the dimensional geometry of the bearing surfaces measurements are completed using a CMM (coordinate measurement machine), this allows the radius and sphericity of the bearing surfaces to be measured. If the measured radius and sphericity values are not within their specified tolerances

this will affect the diametrical clearance and therefore implant performance. Such non-conforming implants are considered scrap.

ISO 21535:2007 and ISO 7206-2 outline the sphericity and diameter tolerances required for hip implant components, MoM and CoC tolerances are not yet included, table 5 [10, 11]. The tolerances for polymer components are less stringent compared to those set for the metal or ceramic femoral components. Manufacturers invariably supersede ISO standards by setting their own much tighter dimensional tolerances. The CMM measurement method outlined in ISO 7206-2 requires a total of 120 measurement points for the femoral head and 100 measurement points for the acetabular cup. The location of the measurement points must be evenly spread over the majority of the surface. ISO standards state that the bearing surface must be split into four quadrants with the measurement points evenly spread among each quadrant. An alternative method is to create a continuous scan of points from the pole of the component, a scan must take place within each quadrant. For the femoral head, a total scan angle of 200° is required and for the acetabular cup a total scan angle of 140° is required. See figure 36 for an example CMM scanning method for quality inspection.

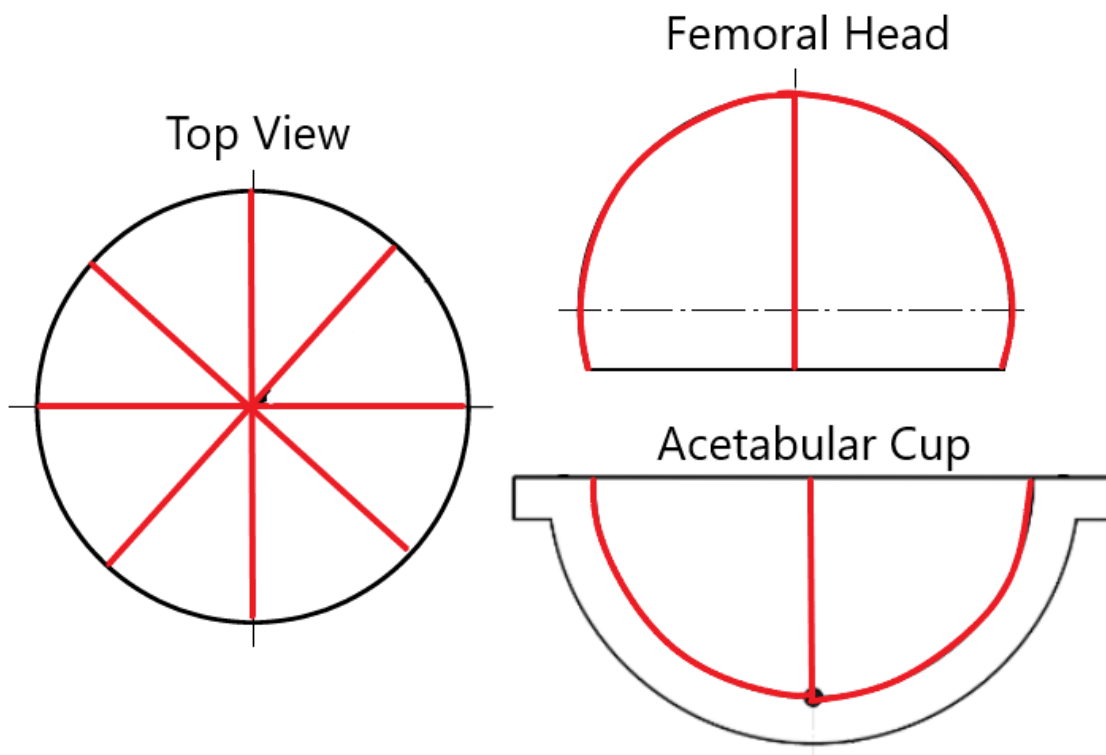


Figure 36: Example quality inspection measurement strategy. Each red line represents a scan line during CMM measurement. The user can determine the number of points required per line. This method ensures that each required quadrant area is measured, this measurement strategy is easy to implement on the CMM.

Large head MoM implants are designed with low diametrical clearance as to promote lubrication and reduce wear, these type of large MoM implants with low diametrical clearance have been shown to suffer from increased failure rates compared to other implant designs. Upon retrieval analysis it was found that a number of these implants were manufactured with lower diametrical clearance than was intended by the manufacturer [104]. This could have resulted in edge loading and increased wearing of these implants. This highlights the importance of accurate geometric measurement to determine the geometry of components. Bearing interfaces designed with low diametrical clearance require the most accurate geometric measurement, with emphasis on suitable fixturing methods and repeating measurements.

Surface Measurement

The surface finish of newly manufactured bearing surfaces also needs to be considered, ensuring the surface finish is within the specified surface roughness tolerances. The surface measurement method outlined in ISO 7206-2 requires a total of 5 surface measurements to be taken, using a cut-off value of 0.08 mm. One at the pole, and one in each quadrant of the component at 30 degrees elevation [10, 11]. Depending on the type of material, the bearing surface finish requirements vary. Ceramic surfaces require the smoothest finish and polymer surfaces the roughest, table 5 outlines the Ra surface finish requirements of hip implant components [10, 11]. Optical surface measurements made must comply with the principles given in ISO ISO 25178-3:2012-Part3 [119]. The simplest surface quality inspection would involve five 2D contact profile measurements with the resulting Ra values, whereas a more detailed analysis could include multiple areal measurements and the use of multiple surface parameters.

Table 5: Manufacturing tolerance requirements set as part of ISO 7206 for hip replacement components [10, 11].

	Metal Femoral Head	Ceramic Femoral Head	Polymer Acetabular Cup
Sphericity	< 10 um	< 10 um	< 100 um
Diameter	-0.2 mm to 0 mm	-0.2 mm to 0 mm	+0.1 mm to + 0.3 mm
Surface Roughness	< Ra 0.05 um	< Ra 0.02 um	< Ra 2 um

2.2.1.2 Experimental Study Analysis

Experimental functional studies incorporating dimensional metrology are completed on new implant designs to quantify their performance. Additionally, dimensional analysis of retrieved implants can provide insight to the performance of previously implanted devices (retrievals/explants).

In-vitro and In-vivo Studies

When considering experimental studies, it is important to first distinguish between in-vitro and in-vivo studies. In-vitro studies use simulator testing, this is where a hip simulator is used to recreate the motion of the natural hip joint, such simulators allow multiple implants to be tested in a short timeframe, figure 37. Hip simulators recreate the natural gait of a human and a variety of gait patterns can be implemented [120]. Regulation requires that designs of joints be subject to an exhaustive set of simulator studies prior to regulatory approval [10]. A key element of simulator studies is to determine the wear performance/material loss of the implant during the simulated “life cycle”. It should be noted that the complexity and subtlety of the human movement over a long period of time e.g. several decades, cannot be exactly simulated.

In-vivo studies, also called retrieval studies, involve the analysis of implants that have been removed during retrieval surgery, figure 37. This type of study can provide valuable retrospective insight into the performance of past implants that cannot be achieved from in-vitro testing. For example, large MoM implant designs performed well during in-vitro testing but poorly in real life patients and have therefore been a particular focus for retrieval studies [76, 77]. The main drawback with retrieval studies is the time required to gather a large cohort size, particularly for modern designs which may be inside the body for several decades before being retrieved.

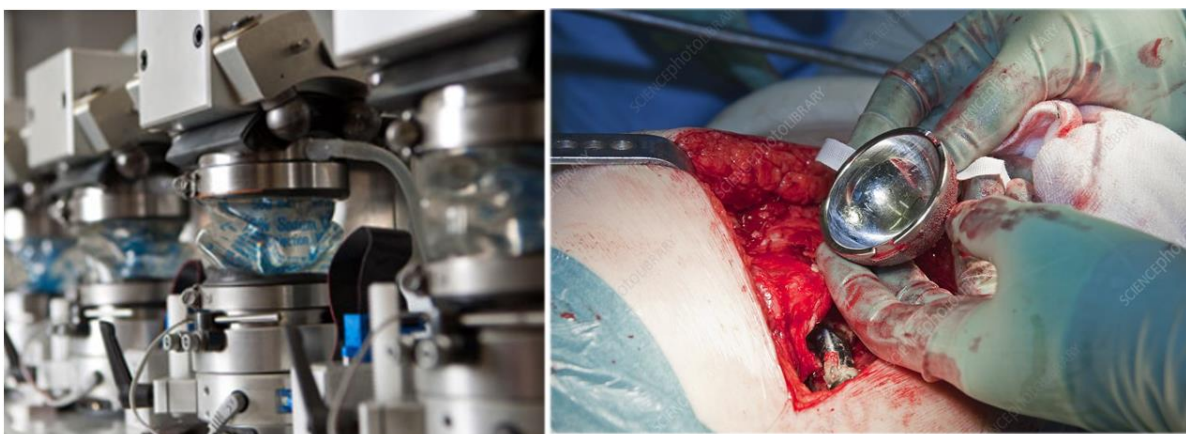


Figure 37: Experimental study types. Left: Hip implant wear simulator [121]. Right: Retrieval of a hip implant (right) [122].

Wear Measurement

As the risk of aseptic loosening, the most common failure mode for hip implants, is increased by higher bearing wear rates, a common focus of experimental study is the wear performance of implants. Wear is the amount of material lost from an implant during its usage, wear measurement is most commonly focussed to the bearing surfaces as this is the location of most wear [8]. Wear measurement is the most common and effective tool in diagnosing implant failure mechanisms and determining long term performance of orthopaedic implants [13]. Using wear measurement analysis, a deeper understanding of failure mechanisms can be achieved, and future implant designs can be improved. The most common parameter calculated is the volume loss (or weight loss) from the bearing component. As previously mentioned, a well-documented wear testing process is a requirement to ensure ISO compliance of new designs [10]. There are two main methods for wear measurement of hip implants: gravimetric and volumetric [12].

2.2.2 Coordinate Measuring Machines

Before discussing the wear measurement methods, it is important to discuss the coordinate measurement machine (CMM), CMMs are utilised to complete volumetric wear measurements for implants. A CMM is a measuring system which most commonly utilises a contact probe to determine spatial coordinates on the surface of a component [123]. CMMs come in a wide range of configurations, some specialise in measuring very large objects of several metres, whereas miniature versions can measure very small objects in the mm^3 range, with measurement resolutions down to 0.1 nm [123].

The most common type of CMM is the moving bridge CMM, figure 38, this CMM utilises three linear axes [123]. The location of the probe is controlled by the linear axes and the probe position is tracked in cartesian coordinates using calibrated optical scales, the CMM records the position when the probe contacts the surface with a given force [123]. The CMM can either measure by direct probing, which is a collection of single points on the surface, or through scanning, where data points are continuously collected as the stylus tip is dragged across the surface [123]. CMMs can sense the surface with a variety of devices, such as: touch trigger probes, analogue probes, continuous scanning, and non-contact systems, the majority of CMMs use a touch trigger probe [124].

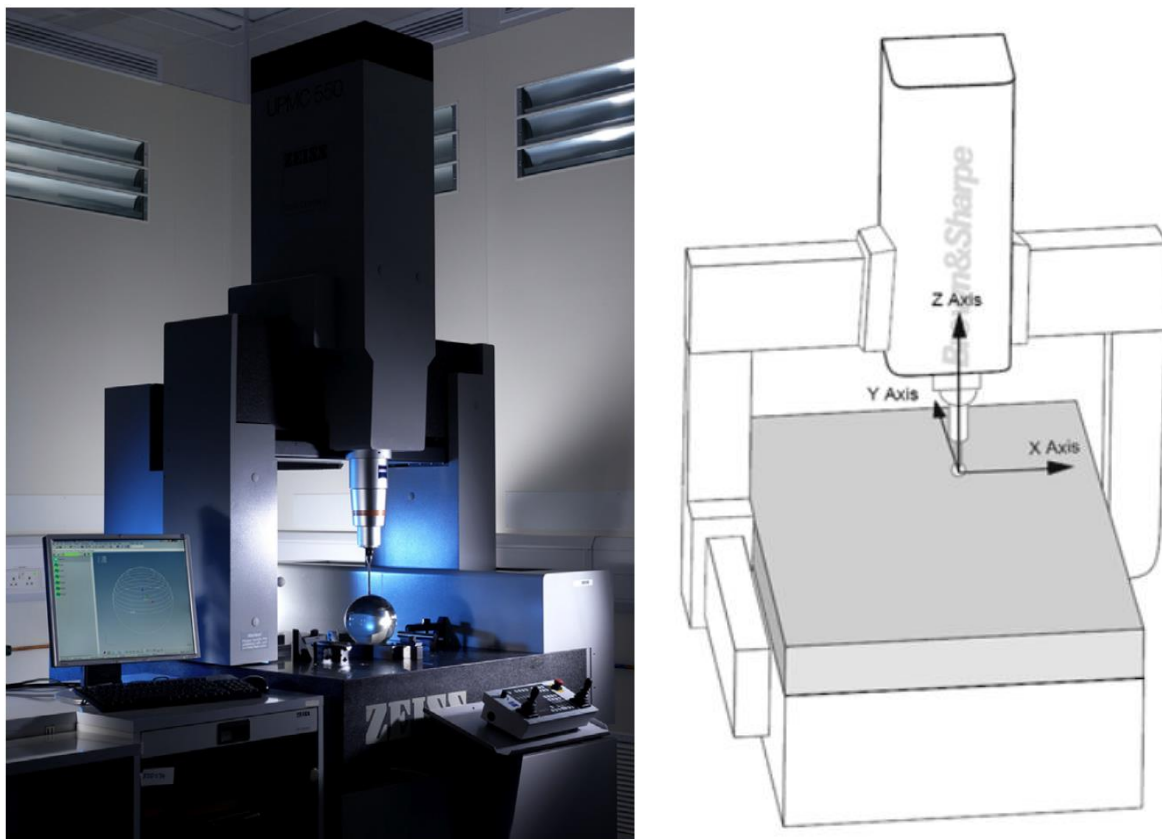


Figure 38: CMMs. Left: A typical moving bridge CMM [123]. Right: Typical axes of a bridge CMM [125].

2.2.2.1 Touch Trigger Probe

A typical touch trigger probe consists of three cylindrical rods, each pressed against pairs of metallic balls. This setup constrains all six degrees of freedom of the stylus, so after the stylus is deflected it returns to the same position [124], figure 39. The touch trigger probe creates an electrical circuit through contacts, as the stylus is deflected in any direction, these contacts are then broken, a trigger signal then notifies the computer to record the cartesian position [124].

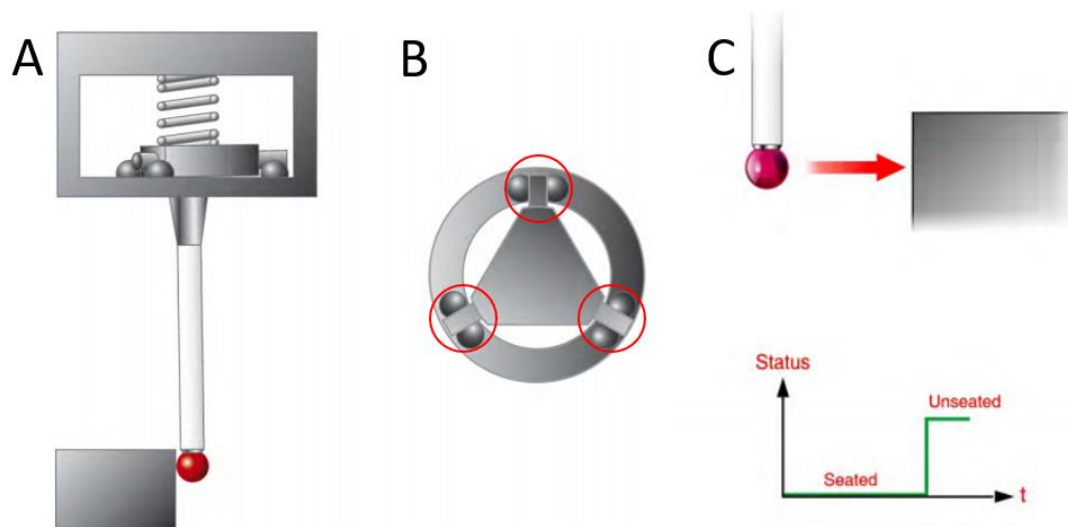


Figure 39: Touch trigger probe system [124]. A: Side view of the probe system. B: Top view of the probe system, red circle indicating the contacts. C: Probe stylus touching surface, lifting 'contacts', and triggering electrical signal for computer to record cartesian position.

2.2.2.2 Analogue Probe

High accuracy CMMs often utilise analogue measuring probes, figure 40. Analogue probes utilise three spring parallelograms that have a deflection of typically ± 3 mm in the direction of the measuring axes. The movements of the probe head during contact are picked up by an inductive measuring system. As the probe head contacts the surface, the spring parallelograms deflect, allowing the probe to remain in contact with the surface. When contact is made, both the machine axes coordinates and the digitised residual deflections of the probe head are saved to the computer. This allows for a more accurate measurement of the cartesian position compared to a touch trigger probe system. A typical measurement uncertainty for an analogue probe CMM is approximately ± 1 micron, but will vary slightly depending on the measurement length [126].

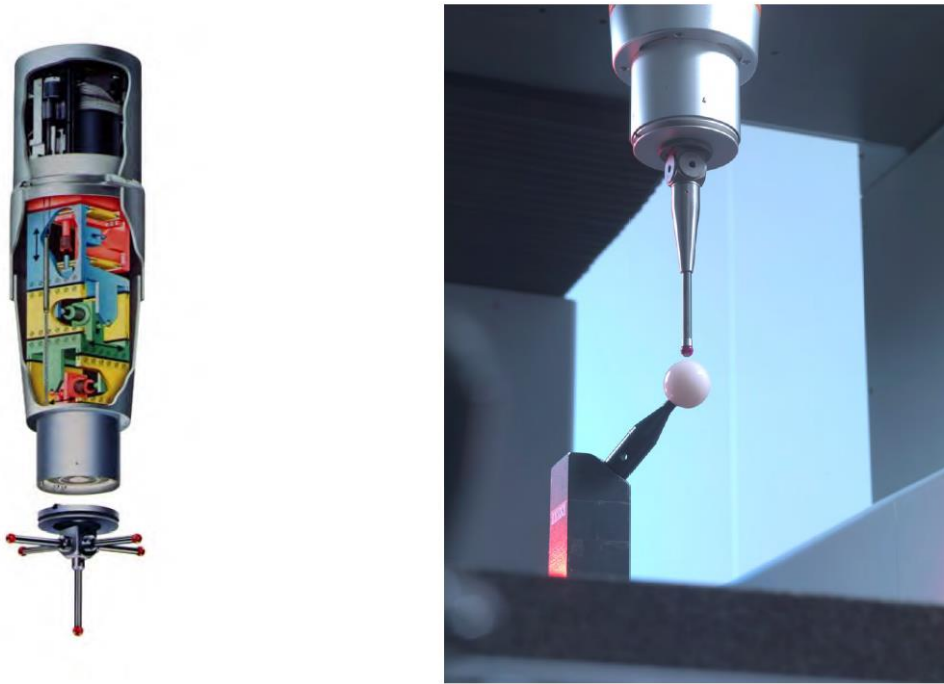


Figure 40: Analogue probe system. Left: Exploded view of analogue probe head. Right: Measurement of qualification artefact.

2.2.2.3 Qualification, Verification, and Calibration

The terms qualification, verification and calibration are often confusingly interchanged when discussing CMMs [127]. Qualification refers to the day-to-day task of determining the stylus tip radius; verification refers to the periodic task (often annually) of determining if the CMM still meets the manufacturers specification; and calibration refers to the task carried out on installation and then as necessary to determine the magnitude of all error sources, otherwise known as error mapping [127].

To maintain the specified uncertainty in any probing system, the stylus needs to be qualified using a reference sphere, this allows the radius of the stylus tip to be determined [124, 127]. As the reference sphere size is defined to a high level of accuracy, the size of the stylus tip can be determined by measuring the reference sphere and calculating the difference between the 'ball centre data' and the reference sphere size [124, 127]. This allows for an accurate determination of the stylus tip radius, which is crucial to low uncertainty CMM measurements [124, 127]. Once the stylus radius is known after qualification, when the stylus tip contacts the surface, the coordinates of the 'ball centre data' are automatically 'offset' by the stylus radius to allow for the actual surface coordinate to be recorded [124, 127], figure 41. CMMs are fully traceable when calibrated and are accompanied by an uncertainty statement [13, 127-129].

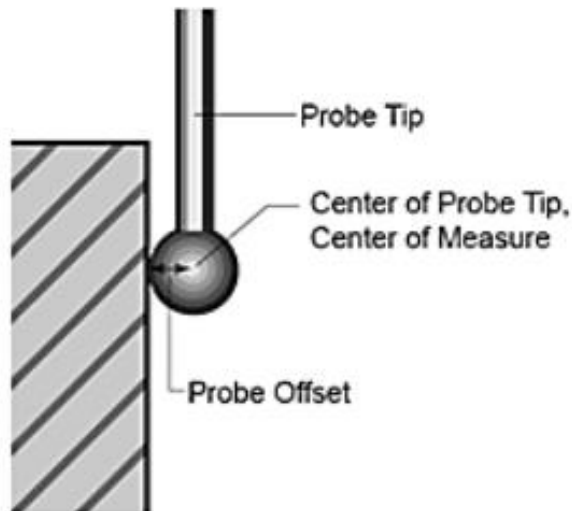


Figure 41: Probe offset during CMM measurement.

2.2.2.4 Non-contact Probes (Optical)

Non-contacting probes are replacing traditional contact probing systems in applications where speed is required or where material properties are not suitable for contact probing [124]. These systems allow for faster measurement, however current traceability is difficult to demonstrate and specification standards relating to performance verification are at the early stages of development [124]. A recently developed non-contact optical CMM has been designed for hip implant bearing surface measurement [130-132], figure 42. Non-contact measurement can be particularly useful as there is no chance of implants being damaged by the measurement stylus. This may be a serious issue when measuring orthopaedic materials such as ultra-high molecular weight polyethylene (UHMWPE). A comparison study between an analogue probe CMM and the modern RedLux optical CMM was completed as part of this project.

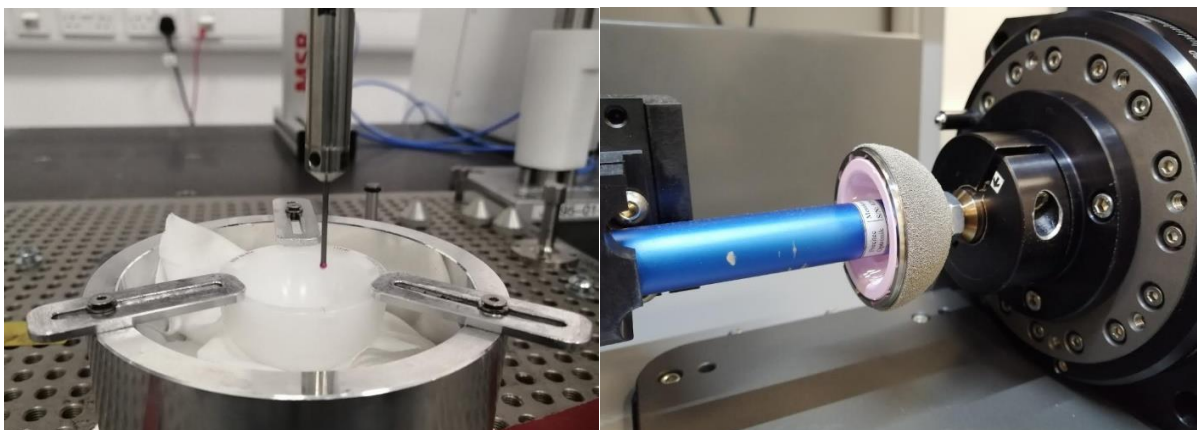


Figure 42: CMM measurement of acetabular liners. Left: CMM analogue probe measuring a polymer liner. Right: Optical CMM measuring a ceramic liner (right).

2.2.3 Wear Measurement Methods

2.2.3.1 Gravimetric Method

The gravimetric method is the most common method to perform wear measurements on in-vitro tested components. The method uses a calibrated microbalance to measure the specimen weight pre-wear and post-wear, figure 43, the resulting weight loss is calculated between the two measurements [12]. Due to the gravimetric method requiring a pre-wear measurement, this method can only be used for in-vitro testing and cannot be used for in-vivo (retrieved implant) testing.



Figure 43: Gravimetric measurement method. Weighing of a polymer knee component [133].

Fluid sorption is the uptake of lubrication into the component, increasing the weight of the component, figure 44. A control specimen, identical to the components being tested, must be soaked in the same lubrication as the other components, to also allow for fluid sorption. This will be used as a control to account for the weight gained from fluid sorption during testing, this control component will be loaded identically as the other components but subjected to no articulation [12].

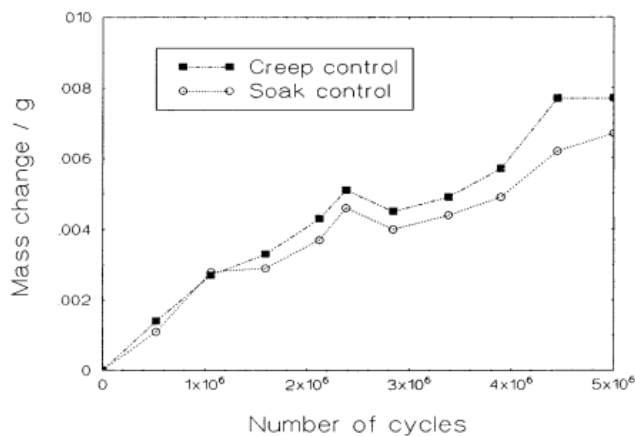


Figure 44: Fluid uptake during simulator testing on UHMWPE acetabular cups [134]. The 'Soak control' set had no loading of the component, whereas 'Creep control' loaded the component identically to the test components.

2.2.3.2 Volumetric Method

The volumetric method, also called the geometric method or the dimensional change method, uses a coordinate measuring machine (CMM) to create a 3D point cloud of the bearing surface [12], figure 45. The measurement points are taken relative to an origin reference point, for example, the spherical centre of the component. All measurement points will have an XYZ value from this origin position, together these measurement points are used to generate a 3D point cloud representative of the surface.

The amount of data points taken is decided by the user and can depend on the scenario. The amount of data points taken, and the resultant mesh shape will contribute to the uncertainty of the measurement [13]. More data points will result in a more representative measurement of the surface but will also increase the measurement time and the processing power required to analyse the data. When a CMM is used for quality inspection purposes less measurement points are required to calculate the radius and sphericity compared to the many points needed for wear measurement.

The generated 3D point cloud from CMM measurement can be converted into a 3D volume using a range of software analysis tools, the change in volume from pre-wear measurement to post-wear measurement can then be approximated. This method can also generate a 3D wear map using the measured data points, allowing the user to quantify wear areas, figure 45.

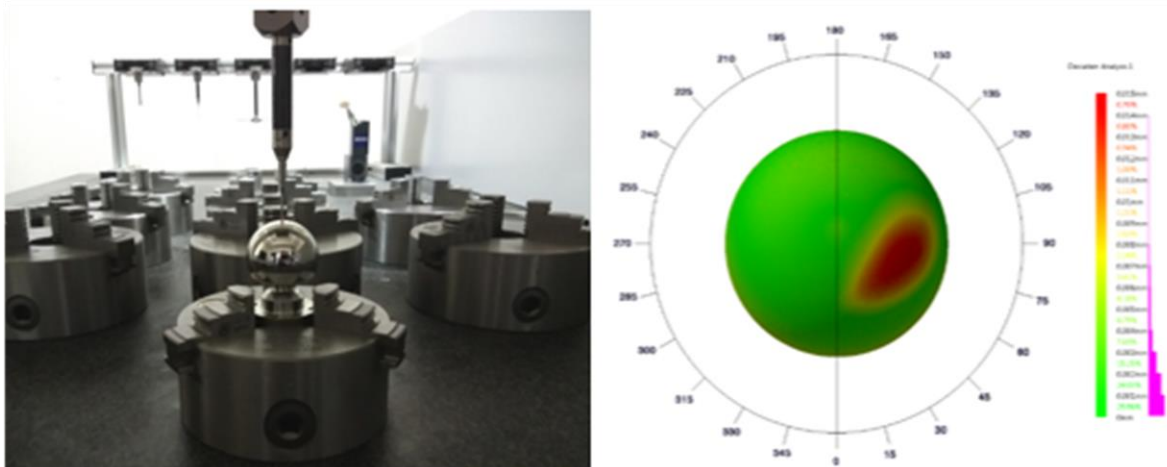


Figure 45: Volumetric measurement of a femoral head. Left: CMM probe tip contacting femoral head during measurement. Right: The resulting wear map generated from the measured data points. Note the wear area clearly visible as a red area.

Volumetric Measurement of Retrieval Implants

The volumetric method was initially developed for the purpose of measuring retrieved MoM implants [13]. At the time in-vivo wear measurements of UHMPWE components were made using radiographic methods [13]. However there is debate over radiographic wear measurement accuracy as these methods were also only developed for high wear rate UHMWPE components, not the small amount of wear on MoM components [13]. Gravimetric measurement was also not applicable due to the requirement of a pre-wear measurement which is not possible with retrieval implants [13].

Pre-wear data is virtually never available for retrieved implants; however, using the volumetric method the pre-wear geometry can be estimated and reconstructed [13, 135, 136]. After initially measuring the component with the CMM, the unworn surface can be identified and separated from wear areas. Using the unworn surface data as reference, the original pre-wear geometry can be reconstructed. This reconstruction allows the pre-wear geometry to be estimated with increased accuracy compared to using the nominal radius values for reconstruction. If the pre-wear geometry is reconstructed using the nominal radius values, the error from manufacturing tolerances will lead to large uncertainty in the pre-wear geometry, affecting the post-wear results, figure 46. It is likely that the size of the manufacturing tolerance will be greater than the depth of wear areas [136]. Therefore, reconstruction of the original pre-wear geometry using volumetric measurement is a necessary step for accurate wear measurement of retrieved implants.

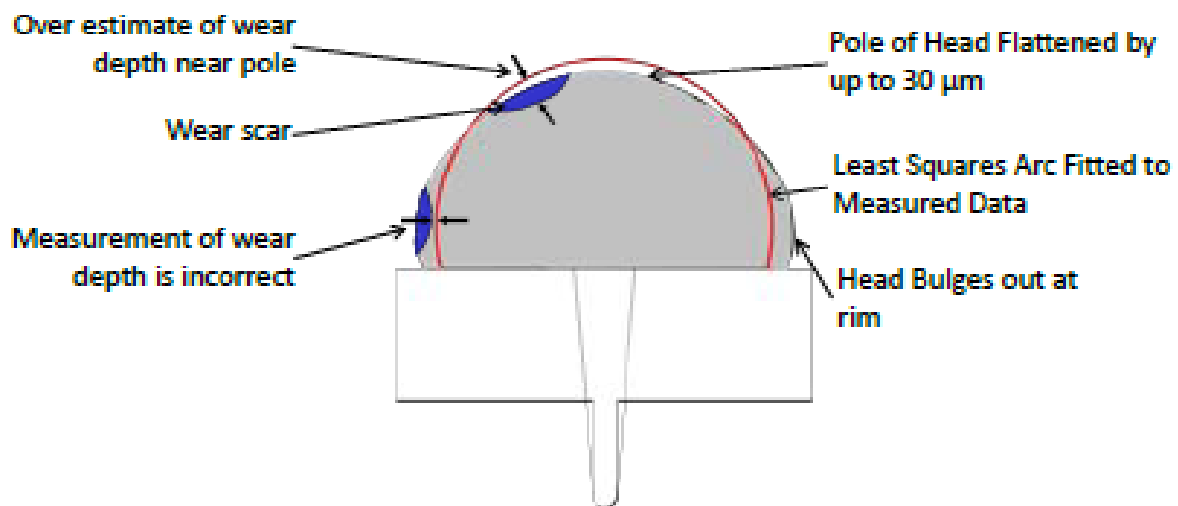


Figure 46: Reconstructing pre-wear geometry for retrieval studies [136]. The red line represents the nominal defined geometry, if this is used as the pre-wear geometry the post-wear values calculated will be inaccurate.

2.2.3.3 Measurement Uncertainty of Volumetric Method

There have been multiple methods developed for retrieval implant wear measurement over the past few decades [13, 19, 135, 137-147]. The advantage of using a CMM for wear measurements is that measurements are traceable back to a measurement standard, in this case the metre [13]. This means the measurement method is deterministic rather than comparative and can therefore be used to compare measurements from different studies [13]. Practically this is not the case because of the range of measurement methods used with different statements of accuracy [13].

A volumetric method by Bills et al [13] was developed for retrieval hip bearing wear measurement, with a focus on assessing and quantifying the measurement uncertainty of the method. Two different studies were completed whilst developing this method: Firstly, the error induced through software analysis was assessed by simulating a perfect sphere and sampling it with different mesh spacing values. Secondly a spherical measurement artefact was measured 20 times with a CMM, the measurement results were assessed in accordance with ISO 15530-3 [148] allowing an expanded measurement uncertainty value to be found.

Software Analysis and Mesh Spacing Study [13]

The mesh spacing was found to have a major influence on the results of volumetric measurement, there are three components which are considered for the mesh spacing: the scanning strategy, the distance between scan lines, and the sampling spacing (points per scan line). A polar grid scanning strategy was selected for the CMM measurement, with all scan lines emanating from the pole of the component, figure 47. This was selected over the square grid scanning strategy, as there was a minimisation of edge effects at the equator (rim) of the component, which is an issue for the square grid strategy, figure 48.

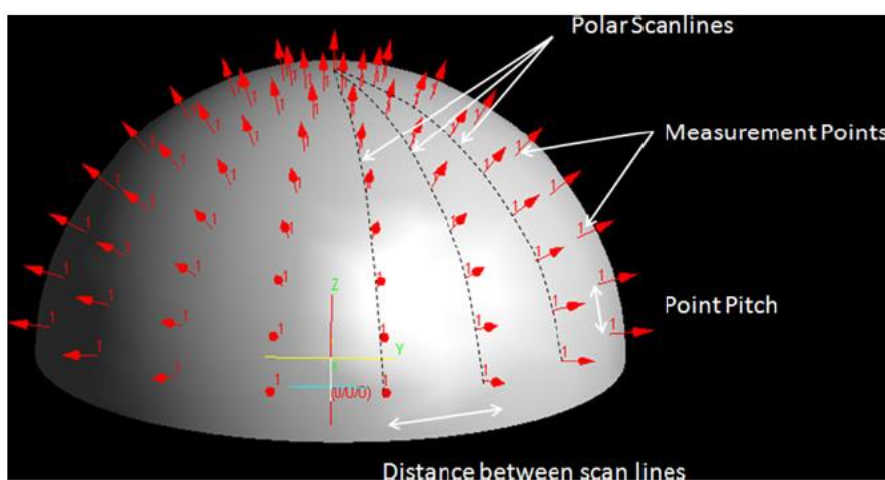


Figure 47: Polar scan strategy, each scan line emanates from the pole to the equator of the component [13].

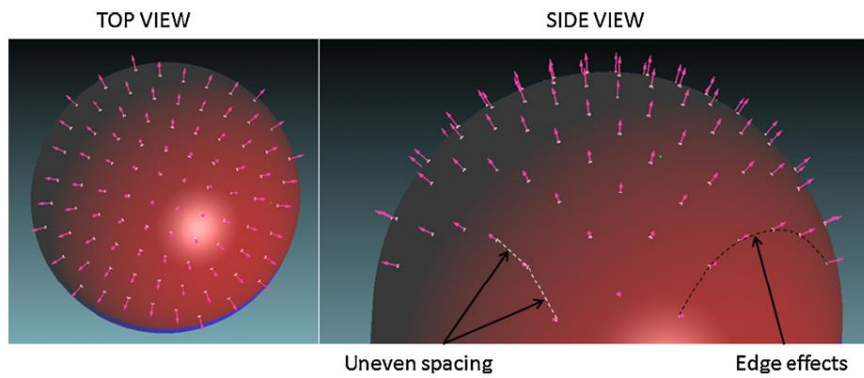


Figure 48: Square scan strategy, highlighting the resultant edge effects [13].

Using simulated data, the effect of mesh spacing was investigated, a perfect 50 mm hemi-sphere was generated, and the volume of the perfect hemi-sphere calculated. Then a range of polar scan meshes were located to the hemi-sphere and the resultant volume of the meshes was calculated. The resultant volume of the meshes was compared to the perfect sphere volume, table 6. This study demonstrated the major influence mesh spacing has on the results of volumetric measurement. It must also be considered that in a real measurement scenario, the greater amount of data points used will increase the CMM measurement time and the processing power needed for analysis.

Table 6: Deviation analysis between perfect 50 mm hemisphere and meshes with different mesh spacing parameters [13].

Number of scan lines	Max point spacing at the equator (mm)	Scan line point pitch (mm)	Total number of points	Total length of scan path (mm)	Volumetric difference (mm ³)
25	6.266	1	1025	981.75	355.895
	6.266	0.5	2000	981.75	346.614
	6.266	0.1	9850	981.75	343.543
50	3.139	1	2050	1963.50	98.627
	3.139	0.5	4000	1963.50	89.272
	3.139	0.1	19700	1963.50	86.176
100	1.570	1	4100	3926.74	34.129
	1.570	0.5	8000	3926.74	24.746
	1.570	0.1	39400	3926.74	21.644
160	0.981	1	6560	6282.78	21.008
	0.981	0.5	12800	6282.78	11.630
	0.981	0.1	63040	6282.78	8.526
	0.981	0.05	125920	6282.78	8.428
200	0.785	1	8200	7853.48	17.981
	0.785	0.5	16000	7853.48	8.603
	0.785	0.1	78800	7853.48	5.499
	0.785	0.05	157400	7853.48	5.401
400	0.392	1	16400	15706.95	13.945
	0.392	0.5	32000	15706.95	4.566
	0.392	0.1	157600	15706.95	1.462
	0.392	0.05	314800	15706.95	1.364
600	0.262	1	24600	23560.43	13.198
	0.262	0.5	48000	23560.43	3.818
	0.262	0.1	236400	23560.43	0.714
	0.262	0.05	472200	23560.43	0.616
800	0.196	1	32800	31413.91	12.936
	0.196	0.5	64000	31413.91	3.557
	0.196	0.1	315200	31413.91	0.453
	0.196	0.05	629600	31413.91	0.355
1000	0.157	1	41000	39267.39	12.816
	0.157	0.5	80000	39267.39	3.435
	0.157	0.1	394000	39267.39	0.332
	0.157	0.05	787000	39267.39	0.233

Measurement Uncertainty Study [13]

ISO 15530-3 [148] and NPL's 'Good Practice Guide' [149] detail the method for calculating the measurement uncertainty, for this study a coverage factor of $k = 2$ was used, allowing for an approximated coverage probability of 95%. Three uncertainty contributions were considered and together formed the expanded uncertainty, U , the three standard uncertainties were:

- U_{cal} : the uncertainty of the calibration of the calibrated work piece.
- U_p : the uncertainty due to the repeatability of the complete measurement procedure, calculated as the standard deviation of the 20 repeated artefact measurements.
- U_w : the uncertainty resulting from material and manufacturing variations.

The systematic error, b , and the mesh volumetric uncertainty, c , are considered separately and this results in the expanded uncertainty equation:

$$U = k \times \sqrt{(u_{cal}^2 + u_p^2 + u_w^2)} + b + c$$

Table 7: Volumetric uncertainty budget contributions [13, 148].

Contributor	Volumetric uncertainty (mm ³)
U_{cal}	0.141
U_p	0.339
U_w	0.198
b	0.311
c	0.714
$U (k=2)$	1.859

To calculate U_p a 30 mm spherical artefact was scanned with the same method as the retrieval components. The measurement was repeated 20 times and the volume of the hemisphere calculated each time. This allowed for the calculation of U_p , the standard deviation of the 20 measurements. The systematic error, b , was also calculated, the difference between the calibrated volume of the artefact and its average measured volume. A white light interferometer was used to measure the root mean square roughness (S_q) of a scratched area of the bearing surface and the surface of the calibration sphere. The maximum difference in S_q was calculated in the order of 0.14 μm , this was then used to calculate the U_w value. For a 50 mm sphere with a measurement of 160 radial lines and a point spacing of 1 mm, this would result in a volumetric error of 21.008 mm³. As wear of an orthopaedic component can be of this magnitude or less, this level of error is not suitable. Instead, 600 radial lines with a point spacing of 0.1 mm, would result in a mesh volumetric uncertainty of 0.714 mm³. A calculation of the expanded uncertainty can be made using the uncertainty sources, for a coverage factor of 2, this would result in an expanded uncertainty of 1.859 mm³.

2.2.3.4 Volumetric Method Variation

Currently the application of the volumetric method has a lack of consistency across user groups, this is a problem for both industry and research, current ISO standards are rather ambiguous allowing for large variations in the application of volumetric wear measurements [12]. Ideally the ISO standard should be stricter allowing for results from different user groups to be comparable with less uncertainty in the accuracy of results. The reasons for variation in the volumetric method can be summarised into three areas: the CMM, the measurement method, and the analysis method.

Range of CMMs

There are a wide range of CMMs available to purchase, with a range of probing systems and with differing levels of measurement uncertainty. The uncertainty of the machines taking the measurement will affect the accuracy of the results, to meet ISO standards the maximum axial-position error of measurement in microns must be: $D = 4 + 4l \times 10^{-6}$ [12]. There are a wide variety of manufacturers and models of CMMs meeting this requirement with varying levels of uncertainty.

Measurement Method

The measurement method outlined in ISO 14242-2016 is rather ambiguous [12]. On the topic of mesh spacing it only states: 'ensure the mesh spacing is no greater than 1mm'. This leaves a large amount of variation on the number of measurement points that could be used. The amount of data points used, and the shape of the mesh will play an important role in the accuracy of the results [13]. If the mesh spacing (distance between the data points) is too far apart, deviations in the surface height will not be captured, figure 49.

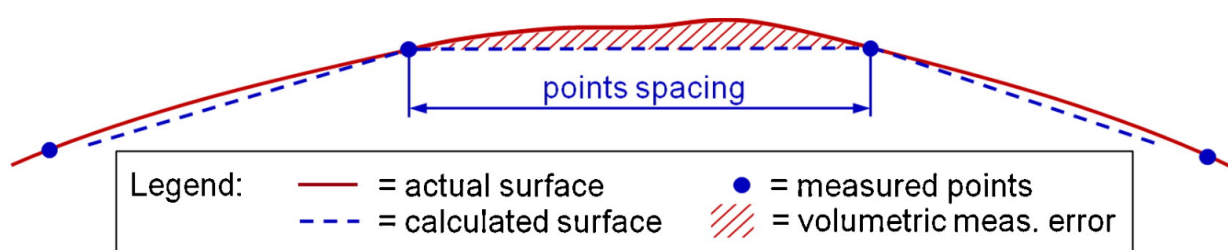


Figure 49: Measurement error caused by insufficient measurement points [150]. The actual surface (red) is not being accurately captured due to the lack of measurement points (blue circles).

Analysis Method and Software

The volumetric method requires analysis software to collate the data points and calculate the enclosed volume. The analysis method is outlined in ISO 14242-2:2016 [12], it simply states: 'Calculate the volume V_n of the acetabular cavity'. This again leaves variation on how this calculation will be

completed. A variety of analysis software tools could be used and the method for calculating the volume could also vary. This could lead to identical measurement data being calculated as different volumes and wear volumes. The analysis method is also more complicated for retrieval studies as the pre-wear geometry has to be quantified from the unworn surface, this will lead to more variation as the method to achieve this could vary. There is no advice from ISO 14242-2:2016 on how to calculate pre-wear geometry from retrieved implants.

2.2.4 Comparing Gravimetric and Volumetric Wear Measurement Methods

When comparing the gravimetric and volumetric methods it is difficult to distinguish which method is more appropriate for wear measurement, this is partly because of the amount of variation that is implemented with the volumetric method. Volumetric measurements from both optical and stylus CMMs however, have shown good agreement with gravimetric measurements [134, 150, 151]. The advantages and disadvantages of the gravimetric and volumetric methods for wear measurement are summarised below [135].

Gravimetric Advantages

- **Lower Cost** - The cost of gravimetric equipment is generally regarded as cheaper than the cost of volumetric equipment (CMM).
- **Wealth of Experience** - As the gravimetric method is more traditional, there is greater experience with this method and processes within the orthopaedic industry.
- **Less User Variance** - The method is more clearly defined compared to the variance that can occur from the volumetric method [12]. There is also no need for analysis software which can introduce further user variance.

Gravimetric Disadvantages

- **No Wear Location Information** - There is no location information data collected from the gravimetric method, only a change in weight. This means a wear map cannot be created and the size and location of the worn areas cannot be analysed.
- **Liquid Sorption Error** - Liquid sorption is a factor that can introduce error even with a control specimen.
- **Tissue Attachment Error** - If biological tissue becomes attached to the component and is not removed during cleaning, this can introduce error. This is more likely to occur in uncemented components which have coatings designed for tissue ingrowth.
- **No Retrieval Studies** - Due to the requirement of pre-wear measurements, retrievals cannot be measured.

- **No Geometric Information** - The radius and sphericity cannot be calculated.
- **Difficult to Assess Hard-on-Hard Bearings** - When assessing hard-on-hard bearings the volume of material removed can be so little it can be hard to measure the change in weight from pre-wear to post-wear.

Volumetric Advantages

- **Wear Location Provided** - The location, size and depth of wear areas can be analysed, and a wear map can be created.
- **Geometric Parameters** - The radius and sphericity can be calculated, which is required for quality inspection.
- **Retrieval Studies** - The measured unworn surface can be used to reconstruct the original pre-wear geometry, analysis of retrieval implants is possible.
- **Reduced Chance of Liquid Sorption Error** - The influence of liquid sorption error is greatly reduced as the volumetric measurement does not rely on weight measurement.
- **Reduced Chance of Biological Tissue Attachment Error** - As the volumetric measurement is isolated to only the bearing surface any biological tissue attachment on the backside of the cup cannot affect results.

Volumetric Disadvantages

- **Increased Cost**
- **Fixturing Error** - If the component is not fixtured securely in place then error can be introduced to the measurement, the component must be firmly secured but not geometrically altered.
- **User Variance** - As previously discussed this method has high user variance as the ISO method outlined is ambiguous, for both the measurement and analysis method.
- **Contact Damage from CMM Probe** - This is not an issue for non-contact CMMs.

2.2.5 Surface Metrology

Surface metrology is used during quality inspection to ensure the components surface finish is within design tolerances. Surface metrology is also useful as part of experimental studies to understand the tribological mechanisms occurring at the bearing surface.

2.2.5.1 Surface Measurement Instruments for Hip Implant Bearing Surfaces

The areal arithmetic mean deviation (S_a) of new bearing surfaces typically ranges from approximately 1 nm to 200 nm depending on the material type [9], CMM measurement cannot provide the level of resolution required to detect these surface deviations, therefore a different type of instrumentation is required.

The Stedman diagram is used to display aspects of the performance of instruments measuring surface roughness [152, 153]. Stedman diagrams are commonly used to compare the features of a range of measuring instruments [152, 153]. The traditional Stedman diagram assumes the surface is made up of sin waves of differing amplitude and wavelength. It plots the surface wavelength in the x axis and surface amplitude in the y axis, with the capabilities of measurement instruments indicated as an area on the plot [153]. Some Stedman diagrams have been adapted to also include data acquisition speed as a factor in the z axis, this demonstrates the clear superiority of areal measurement over profile for data acquisition speed [152].

As shown on the Stedman diagram, figure 50, the required amplitude range for hip implant bearing surfaces, 1-200 nm, is ideally located in the range of optical surface measurement instruments. Also notice the CMM area is lacking in the required level of resolution to achieve these surface measurements.

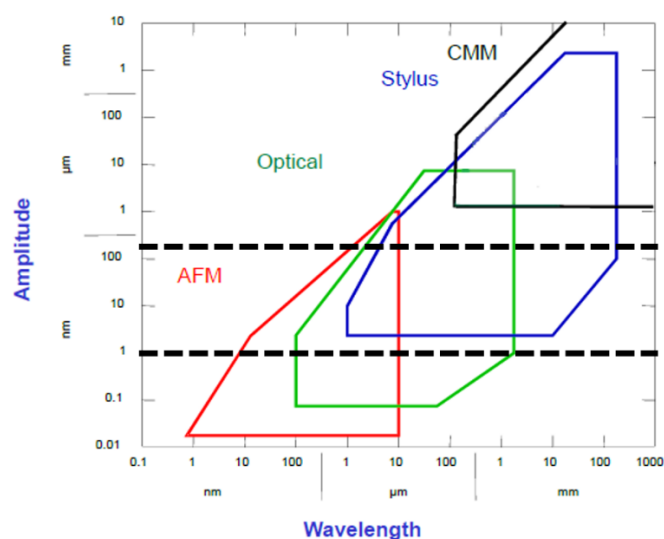


Figure 50: Stedman diagram showing the typical measurement capabilities of measurement instrument groups (adapted from) [153]. Black dashed lines indicate the range of surface amplitude that requires measuring for hip implant bearing surfaces. Note that the optical range ideally captures this range.

2.2.5.2 Profile and Areal Measurement

A surface measurement can be considered a collection of surface point heights. These points can either be taken over a single line, referred to as profile measurement, or they can consist of multiple profile or array measurements built up to form a measurement over a larger area, this is referred to as areal measurement [154].

Profile measurement is the more traditional approach using a contact stylus to measure the surface, it is quicker and simpler in its analysis, but has major limitations, figure 51 [15]. A profile measurement can identify the height and depth of surface features, but it cannot determine if these features are long or short across the surface [15]. Due to the single measurement trace captured by profile measurement there is increased possibility that important surface features are not captured, especially if the surface has multidirectional features. This is particularly the case for worn bearing surfaces as the surface topography can change greatly over a very small distance. Profile measurements are better used for newly manufactured surfaces which tend to be more uniform in their surface topography due to no wearing taking place.

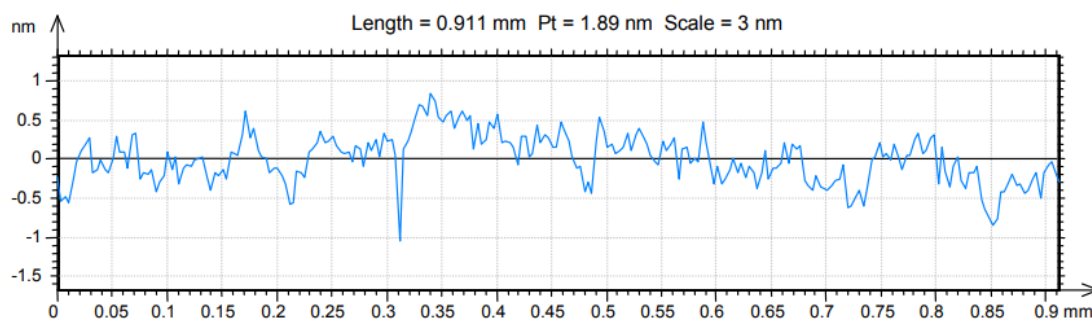


Figure 51: Example of a profile type surface measurement [15].

The areal approach has a range of measurement methods but most commonly for hip implant bearing surfaces a variant of optical interferometry is utilised. The areal measurement produces a 2.5-dimensional representation of a surface, acquiring a larger amount of surface data [15], figure 52. The sampling area refers to the size of the xy plane of the measurement [15]. Areal measurement allows the surface to be analysed in more detail and is a more sophisticated, flexible and statistically representative measurement of the surface [155, 156]. As areal measurement allows surface features to be measured in three dimensions, this reveals the 'length' of surface features, leading to a better understanding of the surface [15], figure 53. For hip implant bearing surfaces, areal surface measurement is desirable and is used widely across manufacturers using internal quality specifications. As areal measurements capture a larger measurement area, this reduces the possibility of important surface features being missed. If required, profile plots can easily be taken from areal measurements using analysis software.

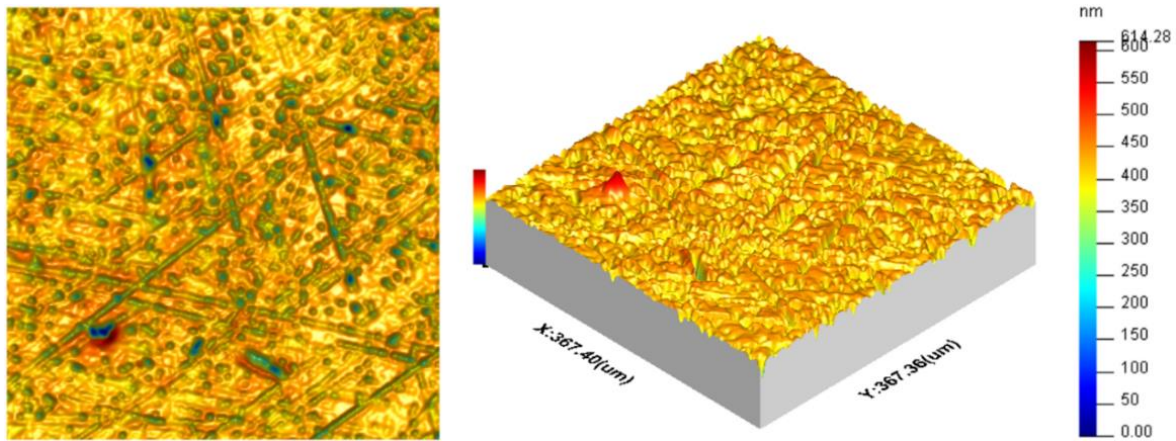


Figure 52: Example areal optical surface measurement of a retrieved CoCr femoral head.

Figure 53 shows an area and profile measurements of the same bearing surface and demonstrates the benefits of the areal measurement compared to profile measurement for hip implant bearing surface measurements. The profile measurement can identify a clear pit, however on the areal surface map the pit can be seen to actually be a valley covering the entire Y length of the areal measurement. The areal measurement captures much more functional information, ensuring anomalies do not greatly affect results, and the areal measurement allows the user to get a better overall judgment of the surface tribology and functional history.

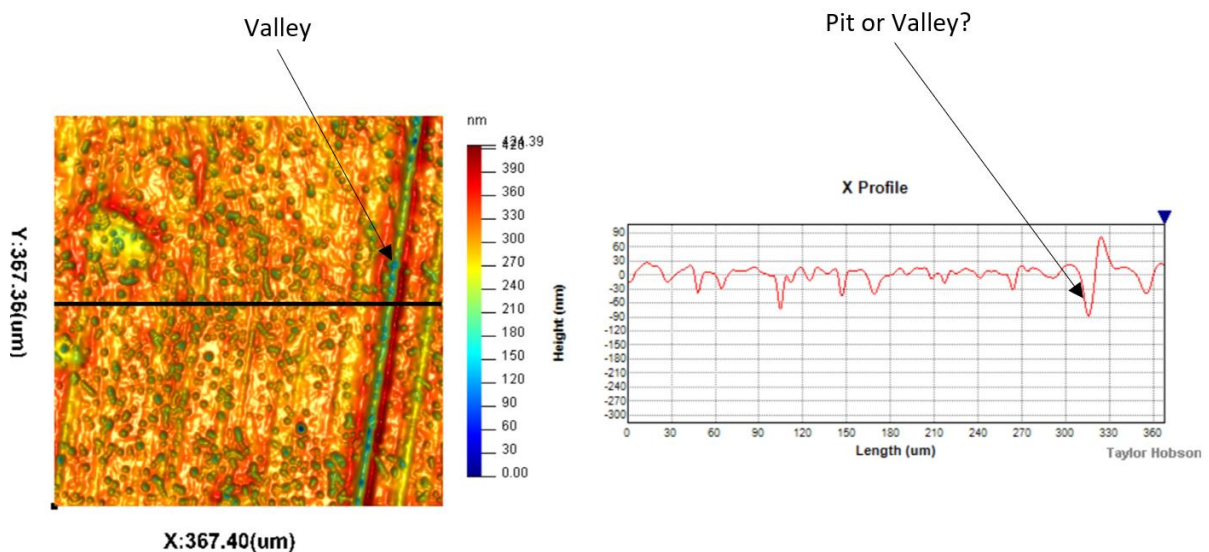


Figure 53: Areal and profile surface measurements of a retrieved CoCr femoral head compared. Areal surface measurement (left) compared to an extracted profile measurement (right). The black line through the areal measurement represents the surface recorded by the extracted profile.

2.2.5.3 Surface Filtering

Traditionally surfaces are considered a summation of several sinusoidal waveforms, they are grouped in three spatial domains, these are: form, waviness, and roughness, figure 54. The form is the longest waveform, this waveform represents the geometric shape of the sample. In the case of a hip implant, this will be the spherical shape of the head and cup component. The waviness is an intermediate wavelength of repeating pattern, it could be manufactured intentionally to have this waviness, or it could be caused during manufacture. Waviness is not always easily detected on a surface, this is particularly the case for very smooth polished surfaces. If present on polished surfaces it is often referred to as mid spatial frequencies. Roughness is the wavelength with the highest frequency and shortest wavelength, roughness is the classical wavelength used for metrological analysis. It usually results from the event pertaining to the materials removal mechanism. Before the roughness can be analysed, according to a specified standard, the form and waviness wavelengths must be removed through surface filtering [15, 154].

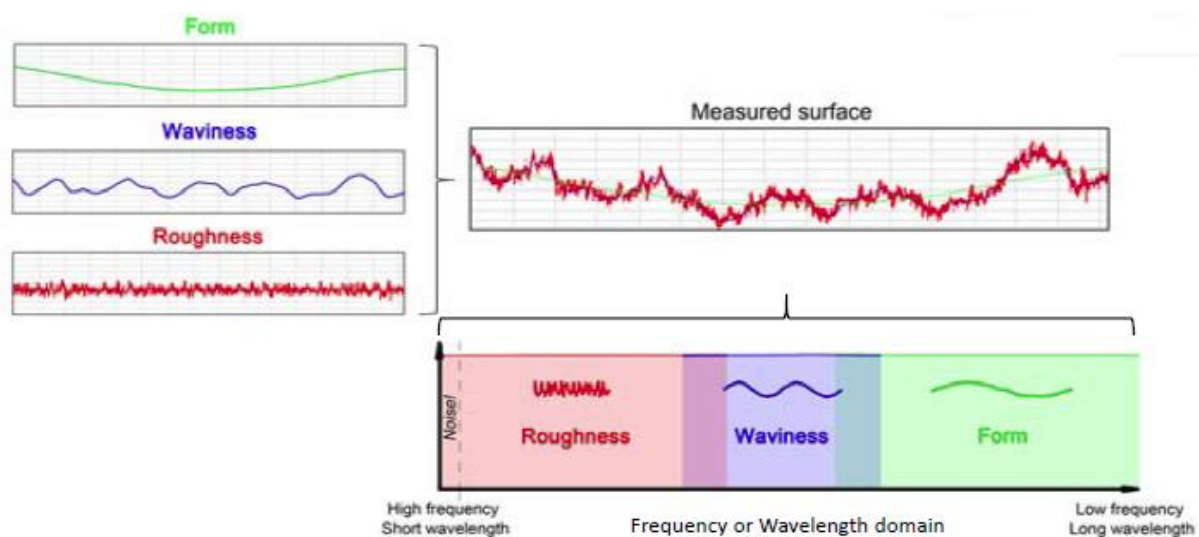


Figure 54: Profile surface measurement split into waveforms. These same filtering principles can apply to areal measurement[155].

Since the uptake of areal measurement, new methods for filtering have been implemented [119, 154]. For areal measurements, two filters are defined, the S-filter and the L-filter, figures 55 and 56. The S filter removes unwanted small-scale/high frequency lateral components, such as measurement noise or functionally irrelevant small features. The L-filter is used to remove unwanted large-scale lateral components of the surface such as waviness. There is also an F-operator that removes the nominal form. An SF surface results from using an S-filter and an F-operator (equivalent to a primary profile), an SL surface (equivalent to a roughness surface) results from using an L-filter on a SF surface. SF and SL surfaces are called scale-limited surfaces. When comparing surfaces in a study, it is crucial that surface measurements use identical filtering methods, otherwise the results will not be comparable

[154, 156]. A Gaussian regression filter is a good general-purpose filter and is the current recommended approach for S-filters and L-filters [15, 119]. In contrast to conventional 2D profile analysis the scale limited approach generalises the approach to implementing filters and consequently does not define specific wavelength boundaries between roughness and waviness. Consequently, the scale limited approach is suited to surfaces ranging from conventionally manufactured to atomic scale topographies. The recommended type of filter that should be applied to a measured surface can be found in ISO 25178-3:2012-Part3 [119]. Once the surface has been successfully filtered e.g. (SL surface) it is then suitable for quantification through the use of areal roughness parameters.

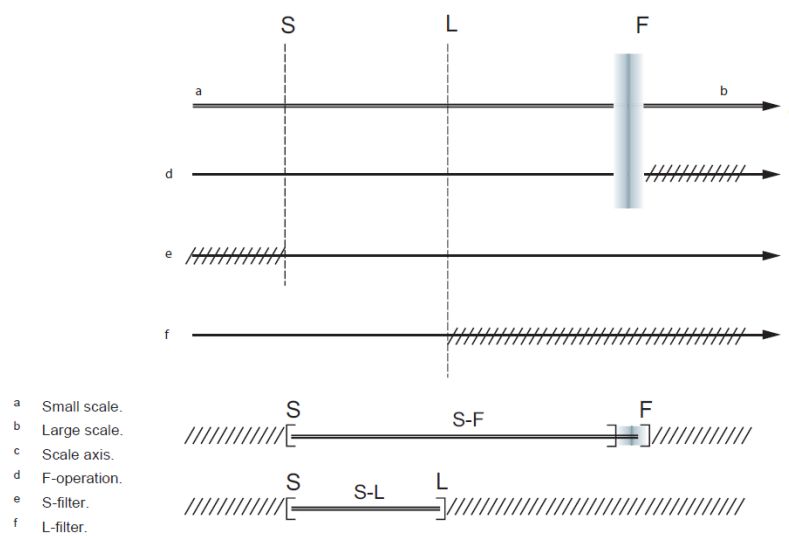


Figure 55: Relationships between S-filter, L-filter, F-operator and SF and SL surfaces [154].

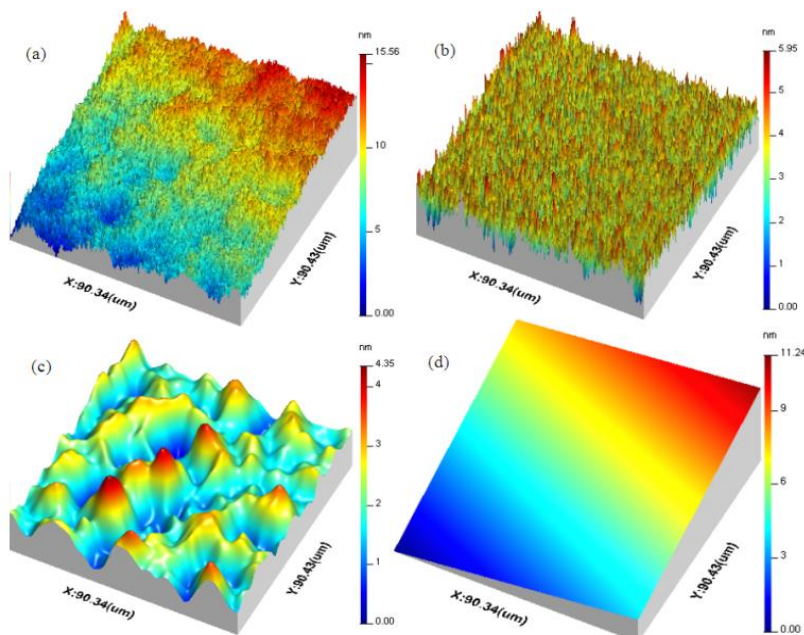


Figure 56: Scale limited surface filtering using a Gaussian filter. Raw measured surface (a), roughness surface (SL-surface) (b), primary surface (SF surface) (c), F-operator (d) [15].

2.2.5.4 Surface Measurement Methods

Michelson Interferometer

Interferometry is an optical measurement method using the phenomenon of light wave interference to measure the distance to a surface at a high level of precision. Interferometry is used for surface measurement but is also applied in calibration, mechanical stage motion, precision machining and precision length measurement scenarios [157, 158].

The first demonstration of using interferometry as a measurement tool was the Michelson interferometer in the 1880's. Although technology has much improved since then, the fundamentals of the measurement method still remain the same, figure 57. A beam splitter is used to split a light source into two beams, one beam is directed into a reference mirror, the other beam is directed to the displaceable mirror. The beams reflect back from each mirror and are superposed at the beam splitter and the resulting interference pattern hits the detector. The path difference between the two beams causes a phase difference and an interference pattern. If the distance to the displaceable mirror is changed, this will result in a change in the interference pattern. The change in the interference pattern is directly related to the change in displacement, allowing for a very precise displacement measurement, this is the basic principle of interferometry measurement [157, 158]. In modern instruments the interference pattern is directed onto an image sensor, creating an interferogram. The pattern of the fluctuating optical interference fringes can be converted into an electrical signal to allow for analysis on a computer [158].

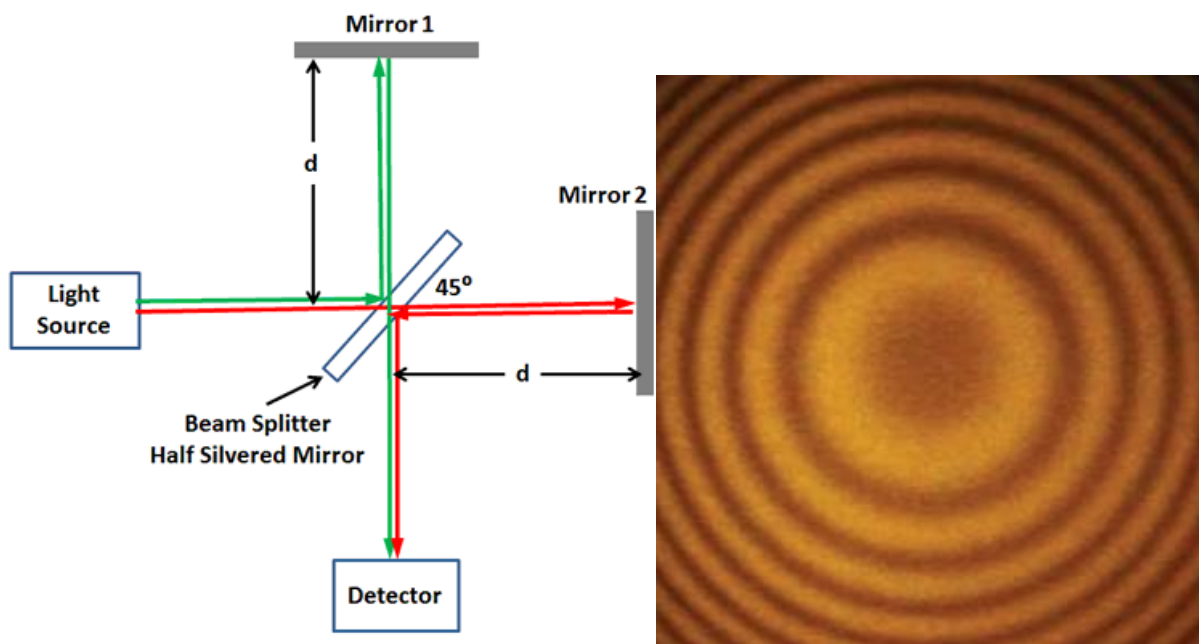


Figure 57: Michelson Interferometer. Left: Diagram of the Michelson interferometer setup [159]. Right: Interference pattern from a Michelson interferometer [160].

Coherence Scanning Interferometry

Coherence scanning interferometry (CSI) is a common term given to a group of interference microscopes which utilise white light interferometry, other common names include: scanning white light interferometry (SWLI) and vertical scanning interferometry (VSI) but many other similar names are used [161]. CSI is currently one of the most common methods for areal surface measurement due to its flexibility and broad application for measurement [14]. CSI can be used to measure smooth surfaces, under 50 nm, which is crucial for measurement of metal or ceramic bearing surfaces [15].

CSI uses a beam splitter to generate an interferogram of the surface, this interferogram is directed onto a digital image sensor, the sensor captures the interferogram and converts it to digital data. The objective lens is moved vertically downwards very precisely using a piezo drive system starting from just above the focal length of the interferometer lens and then moves downwards until all of the surface has been measured. The resulting interferogram detected at the CCD image detector is continuously changing as the highest points of the surface cause interference. The highest interferogram contrast points can be recorded for each pixel using the digital image sensor. As the position of the lens is tracked downwards the surface height of each pixel is recorded and a 2.5 dimensional map of the surface can be generated [15], figure 58. Optical interferometry can resolve surface feature below 1nm and is particularly useful for polished implant surfaces. The methodology however requires enough light to return from the surface to give interference and is not suitable for rougher surfaces or surface with significant slope.

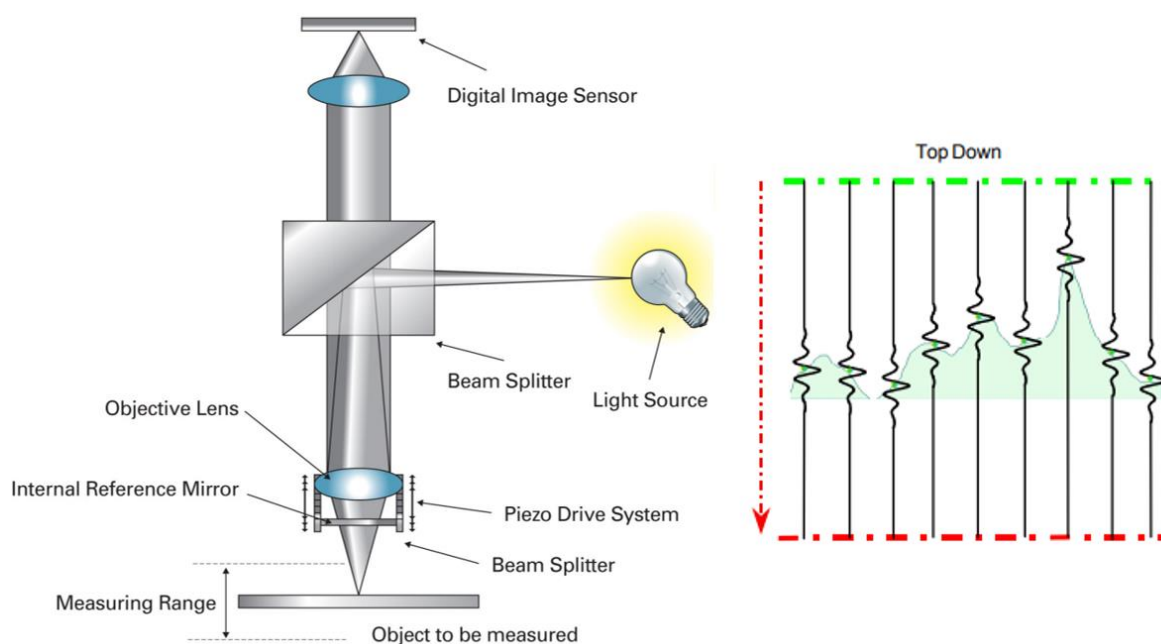


Figure 58: Coherence scanning interferometry. Left: Modern CSI microscope setup [15]. Right: CSI measures the peak height of each pixel as the lens moves downwards, creating a three-dimensional surface topography [15].

Focus Variation

Focus variation is another popular method for measurement of surface topography, focus variation utilises a combination of optics with limited depths of field and vertical scanning [161]. Focus variation is performed by searching for the best focus position whilst measuring a surface, as the measurement is undertaken the optic is moved precisely vertically (similar to the CSI method) and a depth map of the surface is generated [161], figure 59. By moving the lens downwards vertically, the highest points of the surface will come into focus, as the lens continues to move downwards the entire surface topography will come in and out of focus. The highest points can be recorded for each pixel using the digital image sensor to capture the point of maximum contrast with neighbouring pixels. As the position of the lens is tracked downwards the surface height of each pixel is recorded and a 2.5 dimensional map of the surface can be generated [161]. Focus variation is excellent for machined surfaces and surfaces of higher slope as it requires less returned light. It is however poor for the quantification of polished surfaces due to the difficulties of pixel to pixel contrast on light returning from smooth surfaces.

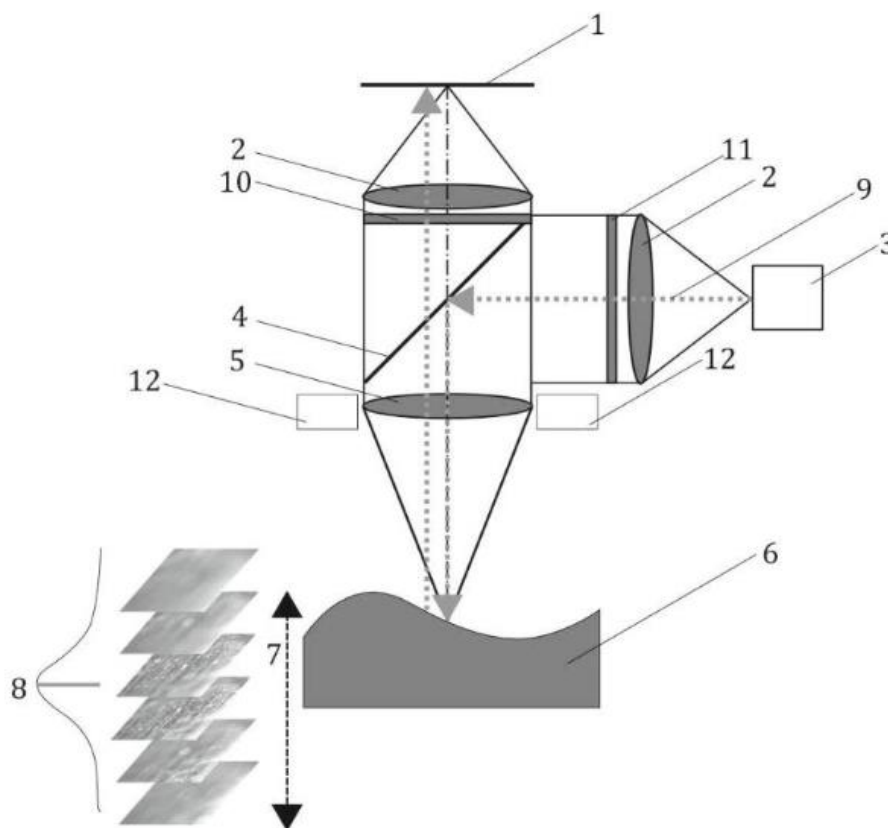


Figure 59: Focus variation surface measurement [161]. (1) CCD sensor, (2) lenses, (3) white light source, (4) semi-transparent mirror, (5) objective lens with limited depth of field, (6) surface, (7) vertical movement with driving unit, (8) contrast curve calculated, (9) light rays, (10) optical analyser, (11) optical polariser, (12) optional light ring.

2.2.5.5 Performance Specifications

Often the performance specifications for confocal microscopes (including focus variation types) and optical interferometers can be confusing and misleading [162]. This is due to the large amount of specification parameters and an inconsistency across manufacturers among which are used [162]. De Groot [162] provides an example performance specification for a CSI instrument, table 8.

It is often considered that the most desired performance parameter would be the vertical resolution, the minimum amount of variation in Z height that can be detected. However, note that vertical resolution is not included in the example specifications table. The term vertical resolution in standardised metrology refers in most cases to the number of digits displayed as the output, consequently it is preferable not to use vertical resolution as a synonym for detectability of small surface heights [162]. It is preferable to actually instead use the repeatability of the RMS parameter or the repeatability of the Sq parameter [162]. More information about performance specification parameters can be found in ISO 25178-604 [163]. The performance specifications of the Bruker Contour GT-X, a CSI instrument, is shown in table 9, note the use of RMS repeatability instead of vertical resolution. Interferometers with sub nanometer RMS repeatability are considered to be highly appropriate to measure and quantify the polished surfaces encountered on hip implant surfaces.

Table 8: Example specifications for a CSI instrument [162].

Specification	Value	Footnotes
Surface topography repeatability	0.1 nm	Repeatability (1σ) for SmartPSI mode, 1 second data acquisition, 1 million image points, 3×3 pixel surface filtering
Repeatability of the RMS	0.005 nm	Repeatability (1σ) of the ISO Sq parameter, same conditions as for the surface topography repeatability
Optical lateral resolution	0.33 μm	100 \times , 0.85 NA objective, Sparrow criterion
Lateral sampling	0.04 μm	100 \times objective, 2 \times zoom
Step height accuracy	0.8 %	Instrument contribution to the uncertainty ($k = 1$) for step height measurement in extended scan mode (0.15 mm to 20 mm range)
Height response linearity	≤ 20 nm	Maximum deviation with respect to the best fit linear response
Step height repeatability	0.1 %	Repeatability (1σ) in reported step height as verified using a 1.8 μm and 24 μm standard artefacts

Table 9: Typical performance of a modern coherence scanning interferometer Bruker Contour GT-X [164].

Max Scan range	<10 mm
RMS Repeatability	<0.03 nm
Lateral Resolution	0.38 μ m
Step Height Accuracy	<0.75%
Step Height Repeatability	<0.1%
Max. Scan	114 μ m/sec
Sample Reflectivity	0.05%-100%
Max. Sample Slope	Up to 40° (shiny surfaces); Up to 87° (rough surfaces)

2.2.5.6 Surface Measurement Parameters

There are a wide array of surface parameters that can be used to define a surface [15, 154], the suitable parameters depend on the performance requirements of that surface.

Surface parameters as defined in ISO25178-Part 2 [154] are split into field and feature parameters. The field parameters use all the XYZ information collected by the metrology instrument in the calculation of parameters. Field parameters on the other hand use only information from previously segmented surface features before quantification of the feature parameters is carried out. In the following section what is considered the most relevant areal surface parameters for analysing worn hip implant bearing surfaces will be discussed.

Maximum Height (S_z), Maximum Peak Height (S_p), Maximum Pit Depth (S_v) (Field Parameters)

The parameters S_z , S_p and S_v are used to define the maximum and minimum height values of the surface, figure 60 [15, 154, 165]. These are basic but powerful parameters when analysing surface measurements. For example, the maximum depth of the deepest scratch on the bearing surface can be measured using the S_v parameter, allowing bearing surfaces to be compared by their deepest scratches.

Arithmetical Mean Height (S_a) and Root Mean Square Height (S_q) (Field Parameters)

The S_a parameter represents the arithmetic mean of the absolute value of the surface departures $Z(x,y)$ within the sampling area relative to a mean fitted surface, figure 60. S_q is a similar parameter to S_a that offers a more statistically significant analysis, despite this S_a remains a popular parameter. The S_q parameter represents the root mean square value of the surface departures, $Z(x, y)$ within the sampling area relative to a mean fitted surface, figure 60. The S_a and S_q parameters are the most commonly used areal parameters as they give a good indication of the overall surface roughness.

When the height distribution is normal, the relationship between the parameters S_q and S_a is approximately $S_a = 0.8 * S_q$ [15, 154, 165].

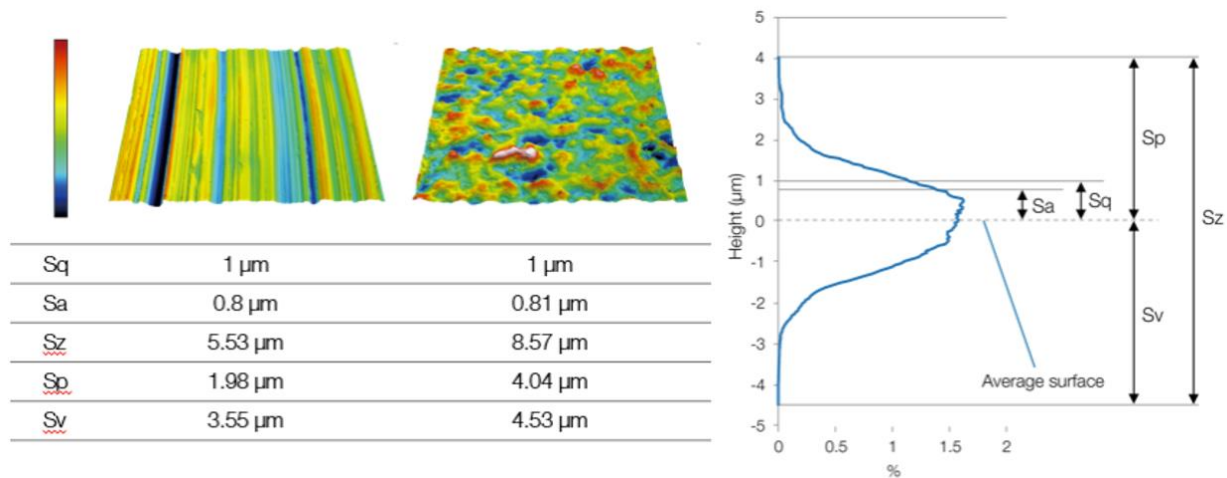


Figure 60: Areal height parameters. Left: Two areal surface measurements and the resulting height parameters. Right: Diagram showing how each parameter relates to the height of the surface [165].

Ideally for implant surfaces the S_a/S_q value should be as low as possible as this indicates the peaks and valleys of the surfaces are smaller. Smaller surface peaks increases the likelihood that the bearing interface is operating in fluid film lubrication mode resulting in better tribological performance conditions. Figures 61–63 show areal surface measurements with identical S_q values, however the surface topography of each measurement is clearly different. This highlights the importance that other parameters are also required to define a surface when analysing to a high level of detail.

Skewness (S_{sk}) (Field Parameter)

The S_{sk} parameter defines the distribution of the surface above or below the mean fitted plane, figure 61. A positive skewness value indicates a greater amount of surface below the mean plane (peak dominated), a skewness of 0 indicates an equal/Gaussian distribution of surface above and below the mean plane and a negative skewness indicates a greater amount of surface above the mean plane (valley dominated) [15, 154, 165]. A negative skewness usually indicates a surface that has been polished as the peaks of the surface have been removed as part of the polishing process.

Ideally a bearing surface should have a negative skewness, a negative skewness results in fewer peaks and more valleys. With less peaks the chance of asperities contacting between bearing surfaces is decreased, therefore also reducing the amount of wear debris production. The increased number of valleys also allows for lubrication to be transported through valleys, improving the presence of lubrication.

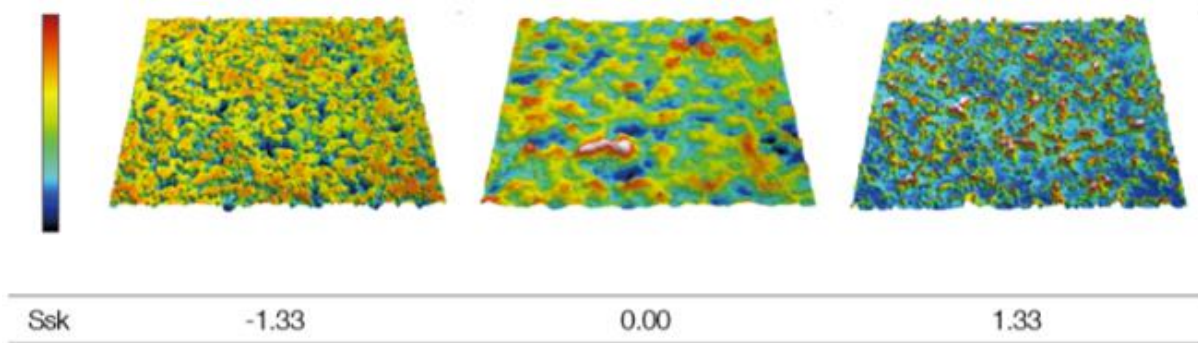


Figure 61: Areal surface measurements with identical S_q values but varying S_{sk} values [165].

Density of Peaks (Spd) and Arithmetic Mean Peak Curvature (Spc) (Feature Parameters)

The Spd field parameter indicates the number of significant peaks per unit area, figure 62. Only peaks that exceed a designated height (Wolf Prune) are included in the count, this set height is most commonly 5% of the maximum height (S_z) but can be adjusted [15, 154, 165]. It is important to note that because the number of peaks counted is set by the maximum height of the surface, as per the 5% of S_z inclusion standard, smoother surfaces will include smaller peaks as part of their Spd count. Therefore, when comparing surfaces to each other, the set height at which peaks are included should be set to the same numerical value across all surfaces as to allow for a fair comparison.

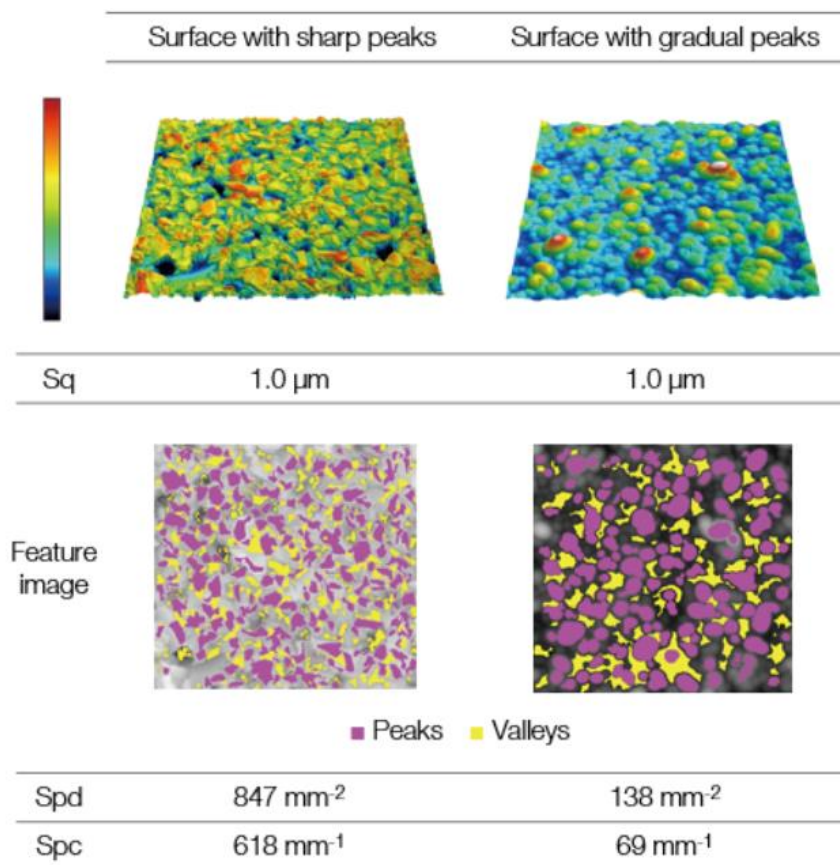


Figure 62: Areal surface measurements with identical S_q values but varying Spd and Spc values [165].

A lower Spd value indicates a lower count of peaks within the measurement area. The Spc parameter indicates the average curvature ($1/\text{Peak Radius}$) of the peaks which are included in the Spd count, a lower Spc value indicates a more rounded peak, figure 62.

Ideally the bearing surface should have as low as possible Spd and Spc values as this indicates a surface with minimal amounts of peaks, which when present have a smooth curvature. A lower number of peaks reduces the chance of asperities contacting between bearing surfaces and therefore reduces the chance of wear particle production.

Root Mean Square Gradient (Sdq) (Field Parameter)

The Sdq parameter indicates the mean magnitude of the local gradient (slope) of the surfaces, if the value increases the local surface is more steeply inclined [15, 154, 165], figure 63. Ideally the Sdq value for implant bearing surfaces should be low as this indicates a smooth surface transition between features which is ideal for a bearing surface.

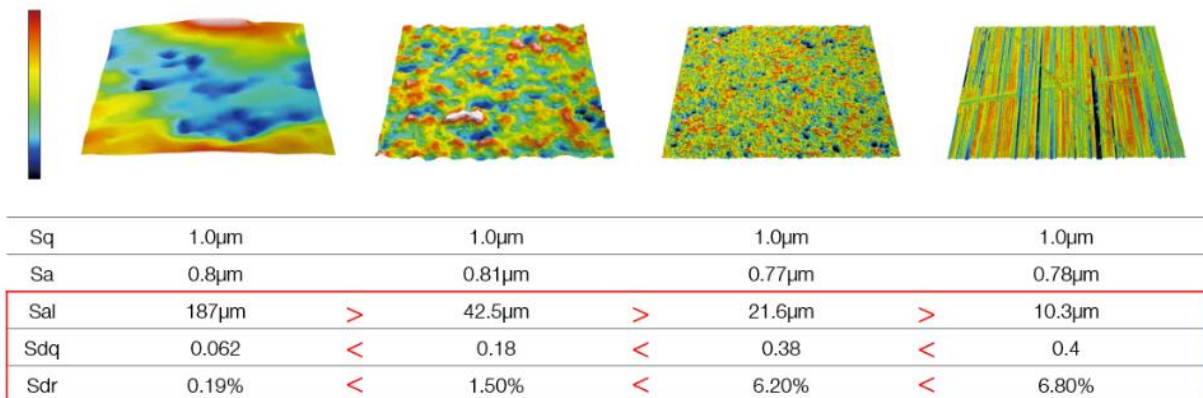


Figure 63: Areal surface measurements with identical Sq values but varying Sdq and Sdr values [165].

Developed Interfacial Area Ratio (Sdr) (Hybrid Parameter)

Sdr, the Developed Interfacial Area Ratio, is expressed as the percentage of additional surface area contributed by the texture as compared to an ideal plane the size of the measurement region [166].

Sdr may further differentiate surfaces of similar amplitudes and average roughness. Typically, Sdr will increase with the spatial complexity of the texture whether or not Sa changes. Sdr is useful for implant bearing surfaces when considering the interface tribology, in other words an ideal smoother surface would have a lower Sdr. Sdr is affected both by texture amplitude and spacing, a higher Sa, with a wider spaced texture may have actually a lower Sdr value than a lower Sa but finer spaced texture, figure 64.

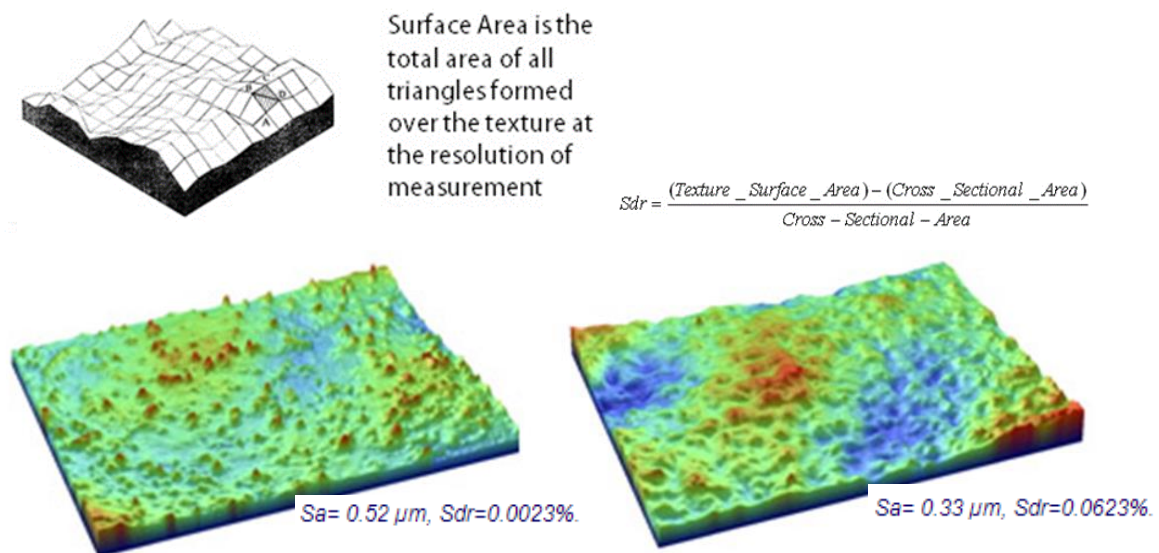


Figure 64: Developed interfacial area ratio (Sdr) [166].

Texture Direction (Std) (Field Parameter)

The texture direction is determined by the APSDF (angular power spectral density function) and is a measure of the angular direction of the dominant lay comprising a surface [167]. Std is defined relative to the Y axis. Thus, a surface with a lay along the Y axis will return a Std value of 0, figure 65. This can be particularly useful to see if surface scratches are uni-directional or multi-directional in their orientation.

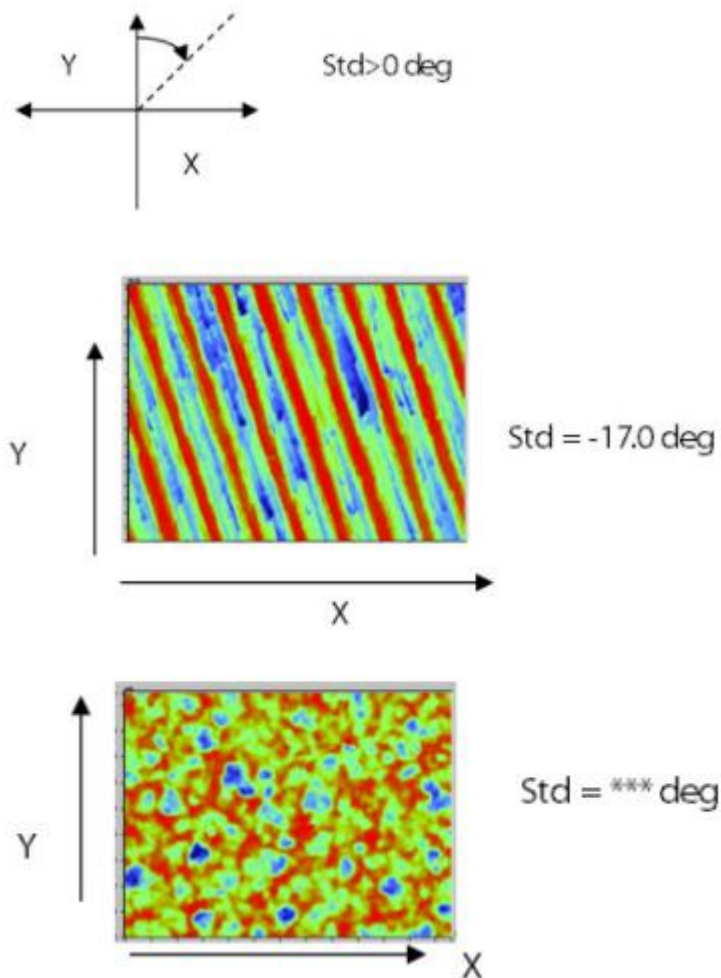


Figure 65: Texture direction (Std) [167].

There are many more surface parameters which can be used, the definitions of these parameters can be found in ISO 25178-2:2012 Part 2 [154].

The surface parameters discussed above demonstrate why using only the Sa/Sq parameters to describe a surface is not ideal and how measurements with identical Sa/Sq values can have very different topographies and therefore different tribological performance.

2.2.6 Chapter Summary

The most common applications of metrology in the orthopaedics industry are during quality inspection of new components and experimental studies of new designs or retrieval implants [10-12].

Due to the prevalence of aseptic loosening induced by wear particles [4-6], a common focus of experimental studies is the wear performance of the implant [12]. Wear measurement is the most effective tool in diagnosing implant failure mechanisms and determining long term performance of orthopaedic implants [13]. Coordinate measurement machines (CMM) are commonly used for volumetric wear measurements [12]. Allowing a wear map of the bearing surface to be created, and the size and location of wear areas to be analysed [13].

To understand wear mechanisms and tribological behaviour at a micro/nano scale, areal surface measurements can be used. Coherence Scanning Interferometry (CSI) is currently one of the most common methods for areal surface measurement due to its flexibility and broad application for measurement [14]. CSI can be used to measure smooth surfaces, under 50 nm, which is crucial for measurement of metal or ceramic bearing surfaces [15]. A range of areal surface parameters can be used to analyse hip implant bearing surfaces [154], allowing quantitative patterns to be studied, using these findings to improve future hip implant design.

2.3 Surface Metrology Studies on Worn Hip Implant Bearings

2.3.1 Changing Surface Topography within Wear Areas

When measuring the surface on worn hip implant bearing components it is important to understand that the surface topography varies considerably within the wear area compared to the unworn surface across the rest of the component. This change in surface topography has been shown in multiple experimental studies for all popular bearing material combinations [17-24, 109]. Depending on the material combinations the surface topography change can be smoothing or roughening. Therefore, when surface measurements are taken on worn bearing surfaces, they need to be positionally targeted both within and outside the wear area to give a comprehensive analysis of the entire component.

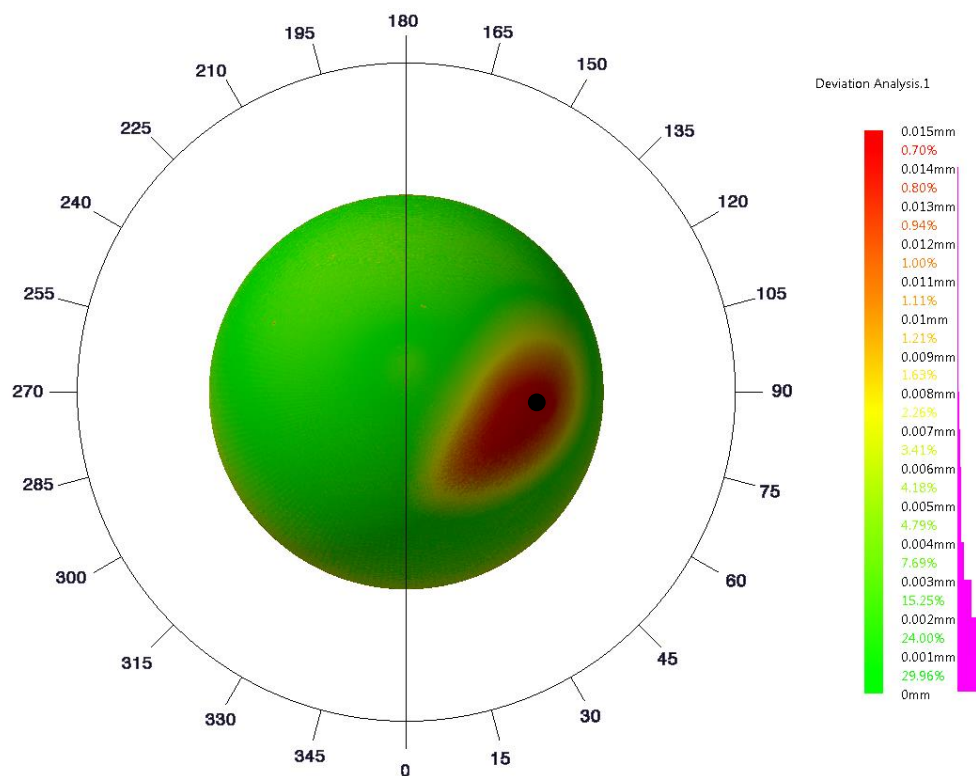


Figure 66: Wear map of a retrieved MoM femoral head, CMM measurement and CATIA analysis. The wear area can be identified as the red area. The maximum linear wear depth within the wear area is indicated by a black dot.

2.3.1.1 Metal-on-Metal

Mckellop et al. [168] collated previous research on MoM hip implant wear and using their own practical examples of wear damage proposed the correct terminology to be used. Example images for each type of wear damage are shown in figure 67.

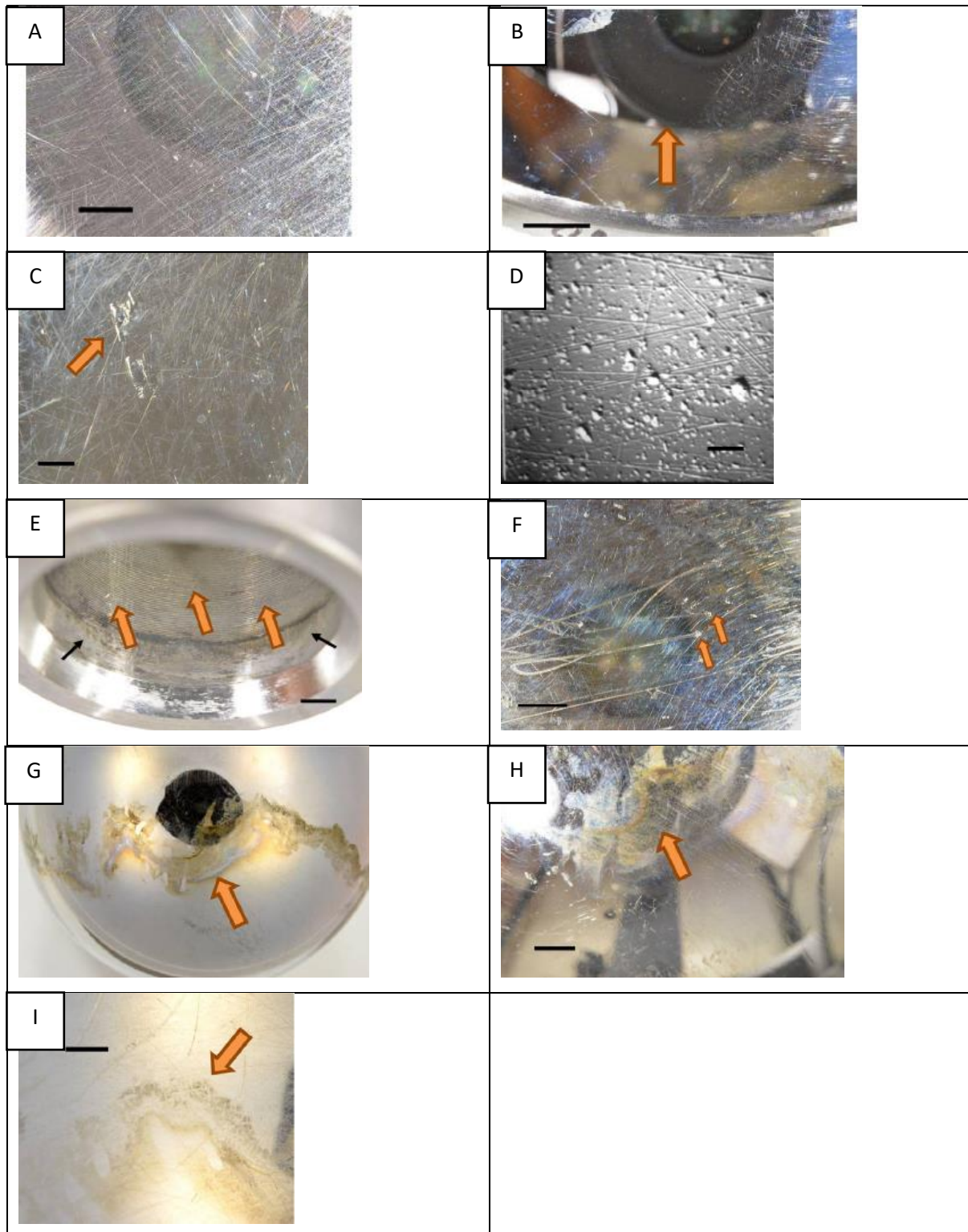


Figure 67: Types of wear damage for MoM hip implant bearings [168]. A: Scratching, B: Polishing, C: Gouging, D: Pitting, E: Etching, F: Embedded Particles, G: Surface Discolouration, H: Surface Deposits, I: Tribo-chemical Reaction Layers.

The change in surface topography within wear areas was first studied by P.S. Walker and B.L. Gold in 1971 [109]. The surface finish was compared for 10 retrieved MoM implants between the unworn areas and within the wear area. The surface roughness increased up to 5x within the wear area compared to the unworn area. The main type of wear occurring was considered to be abrasive wear caused by trapped third body debris within the bearing interface. Scratches across the sample were a wide variety of different widths, depths, and direction. However, the largest scratches tended to be uni-directional in the flexion-extension direction. It was noted that the scratches seen were usually absent of 'scratch lips' this could indicate that once a scratch was produced the 'scratch lip' was either flattened or removed as wear debris.

Witzleb, 2009 [19], analysed the wear rate of retrieved MoM resurfacing components. As well as CMM volumetric analysis of the components, SEM surface images were taken within the wear area and the unworn area, figure 68. On the wear area surface image, fine multidirectional scratches can be observed across the entire surface, then larger unidirectional scratches can be observed emanating from the bottom left to upper right corner of the surface image. There is no indication of block carbides which can be seen on the unworn surface image. These block carbides must have been removed through the wearing of the surface. The evidence of both fine multidirectional scratches and larger unidirectional scratches matches the surface pattern findings by Howie [17].

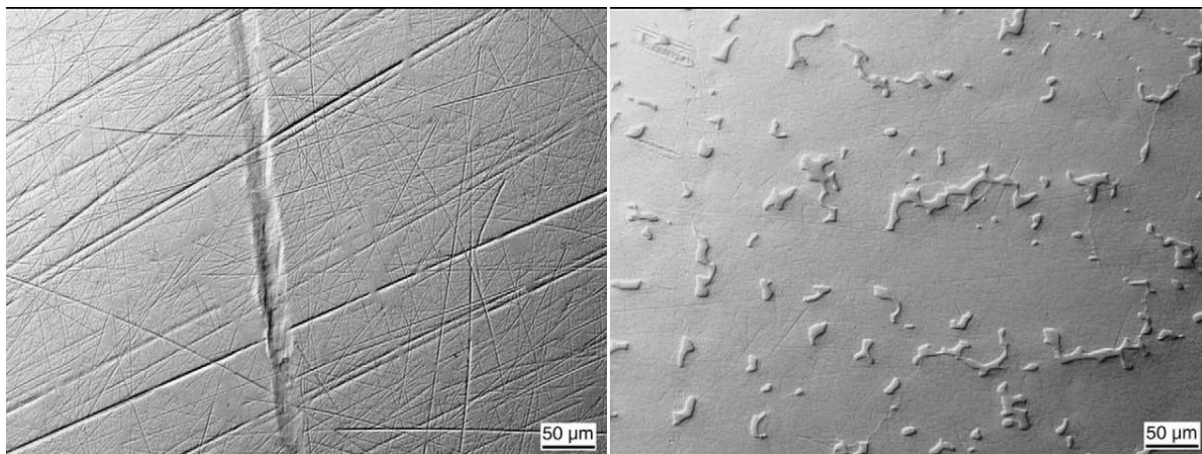


Figure 68: Surface measurement images of retrieved MoM resurfacing components [19]. Left: Wear area. Right: Unworn area.

Howie, 2005 [17], categorised SEM measured surface wear patterns found on 24 MoM retrieval bearings through their visual appearance. The types of wear were separated into four categories: Polishing wear, fine abrasive wear, multidirectional dull abrasive wear, and unidirectional dull abrasive wear, figure 69. The fine abrasive wear was the most commonly found type of wear present on the majority of the surface, but tended to be difficult to visualise using the SEM.

It was shown that the largest increase in roughness occurred within the unidirectional dull abrasive type of wear, approximately a 10-fold increase. This large increase in roughness shown by unidirectional scratches was also noted by Walker in 1971 [109]. According to Howie for fine abrasive wear and multidirectional dull abrasive wear there was only a small increase in roughness and in polishing wear areas there was no change in surface roughness compared to unworn areas of the surface. However other authors would contend that roughness does increase self-evidently in the presence of wear [169].

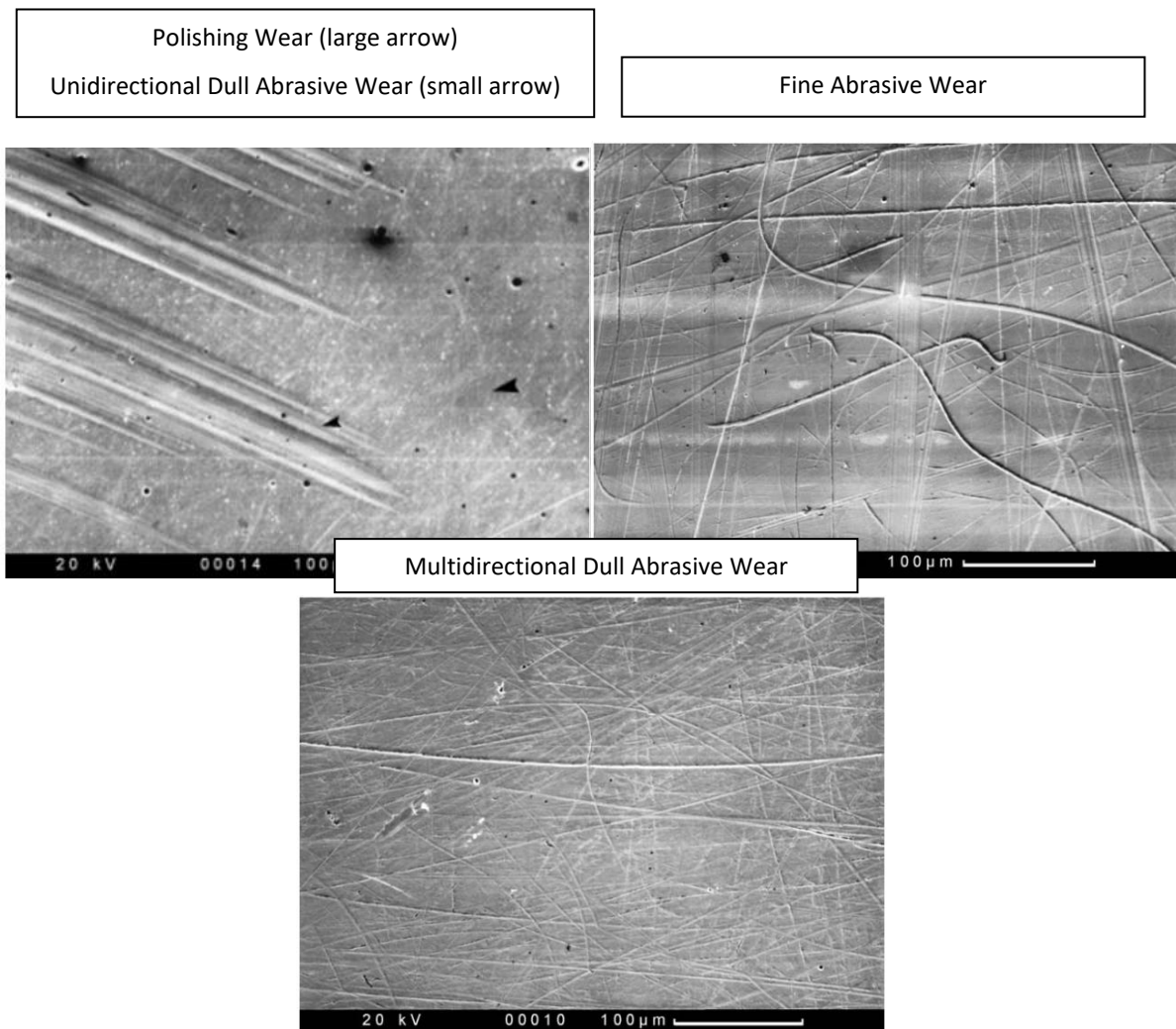


Figure 69: SEM images of types of MoM bearing wear [17].

2.3.1.2 Metal-on-Polymer

Hall, 1997 [18], again noted the most heavily scratched regions of retrieved MoP femoral heads were found within their wear areas, with the majority of scratches smaller than 2 microns in width, figure 69 (left). Evidence of polishing wear was also noted elsewhere on the femoral head, demonstrated by ‘polishing pits’ or ‘polishing tails’, this indicates the removal of surface asperities through wear, or pull out of intermetallic carbide phases creating wear debris but leaving a more polished surface finish, figure 70 (right).

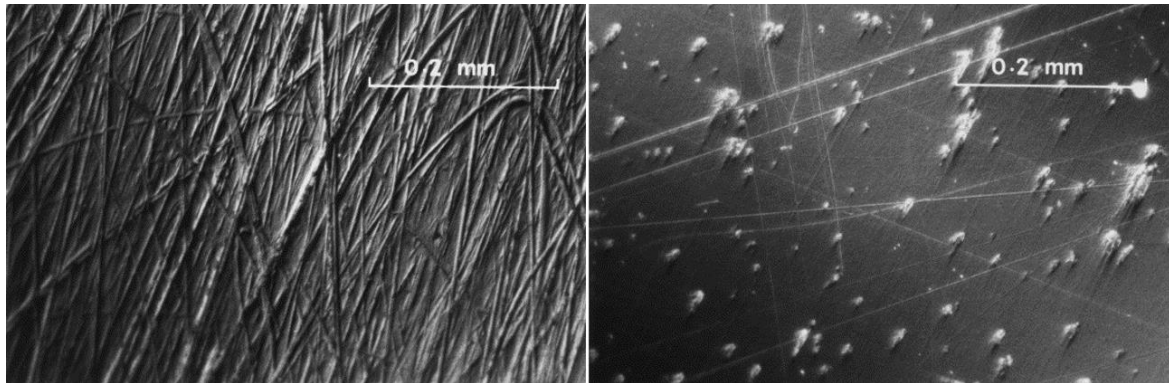


Figure 70: SEM images of retrieved MoP femoral heads. Left: Heavily scratched within the wear area. Right: Evidence of wear polishing, note the tails emanating from the pits, creating wear debris but also polishing the surface [18].

Elfick, 2002 [20], studied the change in surface topography within the wear area for 42 retrieved MoP hip implants, both the metal femoral head and polymer acetabular cup components were analysed, figure 71. The roughness of the metal femoral heads increased within the wear area (Sa unworn - 3.05 nm, wear area - 10.35 nm). Whereas the roughness of the polymer acetabular liner fell dramatically within the wear area (Sa unworn - 212 nm, wear area - 41 nm).

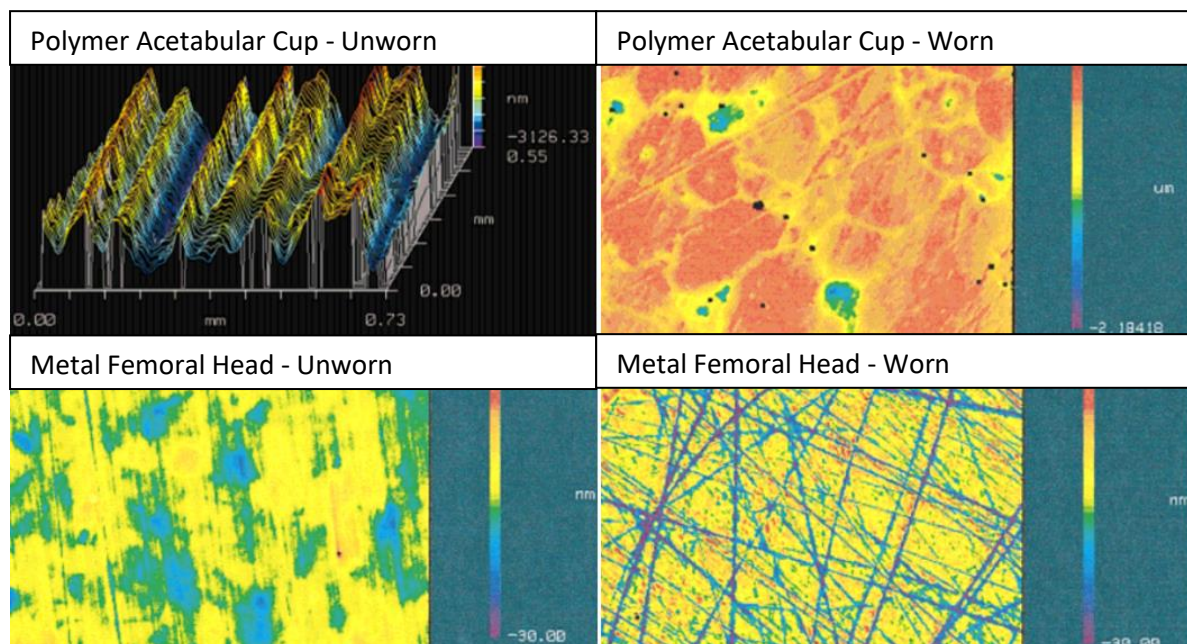


Figure 71: Surface measurements of retrieved MoP components, comparison within unworn areas and the wear area [20].

2.3.1.3 Ceramic-on-Metal

Williams, 2009 [22], analysed 6 CoM bearings through a simulator study up to 5 million cycles. At the end of testing, ceramic third body wear debris was present within the bearing interface, this could be seen as a powder trace by using UV light and a CCD camera. The overall amount of wear measured on the ceramic femoral heads via gravimetric measurement was undetectable, however by using surface measurements, wear scratches were discovered. The surface roughness (S_a) did not increase for the ceramic femoral heads after testing, but faint multi-directional scratches were visible on the ceramic surface, grain pull out was also prevalent within the wear area on the ceramic femoral heads, figure 72. The author theorised that the ceramic femoral heads were likely to polish the metal acetabular cups over time as 'polishing tails' were found on the surface of the metal cups. However, the present author would contend that over a long enough period of time or with inferior tribological conditions both the ceramic and metal surfaces will roughen, particularly within their wear areas.

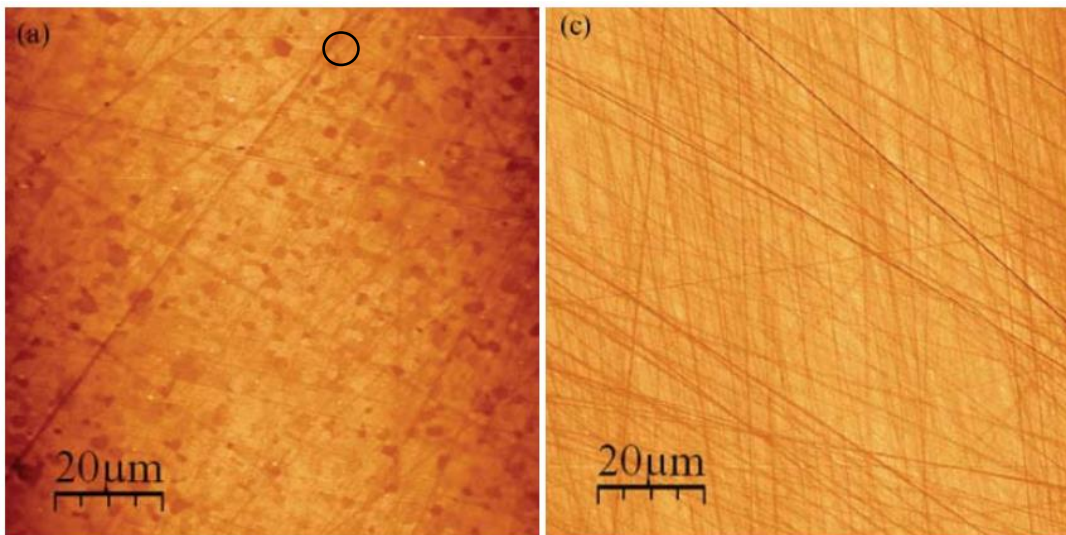


Figure 72: AFM images of a ceramic head [22]. Left: Within the wear area, note the grain pull-out evident on the surface, a single grain pull-out area is circled in black. Right: Unworn area of the head, no grain pull-out, but abrasive scratches present.

2.3.1.4 Ceramic-on-Ceramic

Affatato, 2011 [23], again noted the change in the grain structure of ceramic implants within the wear area, during both simulator and retrieval analysis of CoC hip implants, figure 73. A different superficial grain microstructure was observed within the wear area, emphasizing an inter-granular fracture of the alumina. The grain sizes were typically in the 4 to 6-micron range. As part of this study, no interferometry measurements were taken within the wear area to produce surface measurement parameters. The present author would contend that with the provided SEM images, the roughness appears to have increased within the wear area of the ceramic surfaces.

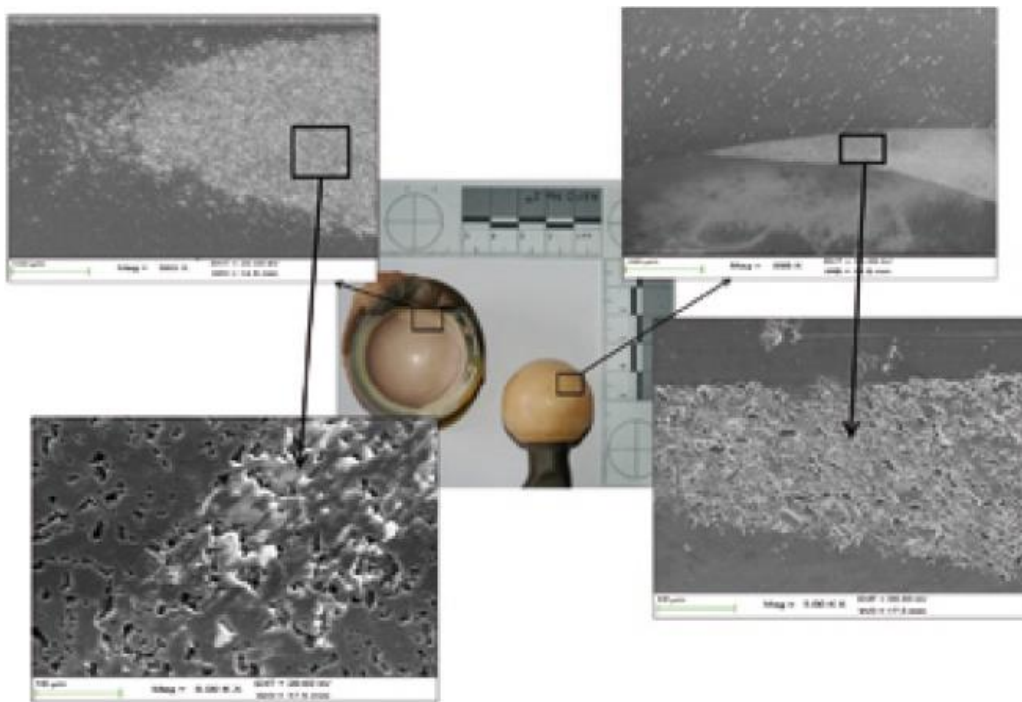


Figure 73: SEM images showing surface damage within the wear area of retrieved CoC implant.

2.3.2 Roughening or Smoothing of the Surface Within the Wear Area

The change in surface topography within the wear area has been shown to vary depending on the materials used at the bearing interface. Evidence from the retrieval and simulator studies, suggest the surfaces of metal and ceramic components tend to become rougher within their wear areas. Whereas polymer acetabular components tend to become smoother within their wear areas.

Niemczewska-Wojcik, 2017 [170], tracked the changing surface topography of a MoP hip bearing throughout several stages of simulator testing, figure 74. After 250,000 simulator cycles, the surface roughness of the metal femoral head increased from Sq - 0.111 μm to 0.527 μm . The surface roughness of the polymer acetabular liner decreased from Sq - 2.5 μm to 0.544 μm . The surface measurements for this study were targeted at the pole of the component, ideally these measurements would have been targeted within the wear area of the components, as this is where the largest change in surface topography is occurring.

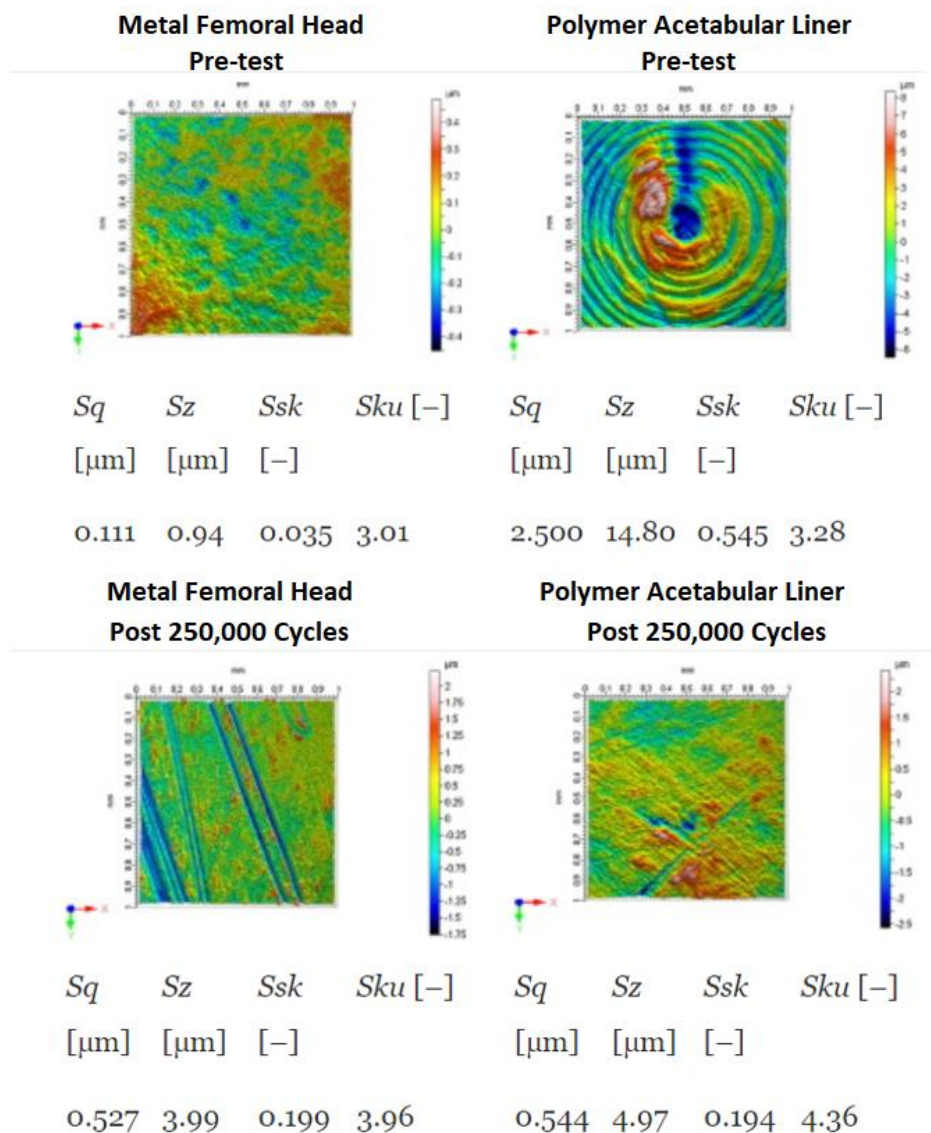


Figure 74: Changing surface topography of a MoP bearing, measured at the pole of the components [24].

The original surface finish of polymer acetabular components is much rougher compared to metal/ceramic components (Polymer: Ra 0.1 - 2 μm [9]). The increased roughness of polymer components is due to spherical manufacturing ridges present on the surface, produced by a turning operation. The present author would contend that as the bearing interface is in motion, the peaks of the machining marks are removed through abrasive wear from the harder metal or ceramic femoral head, leaving a smoother polymer surface finish. Although a smoother surface finish for the polymer component is desirable for tribological performance [9], the production of wear debris should always be avoided. Furthermore, after this initial smoothing of the polymer surface, a second process of roughening could now initiate, with the harder femoral head or any third body debris now damaging the 'smoothed' polymer surface.

Metal and ceramic components, have a highly polished surface finish preimplantation, (Metal: Ra 0.01 - 0.05 μm , Ceramic: Ra 0.001 - 0.005 μm [9]) there are no obvious manufacturing peaks to be removed. It has been shown that metal components tend to become rougher throughout their lifetime, particularly within the wear area where the bearing surfaces are in contact more often. This wear is thought to be a combination of abrasive and adhesive wear, with third body debris trapped within the bearing interface also causing significant damage. Ceramic surfaces have shown roughening within the wear area, through damage to the ceramic grain structure.

2.3.3 Linking Surface Topography and Implant Wear Rates

The surface topography of the bearing components has long been shown to affect the overall wear rates of the bearing through both simulator and retrieval studies.

Dowson, 1985 [171], investigated the effect of changing femoral head surface roughness (R_a) to the wear rates of polymer acetabular components. This was achieved using pin-on-plate simulation, i.e. a polymer pin running on a flat plate metal counter face. The experiment revealed that under wet conditions (presence of lubrication) as the roughness of the metal counterface was increased the wear rate of the polymer increased with high correlation, figure 75. This same correlation was not found when running the pin-on-plate testing in dry conditions.

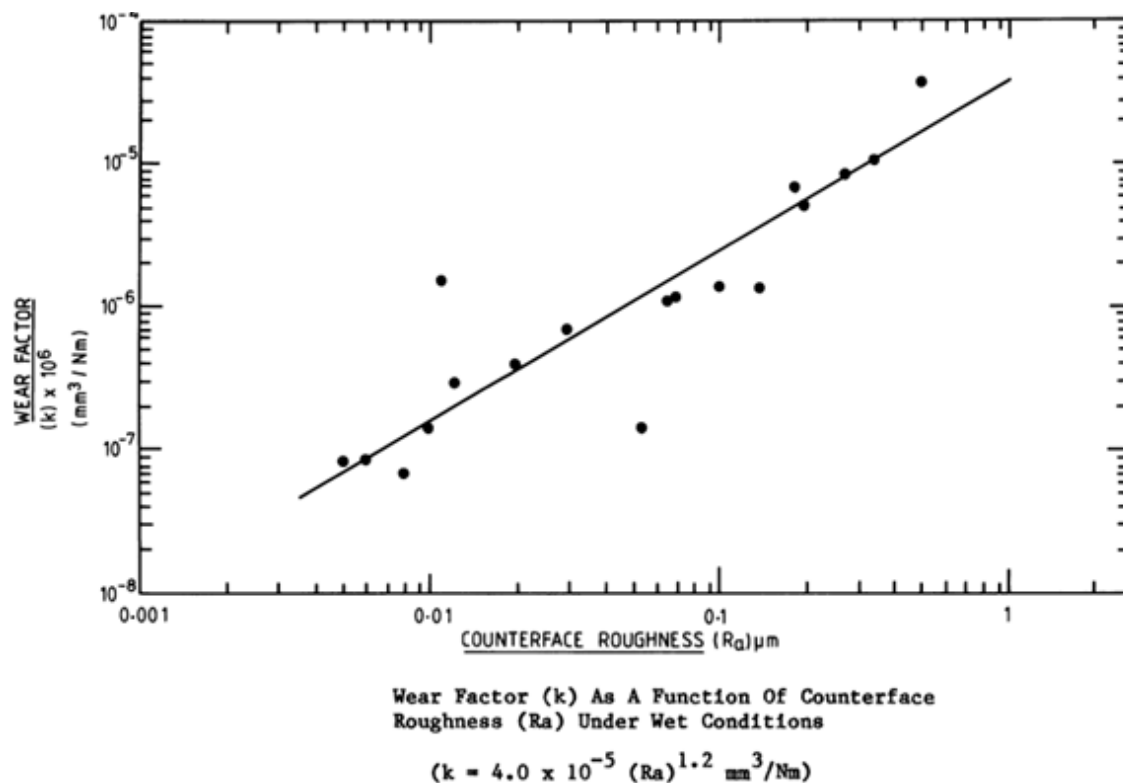


Figure 75: Wear rates of the polymer pin against the metal counterface roughness under wet testing conditions [171].

Hall, 1997 [18], also correlated the roughness of 35 retrieved MoP femoral heads with the overall amount of wear on the corresponding polythene acetabular components, this time using a retrieval study. As the roughness of the retrieved femoral heads increased, the corresponding acetabular components tended to have increased overall wear. This finding matches the theory that increased surface roughness will cause more bearing wear. The surface measurements were targeted within the wear area of the femoral heads and the profile parameters which showed correlation to overall acetabular component wear were arithmetic mean roughness (R_a) and skewness (R_{sk}), figure 76. Correlation was defined using Spearman's rank correlation coefficient, R_a (0.284, $P = 0.099$) and R_{sk}

(0.374, $P=0.027$). Potentially better correlation could have been found between surface parameters and overall acetabular component wear in this retrieval study.

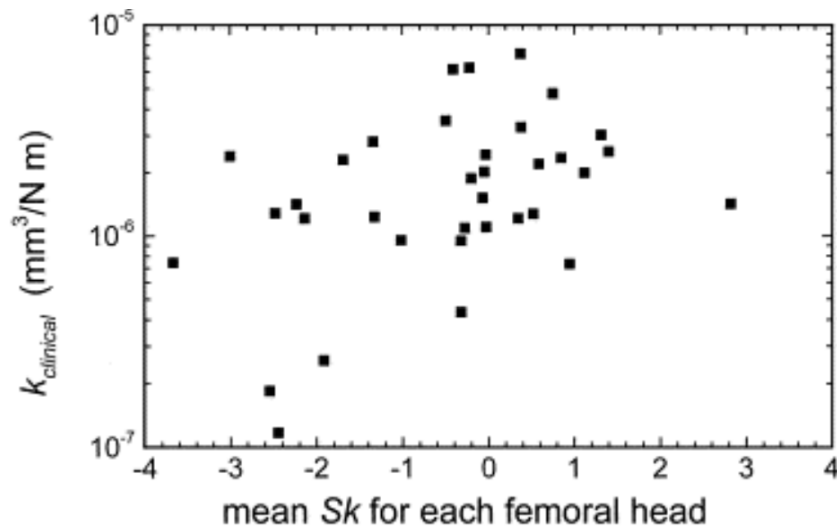


Figure 76: The wear of the polythene socket (k) plotted against the mean skewness (R_{sk}) for each femoral head [18].

Wang, 1998 [172], also tested the theory that increased femoral head roughness increases the wear of the polyethylene liner. Through hip implant simulator testing it was shown that increasing the femoral head roughness from $R_a - 0.01 \mu\text{m}$ to $0.10 \mu\text{m}$ resulted in an approximately 2-fold increase in the wear rate, figure 77.

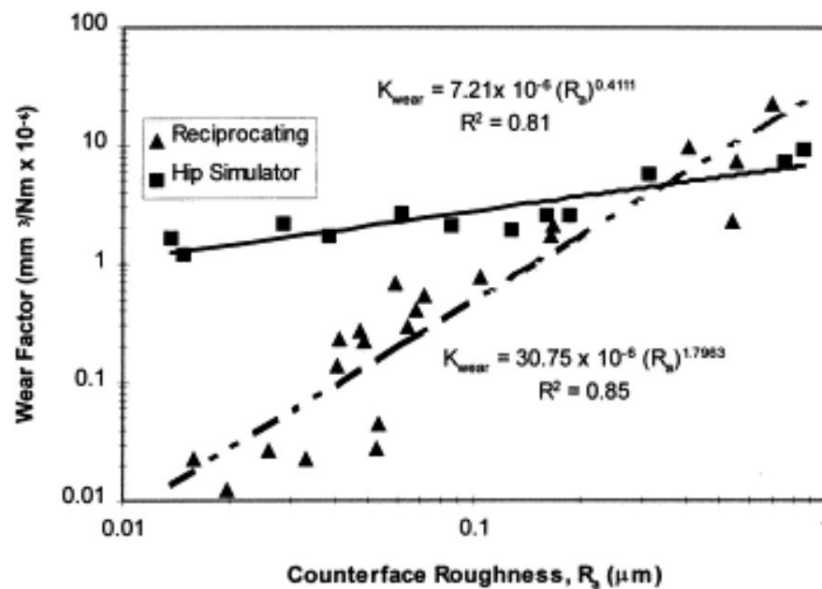


Figure 77: The wear factor of the polymer liners against the roughness of the femoral heads [172]. The values from the hip simulator are labelled as squares with a line of best fit.

2.3.4 Chapter Summary

It has been well established that the surface topography of the hip implant bearing surface changes within the wear area, this has been shown to be true for all popular bearing material combinations [17-24, 109]. Therefore, when surface measurements are taken on worn bearing surfaces, they need to be positionally targeted both within and outside the wear area to give a comprehensive analysis of the entire component.

The change in surface topography within the wear area can vary depending on the materials in use [17-24, 109]. Polymer surfaces tend to undergo an initial smoothing of the surface, due to the removal of manufacturing ridges, potentially followed by later surface roughening. Metal and ceramic surfaces tend to become rougher within their wear areas, due to breakdown of their original highly polished finish.

The correlation between bearing surface topography and wear rates of the bearing has been well established in both retrieval and simulator studies [18, 171, 172]. Demonstrating the great importance of surface measurements for both quality inspection and wear analysis. This correlation could potentially be better demonstrated using more accurate positional targeting of surface measurements and the effective use of modern areal surface parameters. The vast majority of studies declare that surface measurements have been 'targeted' within the wear area but there is no information on the fixturing used and no consideration of the positional error of surface measurements. The surface measurement positional accuracy will have a huge effect on the results of any surface measurement study.

2.4 Wear Map Positional Targeting of Surface Measurements

2.4.1 Spherical Coordinates

Spherical coordinates will be used throughout this project to describe locations on hip implant bearing components. The entire bearing surface can be considered a combination of an azimuth and elevation angle, figure 78. The azimuth angle is taken anti-clockwise from the front of the component. The elevation angle is taken from the pole of the component towards the rim. For the femoral head this is downwards along the surface from the pole to the equator, but for the acetabular cup this is upwards along the surface from the pole to the equator. See figure 78 for spherical coordinates plotted onto a femoral head wear map, for example the maximum wear depth (1) is located at azimuth 90° , elevation 55° .

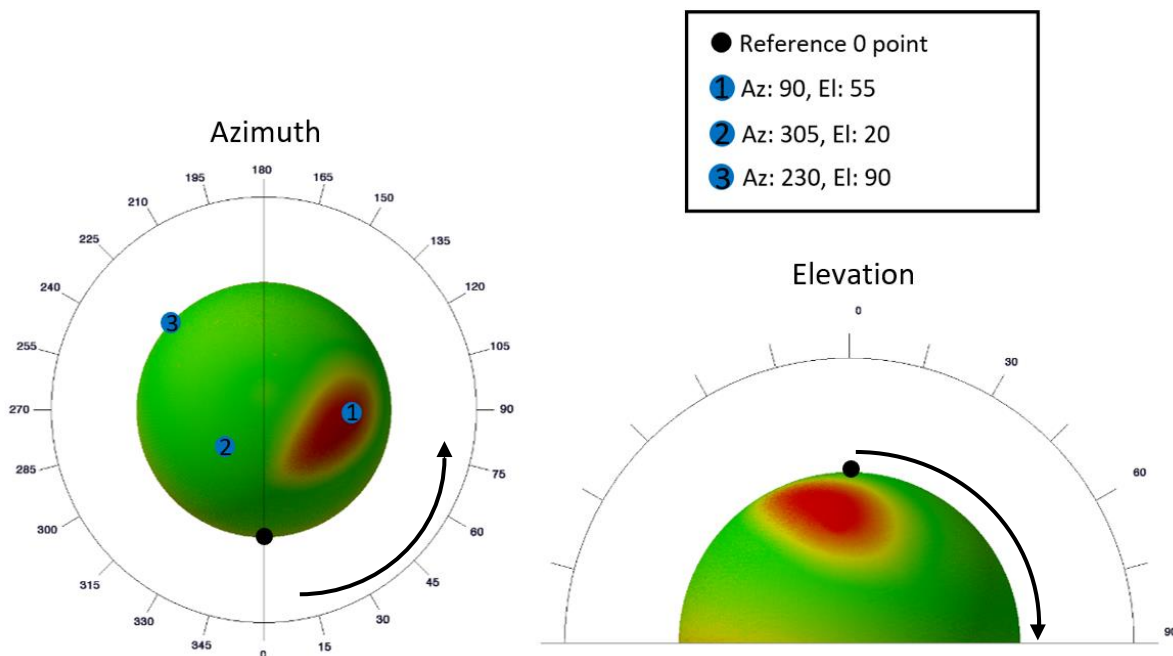


Figure 78: Spherical coordinates of a femoral head. Example spherical coordinate locations are shown on the top view.

2.4.2 Metrology Data Fusion

As the requirements on the complexity and accuracy of dimensional metrology increase, multisensory data fusion is utilised [173, 174]. Multisensor data fusion in dimensional metrology can be defined as the process of combining data from several information sources (sensors) into a common representational format [173]. This means measurement results can be determined, which could not be determined solely on the basis of data from an individual sensor only [173]. By this definition wear map targeted surface measurements can be considered a basic level of complementary data fusion, as data from both the CMM and surface interferometer are combined to represent the results together. A sensor configuration is called complementary if the sensors do not directly depend on each other, but can be combined in order to give a more complete measurement result [173].

2.4.3 Wear Map Targeted Surface Measurements

Volumetric (CMM) wear measurement methods can generate a wear map of the measured component, allowing the size and shape of the wear area to be analysed. The wear map can then be used as a positional reference for targeted surface measurements. This allows surface measurements to be targeted within the wear area and at unworn areas of the component, which is crucial for a comprehensive surface analysis and understanding the development of tribological phenomena.

The wear area must not be assumed to have the same surface topography throughout its entire area, this is very unlikely. For example, assume the point of maximum linear wear depth will undergo the most dramatic surface alteration, and the level of surface change propagates outwards until the edge of the wear area, figure 79. Therefore, there is a small area within the wear scar which is most important to capture with surface measurement. If the surface measurements taken within the CMM defined wear area are not accurately wear map targeted, this area is unlikely to be captured.

Elfick, 2002 [20], states ‘an inherent source of error in all assessments of roughness is the assumption that the entire surface has the same topography as the small sample area that is selected’. This error can be minimised by firstly ensuring the positional targeting of surface measurements is as accurate as possible and positionally fused with the CMM wear map. Secondly by taking many surface measurements across the surface, in particular at wear areas. In addition, a deeper understanding of the salient tribology may be gained by recording a series of surface measurements across the wear area, from unworn, through the wear area, to unworn. This would clearly require careful positional control of the surface measurement with respect to the wear area.

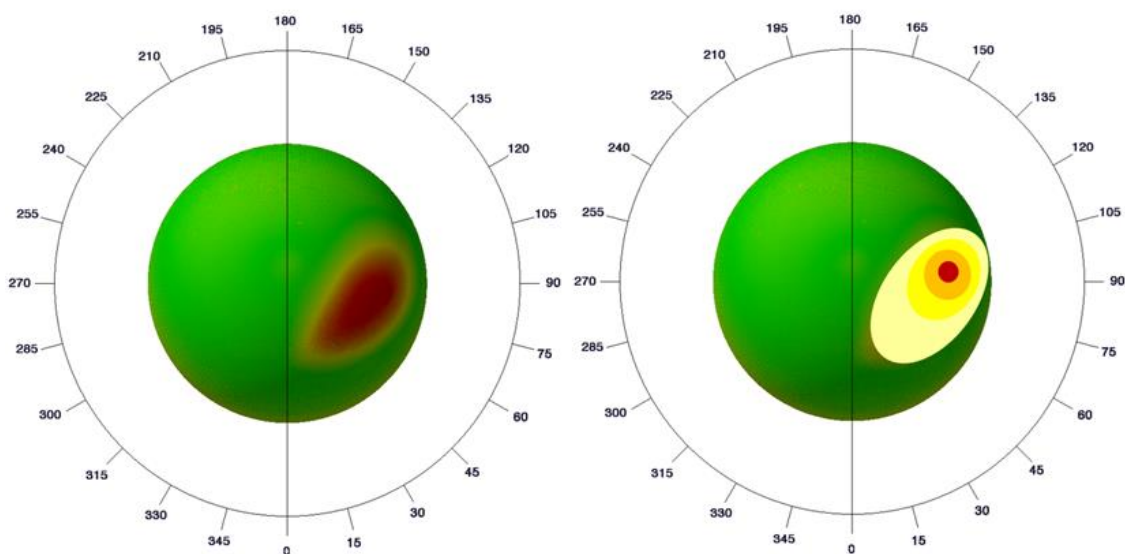


Figure 79: CMM wear map of retrieved femoral head. Left: The original CMM wear map. Right: A representation of the topography changes within the wear area. The highest level of surface topography change (red) at the maximum linear wear point, the level of topography alteration propagates outwards.

2.4.4 Surface Measurement Limitations for Acetabular Cups

The location of surface measurements on the acetabular cup bearing surface are limited as to where they can be collected. This is due to the objective lens of the surface metrology instrument colliding with the rim of the acetabular cup. Figure 80 shows two locations on the acetabular cup being measured, the pole of the component on the left and an area closer to the rim on the right. The pole of the component can easily be measured because the measurement lens can access the measurement area with no contact from the rim of the component. However, when surface measurements are required to be targeted through an elevation angle, towards the rim of the component, the rim of the component can impede the access of the objective lens from accessing the measurement area.

Three factors decide how much of the component is accessible: the diameter of the acetabular cup, the diameter of the measurement objective lens, and the working distance of the objective lens. If the acetabular cup is larger in diameter then more of the bearing surface can be measured, this is because there is more space for the measurement lens to access the surface. If the measurement lens is smaller in diameter this allows it to fit into smaller diameter acetabular cups and allows greater elevation angles to be accessed on the acetabular cup surface. Long working distance objectives are available but they are an additional cost.

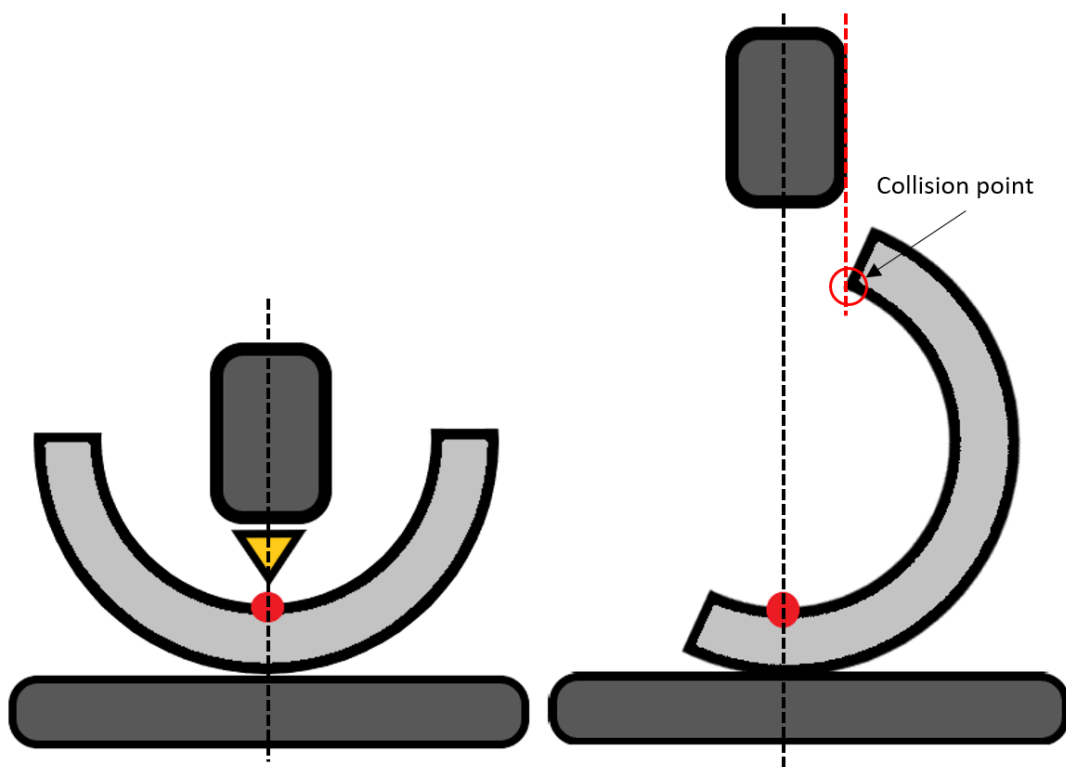


Figure 80: Surface measurement limitations for acetabular cups. Left: Measurement at the pole of the acetabular cup, lens easily fits within the acetabular cup for access to measurement. Right: Measurement at approximately 80° elevation, lens not accessible due to collision with the rim of the acetabular cup.

2.4.5 Fixturing to Support Wear Map Targeted Surface Measurements

The positional targeting of surface measurements can only be achieved by accurately manoeuvring the hip implant component with a highly repeatable fixture (holding device). The measurement lens of a surface measurement instrument is fixed perpendicularly above the measurement surface. Therefore, the hip implant component needs to be manoeuvred so the desired measurement area is positioned perpendicularly under the lens at the desired working distance, figure 81.

Although this positional targeting of surface measurements is crucial, a common theme among scientific studies is the lack of information on the fixturing utilised. The vast majority of studies declare that the surface measurements have been ‘targeted’ within the wear area but there is no information on the fixturing used and no consideration of the possible positional error of the fixture. It is assumed that this positioning is carried out manually with very simple fixturing resulting in a highly subjective measurement location. As previously stated, if surface measurements intended to be taken within the wear area are marginally in the wrong location this could have a great effect on the surface measurement results. Therefore, the accuracy of the fixturing in use is of great importance for a successful surface measurement study.

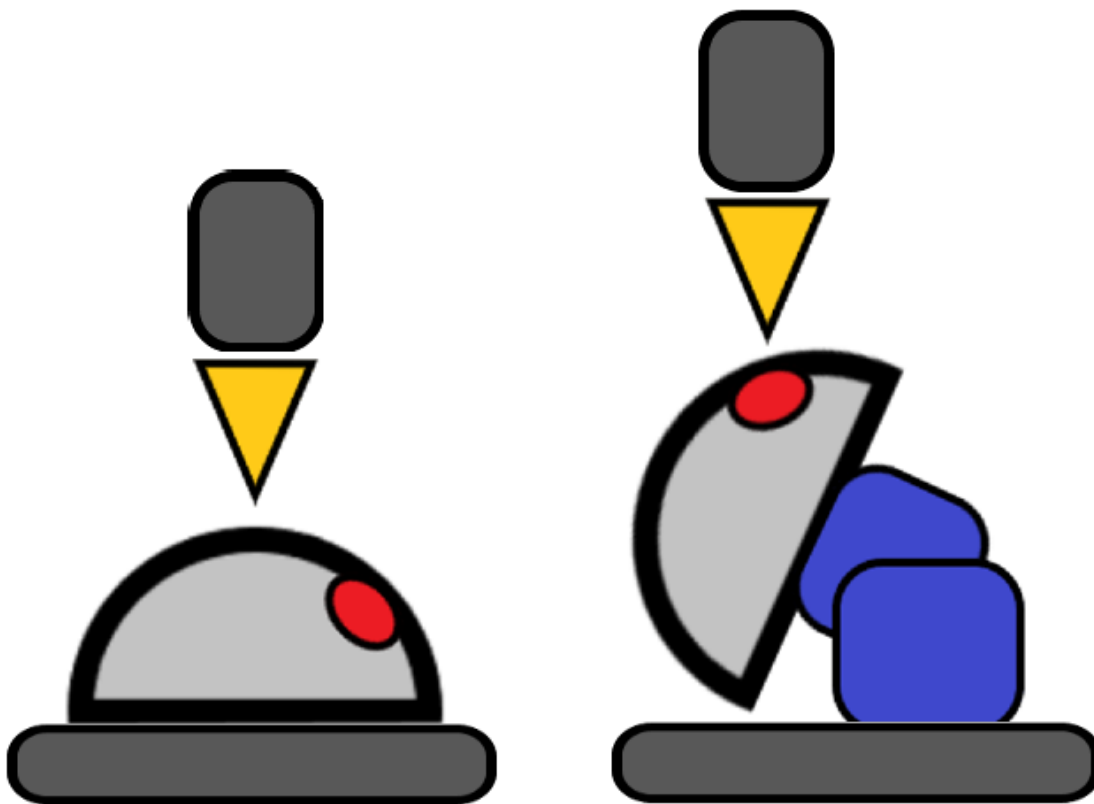


Figure 81: Surface measurement of femoral head. Left: Measurement at pole of the component. Right: Measurement at the wear area of the component, achieved using a fixture to manoeuvre the component as to positionally target the surface measurement within the wear area.

2.4.5.1 Commercially Available Fixturing

Although the fixturing utilised for surface measurement studies is rarely mentioned in published scientific studies, there must be some form of fixturing in use as surface measurements are often targeted within wear areas. There are many commercially available positioning stages, which can vary greatly in price depending on their level of accuracy and the type of drive control. In this section the variety of commercially available fixturing options are discussed.

Basic Tilt Fixture

The most basic fixturing requirement is the ability to tilt the component through its elevation angle. The use of a manual tilt fixture, figure 82, can be utilised, this allows the femoral head to be tilted through any elevation angle, but with poor positional accuracy. Improving the positional accuracy of the fixture can easily be achieved through the use of commercially available manual translation and rotation stages. Note the implant is mounted on a matching taper fit.

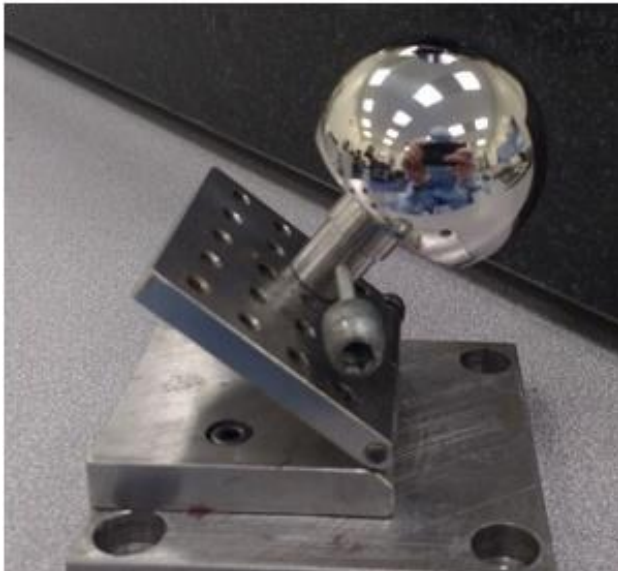


Figure 82: Basic tilt fixture allowing for the elevation angle to be adjusted for the surface measurement of a femoral head.

Manual Translation and Rotation Stages

A superior manual setup compared to the basic tilt fixture would include a combination XY translation stages, and rotational stages combined, figure 83. These stages are often designed to be modular and combined together to create a custom setup for bespoke measurement applications. For example, a potential setup for hip implant surface measurement could be as follows: A rotational platform at the base of the fixture would allow for the adjustment of the azimuth angle of the component. An XYZ translation stage secured on top of the rotational platform can allow for fine directional adjustment to ensure the component is located centrally underneath the surface measurement lens. A second rotational stage can be attached through the use of an angle bracket to the XYZ stage, allowing for the adjustment of the elevation angle of the component. A final angle bracket can be placed on the elevation rotation platform, where the component is placed, allowing the component to now be perpendicular to the measurement lens. This setup relies on human control of the stages, but with improved positional accuracy due to the use of precision scales and fine micrometer type adjustment screws. The main drawback of this setup is that no digital control is available, which allows for advanced control options using CMM data as direct control input. Depending on the size of commercially available fixtures it also can be difficult to create this manual setup within the working height limits of surface measurement machines (approx. 100mm).

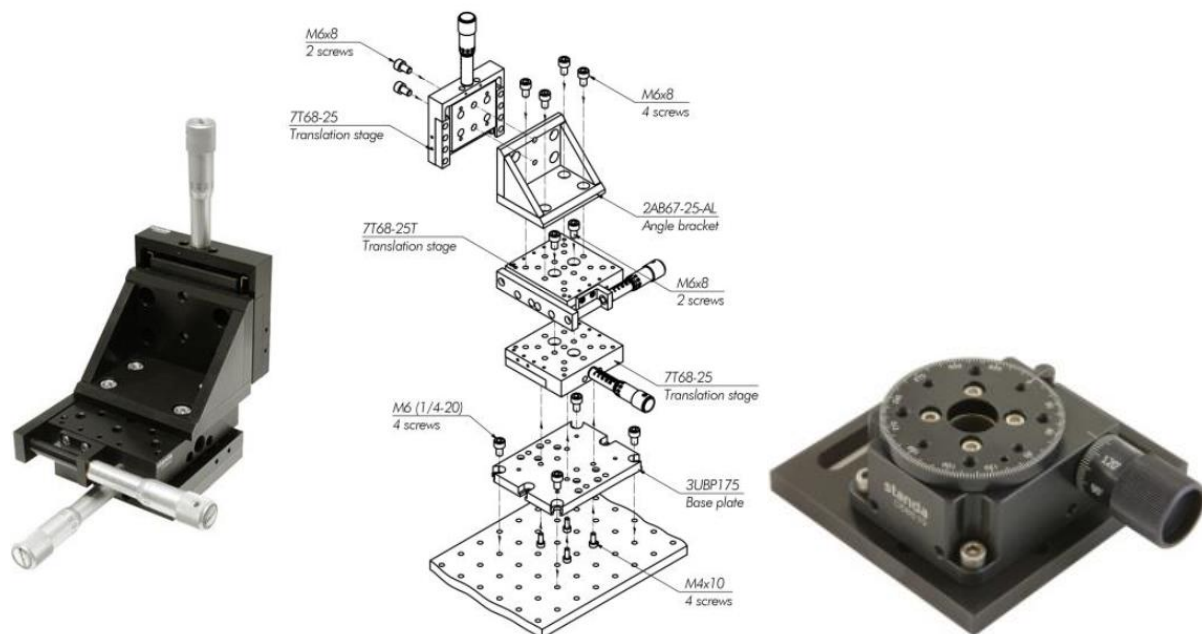


Figure 83: Manual translation and rotation stages. Left: XYZ translation stage. Centre: Explosive view of translation stages to create XYZ translation stage. Right: Corresponding rotation stage for XYZ translation stage.

Digital Control Stages

Digital control stages utilise electric motors to control the movement of the stages, they tend to have increased accuracy compared to manually controlled stages. They are also more expensive and usually larger in size compared to manually driven fixtures. An electronically driven setup allows the user to control the stage using a computer, this allows for more dynamic control options of the fixture. Custom software can even be created, allowing the CMM data to be used as direct control for the fixture, opening the possibility for a multitude of user-friendly data fusion control options, combining CMM information to control the position of surface measurements. The main drawbacks of these stages are the increased cost and the large size of the stages, figure 84. A fixture created with digital control stages is unlikely to fit within the working height limits of most surface measurement machines (approx. 100 mm).



Figure 84: Motorised fixture with digital control, created with a combination of rotary stages. Note the large size of the fixture, in particular in its height.

2.4.6 Modern Measurement Instruments

2.4.6.1 Bruker-Alicona uCMM

The Bruker-Alicona uCMM system is a recently developed measurement machine, it operates similarly to a traditional bridge stylus CMM however the contact probe has been replaced with a focus variation surface measurement sensor, figure 85. This system was not designed specifically for orthopaedic applications, instead it is meant to be applicable across many industries. This machine can be considered a form of complementary data fusion, utilising the geometrical measurement capabilities of a bridge CMM with the surface measurement capabilities of a dedicated surface measurement instrument. The machine allows surface measurement results to be stitched onto geometrical measurement data, figure 85. The sensor however is not at present capable to accurately acquire the nanoscale surface topographies found on orthopaedic bearing surfaces.

Similar to a bridge CMM, measurement points can be taken on the component, however instead of only locational information, a surface measurement can be captured. The location of this surface measurement is stored in cartesian format similar to a single measurement point on a bridge CMM.

A fixturing system has also been developed by Bruker, the 'Real 3D' system, it is able to manoeuvre components through azimuth and elevation angles, which is ideal for measurement of hip implant bearing components, figure 85. Any location on the hip implant bearing surface could be measured through the use of the Real 3D system. This Real 3D system also boasts analysis methods to compare CAD geometries to measured geometries which could in theory be applied to wear measurement scenarios and the generation of wear maps for orthopaedic components.

Using the Bruker-Alicona uCMM, theoretically the entire bearing surface could be measured as a series of surface measurements, however this is likely impractical due to the extremely long measurement time. Instead, the best process would be to firstly measure the entire surface as a geometric point cloud with no surface measurement data required. Then once the geometric point cloud is generated and suitable analysis is completed to generate a wear map, surface measurements could be targeted within the wear area, unworn areas, and at any other desired locations.

This system allows geometrically tracked surface measurements anywhere on the hip implant bearing, this could allow for a complete geometric, wear and surface analysis of the component with one machine. The length measurement errors are also very similar for the Alicona Bruker uCMM, $0.8 + L/600$ μm [131], compared to an analogue probe CMM (Zeiss Prismo 5), $0.5 + L/500$ μm (L in mm) [126]. More information on the uCMM can be found on the Bruker-Alicona website [131].

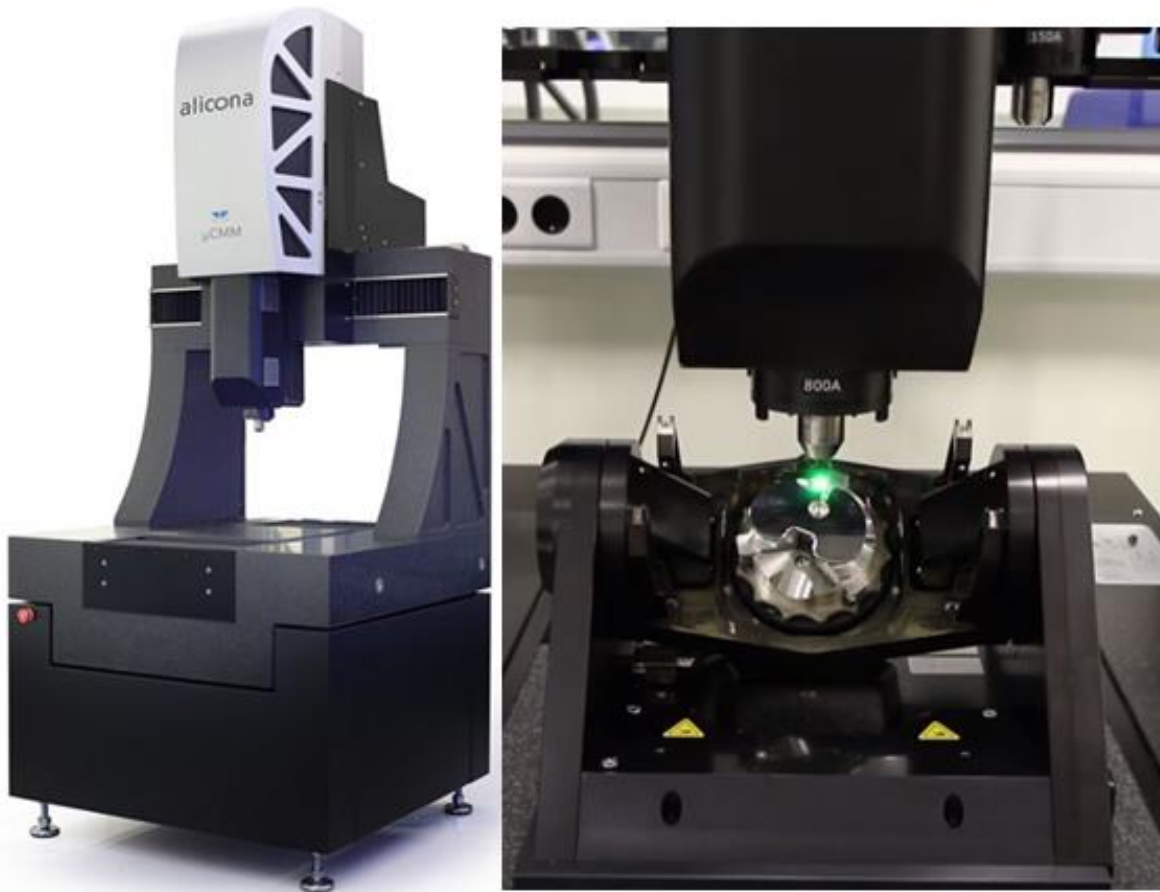


Figure 85: Bruker-Alicona uCMM. Left: Overview of the entire uCMM machine [131]. Right: Detailed view of the 'Real 3D' fixturing device, pictured holding a knee implant component [175].

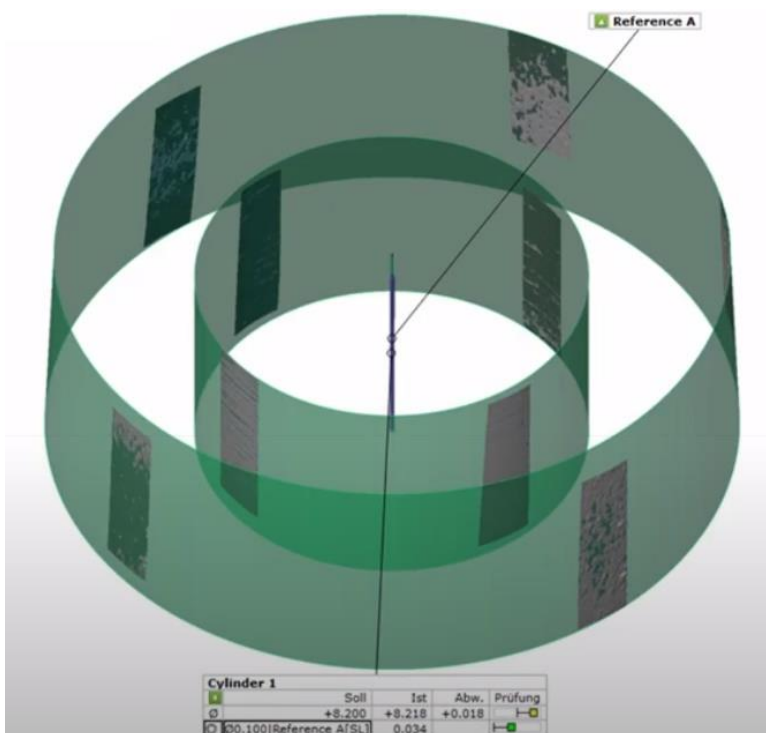


Figure 86: Data fusion of focus variation surface measurements and the positional information of the CMM sensors using the Bruker Alicona uCMM [175].

2.4.7 RedLux OrthoLux

The RedLux OrthoLux instrument is an optical CMM specifically designed for the orthopaedics industry. The use of an optical CMM compared to a traditional stylus CMM is particularly appealing as there is no risk of the component being damaged by the stylus tip during measurement. The opportunity to test the RedLux OrthoLux compared to an analogue probe CMM was provided by DePuy J&J Leeds.

Using the RedLux instrument, the entire bearing surface can be scanned in only a few minutes compared to a similar measurement size on a contact probe CMM taking approximately 20 minutes. The instrument is a 4-axis optical CMM, figure 87. There are two rotary stages which can manoeuvre the component through azimuth and elevation, allowing the component to be rotated around the measurement sensor during measurement. This is the opposite approach of a bridge CMM, where the component remains still and instead the measurement stylus moves to different positions on the component. There are also two linear axis, one main linear axis for large movements of the sensor and a precise linear axis for movement of the sensor during measurement.

The Redlux OrthoLux does not advertise the length measurement error of its system on its website, instead it states the resolution of the system as 20 nm. The sensor is a point based, chromatic confocal sensor with a resolution of 20 nanometres. By combining the sensor signal with the positional information from all 4 stages, a 3D representation of the surface can be created. The data from measurement can be quickly analysed using the in-built software to create a wear map of the component and calculate geometric and wear analysis parameters [130, 132]. Although the RedLux system is an alternative to the bridge CMM it cannot provide areal surface measurements like a dedicated surface measurement instrument can.

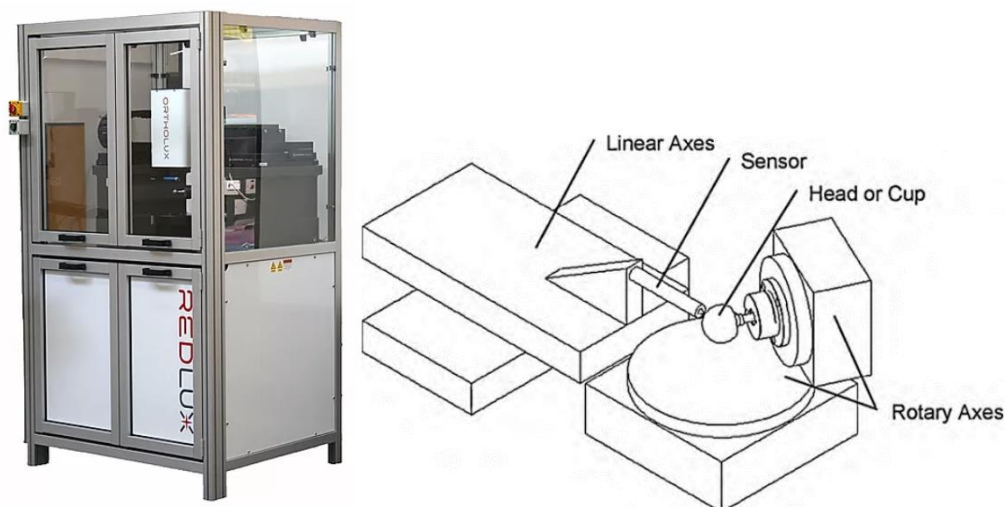


Figure 87: RedLux OrthoLux. Left: Image of the RedLux OrthoLux system which is fully enclosed [130]. Right: Schematic of the RedLux measurement principle [132].

2.4.8 Chapter Summary

The CMM wear map can be used as a positional reference for surface measurements. This allows surface measurements to be targeted within the wear area, which is crucial for a comprehensive surface analysis. If the surface measurements are targeted within the CMM defined wear area, but with poor positional accuracy, this measurement set may not capture the most critical surface topography information.

The positional targeting of surface measurements is achieved by manoeuvring the hip implant component with a fixture (holding device). Although this positional targeting of surface measurements is crucial, a common theme among scientific studies is the lack of information on the fixturing utilised and no consideration of the positional error of the fixturing. Commercially available positioning stages are inadequate for wear map targeted surface measurements either due to their lack of high accuracy digital control or being too large to be compatible with surface metrology instruments.

The modern Bruker Alicona uCMM, seems ideal for wear map targeted surface measurements. However, its performance capabilities are largely unknown and the investment cost to purchase is substantial. The RedLux system is used in industry for its wear measurement capabilities, producing geometrical/volumetric wear parameters, and creating wear maps of bearing components. However, there are currently no useful surface measurement capabilities for the RedLux system. There is also a lack of performance information for the RedLux system, crucially the length measurement error and other CMM specification parameters that are not in the public domain [130].

2.5 Gaps in Knowledge from Literature Review

In this section the current gaps in knowledge shown from the literature review are discussed.

1. Previously completed studies on surface finish of worn hip implants do not discuss the fixture utilised to manoeuvre the bearing component. This means a fixture with poor positional accuracy could have been used which could result in measurements not capturing the most critical data and overall inaccurate results.

Using accurate fixturing, results can be given with more confidence that the most important surface topography data is captured, and the location of surface measurements will be known to a high level of accuracy.

2. Most orthopaedic companies have access to high quality CMMs and surface measurement instruments, however they do not have fixture systems which allow these datasets to be combined accurately.

By creating a fixture system as shown in this project, this allows for CMM wear map data to be used for high accuracy control of surface measurement location. Therefore, allowing for advanced analysis options, and a wide range of other benefits, which is highlighted in this project.

3. A detailed surface measurement across the entire length of a wear area on a hip implant bearing component has currently not been achieved. This is mainly due to stitching not being available over a highly curved surface such as a hip implant bearing component.

Using the newly developed fixture system from this project this has now been achieved and allows the surface to be analysed over the entire length of the wear area, and interesting areas such as the boundary regions to be investigated.

4. The use of optical CMMs for measurement of orthopaedic components is not yet widespread across the industry. There is currently a lack of information comparing an optical CMM to an analogue probe CMM for typical orthopaedic measurements.

As part of this project a comparison is made between an optical CMM and an analogue probe CMM to help compare their effectiveness for measurement of hip implant bearing components.

Chapter 3: Comparison of the RedLux Optical CMM to an Analogue Probe CMM

3.1 Introduction

Typically an analogue probe CMM is used to complete geometric quality inspection and volumetric wear measurements on orthopaedic components [12]. An analogue probe CMM uses a stylus to physically contact and record the position of the component in three-dimensional cartesian coordinates, typically with a measurement error of approximately ± 1 micron [126].

Non-contact optical CMMs have been developed with performance specifications that are capable of bearing surface measurement [130-132]. Non-contact measurement can be particularly useful as there is no chance of the component being damaged by the stylus during measurement. This chapter aims to compare the measurement repeatability of an analogue probe CMM to an optical CMM through wear measurement of hip implant bearing components.

The CMMs used for this study are the RedLux OrthoLux [130, 132] and the Zeiss Prismo 5 with a VAST Gold 2 mm analogue probe [126]. ISO 10360 series [129, 176] sets out the method to calculate a CMMs performance specifications for both contact probe and optical probe systems. This includes the calculation of the most specified CMM parameter, the length measurement error. The Redlux OrthoLux does not advertise the length measurement error of its system on its website, instead it states the resolution of the system as 20 nm, and the ISO10360 [176] specified capability of the RedLux is not in the public domain. The author would reasonably contend that this value is the resolution of the optical probe and not the overall uncertainty of the machine. This only adds to the desire to complete a measurement comparison study between the two instruments.

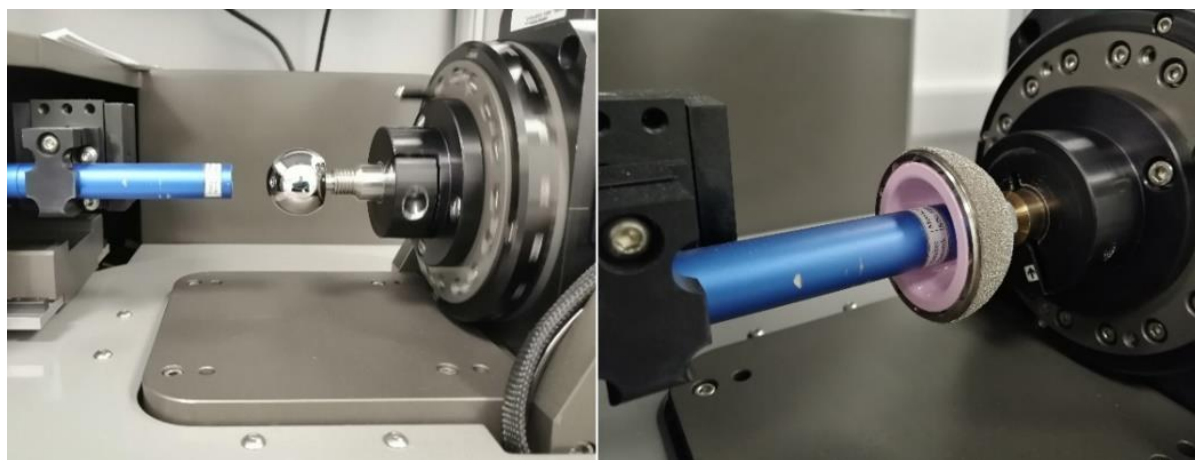


Figure 88: RedLux Optical CMM, measurement of femoral head (left) and acetabular liner (right).

A metal femoral head, polymer acetabular liner and a ceramic acetabular liner will be measured five times by both instruments. The radius, wear depth, measurement volume, and wear volume will be calculated, a wear map of each measurement will also be created. The standard deviation of each parameter dataset will be calculated allowing the instruments to be compared on their measurement repeatability.

Hip implant bearing components can be designed with very high conformity, resulting in small manufacturing tolerance bands such as 20 microns [9], but can be as low as 10 microns for metal bearings [177]. It is therefore crucial that measurement sets of the radius have a standard deviation value well within this tolerance band range. Polymer acetabular liners tend to have less strict manufacturing tolerances, with tolerance bands of approximately 150 microns [9]. Volumetric wear measurements also require a high level of repeatability as the volume loss in retrieved MoM implants can be very low, less than 5 mm³ [13, 110]. Therefore, a reasonable measurement repeatability target for radius/wear depth measurements is a standard deviation of 1 µm, and for volume measurements 2 mm³.

A 2018 study compared the traditional gravimetric method to both analogue probe and optical CMM instruments for wear measurement of ten MoM femoral heads and acetabular cups [151]. The samples were tested on a hip wear simulator up to two million cycles, gravimetric and optical CMM measurements were taken at intervals (0.33, 0.66, 1.0, 1.33 and 2.00 Mc) analogue probe CMM measurements were only taken at the start and finish. There was a high degree of linearity between optical and gravimetric methods ($R^2 = 0.997$ for femoral heads and $R^2 = 0.96$ for cups) from interval testing.

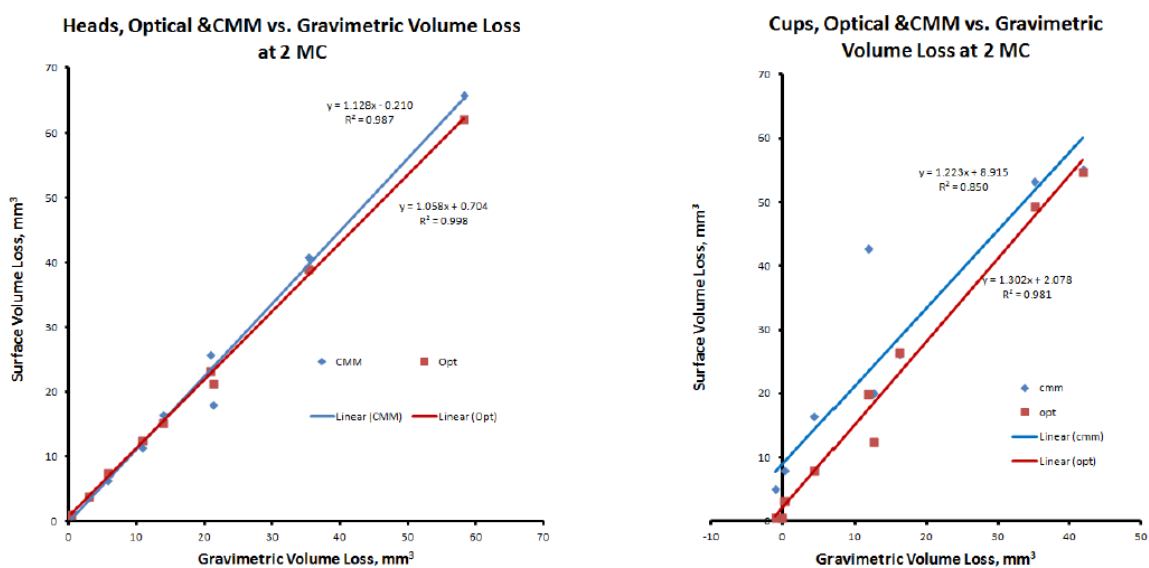


Figure 89: Comparison of Optical and Analogue Probe CMM, volume loss calculations of worn bearing components [178].

When comparing the analogue probe and optical CMM methods, the femoral heads showed no statistically significant difference. However, for the acetabular cups the analogue probe CMM measured significantly more wear than optical ($p = 0.04$). CMM methods measured more material loss than the gravimetric method (optical, $p = 0.01$; CMM, $p = 0.003$). It was theorised that two confounding factors resulted in this increase: burnishing and backside absorption. Burnishing is a type of polymer surface deformation, where geometrically the volume changes are registered, but no wear debris is released. This could account for increased wear measured from CMM methods. Backside absorption of proteinaceous debris on cups will increase the weight of the sample and therefore reduce the amount of weight loss detected by gravimetric measurement [151].

3.2 Methodology

3.2.1 CMM Performance Specifications

As previously discussed the RedLux OrthoLux does not provide a length measurement error value (at time of publication), this is the most common parameter to compare CMM performance. The listed performance specifications for each CMM are shown in table 10.

Table 10: CMM Performance Specifications.

Machine	Zeiss Prismo 5 navigator / VAST gold 2mm Probe [126]	RedLux OrthoLux [130]
Method	Analogue Contact Probe	Non-Contact Optical Chromatic Sensor
Length Measurement Error	$0.5 + L/500$ μm	-
Form Measurement Error	0.5 μm	-
Probing Error	0.5 μm	-
Resolution	-	20 nm

3.2.2 Cohort

Three hip implant bearing samples were measured, a metal femoral head, polymer acetabular liner and a ceramic acetabular liner, figure 90. Each of the components had a nominal radius of 18 mm. Samples were provided by DePuy Synthes, it was unknown whether the samples had been used for any experimental testing. On visual inspection scratches were visible on the surface of the metal femoral head, neither of the acetabular cup components had any visible scratches. Each component was measured five times on both of the CMMs. Latex gloves are worn when handling the components, cleaning is completed pre-measurement using isopropanol and a safe wipe, a hand squeezed air blower is used to remove any debris particles from the samples. Between each measurement the sample is cleaned and re-secured, as to replicate a new component being measured.

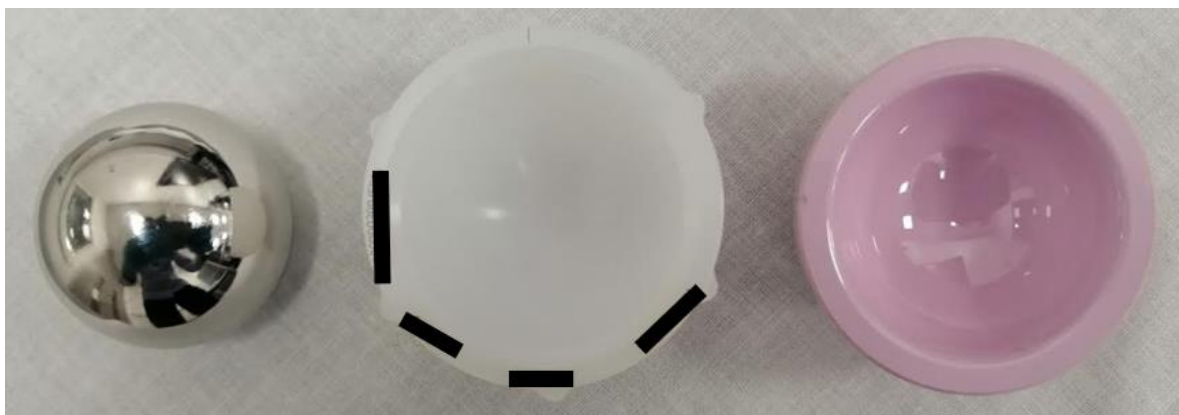


Figure 90: Measurement cohort. Left: Metal femoral head, centre: Polymer acetabular liner, right: Ceramic acetabular liner.

3.2.3 Fixture Setup

A suitable fixture setup is crucial to ensure no movement of the component during measurement. This is particularly important for the Zeiss CMM as the component is being contacted by the probe which could initiate movement if the component is not properly fixated.

The fixturing of the femoral head for the Zeiss CMM is achieved using a taper mount, figure 91, the femoral head is placed firmly on to the taper until it is fully engaged. The taper fixture is secured to the CMM base using tension clamps. The acetabular cup is fixated using a three-pronged holder fixture, figure 91. The acetabular cup is gently pressed into the centre of the three-pronged fixture where it is held by a spring, each prong is then carefully positioned over the rim of the acetabular cup, then each prong is tightened in place using a hex screw. The base of the fixture is secured to the CMM base using tension clamps.

The fixturing of the femoral head for the RedLux CMM is achieved using a taper with a screw base, which is screwed into the azimuth rotary axis of the machine until secure, figure 91. The acetabular cup is placed within a matching sized cup component, this cup component is then screwed onto a threaded mount on the azimuth rotary axis, figure 91. The distance the components are screwed into the azimuth rotary axis may need to be adjusted pre-measurement if prompted by the RedLux CMM.

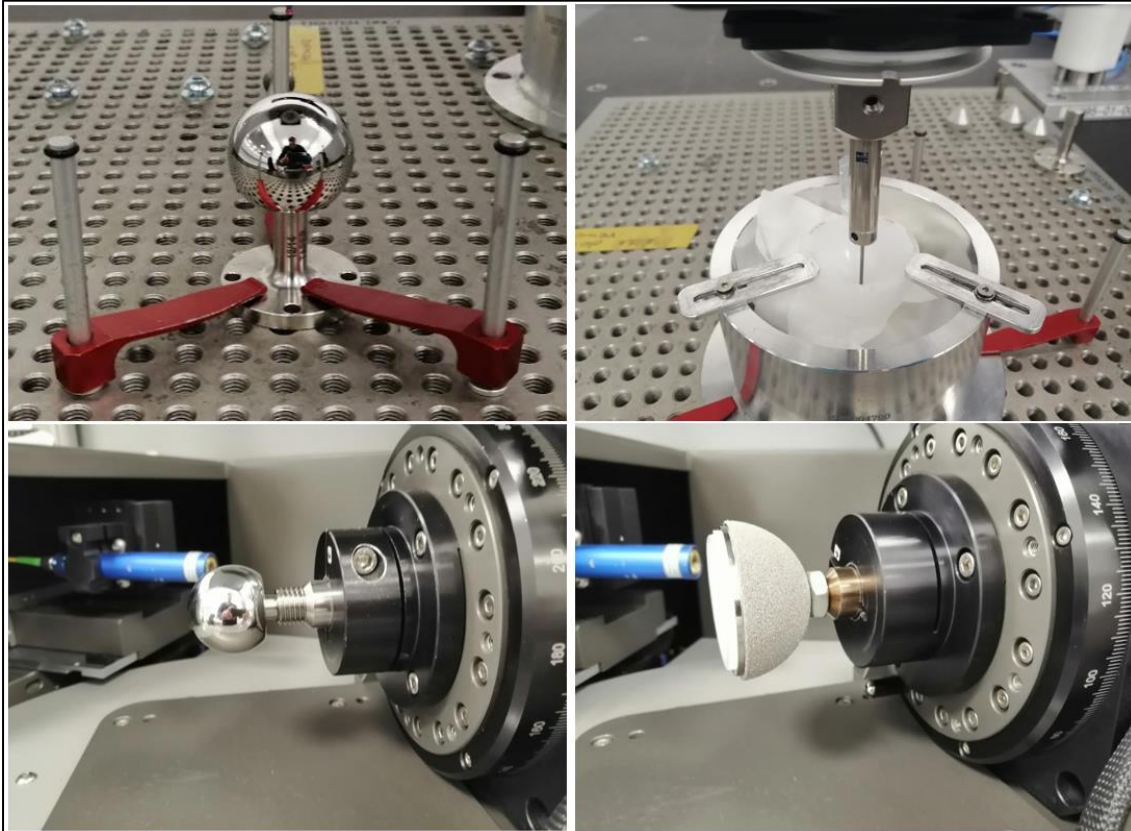


Figure 91: Fixturing setups. Top left: Zeiss CMM femoral head. Top right: Zeiss CMM acetabular liner. Bottom left: RedLux CMM femoral head. Bottom right: Zeiss CMM acetabular liner.

3.2.4 CMM Qualification

Before qualification both CMMs are initialised and left for one hour, this is to ensure all sensors adjust to the ambient room temperature. Both machines are located in the same temperature-controlled room, with the temperature set to 20 C degrees.

The Zeiss CMM is qualified using a reference sphere, this allows the stylus radius tip to be determined. If the radius value is deemed to be outside of the manufacturers required tolerance the user is notified of the issue. The RedLux CMM is qualified using a reference sphere, all measured data points of the reference sphere must lie within ± 250 nm of the reference sphere's nominal radius. The user must check this manually by analysing the deviation map of the reference sphere. Both reference spheres are calibrated, and measurement certificates are available.

3.2.5 Scanning Strategy

As previously discussed the scanning strategy outlined in ISO 14242 is rather ambiguous [12], with the requirement of mesh spacing being no greater than 1 mm. Therefore, the amount of data points used can vary greatly, for this study the same amount of data points are used on both CMMs, 97,188 data points. According to Bills study on CMM measurement uncertainty for hip implant bearings, this should result in approximately 3-4 mm³ of volumetric measurement uncertainty [13].

Although the amount of data points used by both CMMs is identical, the scanning strategy is slightly different on each instrument. The Zeiss CMM uses a polar scanning strategy which was outlined by Bills [13]. This scanning strategy consisted of 364 scan lines originating from the pole of the component up to 90 degrees elevation, each scan line has 267 evenly spaced data points, resulting in 97,188 total data points. The probe scan speed is set to the suggested optimal scan speed recommended by the CMM software (15 mm/s). The RedLux CMM scan is designed to work in a spiral pattern and is also set to measure up to 90 degrees elevation. The centre of the spiral originates at the pole of the component and spirals outwards towards the rim of the component. Both measurement strategies result in very similar mesh spacing, both exhibiting an increased mesh density at the pole of the component, figure 92.

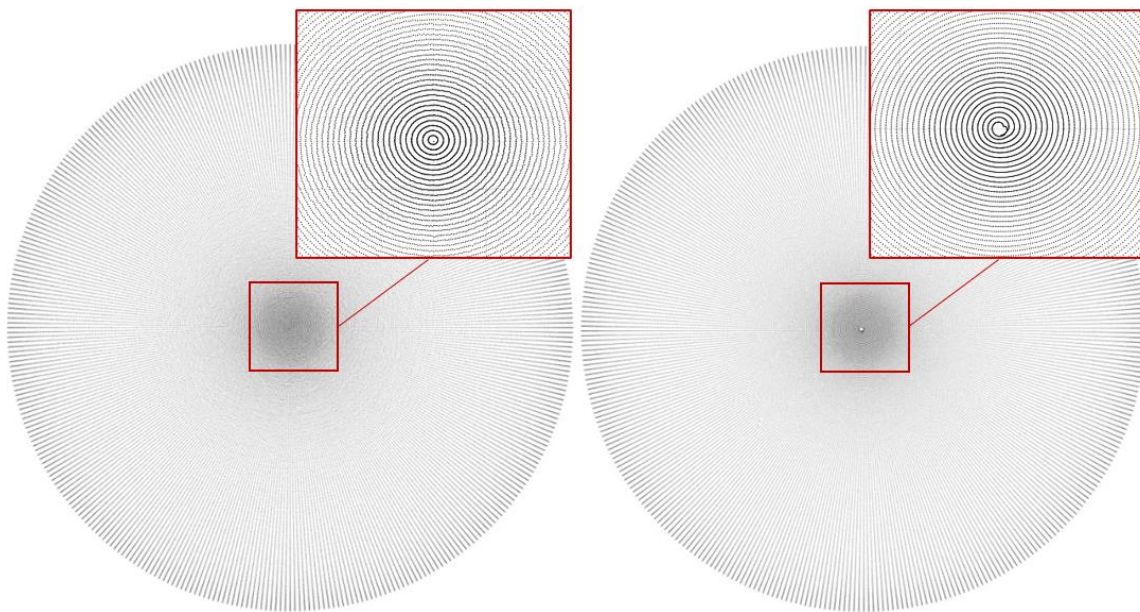


Figure 92: Comparison of scanning strategies. Left: Zeiss CMM, right: RedLux CMM. Zoom view of scan start shown in red.

3.2.6 Data Analysis

The analysis of CMM measurement data is completed using CATIA software [179], an overview of the analysis method is shown in figure 93. This analysis method was created by Bills et al. [13].

Initially the CMM measurement data is imported as a point cloud (A). The point cloud is then converted into a surface representing the measured worn femoral head, this shall be called the 'worn surface' (B). A sphere is then fitted to the worn surface, this will be used to represent the original pre-wear surface, this shall be called the 'pre-wear surface' (C). An initial deviation analysis can be made between the worn surface and the pre-wear surface, this allows the wear area to be identified (D). At this stage, the amount of wear is being underestimated as the pre-wear surface should only be constructed using the unworn portion of the worn surface. Therefore, a new sphere is fitted to the worn surface, however the wear area portion is excluded from the fitting (D). This allows for a more accurate reconstruction of the pre-wear surface to be created. Now a new deviation analysis is completed to create the wear map (E) and calculate the relevant parameters: radius, wear depth, measurement volume, and wear volume. The process of constructing a new pre-wear surface by excluding the wear area portion can be repeated until the wear parameters do not change between each iteration.

When calculating enclosed volumes, both the reconstructed original surface and CMM measurement data are trimmed using the same plane to ensure they have the exact same rim edge starting point (F). A 1 mm trim for the metal and polymer components, whereas a 4 mm trim is used for the ceramic acetabular liner due to an increased radius at the rim.

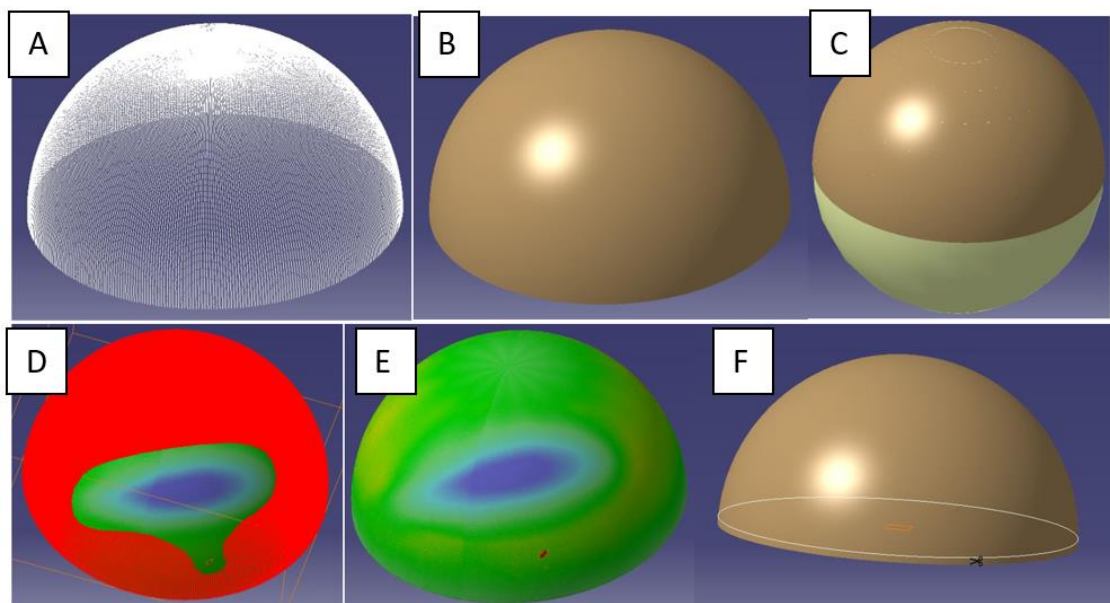


Figure 93: CMM analysis with CATIA, method steps. A: Import of CMM data. B: Fitting of worn surface to CMM data. C: Initial reconstruction of pre-wear surface. D: Exclusion or wear scar from pre-wear surface reconstruction. E: Resulting wear map. F: Trimming of both the worn surface and pre-wear surface by 1 mm to ensure same rim starting point.

3.3 Results

A summary of the parameter values calculated are presented in table 11, the median values and standard deviation for each dataset are recorded. A colour code is used for the standard deviation values to represent whether they are within the defined repeatability targets at the start of this chapter, SD value < 1 μm for radius and wear depth calculations, and SD value < 2 mm^3 for volume calculations. Green is within target, and orange is outside the target, red is when the result is $\geq 5x$ than the target. The full measurement results are found in the appendix.

Table 11: Comparison of Zeiss CMM and RedLux CMM, median values of 5 measurements and the standard deviation.

Metal Femoral Head	Zeiss		RedLux	
	Median	SD	Median	SD
Radius (mm)	17.99898	0.00025	18.00000	0.00020
Wear Depth (μm)	2.20	0.12	6.80	1.32
Total Volume (mm^3)	11195.92	0.91	11197.79	0.58
Wear Volume (mm^3)	0.81	0.04	0.72	0.02
Polymer Acetabular Liner				
Radius (mm)	18.44582	0.00343	18.43447	0.00539
Wear Depth (μm)	76.10	3.60	92.20	14.16
Total Volume (mm^3)	12193.20	11.43	12155.69	8.12
Wear Volume (mm^3)	45.65	3.53	40.41	2.60
Ceramic Acetabular Liner				
Radius (mm)	18.02558	0.00020	18.02566	0.00059
Wear Depth (μm)	6.20	0.40	6.90	0.19
Total Volume (mm^3)	8251.62	0.99	8241.76	7.56
Wear Volume (mm^3)	-0.26	0.06	0.11	0.10

3.3.1 Metal Femoral Head

Figure 94 shows box and whisker plots for the parameter values measured by both CMMs on the metal femoral head. The median radius values for the metal femoral head are calculated as 17.99898 mm (Zeiss) and 18.00000 (RedLux), these are similar median results, with a difference of 1.02 μm . Standard deviation values of 0.25 μm and 0.20 μm respectively, both datasets have high levels of repeatability well within the target of 1 μm for radius measurements.

The median wear depth values are 2.2 μm using the Zeiss and 6.8 μm using the RedLux, this is a large difference of 4.6 μm . This is due to the increased resolution of the RedLux system allowing for the depth of some scratches to be captured. The standard deviation values are 0.12 μm and 1.32 μm , the RedLux has a worse repeatability, however this can again be explained, due to its better resolution, individual scratch depths are sometimes captured but can also be missed when scanning the surface.

The median total volume of the measurement values are 11195.92 mm^3 (Zeiss) and 11197.79 mm^3 (RedLux), this is a difference of 1.87 mm^3 . The standard deviation values are 0.91 and 0.58 mm^3 , both very low and within suggested targets. The median wear volume was measured to be very small from both machines, 0.81 mm^3 (Zeiss) and 0.72 mm^3 (RedLux) a difference of 0.09 mm^3 . The standard deviation values are 0.04 and 0.02, both very low and within suggested targets. As the amount of wear on the component was so minimal, a more heavily worn component would have provided a better test for comparison.

For the metal femoral head, when comparing Zeiss to RedLux, the radius values had a 1 μm difference, and the wear depth was measured deeper on the RedLux, this can be explained due to increased RedLux measurement resolution. Volume calculations from both CMMs are close, with only a 0.09 mm^3 difference in wear volume and 1.87 mm^3 in total volume. Standard deviation values are low on both CMMs and within the recommended targets set at the start of this chapter.

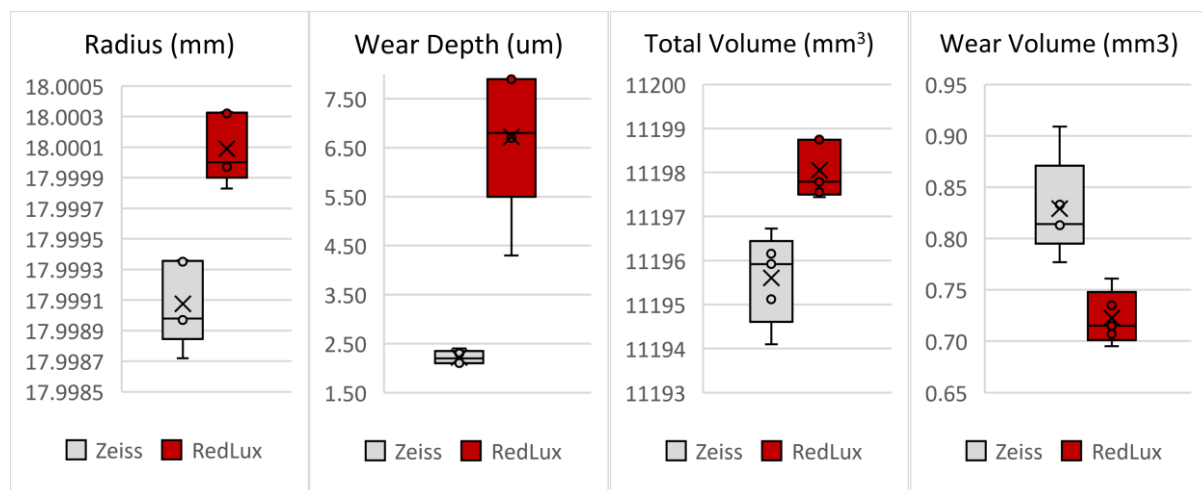


Figure 94: Box and whisker plots for metal femoral head measurement results, exclusive of median for quartile calculations.

3.3.2 Polymer Acetabular Liner

Figure 95 displays the box and whisker plots for polymer acetabular liner measurements. The median radius values are calculated as 18.44582 (Zeiss) and 18.43447 (RedLux), this is a difference of 11.35 μm . This is much greater than the difference between the instruments when measuring the metal femoral head. As the exact size of the liner is unknown, it cannot be determined which measurement set is more accurate. The standard deviation values are 3.43 μm (Zeiss) and 5.39 μm (RedLux), the standard deviation has increased for both instruments when compared to metal femoral head measurements. These standard deviation values are not within the 1 μm target, however as polymer acetabular liners tend to have less strict manufacturing tolerances, these standard deviation values may still be acceptable for a manufacturer.

The polymer acetabular liner is measured to have significant wear, the median wear depth values are calculated as 76.1 μm (Zeiss) and 92.2 μm (RedLux). Again, a greater wear depth is calculated using the RedLux due to its increased resolution. However, we can also see that the spread of measurement data is much larger on the RedLux, a standard deviation of 3.6 μm (Zeiss) compared to 14.16 μm (RedLux). This can again be explained due to the RedLux increased resolution, individual scratch depths are sometimes captured but can also be missed when scanning the surface.

The median total volume of the measurements are 12193.2 mm^3 (Zeiss) and 12155.69 mm^3 (RedLux), the RedLux total volume is lower by 37.51 mm^3 . The standard deviation values are 11.43 mm^3 (Zeiss) and 8.12 mm^3 (RedLux), the RedLux showing better repeatability for this parameter. Compared to the measurements on the metal and ceramic components, again the repeatability is worse, with higher standard deviation values. The wear volume was calculated as 45.65 mm^3 (Zeiss) and 40.41 mm^3 (RedLux), a difference of 5.24 mm^3 , the standard deviation values are 3.53 mm^3 (Zeiss) and 2.6 mm^3 (RedLux). Both CMMs are capable of determining the wear area and calculating the volume loss, with similar median values and repeatability.

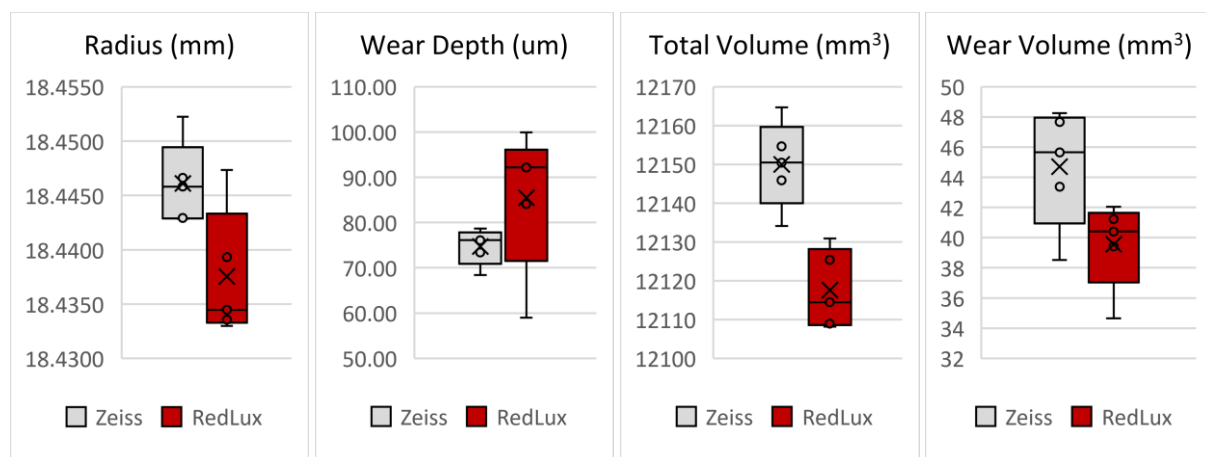


Figure 95: Box and whisker plots for polymer acetabular liner measurement results, exclusive of median for quartile calc.

For the polymer acetabular liner, both the Zeiss and RedLux had a reduction in their agreement with each other and repeatability compared to metal and ceramic component measurements. The radius values had a 11.35 μm difference, and again the RedLux measured a greater amount of wear depth. Wear volume calculations showed better agreement with a 5.24 mm^3 difference and better standard deviation values. Both instruments have a worse repeatability when measuring polymer components, and less agreement in their results, compared to measuring metal or ceramic components. This reduction in repeatability could be explained by light reflection below the semi-transparent surface affecting the RedLux CMM results. Whereas for the Zeiss CMM the softer polymer surface may allow the contact probe to slightly deform the surface before a measurement point is created.

3.3.3 Ceramic Acetabular Liner

Figure 96 displays the box and whisker plots for ceramic acetabular liner measurements. The median radius values are calculated as 18.02558 mm (Zeiss) and 18.02566 (RedLux), this is a difference of 0.08 μm , these results are very close. Standard deviation values are 0.2 μm (Zeiss) and 0.59 μm (RedLux) both well within the recommended repeatability target.

The median wear depth values are calculated as 6.2 μm (Zeiss) and 6.9 μm (RedLux), very similar values, the RedLux measures a slightly deeper wear depth, but not as much as it did for the polymer and metal components, this could be due to the absence of scratches, which are therefore not measured by the increased resolution of the RedLux instrument. The standard deviation values are calculated as 0.4 μm (Zeiss) and 0.19 μm (RedLux), both well within target.

The median total volume of the measurements are 8251.62 mm^3 (Zeiss) and 8241.76 mm^3 (RedLux), a difference of 9.86 mm^3 . With SD values of 0.99 mm^3 (Zeiss) and 7.56 mm^3 (RedLux), clearly the Zeiss showing a better repeatability for this set. Although a wear depth was calculated, the region of wear is thin on the rim of the liner, leading to very low volumetric wear values, so low they are negligible and difficult to differentiate from no wear. The following wear volumes were calculated, -0.26 mm^3 (Zeiss) and 0.11 mm^3 (RedLux), the Zeiss value is indicating negative wear. The SD values are: 0.06 mm^3 (Zeiss) and 0.10 mm^3 (RedLux). In an experimental study these wear values should not be included as they are too low when considering the measurement uncertainty of the CMMs.

For the ceramic acetabular liner, the Zeiss and RedLux had a close agreement in their results and both good repeatability. The median radius values with only a 0.08 μm difference, and similar measurements of wear depth, slightly greater on the RedLux. The amount of volumetric wear on the

ceramic acetabular liner was too small to accurately calculate as only a very thin region at the rim area was worn, leading to a negative median wear volume value on the Zeiss measurements, and one negative wear value from the RedLux set of measurements.

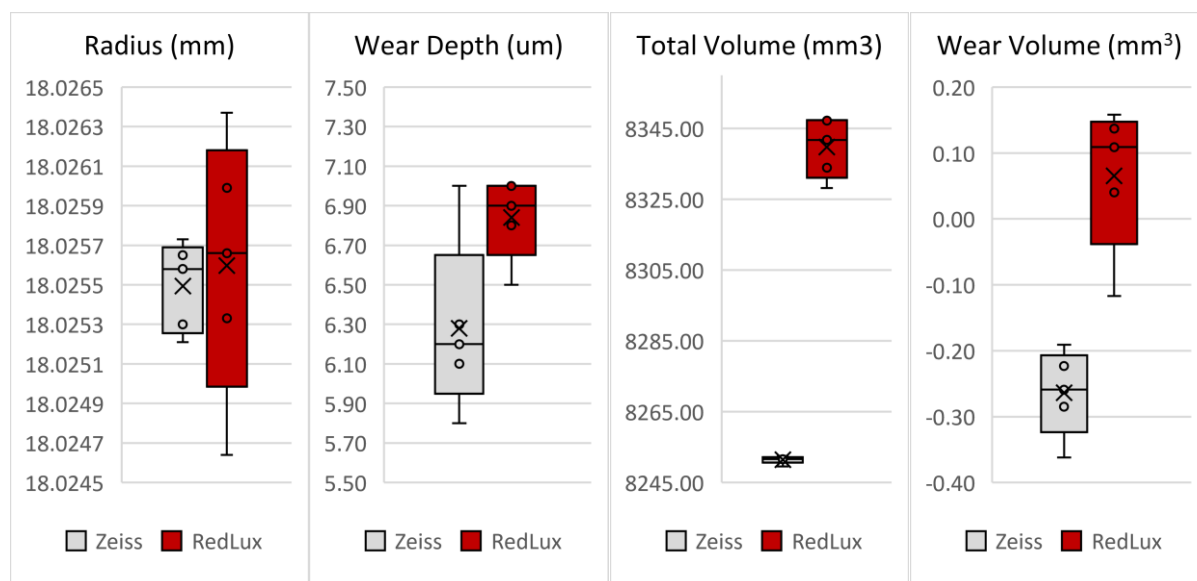


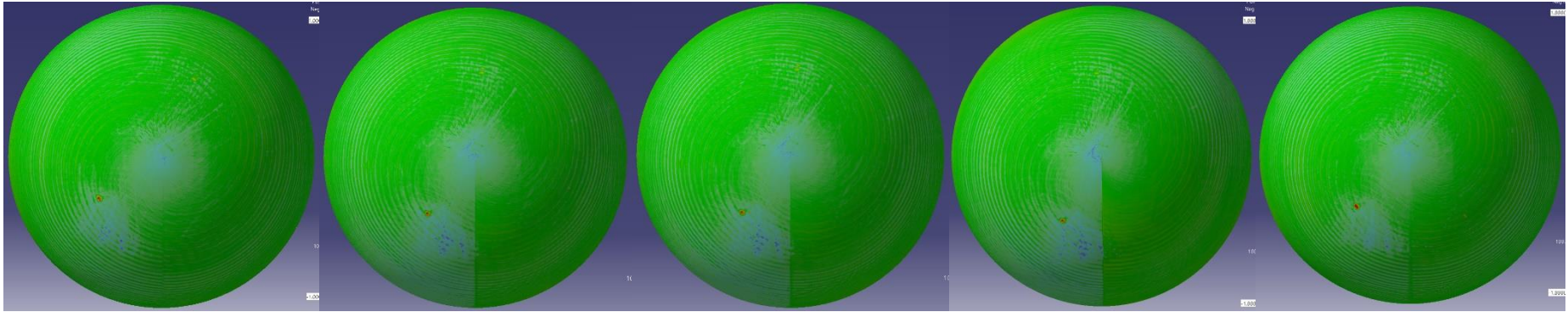
Figure 96: Box and whisker plots for ceramic acetabular liner measurement results, exclusive of median for quartile calc.

3.3.4 Wear Maps

All of the wear maps are shown in figures 97 – 99. For femoral heads, wear is indicated by negative deviation and is therefore blue in colour, whereas for acetabular liners wear is indicated by positive deviation and is therefore red in colour. Note that for some measurements the components are not aligned the same as the previous measurement, therefore the location of wear may appear to change but in reality it has not, the component is aligned differently during measurement.

3.3.4.1 Metal Femoral Head Wear Maps

Zeiss Measurements, Colour Scale: -3 μm to + 5 μm



RedLux Measurements, Colour Scale: -3 μm to + 5 μm

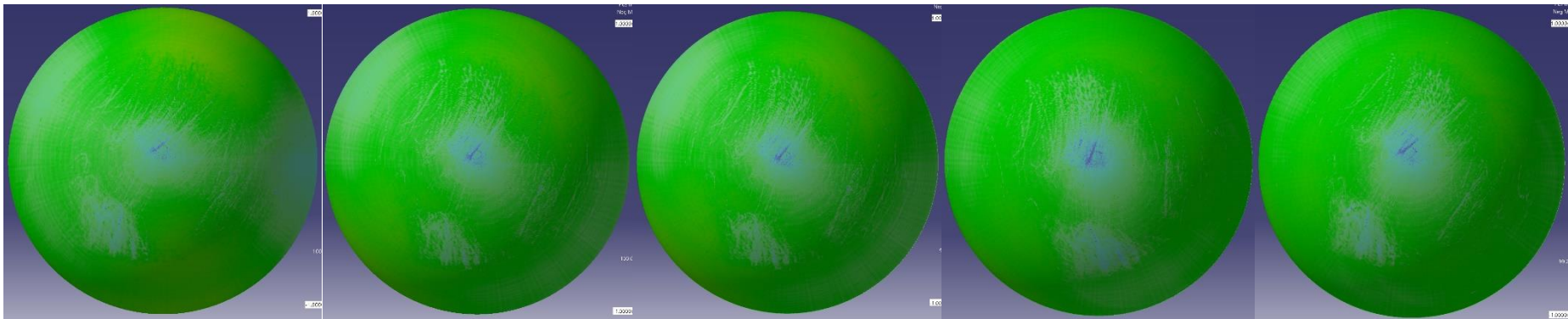
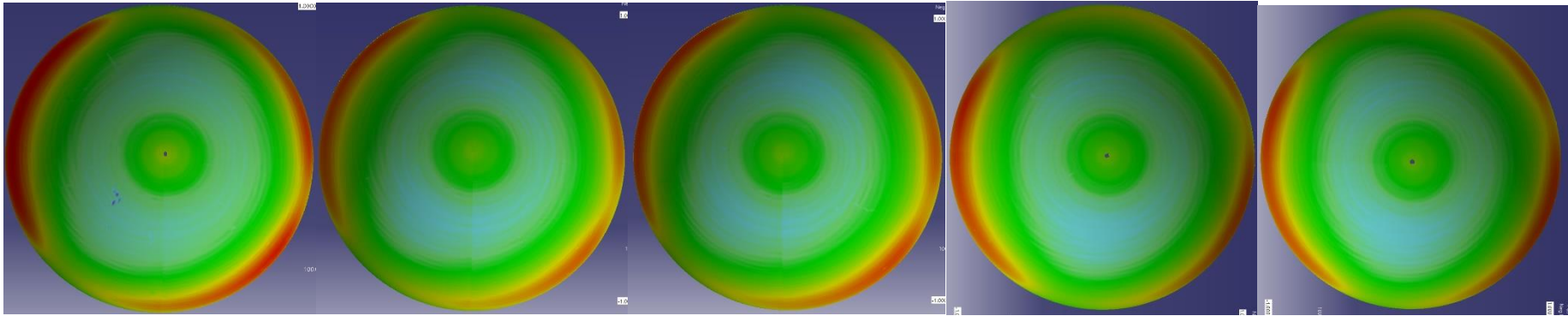


Figure 97: Metal femoral head wear maps.

3.3.4.2 Polymer Acetabular Liner Wear Maps

Zeiss Measurements, Colour Scale: -40 um to + 90 um



RedLux Measurements, Colour Scale: -40 um to + 90 um

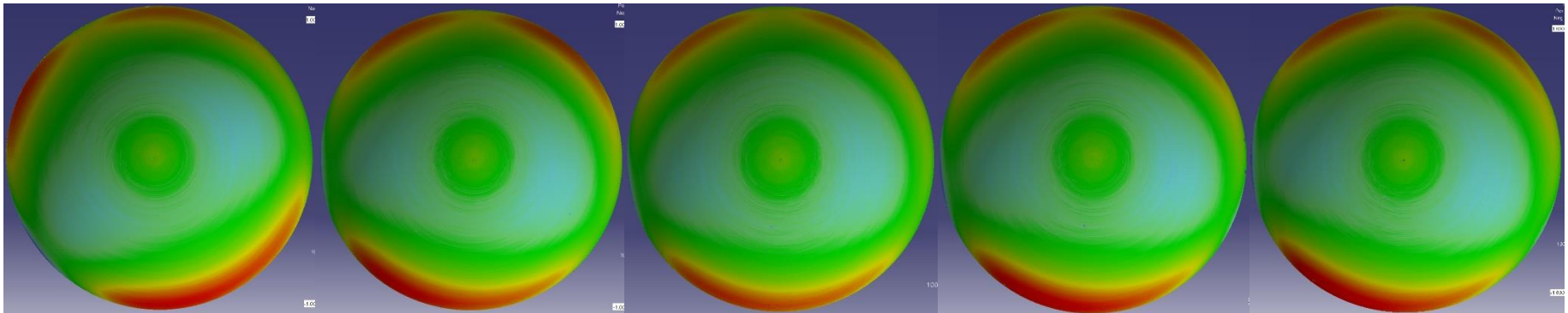
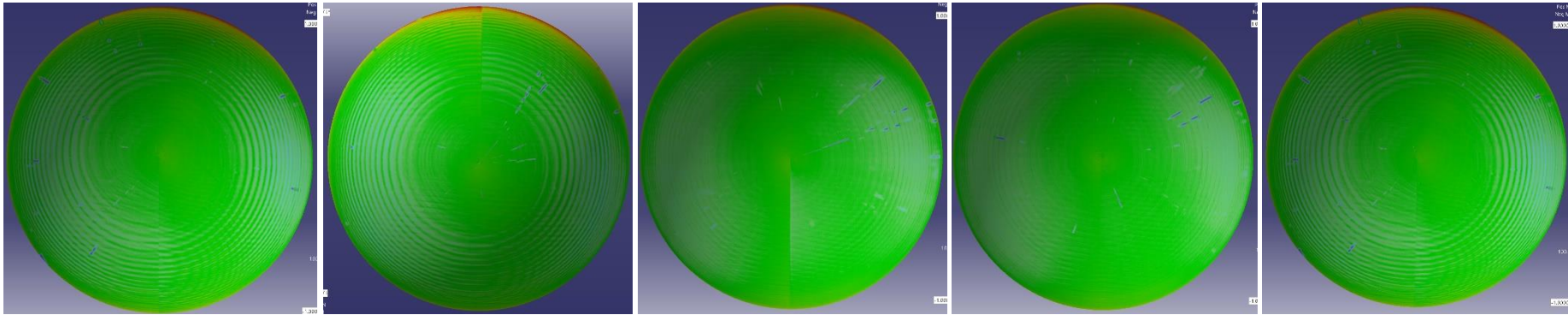


Figure 98: Polymer acetabular liner wear maps.

3.3.4.3 Ceramic Acetabular Liner Wear Maps

Zeiss Measurements, Colour Scale: -7 μm to + 4 μm



RedLux Measurements, Colour Scale: -7 μm to + 4 μm

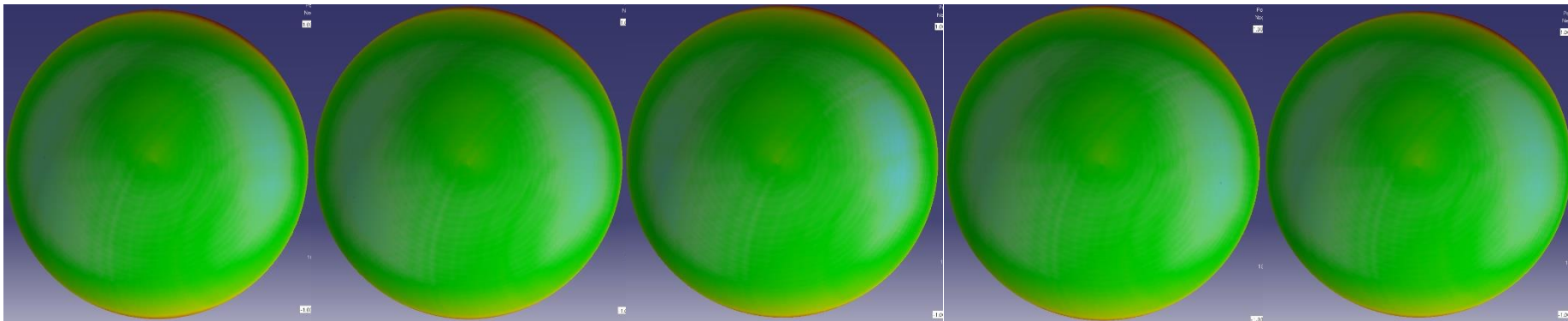


Figure 99: Ceramic acetabular liner wear maps.

3.4 Discussion

3.4.1 Radius Comparison to Tolerance Bands

In this section the median radius values calculated by each of the CMMs will be compared to the corresponding manufacturing tolerance bands for each component, table 12.

For the metal femoral head and the ceramic acetabular liner, the median radius values calculated by both of the CMMs falls within the manufacturing tolerance band. However, for the polymer acetabular liner the median values from both CMMs both are lower than the manufacturing tolerance band. This could indicate that both CMMs are measuring the radius too small compared to the real value. Secondly it could indicate that the polymer acetabular liner was manufactured smaller than the manufacturing tolerance band. There is also the possibility that the manufacturing tolerance band selected did not match the corresponding component.

Table 12: Radius tolerance bands for each component measured.

Component	Manufacturing Tolerance Band (mm)	Zeiss (mm)	RedLux (mm)
Metal Femoral Head	17.99463 - 18.00479	17.99898	18.00000
Polymer Acetabular Liner	18.4858 - 18.6182	18.44582	18.43447
Ceramic Acetabular Liner	18.01 - 18.035	18.02558	18.02566

3.4.2 Measurement Time

The measurement time is significantly lower using the RedLux (approx. 7 minutes) compared to the CMM (approx. 46 mins). The measurement time can be reduced on the CMM using fewer measurement points or a faster scan speed, although this will reduce the measurement accuracy. Despite the CMM being slower for individual measurements, the CMM has a large measurement area which can allow multiple samples to be measured consecutively in one measurement program. Multiple sample measurement cannot be achieved using the RedLux instrument.

3.4.3 CMM Fixture Setup

For 'hard' components the fixturing of samples for CMM measurement is particularly important, this is due to the minimal wear present on these 'hard' components. Even very small instability of the sample can lead to measurement failure. This occurred at times for ceramic liner measurements due to the three-pronged holder fixture not suitably securing the sample.

An alternative to using the previously described three-pronged holder is to place the liner within a corresponding size acetabular shell and clamp the edges of the acetabular shell to the CMM bed. Using the alternative shell setup allowed the components to be consistently secured in less time and there was no measurement failure due to instability of the component. The three-pronged holder fixture was more difficult to setup taking considerably more time and would result in a failure of a successful measurement for approximately 50% of ceramic liner measurements.



Figure 100: Alternative fixture setup for acetabular liners.

3.4.4 RedLux Wear Depth Measurement

The maximum linear wear depth is consistently measured deeper using the RedLux compared to the Zeiss. It is theorised that because the RedLux has a lower measurement width, spot diameter 4 μm , this allows the depth of scratches to be captured, whereas the CMM cannot measure the internal depth of scratches due to the size limit of the 2 mm stylus tip. This also explains the lower repeatability of the RedLux instrument for wear depth measurements, as from one measurement to the next, different scratches could be captured which will affect the wear depth value.

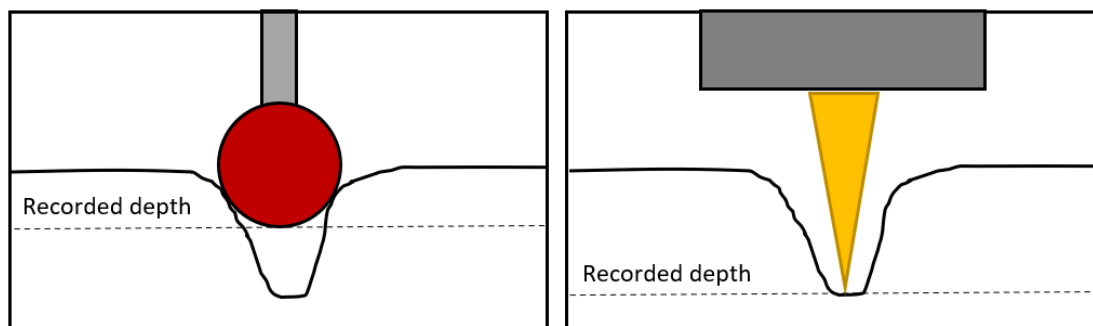


Figure 101: Diagram of scratch measurement on the Zeiss (left) and RedLux (right).

3.4.5 RedLux Analysis Software

An important benefit of the RedLux instrument is the in-built analysis software that can be used to instantly analyse measurement data whilst at the machine or on a computer of the user's choice. It allows the user to create wear maps of the component and calculate parameters such as radius, linear wear, and wear volumes [130]. This is not available on the Zeiss, as it is a multi-use instrument, used in many industries and applications. However, analysis software such as MATLAB and CATIA can be setup to analyse the Zeiss measurement data, as shown in this chapter.

3.4.6 Further Work

Further work that could be completed to improve on this project include:

- **Calibration Ball Measurement**

Measurement of a calibration ball would allow for the accuracy of the CMMs to be better compared. Currently this study covers the repeatability of each machine well, however it is unknown which measurement sets are more accurate when comparing the CMMs. By measuring a calibration ball, the dimensions of the ball will be well determined, and therefore the measurement values calculated can be compared for accuracy with more confidence.

- **Larger Cohort Size and Multiple Test Users**

A larger cohort size will allow results to be determined with more confidence. By completing the same measurements again with different test users, this allows any human influences on the measurement repeatability to be noted.

3.5 Chapter Summary

This study has compared the measurement repeatability of an analogue probe CMM, Zeiss Prismo, to a non-contact optical CMM, RedLux OrthoLux, for geometrical and wear measurement of hip implant bearing components.

A metal femoral head, polymer acetabular liner, and a ceramic acetabular liner were measured five times by both CMMs. The radius, wear depth, measurement volume, and wear volume were calculated, and a wear map of each measurement was also created. The standard deviation of each parameter dataset was calculated allowing the CMMs to be compared on their measurement repeatability.

Both CMMs showed good levels of repeatability when measuring metal and ceramic bearing components, mostly within the targets of a standard deviation value less than 1 μm for radius/wear depth measurements, and a standard deviation values less than 2 mm^3 for volume measurements. Both CMMs showed a decrease in repeatability for polymer component measurements, compared to metal and ceramic components.

Overall, it was shown that both machines can be used to effectively measure the geometry and wear of hip implant bearing surfaces. The RedLux CMM demonstrated a much quicker measurement time and Zeiss CMM measurements were more susceptible to error introduced by imperfect fixturing.

Whilst there are differences highlighted in the presented results reported for the two CMM systems, both techniques are widely used in industry. For both systems, their usefulness would be enhanced by combining their output with detailed surface mapping in areas on the surface where wear is prevalent and combining the metrology techniques would clearly enhance the understanding of the dominant wear mechanisms.

Chapter 4: Development of the Custom Fixture System

4.1 Design Requirements Checklist

In this section the requirements of the custom fixture system are collated into a list and discussed, these requirements will be followed throughout the development of the fixture system. The main aims were previously mentioned in the project aim section:

- Relatively Low Cost
- High Accuracy Positional Control
- Easily Compatible with CMM and Surface Metrology Instruments
- Data Fusion of Captured Data

For the design requirements checklist, more specific fixture design requirements are added:

- Low Fixture Height
- Motorised Stages with Digital Control
- Custom Control Software
- Surface Measurement Stitching Capabilities
- Reverse Coregistration of Datasets
- Compatibility Focus for Femoral Heads

Relatively Low Cost

As this is an initial prototype design, the development costs should be kept relatively low, the fixture system can be improved later on with more expensive components. The fixture system is designed to be a low-cost alternative to a brand new fused metrology instrument. For an initial target, the budget was set at £2,500, with the majority of the cost budgeted to be spent on motorised rotary stages and the supporting control hardware.

High Accuracy Positional Control

The main requirement for the fixture system is to accurately manoeuvre the bearing component, allowing access for surface measurement anywhere on the bearing surface. With suitably high positional accuracy, the fixture system will ensure the most critical surface topography is captured on the component, which would not be possible with poor positional accuracy fixtures.

Easily Compatible with CMM and Surface Metrology Instruments

As this fixture system is designed to be used with both CMM and surface metrology instruments, the fixture system must be easily compatible with both. It must be designed to be compatible with all bridge CMMs and surface metrology instruments on the market, this ensures the fixture system is flexible enough to be used in a multitude of metrology labs setups.

Data Fusion of Captured Data

It is critical to use the generated CMM wear map of the component for positional reference and control of the fixturing system, this allows for wear map targeted surface measurements. As previously discussed, wear map targeted surface measurements are crucial due to the changing surface topography within wear scars. Additionally, combining the outputs from the CMM and surface metrology instrument in a fused data context will allow for a comprehensive investigation into tribological/wear behaviour of the component.

Low Fixture Height

As previously mentioned the fixture system should be flexible to work with all common bridge CMMs and surface metrology instruments. Due to the large measurement volume of bridge CMMs, the physical size requirements of the fixture system are only restricted by the measurement volume of surface metrology instruments. Crucially, the fixture system must have a low height in order to fit within the measurement height limits of common surface metrology instruments. This is typically < 100 mm [164], where the component and fixture need to be situated below the objective lens.

Motorised Stages with Digital Control

Motorised stages with digital control allow for fast, high precision movement, they also allow for a multitude of user-friendly control options, permitting CMM data to control the position of surface measurements. Digitally controlled stages can use input from a computer to control the stages, this is crucial as it allows for the utilisation of custom control software. The main drawback of motorised stages is the increased cost to purchase compared to manual stages.

Custom Control Software

Custom control software will be developed to be used with the motorised stages; this allows CMM measurement data to be used as direct input for control of the fixturing system. Crucially this software will allow for wear map targeted surface measurements and an array of control options which are user-friendly and are crucial to the success of the fixturing system.

Surface Measurement Stitching

A 'stitch' describes a series of surface measurements which have been combined together to increase the surface measurement size. Modern surface measurement instruments have the capabilities to stitch over a larger area than a single measurement but only when the measurement surface is relatively flat. This fixture system aims to provide a high enough level of accuracy to allow multiple surface measurements to be stitched together across the curvature of the bearing component. An area of particular focus is the wear scar of the component, a stitch of areal surface measurements entirely through the wear area has never been reported and would be a novel step forward in analysis of hip implant components. This will allow for a detailed surface analysis throughout the wear area, and see how it varies throughout, including at the boundaries.

Additional Reverse Coregistration of Datasets

Standard coregistration refers to selecting a location on the CMM wear map and using the spherical coordinates to control the fixture system and manoeuvre the component to the defined area of interest for surface measurement at this location. This is how the fixturing system is primarily designed to be used. However, reverse coregistration refers to manoeuvring the component firstly using the fixture system and scanning the surface without any use of the wear map. Once a surface feature of interest is found, the spherical coordinates can then be saved and referred back to a CMM wear map. This is not primarily how the fixture system is intended to be used but provides a useful alternative analysis option.

Compatibility Focus for Femoral Heads

The initial focus for the fixture system is to be compatible for use with femoral heads, this is due to the greater amount of surface accessibility for measurement compared to that available for acetabular cups. In the future the fixture system could be developed with minor adjustments allowing it to be used for acetabular cups, or even knee replacement components.

4.2 Required Positional Uncertainty of the Fixture System

4.2.1 Accuracy, Uncertainty, and Error for Metrology

Commonly the terms 'accuracy' and 'uncertainty' describe how sure we are of something, but in metrology these words have distinct separate meanings and it is important to understand their meanings and use the correct terminology [180]. The accuracy of measurement is an older term, and the agreed definition is: 'the closeness of the agreement between the result of a measurement and a true value of the thing being measured'. The definition also states that accuracy is a qualitative concept and therefore can be expressed as high or low, but numbers should not be used, however in practice this is not the case. Accuracy is often used quantitatively and then the definition changes to: 'the difference between a measured value and the true value'. This definition is not possible as it relies on the fact that a true value can be defined, but in reality true values can never be realised. It is impossible to define or make perfect measurements, there is always a level of uncertainty [149, 180, 181]. The uncertainty of measurement acknowledges that no measurement can be perfect and is defined as: 'a parameter, associated with the result of a measurement, that characterises the dispersion of values that could reasonably be attributed to the thing being measured'. It is usually expressed as a range of values in which the value is estimated to lie, within a given statistical confidence, it does not rely on a true value. For example, the length of a stick measures 20 centimetres, plus or minus 1 centimetre, at the 95 percent confidence level [149, 180, 181]. This can be written as:

20 cm \pm 1 cm, at a level of confidence of 95%

Therefore, for estimates of performance, and to discuss validity of measurement results the parameter uncertainty should be used rather than the term accuracy [149, 180, 181].

To calculate the uncertainty of a measurement, the sources of uncertainty in the measurement must be identified, the combined standard uncertainty can then be calculated from the individual sources. To help in the process of calculation it can be useful to summarise the uncertainty analysis or 'uncertainty budget' in a spreadsheet [149, 180, 181]. A relevant example of this is the calculation of measurement uncertainty for CMM volumetric measurement of hip implant bearings completed by Bills [13]. More information on calculating the measurement uncertainty is found within the NPL's 'Good Practice Guide' [149].

It is important not to confuse the terms 'error' and 'uncertainty'. Error is the difference between the measured value and the 'true value' of the thing being measured. Uncertainty is a quantification of

the doubt about the measurement result. When possible we try to correct for any known errors, but any error whose value we do not know is a source of uncertainty [149].

4.2.2 Calculating the Target Positional Uncertainty

4.2.2.1 Stitching Scenario for the Target Positional Uncertainty

The target positional uncertainty for the fixture system is important to determine before the design is considered. The level of required positional uncertainty can be determined by using stitching as the measurement scenario. As one of the requirements of the fixture system is to stitch together surface measurements, this will be the stage where the highest amount of positional precision is required, figure 102. One important factor is the sampling size of the surface measurement instrument that the fixture system is being used in combination with. A typical surface interferometer sampling size is $918.57 \times 918.57 \text{ um}$, this is based on a 20x lens measurement using the Taylor Hobson TalySurf CCI. This approximately 1 mm^2 sampling size will be used as the basis of calculating the required positional uncertainty of the fixture system.

Assuming that the azimuth angle of the component is kept constant, the required change in elevation angle between stitches can be calculated. The fixture system must maneuverer the component from the initial surface measurement location to the next surface measurement location allowing for a region of overlap between the initial surface measurement and the next surface measurement in the stitching series. This amount of overlap required can vary but to be cautious a large target overlap region of 20% will be used, figure 102.

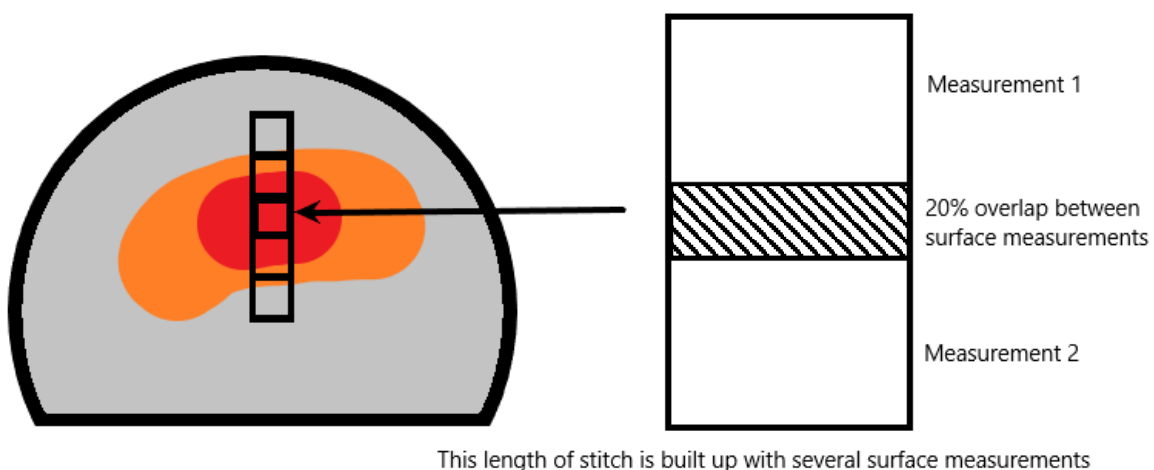


Figure 102: Stitching of surface measurements through the wear area of a femoral head, not to scale.

4.2.2.2 Effect of Component Size

The size of the component being manoeuvred will also make a difference to the required precision of the fixture system. Elevation angle adjustments on a larger bearing component result in a greater change in distance along the surface, figure 103.

Consider figure 103, the left and centre femoral heads are tilted through 30 degrees of elevation angle, the resulting distance changed along the surface can be seen as AB and CD, CD is clearly longer than AB. This shows that as the bearing size becomes larger the change in distance along the surface from adjusting the elevation angle becomes greater. However, when the large right femoral head is tilted only 20 degrees of elevation angle, the resulting distance along the surface EF closely matches the distance along the surface of AB. Therefore, as the bearing becomes larger in diameter a smaller change in elevation angle is required to maintain the 20% overlap measurement area.

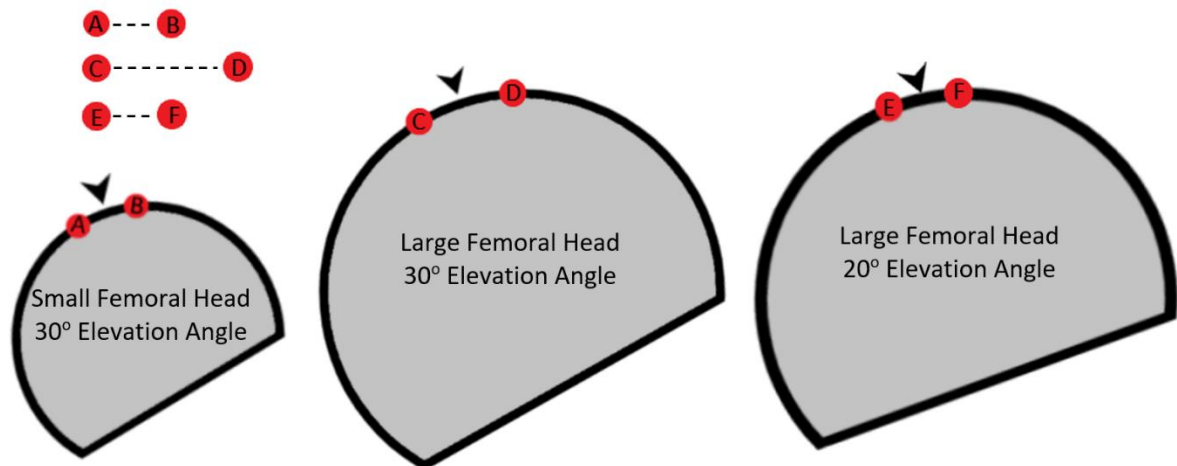


Figure 103: Relationship of bearing size with required elevation angle adjustment.

As a larger bearing component requires greater precision, theoretically large bearing size will be used to calculate the target positional uncertainty. A 60 mm diameter femoral head is used for the calculation of the target positional uncertainty, as this size is larger than any commonly manufactured femoral head, which are usually up to 54 mm [4].

4.2.2.3 Calculating the Target Positional Uncertainty

To calculate the target positional uncertainty, firstly the distance along the surface between two measurements in a stitch series is calculated, figure 104. This equation uses the sampling length of the measurement (ls) and the required overlap percentage ($OL\%$) as part of the calculation. This makes the equation flexible as it allows for the sampling length and overlap percentage parameters to be adjusted. The distance between the two measurements with zero overlap percentage would be equal to the sampling length, to adjust for this the required overlap region must be considered. For example, with a sampling length of 918.57 μm and an overlap percentage of 20% this would result in a distance of 734.856 μm , figure 104.

$$dist = ls \times \left(1 - \frac{OL\%}{100}\right)$$

$$\text{Example 1, } dist = 918.57 \times \left(1 - \frac{20}{100}\right) = 734.856 \mu\text{m}$$

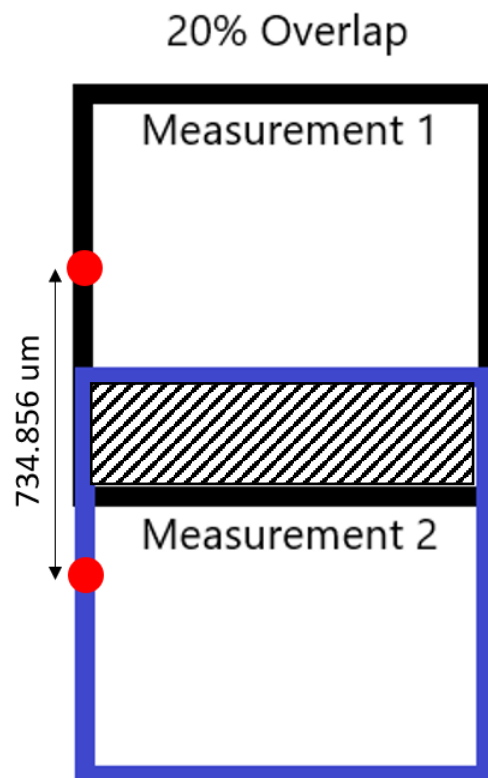


Figure 104: Distance along the surface between two measurements in a stitch series, sampling length of 918.57 μm . The red circles mark the midpoint of the surface measurements, the distance between the midpoints is the required change in distance.

Although the required positional adjustment in length is known, the fixturing system will work by adjusting the component in elevation angle. Therefore, this change in distance needs to be calculated as an angle, figure 105. As previously discussed, the required change in angle is smaller for larger femoral heads, so a large femoral head size of 60 mm is used.

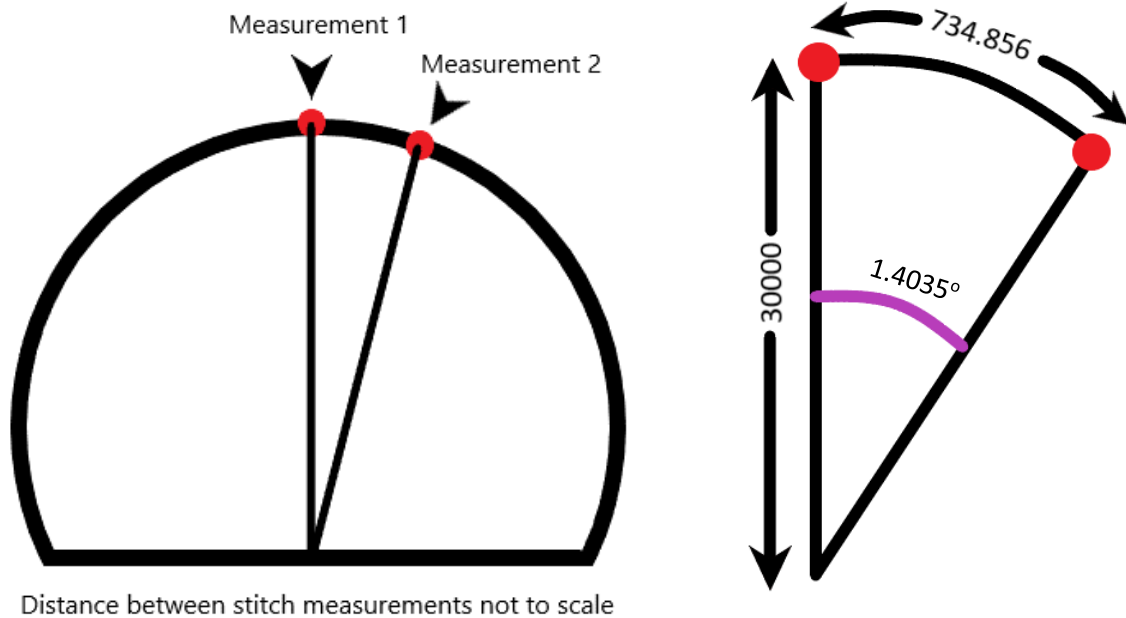


Figure 105: Calculation of the change in elevation angle between stitch measurements.

The change in elevation angle can now be calculated using the arc length formula:

$$\theta = \frac{\text{arclength}}{\text{radius}}$$

$$\theta = \frac{734.856}{30000}$$

$$\theta = 0.024495 \text{ rad}$$

$$\theta = 1.4035 \text{ deg}$$

Now that the required change in elevation angle is known (1.4035°), the level of positional uncertainty can be considered, figure 106. If the target overlap between stitch measurements is 20% we can set the target uncertainty to be within $\pm 5\%$ of this, resulting in an actual overlap of 15-25%. This ensures a suitable amount of overlap is achieved between stitch measurements. The required positional uncertainty distance (u) is calculated by multiplying the measurement sampling length (sl) by the target positional uncertainty percentage ($u\%$), figure 106. Using the same arc length calculation method as earlier, assuming a 60 mm femoral head, this would equate to an angular positional uncertainty of ± 0.0877 degrees or ± 5.262 arcmin. Therefore, a stitch measurement on a 60 mm femoral head will be required to move 1.4035° with a positional uncertainty of $\pm 0.0877^\circ$.

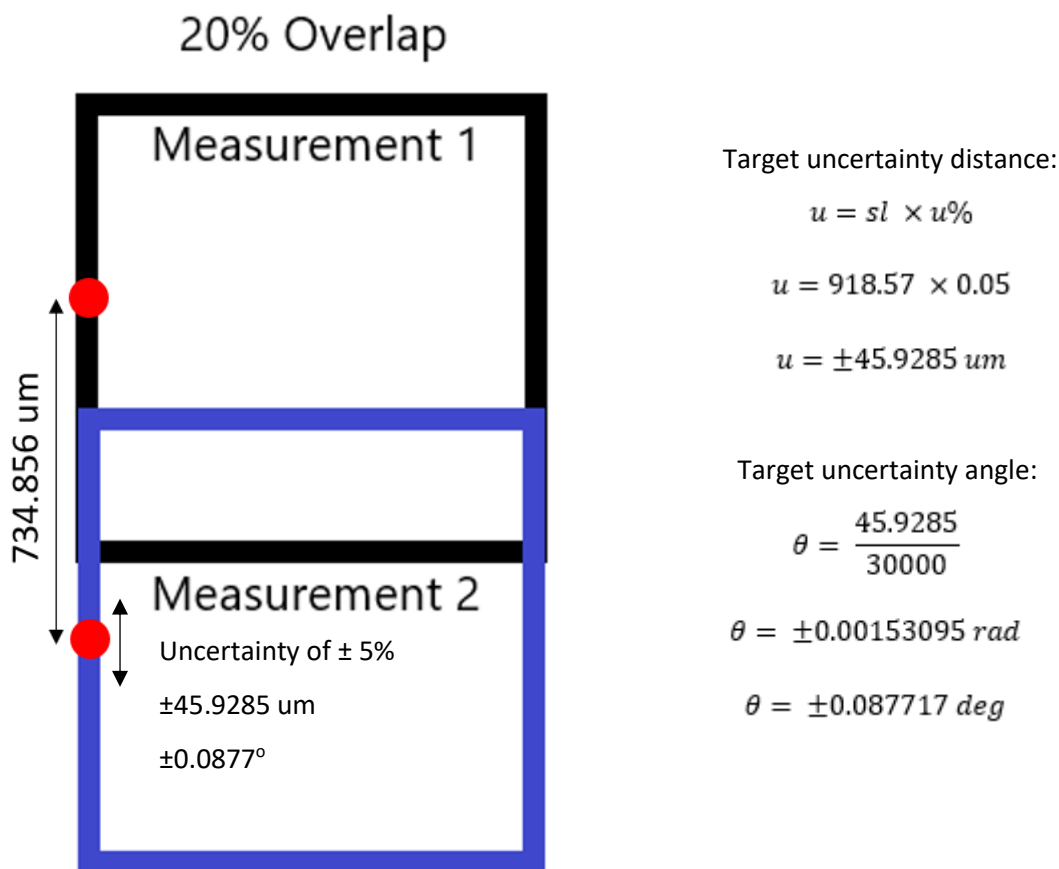


Figure 106: Calculating the target positional uncertainty for the custom fixture system.

4.3 Hardware Development

4.3.1 Initial Designs

The body of the fixture requires custom design and manufacture to adhere to the strict height limits imposed by surface metrology instruments, figure 107. Initial designs for the fixture system were created using the CAD software SOLIDWORKS [182].



Figure 107: Height limit of surface metrology instrument indicated by red arrow (approximately 100 mm), Bruker Contour GT-X [164]. Custom fixture system must fit within this limit, red arrow.

Design 1

At this stage in the design process there was no consideration of the actual rotary stages that would be utilised, instead the focus was only on general concept adaptation. The first design, figure 108, uses two translation stages at the bottom of the fixture (A), this allows the component to be finely adjusted in X and Y if required whilst under the objective lens of the interferometer. Support arches on either side (B) support the rotary stages (C) to manoeuvre the component through the elevation angle. Attached to the elevation rotary stages are vertical translation stages on both sides (D), this allows the z-height of the component to be adjusted which is crucial as it allows the spherical centre of the bearing component to be aligned with the elevation rotary stage axis. Finally, an azimuth rotation stage (E) is attached to the vertical translation stages, this allows the bearing component to be adjusted through any azimuth angle. The total size of this design was too tall to fit within the 100 mm height limit, design changes were obviously required. It was decided that the manual translation stages (A) could be removed, as most modern surface metrology instruments already come with a measurement base equipped with manual or electronic XY control, therefore the need for the translation stages was unlikely.

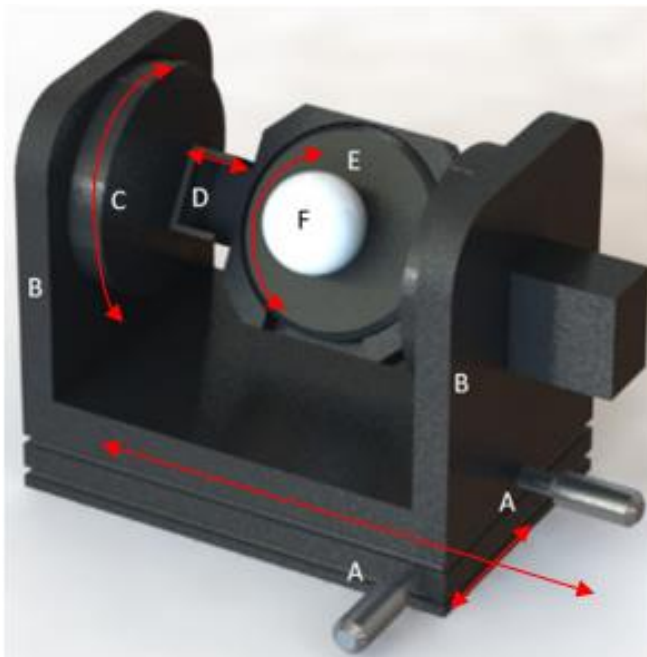


Figure 108: Concept design of fixture system, Design 1: A: Manual translation stages, B: Support arches, C: Elevation rotary stages, D: Vertical translation stages, E: Azimuth rotary stage, F: Femoral head. Red arrows indicate movement.

Design 2

The second design, figure 109, uses actual components for the rotary and translation stages. For design purposes simplified CAD models of the chosen rotary stages and translation stages were created, this allows the size of the rest of the custom components to be designed, ensuring they were compatible with the rotary stages.

Design 2 has a much lower working height compared to design 1, meeting the target of under 100 mm. As well as removing the translation stages from design 1, to save height even further the base of the fixture (A) has a pocket machined into it. This allows the overall fixture height to be reduced as the elevation rotary stage (C) can be mounted lower. This design only supports the azimuth rotary stage (G) from one end, this reduces the complexity of the design and reduces the XY footprint. However, because the azimuth rotary stage is not supported from both ends, a cantilever effect could take place which could potentially reduce the positional accuracy of the fixture system. With only one support this also puts a greater load on the elevation rotary stage which only has a 1.5 kg horizontal load limit. For design 3 the fixture was redesigned with better support of the azimuth rotary stage from both ends, thus reducing the load on the elevation rotary stage and reducing the chance of a cantilever effect impacting the positional accuracy.

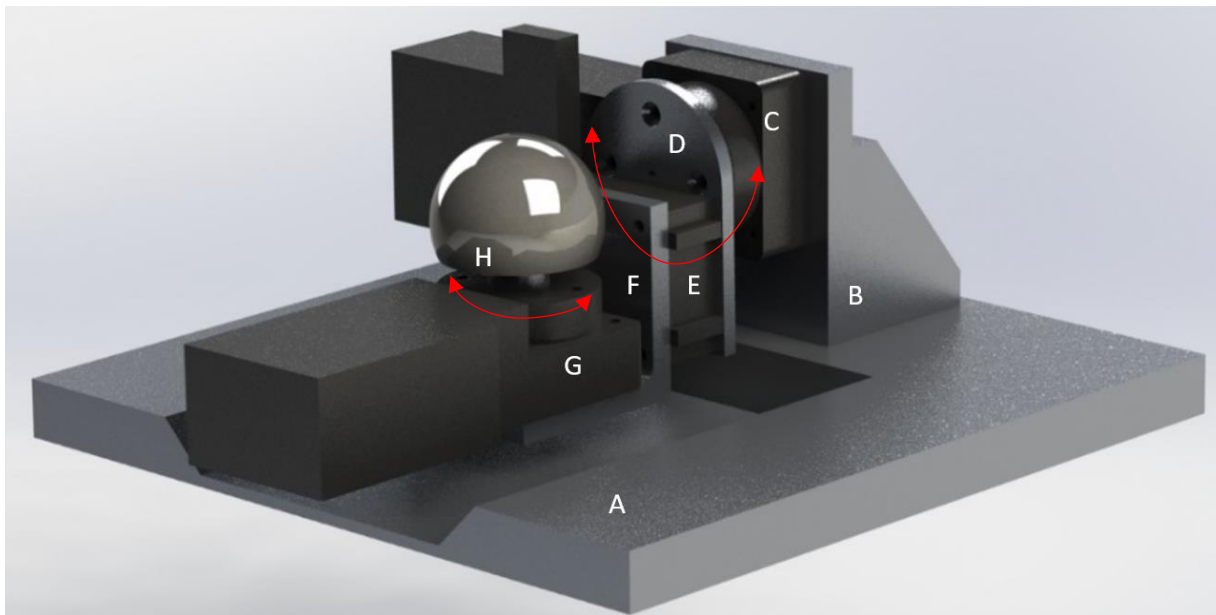


Figure 109: Concept design of fixture system, Design 2: A: Base with central pocket, B: Base right angle support, C: Elevation rotary stage, D: Adaptor face, E: Vertical translation stage, F: Component right angle support, G: Azimuth rotary stage, H: Femoral head.

4.3.2 Rotary Stages Selection

Motorised ‘digitally controlled’ rotary stages were used because of their high speed, high precision control and the possibility for more advanced control options, allowing CMM data to be used as direct control of the rotary stages. For example, the CMM data can be analysed to give the spherical coordinates of the maximum linear wear point. These coordinates can now be used to command the rotary stages to this position, this could be programmed to be a simple button click, ensuring easy to use, high speed, high accuracy control, in a fused data context.

Now the target positional uncertainty has been calculated as 0.0877° (5.262 arcmin), this can be used as a basis for selection of the rotary stages. A number of manufacturers were contacted to enquire about the prices of their electronic rotary stages. After comparing quotes and options the manufacturer Standa were selected, mainly due to the low cost of their stages compared to other manufacturers. It is important to keep costs low for a first prototype in case any problems arise in the design and changes are required.

Although the stages are cheaper than some competitors, the resolution values are well within the required target positional uncertainty range, with a resolution of 0.9 arcmin (0.015°) [183]. The size of the rotary stages were very small (LxWxH, 115x52x29 mm) which is crucial to meet the brief of the fixture system, ensuring the total height is below 100. The total cost of the rotary stages, motor controller and power supply unit is £2365, as predicted this is the majority of the fixture system costs.



Parameter	Value
Resolution Range	360°
Resolution in full step	0.9 arcmin
Uni-direction repeatability	0.4 arcmin
Bi-direction repeatability	1.6 arcmin
Max rotation speed	75°/s
Load	4 kg / 1.5 kg radial

Figure 110: Standa 8MR174-11 Motorized Rotation Stage, summary of specification parameters in accompanying table [183].

4.3.3 3D Printed Prototype

The third design, figure 111, uses a longer support bracket underneath the entire azimuth rotary stage (D), supported from both sides ensuring there is no possible cantilever effect. This middle bracket connects with the elevation rotary stage (C) and the front bracket (B) on one end, and with a bearing housed within the end bracket (F) on the other. This design increases the overall length compared to design 2, however it improves the stability and removes the possibility of a cantilever effect. The vertical translation stage from design 2 has to be removed, as it is not possible to have manual vertical translation stages on each end of the middle bracket as this could cause issues if both the translation stages are not used exactly in unison. Instead a new idea was developed of the Z screw taper mount as part of this design which allows the component to be adjusted in Z. At this stage in the design process is when the idea of a laser measurement sensor (H) was introduced.

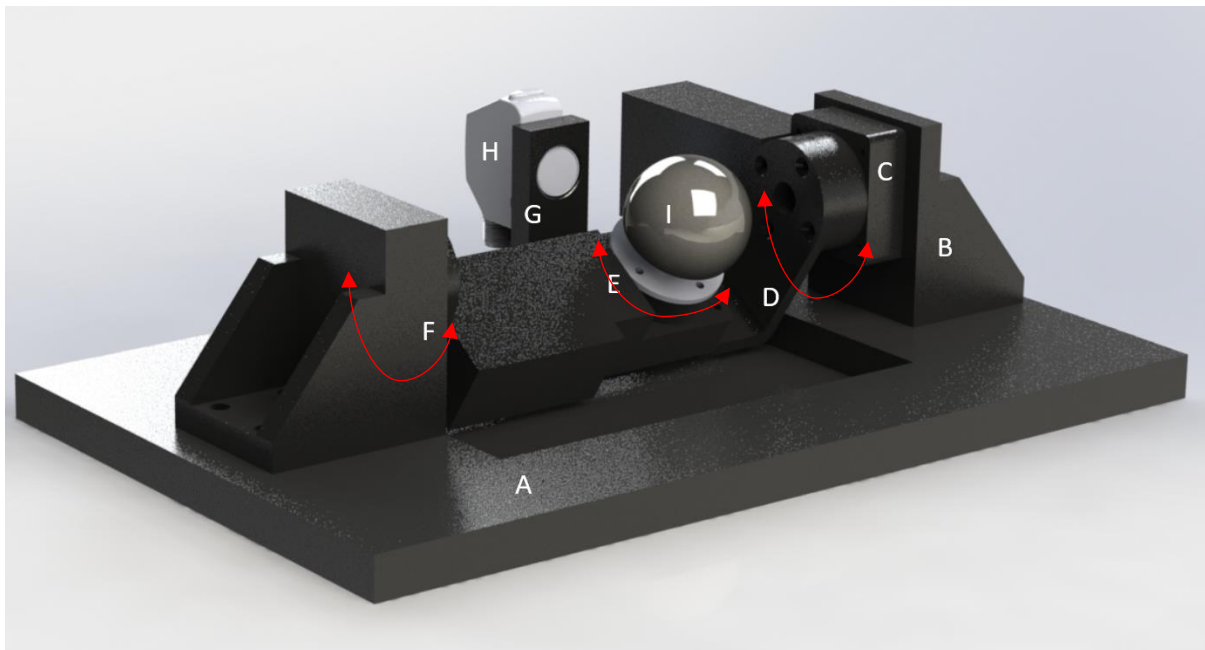


Figure 111: Concept design of fixture system, Design 3: A: Base with central pocket, B: Front bracket, C: Azimuth rotary stage, D: Middle bracket, E: Elevation rotary stage, F: End bracket w/ bearing, G: Laser mount, H: Laser measurement sensor, I: Femoral head.

At this stage the CAD design was ready for prototyping via 3D printing, this would allow for the purchased rotary stages to be tested with the other components and allow the fixture system to be tested with the surface metrology instrument and check if any problems arise or any design improvements should be considered.

3D printing was completed using a Prusa i3 3D printer, with components being printed in PLA, figure 112. This is a low strength material which has much less stiffness compared to aluminium, however it is cheap to 3D print with which is ideal for the prototyping stage. The base of the stage had to be created in two parts due to the size limitations of the 3D printers, these were then glued together.

After assembling the 3D printed design it was clear that the size of the fixture could be further reduced by removing excess material from the edges of the base. This would reduce the weight, allow for easier transportation and allow the fixturing system to fit on the surface metrology instrument base more easily. The 3D printed design was tested underneath the surface metrology instrument, Taylor Hobson Talysurf CCI, to ensure the bearing component was measurable within the working height limits of the instrument, and to ensure there was no risk of impingement during movement of the rotary stages.

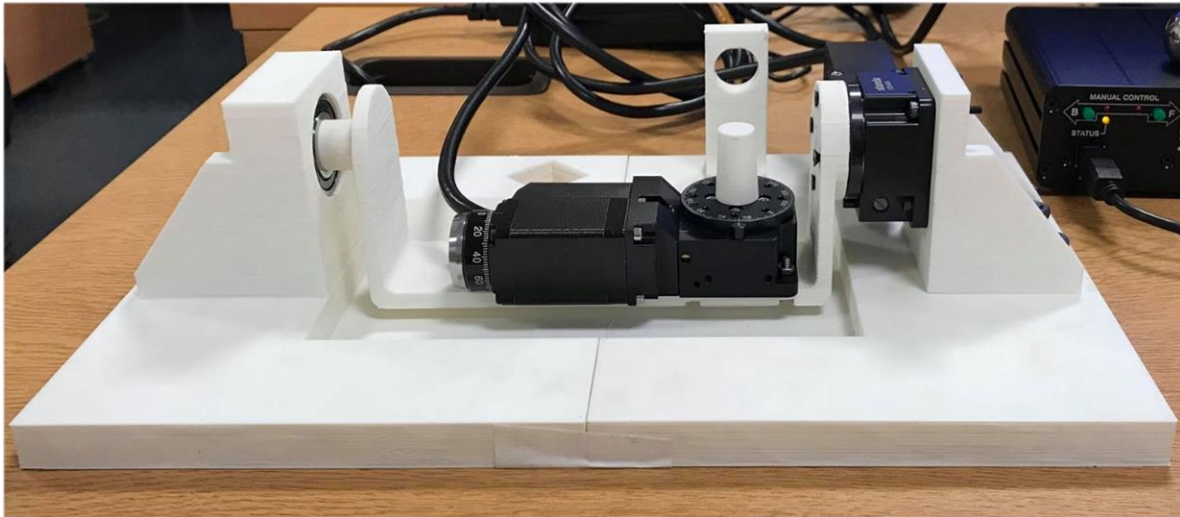


Figure 112: 3D printed prototype of the fixture system using the Standa rotary stages.

4.3.4 Final Design Overview

The final design, figures 113 and 114, is similar to the 3D prototype, but a few crucial design improvements were made. Excess material was removed from around the edge of the base (1) allowing for smaller XY dimensions. To accommodate for this alteration, the front and end support brackets (3,2) were also redesigned to be more compact. The pocket in the centre of the base (1) had all material removed as this allows the overall height of the fixture to be reduced by a further 5 mm. The final design has dimensions of 271 x 155 x 93 mm (LWH), this fits within the target height limit of 100 mm and the XY dimensions of the base fit comfortably on the measurement base of the surface metrology instrument. There are many design features and intricate components that are included in the final design, these are discussed in section 6.3.5.

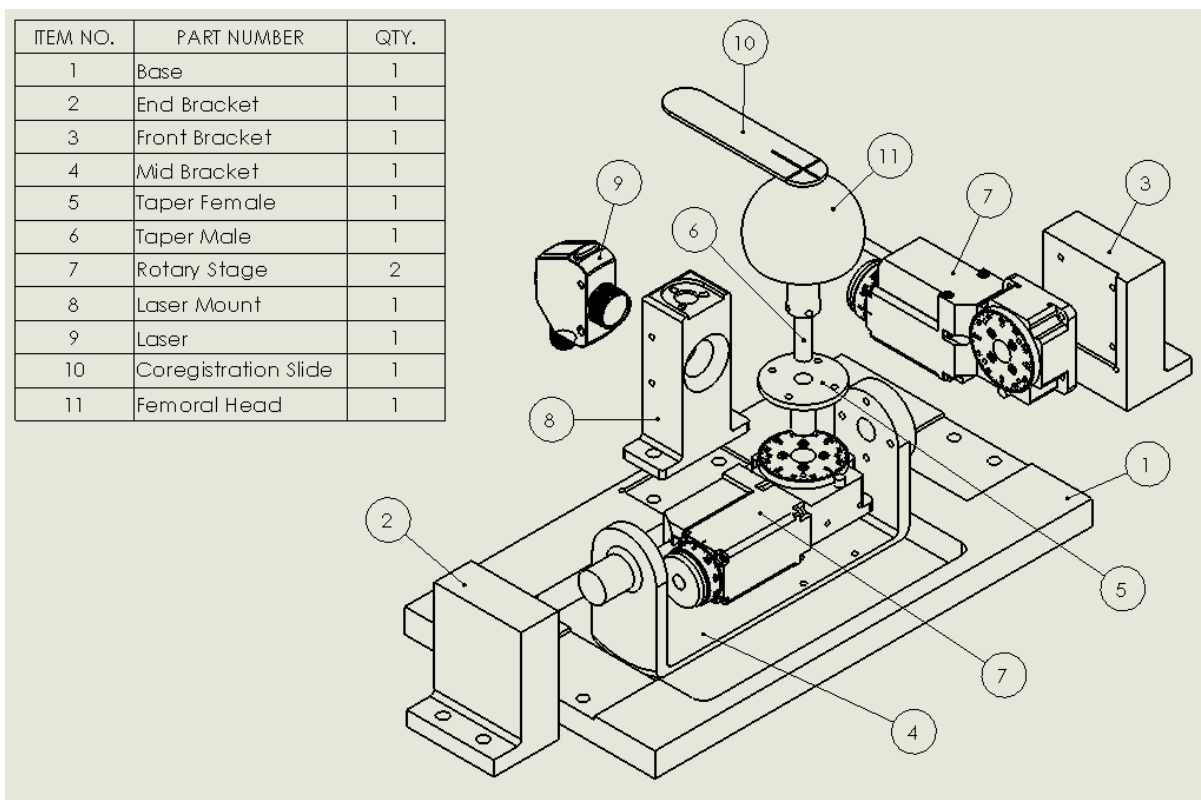


Figure 113: Exploded assembly view of the final fixture system design.

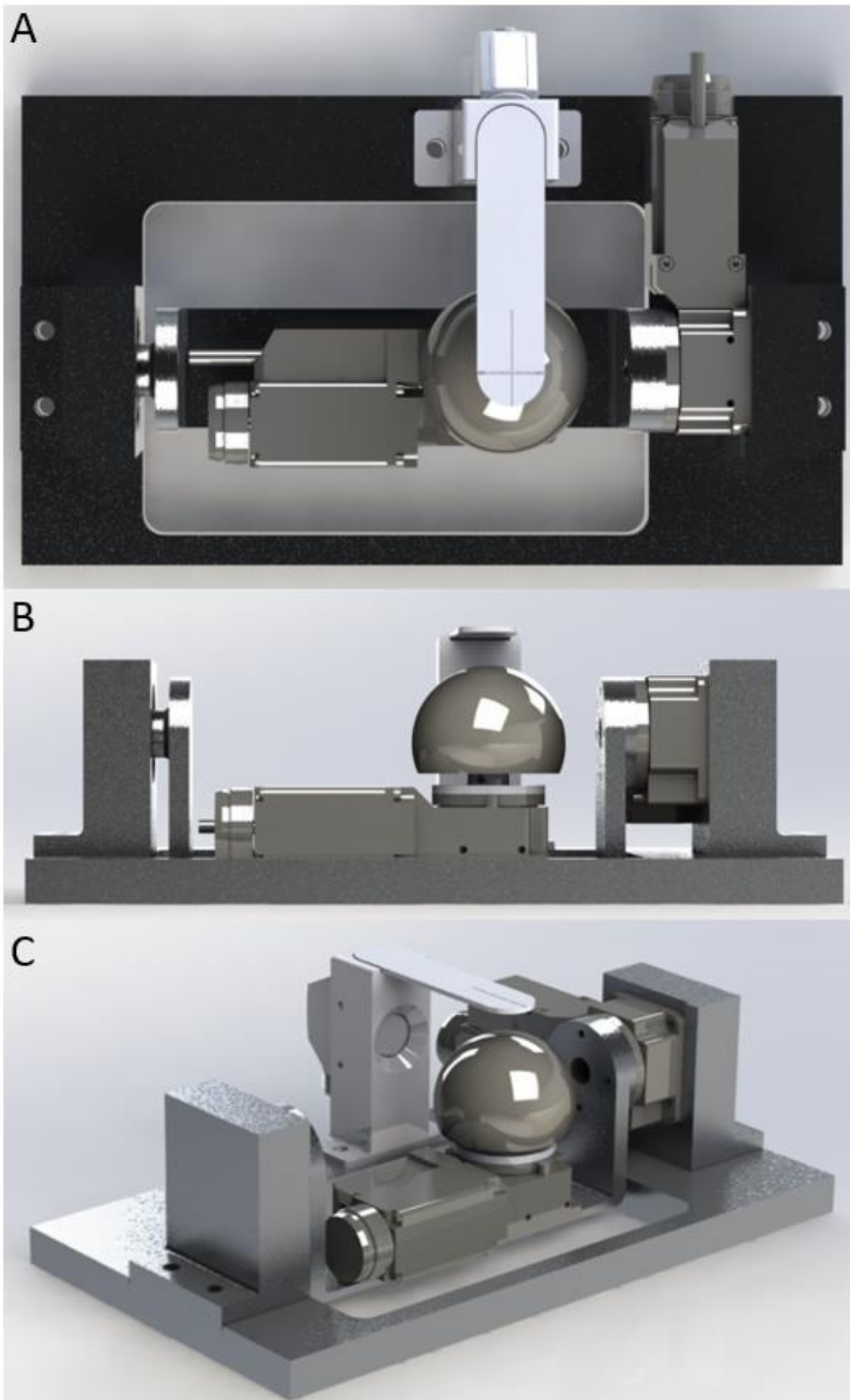


Figure 114: Rendered CAD images of the final fixture system design. A: Top view, B: Side view, C: Isometric view.

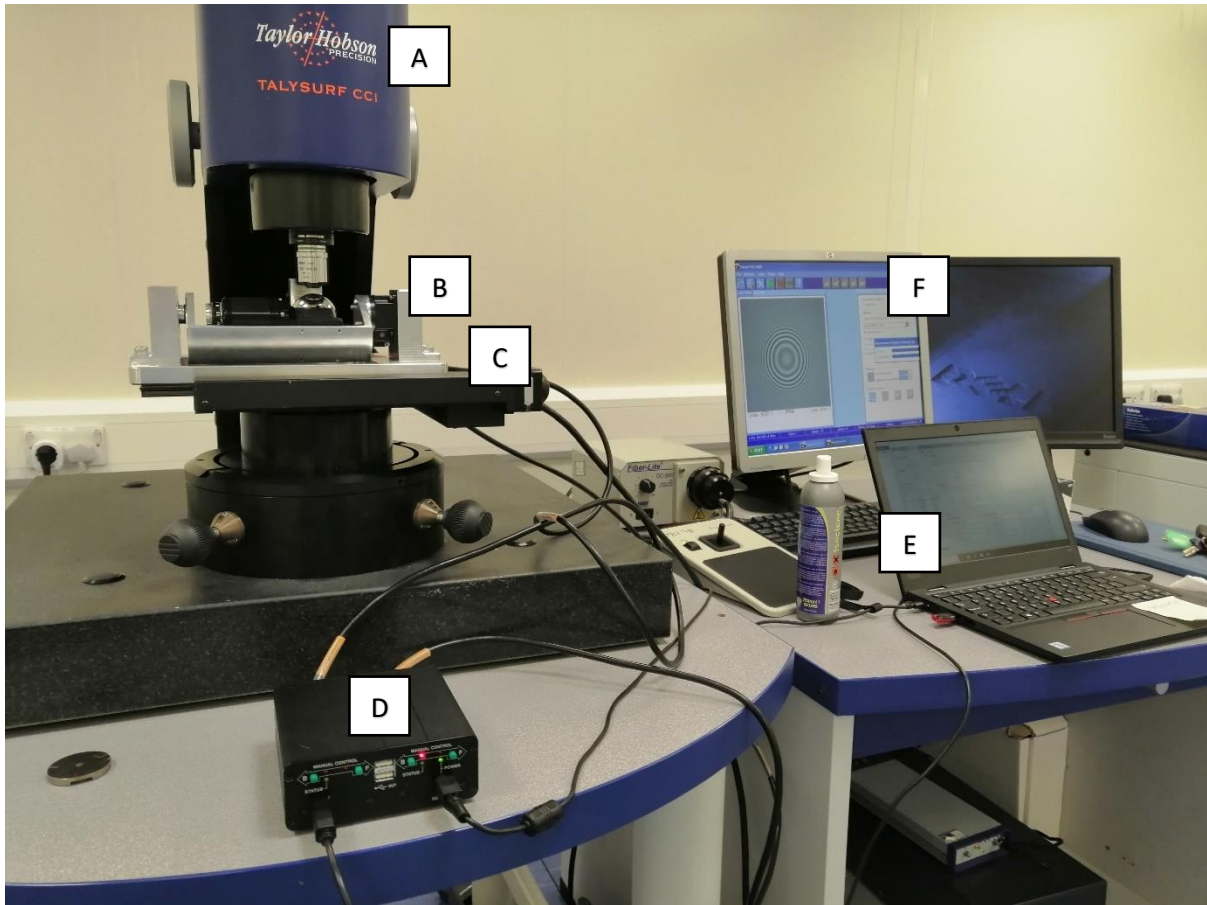


Figure 115: Fixture system in use with the Taylor Hobson Talysurf CCI. A: Talysurf CCI instrument, B: Fixture, C: XY motorised stages, D: Motor controller, E: Laptop controlling fixture system, F: Output from surface measurement sensor.

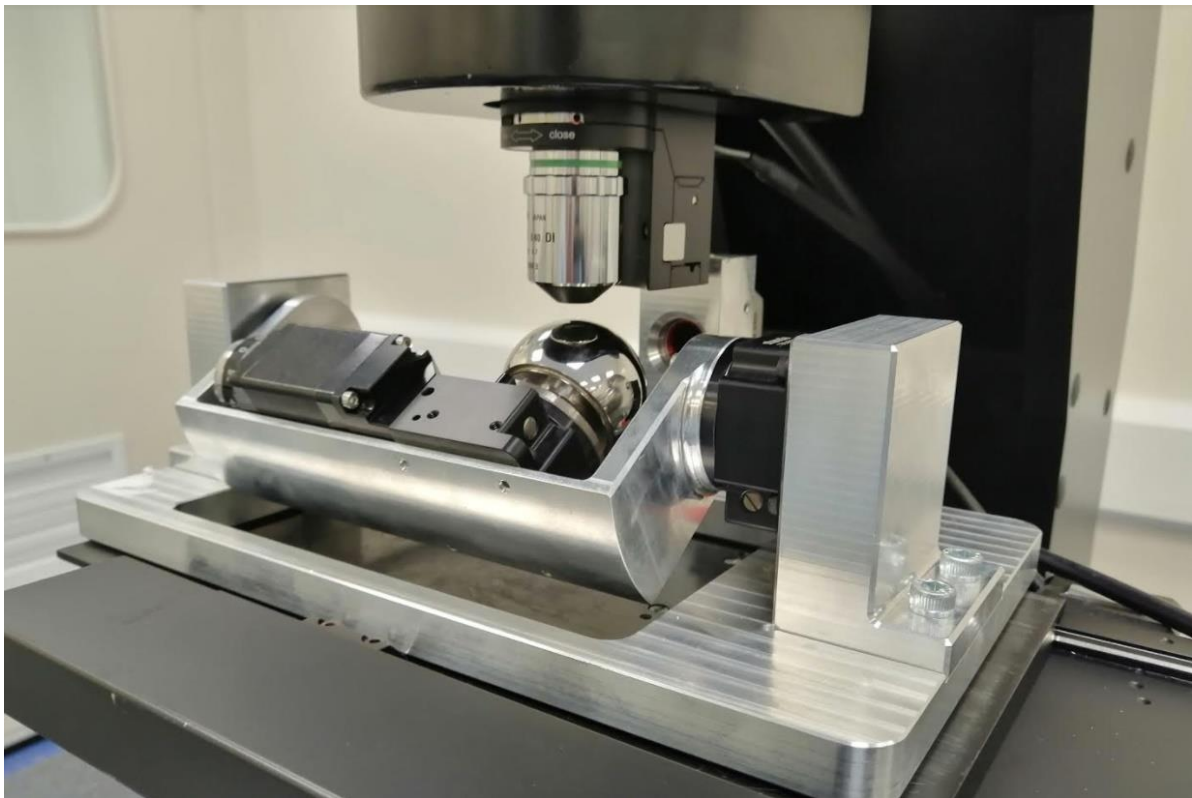


Figure 116: Close up image of the fixture in use with the Taylor Hobson Talysurf CCI, measurement of a femoral head.

4.3.5 Design Features

4.3.5.1 Alignment Pockets

Pockets were introduced onto the base of the fixture system, to allow for better alignment during assembly, figure 117. By using pockets on the base (A) this allows both the front (B) and end brackets (C) and the laser mount (D) to be pushed against an alignment corner (F) during assembly, this ensures that the pockets are aligned accurately with each other, removing the possibility of the brackets being twisted or misaligned during assembly. The front bracket (B) also features a pocket which is machined into it, this ensure that the elevation rotary stage (E) when fastened to the bracket is parallel to the base.

By adding alignment pockets, quicker assembly, with accurate positioning of the components can be achieved, reducing the risk of damage to the fixture system and ensuring it works as expected. Due to the thinness of the middle bracket, supporting the azimuth rotary stage, it was decided not to add a pocket for the azimuth rotary stage. This is not an issue as any rotational assembly error of the azimuth rotary stage will not affect performance, as the stage would be used to rotate the component anyway.

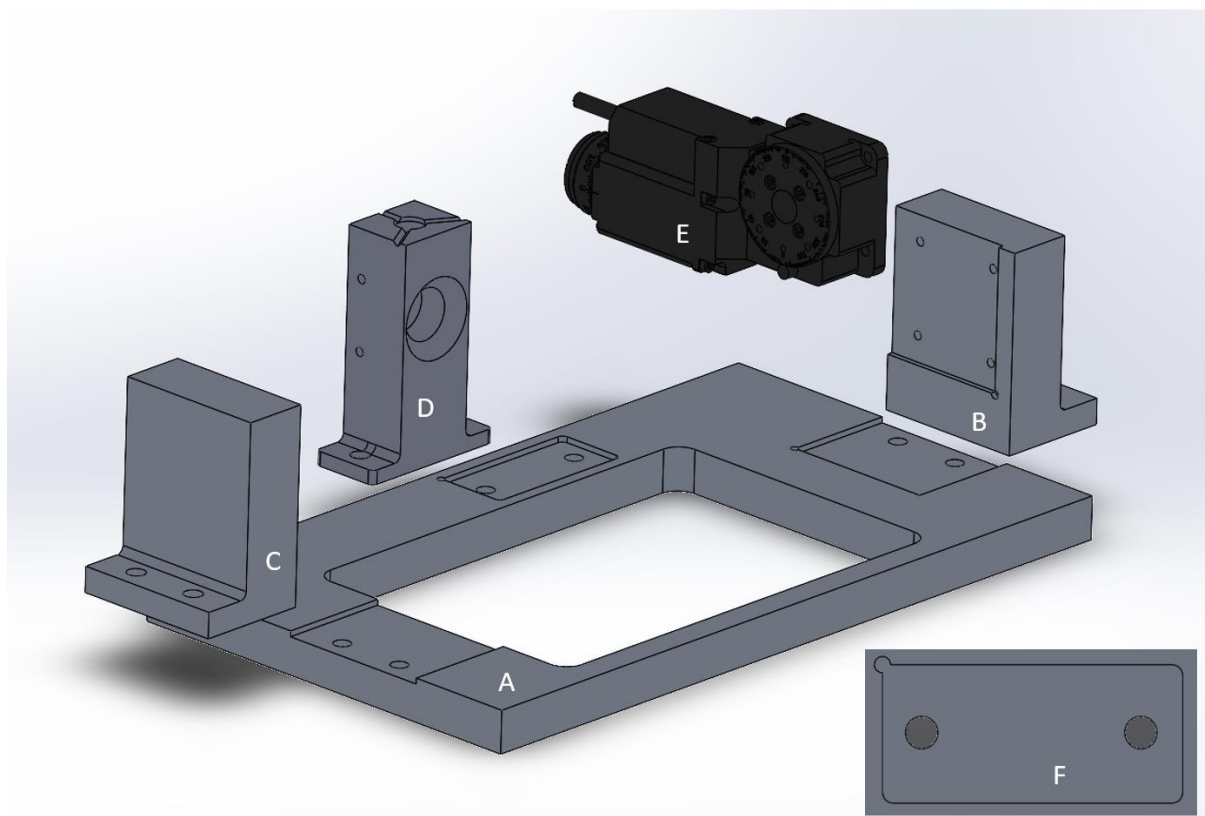


Figure 117: Alignment pockets on the fixture: A: Base, B: Front bracket w/ pocket, C: End bracket, D: Laser mount, E: Elevation rotary stage, F: Detailed view of the laser mount pocket, highlighting the alignment corner in the top left of the pocket.

4.3.5.2 Coregistration Slide

When wear map targeted surface measurements are completed, it must be ensured that the component is aligned as closely as possible on both measurement instruments, the CMM and the surface metrology instrument. If the component is not consistently aligned between the two machines this will introduce a large error in the positional accuracy of surface measurement targeting, this error is called the azimuth alignment error.

Consider figure 118, once a CMM measurement is taken of the component, the alignment of the component has now been set, and the wear area has been located (red area). When the component is moved from the CMM to the surface metrology instrument, if the fixture is twisted, the azimuth angle is adjusted, this results in the alignment being inconsistent. Note the blue line is skewed on the surface measurement diagram compared to the CMM measurement, this is because the azimuth angle of the component has been adjusted. Now when surface measurements are taken that are targeted at the centre of the wear scar (black X) the actual location (green X) is missing the target location and not capturing the desired surface topography. This highlights the importance in reducing the azimuth alignment error as much as possible.

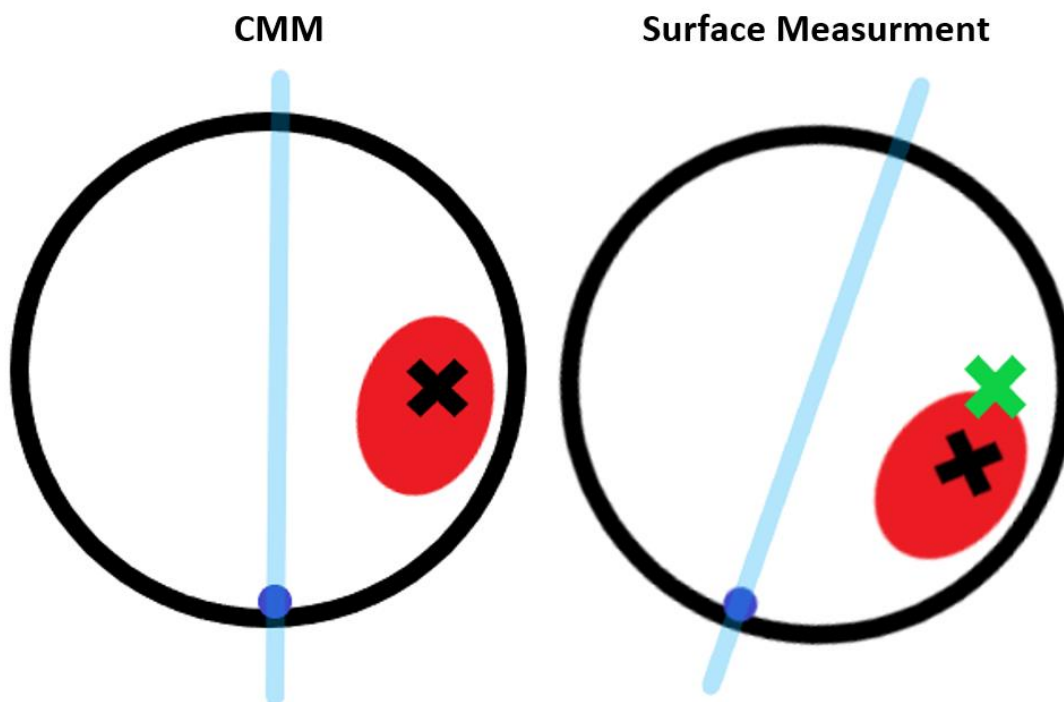


Figure 118: Azimuth alignment error between CMM and surface measurement, resulting in poor positional accuracy for wear map targeted surface measurements.

A simple way to reduce this error is by using a visual reference mark on the component. For example, figure 119 shows the underside of a retrieved femoral head, a reference mark is made using a pen, a cross mark indicates the 'front' reference point of the component. This reference mark is made before the CMM measurement takes place and when using the CMM the femoral head is secured so the

reference mark is at the front position in the measurement plane. For the surface measurements to take place, the femoral head is removed from the CMM and now secured to the surface metrology instrument using the same 'front' visual reference mark to align the femoral head. This ensures the component is aligned closely with how it was originally on the CMM. This method lacks positional accuracy as it relies solely on human visual alignment of the reference mark when fixing the component to both the CMM and surface metrology instrument and will likely result in several degrees of positional error for the azimuth alignment, therefore a design solution was required.



Figure 119: Retrieved femoral head with a visual reference mark on the underside of the component. Cross mark indicates the 'front' azimuth position of the femoral head.

To reduce the azimuth alignment error further it was decided the component would remain secured to the fixture during both the CMM and surface measurement phases, meaning the component would not be touched in between both measurement datasets. This would allow for no alignment of the component to be required and instead the fixture would have to be aligned consistently across the CMM and surface metrology instrument.

Figure 120 shows the process of using fixture alignment to reduce the azimuth alignment error. Firstly, the component is secured to the fixture, and now the CMM measurement procedure can begin (1). Crucially before the CMM measurement takes place the front face of the fixture is used as the X reference plane during CMM measurement. This means that if the fixture is placed skew onto the CMM measurement base, the effect of this skewness will be removed.

Once the CMM measurement is complete, the component is not removed from the fixture, instead the entire fixture is moved to the surface metrology instrument with the component still attached (2). Now the fixture needs to be re-aligned, so the front edge of the fixture is parallel with the surface measurement sensor X axes (3). To initially get this alignment approximately correct the front edge of the fixtured is aligned with the front edge of the surface metrology instrument table.

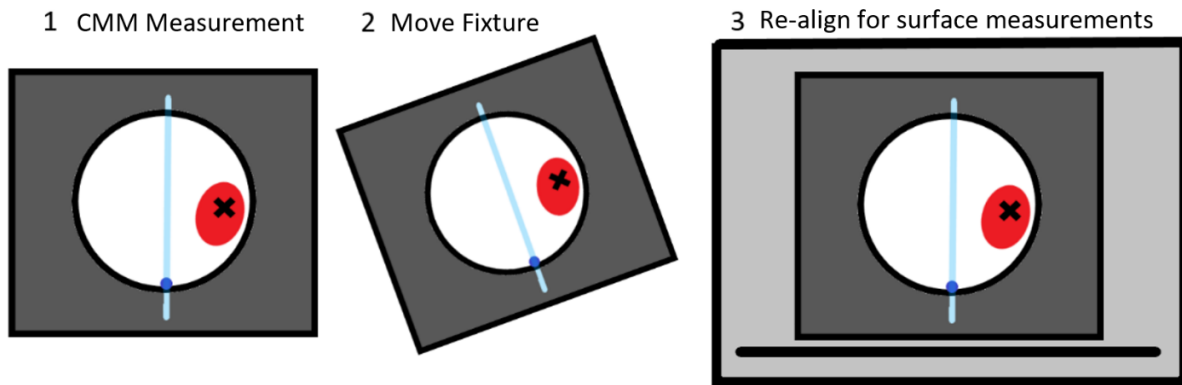


Figure 120: Using fixturing alignment to minimise the effect of rotational azimuth error. A top view of the alignment of a hip bearing component at 1: CMM Measurement, 2: Moving in between measurement machines, 3: Re-aligning for surface measurements.

To further reduce azimuth alignment error, the idea of the coregistration slide was developed. As the surface measurement instrument base will not be perfectly square with the camera sensor the idea is to use the camera sensor itself for alignment purposes. This should result in a further reduction in the azimuth alignment error. To achieve this an alignment mark needs to be made somewhere on the fixture, this alignment mark will then be located and visually aligned square with the camera sensor. This should further reduce the azimuth alignment error. Ideally this alignment mark should be above the component as the sensor needs to access it without risking the sensor hitting the component or the fixture. The alignment mark was made on a thin plate component called the coregistration slide, figure 121.



Figure 121: Coregistration slide component. A: Top view of the component, reference cross mark located on the far end. B: Bottom view of the component, three hemispheres are used for locating and securing the coregistration slide.

The coregistration slide attaches to the top of the laser mounting post, figure 122, allowing the centre of the reference mark to be located above the centre of the component. Once the coregistration slide is attached, the camera sensor is focussed above the coregistration slide and the reference mark is

located, the fixture is then adjusted in X, Y and azimuth angle until the reference mark is square with the camera sensor. The output of the camera sensor can be viewed live from a computer screen, figure 123. This method of aligning the fixture using the camera sensor should result in a further reduction in the azimuth alignment error and is a vast improvement compared to using a visual reference mark on the component.

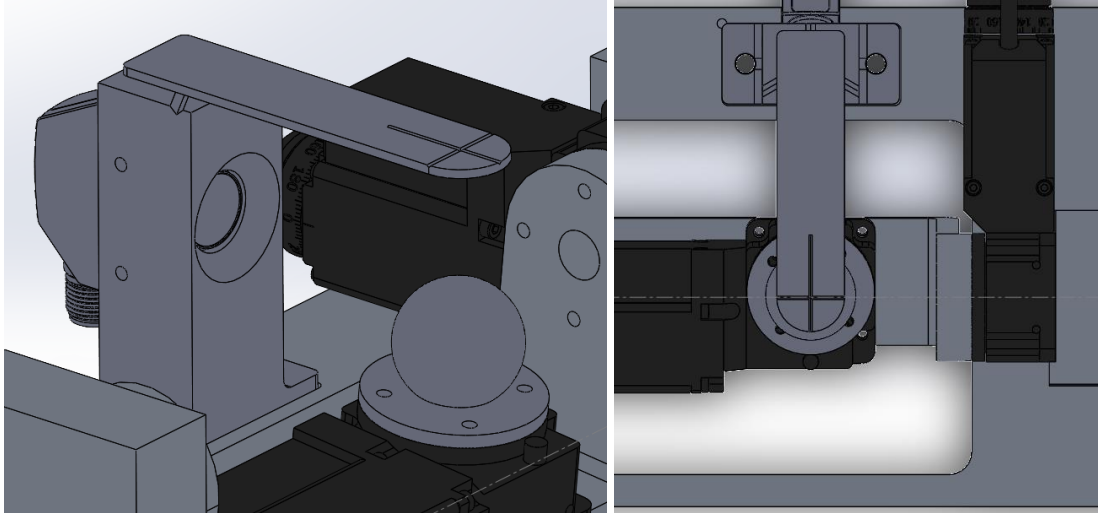


Figure 122: Laser mount with coregistration slide attached. Left: Isometric view, Right: Top view.

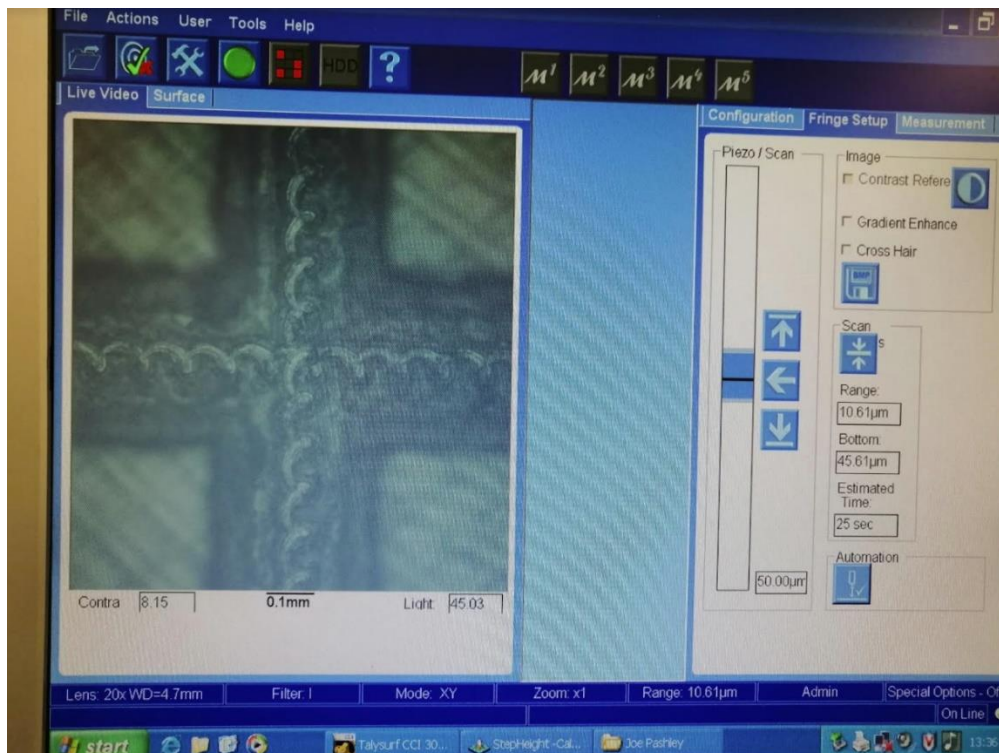


Figure 123: Reference mark from the coregistration slide located using the CCI sensor output. The fixture is adjusted precisely in XY and azimuth rotation until this cross is as square as possible with the sensor output.

As the slide is located above the component, it needs to be easily removable yet positionally accurate, ensuring the reference mark is square with the front edge of the fixture. Initially a design to use small bolts to locate the slide was drafted, however the bolts would allow for small positional uncertainty of the slide which could lead to the reference mark not being square. Instead, the idea of using a magnet, positioning channels and hemispheres to secure the slide was developed, figure 124. This allows the coregistration slide to be secured into place accurately, yet also be removable quickly and easily. A magnet is located on the top of the laser mount, the magnet sits just below the top surface of the laser mount inside a pocket. Three positioning channels are also made in the top surface in a triangular pattern, these channels are designed to locate the position of the slide accurately by centring the hemispheres on the bottom of the coregistration slide.

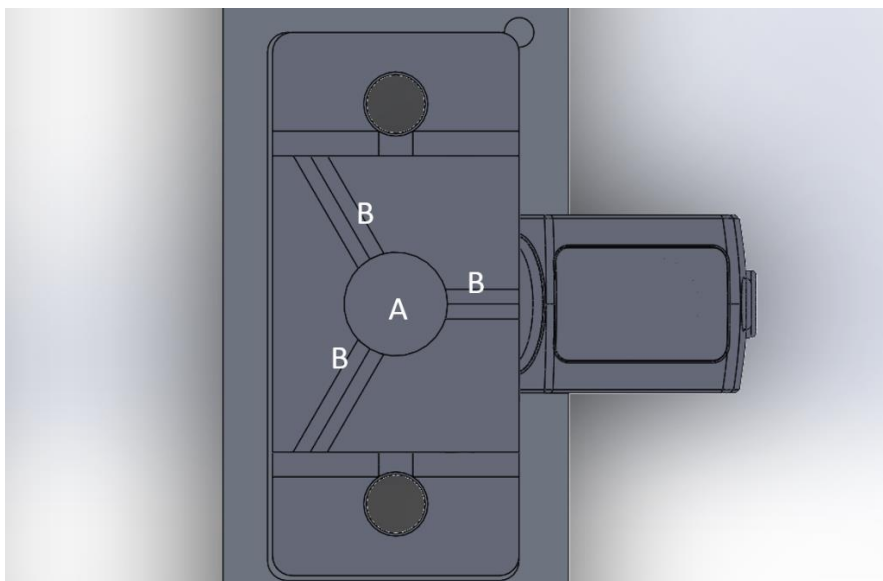


Figure 124: Top view of laser mount component. A: Pocket for magnet, B: Positional channels.

On the slide itself three raised hemispheres are on the underside of the component, these are designed to fit within the channels on the laser mount post, figure 125. As the slide is placed onto the laser mount, the magnet pulls the slide towards the surface. As the slide is pulled towards the surface, the hemispheres slide into the positional channels, quickly and accurately securing the coregistration slide to the laser mount, figure 125. With the triangular setup of the positional channels the coregistration slide is fixed in place in all XYZ movement.

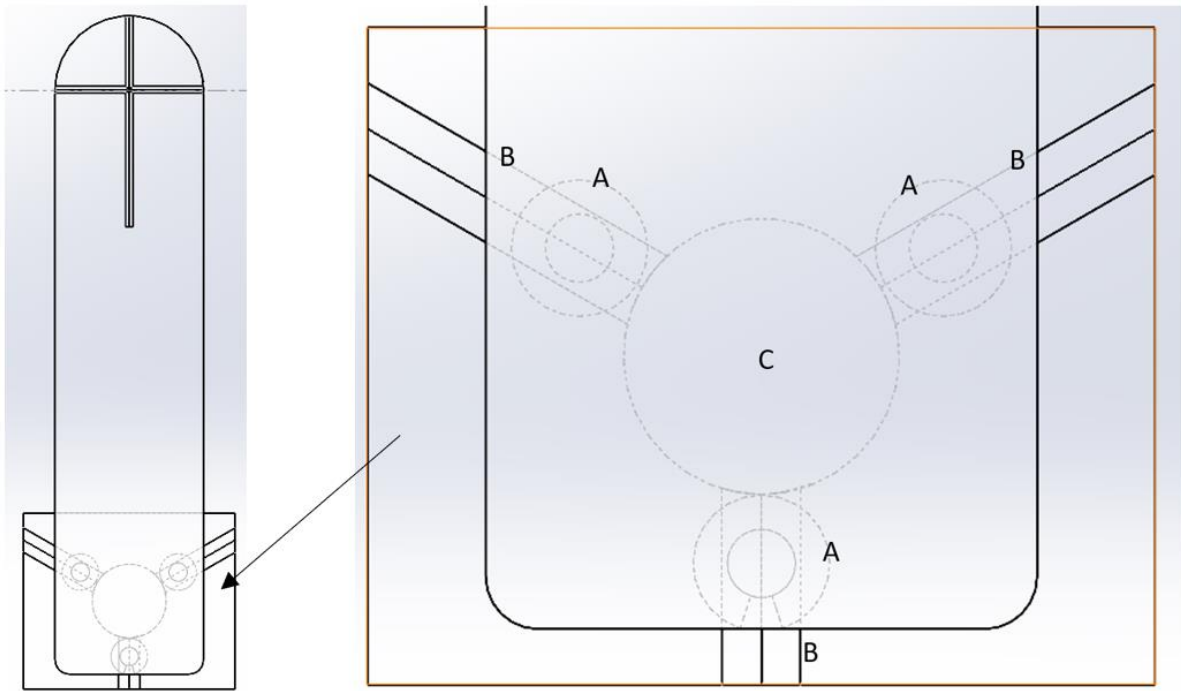


Figure 125: Top wireframe view of the laser mount to coregistration slide interface. Each nodule (A) is fixed within a positioning channel (B), whilst the magnet (C) pulls the coregistration slide towards the surface securing it in place.

4.3.5.3 Z-screw Taper

It is important that the spherical centre of the femoral head is aligned with the elevation rotary axis, if it is not aligned, when the component is moved through an elevation angle it will also move in the Y direction relative to the surface measurement lens. This is not ideal as the fixture then has to be adjusted in the Y direction for the next surface measurement. Ideally, the femoral head needs to be adjustable in Z height compared to the elevation axis, allowing it to be moved up or down until the spherical centre of the femoral head is aligned with the elevation rotary axis. This will speed up surface measurements as no adjustment of the Y direction is required in between measurements.

For example, see figure 126, the femoral head is set too low compared to the elevation rotary axis. This is not an issue when measuring the top dead centre of the femoral head. However, once the elevation axis is adjusted, figure 127, it can be seen that the femoral head is too far below the elevation rotary axis which is causing the target measurement location (black X) to not currently be the focus for measurement. The area the surface metrology instrument sensor is instead measuring on is shown by the green X. To resolve this issue the spherical centre of the femoral head must be as closely aligned with the elevation rotary axis as possible. Otherwise, the fixture has to be adjusted in Y direction precisely using a motorised Y stage, this movement in Y should never be done manually as it will introduce azimuth alignment error.

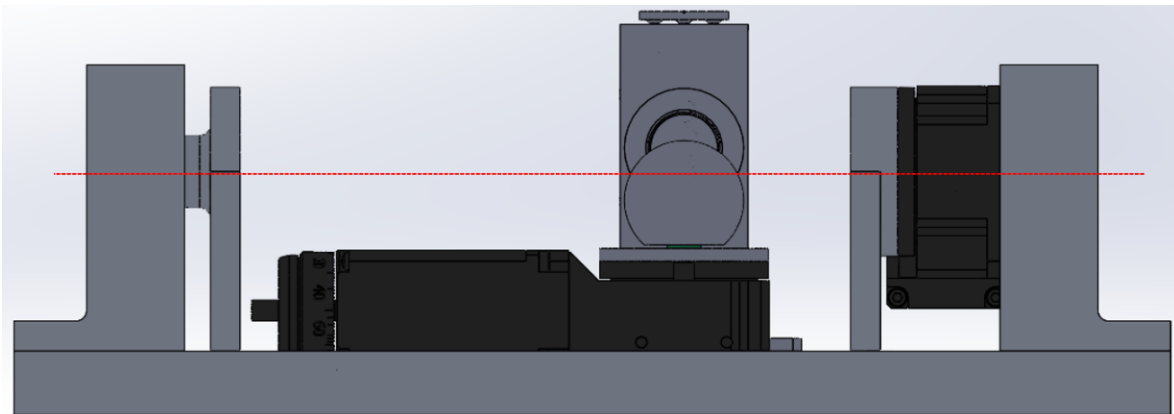


Figure 126: Femoral head spherical centre is too low compared to the elevation rotary axis.

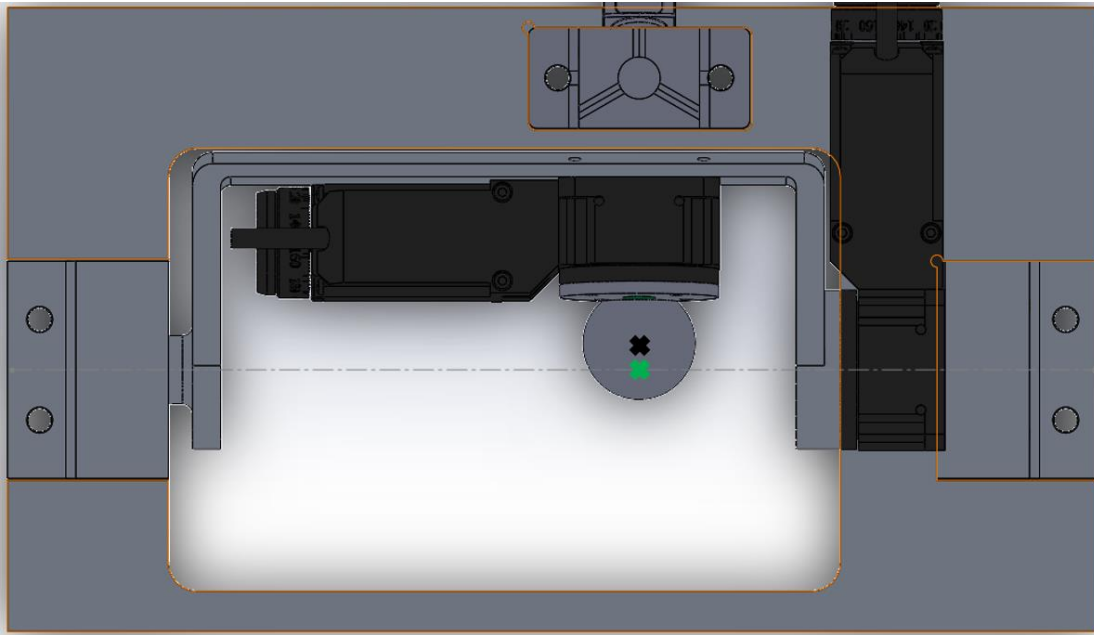


Figure 127: The elevation angle is altered to approximately 80 degrees. The target measurement location (black X) cannot be accessed without moving the fixture in the Y direction. The green X represents the location where the surface metrology instrument sensor is currently measuring.

Initially the idea to allow for adjustment in Z height was to use a motorised Z stage, figure 128. This allows the component to be adjusted up and down precisely and combined with the use of sensors, the fixture system may be able to adjust the z height automatically until the spherical centre of the component is correctly aligned. However, with the current design it was impossible to fit a z stage below the azimuth rotary stage without the height limits being exceeded or the component being too high compared to the elevation axis. It also added further drawbacks such as adding more weight to the middle bracket and therefore a greater load on the elevation rotary stage. Furthermore, the amount of vertical travel available from a suitably sized motorised z stage would only allow for 13 mm of travel, which is not enough to cover the range required for all bearing sizes, therefore a new solution was required.

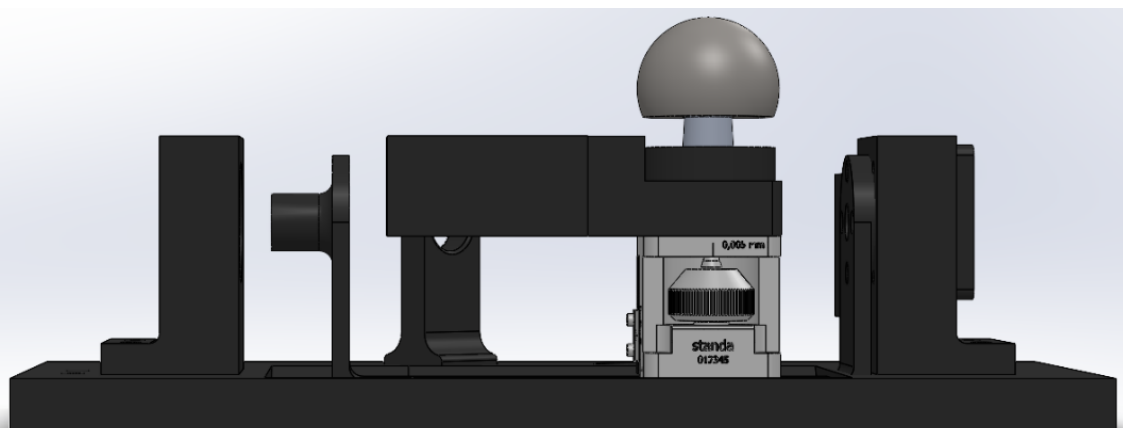


Figure 128: Z adjust stage mounted below the azimuth rotary stage.

Instead, a new two-piece component was developed that would allow adjustment in z height with minimal addition to the overall height where the component sits, the z-screw taper, figure 129. The two pieces of the z screw taper are the cylinder base (A) and the threaded taper (B). The cylinder base sits within the central aperture of the azimuth rotary stage, it is secured to the azimuth rotary stage with 4 screws, the inner cylinder of the cylinder base is threaded. The taper which the femoral head secures to is machined atop a threaded section of bar, this facilitates the femoral head to be adjusted up and down by rotating the threaded taper within the cylinder base, figure 129. A nut is placed underneath the taper to tightly secure the threaded taper in place and ensure no tilting.

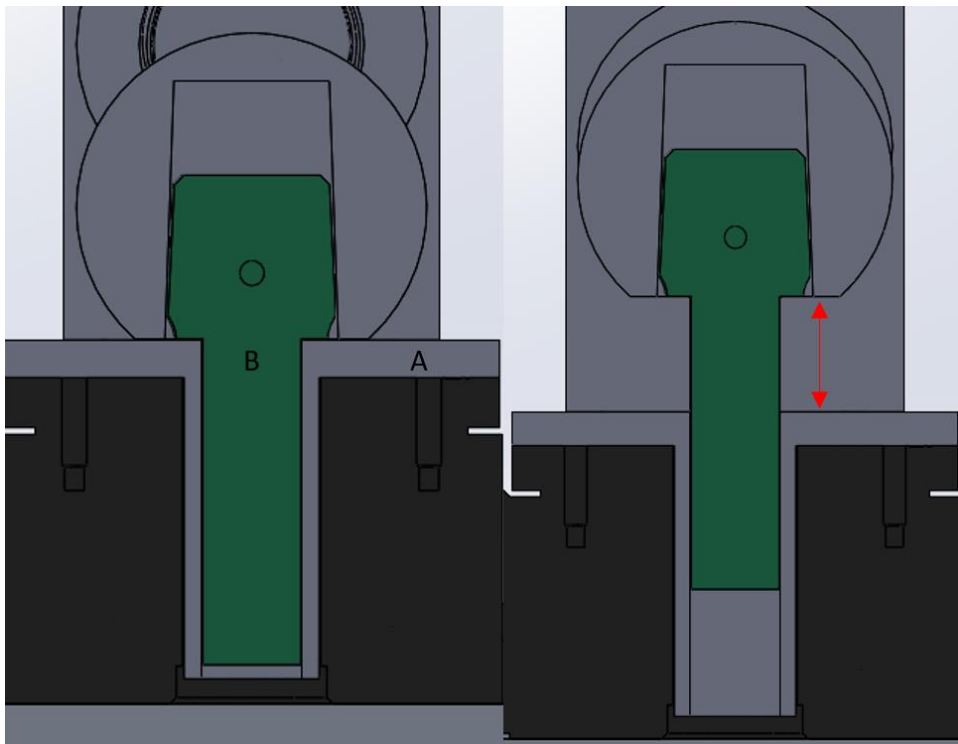


Figure 129: Working principle of the z-screw taper. A: Cylinder base, B: Threaded taper. Left: The femoral head is too low down compared to the elevation rotary axis. Right: The femoral head is raised by rotating the threaded taper.

4.3.5.4 Mounted Laser Measurement Sensor

Now that the femoral head can be adjusted vertically it is important to ensure the spherical centre of the femoral head is aligned as close as possible with the elevation rotary axis. It can be difficult to visually align the spherical centre of the femoral head with the rotary elevation axis. A design feature was developed to allow this alignment to be achieved easily and accurately. Using a mounted laser distance measurement sensor, the distance from the laser to the femoral head can be measured. The laser was mounted so it is aligned at the same height of the elevation axis, this allows the user to know when the femoral head is at the correct height easily, whilst also accommodating different head sizes. As the femoral head is widest, and therefore closest to the laser, at its spherical centre, once the laser distance measurement sensor displays its smallest reading this would indicate that the femoral head is correctly aligned.

Consider figure 130, Initially the femoral head is too low down as seen by the laser not hitting the spherical centre of the component, image A. The femoral head is raised upwards using the Z screw taper, as the femoral head is raised upwards the laser distance measurement device values become smaller until the laser intercepts the spherical centre, image B. When the minimum value is reached the spherical centre of the femoral head is found.

As this fixture is a first prototype a low-cost laser measurement sensor was utilised, Banner Q4X [184], if the working principle is tested and considered to be beneficial, a sensor with a higher measurement resolution can be utilised instead.

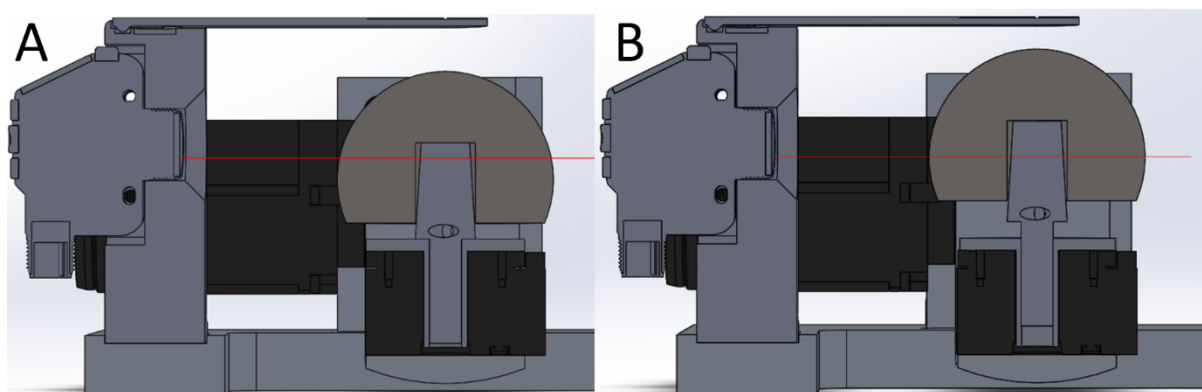


Figure 130: Mounted laser measurement sensor working principle. A: Femoral head is too low. B: Femoral head is raised using the z-screw taper. The display of the laser measurement sensor is checked as the femoral head is raised. Once the smallest distance reading is achieved the femoral head is correctly aligned with the elevation rotary axis.

4.3.6 Material Choice

A review of the possible material types to be used for the custom components was completed before manufacturing took place. Manufacturing of the components from either a polymer or ceramic material was ruled out due to the impracticality to machine to a high level of accuracy with either material. When reviewing the positioning stages on the Standa website the vast majority of the housing for the stages were made from either aluminium or stainless steel. These materials then became the focal point of the material choice investigation: aluminium, or stainless steel.

When comparing aluminium and stainless steel the main factors to consider are the material stiffness, density, and machinability. When comparing the Young's Modulus values of aluminium and stainless steel, the stainless steel has a greater value of 180 GPa compared to aluminium 69 GPa [185], therefore the stainless steel would provide stiffer components which is ideal for a high accuracy fixture. However, because of the modest loads that will be acting on the fixture either material provides adequate stiffness performance and instead the density of the components is a more important factor. When considering the density of stainless steel 7480 kg/m³ and aluminium 2712 kg/m³ [186], clearly the stainless-steel components will add more weight to the fixture. Increasing the weight of the components is undesirable for three reasons. Firstly, any additional weight to the middle bracket will increase the load on the elevation rotary stage, which could reduce the accuracy of the fixture system. Secondly, an increase in weight is not ideal for transporting the fixture in between measurements on the CMM and surface metrology instrument. Thirdly, there are weight limits to the translation stages of commercial interferometers. The use of aluminium also allows for easier machinability compared to stainless steel, potentially allowing for increased accuracy during machining of the components and ensuring the fixture is built to specification accurately. Therefore, after comparing the benefits and drawbacks of stainless steel and aluminium the decision is made to use aluminium for the custom fixture components.

Although stainless steel does provide a lower thermal expansion coefficient, thermal expansion was ruled out as an important factor for the fixture. As the fixture is designed to be used in a temperature-controlled metrology lab any variation in temperature will be minimal. If the fixture had been stored in a warm/cold environment it could then be placed in the temperature-controlled metrology lab for a suitable 24 hour soaking period.

4.3.7 Manufacturing and Assembly

The manufacturing of the components was completed on a 5-axis CNC milling system, by an experienced precision machining technician at the University of Huddersfield, figure 131. Technical drawings were provided for all components.

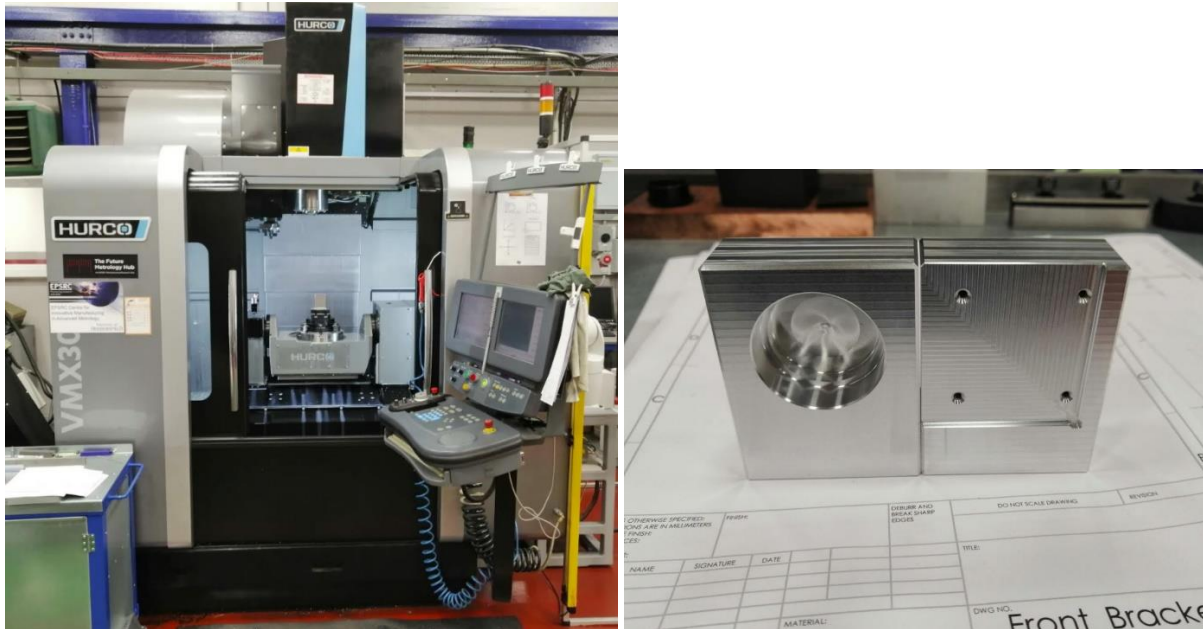


Figure 131: Manufacturing Images. Left: 5-axis CNC milling system. Right: Freshly manufactured front and end brackets.

During assembly of the fixture the alignment pockets were utilised to ensure the components were square with each other and none of the components were incorrectly aligned. The origin location of both the azimuth and elevation rotary stages were adjusted once assembly of the fixture was complete. The elevation rotary stage origin must be set so the middle bracket and therefore the azimuth rotary stage are parallel with the base of the fixture system. If this is misaligned then during CMM measurement the results could be inaccurate as the component will be tilted and not perpendicular with the CMM probe. The adjustment of the azimuth rotary stage origin is not so crucial but was adjusted to ensure the bolts attaching the threaded taper were aligned in a manner that clearly demonstrated a home position.

The CMM is used to assist in adjusting the origin position of the elevation rotary stage, initially using visual judgement the middle bracket is set so it is parallel with the base of the fixture. At this stage, the azimuth rotary stage is removed and a CMM measurement is made on the middle bracket with a scanning pattern, figure 132. This allows the angle of the middle bracket to be measured compared to the base of the fixture system. Using the calculated angle from the CMM measurement, an adjustment of the elevation angle origin position is made in the MATLAB code, the elevation rotary stage then moves to its new origin position. This process is repeated until the middle bracket cannot be adjusted

any closer and any attempt results in a similar level of angular error from the CMM measurement each time. The final measurement value calculated a difference in angle between the middle bracket and the base of the fixture system as 0.0252 degrees.

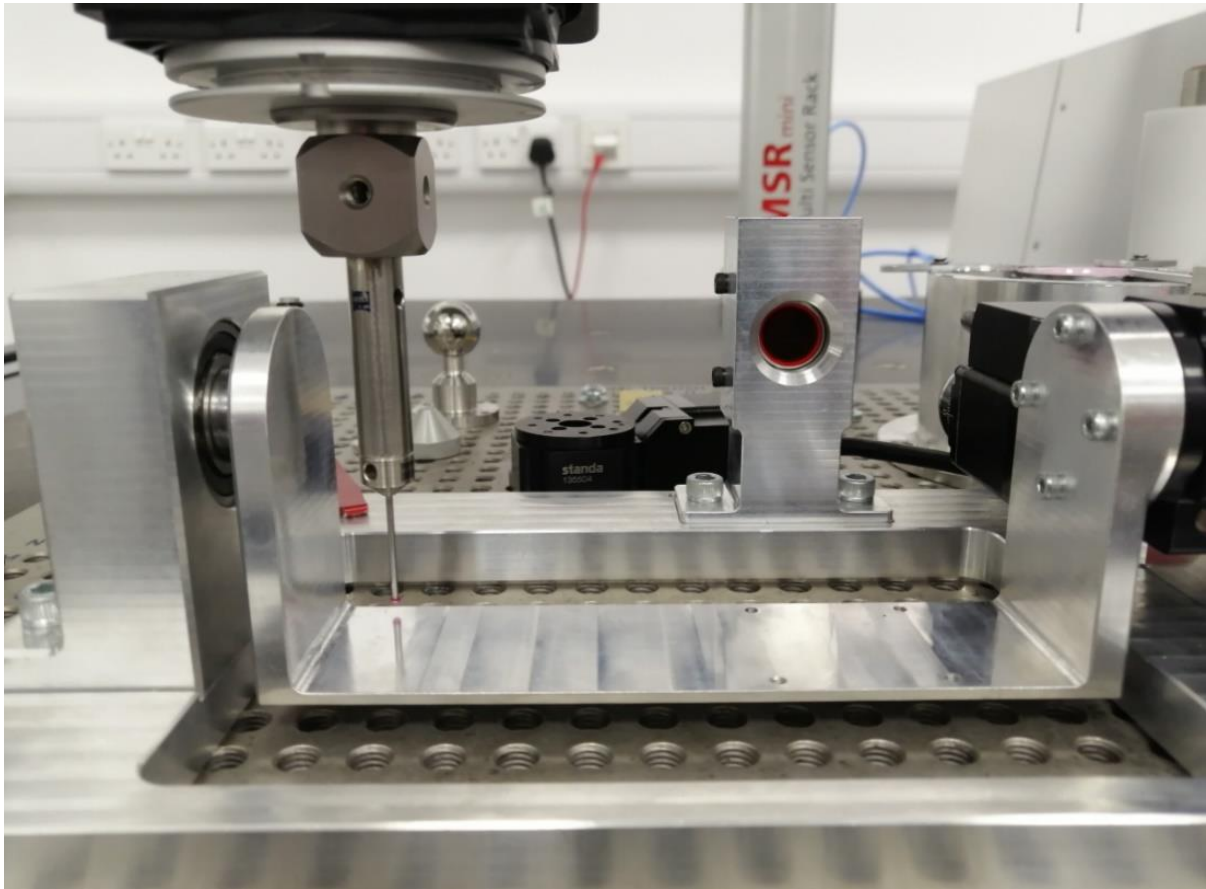


Figure 132: CMM measurement of the middle bracket to set the elevation rotary stage origin position. Note the azimuth rotary stage is removed to allow for a larger scanning area.

4.4 Software Development

Software was developed alongside the fixture hardware. The software aims to analyse CMM data and use this data to control the fixture system, allowing for wear map targeted surface measurements. The software was developed using MATLAB [187], the development process consists of each section being developed as a standalone script, once the scripts are working at a basic level the scripts are converted into app format. The development of the scripts into app format makes the software easier to use, particularly for people that have never used MATLAB before. Using an app also ensures that the code cannot be accessed or altered by the user. Throughout this section an overview of important parts of the code is shown, the full app code is several thousand lines long and would be too long to include entirely as part of this report.

The software is split into three different sections:

- CMM Analysis
- Selecting Surface Measurement Locations
- Control of the Fixturing System

4.4.1 CMM Analysis

The main aim for the CMM analysis section is to import the CMM data and create a wear map using the imported data. The calculation of the volume parameters is also desirable, however the method developed by Bills using CATIA [179] will be used for any official calculations. The 'CMM Measurement' tab is the first displayed in the app, figure 133.

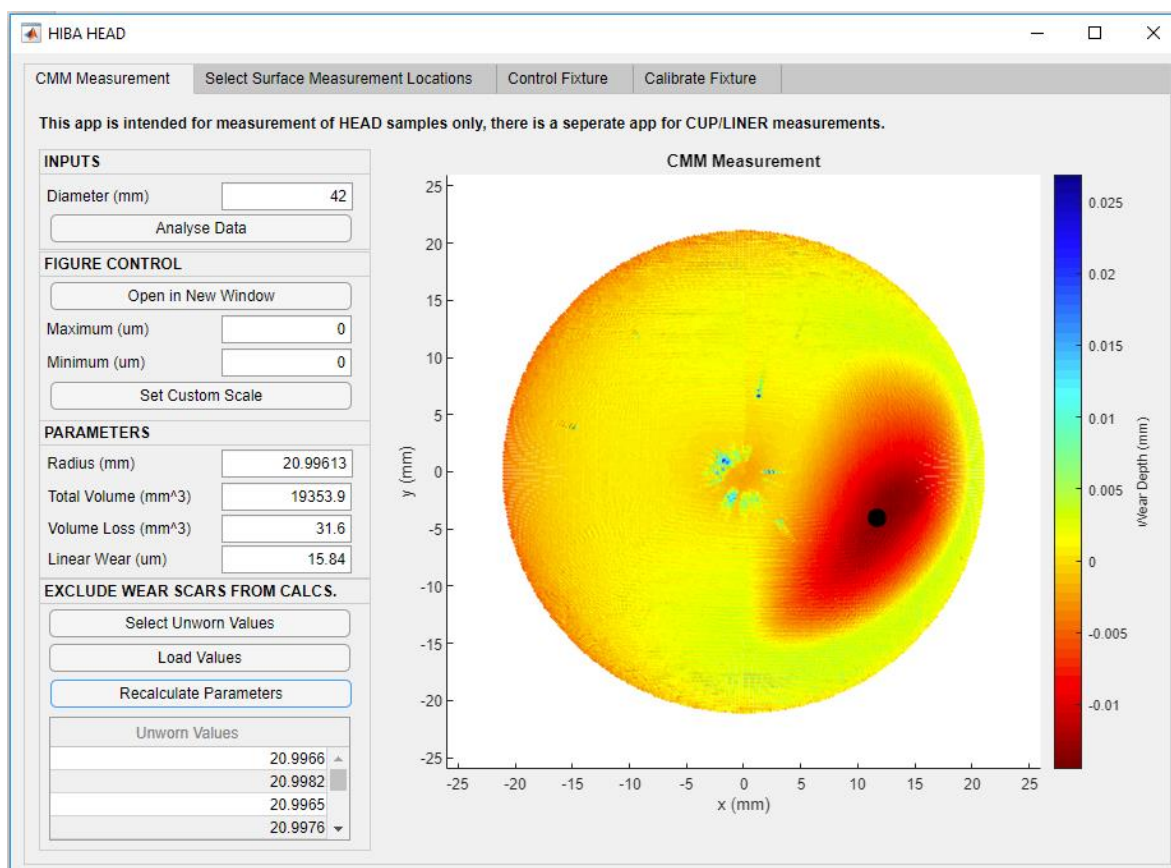


Figure 133: CMM Measurement tab. CMM data has been analysed, wear map and volume parameters produced.

There a number of buttons on the left side of the app and on the right side is a large graphical area, initially empty. The user inputs the diameter of the bearing component being measured in the 'INPUTS' area. Once they select the 'Analyse Data' button a file selection modal dialog box opens automatically at the folder location where the CMM data is stored, the user can then select the desired CMM data. After the CMM data is selected the CMM analysis code is ran, the output CMM wear map is shown in the graphical area and the parameters are displayed in the 'PARAMETERS' area. The user can also set the maximum and minimum values of the wear map colour scale in the 'FIGURE CONTROL' area. This can be particularly useful for comparing a cohort of samples, ensuring they have the same colour scale for a valid comparison.

To calculate the volume parameters more accurately, the wear area must be excluded from the dataset. This allows a more representative radius value to be calculated resulting in a more accurate

calculation of the other parameters. For example, in the case of a femoral head, the data values within the wear area will have a smaller radius value due to the concave wear scar in the surface. This means the radius value when calculated from the entire dataset will be smaller than it actually should be. By excluding the wear area data from the calculation, the radius value will be slightly larger and more accurate.

Firstly the 'Select Unworn Values' button is selected; this opens a window with the wear map and the user can now click on the wear map to select data points, figure 134. Once the user has selected 30 data points in the unworn area of the wear map, the user selects the 'Load Values' button, the radius values of those data points will be calculated and will appear in the 'Unworn Values' table. The 'Recalculate Parameters' button is selected, and the median value of the selected data points is selected as the radius value rather than the median of the entire dataset. This will allow for a more accurate calculation of the volume parameters and reduce the effect of the wear area affecting the outcome of the radius value. To improve this section of code further, rather than custom selecting data points from the unworn surface, the code ideally can include all data points with the exception for the wear area. This will allow for several thousand data points to calculate the radius value rather than just thirty or however many the user manually selects.

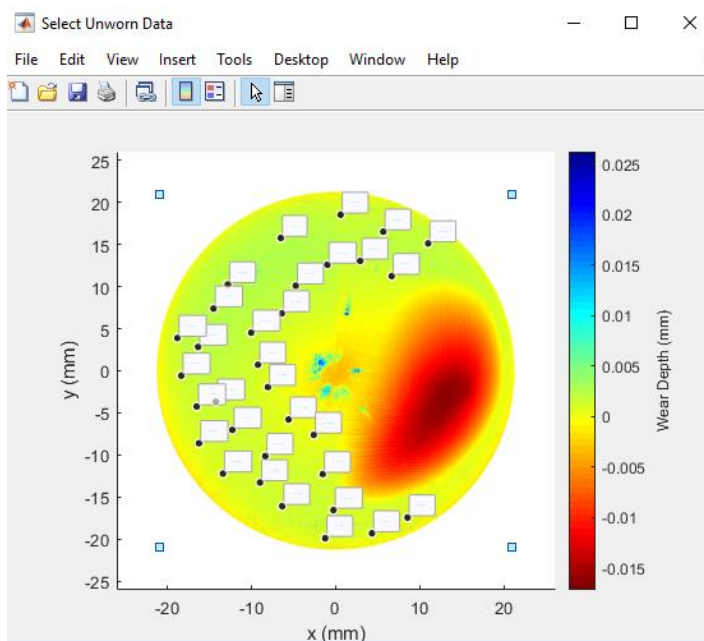


Figure 134: Selecting unworn area data for an improved calculation of the component radius value and volume parameters.

The following code shows an overview of how the wear map is created from the CMM data for a femoral head, figure 135. Annotations are shown alongside the code in green, this explains what each line of code does, this is crucial when coding to ensure when the code is revisited after a long time it can be quickly understood.

```

% User inputs data
diameter = 36          % diameter of componenet in mm
radius = diameter/2   % radius is calculated from diameter value

% The code below opens the CMM data and converts it to a matrix.
% The CMM data must be stored in a text file with the coordinates seprated into 3 columns x,y,z.
% The x,y,z values should be comma seperated.
% This code was designed for CMM values to be in mm.
% Ensure the 'Current Folder' and the uigetfile location is set to where the CMM data is stored.
cmm_data = table2array(readtable(uigetfile('*.txt', 'G:\University\PhD\Software\app4\app')));

% Split the input CMM data into seprate xyz column vectors.
cmm_xdata = cmm_data(:,1)
cmm_ydata = cmm_data(:,2)
cmm_zdata = cmm_data(:,3)

% Calculates the vector sum for each xyz value and the deviation from the perfect diameter sphere.
norm_data = sqrt(sum(cmm_data.^2,2))
norm_deviation = norm_data - radius

% Calculates the maximum normal deviation values, linear wear.
[max_normdev, max_normdev_ind] = min(cmm_data_2(:,5))
[min_normdev,~] = max(cmm_data_2(:,5))
max_normdev_um = -(max_normdev * 1e3)

% Locates maximum deviation point and stores coordinates, both cartesian and spherical.
max_data = cmm_data_2(max_normdev_ind,:)
max_x = max_data(1)
max_y = max_data(2)
max_z = max_data(3)
[max_az, max_el] = cart2sph(max_x,max_y,max_z)

% Plot user CMM data as a point cloud with colour scale representing the ...
% ... amount of deviation from the perfect diameter sphere.
figure('Name', 'CMM Data')
scatter3(cmm_xdata,cmm_ydata,cmm_zdata,[],norm_deviation, '.')
title('CMM Data')
xlim([-radius-5 radius+5])
ylim([-radius-5 radius+5])
xlabel('x (mm)')
ylabel('y (mm)')
zlabel('z (mm)')
view(2)
colormap(flipud(jet))
c = colorbar
c.Label.String = 'Wear Deviation (mm)'
caxis([min_normdev,max_normdev])
daspect([1 1 1])
grid('off')

```

Figure 135: Overview of the coding used to generate a wear map from CMM data for femoral heads.

The code to generate wear maps for femoral heads and acetabular cups is very similar however the use of the max/min functions needs to be selected carefully. For femoral heads, the 'min' function is used to calculate the maximum amount of wear, as femoral head wear is seen as negative compared to the nominal radius of the component. Compared to acetabular cups where the wear is seen as positive compared to the nominal radius, so the 'max' function is used. For this reason, there are two versions of the app, HIBA_HEAD and HIBA_CUP, one which is designed for use with femoral head data and the other is designed to be used with acetabular cup data. The abbreviation HIBA stands for Hip Implant Bearing Analysis.

Name	Date modified	Type	Size
ximc	18/04/2020 14:00	File folder	
HIBA_CUP	01/04/2020 18:44	MATLAB App	193 KB
HIBA_HEAD	07/08/2020 15:51	MATLAB App	160 KB

Figure 136: App versions, separate app for femoral head and acetabular cup samples.

4.4.2 Selecting Surface Measurement Locations

Now that the wear map of the CMM data is fully developed, the user can then select where to target the surface measurements, figure 137. As previously discussed because of the spherical shape of the bearing components, spherical coordinates are used (azimuth and elevation).

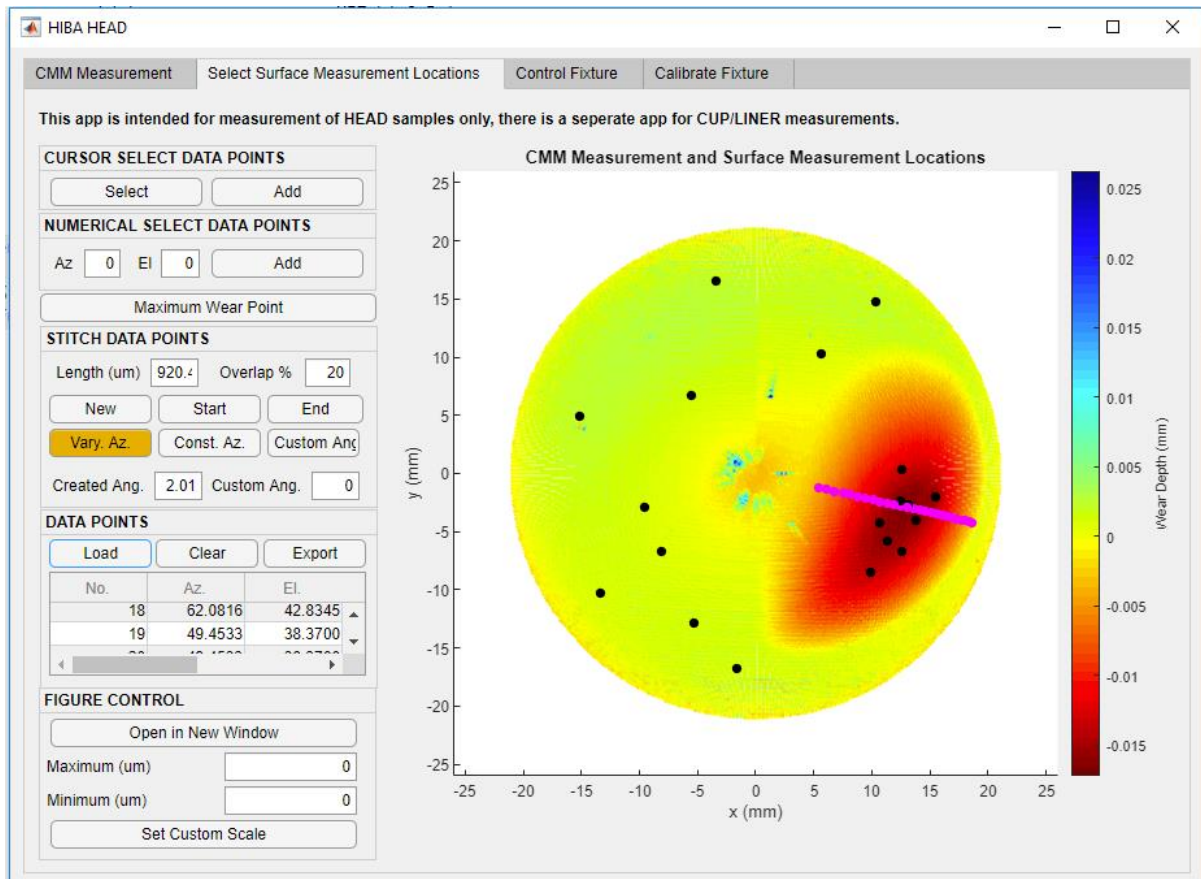


Figure 137: Select Surface Measurement Locations tab. The desired locations for surface measurement are selected by the user. In this example, 10 measurements in the unworn area, 10 measurements in the wear area, and a stitch of measurements through the centre of the wear area.

To make the software easy to use and flexible there are multiple ways for the user to select the surface measurement locations:

- **Cursor Select**

The cursor select option is likely to be the most commonly used method of selecting surface measurement locations. A wear map is visible on the app, once the 'Select' button is clicked in the 'CURSOR SELELCT DATA POINTS' area, a new window of the wear map is produced. The user can now select data points using their cursor, once the desired location on the wear map is selected via the cursor, the 'Add' button is clicked and the spherical coordinates are saved.

- Numerical Input

This is the simplest of methods, the user manually enters the required spherical coordinates in the 'NUMERICAL SELECT DATA POINTS' area, and then selects the 'Add' button.

- Maximum Linear Wear Point

Using the code in the CMM analysis tab the maximum linear wear location is calculated as spherical coordinates, these can then be used so the user can quickly and accurately select the location of maximum linear wear for surface measurement. To do this the user selects the 'Maximum Wear Point' button.

- Stitching Data

The 'STITCH DATA POINTS' area allows the user to create the coordinates for a stitch of measurements. The following code shows an overview of how the stitching coordinates are created using the app:

When the 'New' button is selected a wear map of the sample is created and opened in a new window, figure 138. The wear map is made interactive with the cursor so data points can be stored using cursor select.

```
% Button pushed function: NewButton
function NewButtonPushed(app, event)
    % Create wear map in new window, with data cursor mode turned on.
    figure('Name','Stitch Custom Surface Locations','NumberTitle','off'); % Set figure name
    scatter3(app.x,app.y,app.z,[],app.normd2, '.') % Create wear map with colour scale set to radius deviation data.
    xlim([-app.in_radius-5 app.in_radius+5]); % Set x limit.
    ylim([-app.in_radius-5 app.in_radius+5]); % Set y limit.
    zlim([0 app.in_radius+5]); % Set z limit.
    xlabel('x (mm)');
    ylabel('y (mm)');
    zlabel('z (mm)');
    view(2); % Set top view.
    colormap(flipud(jet)); % Set type of colour scale.
    c = colorbar();
    c.Label.String = 'Wear Depth (mm)';
    caxis([app.max_normd2 app.min_normd2]); % Set the max and min of colour scale to max and min value of radius dev
    daspect([1 1 1])
    grid('off');
    app.dcm_obj = datacursormode; % Turn on data tip to allow for cursor data to be stored.
    set(app.dcm_obj,'DisplayStyle','datatip',...
        'SnapToDataVertex','off','Enable','on');
end
```

Figure 138: Opening a new figure and allowing data to be selected by the cursor.

The user hovers over the area they would like the stitch of measurements to start, once this is done the 'Start' button is selected, the spherical coordinates of this starting location are saved. The user also selects an ending point for the stitch via the cursor and the 'End' button is selected to store the spherical coordinates, figure 139. When a stitch is created the azimuth value for all coordinates will be identical. The azimuth angle used for the stitch will always be the azimuth angle from the starting location regardless of the end location, the end location is used only to determine the amount of elevation angle change required.

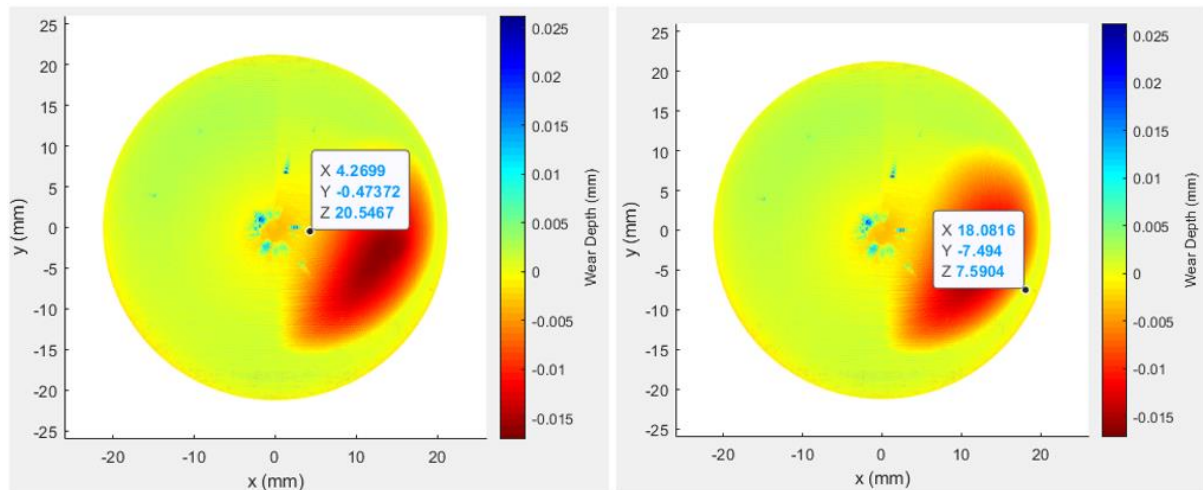


Figure 139: Selecting the start and end points of the stitch.

```
% Button pushed function: StartButton
function StartButtonPushed(app, event)
    % Select start point of stitch.
    c_info = getCursorInfo(app.dcm_obj);
    cx = c_info.Position(1);
    cy = c_info.Position(2);
    cz = c_info.Position(3);
    app.stitch_start_x = cx;
    app.stitch_start_y = cy;
    app.stitch_start_z = cz;

    % Converts this point to spherical, finds start az and el.
    [startaz,startel,~] = cart2sph(cx,cy,cz);

    % Converts rad2deg.
    startaz2 = rad2deg(startaz);
    startel2 = rad2deg(startel);

    % Converts azimuth so is from front of jig reference location.
    app.startaz3 = startaz2 + 90;
    % Converts elevation so is measure from top down, not bottom up.
    app.startel3 = 90 - startel2;
end

% Button pushed function: EndButton
function EndButtonPushed(app, event)
    % Select end point of stitch.
    c_info = getCursorInfo(app.dcm_obj);
    cx = c_info.Position(1);
    cy = c_info.Position(2);
    cz = c_info.Position(3);
    app.stitch_end_x = cx;
    app.stitch_end_y = cy;
    app.stitch_end_z = cz;

    % Converts this point to spherical, finds start az and el.
    [endaz,ende1,~] = cart2sph(cx,cy,cz);

    % Converts rad2deg.
    endaz2 = rad2deg(endaz);
    ende12 = rad2deg(ende1);

    % Converts azimuth so is from front of jig reference location.
    app.endaz3 = endaz2 + 90;
    % Converts elevation so is measure from top down, not bottom up.
    app.endel3 = 90 - ende12;
end
```

Figure 140: Collecting the start and end stitch coordinates. The cartesian coordinates from the cursor data are converted into spherical coordinates.

Before creating the stitch, the user has to enter the desired amount of overlap between stitch measurements, as standard set to 20%, and the sampling size of the surface measurement sensor being used. These variables must be known for the code to calculate the required elevation angle change in between measurements. The user can now select the 'Const. Az.' Button and the spherical coordinates for the stitch will be calculated and stored, figure 141.

```

function ConstAzButtonPushed(app, event)
% OL = overlap percentage.
OL = app.OverlapEditField.Value;
% OL2 = overlap percentage as decimal ex: 20% = 0.8.
OL2 = 1 - (OL / 100);
y0 = app.LengthEditField.Value * 1e-3;
% y = optical length in mm including overlap percentage.
y1 = y0 * OL2;
% Calculating change in z according to radius and y length.
z1 = sqrt((app.radius^2)-(y1^2));
z2 = app.radius - z1;
% Converting cartesian values to spherical, elevationdeg is the amount of needed elevation change in deg for each stitch.
single_angle_rad = atan2(z2, (sqrt(y1^2))); |
single_angle_deg = rad2deg(single_angle_rad) * 2;
% Total stitch distance for elevation only.
el_travel = app.endel3 - app.startel3;
% Calculating number of points needed for stitch.
numpoints = el_travel / single_angle_deg;
numpoints2 = round(numpoints);
% Calculating elevation coordinates, has been altered to maintain a consistent angular change, old method linspace
% Newcode Calcualte new actual end point
end_point = app.startel3 + (single_angle_deg*numpoints2);
%el_co = linspace(app.startel3, app.endel3, numpoints2);
el_co = app.startel3:single_angle_deg:end_point;
numpoints3 = numel(el_co);
% converts row vector into column vector
el_co2 = (el_co)';
% create az_co for needed amount of value
az_co = repmat(app.startaz3,numpoints3,1);
%final coordiante values
stitch_coords = [az_co el_co2];
% This code here converts the stitch data to cartesian.
% Renaming some variable names
stitch_az = az_co;
stitch_el = el_co2;
% Converting spherical coords back to cartesian.
stitch_el2 = 90 + stitch_el;
stitch_az2 = stitch_az - 90;
% Converting from deg 2 rad.
stitch_el2_rad = deg2rad(stitch_el2);
stitch_az2_rad = deg2rad(stitch_az2);
[app.stitch_x, app.stitch_y, app.stitch_z] = sph2cart(stitch_az2_rad,stitch_el2_rad,app.radius);
% Save data into table
currentdata = app.UITable2.Data;
[rowcount, ~] = size(currentdata);
newrow = rowcount+1;
totalrows = rowcount+numpoints3;
newrows = [newrow:1:totalrows]';
[fillcount,~] = size(stitch_coords);
fill = zeros(fillcount,1);
app.UITable2.Data = [currentdata; newrows stitch_coords fill fill fill];

```

Figure 141: Calculating the stitch coordinates and storing them in the 'DATA POINTS' table.

Despite which method is used to generate the spherical coordinates, the code collects the spherical coordinates into the 'DATA POINTS' table to then be used in the next tab to control the fixture system. Different methods of location selection can be used simultaneously, once all surface measurement locations have been selected, the user can then view all of the selected surface measurement locations on the wear map by selecting the 'Load' button in the 'DATA POINTS' area. Single surface measurements are seen as black circles, whereas stitch measurements are shown in magenta to differentiate from each other. If the user is not happy with the surface measurement locations they have selected, they can use the 'Clear' button in the 'DATA POINTS' area, to remove all spherical coordinates and start the process again. The user can also use the 'Export' button to save the selected spherical coordinates to their computer desktop in a text file. This can be useful when completing reports or if data needs to be transferred to MS Word or Excel.

4.4.3 Control of the Fixture System

The spherical coordinates of the selected locations are now used to drive the fixture system. This section of the app is used when the fixture is secured underneath the surface metrology instrument, allowing the user to accurately manoeuvre the component to the desired measurement locations.

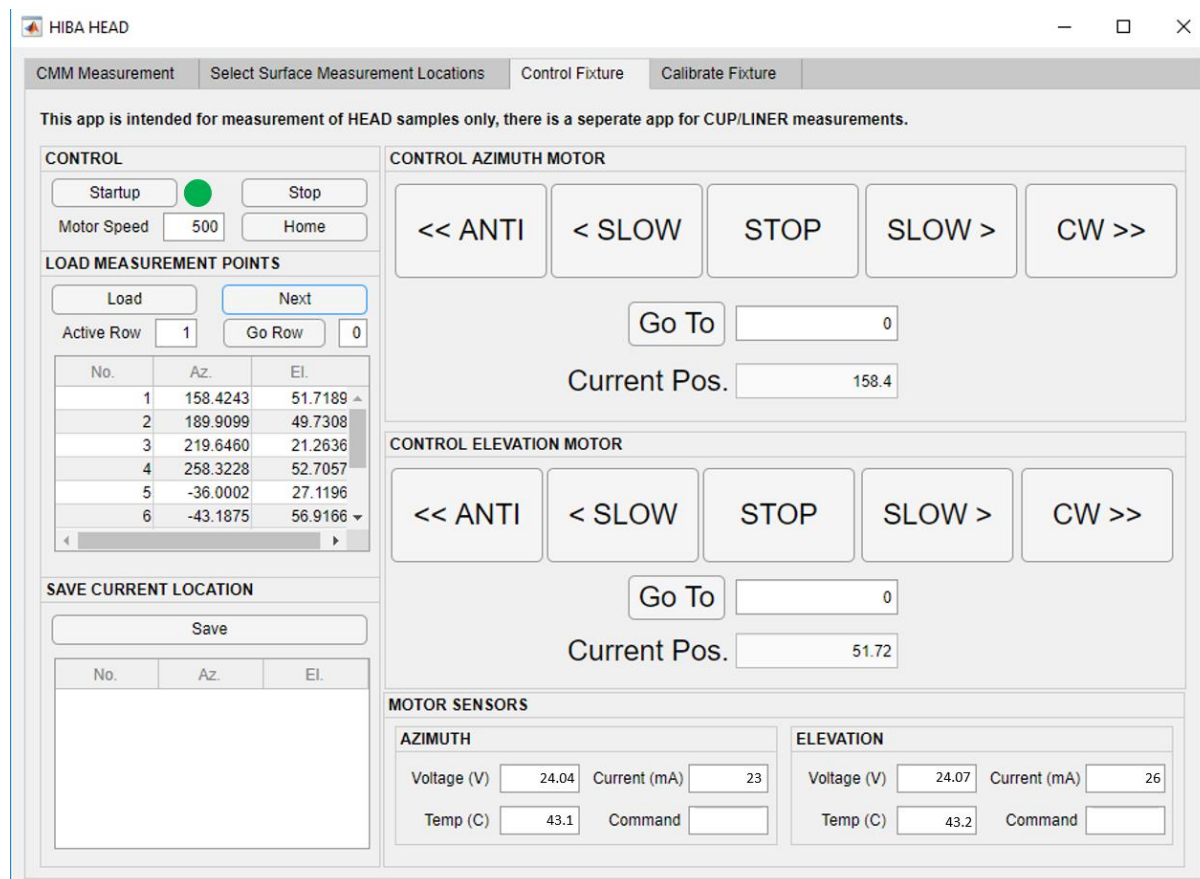


Figure 142: Control fixture tab. The locations selected from the previous tab are used to control the fixturing system.

When this tab is first opened, the rotary stages need to be activated to ensure they are working with the software. To do this the 'Startup' button in the 'CONTROL' section is selected. If the stages are working as intended then the lamp next to the 'Startup' button will turn from red to green. The speed of the motors can be adjusted in the 'CONTROL' section, between 500 and 2000 steps per second, the motors can also be sent to their home position or stopped immediately from any movement with the 'Home' and 'Stop' buttons.

The measurement locations selected from the previous tab can be loaded into this tab with the 'Load' button in the 'LOAD MEASUREMENT POINTS' section. The selected measurement locations can be used to control the rotary stages. The 'Next' button automatically commands the rotary stages to the next selected location, this allows the user to quickly send the rotary stages to each of the desired locations one by one. If a specific location needs to be revisited, for example, if the surface

measurement taken had a measurement error, then the 'Go Row' button can be used. The user enters the row no. of the desired measurement location into the edit field and selects the 'Go Row' button.

If the user does not want to use the selected locations from the previous tab they can control either the azimuth or elevation rotary stages with the large buttons in the centre of the app. With these buttons the rotary stages can be controlled in anti-clockwise and clockwise movement or a custom coordinate can be entered into the 'Go To' field.

The rotary stages are linked to the app using a range of external matlab functions that are provided by the rotary stage's manufacturer Standa, figure 143. The 'enumerate_devices_wrap' connects the rotary stages to the software and can be used to check that both rotary stages are connected. The 'set_microstep_256' function sets the motor into the most precise stepper motor setup type. The other matlab functions are fairly self-explanatory with the names they have been given. The 'get_speed', 'get_status', and 'get_status_calb' functions, all allow for information about the rotary stages to be seen by the user, such as the speed, current, voltage, temperature and command type, these can then be viewed on the app for the user to see. The 'set_speed' and 'go_home' functions allow the rotary stages speed to be altered and the rotary stages go to their home position. The 'go_home' function is not used in the app, as the origin positions have been altered and therefore the 'go_home' function would take the rotary stages to the wrong original home position.







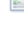
 ximc_enumerate_devices_wrap	16/04/2018 13:29	MATLAB Code	1 KB
 ximc_get_speed	16/04/2018 13:29	MATLAB Code	1 KB
 ximc_get_status	16/04/2018 13:29	MATLAB Code	1 KB
 ximc_get_status_calb	16/04/2018 13:29	MATLAB Code	1 KB
 ximc_go_home	08/01/2019 11:51	MATLAB Code	1 KB
 ximc_set_microstep_256	16/04/2018 13:29	MATLAB Code	1 KB
 ximc_set_speed	16/04/2018 13:29	MATLAB Code	1 KB

Figure 143: Standa MATLAB functions linking the rotary stages to the app.

The library 'libximc' is also provided by Standa which provides a range of command functions which are used to control the rotary stages. Each function requires inputs which are given through the use of the app, the command functions used to control the rotary stages are:

- command_sstp - stops the input rotary stage.
- command_move - moves the input rotary stage to the input steps position.
- command_right - moves the input rotary stage to the right.
- command_left - moves the input rotary stage to the left.

```

% Set bindy (network) keyfile. Must be called before any call to "enumerate_devices" or "open_device" if you
% wish to use network-attached controllers. Accepts both absolute and relative paths, relative paths are resolved
% relative to the process working directory. If you do not need network devices then "set_bindy_key" is optional.
calllib('libximc','set_bindy_key','E:/University/PhD/Software/app/launch/ximc/win64/keyfile.sqlite')

probe_flags = 1 + 4; % ENUMERATE_PROBE and ENUMERATE_NETWORK flags used
enum_hints = 'addr=192.168.1.1,172.16.2.3';

% enum_hints = 'addr='; % Use this hint string for broadcast enumeration
device_names = ximc_enumerate_devices_wrap(probe_flags, enum_hints);
devices_count = size(device_names,2);

if devices_count ~= 2

    app.Lamp.Color = 'red';
    app.Lamp_2.Color = 'red';
    app.CommandEditField.Value = 'FAIL';
    app.CommandEditField_2.Value = 'FAIL';

return
end

if devices_count == 2

    app.Lamp.Color = 'green';
    app.Lamp_2.Color = 'green';
    app.CommandEditField.Value = 'ACTIVE';
    app.CommandEditField_2.Value = 'ACTIVE';

end

az_device_name = device_names{1,1};
el_device_name = device_names{1,2};

```

Figure 144: Start-up of the rotary stages. The folder location for the 'libximc' library and the command functions is set using 'calllib'. The code checks that the motors can be linked to the software using the 'ximc_enumerate_devices_wrap', if both rotary stages are connected then a green lamp on the app indicates to the user they can proceed.

```

% SET STANDARD SPEED
cus_speed = app.MotorSpeedEditField.Value;
cus_uspeed = 0;
ximc_set_speed(app.az_device_id, cus_speed, cus_uspeed);

% GO TO HOME POSITION FOR AZIMUTH
custom_uperposition = 0;
result = calllib('libximc','command_move', app.az_device_id, app.az_zero, custom_uperposition);
if result ~= 0
    app.Lamp.Color = 'red';
end
% GO TO HOME POSITION FOR ELEVATION
custom_elevation = 0;
result = calllib('libximc','command_move', app.el_device_id, app.elev_zero, custom_elevation);
if result ~= 0
    app.Lamp.Color = 'red';
end

app.CurrentPosEditField.Value = 0;
app.CurrentPosEditField_2.Value = 0;

```

Figure 145: Sending the rotary stages to their home/origin positions using the 'command_move' function.

```

% SOFT STOP AZIMUTH
result = calllib('libximc','command_sstp', app.az_device_id);
if result ~= 0
    app.Lamp.Color = 'red';
end

% SOFT STOP ELEVATION
result = calllib('libximc','command_sstp', app.el_device_id);
if result ~= 0
    app.Lamp.Color = 'red';
end

```

Figure 146: Stopping both rotary stages using the 'command_sstp' function.

4.4.3.1 Controlling the Rotary Stage Motors

The motors do not use spherical coordinates as input for control, instead the rotary stages use 'steps' as their control input. The motors for the rotary stages are stepper motors, these types of motors divide a full rotation into a number of equal steps. Stepper motors are very easy to control with each pulse of electricity turning the motor one step. One crucial feature of a stepper motor is that error does not accumulate from step to step. For example, a standard stepper motor travels one step it will go $1.8^\circ \pm 0.05^\circ$, if the same motor travels one million steps, it travels $1,800,000^\circ \pm 0.05^\circ$. The error does not accumulate [188].

To convert the spherical coordinates into steps there are two things that need to happen. Firstly, the spherical coordinate system needs to be adjusted into steps. Secondly the new origin locations of both the rotary stages in terms of steps need to be stored and used for all future movements of the motors. To adjust the spherical coordinates (degrees) into steps, we consult the motor specifications. The specification states that 200 steps equate to 3 degrees of rotation. Therefore, spherical coordinates in degrees can be converted into steps as follows:

$$P_{steps} = \left(\frac{P_{deg}}{3} \right) \times 200, \text{ For example, } 0.5 \text{ degrees of rotation} = (0.5 / 3 * 200) = 33.3 \text{ steps.}$$

The origin locations of both motors are set as shown in figure 147. These origin locations were set during the assembly of the fixture. The origin locations can easily be adjusted by altering this code.

```
% Set zero positions here for the stage.
app.az_zero = (-154 / 3) * 200;
app.elev_zero = (-141.7513 / 3) * 200;
```

Figure 147: Origin positions of both the azimuth and elevation rotary stages. Note negative values represent anti-clockwise movement.

Before any movement of the rotary stage, the initial origin positions are input, then the new position in steps is input afterwards as an addition. This is done automatically with the code created, this is the basis for all movements of the rotary stages. For example, consider figure 148, the position the user wants the stage to go to is either entered manually or is selected from the list of collated measurement locations from the previous tab, 'app.CurrentPosEditField.Value'. The spherical coordinate of this value is converted into steps, the origin location value is added to the value to give the actual desired location in steps, the 'custom_position' value. The 'custom_position' and the correct motor ID, 'app.az_device_id', are used as an inputs for the 'command_move' function, allowing for machine code to control the stepper motor with the inputs controlled by the user via MATLAB.

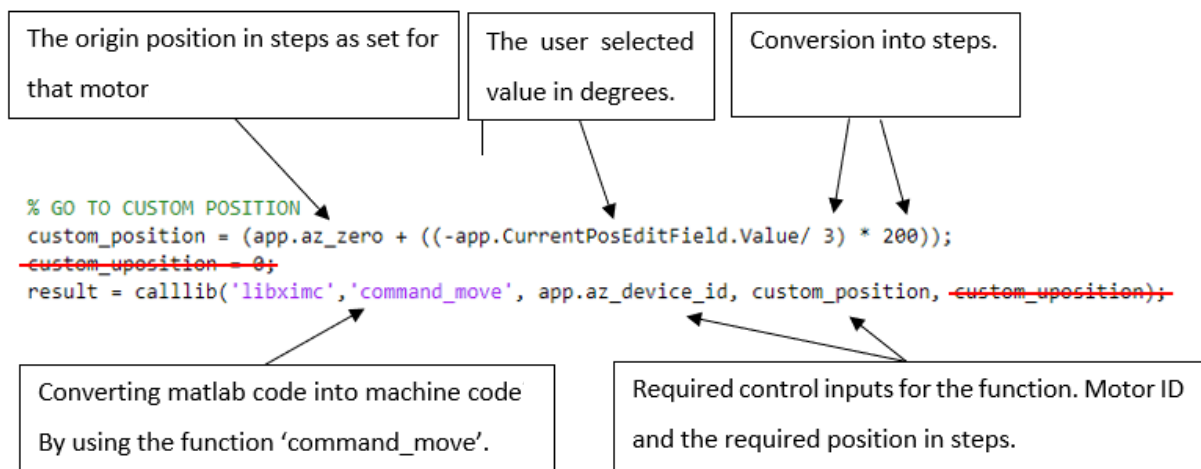
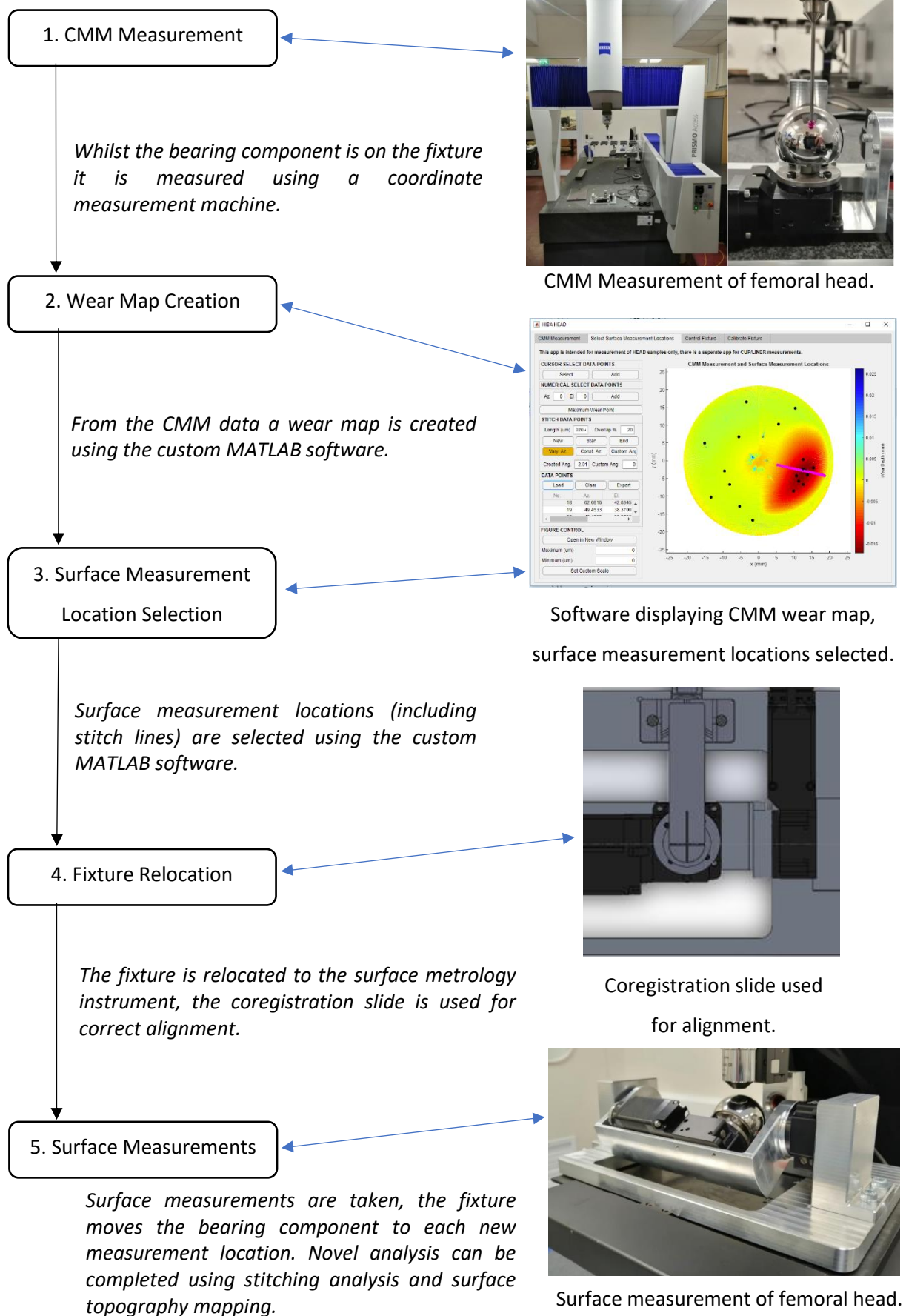


Figure 148: Control of the rotary stages, moving the azimuth rotary stage to a custom position.

4.5 Method Flowchart

The method for using the custom fixture system is detailed below in a flowchart.



4.6 Chapter Summary

Before the development of the custom fixture system began, the design requirements were clearly laid out to be followed as part of the development process. The target positional uncertainty of the fixture was calculated as $\pm 0.0877^\circ$. This was calculated using the stitching of surface measurements as the basis for the required positional uncertainty.

The fixture utilises two rotary stages to manoeuvre the bearing component, allowing access to the entire bearing surface. The size of the fixture is minimal, 271 x 155 x 93 mm (LWH), ensuring it is compatible with the majority of surface metrology instruments. The hardware was designed using SolidWorks, 3D printing was utilised to test the hardware and make further improvements. The rotary stages selected were Standa 8MR174-11, allowing high precision control, with a stated resolution of 0.015° . The final design was machined from aluminium, and during assembly the fixture was measured using the CMM to set the rotary stages origin positions correctly.

The software for the fixture system was developed on MATLAB, the main functions of this software is to: Analyse CMM data and convert it to a wear map; Select surface measurement locations on the wear map; Control the fixture system to the selected surface measurement locations. The software is created in an app format, which is designed to be easy to use for novice users.

Chapter 5: Testing of the Custom Fixture System

5.1 Statistics

In this chapter measures are used to define the variability and spread of positional accuracy data for the fixture system, it is important that these measures are clearly understood.

Mean Value – the arithmetic average value from a dataset, calculated by the sum of all the values in the dataset divided by the number of values.

Median Value – the average value from a dataset, calculated by selecting the middle value in a dataset when ordered from lowest to highest in value.

Range – The range is the difference between the largest and smallest value in the dataset.

Standard Deviation (SD) – The standard deviation is a measure of how spread out a dataset is. If all the values in a dataset are grouped close to the mean then the standard deviation value will be lower. If the values vary a lot and are not close to the mean then the standard deviation value will be greater. The standard deviation is calculated using the following formula:

$$\sigma = \sqrt{\frac{1}{N} \sum_{i=1}^N (x_i - \mu)^2}$$

3 Sigma Rule – The 3-sigma rule is a statistical rule that can help understand the spread of a dataset. The rule states that for a normal distribution 68% of data will fall within \pm one standard deviation from the average value, 95% within \pm two standard deviations and 99.7% within \pm three standard deviation. This is particularly useful to understand the uncertainty of a dataset, in this chapter this rule will be applied for describing measurement error of the CMM and positional error of the custom fixture system.

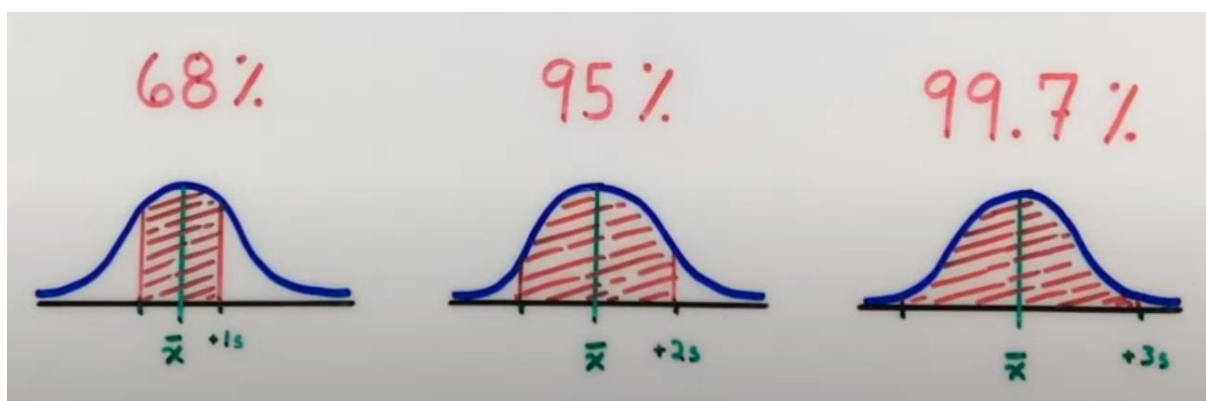


Figure 149: The empirical rule diagram. The shaded area within the graph shows the amount of data falling within the standard deviation limits [189].

5.2 Testing Phases

To test the positional error of the custom fixture, a CMM is used to measure the rotational movement from each of the rotary stages on the fixture. To do this a square faced artefact (or a gauge block in phase 2) is attached to the fixture and measured. The rotary stages manoeuvre the artefact to a new position and the amount of rotation is measured using the CMM, the positional error value is calculated to see if the rotary stage is overshooting or undershooting its target rotation value.

Initially only one phase of testing was expected, however improvements to the testing method were implemented, this led to three separate testing phases being completed:

Phase 1 – Initial Measurement Testing

Measurement test using a square artefact and a five-point probing strategy with the CMM.

Phase 2 – Improved Method Testing

Measurement method is improved by using a gauge block and a scanning pattern strategy.

Phase 3 – Post Error Compensation Testing

Using the measurement results from phase 2 error compensation is applied to the fixture, then final testing is completed to calculate the positional error of the fixture.

5.3 Phase 1 – Initial Measurement Testing

5.3.1 Method

The CMM used for this testing is the Zeiss Prismo Access with a VAST XT analogue probing system, figure 150, the radius of the probe tip is 2 mm. The performance specifications of this CMM states a length measurement error of $0.9 + L/350$ μm [126].

A square faced artefact is manufactured that can be screwed into the top of the azimuth rotary stage, figure 151. Once this artefact is screwed into place the front face of the artefact is aligned over the centre of the azimuth rotary stage from left to right. When either of the rotary stages are driven this will manoeuvre the artefact allowing the CMM to measure the front face of the artefact and calculate the amount of rotation that has occurred in either azimuth or elevation direction.



Figure 150: Zeiss PRISMO Access CMM, used for testing of the fixturing system.

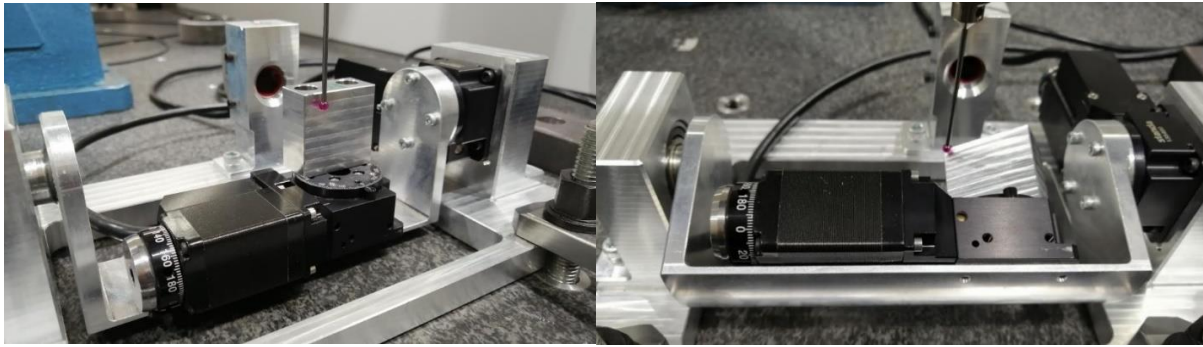


Figure 151: CMM measurement of the square artefact

5.3.1.1 Pre-measurement Procedure

The following procedure is followed before all measurements:

1. The control PC is turned on and the Zeiss Calypso software is loaded on the PC.
2. If the CMM is not initialised the drives are turned on and the controller is used to check all movement axis are active.
3. The master probe is loaded into the stylus system and the reference sphere position is measured.
4. The selected measurement probe, 2 mm radius, is loaded into the stylus system and the reference sphere is again measured to determine the radius of the measurement probe.
5. The fixture is securely attached to the CMM base using clamps as shown in figure 152.
6. The coordinate system of the CMM is set so the top left corner of the square artefact is the origin of the coordinate system, the fixture is at its home position. To achieve this, a measurement is made on the front face, left face, and top face of the square artefact and planes are created for

each face. The X origin is set to the front face plane, the Y origin is set to the left face plane and the Z origin is set to the top face plane. The resulting coordinate system can be seen in figure 152.

7. A suitably sized clearance volume is set around the square artefact to reduce the chance of the probe colliding with the fixture during measurement.

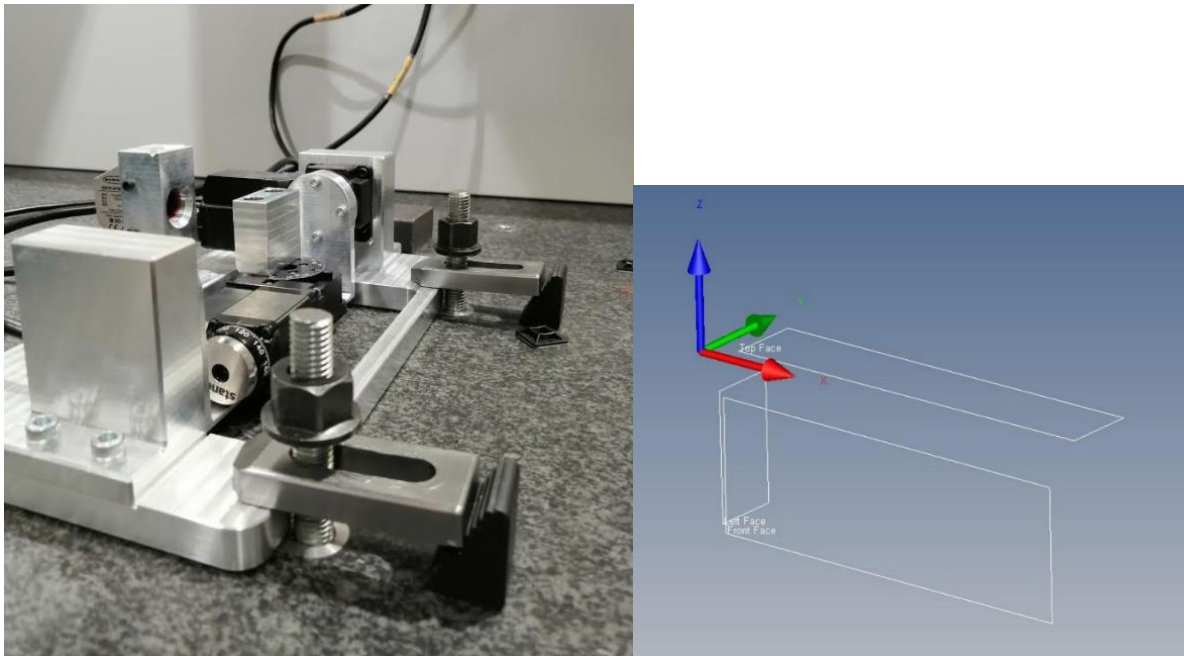


Figure 152: Pre-measurement procedure. Left: Two clamps attached to the fixture to secure it to the CMM base. Right: Coordinate system setup for measurement of the artefact.

5.3.1.2 Probing Strategy and Calypso Angle Deviation Analysis

A five-point plane probing strategy is utilised during phase 1 of testing (this is replaced with a scanning strategy in phase 2 as it improves measurement accuracy), this consists of a probing point in each corner of the face and one in the centre, figure 153. These probing points are then converted into a plane of best fit using the CMM software Calypso. The angle between any two planes can be calculated using the Calypso analysis option: 'Calculate angle between features', figure 154. This analysis method works when only one rotation angle is manoeuvred at a time. If both rotary stages are used at the same time, then the resultant measurement plane has a compound angle, and the azimuth and elevation angles cannot be calculated separately, for this reason only one rotary stage is driven at either time.

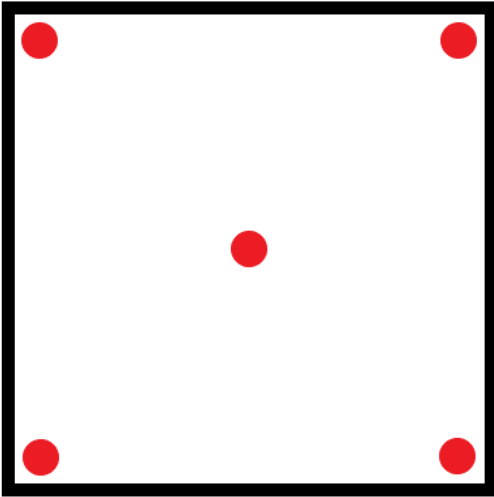


Figure 153: Five-point plane probing strategy.

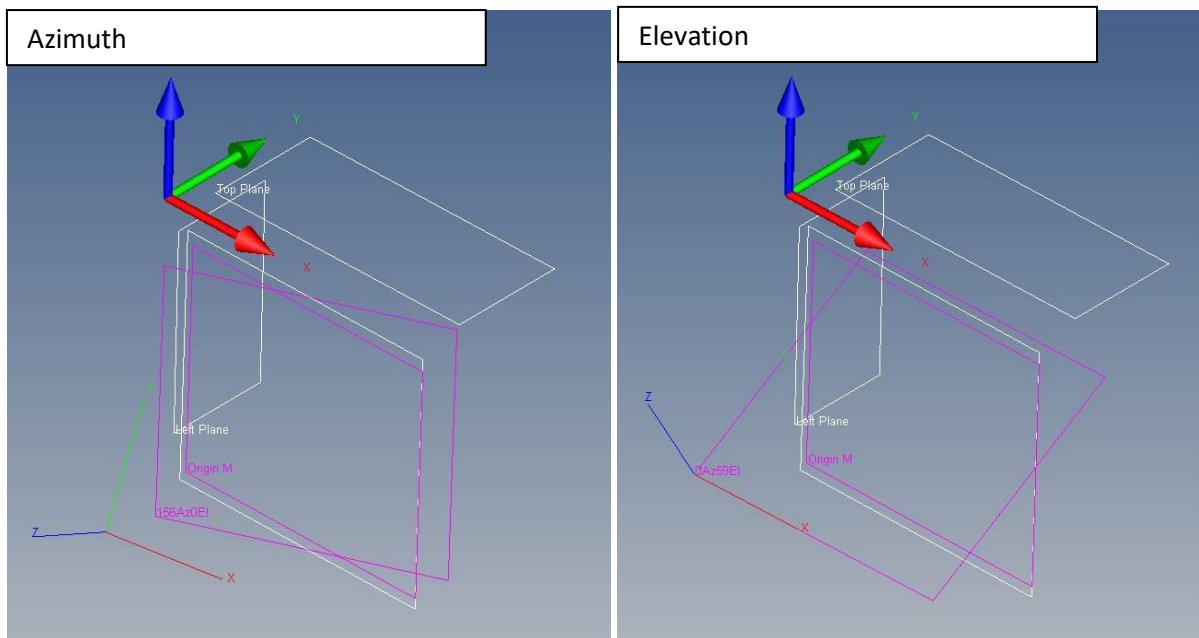


Figure 154: Measurement of angular deviation between planes using Calypso. Angle between the two pink planes is calculated.

5.3.2 CMM Angular Measurement Repeatability

Although the performance specification is already well defined for the CMM, there is no specified value for the angular measurement repeatability of the CMM. We can estimate this value by completing a repeated measurement set of the square artefact.

To complete this test the front face of the square artefact is measured repeatedly 10 times with the five-point plane probing strategy whilst the artefact is at the home position. Each of the measurements is taken using the CNC mode of the CMM, this ensures the same probing points are taken during each measurement. The azimuth and elevation angles between the measurement plane and the datum front plane is calculated for each measurement using Calypso. The median value and

the standard deviation of the dataset are calculated. The angular measurement repeatability of the CMM can be estimated using the 3-sigma rule. The results from this testing can be seen in table 13 and figure 155.

Table 13: Repeated measurements at the origin position.

No.	Az. (°)	El. (°)
01	0.00400	0.01990
02	0.00380	0.01980
03	0.00370	0.01950
04	0.00360	0.01970
05	0.00390	0.01920
06	0.00380	0.01970
07	0.00380	0.02020
08	0.00310	0.02060
09	0.00390	0.02010
10	0.00390	0.02010
Maximum	0.00400	0.02060
Median	0.00380	0.01985
Standard Deviation	0.000242	0.000374
2SD	0.000484	0.000748

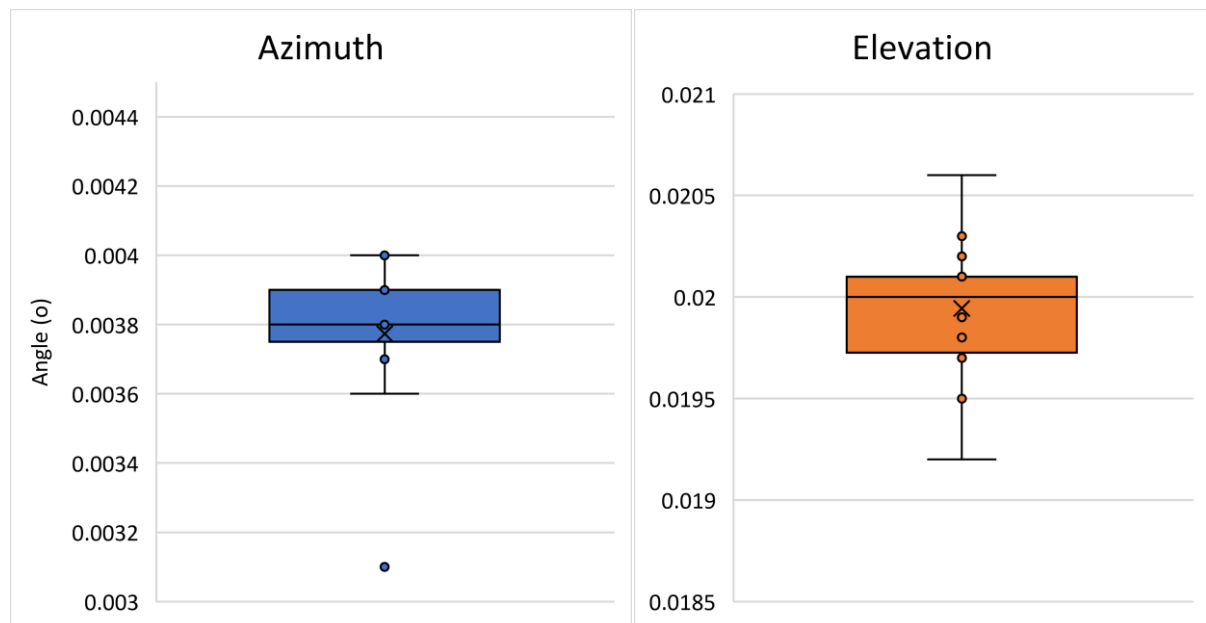


Figure 155: Box and whisker plot of the azimuth measurements and elevation measurements.

Figure 155 uses a box and whisker plot so all repeated measurements can be seen graphically for both the azimuth and elevation deviation and allows the spread of the measurements be visualised.

The 2SD values of the repeated measurements are 0.000484° and 0.000748° for the azimuth and elevation datasets respectively, this results in a combined value of 0.000891° . This gives a good estimation of the angular measurement repeatability for CMM measurements when the same probing points are used each time.

Considering the target positional error of the fixture is $\pm 0.0877^\circ$, the angular measurement repeatability is well below this amount, approximately 98x lower, therefore the CMM is easily capable of calculating the positional error of the fixture to the required level of measurement accuracy.

CMM Angular Measurement Repeatability: 0.000891°

5.3.3 Angular Measurement Error Caused by Inconsistent Probing

5.3.3.1 Inconsistent Probing

Inconsistent probing will occur each time the square artefact is moved to a new position and new probing positions are manually taken by the user on the square artefact. The user will still manually probe in each corner and the centre of the square face however the exact same location cannot be achieved, figure 156. As the square artefact cannot be manufactured perfectly flat, there will always be slight deviations in the surface. If the probing positions are in slightly different locations this results in a slightly different measurement plane being created each time. As the measurement plane being created is different this will also result in different angular deviation calculations. This error does not occur when repeated measurements are taken at each location, as for repeated measurements the CNC mode of the CMM is utilised and this ensures the same probing locations are touched each time.

Ideally the same exact probing points should be used each time, however this is very difficult to program on the Zeiss CMM when the square artefact is being rotated in azimuth and elevation. To understand if the inconsistent probing will be an issue for the upcoming testing the measurement error it causes needs to be estimated and compared with the target positional error of the fixture.

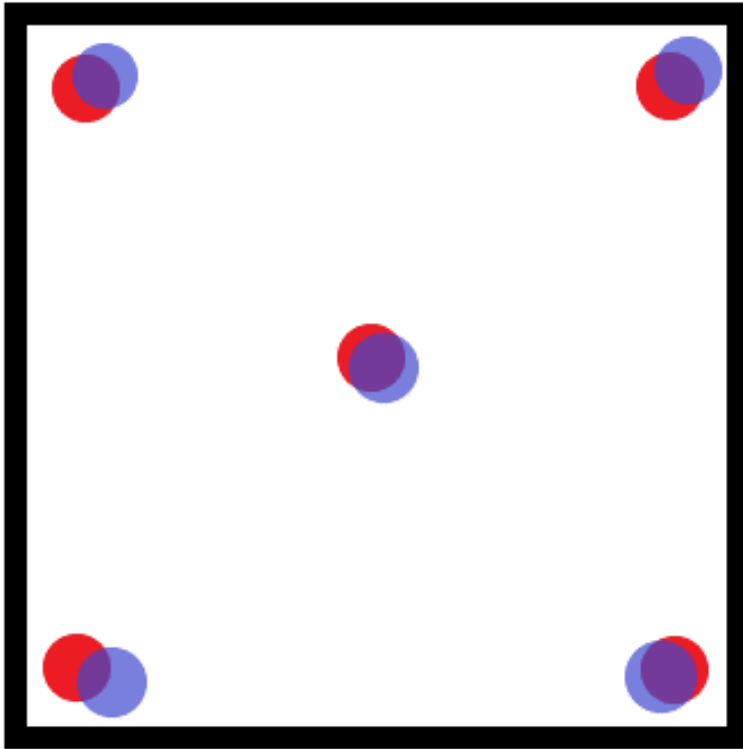


Figure 156: Inconsistent probing diagram. Red circles: Measurement set 1, Blue circles: Measurement set 2.

5.3.3.2 Calculating the Angular Measurement Error Caused by Inconsistent Probing

The measurement error caused by inconsistent probing can be estimated by taking two measurement sets on the square artefact whilst it is at the same position but with new probing positions, 10 measurements are taken for each measurement set.

The angular deviation between the median value of the first measurement set and the median value of the second measurement is 0.0038° for the azimuth value and 0.01985° for the elevation value, figure 157.

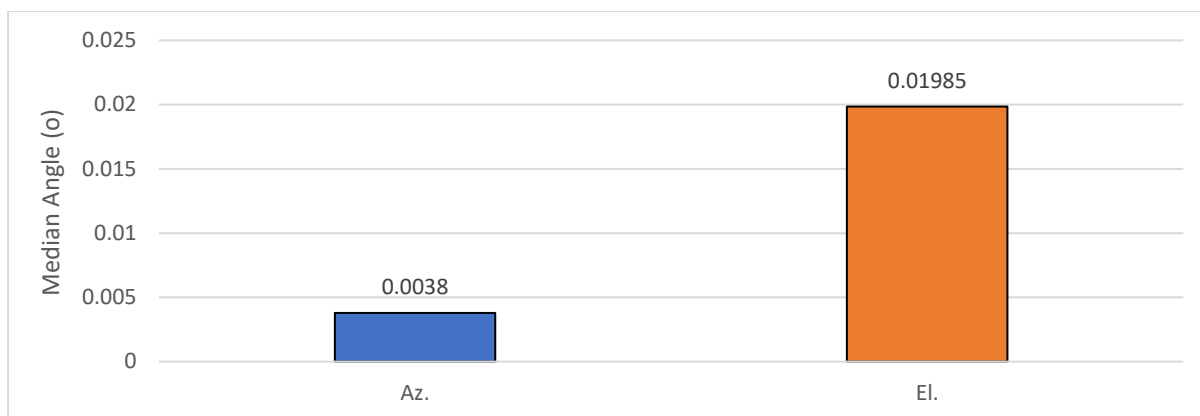


Figure 157: Median error values from the 10 repeated measurements for the azimuth and elevation angular deviation.

These error values can be combined to give a total error value of 0.0202° , this is much larger than the measurement repeatability of the CMM with the same probing points (0.000891°). These values are useful to know before the upcoming repeatability and positional error tests on the fixture.

Angular Measurement Error Caused by Inconsistent Probing: 0.0202°

We must now consider if this level of measurement error is suitable for the task of measuring the positional error of the custom fixture system. Ideally the measurement error should be significantly lower than the target positional uncertainty of the fixture so it can be calculated with good confidence.

When comparing the measurement error value, 0.0202° , to the target positional uncertainty of the fixture, $\pm 0.0877^\circ$, the measurement error is 4.34x lower. This was deemed suitable at the time and positional error testing of the fixture was carried with this method. However, in phase 2 the method is improved, specifically to reduce the measurement error.

5.3.4 Phase 1 Positional Error Testing Results Summary

As the phase 1 testing is superseded by the phase 2 testing, the phase 1 testing results are only included as a summary. **The full results for phase 1 testing are included in the appendix section.**

5.3.4.1 Positional Repeatability of the Fixture

A measurement set is made at the home position (0 Az, 0 El). The rotary stages are then driven to 30 different spherical coordinates. These movements are made over a period of two days (as they were used for the positional error testing of the fixture). Once these movements are completed, the fixture

is sent back to its home position and the artefact is remeasured. For this testing, the same probing points could be used as the measurement was occurring at the same fixture position. When comparing the two measurement sets at the home position, the difference between the median measurement values is 0° (azimuth) and 0.00025° (elevation). This shows that even after two days of testing and 30 movements, the repeatability of the fixture is very good.

This same repeatability test was completed again, however at a random spherical coordinate position, 57° azimuth and 73° elevation. The method was the same, apart from the time between measurement sets was only a few hours. When comparing the two measurement sets at the random position, the difference between the median measurement values is 0.002° and 0.0018° . This is not as good as the repeatability at the home position; however, the values are still very low when compared to the target positional uncertainty.

Combined Positional Repeatability (Home Position): 0.00025°

Combined Positional Repeatability (Random Position): 0.0027°

5.3.4.2 Positional Error of the Fixture

To calculate the positional error of the fixture, the rotary stages are driven to 10 different positions and the square artefact is measured at each location to see how accurately the fixture has actually manoeuvred. The testing is split into two phases, firstly only the azimuth rotary stage is tested, then the elevation rotary stage. The spherical coordinates used were randomly generated as this better represents the manner in which the fixture system will be used. Usually, the spherical coordinates selected are in completely different areas of the bearing and the rotary stages are not manoeuvred in a uniform manner, unless during stitching. This method ensures the rotary stages are driven both forward and backwards during the testing and are not just moved in one single direction which would occur if successive increments were used.

For the azimuth positional error, the maximum error value was calculated as 0.0308° , with a spread of the error in both positive and negative values (overshooting and undershooting the target). The median error value was calculated as -0.0055° . The 2 standard deviation value of the dataset is 0.0378° , therefore using the 3-sigma rule we can calculate the azimuth positional error as $\pm 0.0433^\circ$ (median error + 2SD). This value should cover approximately 95% of movements. For the elevation positional error, the maximum positional error was calculated as -0.746° , this is below the target positional error (± 0.0877), but relatively close. The error values from this dataset are all negative, therefore all movements are undershooting their targets. The median error value was calculated as -0.047° , and the 2SD value of the dataset is 0.0375° . Therefore, we can calculate the elevation

positional error as ± 0.0845 (median error + 2SD). This value should cover approximately 95% of movements. We can see that the elevation rotary stage is performing with worse positional error and is very close to the target positional uncertainty value. We can calculate the combined positional error as $\pm 0.0949^\circ$.

Combined Positional Error: $\pm 0.0949^\circ$ (Currently over the target)

5.4 Phase 2 – Improved Method Testing

5.4.1 Method Improvements

Phase 2 testing will complete the same measurements tests as carried out in phase 1, however important improvements have been made to improve the accuracy of the measurement method. The improvements made to the testing method are as follows:

Scanning Pattern Strategy

Instead of using the five-point probing strategy, a scanning pattern is used on the face of the artefact. This is to reduce the inconsistent probing error which was decreasing the measurement accuracy of the angular calculations. The scanning pattern will allow for more measurement points to cover a larger area of the face, this should ensure that the measurement plane created is more consistent. By

initially only using five points, if any of these five points was an anomaly, from either a surface deviation in the artefact face or the effect of dust particles, this could greatly affect the results of the entire plane. By using more measurement points with the scanning strategy this covers a much larger area with many more points and reduces the chance of an anomaly affecting the resultant measurement plane. With this new scanning strategy, the measurement error caused by inconsistent probing should be drastically reduced and the measurement method should become more accurate. This will allow for a more accurate value to be determined for the positional error of the fixture system.

Figure 158 compares the two probing strategies. For the scanning pattern strategy, initially five probing points are made, once the plane is defined, the 'Grid' tool is used on Calypso to create a scanning mesh within the borders of the five points. The CNC mode is then used to complete the scanning strategy and complete the measurement.

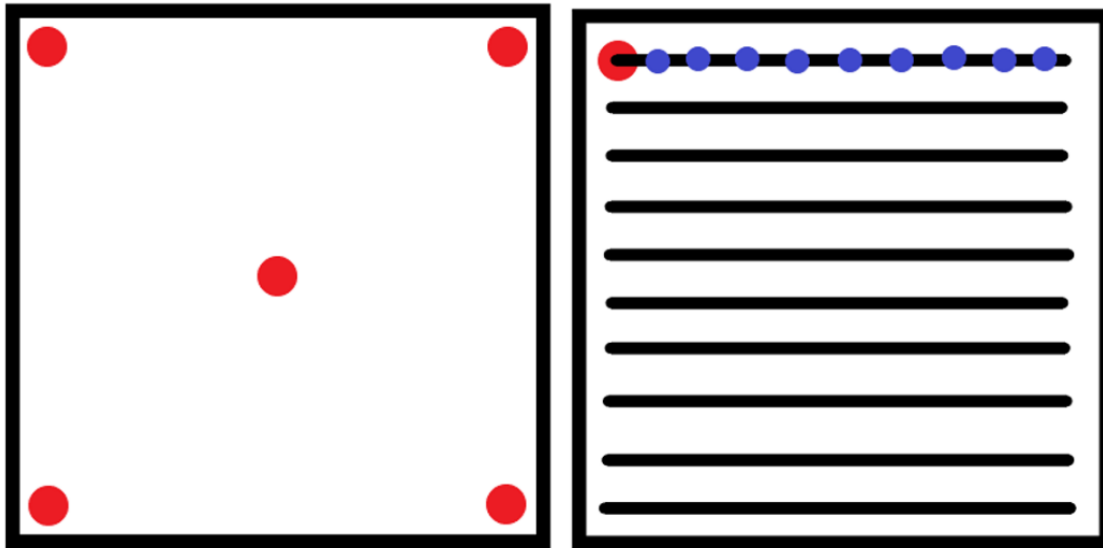


Figure 158: Comparison of probing strategies. Left: Original five-point strategy. Right: Scanning pattern strategy.

Gauge Block Measurement

The results from the phase 1 testing showed a consistent trend for the elevation rotation to undershoot its target, in particular as the elevation rotation extends out towards 90° the rotary stage undershoots its target increasingly. This error may be coming from the rotary stage but could also indicate that the measurement artefact may have a flatness deviation in its Y direction. To determine whether this positional inaccuracy is caused by the rotary stage or the square artefact a new measurement artefact is used for this testing phase. Gauge blocks are metal or ceramic blocks that are precision ground and lapped to specific thicknesses, they are used often for calibration of measurement equipment. A gauge block is manufactured very precisely with specific lengths and flat

faces, for this reason the gauge block will likely be much flatter and have less surface deviations than the square artefact from the first phase of testing.

For this testing, a 25 mm size gauge block, grade 2, is used with the fixture, figure 159. The gauge block is attached to the fixture by using a sacrificial plate to ensure no glue can damage the azimuth rotary stage. The sacrificial plate is screwed into the azimuth rotary stage and the gauge block was glued to the plate. The gauge block was glued on both the front and back edge to the plate and was left 24 hours to fully cure before measurements were taken.

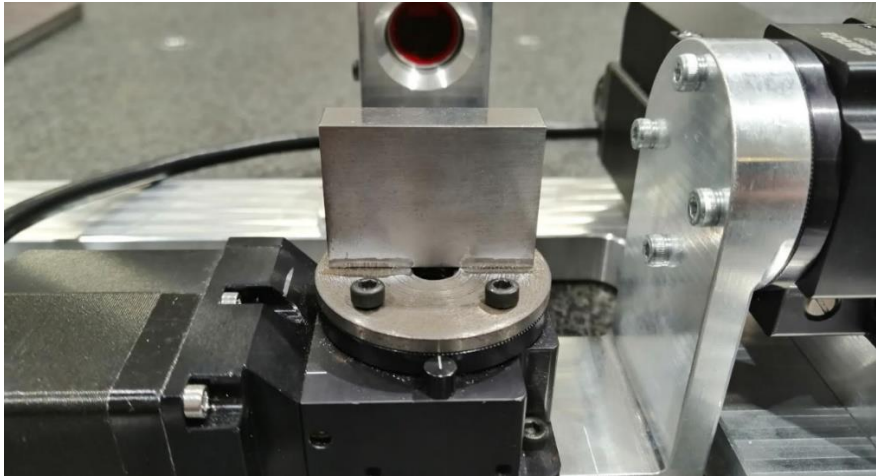


Figure 159: 25 mm gauge block attached to the fixture using glue.

When scanning the front face of the gauge block only the top 2/3 of the surface is measured, the bottom 1/3rd is avoided in case the super glue has altered the flat surface. The approximate bottom edge of the measurement area is shown by the CMM probe, figure 160, The edge of the glue line is marked by a red arrow.

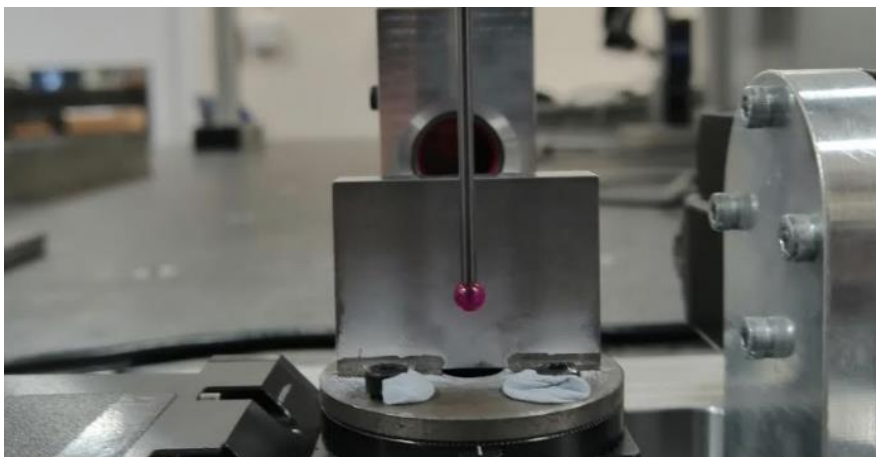


Figure 160: Lowest scan point on the gauge block.

The scanning strategy applied to the face of the gauge block consists of 100 total measurement points, that are located within the boundary of the initial five probing points. The data points are collected by a scanning method that can be seen in figures 161 and 162.

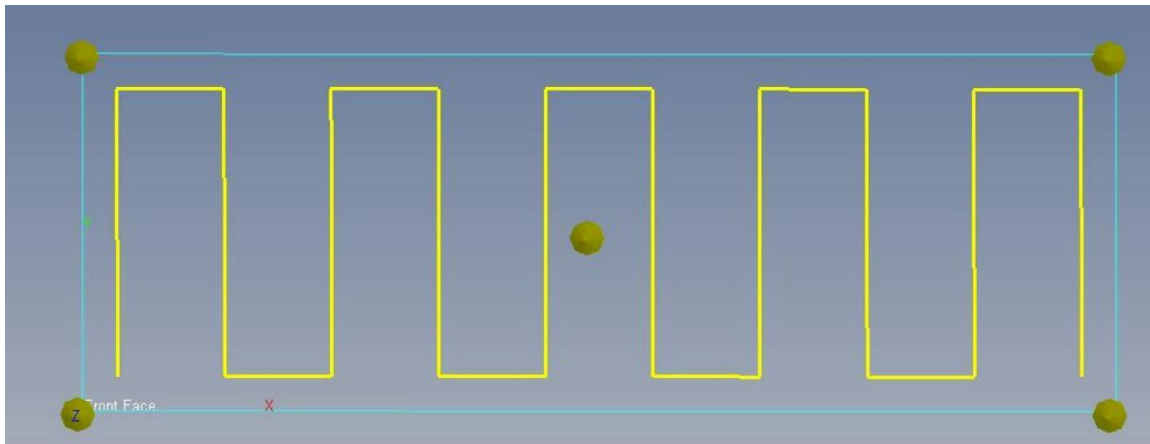


Figure 161: Measurement scanning strategy. Scan starts from lower left side and follows the path.

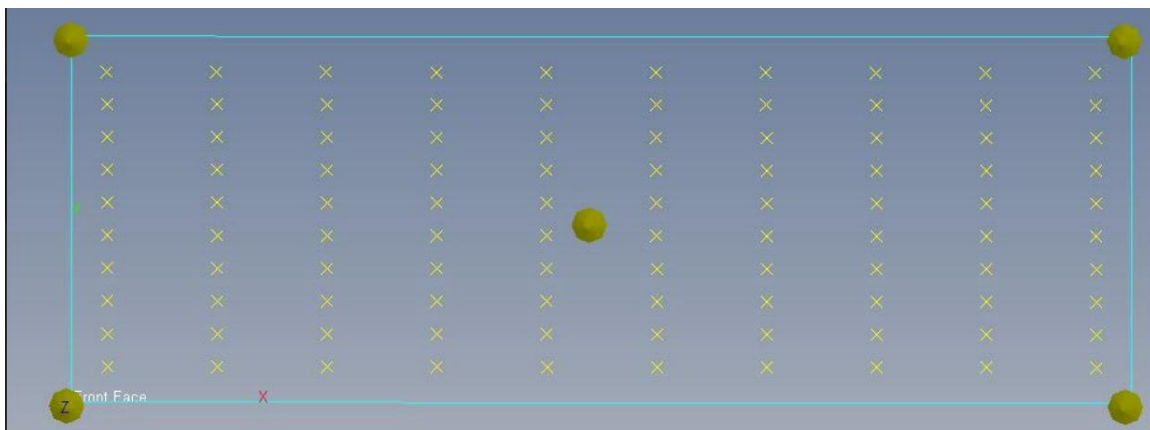


Figure 162: Resultant measurement points from the scanning strategy.

5.4.2 Angular Measurement Repeatability of the CMM

The same measurement is completed 10 times at each of the origin positions, (10 Az, 0 El / 0 Az, 10 El). Each of these measurements is completed using the exact same scan strategy using the CNC mode of the CMM. This is to test the angular measurement repeatability of the CMM and this method.

Table 14: CNC repeated measurement set at Az 10, El 0.

No.	Az. Value (°)	Az. Error (°)
01	9.9928	-0.0072
02	9.9926	-0.0074
03	9.9925	-0.0075

04	9.9930	-0.0070
05	9.9930	-0.0070
06	9.9932	-0.0068
07	9.9932	-0.0068
08	9.9929	-0.0071
09	9.9929	-0.0071
10	9.9930	-0.0070
Maximum	-	-0.0075
Median	-	-0.00705
Standard Deviation	-	0.000217
2SD	-	0.000434

Table 15: CNC repeated measurement set at Az 0, El 10.

No.	El. Value (°)	El. Error (°)
01	9.9761	-0.0239
02	9.9749	-0.0251
03	9.9758	-0.0242
04	9.9770	-0.0230
05	9.9758	-0.0242
06	9.9761	-0.0239
07	9.9744	-0.0256
08	9.9730	-0.0270
09	9.9757	-0.0243
10	9.9780	-0.0220
Maximum		-0.027
Median		-0.0242
Standard Deviation		0.001301
2SD		0.002602

Figure 163 plots the repeatability measurements as box and whisker plots to allow the spread of the measurements to be seen graphically, it is important to note that the range of the Y scale for both box and whisker plots is very different. Although on the box and whisker plots the spread initially seems similar the spread is much greater for the elevation measurements, but this is visually compensated by the larger Y scale on the elevation plot. The standard deviation values of the repeated measurements are 0.000217° for the azimuth measurements and 0.001301° for the elevation measurements.

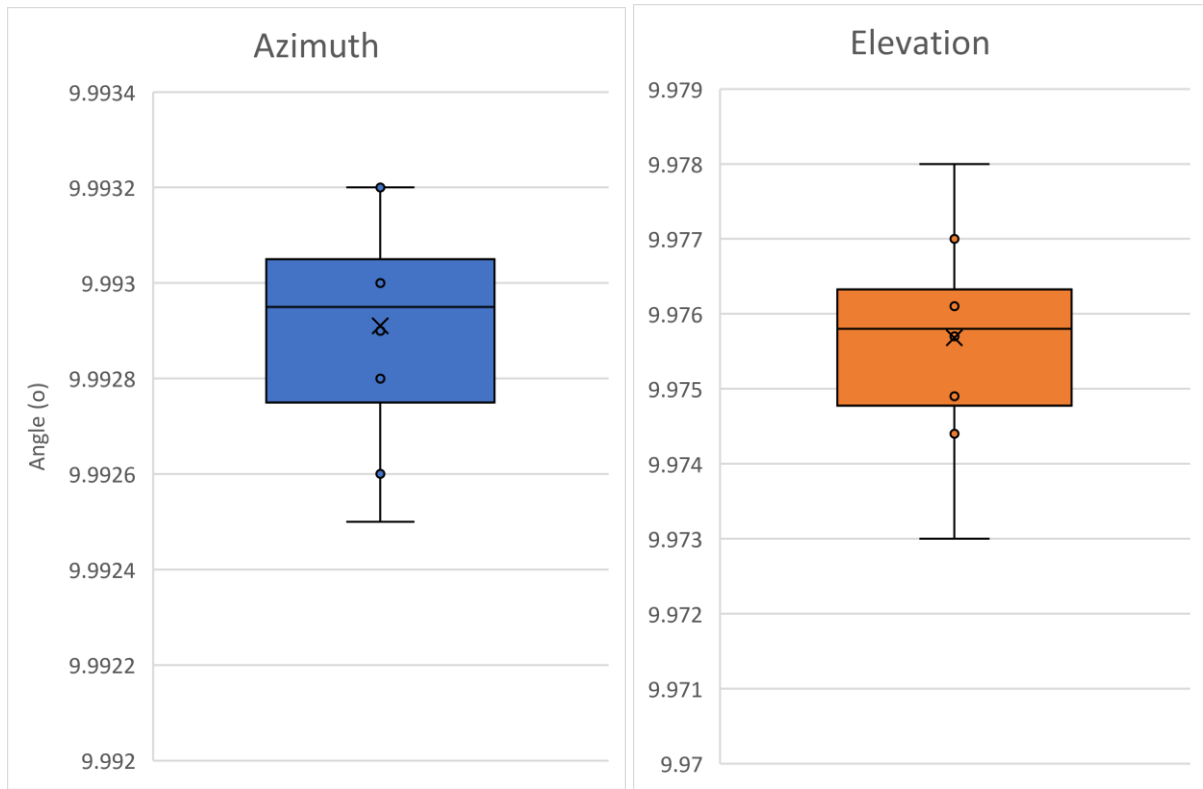


Figure 163: Box and whisker plots of CNC repeated measurements from phase 2 testing.

When we compare this test with the phase 1 testing we can see that for the azimuth rotary stage the standard deviation of the measurements is in the same magnitude as the phase 1 testing results (0.000242° for phase 1, 0.000217° for phase 2). However, the standard deviation of the elevation measurements has increased during phase 2 compared to phase 1 (0.000374° for phase 1, 0.001301° for phase 2). The author contends that as the elevation angle is at 10° compared to 0° , the fixture is less stable at this position compared to at 0° and very small movements have occurred during measurement, this adds further evidence that the reason for the elevation rotary stage to undershoot is because of the load created on the elevation rotary stage. For the combined angular measurement repeatability, 2 standard deviations are used for both of the rotary stages, and this is calculated as 0.00264° , approximately 33x lower than the fixtures target positional uncertainty.

CMM Angular Measurement Repeatability: 0.00264°

5.4.3 Angular Measurement Error Caused by Inconsistent Probing

For this test 5 sets of measurements are taken at each of the origin positions (10 Az, 0 El and 0 Az, 10 El). Each of these measurements uses new probing points to define the measurement plane and therefore slightly different scanning points. For each measurement, three measurements are taken in CNC mode and the median value is recorded.

The spread of the median values is analysed to estimate the measurement error caused by inconsistent probing. Through the use of a scanning strategy, it is expected that the measurement error caused by inconsistent probing will be significantly reduced compared to phase 1 testing.

Table 16: 5 separate measurements at the azimuth origin position (10 Az, 0 El).

No.	Az. Value (°)
1_1	9.9924
1_2	9.9926
1_3	9.9924
1_Median	9.9924
2_1	9.9927
2_2	9.9928
2_3	9.993
2_Median	9.9928
3_1	9.9936
3_2	9.9932
3_3	9.9929
3_Median	9.9932
4_1	9.9934
4_2	9.9931
4_3	9.994
4_Median	9.9934
5_1	9.9919
5_2	9.992
5_3	9.9921
5_Median	9.992
Standard Deviation	0.000512
2SD	0.001024
Range	0.0014

Table 17: 5 separate measurements at the elevation origin position (0 Az, 10 El).

No.	El. Value (°)
1_1	9.9770
1_2	9.9763
1_3	9.9769

1_Median	9.9769
2_1	9.9778
2_2	9.9772
2_3	9.9782
2_Median	9.9778
3_1	9.9761
3_2	9.9753
3_3	9.9774
3_Median	9.9761
4_1	9.9722
4_2	9.9697
4_3	9.9711
4_Median	9.9711
5_1	9.9695
5_2	9.9717
5_3	9.9729
5_Median	9.9717
Standard Deviation	0.00277
2SD	0.00554
Range	0.0067

When comparing the measurement data, we can see that the elevation measurements have a larger spread compared to the azimuth measurements. The standard deviation value of the five measurements is 0.000512 and 0.00277 for the azimuth and elevation measurements respectively, the total range from the datasets are 0.0014 and 0.0067.

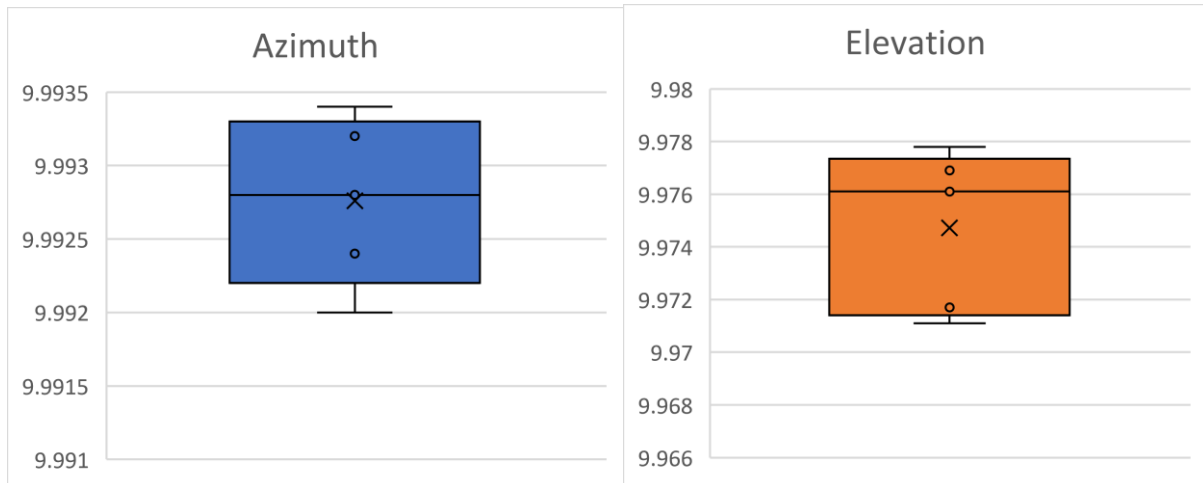


Figure 164: Box and whisker plots of the median values from the inconsistent probing testing.

When comparing the measurement data from phase 1 testing to phase 2 we can see that for both the azimuth and elevation measurements the spread has significantly reduced, this is clearly demonstrated in figure 165. For phase 1 testing only two separate measurements were made with new probing positions, compared to five measurements with new probing measurements in phase 2. The total range has reduced from 0.0038° in phase 1 to 0.0014° in phase 2 for the azimuth measurements. The total range has reduced from 0.01985° in phase 1 to 0.0067° in phase 2 for the elevation measurements. The spread of the elevation data has been reduced more significantly compared to the azimuth measurements.

This confirms that using the scanning measurement strategy compared to just five probing points reduces the issue of inconsistent probing significantly and will allow for much more accurate calculation of the positional error of the fixture in the upcoming tests.

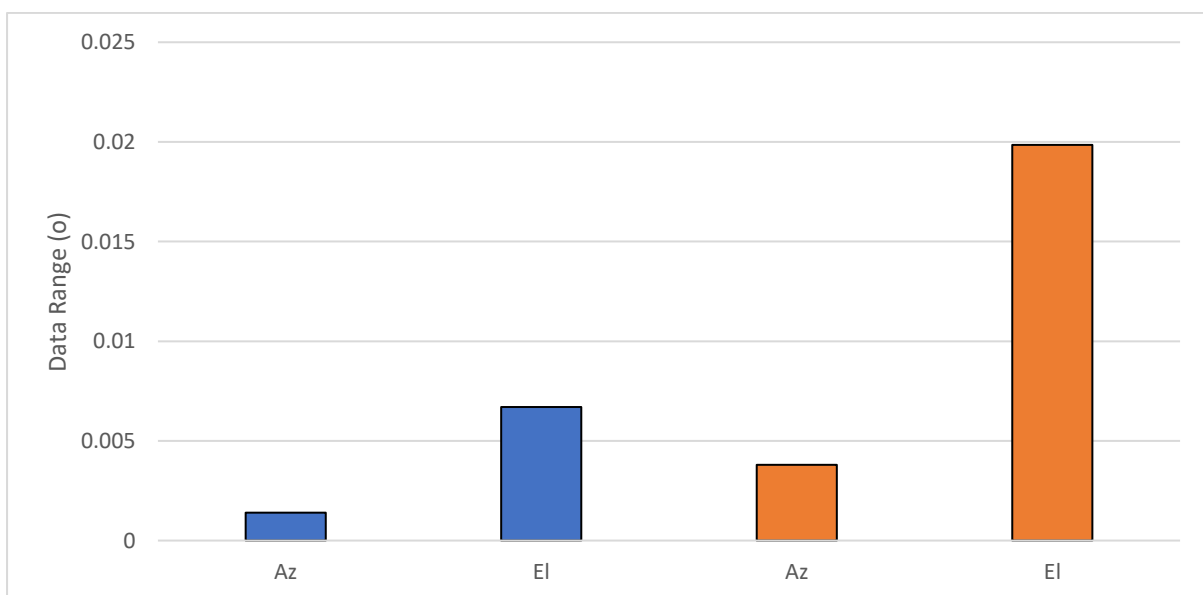


Figure 165: Comparing the measurement error created by inconsistent probing from phase 1 and phase 2 testing. Range of the datasets is plotted and compared from phase 1 testing (orange) to phase 2 testing (blue).

The total angular measurement error was calculated as 0.00563° for the phase 2 measurement method, this gives a good estimation of the total measurement error and covers approximately 95% of measurements. This is much improved from the phase 1 testing, 0.0202° . With the new measurement error, this value is approximately 16x lower than the fixture target positional uncertainty, and therefore should provide a much more accurate measurement of the fixture's positional movements.

Angular Measurement Error Caused by Inconsistent Probing: 0.00563°

5.4.4 Positional Repeatability of the Fixture

To test the positional repeatability of the fixture a measurement set (consisting of 5 CNC measurements) is made at the azimuth and elevation positions (10 Az, 0 El, and 0 Az, 10 El). After these measurement sets, the fixture is driven to 30 different random positions over two days, and then driven back to the original positions. The measurement set is then repeated to see how much deviation has occurred.

Azimuth (10 Az, 0 El)

Table 18: Phase 2 repeatability measurements for the azimuth rotary stage.

No.	Value
1_1	9.9913
1_2	9.9917
1_3	9.9919
1_4	9.9918
1_5	9.9913
1_Median	9.9917
2_1	9.9742
2_2	9.9749
2_3	9.9743
2_4	9.9731
2_5	9.9748
2_Median	9.9743
Difference	-0.0174

Elevation (0 Az, 10 El)

Table 19: Phase 2 repeatability measurements at the elevation position.

No.	Value
1_1	9.9856
1_2	9.9851
1_3	9.9849
1_4	9.9852
1_5	9.9859
1_Median	9.9852
2_1	9.9714
2_2	9.9732
2_3	9.9762
2_4	9.9768
2_5	9.9778
2_Median	9.9762
Difference	-0.009

For the azimuth rotary stage, the difference between the median values of the datasets is -0.0174° . For the elevation rotary stage, the difference is -0.009° , this is much better than the repeatability shown by the azimuth rotary stage. Although both rotary stages show good repeatability compared to the target positional uncertainty of the fixture (0.0877°). We can calculate the combined positional repeatability of the fixture as 0.0196° .

Combined Positional Repeatability: 0.0196°

5.4.5 Positional Error of the Fixture

To calculate the positional error of the fixture the fixture is driven to 15 different positions in azimuth and 15 different positions in elevation. A set of three measurements are taken at each position and the median value is recorded.

Azimuth Measurements

Table 20: Phase 2 azimuth positional error measurements.

No.	Target	Value	Error
1_1	68	67.9645	-0.0355
1_2	68	67.9633	-0.0367
1_3	68	67.961	-0.039
1_median	68	67.9633	-0.0367
2_1	51	50.9605	-0.0395
2_2	51	50.9572	-0.0428
2_3	51	50.9547	-0.0453
2_median	51	50.9572	-0.0428
3_1	344	344.0081	0.0081
3_2	344	344.0096	0.0096
3_3	344	344.0099	0.0099
3_median	344	344.0096	0.0096
4_1	83	82.9607	-0.0393
4_2	83	82.9661	-0.0339
4_3	83	82.9656	-0.0344
4_median	83	82.9656	-0.0344
5_1	240	239.9891	-0.0109
5_2	240	239.9898	-0.0102
5_3	240	239.9895	-0.0105
5_median	240	239.9895	-0.0105
6_1	227	227.0126	0.0126
6_2	227	227.0134	0.0134
6_3	227	227.013	0.013
6_median	227	227.013	0.013
7_1	107	106.9626	-0.0374
7_2	107	106.9664	-0.0336
7_3	107	106.9621	-0.0379
7_median	107	106.9626	-0.0374
8_1	6	5.9741	-0.0259
8_2	6	5.9733	-0.0267

8_3	6	5.9751	-0.0249
8_median	6	5.9741	-0.0259
9_1	302	301.9877	-0.0123
9_2	302	301.9882	-0.0118
9_3	302	301.9885	-0.0115
9_median	302	301.9882	-0.0118
10_1	192	191.976	-0.024
10_2	192	191.9815	-0.0185
10_3	192	191.9792	-0.0208
10_median	192	191.9792	-0.0208
11_1	333	332.9801	-0.0199
11_2	333	332.9825	-0.0175
11_3	333	332.9834	-0.0166
11_median	333	332.9825	-0.0175
12_1	264	263.9822	-0.0178
12_2	264	263.9818	-0.0182
12_3	264	263.9826	-0.0174
12_median	264	263.9822	-0.0178
13_1	10	9.9873	-0.0127
13_2	10	9.9874	-0.0126
13_3	10	9.9879	-0.0121
13_median	10	9.9874	-0.0126
14_1	140	139.9722	-0.0278
14_2	140	139.9759	-0.0241
14_3	140	139.9673	-0.0327
14_median	140	139.9722	-0.0278
15_1	279	278.9835	-0.0165
15_2	279	278.9843	-0.0157
15_3	279	278.9844	-0.0156
15_median	279	278.9843	-0.0157
Maximum			-0.0428
Median			-0.0178
Standard Deviation			0.015501
2SD			0.031002

When considering the azimuth results, figure 166, we can see that the maximum error value is -0.0428 and the median error value is -0.0178. The majority of error values undershoot the target value (13/15 measurements). The standard deviation value of the data is 0.015501, we can use the 3-sigma rule and the median value to calculate the positional error of the azimuth rotary stage as 0.048802° . This calculation of the uncertainty uses 2SD which covers approximately 95% of all error values.

$$\text{Median} + 2\text{SD} = 0.0178 + 0.031002 = 0.048802^\circ$$

The positional error of the azimuth rotary stage lies within the boundaries of the target positional uncertainty, however improvements to reduce the amount of error will be attempted through error compensation.

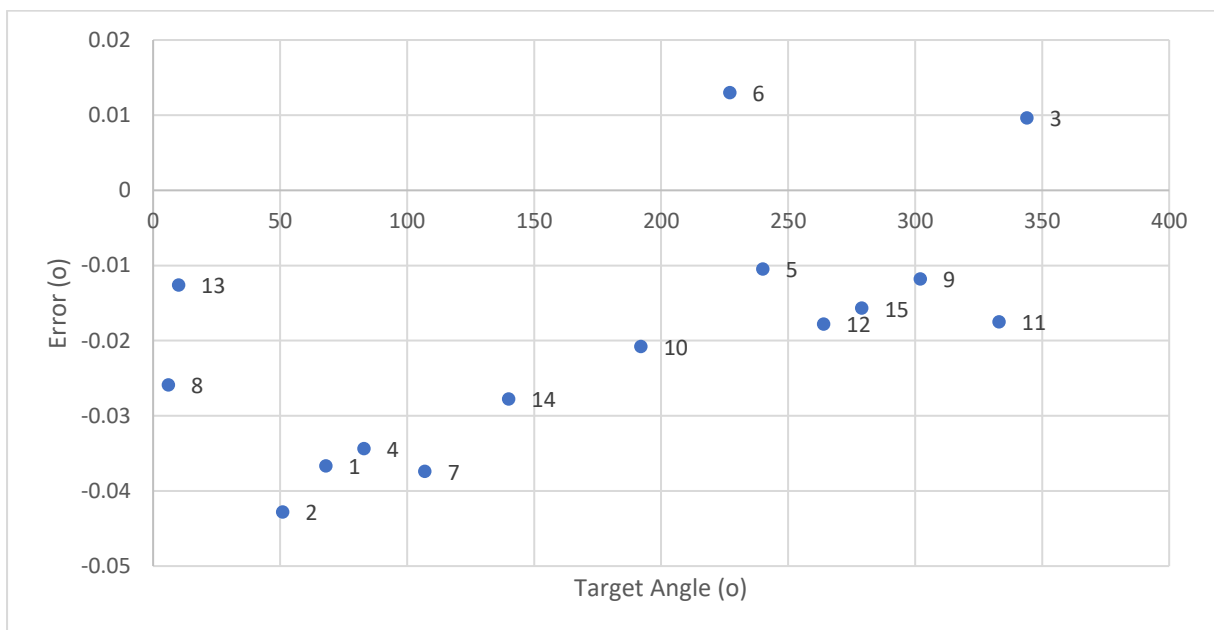


Figure 166: Scatter plot of azimuth measurements during phase 2 positional error testing. Each point on the scatter plot is labelled with a number to show the chronological order in which the measurements were taken.

Elevation Measurements

Table 21: Phase 2 elevation positional error testing.

No.	Target	Value	Error
1_1	67	66.9226	-0.0774
1_2	67	66.9233	-0.0767
1_3	67	66.9227	-0.0773
1_median	67	66.9227	-0.0773
2_1	18	17.9959	-0.0041
2_2	18	17.9966	-0.0034
2_3	18	17.9959	-0.0041
2_median	18	17.9959	-0.0041
3_1	72	71.9481	-0.0519
3_2	72	71.947	-0.053
3_3	72	71.9491	-0.0509
3_median	72	71.9481	-0.0519
4_1	8	7.9818	-0.0182
4_2	8	7.9796	-0.0204
4_3	8	7.982	-0.018
4_median	8	7.9818	-0.0182
5_1	77	76.9418	-0.0582
5_2	77	76.9389	-0.0611
5_3	77	76.9378	-0.0622
5_median	77	76.9389	-0.0611
6_1	40	39.9382	-0.0618
6_2	40	39.9364	-0.0636
6_3	40	39.9359	-0.0641
6_median	40	39.9364	-0.0636
7_1	25	24.9553	-0.0447
7_2	25	24.9582	-0.0418
7_3	25	24.9573	-0.0427
7_median	25	24.9573	-0.0427
8_1	36	35.9697	-0.0303
8_2	36	35.9677	-0.0323
8_3	36	35.9664	-0.0336
8_median	36	35.9677	-0.0323
9_1	89	88.9317	-0.0683
9_2	89	88.9319	-0.0681

9_3	89	88.9318	-0.0682
9_median	89	88.9318	-0.0682
10_1	33	32.9767	-0.0233
10_2	33	32.978	-0.022
10_3	33	32.9783	-0.0217
10_median	33	32.978	-0.0220
11_1	53	52.9298	-0.0702
11_2	53	52.9308	-0.0692
11_3	53	52.9294	-0.0706
11_median	53	52.9298	-0.0702
12_1	49	48.9325	-0.0675
12_2	49	48.9304	-0.0696
12_3	49	48.9308	-0.0692
12_median	49	48.9308	-0.0692
13_1	82	81.9335	-0.0665
13_2	82	81.9369	-0.0631
13_3	82	81.9346	-0.0654
13_median	82	81.9346	-0.0654
14_1	59	58.9275	-0.0725
14_2	59	58.9314	-0.0686
14_3	59	58.9325	-0.0675
14_median	59	58.9314	-0.0686
15_1	65	64.9326	-0.0674
15_2	65	64.9333	-0.0667
15_3	65	64.9376	-0.0624
15_median	65	64.9333	-0.0667
Maximum			-0.0773
Median			-0.0645
Standard Deviation			0.0220
2SD			0.0439

When considering the elevation results, figure 167, we can see that the maximum error value is -0.0773 and the median error is -0.0645. When comparing to the azimuth results both the maximum and median values are greater for the elevation rotary stage, most significantly the median error is

much greater at -0.0645 compared to -0.0178 . The positional error of the elevation rotary axis is calculated as 0.1084° using the same method as before.

Crucially all values are undershooting the target angle and the values appear to show a good correlation shown by the dotted line of best fit, this undershooting also occurred during phase 1 testing. Due to this clear correlation error compensation will be applied to this rotary stage. The standard deviation of the values is 0.0220 , which is similar to the standard deviation of the azimuth rotary stage, therefore we can assume that the rotary stages are performing to similar levels of positional uncertainty if the undershooting of the target can be corrected.

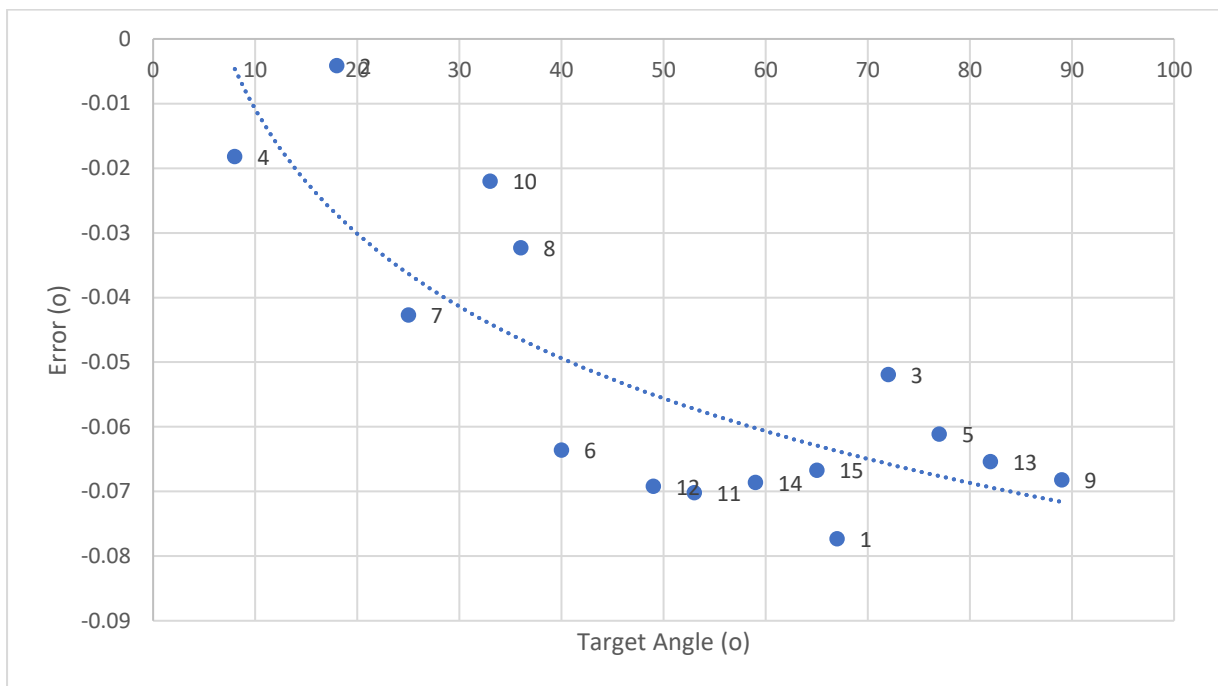


Figure 167: Scatter plot of elevation measurements during phase 2 positional error testing. Each point on the scatter plot is labelled with a number to show the chronological order in which the measurements were taken.

The combined positional error is calculated as 0.119° , this is a combination of the positional error from the azimuth and elevation rotary stages. This is outside the target positional uncertainty value for the fixture system; therefore, error compensation is crucial to improve the accuracy of the fixture system.

Combined Positional Error: $\pm 0.119^\circ$ (Currently over the target)

5.5 Phase 3 – Error Compensation

Error compensation will be utilised to increase the accuracy of the rotary stages. To do this the positional error results from phase 2 testing will be analysed, and any patterns of error can be used to complete the error compensation.

5.5.1 Error Compensation Adjustment

5.5.1.1 Elevation Rotary Stage

A consistent error from both phase 1 and phase 2 testing was the undershooting of the elevation rotary stage. The most likely reason for this undershooting that as a torque moment is applied through the rotary stage as it attempts to rotate upwards the load is causing the rotary stage to undershoot, particularly at higher angles as this has a greater moment due to it swinging outward away from the centre of rotation. The other reason could be due to a slight slackness in the fastening of one of the components.

To counteract this an error compensation was made to the MATLAB code when the elevation rotary stage is used. When we consider the results from phase 2 testing we can see a clear correlation that as the elevation angle increases the amount of undershoot also increases, figure 168. However, the correlation is not perfectly positive, it appears to occur in three main stages. Rotation close to the origin location between 0-20 degrees has the smallest amount of undershoot. Then between 20 to 40 degrees the undershoot averages approximately -0.03 degrees, the amount of undershoot is largest between 40-90 degrees where it averages -0.065 with good consistency.

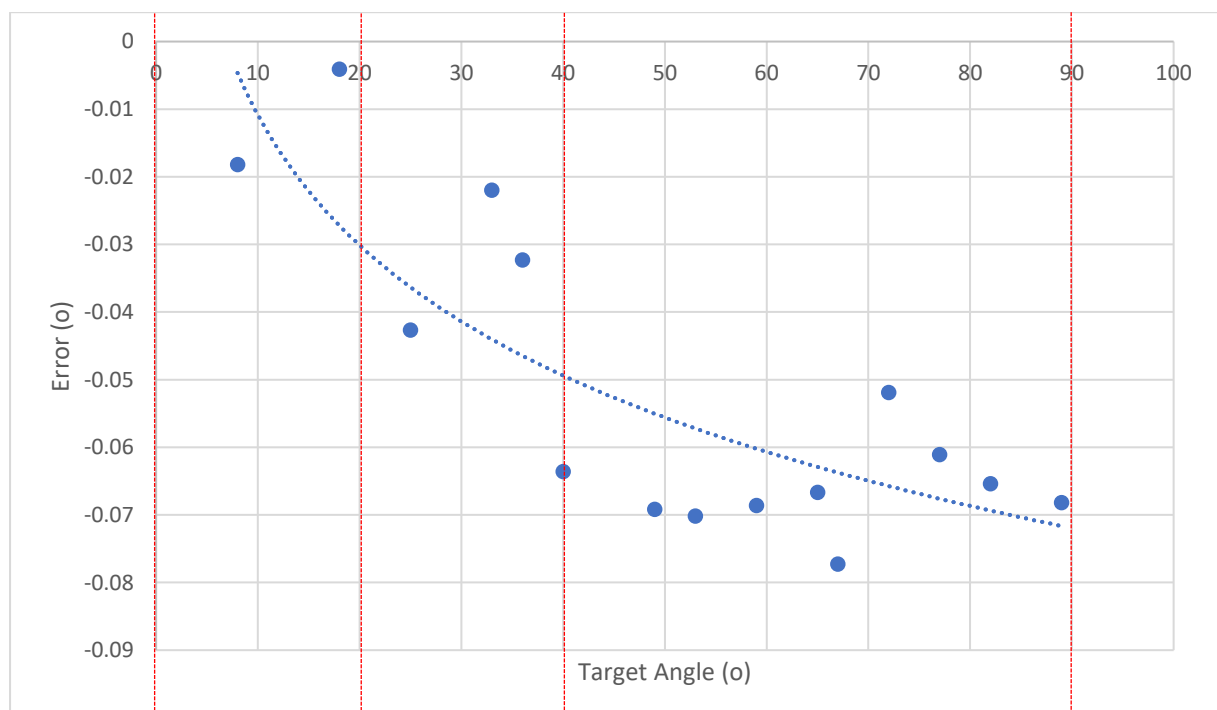


Figure 168: Phase 2 testing results for the elevation rotary stage.

We can use the findings from this testing to improve the accuracy of the elevation rotary stage. As the spread of the error is very small but is consistently undershooting, we can resolve this by telling the rotary stage to purposefully overshoot its target. This should result in it manoeuvring closer to the target value.

By looking at the results we can separate the error adjustment into two sections. Firstly between 20 and 40 degrees the elevation angle is commanded to overshoot by +0.03 and between 40 degrees and 90 degrees the elevation angle is commanded to overshoot by +0.065 degrees. To tell the fixture to overshoot a change is made to the MATLAB coding of the fixture. We use IF commands to check the input elevation angle and adjust accordingly, figure 169. By applying these adjustments to the phase 2 testing results we can estimate what the results would have looked like if we had applied the error compensation beforehand, figure 170.

```
elev_orig = 14

if (20 < elev_orig) && (elev_orig < 40)
    elev_new = elev_orig + 0.03
elseif elev_orig >= 40
    elev_new = elev_orig + 0.065
else
    elev_new = elev_orig
end
```

Figure 169: Error compensation code for elevation rotary stage.

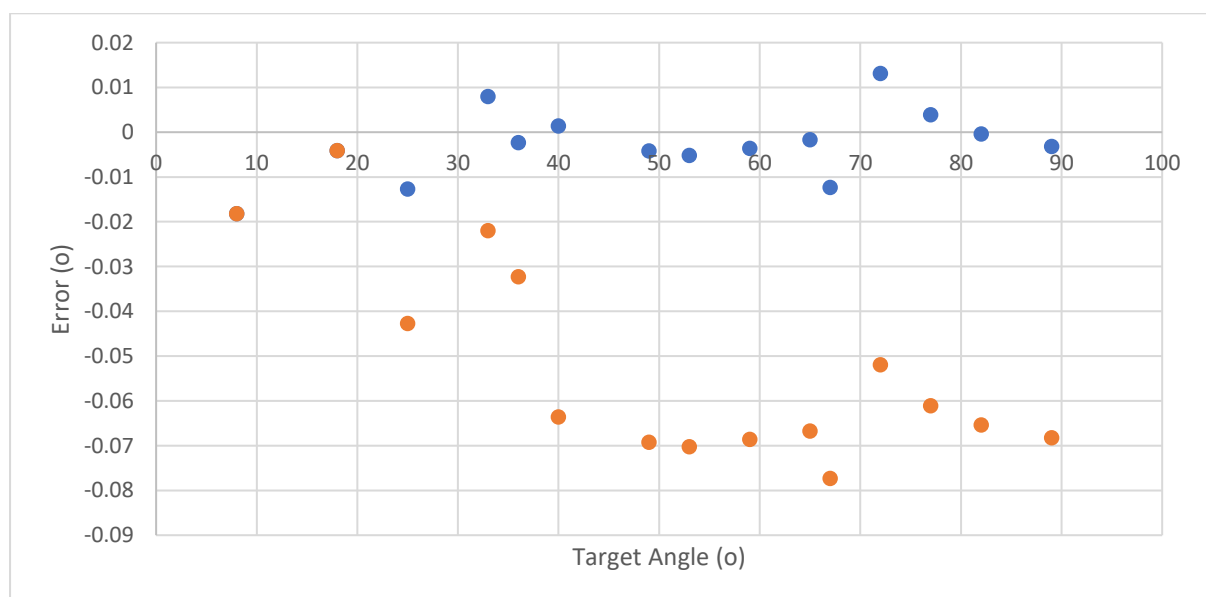


Figure 170: The predicted elevation positional error results post error compensation. Orange: Original values, Blue: Predicted values post error compensation.

5.5.1.2 Azimuth Rotary Stage

The error values are evenly split both positive and negative during phase 1 testing of the azimuth rotary stage, however during phase 2 testing most of the error values are slightly negative (undershooting). To compensate for this the azimuth rotary stage was targeted to overshoot by $+0.01^\circ$ by altering the MATLAB code.

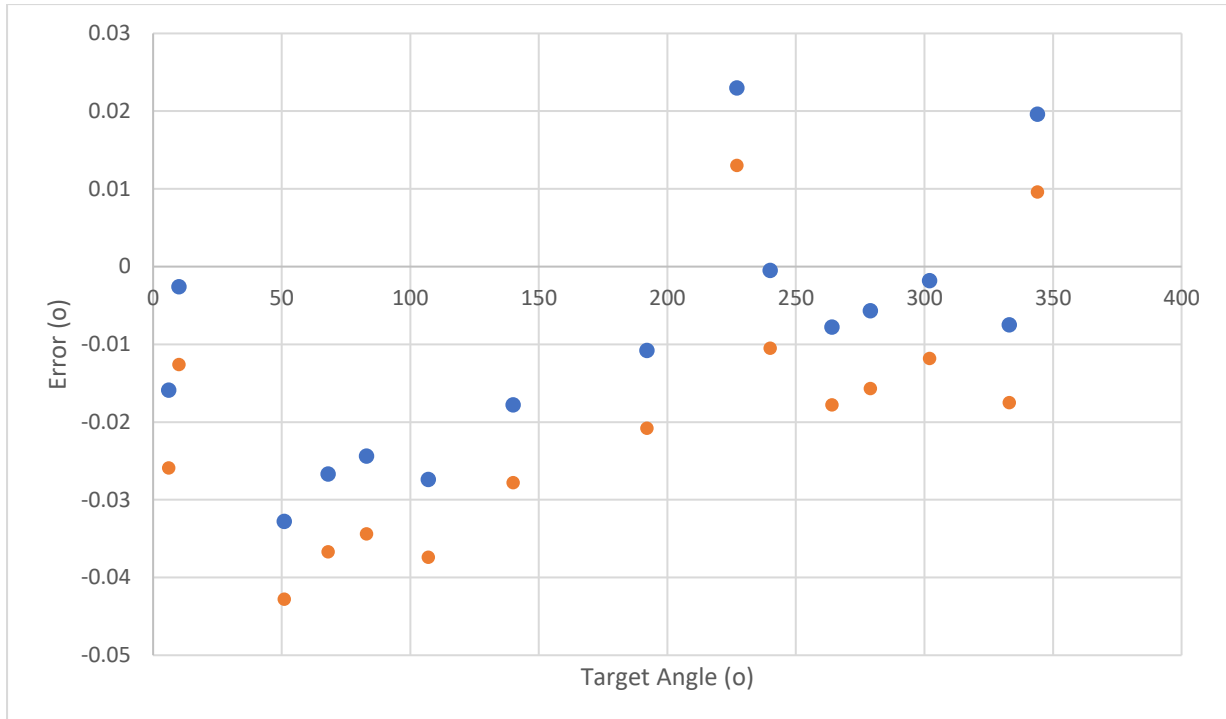


Figure 171: The predicted azimuth positional error results post error compensation. Orange: original values, Blue: Predicted values post error compensation.

5.5.2 Post Error Compensation Testing

Now that the error compensation code has been applied, the positional error testing is completed again. A series of measurements are taken at varying azimuth and elevation coordinates, identical to the phase 1 and 2 positional error testing previously completed. This test consists of 10 measurement sets at varying azimuth or elevation coordinates, with 3 measurements at each position and the median values recorded.

Azimuth Measurements

Table 22: Phase 3 azimuth positional error testing.

No.	Target	Value	Error
1_1	55	55.0229	0.0229
1_2	55	55.0242	0.0242
1_3	55	55.0238	0.0238
1_median	55	55.0238	0.0238
2_1	341	341.0035	0.0035
2_2	341	341.0037	0.0037
2_3	341	341.0025	0.0025
2_median	341	341.0035	0.0035
3_1	129	129.0041	0.0041
3_2	129	129.0033	0.0033
3_3	129	129.0031	0.0031
3_median	129	129.0033	0.0033
4_1	345	345.0289	0.0289
4_2	345	345.0299	0.0299
4_3	345	345.0301	0.0301
4_median	345	345.0299	0.0299
5_1	183	182.9926	-0.0074
5_2	183	182.9987	-0.0013
5_3	183	182.9927	-0.0073
5_median	183	182.9927	-0.0073
6_1	200	200.0138	0.0138
6_2	200	200.0141	0.0141
6_3	200	200.0151	0.0151
6_median	200	200.0141	0.0141
7_1	71	71.0034	0.0034

7_2	71	71.0023	0.0023
7_3	71	71.0031	0.0031
7_median	71	71.0031	0.0031
8_1	293	293.0171	0.0171
8_2	293	293.0178	0.0178
8_3	293	293.0187	0.0187
8_median	293	293.0178	0.0178
9_1	2	2.012	0.012
9_2	2	2.0123	0.0123
9_3	2	2.0128	0.0128
9_median	2	2.0123	0.0123
10_1	103	103.013	0.013
10_2	103	103.0137	0.0137
10_3	103	103.0132	0.0132
10_median	103	103.0132	0.0132
Maximum			0.0299
Median			0.01275
Standard Deviation			0.010464
2SD			0.020928

When considering the post error compensation azimuth results, figure 172, we can now see that the majority of values now slightly overshoot the target. When we compare the median error value from phase 2 testing, -0.0178, and now post error compensation, 0.01275, we can see that the median error is slightly lower but very similar in magnitude. The maximum error is also slightly lower in magnitude from -0.0428 in phase 2, to 0.0299° post error compensation. There has only been a slight increase in performance for the azimuth rotary stage post error compensation. As the majority of the values are now overshooting (9/10) compared to undershooting during phase 2, the amount of error compensation will be very slightly reduced from +0.01 to +0.005. No more testing will be completed on the azimuth rotary stage after this alteration as it is a very minor adjustment. The positional error of the azimuth rotary stage can be calculated using the median error value + 2SD, this should cover approximately 95% of movements, this value is calculated as 0.03368°.

Azimuth Positional Error: ±0.03368°

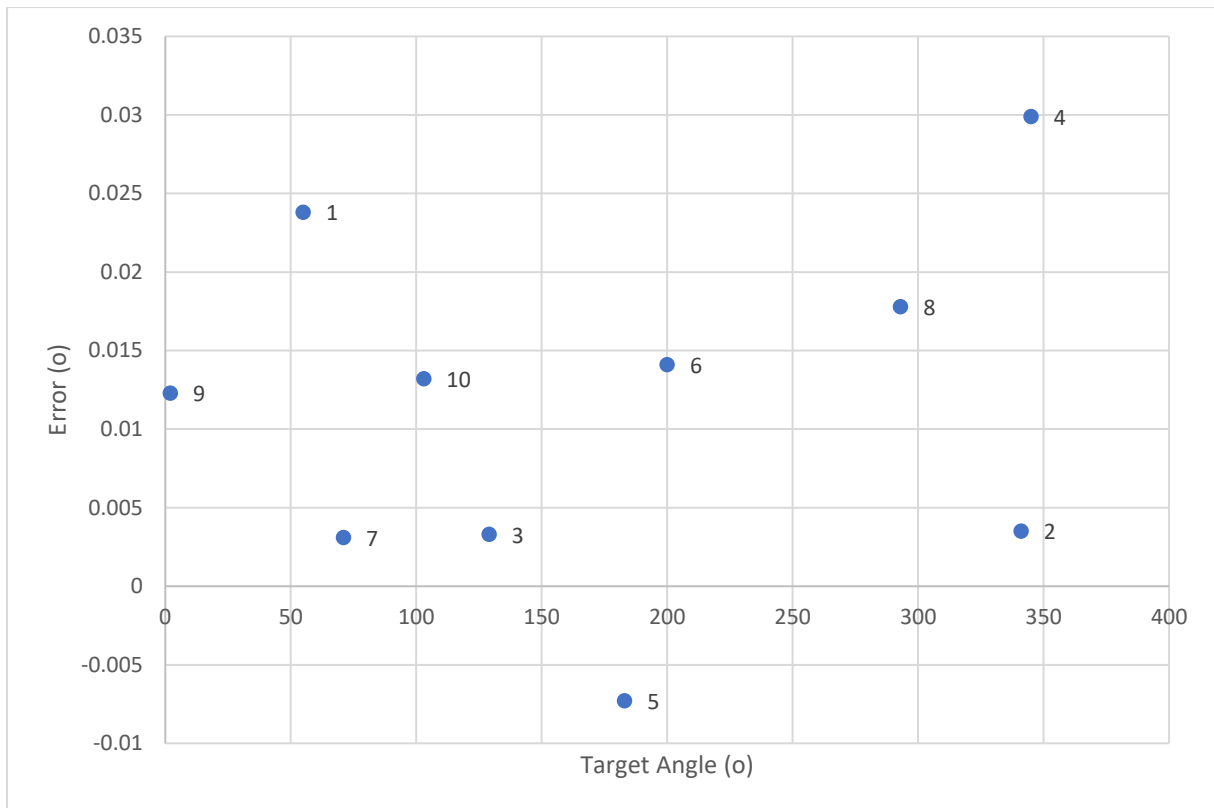


Figure 172: Azimuth positional error testing post error compensation adjustment.

Elevation Measurements

Table 23: Phase 3 elevation positional error testing.

No.	Target	Value	Error
1_1	60	60.0088	0.0088
1_2	60	60.009	0.009
1_3	60	60.009	0.009
1_median	60	60.009	0.009
2_1	24	24.0072	0.0072
2_2	24	24.0087	0.0087
2_3	24	24.0098	0.0098
2_median	24	24.0087	0.0087
3_1	5	4.9866	-0.0134
3_2	5	4.9846	-0.0154
3_3	5	4.9858	-0.0142
3_median	5	4.9858	-0.0142
4_1	30	29.9998	-0.0002
4_2	30	30.0002	0.0002

4_3	30	29.9992	-0.0008
4_median	30	29.9998	-0.0002
5_1	86	86.0132	0.0132
5_2	86	86.0127	0.0127
5_3	86	86.0132	0.0132
5_median	86	86.0132	0.0132
6_1	75	75.0254	0.0254
6_2	75	75.0254	0.0254
6_3	75	75.0254	0.0254
6_median	75	75.0254	0.0254
7_1	18	18.0042	0.0042
7_2	18	18.0028	0.0028
7_3	18	18.0024	0.0024
7_median	18	18.0028	0.0028
8_1	40	39.9946	-0.0054
8_2	40	39.9949	-0.0051
8_3	40	39.9958	-0.0042
8_median	40	39.9949	-0.0051
9_1	67	66.9838	-0.0162
9_2	67	66.9844	-0.0156
9_3	67	66.9859	-0.0141
9_median	67	66.9844	-0.0156
10_1	43	42.9971	-0.0029
10_2	43	42.9964	-0.0036
10_3	43	42.9971	-0.0029
10_median	43	42.9971	-0.0029
Maximum			0.0254
Median			0.0013
Standard Deviation			0.01318395
2SD			0.026367899

When considering the results for post error compensation elevation measurements we can see that the undershooting error has been removed from the elevation rotary stage. During phase 2 testing all 15 values undershot the target angle, now the error is evenly split above and below the target line (5

undershoot, 5 overshoot). This error compensation has greatly increased the accuracy of the rotary stage, with the median error value going from -0.0645 during phase 2, to 0.0013 post error compensation. The maximum error has also greatly decreased from -0.0773 to 0.0254. The positional error of the azimuth rotary stage can be calculated using the median error value + 2SD, this should cover approximately 95% of movements, this value is calculated as 0.0277°.

Elevation Positional Error: $\pm 0.02767^\circ$

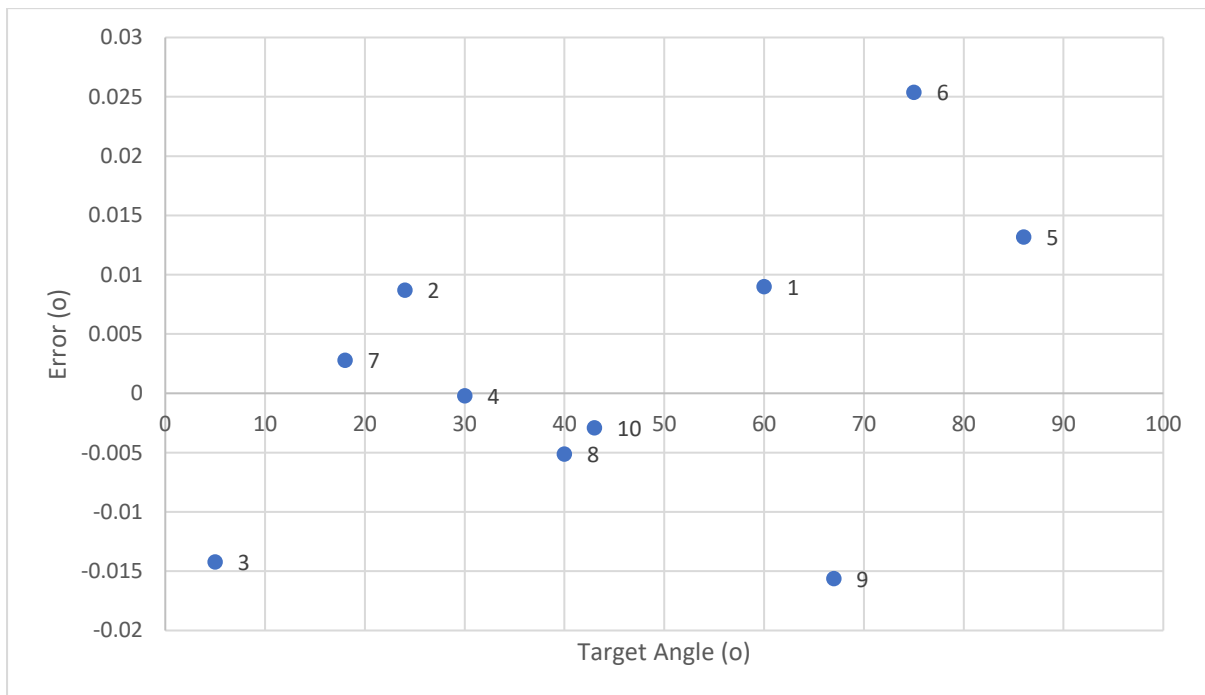


Figure 173: Elevation positional error testing post error compensation adjustment.

5.6 Calculating the Combined Positional Error of the Fixture System

Now that error compensation has been completed on the rotary stages, using the positional error testing results the combined positional error of the fixture system can be re-calculated. The combined positional error will be estimated using the 3-sigma rule, with 2 standard deviations. If 2 standard deviations are used around the median value this will give a good estimate of 95% of values to fall within this level of positional error. As the median value will not be exactly 0, the upper and lower limits will be different, to simplify the calculation of the positional error and to add a further factor of safety, the highest magnitude limit will be used for both the +/- values of the positional error.

5.6.1 Azimuth Rotation Error

Median Error Value: 0.01275°

Standard Deviation: 0.01046°

Example Calc. of 95% Positional Error:

$$\text{Upper Limit} = \text{Median} + 2\text{SD} = 0.01275 + 0.020928 = \mathbf{0.033678^\circ} \text{ (larger magnitude)}$$

$$\text{Lower Limit} = \text{Median} - 2\text{SD} = 0.01275 - 0.020928 = -0.008178^\circ$$

Azimuth Positional Error = $\pm 0.03368^\circ$ (95% movements within this limit)

5.6.2 Elevation Rotation Error

Median Error Value = 0.0013°

Standard Deviation = 0.013184°

Example Calc. of 95% Positional Error:

$$\text{Upper Limit} = \text{Median} + 2\text{SD} = 0.0013 + 0.02637 = \mathbf{0.02767^\circ} \text{ (larger magnitude)}$$

$$\text{Lower Limit} = \text{Median} - 2\text{SD} = 0.0013 - 0.02637 = -0.02507^\circ$$

Elevation Positional Error = $\pm 0.02767^\circ$ (95% movements within this limit)

5.6.3 Combining Azimuth and Elevation Positional Error

5.6.3.1 Pythagoras Method

To combine these azimuth and elevation error values, the simplest way is to use Pythagoras, this assumes a flat surface, figure 174.

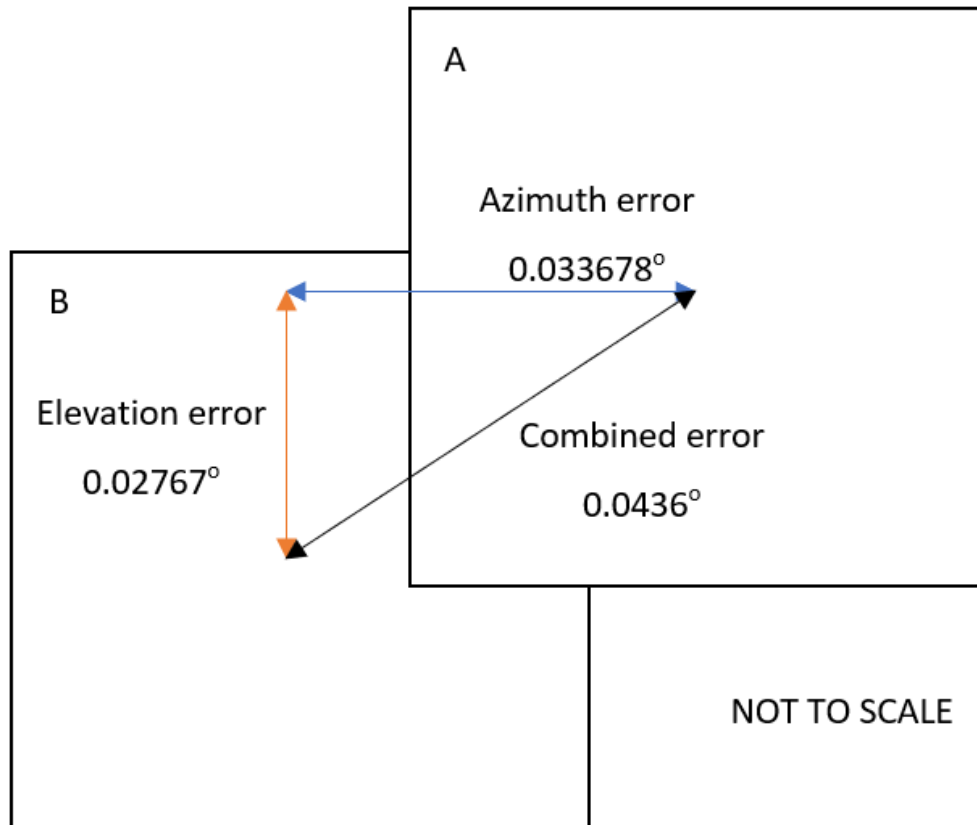


Figure 174: Calculation of the combined positional error. A: Target surface measurement location. B: Actual surface measurement location assuming highest positional error.

Target Positional Uncertainty: 0.0877°

Combined Positional Error: $\sqrt{az. error^2 + el. error^2} = \sqrt{0.033678^2 + 0.02767^2}$

Combined Positional Error: 0.0436°

5.6.3.2 Haversine Method

As the femoral head surface is spherical and not flat, the values from the Pythagoras method are not exact. Instead, the haversine formula, figure 175, can be used to calculate the combined positional error, whilst considering the curvature of the bearing surface. The haversine formula is used to calculate the great circle distance between two points on a sphere using their longitude and latitude coordinates. This formula is commonly used to calculate the distance between two locations on Earth, however by adjusting the radius value to the size of the component, this equation can be used to calculate the distance between two surface measurements on the bearing surface. The error values in degrees need to be converted into longitude and latitude values in radians before calculation.

$$= 2r \arcsin \left(\sqrt{\sin^2 \left(\frac{\varphi_2 - \varphi_1}{2} \right) + \cos(\varphi_1) \cos(\varphi_2) \sin^2 \left(\frac{\lambda_2 - \lambda_1}{2} \right)} \right)$$

Figure 175: Haversine formula.

Using this formula, the distance of the error is calculated as 0.01895 mm, this can then be converted into an angular distance of 0.04021°, using the arc length formula. This value is slightly smaller than the Pythagoras method, as when considering the curvature of the bearing the error distance will be slightly reduced.

Combined Positional Error: ±0.04021°

When we compare the combined positional error of the fixture system (±0.04021°) to the target positional uncertainty (0.0877°) we can see that the combined positional error value is well below the target. This gives us good confidence that the vast majority of positional movements from the fixture system will meet the target positional uncertainty required.

5.6.4 Positional Error from Azimuth Alignment Error

The positional error from the azimuth alignment error is expected to be much larger than the positional error produced from the movement of the rotary stages (the use of the fixture itself). This is because the azimuth alignment error relies on human judgement to align the fixture correctly with the help of the coregistration slide. To calculate the positional error produced from the azimuth alignment error a method was developed using a surface metrology instrument.

A roughness guide, figure 176, is measured repeatedly using the Taylor Hobson Talysurf CCI. The roughness guide is usually used to compare the surface finishes produced by different manufacturing techniques. For this test, the smoothest section of the roughness guide is measured, the surface finish has linear ridges aligned parallel with each other produced from its manufacturing operation, figure 177.

The roughness guide is attached so the smoothest section of the roughness guide is positioned directly under the crosshair of the coregistration slide. This allows the coregistration slide to be used for alignment and then the sensor is lowered to the measurement surface without having to complete any XY repositioning.

To replicate the azimuth alignment error produced from moving the fixture between the CMM and the surface metrology instrument a series of measurements are made on the roughness guide. In between each measurement the fixture is removed from the CCI and is then placed back on the CCI with the coregistration slide used to align the fixture square with the CCI sensor. This replicates the movement from the CMM to the CCI and the use of the coregistration slide to reduce the azimuth alignment error as much as possible. Once the coregistration slide is deemed to be as square as possible with the CCI sensor, it is then removed, the sensor is then lowered over the surface of the roughness guide. The angle the of the surface ridges can then be calculated by analysing the surface measurement taken of the surface. Any rotation of the fixture will in turn rotate the angle of the surface ridges. All surface analysis is completed on the software Mountains.

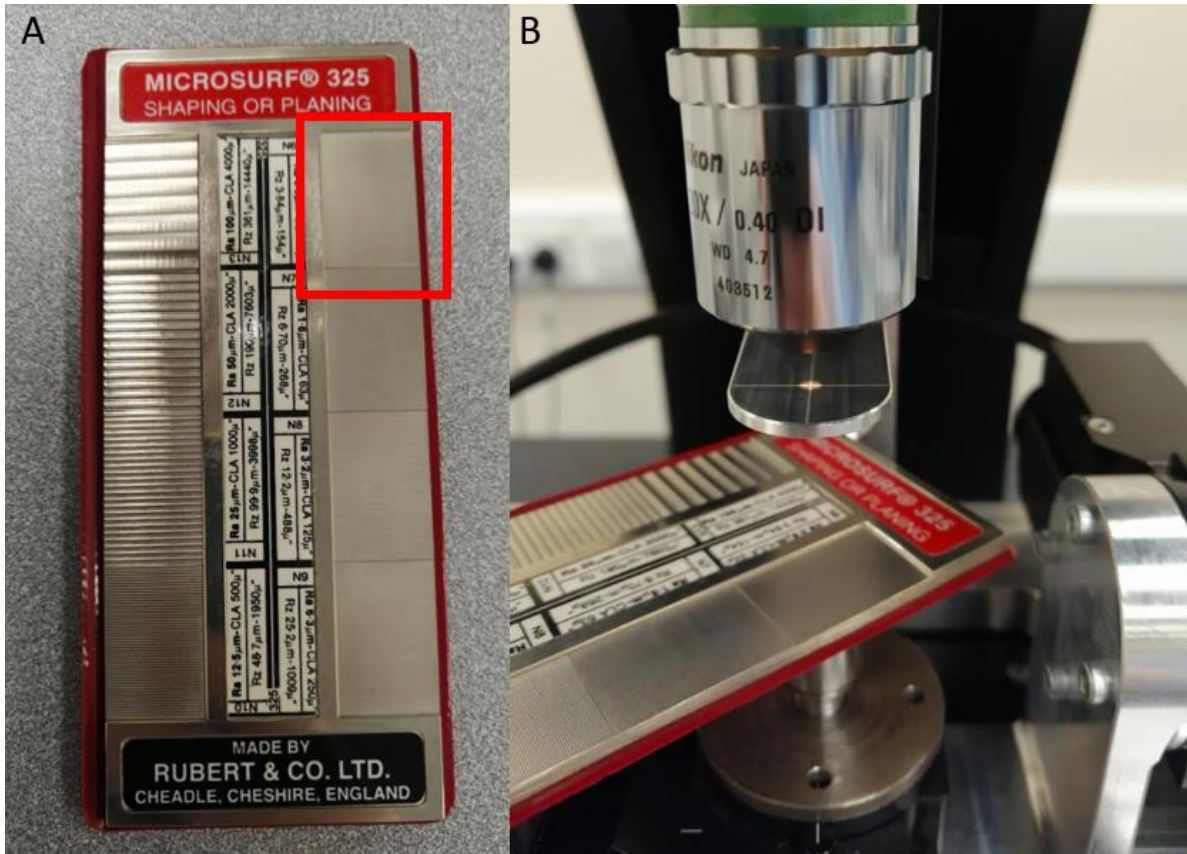


Figure 176: Roughness guide. A: The section for measurement is highlighted by a red square. B: The roughness guide is attached to the fixture using plasticine, the measurement section is located directly below the coregistration slide crosshair.

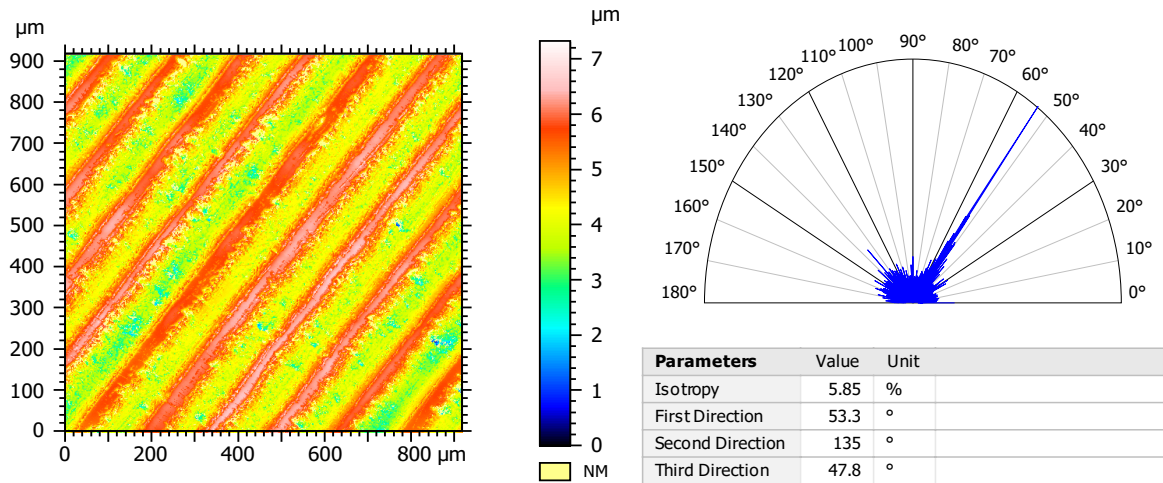


Figure 177: CCI measurement of the roughness guide. Origin measurement, texture direction value is calculated as 53.3°.

A total of 21 surface measurements are taken, with the first surface measurement used as the origin value, and the following 20 measurements used to test the amount of azimuth alignment error, table 24. The change in angle from the origin measurement is the estimated azimuth alignment error produced by removing the fixture and then aligning it back on the CCI. Once all measurements are complete the median and the maximum azimuth alignment error values can be calculated.

Table 24: Resulting angles from the azimuth alignment error testing.

Measurement No.	Calculated angle (o)	Error (o)
0	53.3	-
1	54.0	+0.7
2	53.5	+0.2
3	53.7	+0.4
4	53.5	+0.2
5	53.7	+0.4
6	54.0	+0.7
7	53.8	+0.5
8	53.7	+0.4
9	54.0	+0.7
10	53.8	+0.5
11	53.8	+0.5
12	53.7	+0.4
13	54.5	+1.1
14	54.0	+0.7
15	53.7	+0.4
16	53.8	+0.5
17	53.5	+0.2
18	53.8	+0.5
19	53.3	0
20	53.7	+0.4
Maximum	-	1.1
Median	-	0.45
Standard Deviation	-	0.232594
2SD	-	0.465188

The maximum deviation from the origin measurement was 1.1° occurring on the 13th measurement, the median deviation for the entire set was 0.45° . Importantly the amount of error did not increase as the number of movements took place, the level of error was similar throughout and in fact the lowest error occurred on the 19/20th measurement. This shows that the use of the coregistration slide can allow for a good amount of consistency when repositioning.

The 3-sigma rule can be used to estimate the amount of positional error introduced by the azimuth alignment error. For this scenario, the upper limit will be applied to both the positive and negative limits as human error could allow this error to be applied either clockwise or anticlockwise, two standard deviations will be used to cover approximately 95% of movements.

$$\text{Limit} = \text{Median} + 2\text{SD} = 0.45^\circ + 0.465188^\circ = 0.915188^\circ$$

Azimuth Positional Error = $\pm 0.915188^\circ$ (95% of movements)

When the positional error from the azimuth alignment error ($\pm 0.915188^\circ$) is compared to the combined positional error of the fixture ($\pm 0.04021^\circ$), we can see that the azimuth alignment error is much larger, approximately 23x greater. It is important to understand that this azimuth alignment error is applied equally to all surface measurements of the same component, therefore not affecting stitching capabilities.

5.7 Testing with the Surface Metrology Instrument

Now that the positional error of the fixture system has been calculated, a number of tests are completed using the surface metrology instrument, to check the initial effectiveness of the fixture.

5.7.1 Re-locating Features Test

The first test uses an explant femoral head component and tests the ability of the fixture system to move to the same location twice, similar to the repeatability test completed on the CMM. Once the femoral head component is secured to the fixture, the component is manoeuvred through azimuth and elevation until a small surface feature is located on the measurement sensor. The surface feature located is a sharp pit highlighted by a red circle on figure 178, the spherical coordinates of this location are recorded. Now the component is manoeuvred to five random spherical coordinate locations, after this the component is manoeuvred back to the original spherical coordinates where the surface feature was located. This results in the same surface feature being found on both measurements; however, the exact position of the surface feature within the surface measurement area is not identical for both measurements. The surface feature has moved slightly higher on the output surface measurement; however, this distance is minimal. This experiment confirms that the fixturing system can accurately relocate surface features with good accuracy.

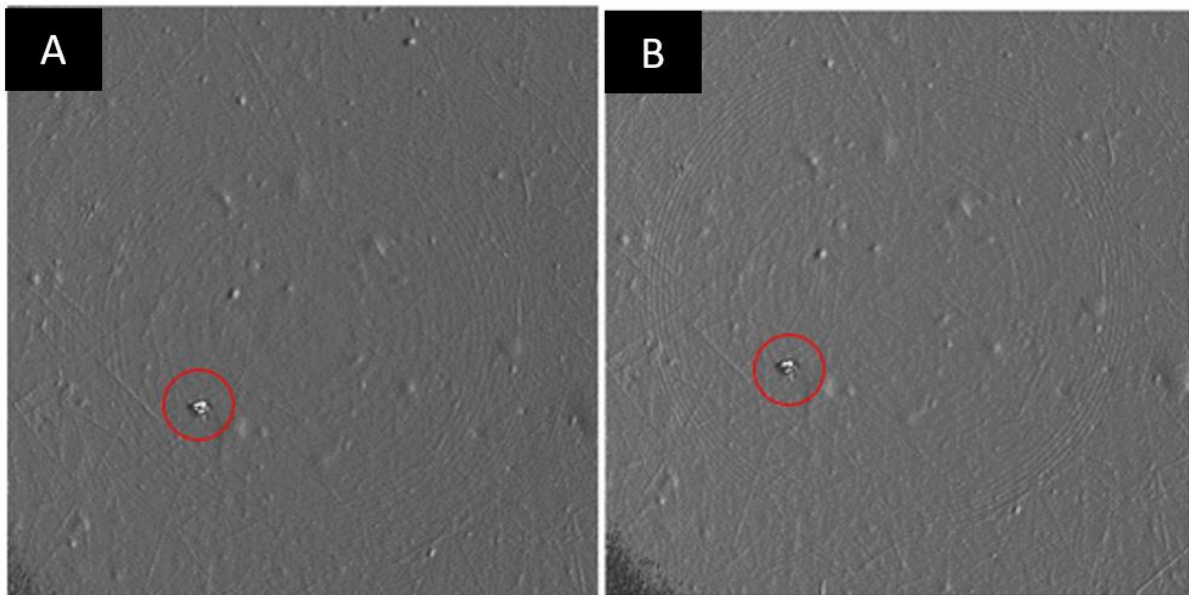


Figure 178: Relocating the same feature using the CCI sensor and fixturing system. A: Original measurement of the surface feature. B: Second measurement of the surface feature, component was manoeuvred to five random positions in between measurements with the same exact input coordinates used for the second measurement.

5.7.2 Stitching Test

The second test is to check the stitching capabilities of the fixture system, to do this a stitch is created along the surface of an explant femoral head. The stitch in this example was randomly selected along a length of a femoral head as no CMM scan had been completed beforehand, therefore no wear area was identified. To create the stitch coordinates the custom MATLAB app was used, and the desired overlap region was set to 20%.

Once all measurements were completed analysis was completed on MATLAB, on initial viewing of the data, surface measurements appeared to be taken with overlapping regions close to the target of 20%. The overlap region was then removed through manual stitching, figure 179. The scratch begins on the top surface measurement and travels all the way down to the third surface measurement. This confirms that the positional accuracy of the fixture was suitable to perform surface stitching. At this stage the stitching analysis was completed manually using MATLAB, in the future Mountains software was used for the analysis of worn MoM femoral heads.

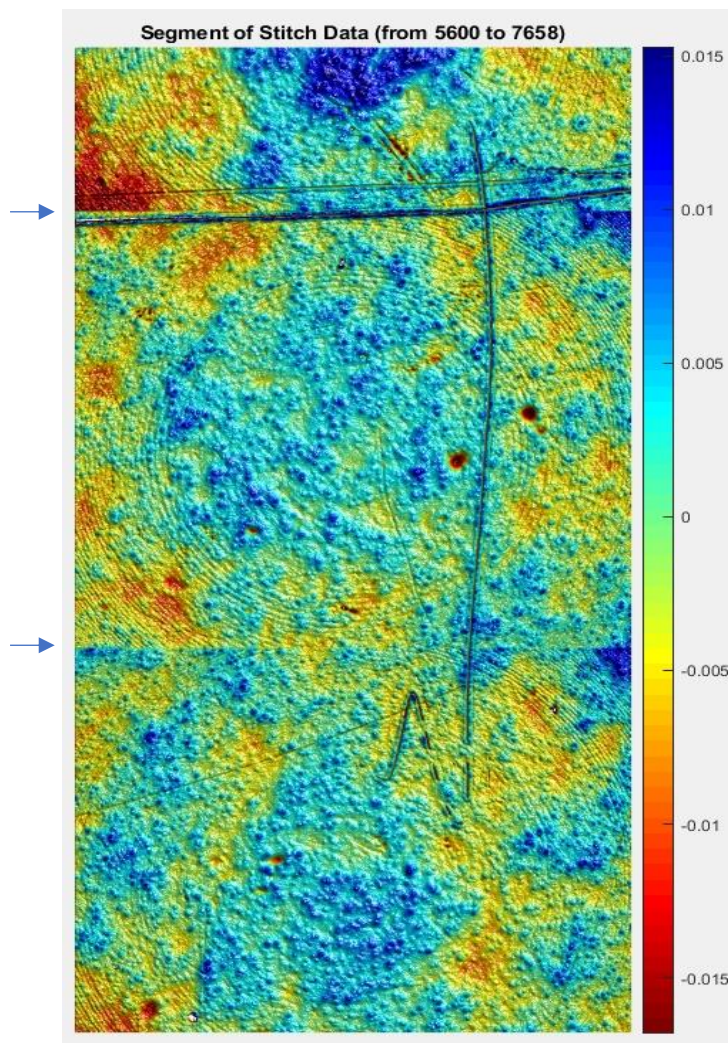


Figure 179: Stitch of three surface measurements, meeting points of surface images marked by blue arrows.

5.8 Chapter Summary

The testing of the fixture system was completed using a CMM to measure the movements of the two rotary stages. The first phase of testing utilised only five probing points and a custom square artefact was measured. After the first phase of testing, the initial measurement method was improved upon to increase the measurement accuracy. Using a scanning strategy and a gauge block to measure, replacing the five-point probing and custom square artefact.

From the second phase of testing the positional error of the fixture system was calculated as $\pm 0.119^\circ$, this is outside the target positional uncertainty. Therefore, error compensation of the rotary stages was applied by altering the MATLAB control code. This significantly improved the positional error of the fixture system, resulting in a final positional error value of $\pm 0.04021^\circ$, well within the target positional uncertainty, $\pm 0.0877^\circ$.

The positional error caused by the azimuth alignment error was also calculated, this was done by measuring the fixtures position in relation to the surface metrology instrument sensor. This replicated the movement of the fixture from the CMM to the surface metrology instrument, introducing azimuth alignment error. The amount of positional error caused by the azimuth alignment error was calculated as $\pm 0.915188^\circ$, much greater than the positional error of the fixture itself ($\pm 0.04021^\circ$). It is important to understand that this azimuth alignment error is applied equally to all surface measurements of the same component, therefore not affecting stitching capabilities.

Once the positional error values were calculated, initial testing with the surface metrology instrument was completed. This consisted of a repeatability test, to see if the fixture could relocate the same surface feature accurately. Also, a stitching test, to see if the fixture could stitch together continuous surface measurements. Both tests were completed successfully, indicating the fixture was working as intended.

Chapter 6: Analysis of Retrieved Metal-on-Metal Bearings

In this section the effectiveness of the fixture system will be tested by measuring a cohort of retrieved hip implant MoM bearings. Using the fixture system, the positional accuracy of wear map targeted surface measurements are demonstrated to be vastly superior compared to any manual fixture options.

This study will act as both a test of the fixture system and as a detailed surface analysis of the cohort of retrieved MoM hip bearings. Using the fixture system stitches of surface measurements will be taken through the wear scar, this will allow for a novel insight into the tribological mechanisms of MoM hip implant bearings.

6.1 Cohort

10 large MoM hip implant bearings were donated by patients to the London Implant Retrieval Centre, with permission to be measured at the University of Huddersfield, no patient specific information is available at this time. The bearing size of the components vary from 42 to 54 mm, these sizes are much larger than the most popular bearing size in use today, 28 – 32 mm [4].

Upon visual inspection no obvious wear areas are visible on the femoral heads, small scratches are visible on the surface, the location and direction of scratches appears multi-directional. Component 082 has a large volume of material missing from the femoral head, it is unknown whether this damage occurred during usage, or during retrieval.

6.2 Methodology for Wear Assessment

6.2.1 Summary

The method can be summarised into three main stages:

Stage 1 - Initial CMM Measurement

Firstly, all femoral heads are measured using the Zeiss Prismo coordinate measuring machine (CMM), without the use of the custom fixture, this allows a wear map to be created for each femoral head and the volumetric parameters to be calculated.

Stage 2 - Unworn Surface Analysis

A surface analysis is made on the unworn areas of all femoral heads, 25 surface measurements are taken equally spaced over the bearing surface, with 5 surface measurements at the rim. If a wear area is present on the femoral head, the wear area is avoided.

Stage 3 - Wear Map Targeted Surface Analysis

For the femoral heads that exhibited a clear measurable wear area delineated by the wear map from stage 1 CMM measurement, a more detailed surface analysis is now completed using the custom fixture system. The worn femoral heads are re-measured on the CMM whilst attached to the custom fixture system, once the measurement is complete and the wear map is generated, the fixture is moved to the surface metrology instrument (Taylor Hobson CCI) for wear map targeted surface measurements. Two sets of surface measurements are then taken, grouped measurements and stitch measurements, providing a detailed analysis of the surface, in particular the wear area.

6.2.2 CMM

6.2.2.1 Zeiss Prismo Access CMM

The CMM used for this testing is the Zeiss Prismo Access with a VAST XT 2 mm analogue probing system, figure 180. This instrument has a length measurement error of $0.9 + L/350$ μm [126]. With the cohorts largest bearing size of 54 mm, the maximum length measurement error should be 0.97714 μm .

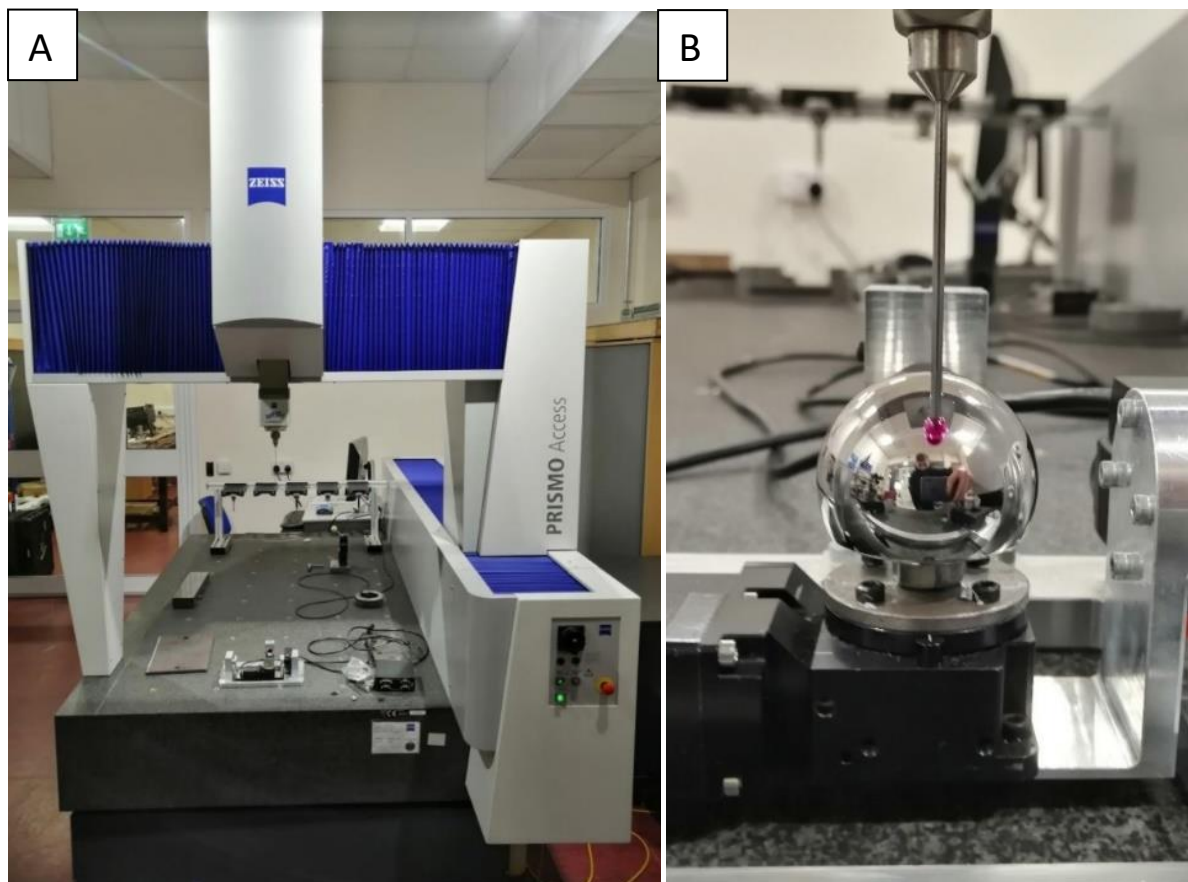


Figure 180: Zeiss Prismo Access CMM. A: CMM overview. B: Measurement of femoral head with probe tip.

6.2.2.2 CMM Method

The femoral heads are secured to the CMM base using either a taper connection within a three-jaw chuck (for the initial CMM measurement – stage 1) or by using the custom fixture system (wear map targeted surface analysis – stage 3). A polar measurement strategy is utilised, with scan lines from the rim to the pole of the femoral head, figure 181. A total of 400 equally spaced scan lines are used with 394 points per line, resulting in a total of 157,600 probing points, a scan speed of 10 mm/sec is applied. This strategy results in an estimated mesh spacing uncertainty of 1.462 mm^3 and a total measurement uncertainty of 2.607 mm^3 according to Bills measurement uncertainty study [13].

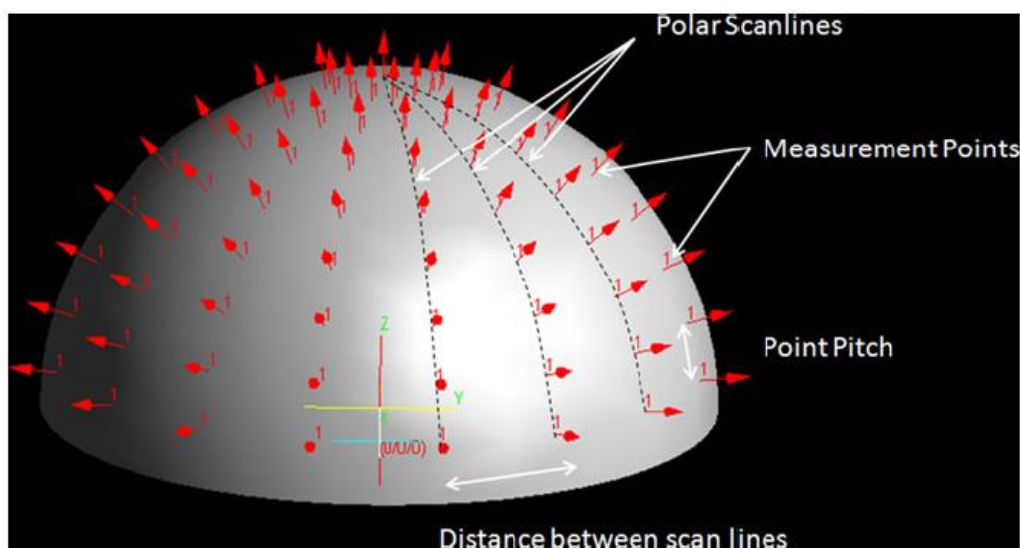


Figure 181: CMM Polar Measurement Strategy [13].

The analysis of CMM measurement data is completed using CATIA software [179], an overview of the analysis method is shown in figure 182. This analysis method was created by Bills et al [13].

Initially the CMM measurement data is imported as a point cloud (A). The point cloud is then converted into a surface representing the measured worn femoral head, this shall be called the 'worn surface' (B). A sphere is then fitted to the worn surface, this will be used to represent the original pre-wear surface, this shall be called the 'pre-wear surface' (C). An initial deviation analysis can be made between the worn surface and the pre-wear surface, this allows the wear area to be identified (D). At this stage, the amount of wear is being underestimated as the pre-wear surface should only be constructed using the unworn portion of the worn surface. Therefore, a new sphere is fitted to the worn surface, however the wear area portion is excluded from the fitting (D). This allows for a more accurate reconstruction of the pre-wear surface to be created. Now a new deviation analysis is completed to create the wear map (E) and calculate the relevant parameters: radius, wear depth, measurement volume, and wear volume. The process of constructing a new pre-wear surface by excluding the wear area portion can be repeated until the wear parameters do not change between

each iteration. When calculating enclosed volumes, both the reconstructed original surface and CMM measurement data are trimmed using the same plane to ensure they have the exact same rim edge starting point (F).

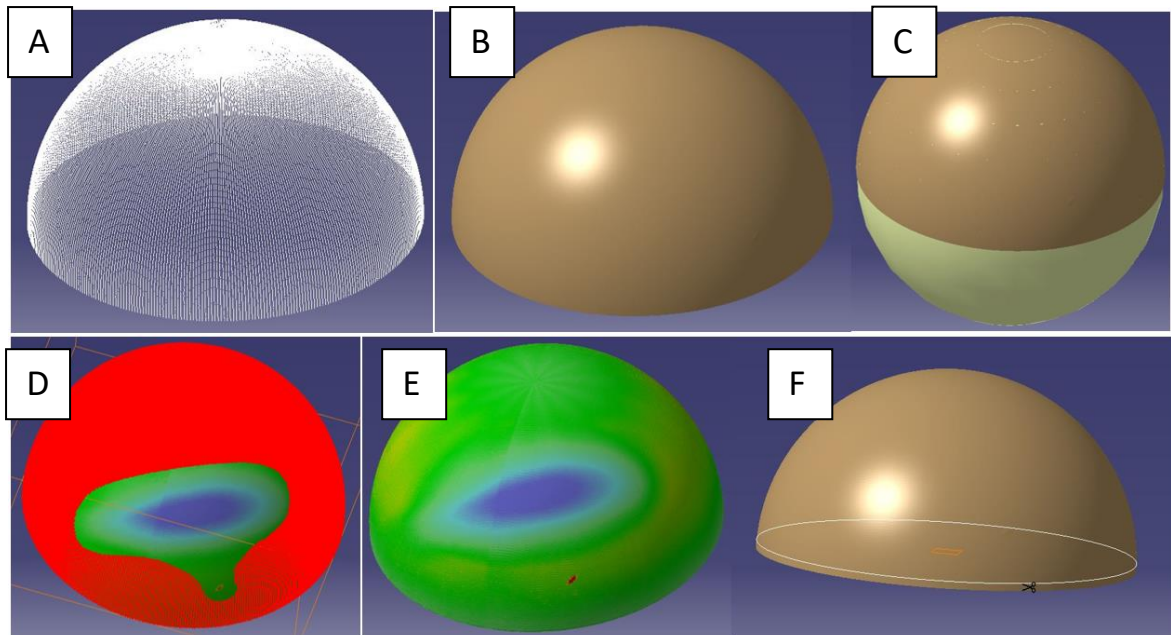


Figure 182: CMM analysis with CATIA, method steps. A: Import of CMM data. B: Fitting of worn surface to CMM data. C: Initial reconstruction of pre-wear surface. D: Exclusion or wear scar from pre-wear surface reconstruction. E: Resulting wear map. F: Trimming of both the worn surface and pre-wear surface by 1 mm to ensure same rim starting point.

6.2.3 Surface Measurement

6.2.3.1 Taylor Hobson Talysurf CCI MP

For surface measurements a Taylor Hobson Talysurf CCI MP is utilised [190], a white light interferometer instrument, equipped with a 20x lens, resulting in a sampling size of 918.57 x 918.57 μm . The base of the CCI can be adjusted in XY via digital control ensuring the alignment of the fixture is not adjusted if any Y movement is required.



Taylor Hobson Talysurf CCI MP Performance Specifications

Repeatability of surface RMS:	<0.02 nm
Number of measurement points:	1024
Step height repeatability:	<0.1%
Surface reflectivity:	<0.3% - 100%

Figure 183: Taylor Hobson Talysurf CCI MP measuring a femoral head with the custom fixture system.

6.2.3.2 Surface Measurement Method

The surface measurement lens is lowered until circular fringes appear on the camera output and the surface is in focus, the Z height boundaries for the measurement are then adjusted using the control software, the measurement is now run. Between each measurement the custom fixture system is used to manoeuvre the femoral head to its next measurement position. If the custom fixture is correctly aligned about the bearing centre of rotation, there should be no need to refocus the objective lens.

All surface measurements are analysed using the software SurfStand [191], form removal is applied to the measurement, and a cut-off Gaussian SF filter is applied, following ISO recommendations [119], for each surface measurement the Sa, Sdr and Ssk parameters are recorded. Surface images are stitched together using the software Mountains [192]. The Mountains software automatically detects overlapping regions of surface measurements and removes the overlap area from the resulting stitch.

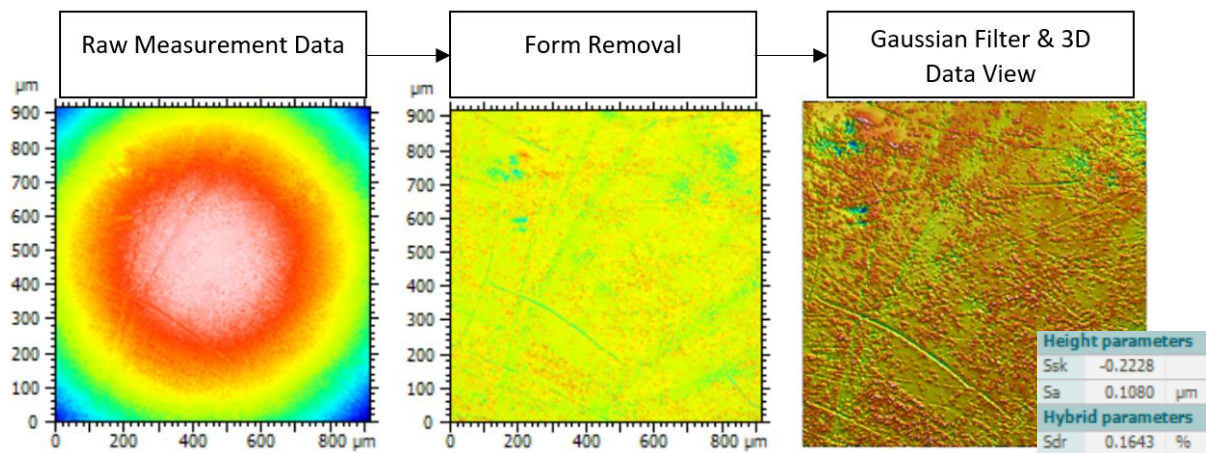


Figure 184: Surface measurement analysis stages.

6.2.4 Custom Fixture System

The fixture system is used to manoeuvre the femoral heads for surface measurement, allowing for accurate wear area targeted surface measurements, facilitated by data fusion of the CMM and surface measurement datasets. The positional error of the fixture system is $\pm 0.04021^\circ$, easily capable of stitching together surface measurements. Another positional error to consider is the coregistration error when moving from the CMM to the surface metrology instrument, this is called the azimuth alignment error. This error is $\pm 0.915188^\circ$ in the azimuth rotation, and this error value is applied equally to all surface measurements of the same component, therefore not affecting stitching capabilities.

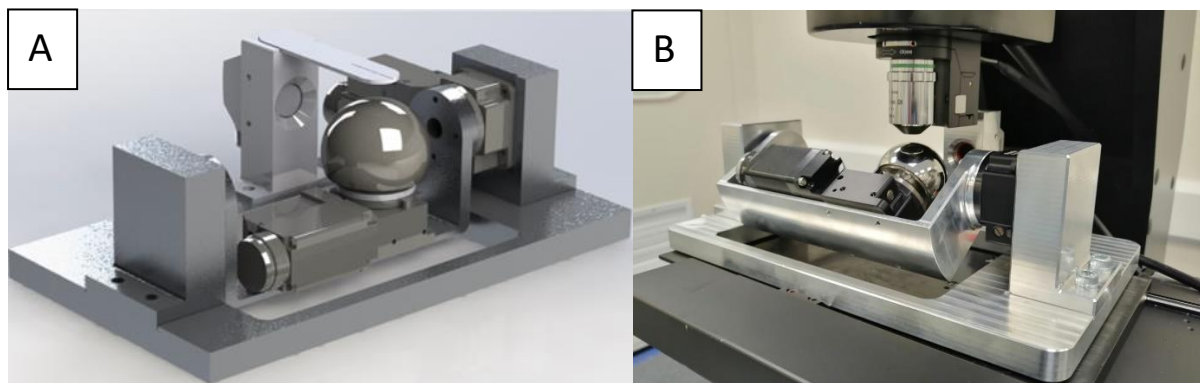


Figure 185: Custom fixture system. A: CAD image. B: Custom fixture system in use with Taylor Hobson CCI.

6.2.4.1 Custom Fixture System Method

Before using the custom fixture system, the femoral head is aligned as closely as possible with the elevation rotary axis by adjusting the taper up or down, the laser measurement sensor may be used to help during this alignment. This ensures minimal adjustment in the Y direction is needed during surface measurements (as the elevation stage and the bearing centre of rotation are aligned). When the fixture system is moved from the CMM to the surface measurement instrument the coregistration procedure is followed. The coregistration slide is placed on the top of the laser mount and the CCI lens is aligned centrally over the crosshair of the coregistration slide. The alignment of the fixture is adjusted until the crosshair is squarely aligned with the CCI sensor axes. This ensures the fixture is closely aligned with its previous position during CMM measurement.

The custom fixture system is used for both the unworn measurements taken on all femoral heads, and for the wear area targeted measurements taken on the worn femoral heads. The fixture is controlled using MATLAB software on a laptop, the laptop is connected to the rotary stages, via a USB connection and control box. Using the MATLAB software, the surface measurement locations are selected with reference to the CMM wear map. These locations can be selected using spherical coordinate input, or via cursor select on the wear map.

6.2.4.2 Surface Measurement Sets

Unworn Measurements

Each component has 25 surface measurements taken equally spaced over their surface, if the femoral head has a wear area then this is avoided. This is to create a baseline for the surface finish in unworn areas. The location of unworn surface measurements for both an unworn and worn femoral head is shown in figure 186.

For the unworn femoral head, the surface measurements are taken in steps of $10, 30, 50, 70, 95^\circ$ of elevation at five azimuth positions of $0, 72, 144, 216, 288^\circ$, resulting in 25 measurements equally spaced on the bearing surface, with five at the rim area.

If there is a wear area on the femoral head, the wear area is avoided during measurement. Instead, 20 surface measurement locations are selected manually via cursor select on the MATLAB software, spread evenly across the surface. The rim locations are taken at the same positions as the unworn components, 95° elevation, $0, 72, 144, 216, 288^\circ$ azimuth.

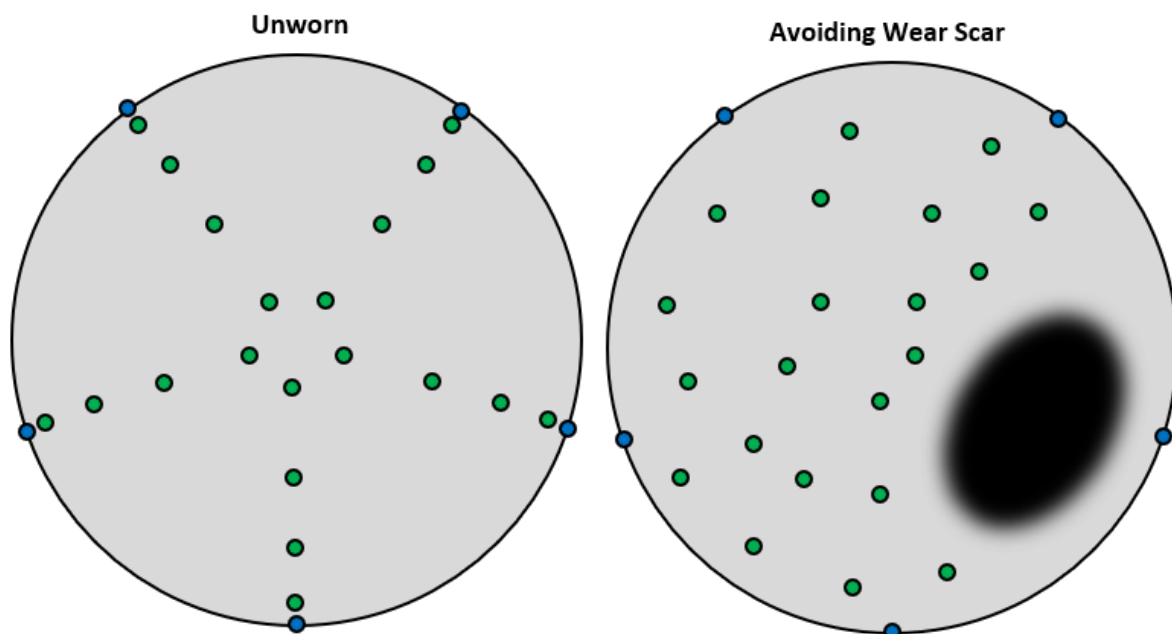


Figure 186: Unworn measurement locations, rim area measurements (blue), wear area (black).

Wear Area Measurements

Any femoral heads that exhibited a clear wear area on their CMM wear maps are firstly remeasured on the CMM whilst attached to the custom fixture. This allows the CMM generated wear map to be positionally linked to the fixture, ensuring good positional coregistration between CMM and surface datasets. Once the CMM measurement is complete the fixture is moved to the surface measurement instrument, without removing the femoral head. At this stage, wear map targeted surface

Grouped Measurements	Stitch Measurements
<ul style="list-style-type: none"> • 10 measurements are taken at the central wear area (red). • 10 at the outer wear area (orange). 	<p>20% overlap used between each surface measurement along the stitch line.</p> <ul style="list-style-type: none"> • Four stitches through the wear area, including

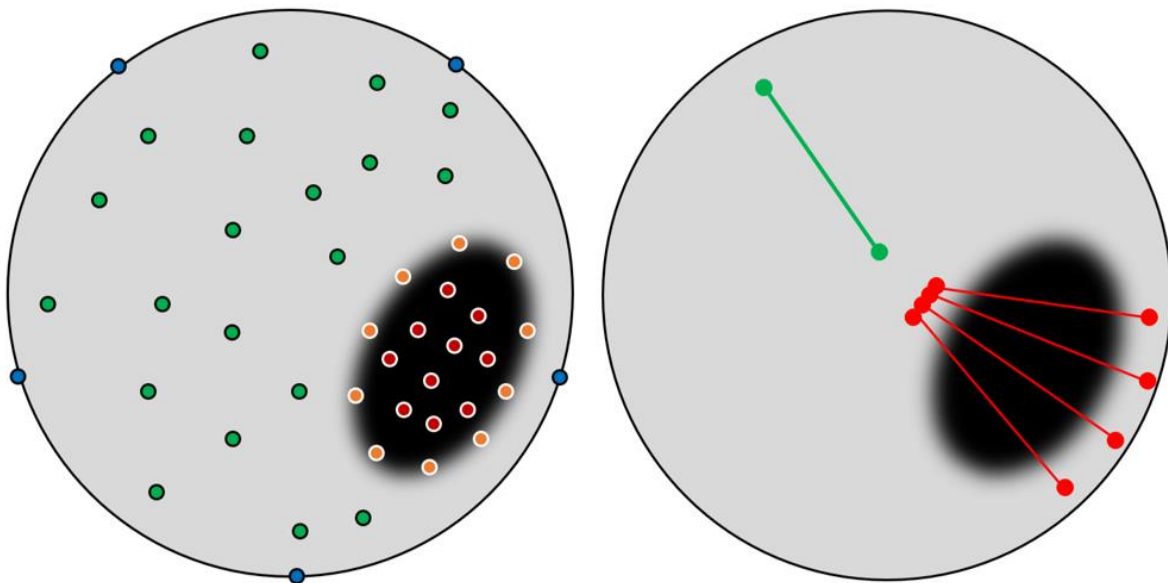


Figure 187: Wear scar measurement locations, wear scar is represented by the black area.

6.3 Hypothesis

6.3.1 Wear

MoM implants are known to have low wear rates when running in ideal tribological conditions, with in vitro wear rates of $0.05 - 4 \text{ mm}^3/\text{Mc}$ in steady state conditions [9]. However retrieval studies have shown that the levels of wear can vary greatly in-vivo, Gascoyne [110], studied 24 retrievals and demonstrated the amount of wear ranged from $0.15 \text{ mm}^3 - 338.2 \text{ mm}^3$, median: 2.19 mm^3 . Bills [13], studied 6 retrievals and showed the amount of wear ranged from $21.78 \text{ mm}^3 - 556.25 \text{ mm}^3$, mean: 23.98 mm^3 , potentially low wear bearings were excluded from the cohort, leading to a larger average wear value compared to Gascoyne. Therefore, for this study it is expected that many of the femoral heads will show minimal or no wear.

The wear area is expected to be on the supero-lateral area of the femoral head, with an elliptical shape, at an elevation angle of approximately 33° . Howie [17], recorded the location of MoM wear scars which ranged from $6^\circ - 50^\circ$ of elevation (elevation angle adjusted to match definition from this report). This gives a good description of the location of the expected wear, this may be useful when analysing wear maps, to distinguish minimal wear from potential measurement error.

6.3.2 Surface Topography

It is expected that the surface roughness will increase within the wear area compared to unworn areas of the worn femoral heads, this has been well established for multiple MoM studies [17, 19, 21, 22, 24]. First studied by Walker and Gold [109], the surface roughness was shown to increase up to 5 times within the wear area, the largest scratches were noted to be uni-directional. Howie [17], noted approximately 10 times increase in roughness, surface wear patterns were also categorised using SEM images, uni-directional dull abrasive wear areas showing the largest increase in roughness. Witzleb [19], produced SEM images of surface wear patterns on unworn and wear scar areas, within the wear area large uni-directional scratches were present. On the unworn surface, block carbides were present, and scratching was minimal.

The author contends these previous surface measurement studies could have missed the most critical surface topography as positional accuracy of the fixture setups was not considered. However, a clear pattern has been demonstrated that the wear area is expected to roughen, with uni-directional scratches indicating the roughest area.

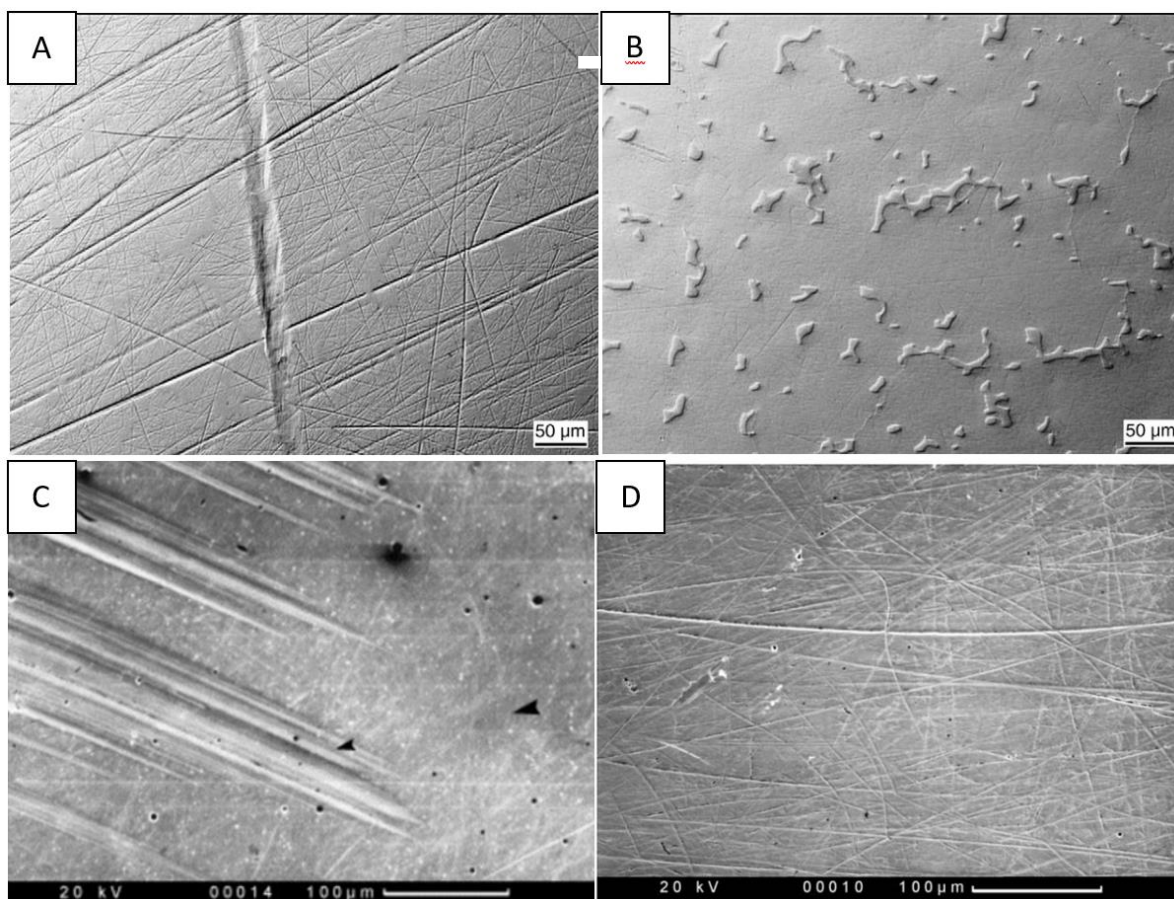


Figure 188: Previous surface measurement studies, SEM images. A: Uni-directional scratches and multi-directional scratches [19]. B: Block carbides [19]. C: Uni-directional scratches [17]. D: Multi-directional scratches 'dull abrasive wear' [17].

6.4 Results

6.4.1 CMM Measurement

Table 25 shows the CMM measurement results for all 10 femoral heads, measuring the radius, linear wear, and volumetric wear of the femoral head. If no wear area was found then the linear wear and volumetric wear parameters are not calculated. In the 'Wear Scar' column, CWS stands for clear wear scar, MWS stands for minimal wear scar, and UN stands for unworn. A wear map for every femoral head is shown in the appendix.

Table 25: CMM measurement results.

Component No.	Wear Area	Unworn Radius (mm)	Linear Wear (um)	Volumetric Wear (m m ³)	Wear Scar Centre Location (Az°/EI°)
135	CWS	24.996	22.6	3.5	19.87/41.97
294	CWS	20.994	16.1	3.0	103.49/38.22
213	MWS	21.993	7.1	1.8	33.30°/32.07°

608	MWS	24.995	9.6	2.0	13.49°/45.83°
082	UN	26.990	-	-	-
109	UN	25.994	-	-	-
131	UN	24.998	-	-	-
162	UN	24.993	-	-	-
550	UN	24.987	-	-	-
618	UN	24.991	-	-	-

The cohort can be split into three groups, those with a clear wear area, a minimal wear area, and those with no detectable wear. From the 10 femoral heads, two showed clear wear areas, femoral heads 135 and 294, figure 189. Both of these femoral heads exhibited an elliptical shaped wear area, the centre of these wear areas at elevation angles of 41.97° (135) and 38.22° (294). The maximum depth of the wear areas is 22.6 μm (135) and 16.1 μm (294). The total volumetric loss from the wear area was calculated as 3.5 mm^3 (135) and 3.0 mm^3 (294), both still low wear values. Due to the clear outline of these wear areas, these two femoral heads were selected to undergo more detailed wear map targeted surface measurements using the custom fixture system.

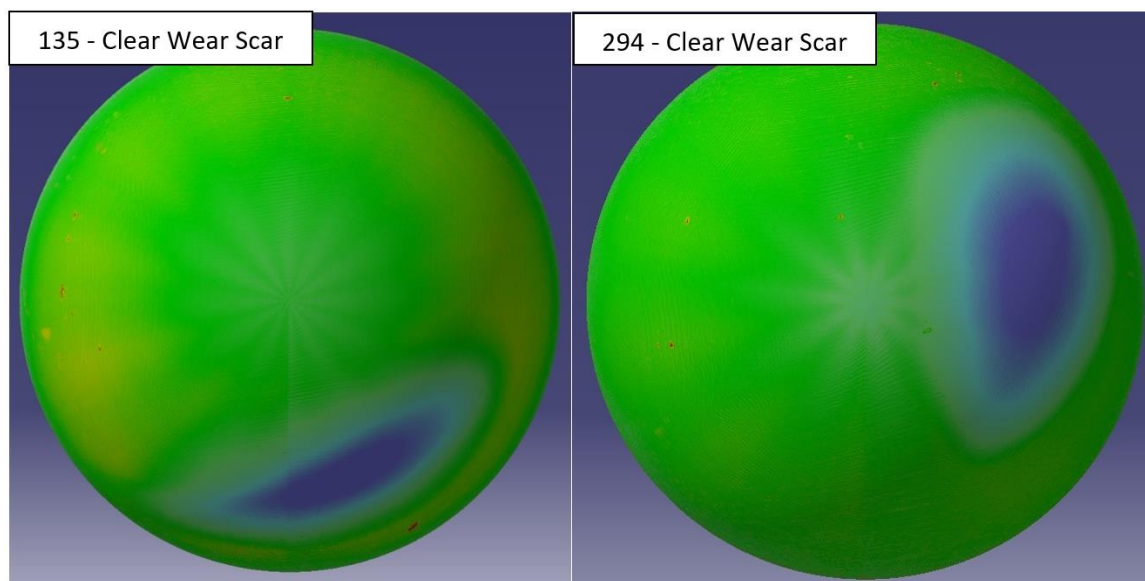


Figure 189: Clear wear area femoral heads. 135 Colour Scale: -22.6 to +10 μm , 294 Colour Scale: -16.1 to +10 μm

Femoral heads 213 and 608, figure 190, showed evidence of minimal wear areas, the depth of the wear areas were minimal and the calculated wear volumes are less than the total measurement uncertainty ($\pm 2.607 \text{ mm}^3$). The centre of the wear areas are located at elevation angles of 32.07° (213) and 45.83° (608). The depth of the wear areas are 7.1 μm (213) and 9.6 μm (608), and the volumetric wear is 1.8 mm^3 (213) and 2 mm^3 (608).

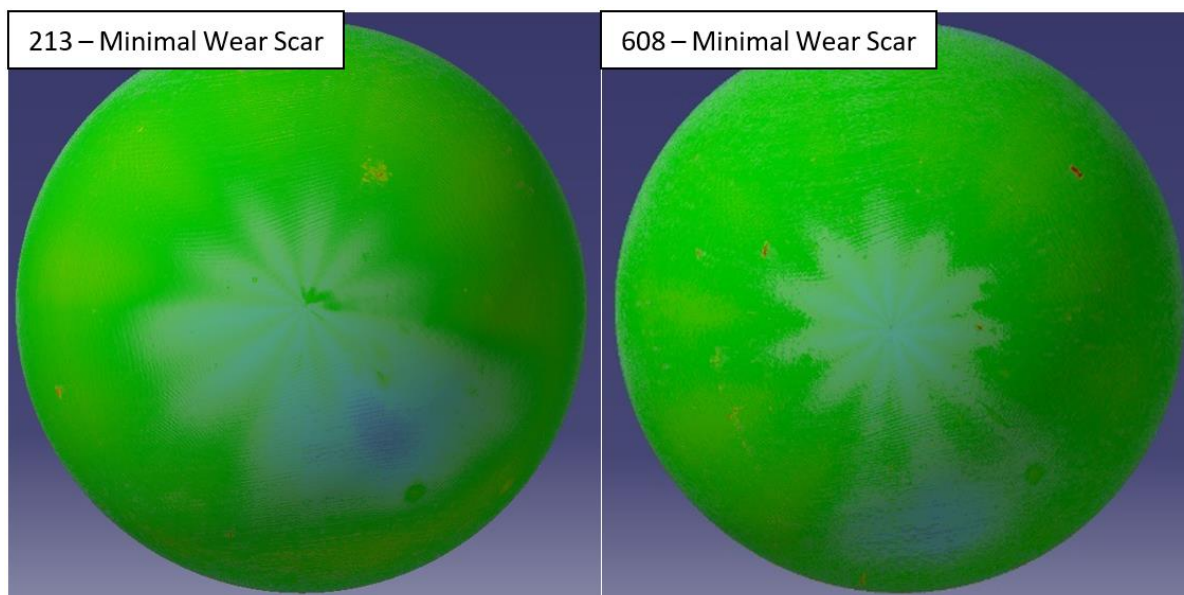


Figure 190: Minimal wear area femoral heads. 213 Colour Scale: -7.1 to + 10 μm , 608 Colour Scale: -4 to 10 μm .

The remaining six components did not show any measurable wear; however, all femoral heads, including those with wear areas, did show slight deviation at the pole of the component. The deviation is unlikely to be wear as due to the hip inclination angle; wear is unlikely to occur at the pole of the femoral head. This could instead indicate slight manufacturing deviation from a perfect hemisphere shape.

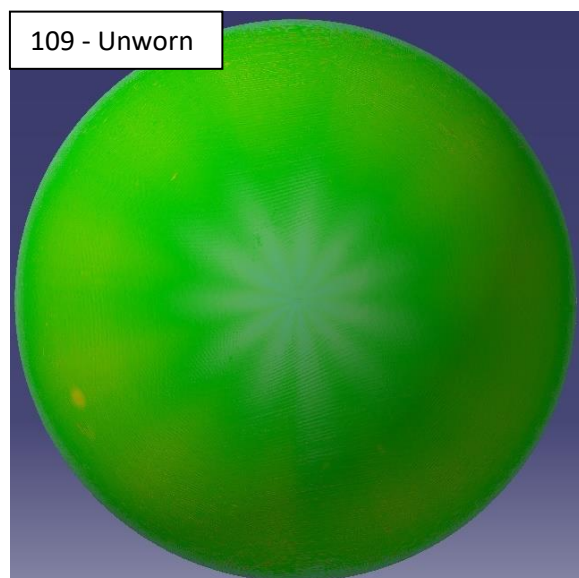


Figure 191: Femoral head 109 wear map, unworn component. Slight negative deviation at the pole of the component. 109 Colour scale: $\pm 10 \mu\text{m}$.

6.4.2 Unworn Surface

Table 26 summarises the **unworn** surface measurement results, the median Sa, Ssk, and Sdr values for each femoral head are shown and the range/standard deviation values are displayed underneath in italics. The full surface measurement results for each femoral head can be found in the appendix.

Table 26: Median surface parameter values for each component from the 25 unworn area surface measurements. Median values are shown in bold, with the range and SD values underneath in italic. Note the Sdr values are multiplied by $\times 10^{-3}$, due to them being very small values. CWS = clear wear scar, MWS = minimal wear scar, UN = unworn.

Component No.	Wear Scar	Sa (nm)		Sdr ($\times 10^{-3}$)		Ssk	
135	CWS	32.49		16.000		-0.46	
		<i>(3.14 - 125)</i>	<i>27.16</i>	<i>(0.017 - 195)</i>	<i>42.483</i>	<i>(-32.83 - 3.94)</i>	<i>7.04</i>
294	CWS	11.10		5.000		-2.03	
		<i>(4.88 - 50)</i>	<i>10.99</i>	<i>(0.095 - 38)</i>	<i>10.239</i>	<i>(-34.47 - 24.48)</i>	<i>10.54</i>
213	MWS	8.00		3.000		-5.75	
		<i>(3 - 21)</i>	<i>5.52</i>	<i>(0.190 - 126)</i>	<i>24.178</i>	<i>(-49.1 - 7.07)</i>	<i>14.34</i>
608	MWS	8.00		3.000		-0.52	
		<i>(1.51 - 18)</i>	<i>4.99</i>	<i>(0.005 - 19)</i>	<i>5.566</i>	<i>(-18.98 - 31.57)</i>	<i>13.46</i>
82	UN	18.00		12.000		-3.81	
		<i>(8.58 - 45)</i>	<i>9.11</i>	<i>(1 - 48)</i>	<i>13.425</i>	<i>(-13.13 - 16.79)</i>	<i>8.25</i>
109	UN	6.00		2.000		-1.33	
		<i>(3.08 - 36)</i>	<i>8.26</i>	<i>(0.03 - 38)</i>	<i>7.779</i>	<i>(-32.97 - 11.33)</i>	<i>10.58</i>
131	UN	22.00		13.000		-0.45	
		<i>(9.66 - 235)</i>	<i>50.63</i>	<i>(0.55 - 41)</i>	<i>12.070</i>	<i>(-18.45 - 2.91)</i>	<i>6.29</i>
162	UN	14.00		10.000		-2.21	
		<i>(4.58 - 409)</i>	<i>86.20</i>	<i>(0.53 - 358)</i>	<i>79.807</i>	<i>(-21.98 - 9.25)</i>	<i>7.25</i>
550	UN	5.01		1.000		-6.31	
		<i>(2.16 - 58.82)</i>	<i>13.83</i>	<i>(0.026 - 73)</i>	<i>17.774</i>	<i>(-32.9 - -0.21)</i>	<i>7.06</i>
618	UN	3.55		0.140		-2.49	
		<i>(1.23 - 13)</i>	<i>3.01</i>	<i>(0.01 - 10)</i>	<i>2.735</i>	<i>(-23.38 - 24.19)</i>	<i>10.24</i>
Median	-	9.55		4.00		-2.12	
Range	-	<i>(3.55 - 32.49)</i>		<i>(0.140 - 16)</i>		<i>(-6.31 - -0.45)</i>	
SD	-	8.61		5.41		2.02	

When considering the median Sa values for the unworn surface on each femoral head, figure 192, the values range from 3.55 nm to 32.49 nm, with an overall median value of 9.55 nm. This median value is in the expected range for freshly manufactured metal surfaces [9]. However, this does not mean that the majority of the surface is 'as manufactured', firstly as the lowest Sa value for each component

is considerably lower than the median value, this indicates that some roughening has occurred, even on the unworn surface. Secondly the surface images clearly show that the majority of surface measurements show evidence of scratches. One of the two femoral heads which has a clear wear area, 135, has the highest Sa value of the cohort, with a median value of 32.49 nm, approximately 3x greater than the average unworn surface. However, the other clearly worn femoral head, 294, has a median unworn surface Sa value of 11.10 nm, similar to the average unworn surface. Therefore, it is unclear whether the unworn surface is consistently rougher on worn femoral heads.

The standard deviation (SD) values can vary greatly from one femoral head to the next. This is most likely due to a high Sa value being captured by chance as part of the random 25 surface measurements, this greatly influences the SD value but does not affect the median value. Due to the 25 surface measurements only covering a small surface area of the femoral head the SD values could be misleading.

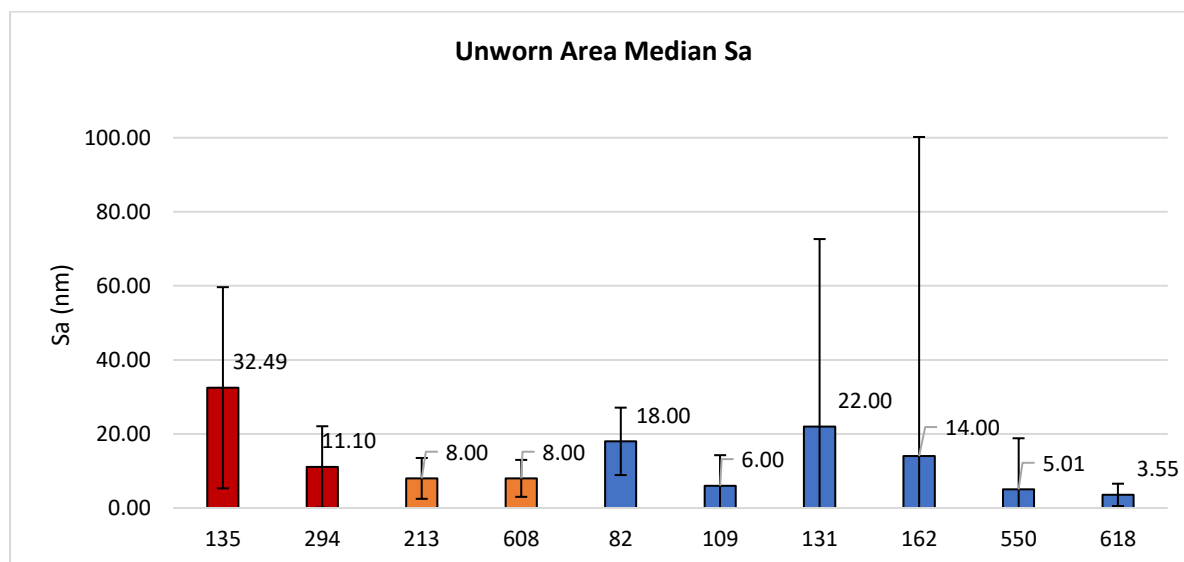


Figure 192: Median Sa Values of each component, 25 measurements, wear scars excluded from measurement area. Clear wear area femoral heads (red), Minimal wear area femoral heads (orange).

When comparing the Sa values on the unworn main bearing surface compared to the rim surface, figure 193, for the majority of the femoral heads (6 out of 10) the median Sa value is greater on the rim of the component compared to the main bearing surface. For 2 of the femoral heads the Sa value is practically identical, and for the remaining 2 femoral heads the Sa value is greater on the main bearing area and lower on the rim surface. The 2 femoral heads which were smoother on the rim surface compared to the main bearing surface were the worn femoral heads. This would suggest the worn femoral heads have a roughened unworn main bearing surface compared to their original surface finish.

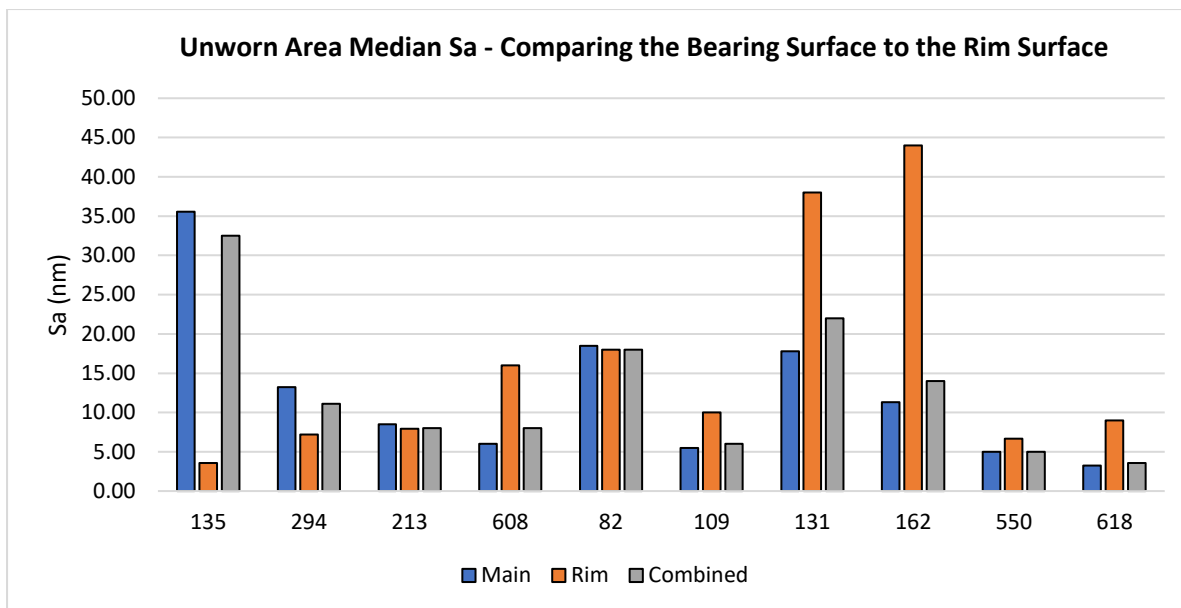


Figure 193: Median Sa Values of each component, 20 measurements on the main bearing, 5 measurements on the rim.

The median Sdr values of each femoral head are shown in figure 194. The values range from 0.140×10^{-3} to 16×10^{-3} , with an overall median value of 4×10^{-3} . The Sdr values closely match the pattern of the Sa values, this is to be expected as usually when Sa values increase, an increase in Sdr will also occur.

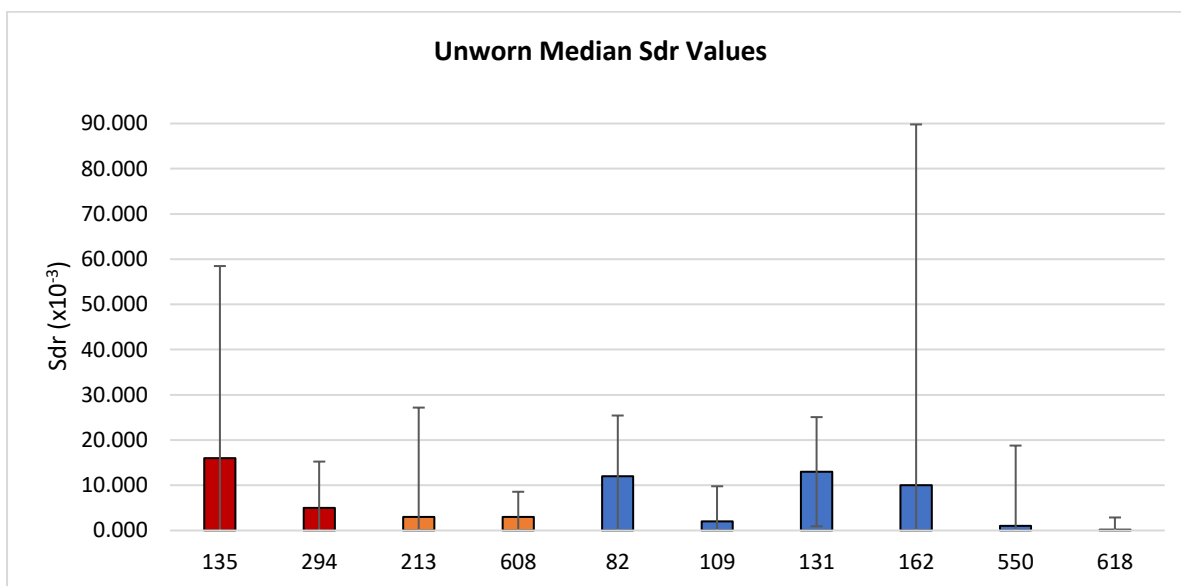


Figure 194: Median Sdr Values of each component, 25 measurements, wear scars excluded from measurement area. Clear wear area femoral heads (red), Minimal wear area femoral heads (orange).

The median Ssk values of each femoral head are shown in figure 195. The values range from -6.31 to -0.45, with an overall median value of -2.12. The median Ssk values do not show a clear difference between the worn femoral heads and the unworn femoral heads, but show the general value consistent with polished surfaces.

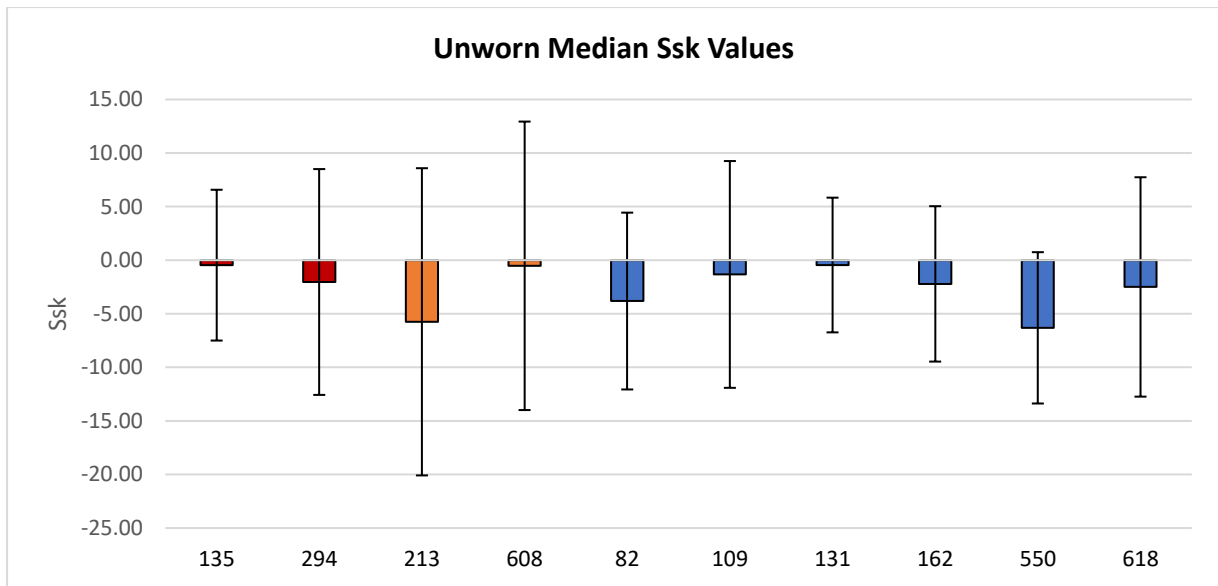


Figure 195: Median Ssk Values of each component, 25 measurements, wear scars excluded from measurement area.

At this stage, a baseline understanding of the unworn area of all the femoral heads has been gained, a detailed surface analysis of the worn femoral heads will now be made to see how the surface finish varies within the wear area.

6.4.3 Wear Area Surface

In this section, the worn femoral heads undergo a more detailed surface measurement analysis to understand how the surface finish within the wear area differs from the unworn surface. Two sets of measurement tests were completed on the worn femoral heads, these are grouped measurements and stitch measurements.

6.4.3.1 Measurement Locations

Grouped Measurement Locations

Figure 196 shows the locations of the grouped measurements taken on the worn femoral heads, the location and amount of surface measurements are as follows:

- 10 at the central area of the wear scar, shown in red.
- 10 at the outer area of the wear scar, shown in orange.
- 20 at unworn areas, shown in green.
- 5 at the rim of the component (95° elevation), shown in blue.

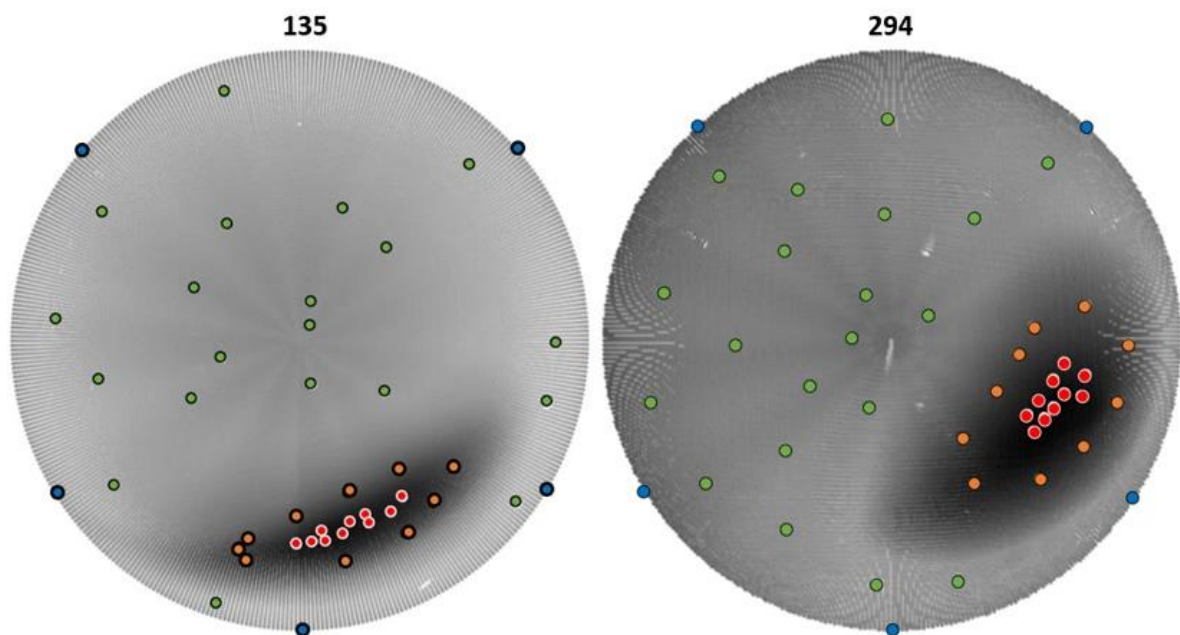


Figure 196: Grouped measurement locations on the wear maps of worn femoral heads. The wear map is set to greyscale mode to allow for the surface measurement locations to be easily seen, the wear area is the black surface.

Stitch Measurement Locations

The location of the stitch measurements can be seen in figure 197, each worn femoral head has four stitches taken through the wear scar (orange/red lines) and one stitch of identical length through an unworn area of the component (green line). The red line indicates the stitch line through the location of maximum wear depth, note this is not necessarily through the centre of the wear scar. The reason a stitch is taken through an unworn area is to ensure that any change in surface topography within the wear area, is not also happening elsewhere on the femoral head at similar elevation angles.

For femoral head 135 each stitch starts at an elevation angle of 13.697° and travels through to 71.091° , each stitch consists of 35 separate surface measurements with a 20% overlap region between each measurement. The azimuth angle of each of the stitch lines are as follows: 2° , 7.29° , 15° , 25° , 200° .

For femoral head 294 each stitch starts at an elevation angle of 8.44° and travels through to 74.77° , each stitch consists of 34 separate measurements with a 20% overlap region between each measurement. The azimuth angle of each of the stitch lines are as follows: 55° , 65° , 73.9° , 85° , 200° .

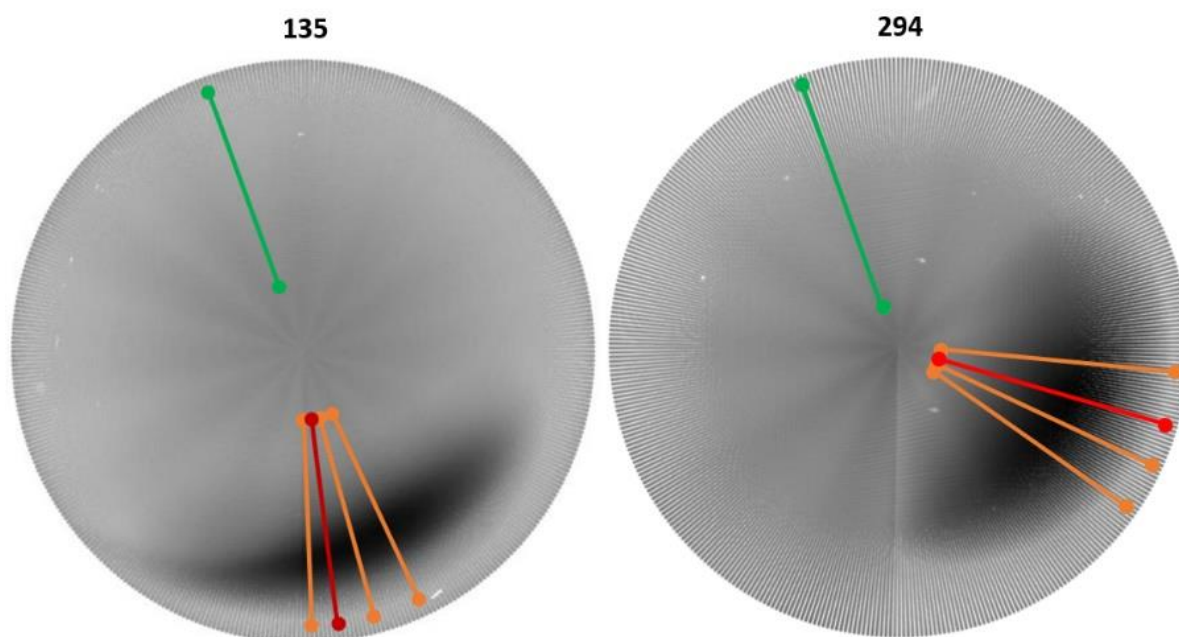


Figure 197: Stitch measurement locations displayed on the wear map. The wear map is set to greyscale mode to allow for the surface measurement locations to be easily seen, the wear area is the black portion of surface.

6.4.3.2 Grouped Measurements Results

A summary of the surface parameter results from the grouped measurements on both worn femoral heads is shown in table 27. It should be noted from CMM analysis that femoral heads chosen for surface measurement (135 and 294) had the greatest measurable volumetric wear of 3.5 mm³ and 3.0 mm³ respectively. The standard deviation and range of values are recorded in italic underneath the median values for each of the datasets. The full surface measurement results of all the individual grouped measurements can be found in the appendix.

Table 27: Grouped measurements, median surface parameter values.

	Femoral Head 135			Femoral Head 294		
	Sa (nm)	Sdr (x10 ⁻³)	Ssk	Sa (nm)	Sdr (%)	Ssk
Central Wear Area						
Median	121.50	94.00	-0.35	67.00	56.00	-0.25
<i>Range</i>	<i>(85 - 150)</i>	<i>(54 - 143)</i>	<i>(-0.96 - 1.55)</i>	<i>(23.02 - 117.60)</i>	<i>(17 - 164)</i>	<i>(-1.08 - 0.56)</i>
<i>SD</i>	<i>18.23</i>	<i>28.11</i>	<i>0.65</i>	<i>29.88</i>	<i>43.852</i>	<i>0.59</i>
Outer Wear Area						
Median	76.00	46.00	-0.93	14.45	7.00	-4.13
<i>Range</i>	<i>(38.23 - 129)</i>	<i>(8 - 58)</i>	<i>(-1.54 - 1.25)</i>	<i>(4.37 - 57)</i>	<i>(0.68 - 69)</i>	<i>(-11.56 - 1.47)</i>
<i>SD</i>	<i>34.65</i>	<i>19.37</i>	<i>1.04</i>	<i>20.10</i>	<i>22.13</i>	<i>3.59</i>
Unworn Area						
Median	35.54	21.00	-0.22	13.21	5.50	-1.82
<i>Range</i>	<i>(20.34 - 125)</i>	<i>(1 - 195)</i>	<i>(-3.35 - 3.94)</i>	<i>(5.69 - 50)</i>	<i>(0.20 - 38)</i>	<i>(-34.47 - 24.48)</i>
<i>SD</i>	<i>24.03</i>	<i>44.74</i>	<i>2.08</i>	<i>11.68</i>	<i>10.97</i>	<i>10.35</i>
Rim Area						
Median	3.57	0.09	-3.34	7.20	2.00	-11.67
<i>Range</i>	<i>(3.14 - 5)</i>	<i>(0.02 - 3)</i>	<i>(-32.83 - -0.15)</i>	<i>(4.93 - 13)</i>	<i>(0.12 - 14)</i>	<i>(-22.31 - 1.77)</i>
<i>SD</i>	<i>0.64</i>	<i>1.17</i>	<i>12.02</i>	<i>-2.80</i>	<i>-5.26</i>	<i>-8.81</i>
Unworn and Rim Area Combined						
Median	32.49	16.00	-0.46	11.10	5.00	-2.03
<i>SD</i>	<i>27.16</i>	<i>42.48</i>	<i>7.04</i>	<i>10.99</i>	<i>10.24</i>	<i>10.51</i>

Comparing Sa in the Unworn Area to the Central Wear Area

The results from the grouped measurements are now shown in a bar graph for each of the three parameters (Sa, Sdr, and Ssk). The bar graph displays the median parameter value from each of the measurement groups and a 1 SD error bar is used.

When comparing the wear area surface to the unworn area, figure 198, we can see that for both femoral heads the Sa value increases greatly within the central wear area. For component 135 the median Sa value increases from 32.49 nm to 121.50 nm, for component 294 the Sa value increases from 11.10 nm to 67 nm.

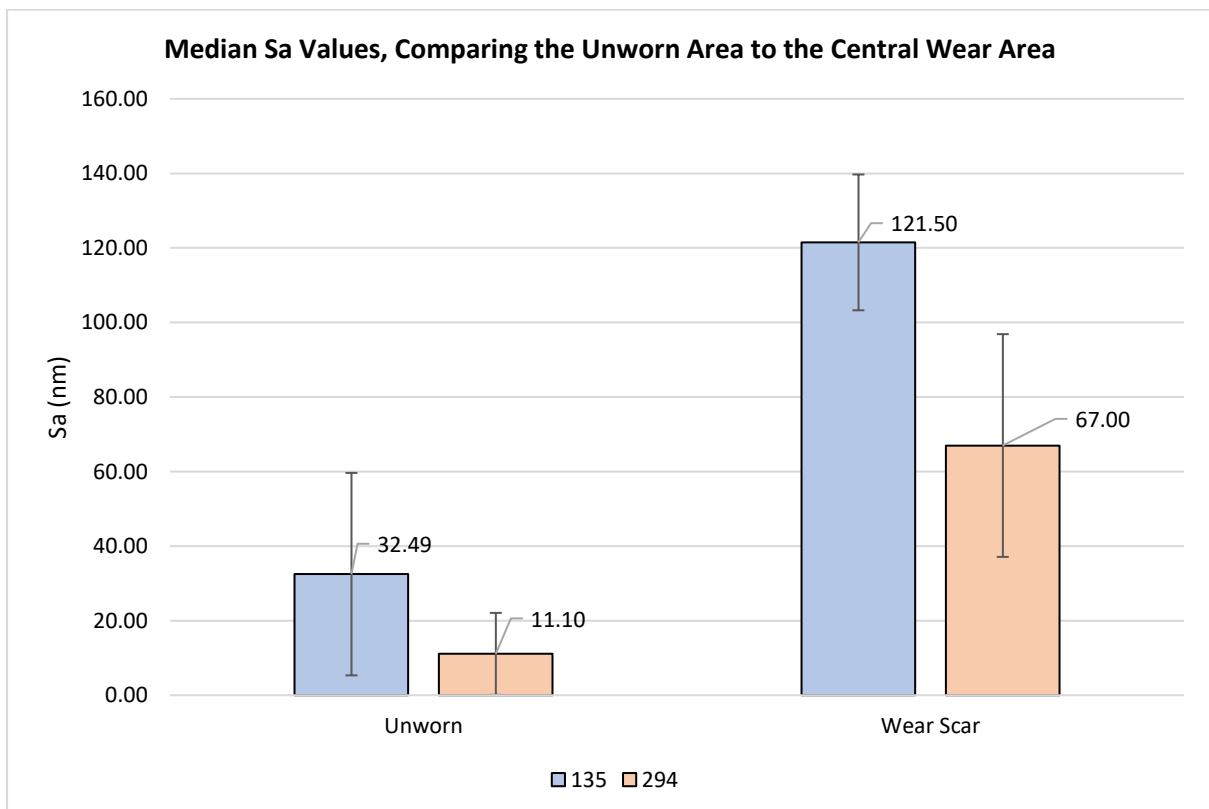


Figure 198: The median Sa values in both the unworn/rim area and the central wear area, 1 SD error bars.

Comparing Sa in all Group Locations

This can be broken down further into the four location groups, the central wear area, the boundary wear area, the unworn area, and the rim surface, as shown on figure 199. For femoral head 135 the rim surface is significantly smoother (3.57 nm) than the unworn main bearing surface (35.54 nm). At the outer wear area, the roughness has increased significantly (76 nm) and continues to increase into the central wear area (121.5 nm).

For femoral head 294 the rim surface is slightly smoother (7.20 nm) compared to the unworn bearing surface (13.21 nm), but this is not a significant difference. At the boundary wear area, the roughness does not increase significantly (14.45 nm). At the central wear area of the roughness significantly increases (67 nm).

For femoral head 294 it is particularly interesting that the boundary wear area does not show a significant increase in Sa, this likely indicates that the shape of the CMM wear area, does not accurately match the shape of the change in surface topography. This will be proven in section 8.4.3.4 and demonstrates why stitching of surface measurements through the wear area are so beneficial.

The Sa values in the rim region gives a good estimate of the original surface finish of the femoral heads as there is little evidence of any damage in the surface images. As can be seen the 'unworn area' of femoral head 135 has become significantly rougher through its lifetime compared to the pristine surface on the rim.

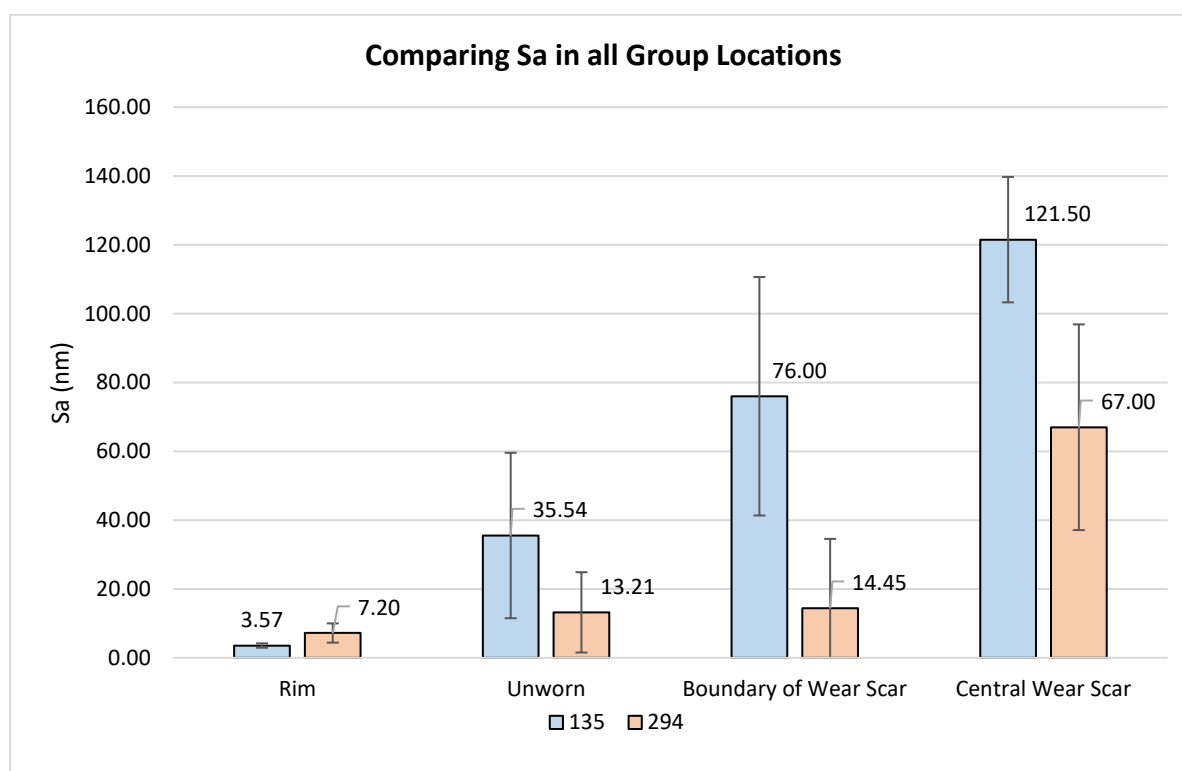


Figure 199: The median Sa values in each of the location groups, 1 SD error bars.

Comparing Sdr in all Group Locations

Figure 200 shows the median Sdr values from each of the group measurement sets. The same correlation as the Sa values has occurred, this is to be expected due to the high correlation between Sdr and Sa for these specimens. The main noticeable difference between Sdr and Sa is that the Sdr is much smaller in the rim region, this is because of the pristine surface finish has a lack of any surface perturbations leading to a very low Sdr value. The use of the Sdr parameter may differentiate smoother and longer wavelength surfaces more than Sa, and is particularly valuable when individual surface measurements are compared later in this chapter.

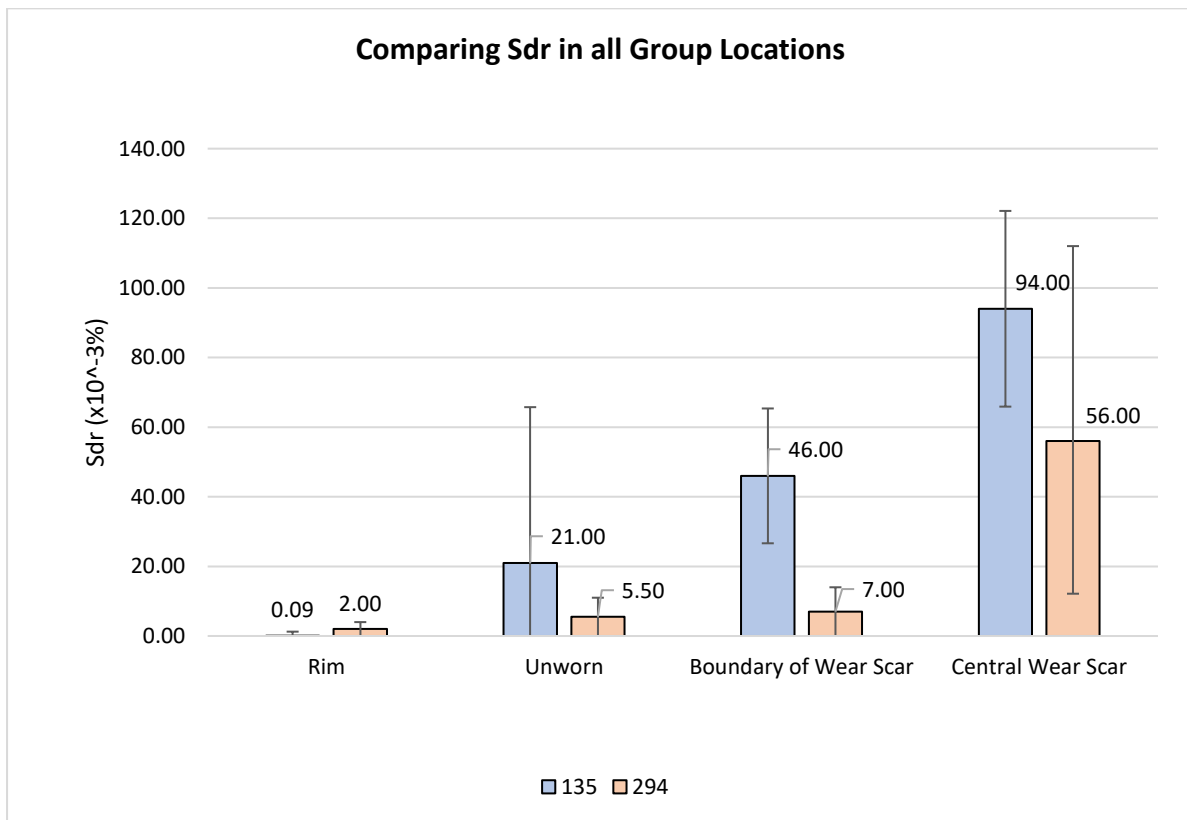


Figure 200: Median Sdr Values by Location Group, 1 SD Error Bars.

Comparing Ssk in all Group Locations

Figure 201 shows the median Ssk values from each of the group measurement sets. Firstly, it can be noted that overall, the median values for all groups are negative, however the error bars indicate that both positive and negative Ssk is still possible. For a freshly manufactured metal femoral head a negative skewness would be expected due to the polishing process removing peaks from the surface and the surface topography becoming negatively skewed towards a valley orientated surface.

Both femoral heads have a similar pattern of results, at the rim area the median Ssk is lowest (-3.34 and -11.67), with a large SD value indicating a wide range of possible Ssk values in this area. In the unworn area the median Ssk is closer to 0 (-0.22 and -1.82), but again there is a large SD value indicating again a wide range of skewness values (the values of Ssk can be affected by a few peak data points), in both a positive and negative [193]. At the outer wear area, the median Ssk values are still close to 0 (-0.93 and -4.13) however the SD values have shrunk greatly, indicating the surface is becoming more consistent in this area. Finally, in the central wear area, the Ssk values are closest to 0 (-0.35 and -0.25) with very small SD values, showing the Ssk is most consistent across all measurements in this area as the surface is more Gaussian in nature as expected for an abrasively worn surface.

The SD value is clearly largest in the rim/unworn region and then reduces within the wear areas. This indicates that in the wear area where the roughness is greatest, the Ssk is consistently close to 0 (random wear events), whereas in the unworn area where the surface is smoother and consistent with a polished surface [193], as pointed out above a small number of peaks or valleys can influence the Ssk greatly in either a positive or negative direction.

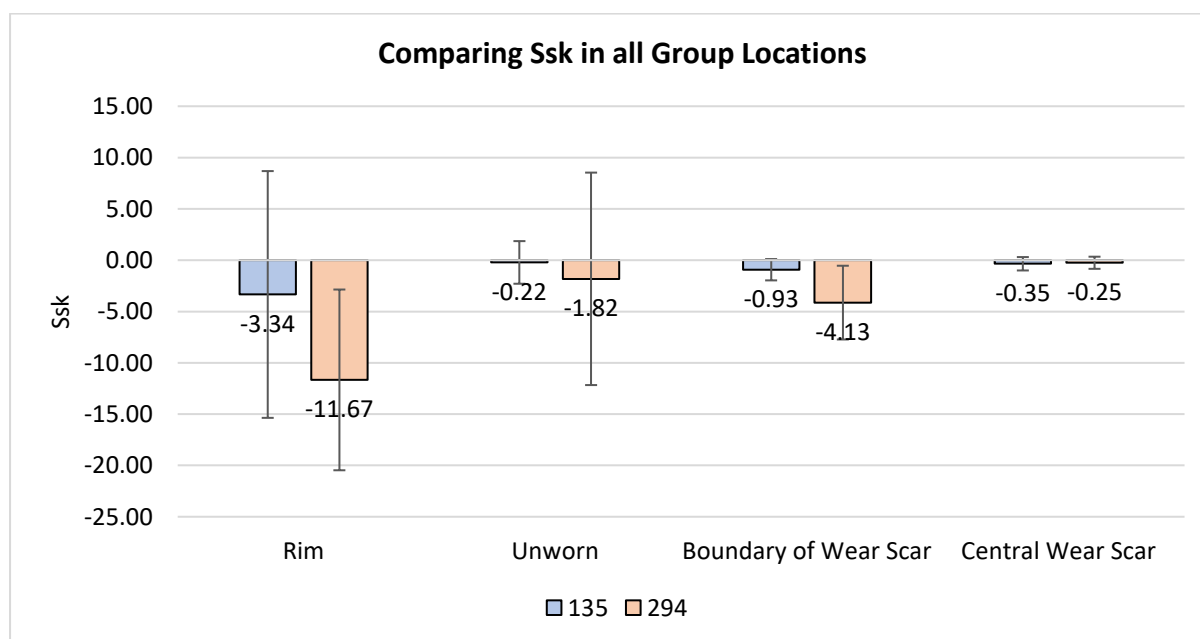


Figure 201: Median Ssk Values by Location Group, 1 SD Error Bars.

Overlay Plots

As the surface measurement locations are precisely tracked in relation to the CMM wear map, we can combine these datasets in a fused output as an overlay plot. This allows the surface parameter values to be plotted as a colour value on top of the wear map, red circles represent a high Sa value whereas blue represent a low Sa value. On the wear map, the black area indicates the wear area. Overlay plots are useful to help understand positional size and shape of areas of surface topography change and will later be used for surface topography mapping. The overlay plots were created by using a custom-made code on MATLAB.

Figure 202 shows the grouped measurement Sa values for the worn femoral heads 135 and 294. For femoral head 135 the increase in roughness appears to be greater on the lower half of the wear area compared to the upper half (closer to the pole). This is indicated by the lower wear area boundary measurements having high Sa values, to a similar amount of those in the centre. We can also see that two measurements taken in the unworn area, between the wear area and the pole have high Sa values more representative of the wear area.

For component 294 the increase in roughness appears to be greatest in the top right of the wear area. The size of the area with increased roughness appears to be small, as the wear area boundary measurements and central wear area measurements in the lower left of the wear area have a similar Sa values to the unworn surface. These examples show that while the roughness does clearly increase within the wear area, the amount of roughening can vary within the wear area.

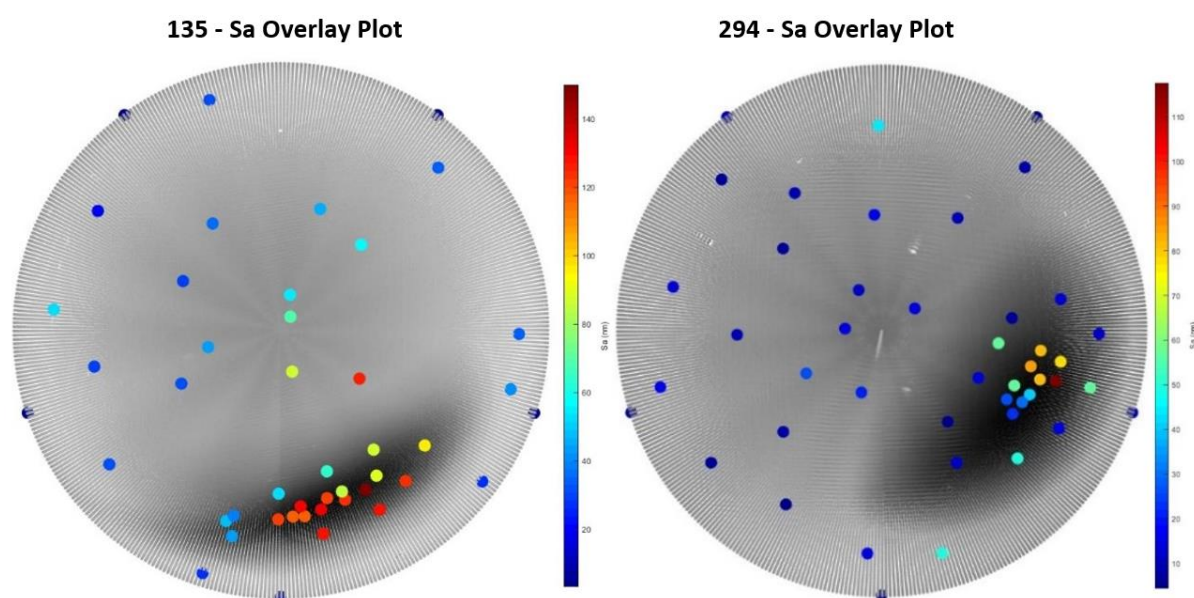


Figure 202: Sa overlay plots of grouped measurements on femoral heads 135 and 294.

Figure 203 shows the Sdr values as an overlay plot, a similar relationship is shown with the Sdr values that was shown with the Sa values, an increase within the wear area compared to the unworn area.

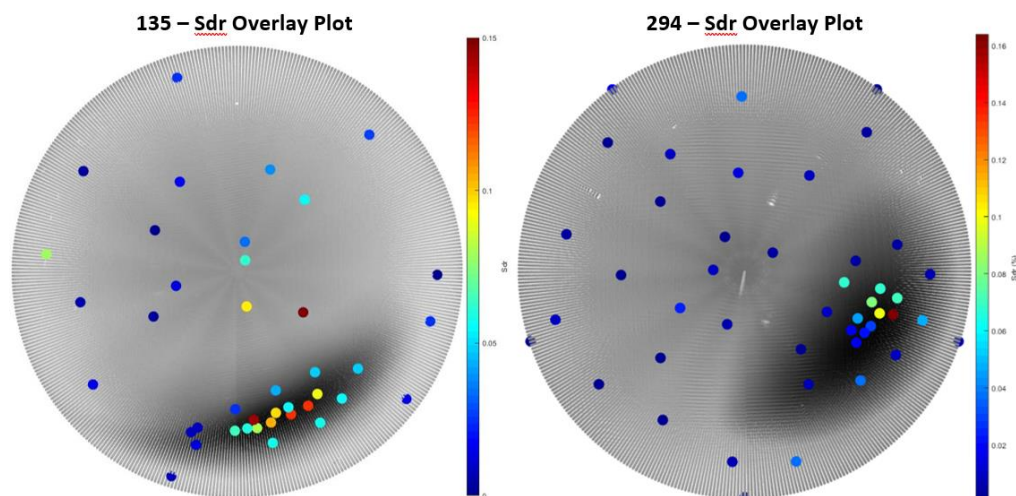


Figure 203: Sdr overlay plots of grouped measurements on femoral heads 135 and 294.

Figure 204 shows the Ssk values as overlay plots, the relationship between Ssk and the wear area is not as obvious as the Sa and Sdr parameters. However, it is clear that all of the values within the central wear area and the outer wear area all had values close to 0, whereas in the unworn areas there was the possibility that the Ssk would significantly change. This is shown by a consistent light green colour within the wear area. For both plots the colour scale was reduced in size, lower than the max/min values, as this allows for a better comparison to be made between surface measurements.

Within the wear area the consistent scratches covering the entire measurement leads to a Ssk close to 0. Whereas the less damaged surface on the unworn area means that features such as scratches or ridges influence the Ssk greatly. The unaffected areas of the rim of the femoral head retain characteristic negative Ssk values associated with a lapped/polished surface.

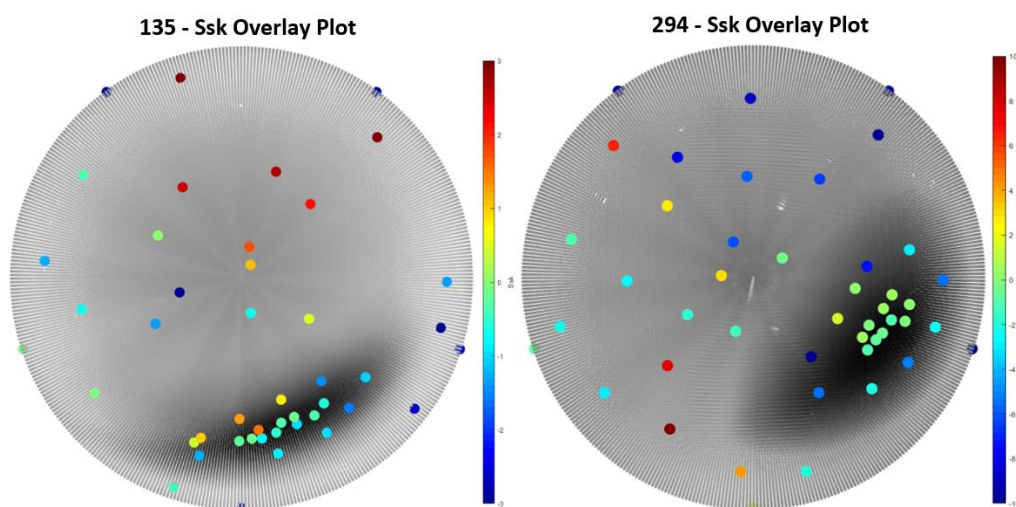


Figure 204: Ssk overlay plots of grouped measurements on femoral heads 135 and 294.

6.4.3.3 Stitch Measurements

A downside of grouped measurements is that the boundary of the wear area is unlikely to perfectly match the change in the surface topography on the femoral head. This can lead to measurement groups having median surface parameter values that do not truly reflect the surface topography, unless many more measurements are taken. Consequently, stitching of a linear band of surface measurements can provide a better analysis, ensuring a full line of measurements is taken through the wear area, including both the start and end boundaries and a portion of measurements in the unworn area.

Due to the large number of measurements taken during the stitch measurements phase a full results table is not featured in the thesis main body, the full results can be found in the appendix. The results from the stitch measurements are best displayed as overlay plots, figure 205 shows the Sa values from stitched measurements for both femoral heads. For both femoral heads, the roughness clearly increases within the wear area compared to the stitch in the unworn area which has no increase in roughness. This shows that the roughness does not increase all the way around the femoral head beyond a specific elevation angle, the increase in roughness is only significant within the wear area.

There are some important differences between the two femoral heads. For femoral head 135, each of the four-stitch lines through the wear area show a significant increase in roughness, in particular on the lower half of the wear area. Femoral head 135 also shows clear roughening between the pole of the femoral head and the wear area, this roughening is not matched underneath the wear area.

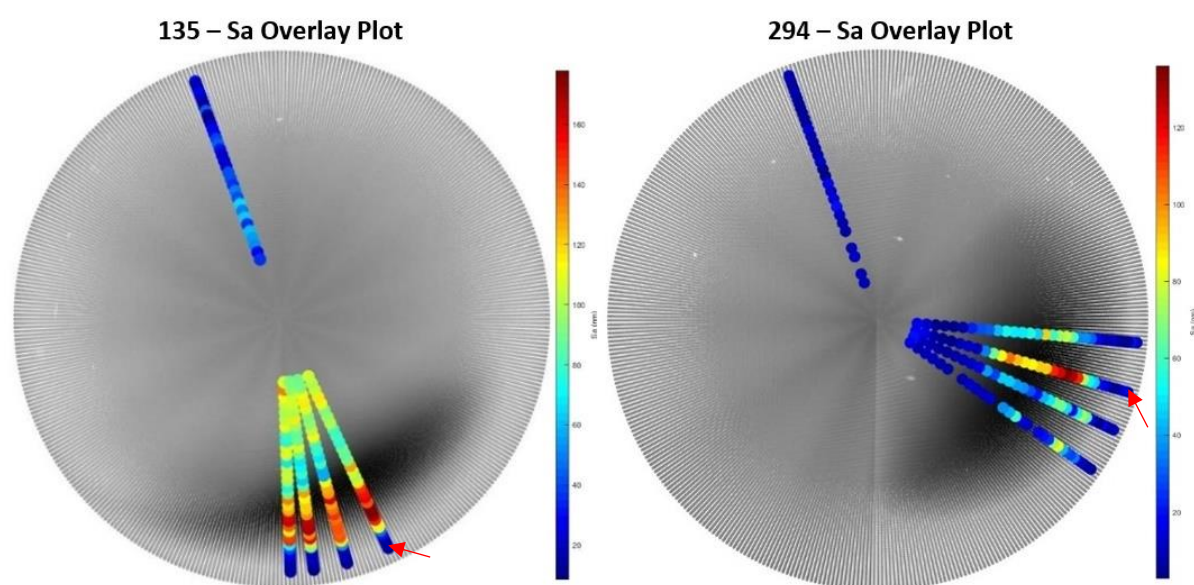


Figure 205: Sa overlay plots of stitch measurements on femoral heads 135 and 294.

For femoral head 294, one stitch line in particular (the third through the wear area) shows a much greater increase in roughness compared to the other stitch lines through the wear area. This indicates that the area of maximum increased roughness is smaller than the wear area shown from the CMM wear map. The increase in roughness was again greatest at the bottom half of the wear area, similar to that of femoral head 135.

The results can also be plotted as a scatter graph to allow the Sa values to be seen in more detail, figure 206. One stitch line is selected for each of the femoral heads, the selected stitch line is highlighted by a red arrow on the overlay plots, figure 205. For femoral head 135 the stitch line selected is at azimuth angle 25° , for femoral head 294 the stitch line selected is at azimuth angle 73.9° . The X axis represents the elevation angle of the measurement, and the Y axis plots the Sa values. The start and end point of the CMM defined wear area is indicated by black dashed lines on the scatter plot.

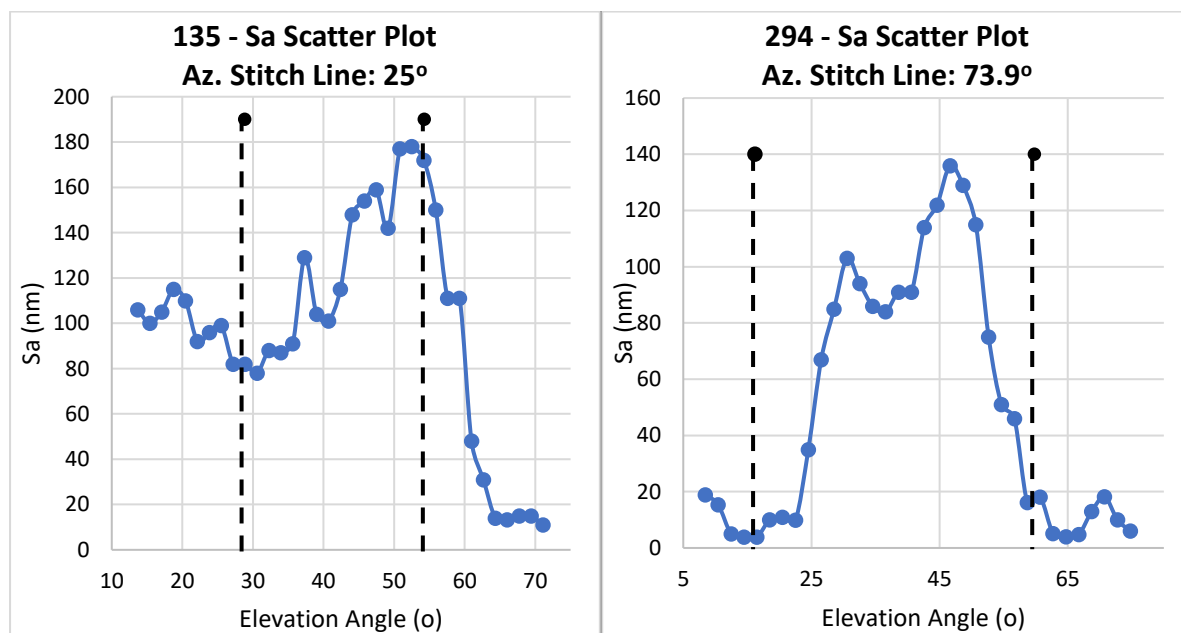


Figure 206: Sa Scatter plots of a selected stitch line through the wear area, the stitch line selected is highlighted by a red arrow on each of the overlay plots (figure 205). Black dashed lines represent the start and end point of the CMM defined wear area.

For femoral head 135, the initial Sa value is high (80 – 120 nm), this indicates that roughening has occurred outside of the wear area and towards the pole. There is a slight drop in the Sa as the measurements begin to enter the wear area (60 – 100 nm). The Sa values then increase in the second half of the wear area reaching up to 180 nm, this peak is reached at the wear area end boundary. After this peak the Sa values decrease rapidly, with the Sa levels reaching their lowest point (10 – 15 nm) 15 elevation degrees past the end of the wear area. This shows that the main area of roughening occurred at the end of the wear area, and continued outside of the CMM defined wear area, again confirming that the change in surface topography does not perfectly match the wear area shape.

For femoral head 294, the initial Sa value is low (5 – 15 nm), initially as the measurements enter the wear area, no increase in roughness occurs. At 25° elevation the Sa values begin to increase, they increase up to 103 nm at the centre of the wear area, at this stage the Sa values level off (80-100 nm). At the lower half of the wear area (closer to the rim), the values then increase again to a maximum of 136 nm. After this peak the surface becomes smooth again in a short distance (5 – 15 nm). Both examples show that the peak of roughening is achieved closer to the rim side of the wear area, then after this peak the surface quickly becomes smooth again.

Instead of plotting just one of the stitch lines, all five of the stitch lines can be plotted, figure 207. All of the stitch lines through the wear area are plotted in red, whereas the stitch line through the unworn area is plotted in green. For femoral head 135 all of the four stitch lines through the wear scar follow a similar pattern to the one described in figure 206. For femoral head 294 the rest of the stitch lines through the wear area, show an increase in Sa, however to a significantly lower extent compared to the stitch through 73.9° azimuth, the stitch through the maximum linear wear point. This shows that the area of most roughening is smaller than the size of the entire wear area.

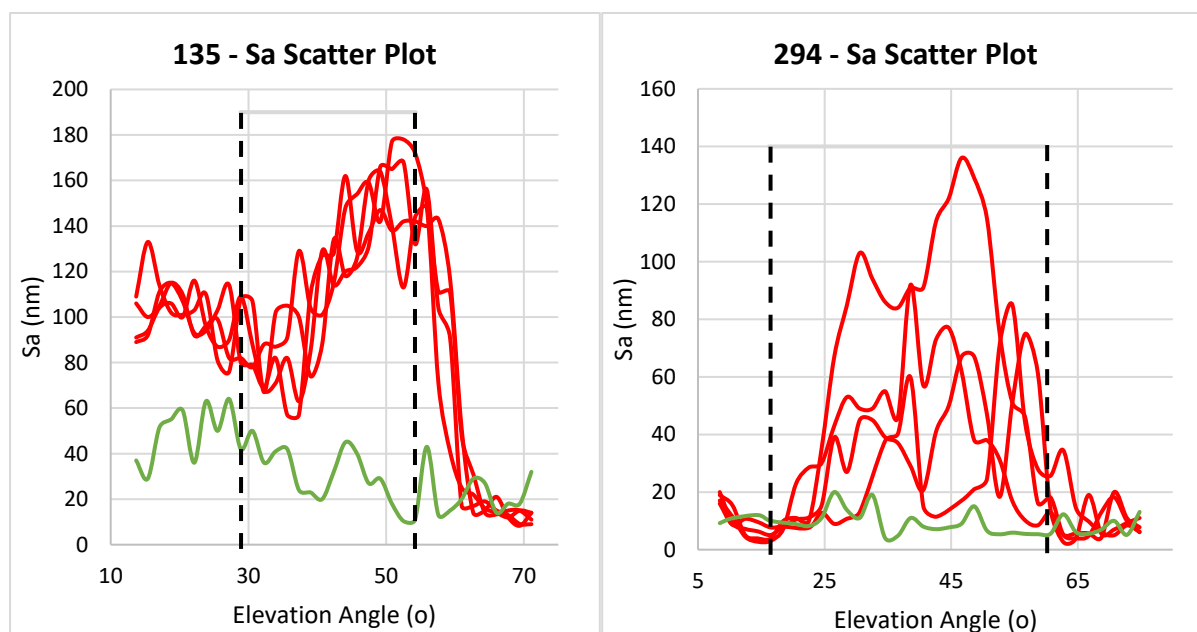


Figure 207: Sa scatter plots of all stitch lines. Red lines represent the stitches through the wear area, the green line represents the stitch taken through the unworn area. Black dashed lines represent the start and end point of the wear area.

The Sdr values are now plotted as overlay plots and scatter plots. For component 135 all four stitches through the wear scar follow a similar Sdr pattern. The Sdr values are greatest in the roughened region between the wear area and the pole. This indicates the complexity of the surface, number of surface features, is greater in this region. The Sdr values gradually drop throughout the wear area, before suddenly dropping at the end of the wear area as the surface becomes smooth. The stitch through the unworn area has low Sdr values throughout. The main difference between the Sa and Sdr values is

that the Sdr is greatest in the pole to wear area, and that the variation from one measurement to the next is greater for this parameter.

For component 294, the Sdr values match very closely with the pattern shown from the Sa values, with one of the stitches through the wear area showing a much greater increase in roughness compared to the others. Both above and below the wear area the surface appears smooth with very low Sdr values either side, with clear increase in Sdr only shown within the wear area. The increase in Sdr is maximum at the lower side of the wear scar, closer to the rim. The maximum increase in Sdr occurs for the stitch through the maximum linear wear point with an Sdr value reaching 0.2130%, compared to the other stitches through the wear scar reaching 0.073% – 0.096%.

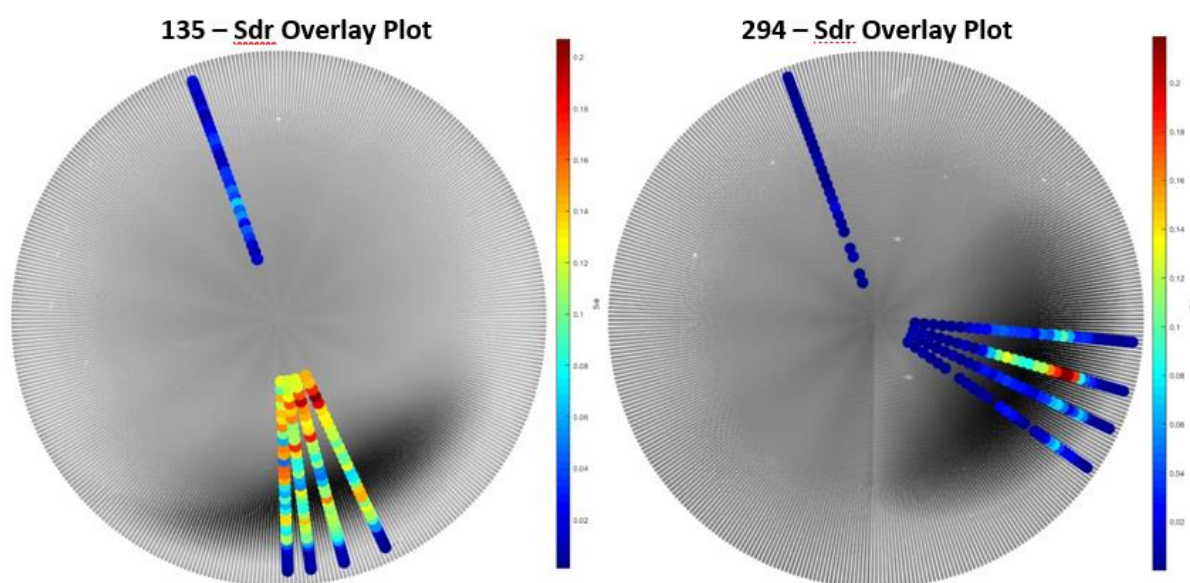


Figure 208: Sdr overlay plots of stitch measurements on femoral heads 135 and 294.

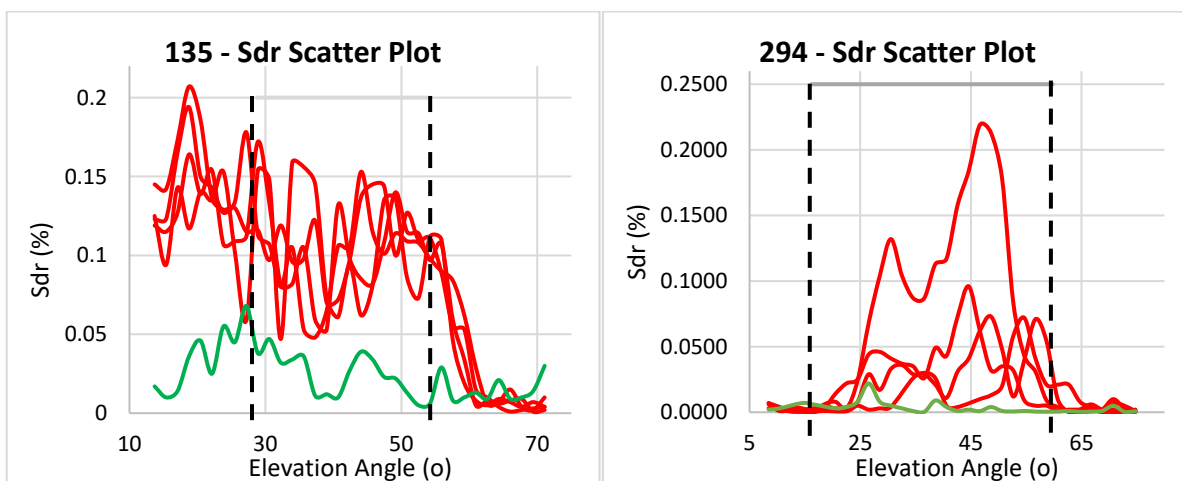


Figure 209: Sdr scatter plots of all stitch lines. Red lines represent the stitches through the wear area, the green line represents the stitch taken through the unworn area. Black dashed lines represent the start and end point of the wear area.

The Ssk values are now plotted as overlay plots and scatter plots. For femoral head 135 the Ssk values are all close to 0 within the wear area and the roughened region between the wear area and the pole. This would indicate a general change in the surface topography. This can be seen on the scatter plot as the stitch lines (shown in red) all remain close to 0, until they leave the wear area and generally decrease in a negative Ssk similar to the virgin polished surface.

For femoral head 294 the Ssk values for the stitch lines are also closest to 0 within the wear area. The two stitch lines at the top of the wear area have the values closest to 0. The stitch through the unworn area has both high and low Ssk values. On the scatter plot the stitch lines through the wear area (red lines) all remain close to 0 when they are within the wear area (start and end points shown by black dashed line).

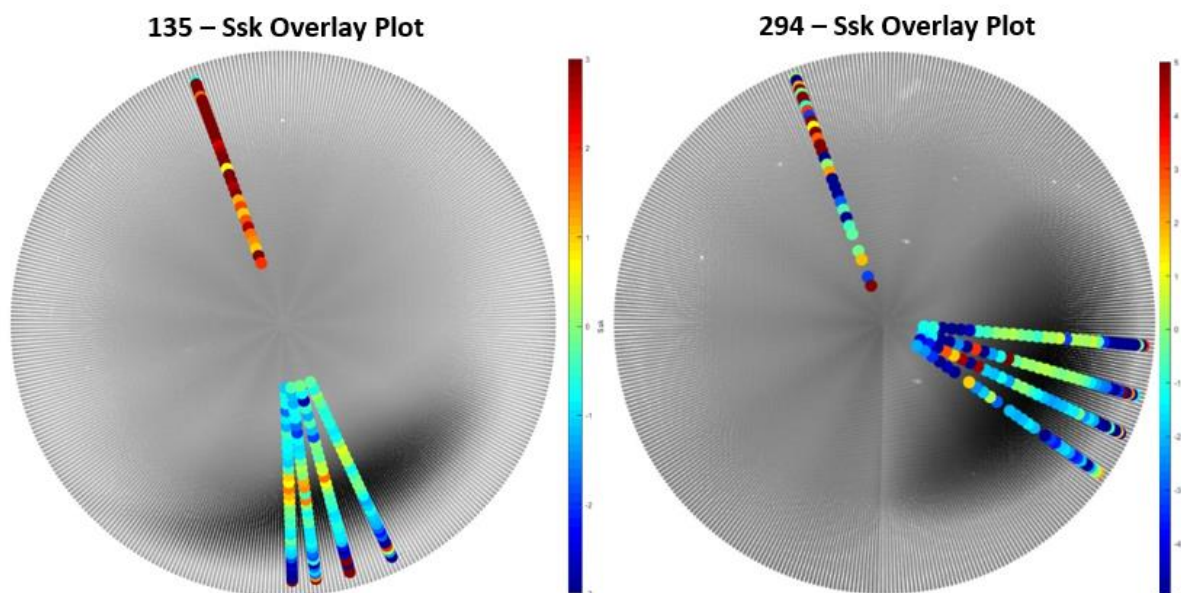


Figure 210: Ssk overlay plots of stitch measurements on femoral heads 135 and 294.

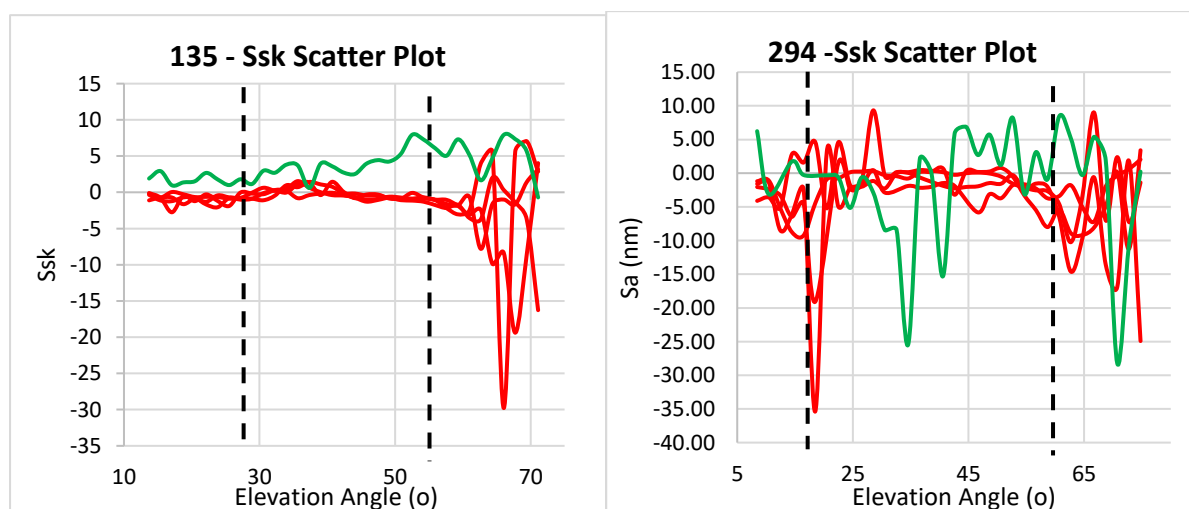


Figure 211: Ssk scatter plots of all stitch lines. Red lines represent the stitches through the wear area, the green line represents the stitch taken through the unworn area. Black dashed lines represent the start and end point of the wear area.

6.4.3.4 Surface Topography Mapping

The wear area is defined by CMM measurement and indicates where the measurable loss of material has occurred. This wear area is likely to contain the location of most roughening, however its shape does not perfectly represent the shape of the surface topography change. By creating an overlay plot of all the surface measurements taken on the worn femoral heads, both the grouped measurements and stitch measurements, the area of roughening can be estimated and compared to the shape of the CMM measured wear area, figure 212. The more surface measurements that are taken allows for a more precise estimation of the surface topography areas.

Within each defined area we can recalculate the median surface parameter values, by using only the surface measurements within each area. This provides a better dataset compared to the grouped measurement datasets that were previously used, as they were based around the CMM defined wear area shape, whereas these groups are based upon the shape of the change in surface topography areas.

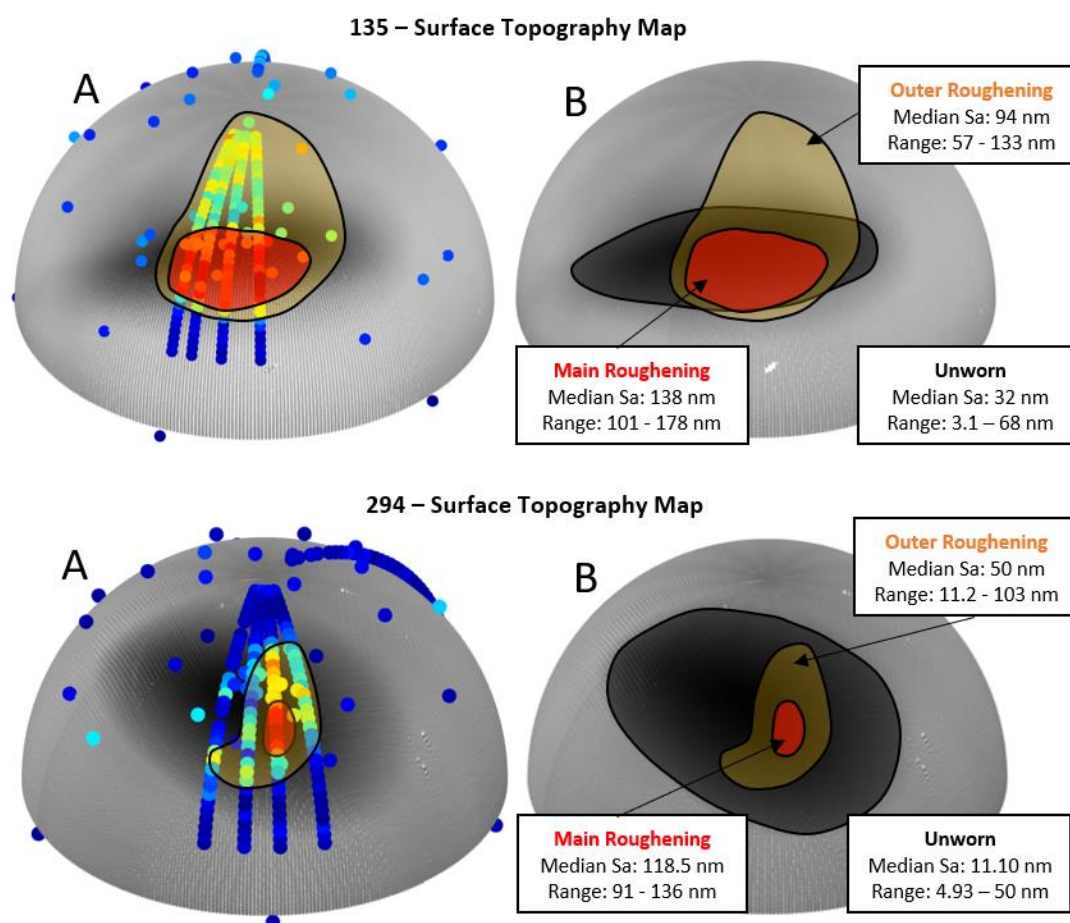


Figure 212: Surface topography maps. A: Surface topography areas plotted using surface measurements. B: Areas of surface topography change (red/orange areas) compared to the wear scar area (black area).

For femoral head 135, we can see that the area of most roughening (Median Sa: 138 nm) is at the lower centre of the wear area, there is also a lower but significant level of roughening (Median Sa: 94

nm) from the centre of the wear area towards the pole. Underneath the wear area it can be observed that the roughening stops abruptly, and the surface becomes smooth. For femoral head 294, we can see that the area of most roughening (Median Sa: 118.5 nm) is very small in size and is located towards the lower right of the wear area. The lower level of roughening (Median Sa: 50 nm) is also relatively small in size, leaving plenty of the wear area having little to no increase in roughness compared to the unworn surface.

Both examples also show that the area of roughening does not clearly match the shape of the CMM defined wear area. The area of roughening can extend out of the wear area as shown by femoral head 135. The area of roughening can also be very small within the wear area as shown by femoral head 294, main roughening area size: 1.84 x 5.51 mm. This demonstrates how easy it is to miss critical surface topography, highlighting the importance of accurate positioning of measurements, and taking many measurements, in particular stitching measurements through the wear area.

As previously discussed the median surface parameter values for each surface topography area have been recalculated using only the surface measurements within each determined area. Figure 213 compares the Sa values in the unworn area compares to the main roughening area as defined from the surface topography mapping. For component 135 the Sa increases from 32 to 138 nm, whereas for component 294 the Sa increases from 11.1 to 118.5 nm. Previously the increase from the unworn to the wear area was calculated using grouped measurements as 32.49 to 121.5 nm (135) and 11.1 to 67 nm (294). For femoral head 294 the increase in roughening was poorly represented by the median value from the grouped measurements within the central wear area. By using surface topography mapping, a larger median value of the main area of roughening is calculated at 118.5 nm.

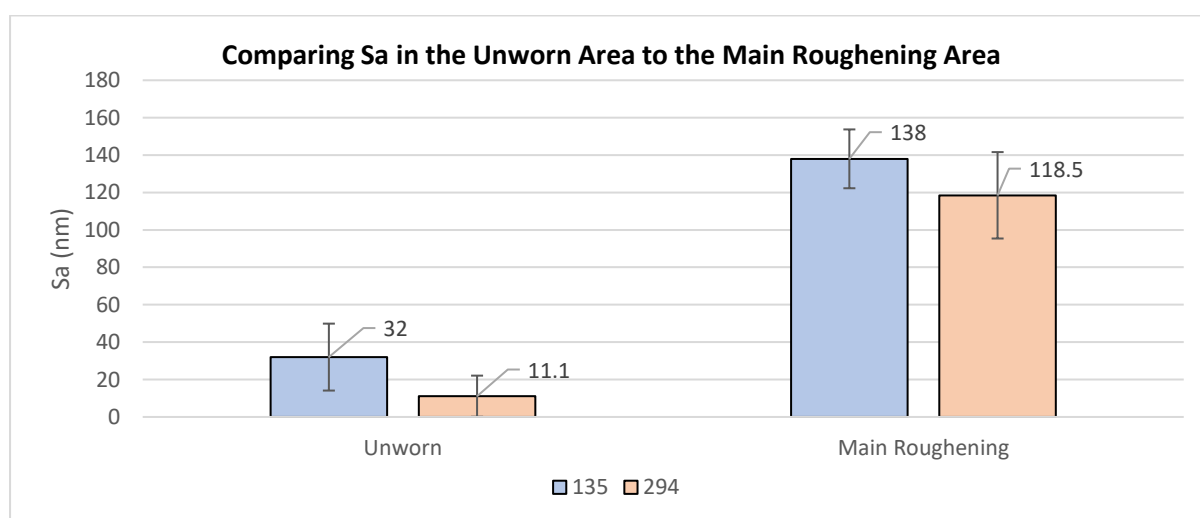


Figure 213: The median Sa values in both the unworn area and the main roughening area, 1 SD error bars.

We can also plot the outer roughening area values in the bar graph, the values from this show that there is an area of lesser roughening around the main roughening area which is to be expected.

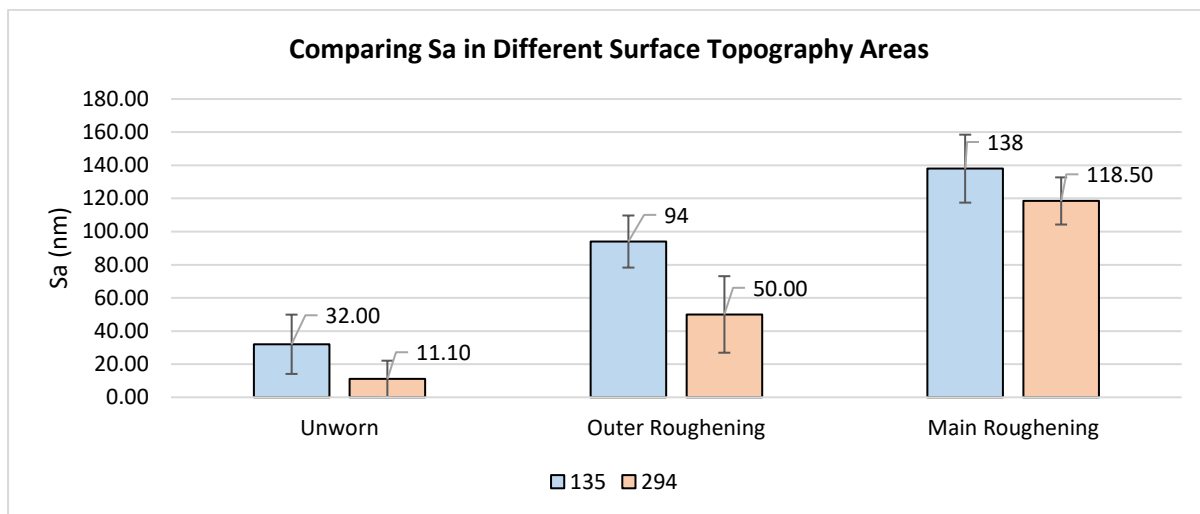


Figure 214: Median Sa values in surface topography areas, 1 SD error bars.

The Sdr values are now plotted as bar charts for the defined surface topography areas. It is clear that in the unworn areas the median Sdr values are very low for both femoral heads 0.012% (135) and 0.05% (294), representing a smooth surface with low complexity. In the roughened areas the median Sdr values increase for both femoral heads, as the roughened surface has more complexity. For femoral head 135 the median Sdr is slightly greater in the outer roughening area 0.1240% compared to the main roughening area 0.1030%, this indicates a greater level of complexity in the outer roughening area, and more surface features. For femoral head 294 the outer roughening area has a lower median Sdr value 0.0410% compared to the main roughening area 0.1810%.

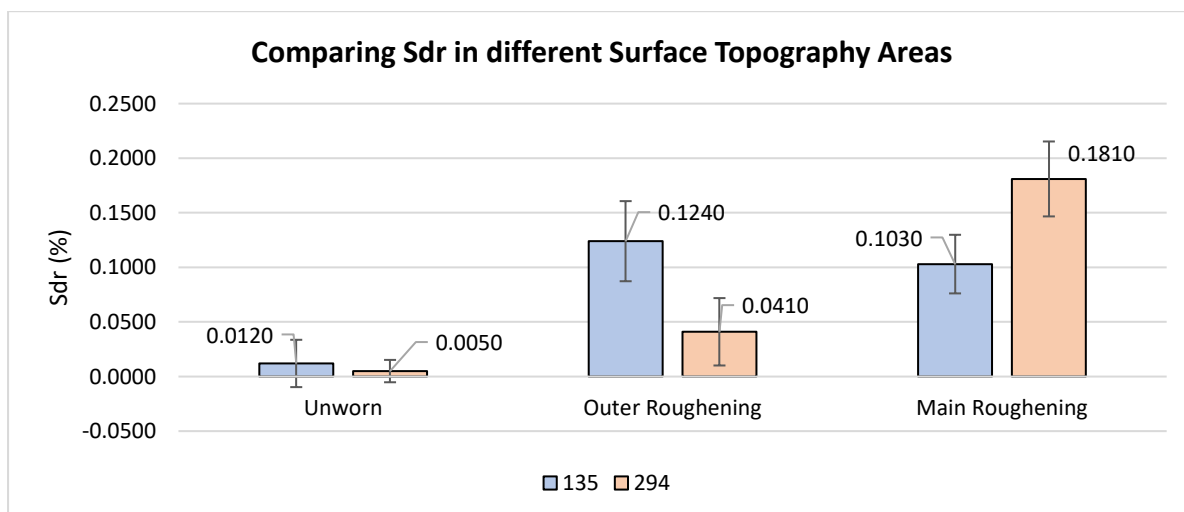


Figure 215: Median Sdr values in surface topography areas, 1 SD error bars

The Ssk values are now plotted as bar charts for the defined surface topography areas. The median values in all areas for both femoral heads are all relatively close to 0, more important to consider rather than the median value is the size of the error bars. We can see that in the unworn areas the large amount of variation shown by the error bars 7.31 SD (135) and 10.51 SD (294). This level of variation reduces in the outer roughening area 0.858 SD (135) and 2.03 SD (294) and main roughening area 0.7 SD (135), 0.22 SD (294). This indicates that in the unworn area, the Ssk can vary greatly, due to the high influence of a small number of features on the unworn surface, whereas in the rougher areas the Ssk values are consistently closer to 0, due to the surface being more random (Gaussian) in nature.

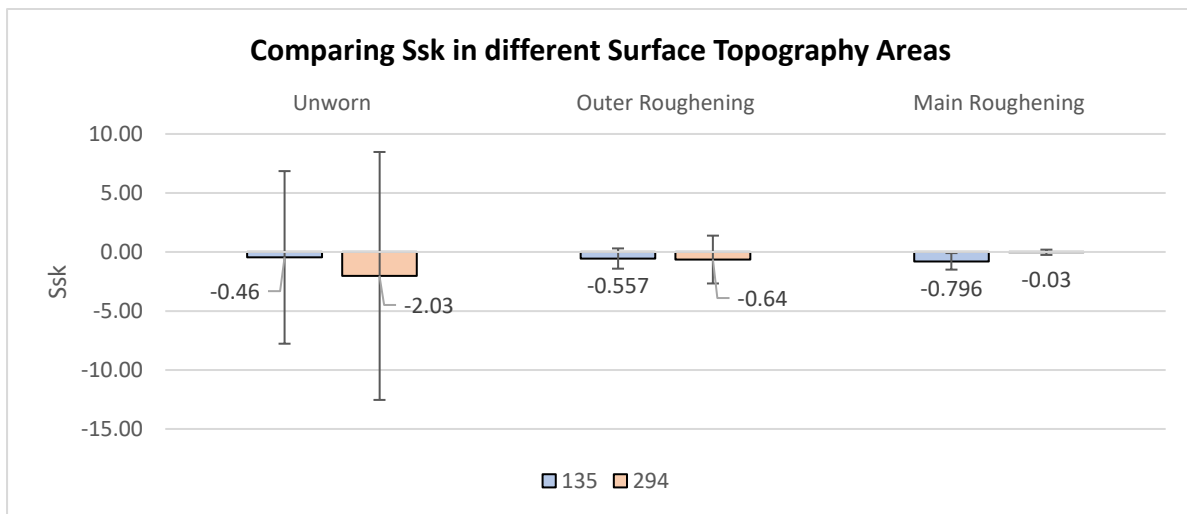


Figure 216: Median Ssk values in surface topography areas, 1 SD error bars.

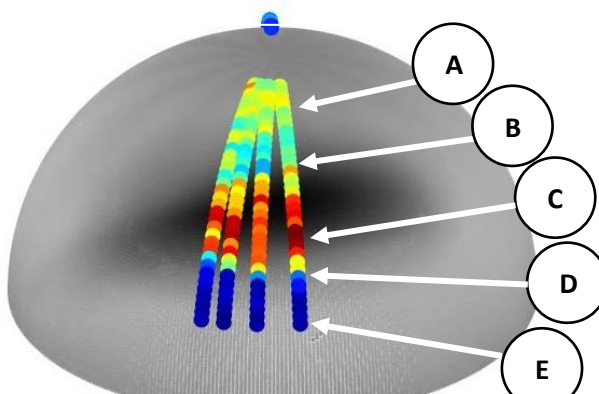
6.5 Discussion

6.5.1 Stages Through the Wear Area

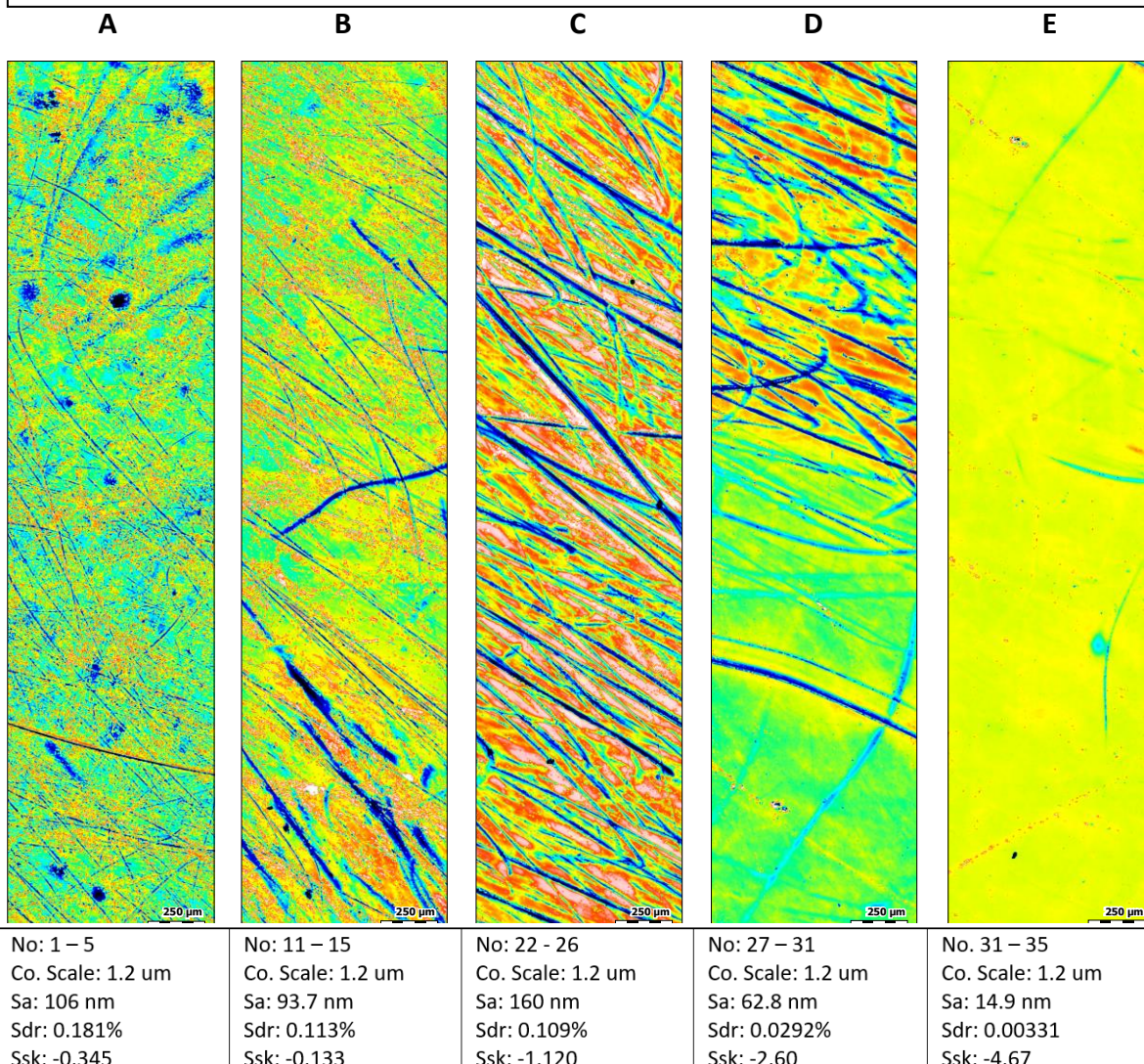
By stitching together surface images we can create a continuous surface measurement through the wear area. Allowing crucial stages through the wear area to be highlighted and analysed in terms of tribological mechanisms potentially occurring. The following surface images are taken from the 4th stitch line through the wear area of femoral head 135.

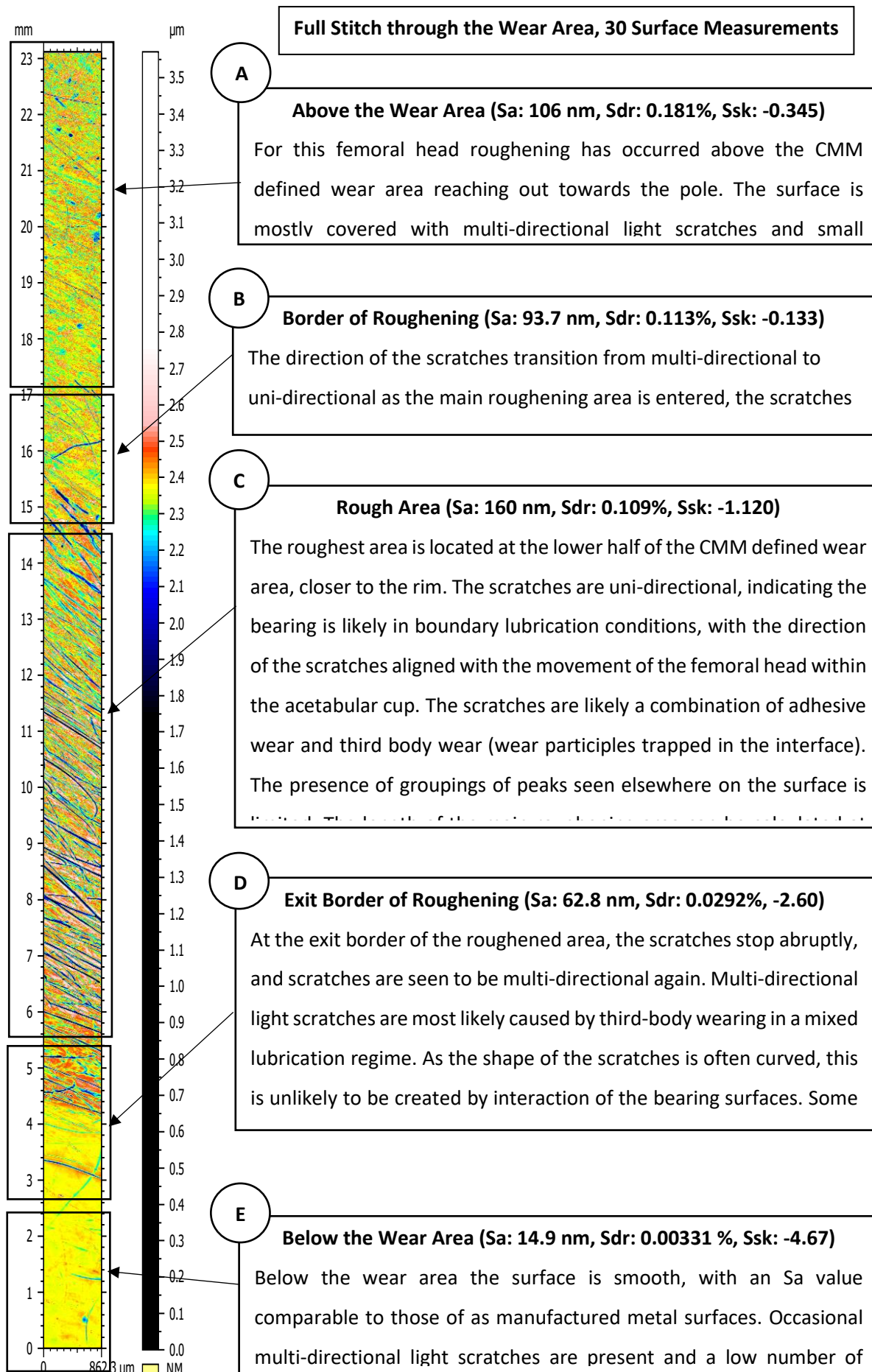
Femoral Head 135 – Stages Through the Wear Area

4th stitch line, start angle: 13.7°, end angle: 71.1°, 35 measurements.



Key Sections of the Stitch Through the Wear Area – 5 Surface Measurements Each

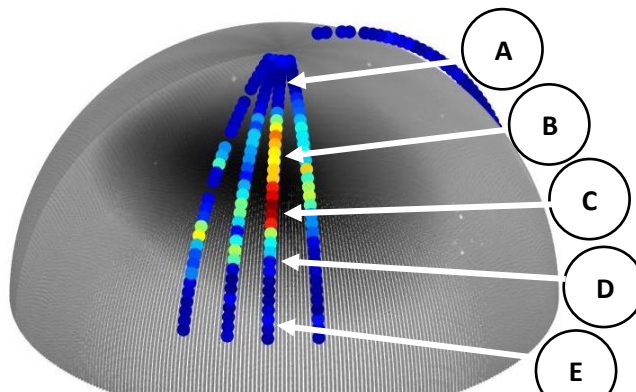




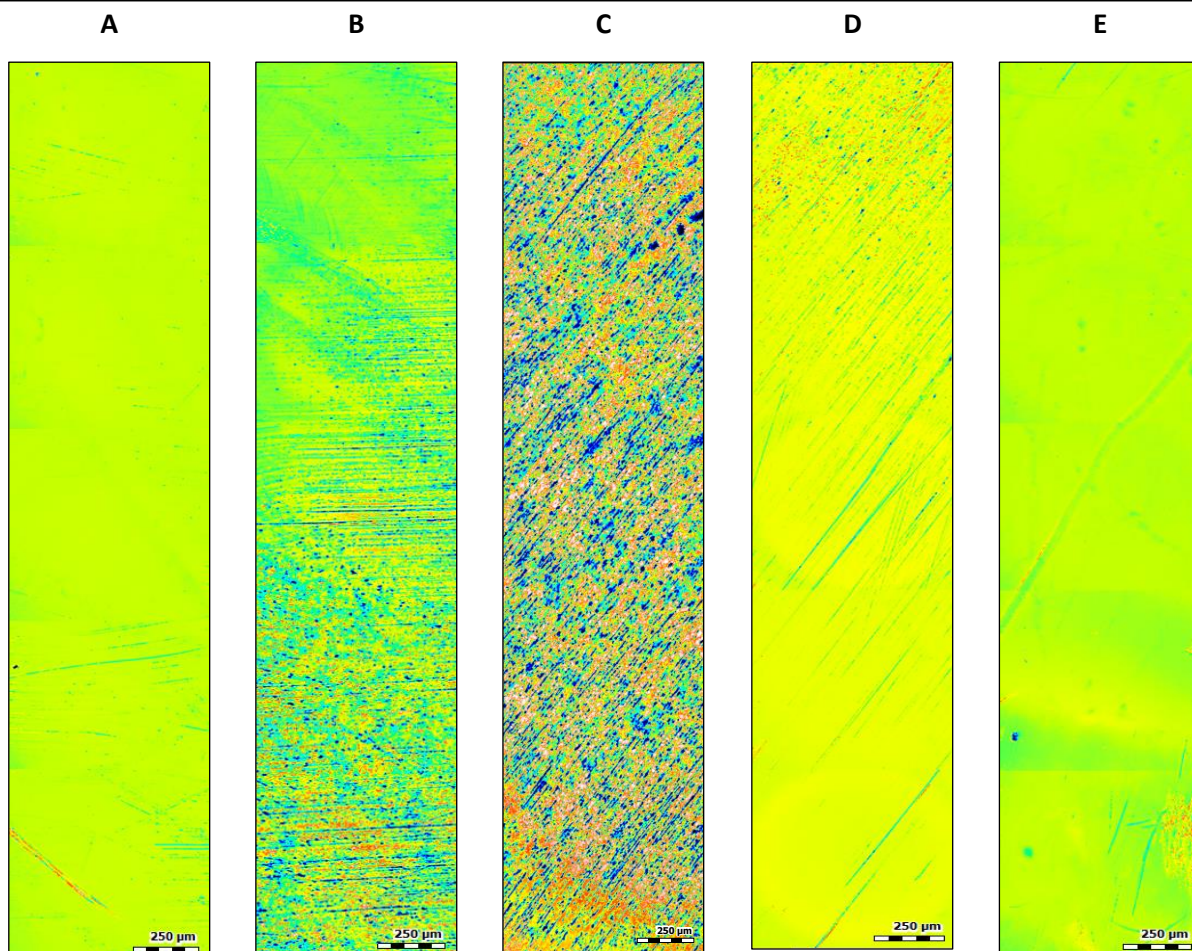
The following surface images are taken from the 3rd stitch line through the wear area of femoral head 294. For the full-length stitch, automated stitching was not possible due to the lack of surface features in smooth regions, therefore some of the overlap regions are still included in smooth areas.

Femoral Head 294 – Stages Through the Wear Area

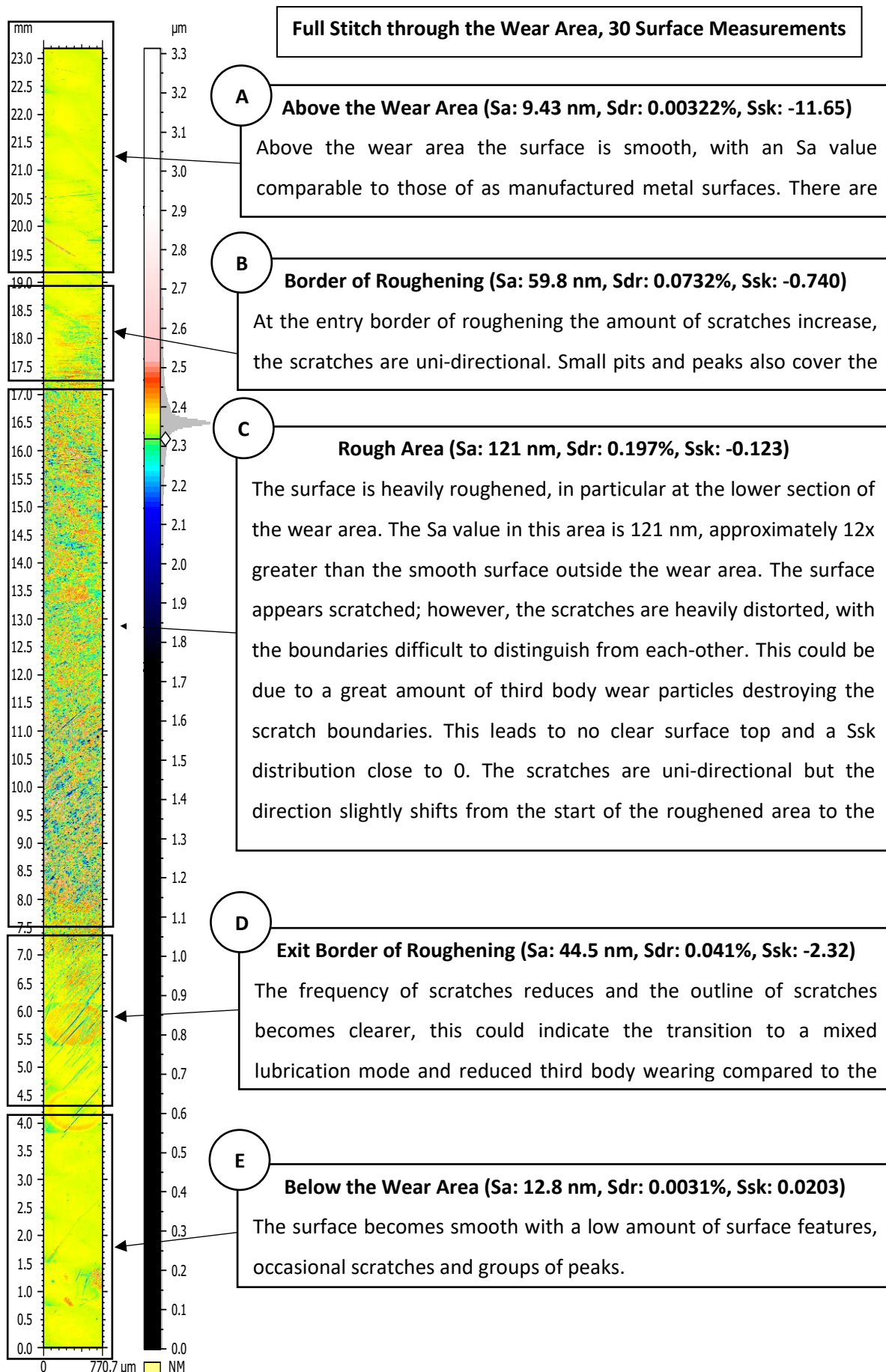
3rd stitch line, start angle: 8.44°, end angle: 74.8°, 34 measurements.



Key Sections of the Stitch Through the Wear Area – 5 Surface Measurements each



No: 3 - 7 Co. Scale: 1.2 um Sa: 9.43 nm Sdr: 0.00322 % Ssk: -11.65	No: 8 - 12 Co. Scale: 1.2 um Sa: 59.8 nm Sdr: 0.0732 % Ssk: -0.740	No: 18 - 22 Co. Scale: 1.2 um Sa: 121 nm Sdr: 0.197 % Ssk: -0.123	No: 23 - 27 Co. Scale: 1.2 um Sa: 44.5 nm Sdr: 0.041 % Ssk: -2.32	No: 29 - 32 Co. Scale: 1.2 um Sa: 12.8 nm Sdr: 0.0031 % Ssk: 0.0203
--	--	---	---	---



6.5.2 Surface Pattern Groups

Individual surface measurements can be analysed and grouped together in terms of the common surface patterns found on the retrieved femoral heads. It is important to note that often the surface topography is a mixture of these surface patterns.

Pristine Condition

Figure 217 shows a pristine surface example. There are no scratches on the surface, with a low Sa value, < 10 nm, as smooth as a freshly manufactured metal surface. This type of surface is most likely to be found on the rim of the femoral head, it will not be found in or near the wear area. Scratches are not present, but pitting holes (circled in red) or groups of peaks (circled in blue) could be present on the surface.

This surface is ideal for a bearing as there are very few asperities to be removed through wearing and low roughness is ideal to improve the presence of lubricant, keeping bearing surfaces separate in a full fluid lubrication mode.

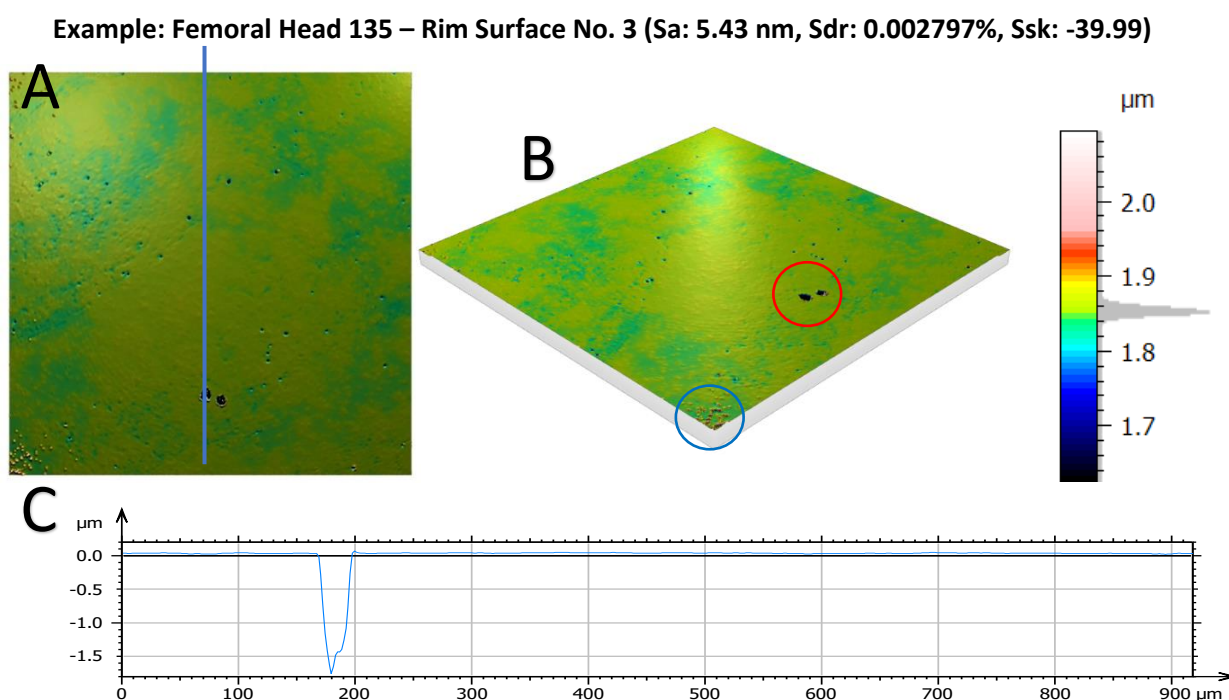


Figure 217: Pristine Condition, Surface Image. A: Top View, B: Angled View, C: Profile Line Result.

Multi-directional Light Scratches

Figure 218 shows a multi-directional lightly scratched surface, this is the most common surface type found on the worn femoral heads, commonly found on the unworn surface area. Although the presence of scratches on the surface is clear, these scratches are very light and do not significantly increase the Sa value.

The author contends that the multi-directional light scratches are caused by third body wear debris in a mixed lubrication mode. As the multi-directional scratches are often curved and random in direction it is unlikely these scratches are within the area of most contact pressure or boundary lubrication conditions. Instead wear debris within the interface moves relatively freely in this portion of the femoral head, creating light scratches. The multi-directional light scratches often lack raised edges on the sides of the scratch, this could indicate the ridges have been removed or the scratch is light.

Multi-directional light scratches still allow for a good bearing surface when scratches are light and are formed as indentations, however the depth and severity of the scratches can vary. Deeper scratches can also occur (circled in red), which have scratch edges formed, due to ploughed material during third body cutting, indicating wear and the creation of new surface asperities as raised edges.

Example: Femoral Head 109 – Unworn Surface No. 12 (Sa: 6.098 nm, Sdr: 0.004527, Ssk: -7.927)

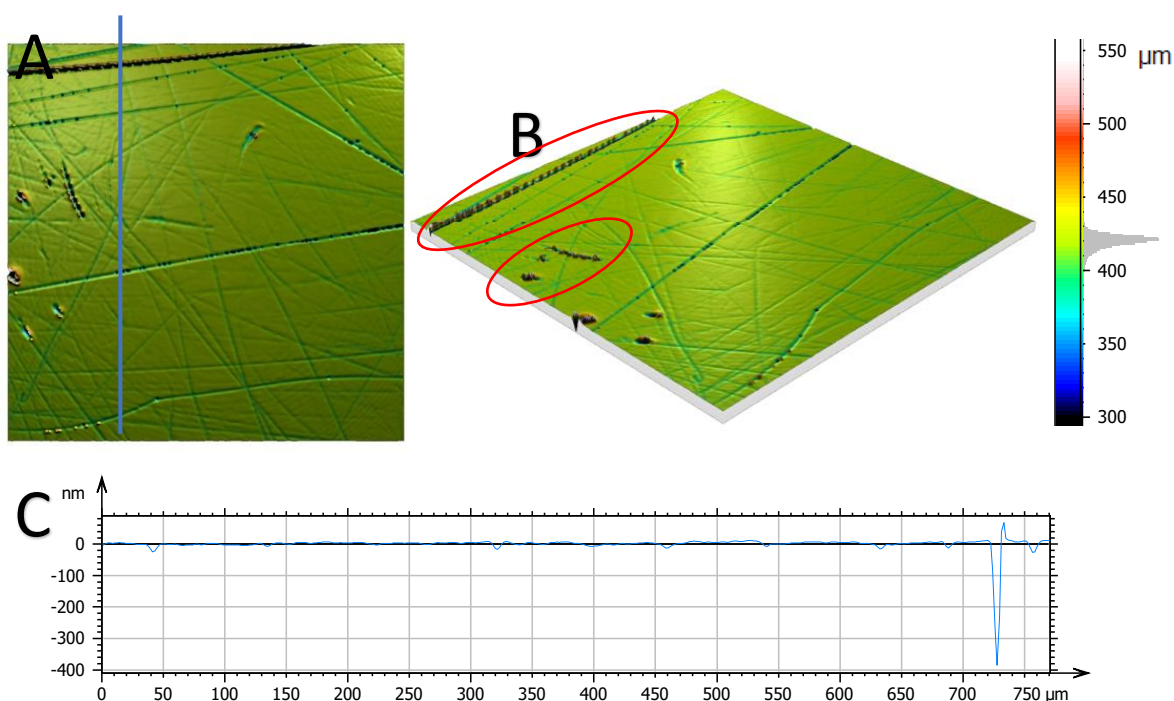


Figure 218: Multi-directional Light Scratches, Surface Image. A: Top View, B: Angled View, C: Profile Line Result.

Groups of Peaks / Metallic Carbides

Figure 219 shows a surface covered with small peaks, this is a relatively common surface type found on the retrieved metal femoral heads. Usually the peaks are grouped together in an area smaller than the example shown. Individual peaks are 8-15 μm in diameter and usually spherical. It seems unlikely that this surface was created through wearing of the surface as there is no evidence of scratching, it is more likely that this surface is as manufactured. It is likely that these peaks are metallic carbides that have been previously measured on CoCr surfaces [19]. These peaks are not ideal for the bearing surface as it creates many surface asperities which can be removed as wear debris. The carbides are generally harder than the surrounding material and are not efficiently removed during polishing. Conversely there is evidence of carbide pull out during over polishing and this leaves the reported comet tails on the as manufactured surface [194].

Example: Femoral Head 131 – Unworn Surface No. 15 (Sa: 33.71 nm, Sdr: 0.02496%, Ssk: 1.419)

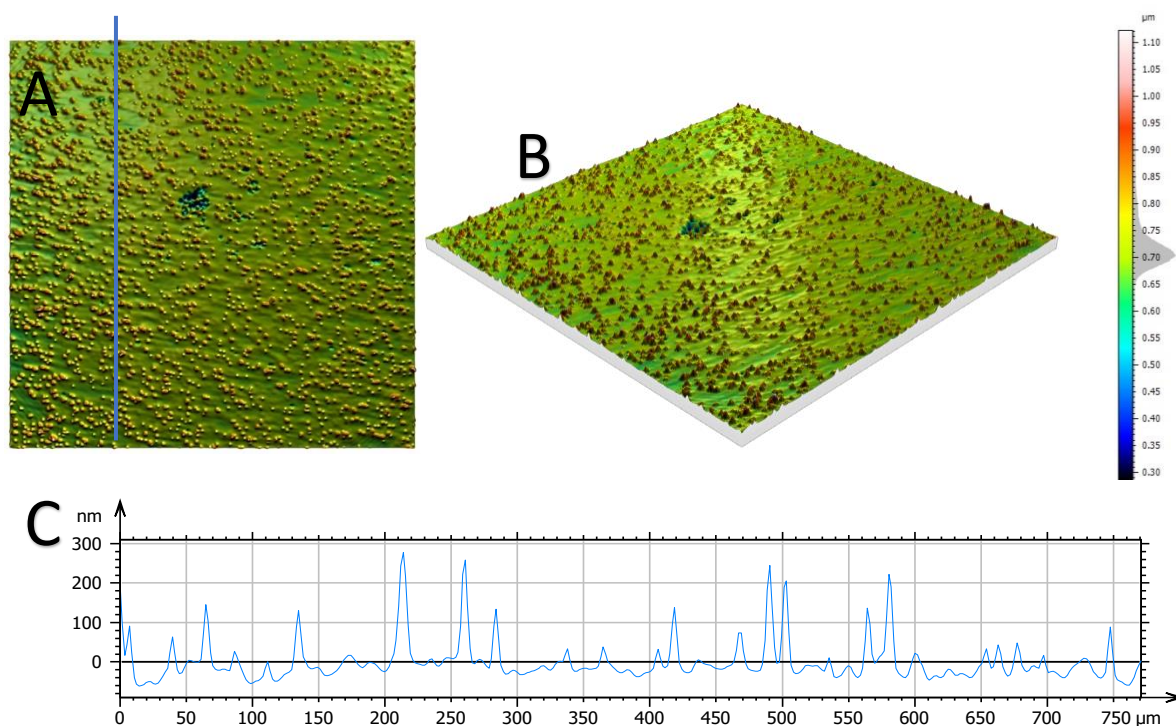


Figure 219: Groups of Peaks, Surface Image. A: Top View, B: Angled View, C: Profile Line Result.

Pitting / Pull Out Metallic Carbides

Figure 220 shows an example surface with pitting, the presence of pitting causes a slight increase in S_a , but still allows for a good bearing surface as no surface asperities are created. The size of the pitting holes closely match the peaks shown in figure 219. Potentially the pitting holes are created by the adhesive pull out of the metallic carbides, this explains the similar sizing and groupings of the holes to that shown in figure 219. This would mean the pull out of the metallic carbides is creating wear debris and leaving these pitting holes, often termed comet tail defects, behind. These pitting holes have been noted on freshly manufactured components and would therefore could be created during the polishing process, pre-implantation, possibly by excessive loads or excessive polishing times [194].

Example: Femoral Head 213 – Unworn Surface No. 18 (S_a : 19.3 nm, S_{dr} : 0.01454%, S_{sk} : -10.1)

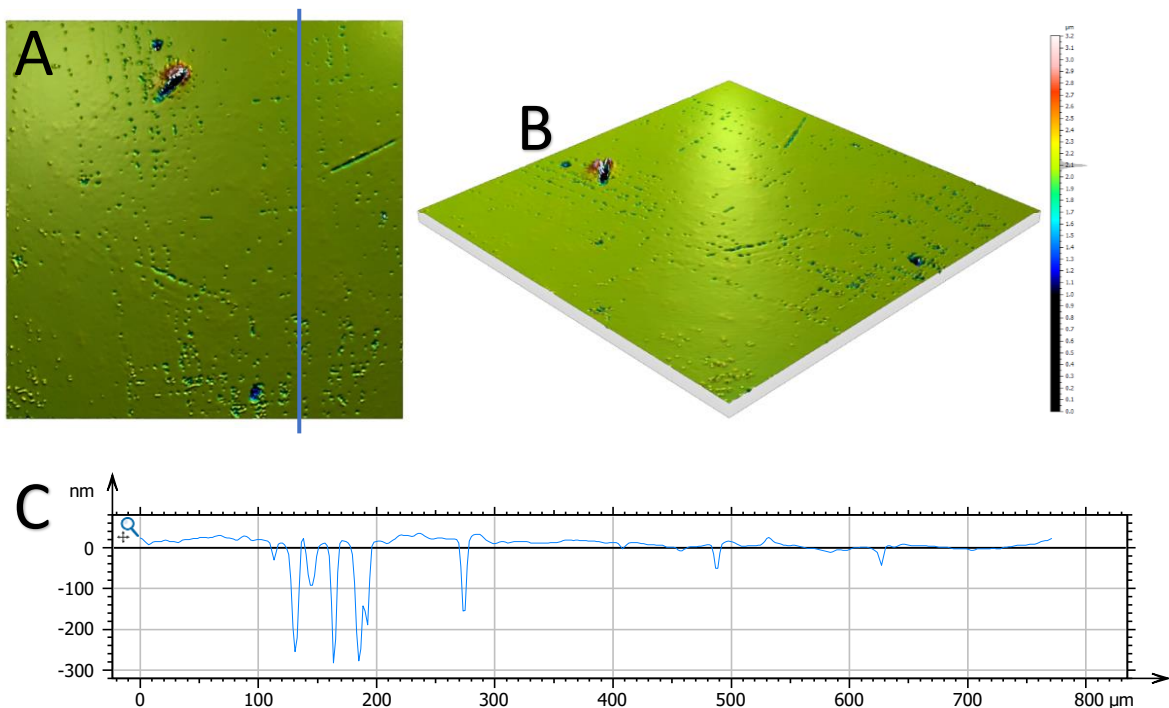


Figure 220: Pitting Holes, Surface Image. A: Top View, B: Angled View, C: Profile Line Result.

High Roughness Uni-directional Scratches

Figure 221 shows an example of high roughness uni-directional scratches, this type of surface is found within the wear area. The uni-directional scratches indicate that the bearing is acting in a boundary lubrication mode, the scratches aligned with the movement of the femoral head within the acetabular cup. The scratches will be a combination of adhesion and third body wear.

This surface is not ideal for the bearing interface, the high Sa value will increase the chance of surface asperities interacting at the bearing. The Sa value in this area, 169 nm, is approximately 47x greater than the pristine surface found on the rim of this component, 3.57 nm. The author contends that the surface will continue to change as wearing takes place, creating more uni-directional scratches, this could potentially lead to a temporary smoothing of the surface, before roughening again takes place. This cycle of roughening and smoothing is not ideal as it leads to the continual production of wear debris.

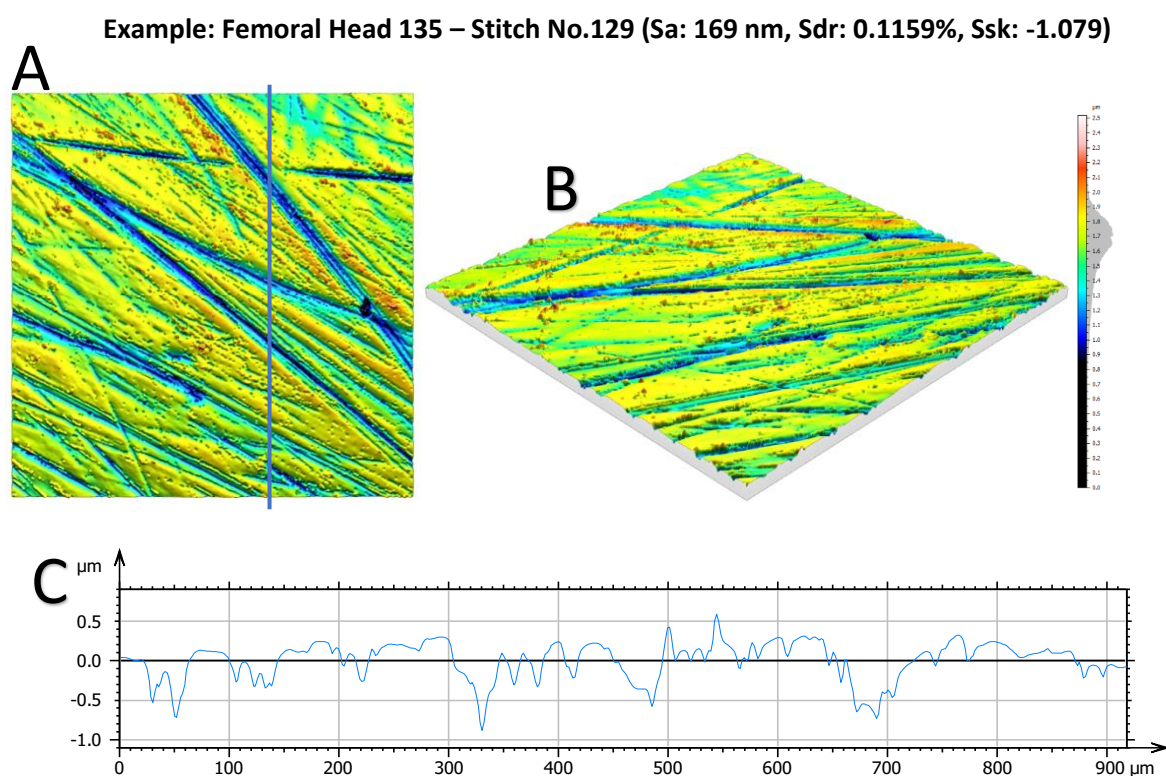


Figure 221: High Roughness Uni-directional Scratches, Surface Image. A: Top View, B: Angled View, C: Profile Line Result.

High Roughness Distorted Uni-directional Scratches

Figure 222 shows an example of high roughness distorted uni-directional scratches. This surface is found within the wear area. Similar to figure 221, the uni-directional scratches indicate the bearing is acting in boundary lubrication mode, the scratches aligned with the movement of the femoral head within the acetabular cup. During boundary lubrication, the scratches are likely to be a combination of adhesive and third body wear. Crucially the scratches on this surface are distorted with often no clear scratch edge, this is what distinguishes it from figure 221. The author contends this distortion is from either an increased amount of third body wear, with a large amount of trapped debris, continually modifying and wearing the scratch boundaries, leading to this distorted surface. Potentially after an initial roughening period, smoothing of the surface can occur through more wearing, this behaviour would continue to cycle. This would also flatten/remove the scratch boundaries, leading to this distorted surface.

This surface is not ideal for the bearing interface, the high Sa value increasing the chance of the bearing surfaces interacting. Also, a very high amount of surface asperities, leading to a potential large amount of wear debris creation. The Sa value in this area, 135 nm, is approximately 19x greater compared to the pristine rim surface, 7.2 nm. Similar to the previous rough surface example, a heavy wear cycle of roughening to smoothing could occur at this area.

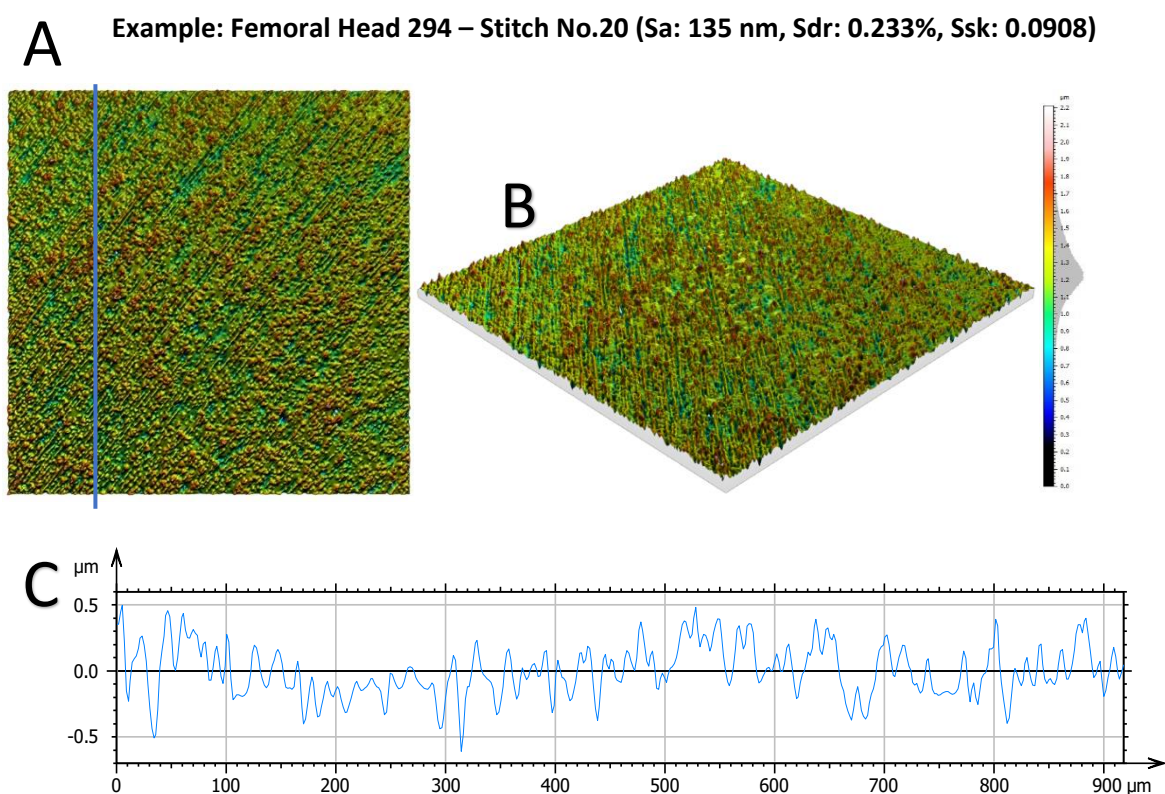


Figure 222: Destroyed Surface Uni-directional Scratches, Surface Image. A: Top View, B: Angled View, C: Profile Line Result.

6.5.3 MoM Wear Mechanism Theory

Examples of the roughened surface on the femoral heads have been shown above, figures 221 and 222, it is now possible to theorise the stages of how the surface reached this state. It is important to note that both these worn femoral heads exhibited relatively low wear rates, 3.5 and 3.0 mm³, therefore more heavily worn bearing surfaces may show greater levels of surface roughening.

Stage 1 – As Manufactured Pristine Surface

The initial surface begins with a highly polished smooth finish, with Sa values lower than 5 nm and no scratches on the surface. The only surface features noted are the pitting holes as described earlier, these are considered to be pull out of metallic carbides, which could occur during the polishing process. Figure 223 shows example surface measurements of the pristine surface.

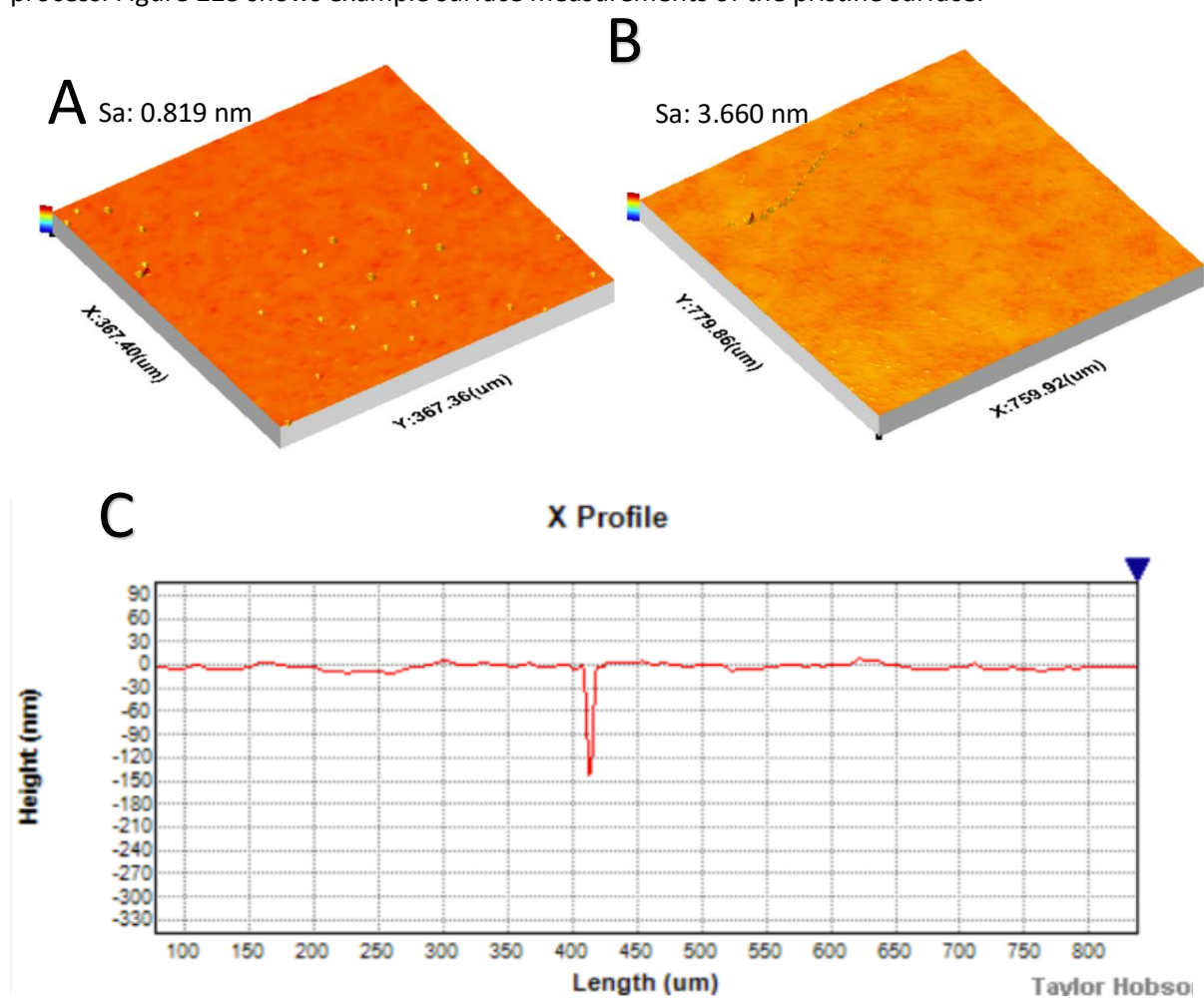


Figure 223: Pristine Metal Femoral Head Surface. A: Unused femoral head surface. B: Pristine surface at rim of retrieved femoral head 135. C: Profile plot of surface B, capturing a single pitting hole feature.

Stage 2 – Wear Area Creation

Ideally the bearing should operate in a full fluid lubrication regime, meaning the load is carried by the lubricating fluid and no contact is made between surface asperities. To achieve this, larger sized, more conformal MoM bearings were first designed. Hard-on-soft bearings typically do not achieve full fluid lubrication, instead operating in mixed/boundary modes, leading to higher wear rates. However due to the softer polymer material the contact pressure is lower compared to that of hard-on-hard bearings acting in similar mixed/boundary lubrication conditions. The chances of boundary lubrication conditions occurring increases with steeper inclination angles, increased load on the bearing, and out of tolerance sized femoral head/acetabular cup components.

The contact area will occur at the area of maximum load, this is on the supero-lateral aspect of the femoral head, figure 224. If full-fluid lubrication conditions are not achieved, wearing of the contact area will begin, increasing the roughness of the contact area surface.

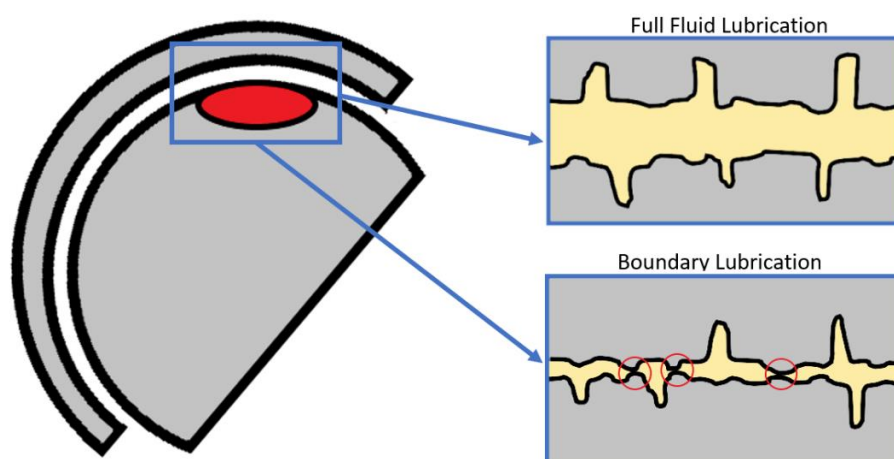


Figure 224: Contact area at the bearing interface and the possible resultant lubrication regimes.

Stage 3 – Roughening of the Wear Area

For MoM implants the bearing wear will be a combination of adhesive wear and third body wear. Initially adhesive wear will occur at the contact area between the head and the cup if boundary/mixed lubrication modes occur. This will create debris which can become trapped within the bearing, causing further third body wear, or disperse outside the bearing potentially causing adverse tissue reaction and aseptic loosening.

Uni-directional scratches are typically found within the wear area, creating the roughest surface, as the uni-directional scratches are aligned with the general movement of the femoral head within the acetabular cup. Whereas light multi-directional scratches tend to occur outside of the wear area, as third body debris moves around the unworn area of the bearing interface. These findings are further supported by the retrieval studies from Witzleb and Howie [17, 19].

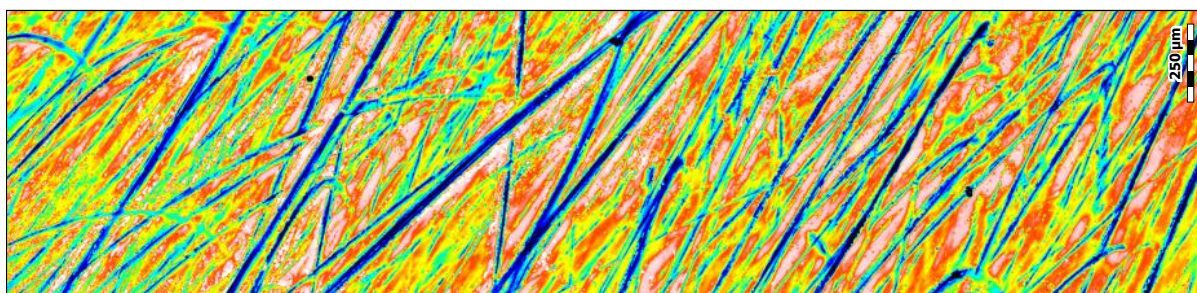


Figure 225: Roughened wear area from retrieval femoral head 135, Sa: 160 nm.

From this project the two worn femoral heads both have clear roughening within their wear areas. However, the roughened surface topography is clearly different. Figure 226 shows the roughened surface of femoral head 294, uni-directional scratches are again shown, however the scratch boundaries are not clear. It is theorised that this is due to either a large amount of third body wear trapped within the interface, this causes further wearing and distortion of the scratch boundaries. Another theory is that after an initial period roughening a smoothing period can occur, see stage 5b.

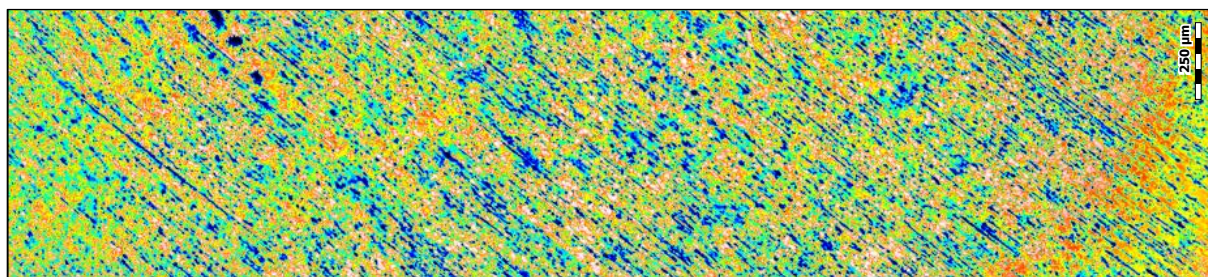


Figure 226: Roughened wear area from retrieval femoral head 294, Sa 121 nm.

Stage 4a – Roughening to Smoothing Cycle

It is considered that after an initial period of roughening, the surface finish could become smoother. See figure 227, once the surface is roughened, large peaks and troughs will cover the surface (A). At this stage, the peaks can be removed through wearing (B), this will leave a smoother surface (C). Now the surface can again become roughened, and the cycle will continue. This process releases wear debris into the interface which is likely to increase wear in specific areas in the future and could initiate osteolysis. The presence of more debris e.g., femoral head 135 may reduce the cycling effect.

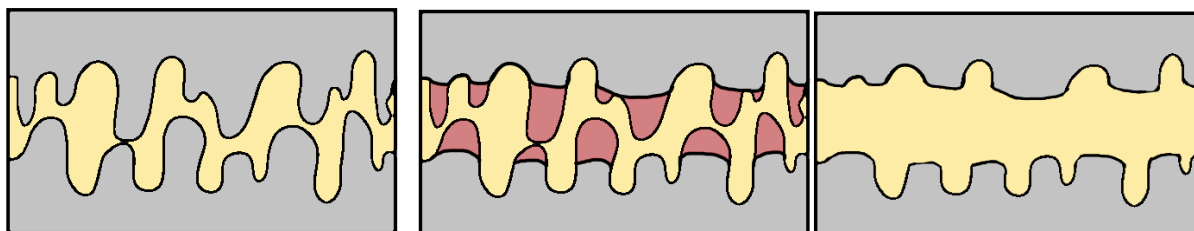


Figure 227: Roughening to smoothing cycle. A: Rough surface. B: Removal of peaks. C: Resultant smooth surface.

Stage 4b – Outwards Spread of the Wear Area

A rough surface is not good for a bearing, there is an increased amount of surface asperities, thus leading to increased risk of asperities being removed as wear debris. However, through enough wearing, the bearing surfaces should separate further away from each other, therefore if enough wear occurs the surfaces will no longer contact, figure 228. The wearing will now occur at the edges of the wear area, this process of the wear area spreading out will continue as the surfaces wear away. However, as this process is occurring, wear debris is being released into the interface which can become trapped as third body debris causing deep scratches. The wear debris could also leave the wear area, interacting with the rest of the bearing surface, causing light multi-directional scratches. Or wear debris could leave the bearing interface completely and potentially initiate aseptic loosening.

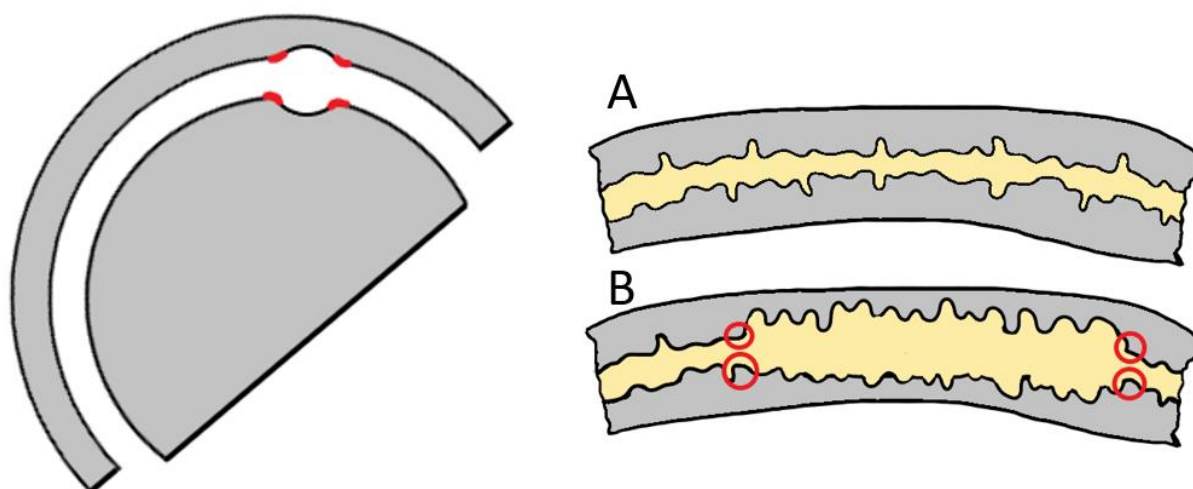


Figure 228: Outwards spread of the wear area. A: Original bearing interface. B: The distance between the bearing surfaces is increased at the wear area, leading to the wear to now occur at the edges of the wear area (circled in red).

6.6 Chapter Summary

Ten large MoM femoral heads were measured to test the effectiveness of the custom fixture system. The method was split into three stages: Firstly, all femoral heads were measured using a CMM to measure the wear of the component and create a wear map. Secondly surface analysis was made on all femoral heads, excluding any wear areas, to determine a baseline of the unworn surface topography. Finally, the femoral heads with a clear measurable wear area delineated by the wear map, were measured again, this time using the custom fixture system for a more detailed surface analysis.

From the initial CMM measurement, two of the ten femoral heads exhibited a clear measurable wear area, with a total volume loss of 3.5 mm^3 (femoral head 135) and 3.0 mm^3 (femoral head 294). These two femoral heads were selected to undergo more detailed surface analysis using the custom fixture system. Two sets of surface measurements were completed on the worn femoral heads, grouped measurements and stitch measurements. The grouped measurement set consists of ten measurements taken within the central wear area, ten at the CMM defined border of the wear area, 20 at unworn areas, and five on the rim of the femoral head. The stitch measurement set consists of four stitch lines through the wear area, and one stitch line through an unworn area.

The grouped measurements indicated a clear increase in roughness for both femoral heads within their wear areas. A downside of grouped measurements is that the boundary of the wear area is unlikely to perfectly match the change in the surface topography on the femoral head. This can lead to measurement groups having median surface parameter values that do not truly reflect the surface topography, unless many more measurements are taken.

Consequently, stitching of a linear band of surface measurements can provide a better analysis, ensuring a full line of measurements is taken through the wear area, including both the start and end boundaries and a portion of measurements in the unworn area. This allowed crucial stages through the wear area, such as the border of the wear area, to be analysed in depth in terms of tribological mechanisms.

The analysis tool, surface topography mapping, was developed by overlaying the surface measurement data onto the CMM wear map, the areas of roughening were compared to the shape of the CMM measured wear area. The more surface measurements that are taken allows for a more precise estimation of the surface topography areas. For both femoral heads, the CMM defined wear area did not closely match the areas of roughening. For femoral head 135 the area of most roughening was at the lower centre of the wear area, however the roughening extended out of the CMM defined wear area and towards the pole of the femoral head. For femoral head 294 the area of roughening

was much smaller than the CMM defined wear area and was limited to the lower right of the wear area. Within each surface topography area, the median surface parameter values were calculated. The surface parameter results showed an increase in S_a from 32 nm in the unworn areas to 138 nm in the main roughening area (femoral head 135) and 11.1 nm to 118.5 nm (femoral head 294). Using this surface measurement data, in particular the results from the stitch measurements, the tribological wear mechanisms occurring for MoM implants were theorised.

Chapter 7: Project Conclusions

7.1 Attainment of Aim and Objectives

The originally set aims and objective have been successfully achieved:

Aims

- The main aim of developing an advanced fixture system has been successfully achieved.
- The cost of the fixture system was kept low, below £3000.
- The fixture system allowed for high accuracy positional control, with a total positional error of $\pm 0.04021^\circ$.
- The fixture system is compatible with most common CMMs and surface metrology instruments.
- Using the developed custom software, data fusion of captured CMM and surface data is achieved.
- The fixture system allows for surface measurements to be stitched together across the hip implant bearing surface.

Objectives

- The fixture system hardware was successfully designed and manufactured.
- The fixture system software was successfully developed.
- The fixture system was thoroughly tested, and the resultant positional error was calculated.
- The fixture system was used to analyse a range of MoM retrieval femoral heads.

7.2 Major Conclusions

Through the successful development of the custom fixture system, a novel surface measurement method for worn hip implant bearings has been created, facilitating accurate data fusion of CMM and surface measurement datasets. Surface analysis tools such as surface topography mapping and stitching through the wear area now allows the worn bearing surface to be studied at a level of detail previously unattainable.

Testing of the custom fixture system has been completed, calculating the positional error of the custom fixture system as $\pm 0.04021^\circ$. This was well within the target positional uncertainty value, $\pm 0.0877^\circ$, therefore stitching of surface measurements was achievable. The azimuth positional error caused by the relocation of the fixture from the CMM to the surface metrology instrument was calculated as $\pm 0.915188^\circ$.

A cohort of ten MoM femoral heads were measured to test the effectiveness of the custom fixture system. From the cohort, two of the ten femoral heads exhibited a clear measurable wear area. Using the custom fixture system these two femoral heads underwent extensive surface analysis, including surface topography mapping and stitching of surface measurements through the wear area. The femoral heads were shown to roughen within their wear areas, and crucially it was noted that the areas of roughening did not closely match the shape of the CMM defined wear area. Using the stitch measurements through the wear area was particularly effective to theorise tribological wear mechanisms for MoM implants.

This new method allows for better judgment of hip implant performance and can be utilised for both in-vitro and in-vivo testing for all material types. As the development costs of the fixture were kept minimal, redevelopment across industry or research environments is achievable. Alternatively, instead of use for wear testing, the fixture system can also provide useful for quality inspection of newly manufactured components.

7.3 Benefits of the Custom Fixture System

Increased Surface Topography Data Capture

It has been shown in previous literature and in this project that the area of greatest surface topography change is at the wear area of the component. However, this project has shown that the area of roughening does not closely match the shape of the CMM measured wear area, the area of roughening can be smaller than the wear area (femoral head 294) or extend out of the wear area (femoral head 135).

A common surface measurement method for analysis of the wear area would consist of 5-10 equally spaced measurements within the wear area, using a manual adjustment fixture with poor positional accuracy, this could lead to multiple measurements, or all, missing the area of roughening, leading to an inaccurate analysis. For example, figure 229 shows the surface measurements taken using the custom fixture system on femoral head 294 (A). This includes four stitches through the wear area and a set of grouped measurements, this allows the surface topography areas to be defined. If a manual fixture is used with poor positional accuracy (B) for 10 surface measurements, then the measurements may not capture the roughening, and the area of most increased roughness (red area) could be missed entirely. This leads to an inaccurate surface analysis of the femoral head wear area, with a significant underestimation of the roughening. The average surface parameter values from the 10 measurements using the manual fixture will not accurately represent the actual surface topography.

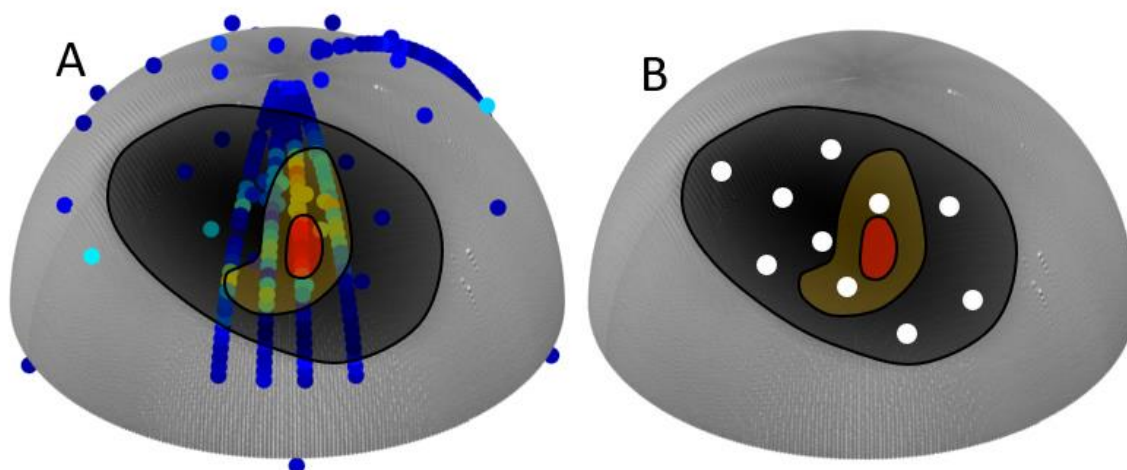


Figure 229: Comparison of fixture methods. A: Custom fixture system. Black area represents CMM defined wear area, whereas orange and red areas represent areas of roughening, defined via surface measurements. B: Manual fixture. White circles represent example locations of surface measurements taken within the wear area. Only two are taken in areas of roughening, none capture the main roughening area (red area).

Quicker Surface Measurement Time

It should also be noted that as the fixture system is motorised and surface measurement locations can be pre-selected on the control software, surface measurements can be taken much quicker compared to when using traditional fixture setups. There is no need for fixture/component adjustment between each measurement, simply the push of a button tells the fixture to move the bearing component to its next pre-determined location. This allows for more surface measurements to be taken in a similar time span.

Advanced Surface Analysis Tools

By using the custom fixture system advanced surface analysis tools such as surface topography mapping and stitching through the wear area have been developed. These analysis tools allow the bearing area to be studied at a level of detail previously unattainable and allow for better judgement of hip implant performance.

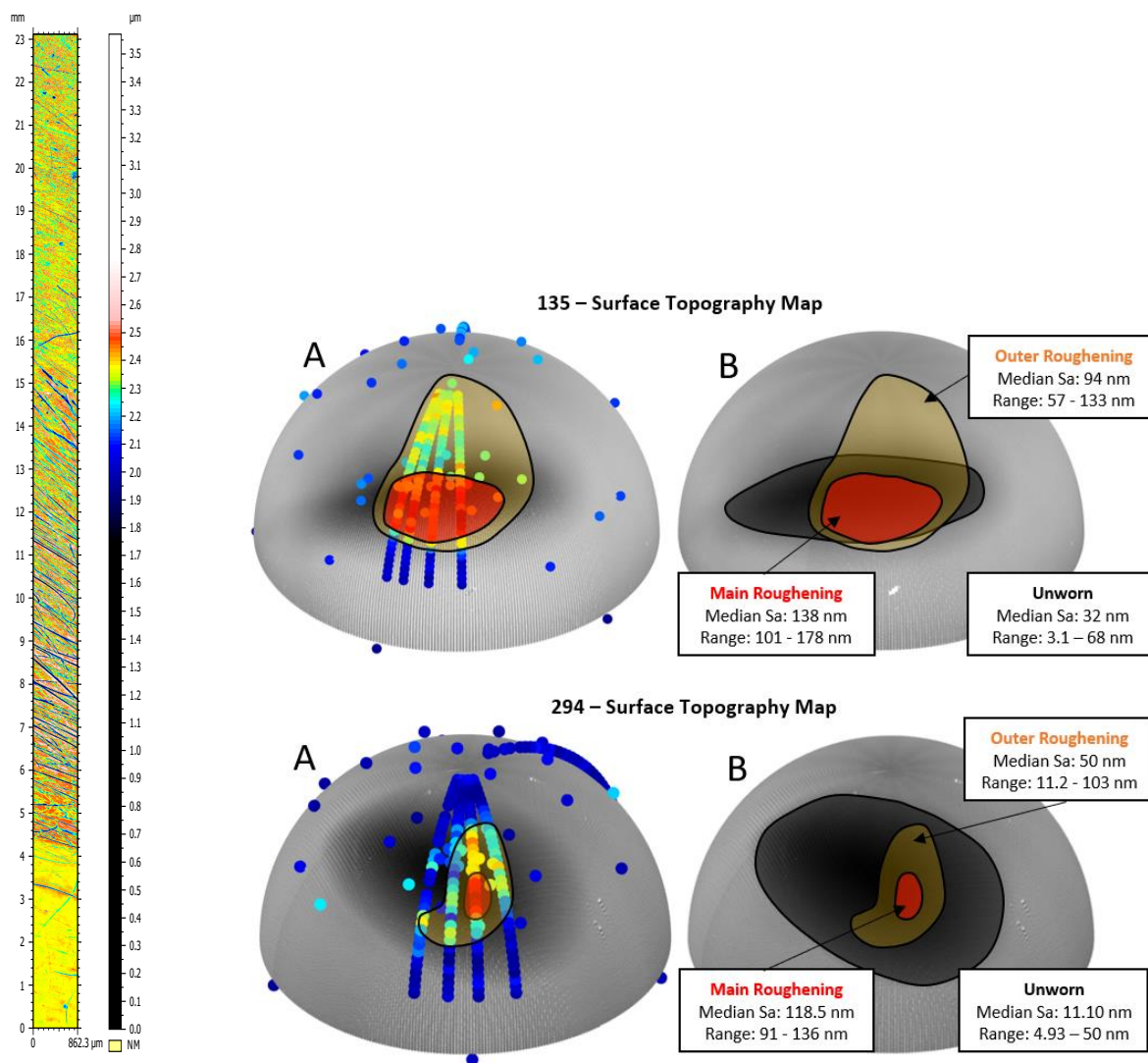


Figure 230: Advanced surface analysis tools. Left: Stitch of surface measurements through the wear area of femoral head 135. Right: Surface topography maps created for femoral heads 135 and 294.

Quality Inspection

Although this fixture was primarily designed for wear analysis of hip implant bearings, it can also provide useful for quality inspection of newly manufactured components. The software can be used to quickly relocate the implant to pre-determined surface measurement locations that are determined by the manufacturer. A stitch (or multiple stitches) can also be created across the entire bearing surface allowing for a detailed inspection of the surface topography, figure 231.

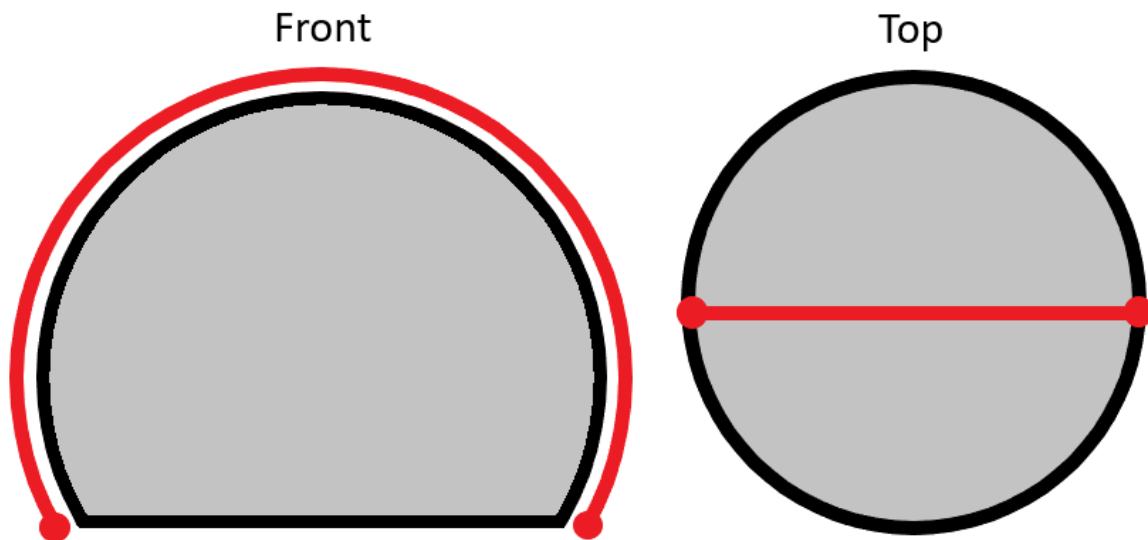


Figure 231: Quality inspection of femoral heads. Red line indicates example stitch line.

Low-Cost Design

The cost of the custom fixture system was kept low, < £3000. This means it can be replicated or further developed relatively easily in research and industry environments. Similar fused metrology instruments that have been developed cost much more, such as the Bruker uCMM [131].

Use of Proven Measurement Instruments

The custom fixture system utilises proven measurement instruments. Instead of creating an entirely new fused measurement instrument, a custom fixture is created to fuse the data from two, tried and tested instruments, the CMM, and the white light surface interferometer. This reduces the cost of the project and ensures measurement data can be considered accurate.

7.4 Novel Contributions

1. Creation of an advanced fixture system for novel surface analysis

The main novel contribution is the development of the fixture system. The creation of this fixture system in turn allowed for novel surface analysis tools to be developed: surface topography mapping and stitching through the wear area. These tools are used for advanced analysis and better judgement of hip implant performance, and these can be implemented for in-vitro and in-vivo testing.

The fixture system also allows for highly accurate positional control of hip implant bearing components during surface measurement, for a relatively low investment cost. The fixture can now be used again for any future hip implant bearing surface analysis.

2. Stitching of surface measurements through the wear area

The stitching of surface measurements through the wear area has always been particularly difficult to achieve for two reasons. Firstly auto-stitching achieved using modern surface measurement instruments is only possible on relatively flat surfaces, therefore the curved surface of the hip implant bearing is not possible for auto-stitching. Secondly manual stitching of surface measurements is a lengthy process and requires very precise positional adjustment of the component, where you can easily lose the position of the original stitch line.

The fixture system solves both issues by allowing for the precise movement of the hip implant component, with smart software for the automatic calculation of each surface measurement location. Simply the user must select the start and end point of the stitch, and the software will calculate each surface measurement location and drive the component to each location, speeding up and easing the process for the user.

3. Novel analysis of worn MoM retrieval implants

By using the newly developed fixture system a novel surface analysis was made of worn MoM retrieval implants. The surface analysis utilised the newly developed analysis tools, surface topography mapping and stitching through the wear area. Novel findings were made about the surface topography within the wear area, the roughened portion of the wear area did not closely match the shape of the CMM wear area. Furthermore, the boundary portion of the wear area was captured and analysed as part of the stitch measurements. MoM implants are a topic of particular interest due to their high failure rates in vivo, therefore it is hoped this information will be of high interest to the orthopaedic community.

7.5 Limitations of the Work

Small Cohort Size

The main limitation of this project is the small cohort size of the femoral heads that underwent detailed surface analysis using the fixture system. As the femoral heads initially measured using the CMM were retrieval femoral heads it was not known whether they had a determinable wear area. Therefore, only two of the ten femoral heads had determinable wear areas and could undergo detailed surface analysis using the fixture system. If more femoral heads could undergo detailed surface analysis, then surface topography patterns could be investigated which could be useful for the orthopaedic community or influence future design decisions. To achieve a larger cohort size more easily, the use of hip simulators would allow all femoral head to be worn down significantly and then analysed. However, it cannot be known if this simulation of wear accurately recreates the wear mechanisms and surface topography of naturally worn femoral heads. Although the cohort size for this project was small it is hoped that now the fixture is developed it can be used in industry or research for larger analysis projects.

Outdated Coherence Scanning Interferometer

The Taylor Hobson Talysurf instrument is a rather old model of optical profiler, originating in the early 2000s. A modern alternative instrument would provide more visually appealing surface images due to improved camera technology, and would allow for surface measurements to be taken much quicker.

7.6 Potential Improvements to the Custom Fixture System

As the fixture system developed for this project was a first prototype there are potential improvements that could be considered and implemented to a new design.

Software Improvements

Currently the control software developed on MATLAB provides a low level of CMM analysis, CATIA was instead used for the analysis section of the MoM retrieval study. Further analysis sections could be added to the MATLAB software for both CMM and surface data analysis, with the results compared to CATIA and SurfStand for validation. This would allow for an all-in-one software package that can handle both the control, analysis, and results output stages.

Alternatively, rather than adding more features to the software, the focus could be on improving the current graphical user interface. By reducing the number of buttons and streamlining the software this could make the software easier to use and simpler to the end user. To encourage use of the fixture system in industry the software could be split into two options: researcher and operator. The researcher option would have more detail and advanced control options, whereas the operator option would have limited advanced control but a simpler operation of the system.

Reduction of Azimuth Alignment Error

The largest positional error source from this method is azimuth alignment error caused by relocating the fixture from the CMM to the surface metrology instrument. This error can be removed by using a fully fused instrument such as the Bruker uCMM previously discussed [131], but comes at a large increase in monetary cost. Alternative options could be investigated with the aim to reduce the azimuth alignment error through new alignment methods.

Height Adjustment of End Brackets

By increasing the height of the front and end brackets the azimuth rotary stage can be set lower compared to the elevation rotary axis. This allows larger components to be held by the fixture and correctly lined up with the centre of the elevation rotary axis, this is particularly useful for acetabular cups. Currently acetabular cups are measurable with the fixture system but depending on their size could be too large to be aligned correctly with the elevation rotary axis. They can still be measured but correction of the drift is required by moving the fixture in the Y direction.

Measurement Laser Upgrade

The laser used to check the Z height of the femoral head requires a higher measurement resolution to increase its effectiveness. The current measurement laser was selected due to its low cost. Although the process with the laser is effective, the fixture system still works effectively even if the laser sensor

is not used. The femoral head z height can be effectively manually aligned using the user and error accounted for using the interferometers motorised stages.

Professional Finish

By anodising the surface of the aluminium components to black, the colour of the rotary stages will match the rest of the components, giving the fixture system a more professional look. Other improvements to the aesthetics could include a carry case for the fixture system, and the use of a touchscreen rather than a laptop for reduced size of the hardware.

Lower Cost Manual Version Alternative

Although the digitally controlled rotary stages bring obvious benefits: superior positional accuracy, custom digital control using the wear map, proven stitching capabilities through the wear scar. A lower cost manual version of the fixture system can be developed for under £1000; this could still provide enough precision to allow for stitching of surface measurements at a reduced cost. There will however be downsides to the manual version: reduced positional accuracy, slower speed, no digital control options.

7.7 Future Work

Use of Alternative Surface Measurement Instruments

As well as measurement of the femoral heads through coherence scanning interferometry, measurement through scanning electron microscopy (SEM) would be beneficial. SEM provides higher resolution images which could allow more detail to be seen on the surface and potentially a better tribological understanding. Furthermore, the use of a modern digital microscope would allow for 4K image to be captured of the surface.

Acetabular Cup Measurement

Now that measurement of the femoral heads has been completed the matching acetabular cups could be measured the same way. A slight alteration to the fixture system holding device, and small alterations to the MATLAB code would be required. There is also less access to the acetabular cup surface area compared to the femoral head surface. This would allow for useful surface analysis of the acetabular cups to see if there is correlation between the acetabular cups and the matching femoral heads.

Different Bearing Materials

This type of analysis can be replicated for different bearing material types (MoP, CoP, etc.) these samples could be from either in-vitro or in-vivo testing. The benefit of an in-vitro testing setup is that the components could be measured at set intervals, for example every 1 million cycles up to 8 million cycles, this way the wear area can be studied as it grows. Furthermore, the case study of MoM implants in this project were measured to have low wear rates. An in-vitro study can ensure a high

wear scenario for all implants in the cohort, which will allow for more implants to be measured and analysed.

Knee Replacement Components

Between 2003 and 2017, 1,087,611 primary knee replacements were completed in the UK, compared to 992,090 total hip replacements [4]. Therefore, it is equally useful to replicate this method for knee bearing components. This would require a re-design of the custom fixture system, however, this project provides the foundations for redevelopment.

Method Replication in Industry

It is hoped that the promising results from this project will encourage other companies and research institutes to replicate this method of advanced fixturing and data fusion.

Firstly, the hardware would require development, the fixture could be designed to be bespoke for the users own CMM and surface metrology instrument, for example mounting holes on the base that match both instruments. The use of a gimbal design with two rotary stages, as shown in this project, seems to be the most effective way of manoeuvring the component. Replication could be achieved as either a manual or motorised version of the current design. The manual version could be developed quicker and at a lower cost, however the analysis of CMM data into a wear map is still required to allow for output of surface measurement location coordinates.

The software development would be simpler for a manual version of the fixture system, the only requirement would be analysis software to convert CMM data into a wear map, and to extract desired azimuth/elevation coordinates. It is possible this could be done on already existing CAD software, for example CATIA. These coordinates could then be used as guidance for manually manoeuvring the fixture systems rotary stages.

For a motorised version of the fixture system, either a bespoke software solution could be created, as shown in the project using MATLAB, this solution handles both the CMM analysis and control of the fixture system, linking them together in one software. Or already available software could be used to save time, for example the use of CATIA to analyse wear maps, and then the use of manufacturers included software for control of the rotary stages. This alternative approach would not be as streamlined but would save time on development and custom software could be considered later in the future.

References

1. L. Drake, R., W. Vogl Adam, and A. W. M. Mitchell, *GRAY'S ANATOMY FOR STUDENTS*. 2nd ed. 2010: Churchill Livingstone Elsevier.
2. Kurtz, S.M., Lau, E., Ong, K. et al, *Future Young Patient Demand for Primary and Revision Joint Replacement: National Projections from 2010 to 2030*. Clinical Orthopaedics and Related Research, 2009. **467**(10): p. 2606–2612.
3. Jonathan T Evans, J.P.E., Robert W Walker, Ashley W Blom, Michael R Whitehouse*, Adrian Sayers*, *How long does a hip replacement last? A systematic review and meta-analysis of case series and national registry reports with more than 15 years of follow-up*. Lancet, 2019. **393**: p. 647–654.
4. National Joint Registry for England, W., Northern Ireland and the Isle of Man, *15th Annual Report 2018*.
5. Dattani, R., *Femoral osteolysis following total hip replacement*. Postgrad Med J, 2007. **83**(979): p. 312-6.
6. Sundfeldt, M., et al., *Aseptic loosening, not only a question of wear: a review of different theories*. Acta Orthop, 2006. **77**(2): p. 177-97.
7. Dumbleton, J., M. Manley, and A. Edidin, *A literature review of the association between wear rate and osteolysis in total hip arthroplasty*. J Arthroplasty, 2002. **17**(5): p. 649-61.
8. A. J. Hart, A.K.M., Radu Racasan, Paul J. Bills, A Panagiotidou, Liam Blunt, Gordon Blunn, John Skinner, *Taper wear contributes only a third of the total volumetric material loss in large head metal on metal hip replacement*. Bone and joint journal: Orthopaedic Proceedings, 2013. **95-B**(Sup 13).
9. Puccio, F. and L. Mattei, *Biotribology of artificial hip joints*. World J Orthop, 2015. **6**(1): p. 77-94.
10. BS ISO, *Non-active surgical implants — Joint replacement implants — Specific requirements for hipjoint replacement implants (ISO 21535:2007)*. 2007.
11. BS ISO, *Specification for articulating surfaces made of metallic, ceramic and plastics materials of hip joint prostheses*. 1997.
12. BSI ISO, *ISO 14242:2016 Implants for surgery - Wear of total hip-joint prostheses*, in *Methods of measurement*. 2016.
13. Bills, P.J., et al., *Volumetric wear assessment of retrieved metal-on-metal hip prostheses and the impact of measurement uncertainty*. Wear, 2012: p. 212-219.
14. de Groot, P., *Principles of interference microscopy for the measurement of surface topography*. Advances in Optics and Photonics, 2015. **7**(1): p. 1-65.
15. National Physical Laboratory, *Guide to the Measurement of Smooth Surface Topography using Coherence Scanning Interferometry*. 2008.
16. Walker, P.S., B.L. Gold, and H.C. Amstutz, *The Tribology (Friction, Lubrication and Wear) of All-Metal Artificial Hip Joints*. Clinical orthopaedics and related research, 1971. **329**.
17. Howie, D., et al., *The Long-Term Wear of Retrieved McKee-Farrar Metal-on-Metal Total Hip Prostheses*. Arthroplasty, 2005. **20**(3): p. 350-357.
18. Hall, R., et al., *The effect of surface topography of retrieved femoral heads on the wear of UHMWPE sockets*,. Medical Engineering & Physics,, 1997. **19**(8): p. 711-719.
19. Witzleb, W., *In vivo wear rate of the birmingham hip resurfacing arthroplasty: a review of 10 retrieved components*. J. Arthroplasty, 2009. **24**: p. 951-956.
20. Elfick, A., et al., *The Influence of Femoral Head Surface Roughness on the Wear of Ultrahigh Molecular Weight Polyethylene Sockets in Cementless Total Hip Replacement*. Journal of Biomedical Materials Research, 2002. **48**(5).
21. Racasan, R., et al., *Characterisation of Wear Morphology at the Head Cup Bearing Interface in Retrieved Metal-on-Metal Hip Replacements*. Bone and joint journal: Orthopaedic Proceedings, 2013: p. p. 488.

22. Williams, S., et al., *Tribological and surface analysis of 38 mm alumina–as-cast Co–Cr–Mo total hip arthroplasties*. Proceedings of the Institution of Mechanical Engineers, Part H: Journal of Engineering in Medicine, 2009. **223**(8).
23. Affatato, S., F. Traina, and A. Toni, *Microseparation and stripe wear in alumina-on-alumina hip implants*. Int J Artif Organs, 2011. **34**(6): p. 506-512.
24. Magdalena Niemczewska-Wójcik, W.P., *The surface topography of a metallic femoral head and its influence on the wear mechanism of a polymeric acetabulum*. Archives of Civil and Mechanical Engineering, 2017. **17**(2): p. 307-317.
25. BSI ISO, *14242-2:2000- Implants for surgery - Wear of total hip joint prostheses - Part 2: Methods of measurement*. 2000.
26. Jones, O. *Anatomical Terms of Movement*. 2019; Available from: <https://teachmeanatomy.info/the-basics/anatomical-terminology/terms-of-movement/>.
27. OrthoInfo. *Osteoarthritis of the Hip*. NA; Available from: <https://orthoinfo.aaos.org/en/diseases--conditions/osteoarthritis-of-the-hip/>.
28. NHS. *Arthritis*. 2018; Available from: <http://www.nhs.uk/Conditions/Arthritis/Pages/Introduction.aspx>.
29. NHS. *Hip Fracture*. 2019; Available from: <https://www.nhs.uk/conditions/hip-fracture/>.
30. NHS. *Osteoporosis*. 2019; Available from: <https://www.nhs.uk/conditions/osteoporosis/>.
31. A. Singh, J., et al., *Rates of Total Joint Replacement in the United States: Future Projections to 2020–2040 Using the National Inpatient Sample*. The Journal of Rheumatology, 2019. **46**: p. 1134-1140.
32. Richard Knight, S., R. Aujla, and S. Prasad Biswas, *Total Hip Arthroplasty - over 100 years of operative history*. Orthopedic Reviews, 2011. **3**.
33. Eynon-Lewis, N., D. Ferry, and P. M., *Themistocles Gluck: an unrecognised genius*. BMJ, 1992. **305**: p. 1534-1536.
34. Hernigou, P., *Smith–Petersen and early development of hip arthroplasty*. International Orthopaedics, 2014. **38**(1): p. 193 - 198.
35. Gomez, P. and J. Morcuende, *Early Attempts at Hip Arthroplasty*. Iowa Orthop J., 2005. **25**: p. 25-29.
36. American Academy of Orthopaedic Surgeons. *One Hip Doctor - Sir John Charnley, MD*. NA; Available from: http://www.aaos75.org/stories/physician_story.htm?id=12.
37. Caton, J. and J.L. Prudhon, *Over 25 years survival after Charnley's total hip arthroplasty*. International Orthopaedics, 2011. **35**(2): p. 185-188.
38. Delaunay, C. *THE CHARNLEY TOTAL HIP REPLACEMENT*. ND; Available from: <http://www.luigigentilemd.com/HipKnee/THE%20CHARNLEY%20TOTAL%20HIP%20REPLACEMENT.htm>.
39. University of Missouri Health Care. *Hip Parts and Materials*. ND; Available from: <https://www.muhealth.org/conditions-treatments/orthopaedics/hip-pain/hip-replacement-surgery/hip-parts-and-materials>.
40. Foran, J.R.H. *Total Hip Replacement*. 2015; Available from: <http://orthoinfo.aaos.org/topic.cfm?topic=a00377>.
41. Petis, S., et al., *Surgical approach in primary total hip arthroplasty: anatomy, technique and clinical outcomes*. Can J Surg, 2015. **58**(2): p. 128–139.
42. Karadsheh, M. *THA Approaches*. 2019; Available from: <https://www.orthobullets.com/recon/12116/tha-approaches>.
43. Hansen, E. *Total Hip Replacement Surgical Procedure*. 2020; Available from: <https://www.arthritis-health.com/surgery/hip-surgery/total-hip-replacement-surgical-procedure>.
44. Maggs, J. and M. Wilson, *The Relative Merits of Cemented and Uncemented Prostheses in Total Hip Arthroplasty*. Indian J Orthopaedics, 2017. **51**(4): p. 377–385.

45. Eldesouky, I., O. Abdelaal, and H. El-Hofy, *Femoral hip stem with additively manufactured cellular structures*, in *IEEE Conference on Biomedical Engineering and Sciences*. 2014.
46. Reese, A. and W. Macaulay, *Hybrid total hip arthroplasty: state-of-the-art in the new millennium?* J South Orthop Assoc., 2003. **12**(2).
47. Wangen, H., et al., *Reverse hybrid total hip arthroplasty*. Acta Orthop., 2017. **88**(3): p. 248–254.
48. Bessa, F., et al., *Clinical and radiographic outcomes of hip resurfacing arthroplasty after eight years – a retrospective study*. Rev Bras Ortop, 2018. **53**(6): p. 768–772.
49. LINK, *Lubinus SP II*. 2017.
50. Depuy Synthes, *CORAIL Hip System*. 2017.
51. Yong Hu, C. and T.-R. Yoon, *Recent updates for biomaterials used in total hip arthroplasty*. Biomaterials Research, 2018. **22**(33).
52. Kumar, N., G. Arora, and B. Datta, *Bearing surfaces in hip replacement-evolution and likely future*. Med J Armed Forces India., 2014. **70**(4): p. 371–376.
53. London Implant Retrieval Centre, *Hip Implants Explained*. ND; Available from: <http://www.lirc.co.uk/hips>.
54. Dumbleton, J., et al., *The basis for a second-generation highly crosslinked UHMWPE*. Clin Orthop Relat Res, 2006. **453**: p. 265-271.
55. McKellop, H., et al., *Development of an extremely wear-resistant ultra high molecular weight polyethylene for total hip replacements*. J Orthop Res, 1999.
56. D’Antonio, J., W. Capello, and R. Ramakrishnan, *Second-generation annealed highly cross-linked polyethylene exhibits low wear*. Clin Orthop Relat Res, 2012. **470**: p. 1696-1704.
57. Reynolds, S., et al., *Wear analysis of first-generation highly cross-linked polyethylene in primary total hip arthroplasty: an average 9-year follow-up*. J Arthroplasty, 2012. **27**: p. 1064-1068.
58. Chan, F., et al., *The Otto Aufranc Award. Wear and lubrication of metal-on-metal hip implants*. Clin Orthop Relat Res, 1999. **369**: p. 10-24.
59. Firkins, P.J., et al., *Quantitative analysis of wear and wear debris from metal-on-metal hip prostheses tested in a physiological hip joint simulator*. Biomed Mater Eng, 2001. **11**(2): p. 143-57.
60. Jenabzadeh, A.-R., S. Pearce, and W. Walter, *Total hip replacement: ceramic-on-ceramic*. Semin Arthroplasty, 2012. **23**: p. 232-240.
61. Willert, H., G. Buchhorn, and A. Fayyazi, *Metal-on-metal bearings and hypersensitivity in patients with artificial hip joints. A clinical and histomorphological study*. J Bone Joint Surg Am, 2005. **87**(28): p. 28-36.
62. Jacobs, J. and N. Hallab, *Loosening and osteolysis associated with metal-on-metal bearings: a local effect of metal hypersensitivity?* J Bone Joint Surg Am, 2006. **88**.
63. Kurtz, S. and K. Ong, *Contemporary total hip arthroplasty: Hard-on hard bearings and highly crosslinked UHMWPE*. 2nd ed. 2009: Academic(Elsevier).
64. Yang, C., R. Kim, and D. Dennis, *The squeaking hip: a cause for concern-disagrees*. Orthopedics, 2007. **30**.
65. Cuckler, J., et al., *Large versus small femoral heads in metal-on-metal total hip arthroplasty*. The Journal of Arthroplasty, 2004. **19**(8).
66. Cho, M., W. Choi, and J. Kim, *Current Concepts of Using Large Femoral Heads in Total Hip Arthroplasty*. Hip Pelvis, 2016. **28**(3): p. 134–141.
67. Smith, S.L., D. Dowson, and A.A.J. Goldsmith, *The lubrication of metal-on-metal total hip joints: a slide down the Stribeck curve*. Proc Instn Mech Engrs, 2001. **215**: p. 483-493.
68. Affatato, S., *Perspectives in Total Hip Arthroplasty - Contemporary designs in total hip arthroplasty (THA)*. 2014: Woodhead Publishing Limited.
69. Springer, B., et al., *Why revision total hip arthroplasty fails*. Clin Orthop Relat Res, 2009. **467**(1): p. 166-173.

70. Ast, M., et al., *Weight changes after total hip or knee arthroplasty: prevalence, predictors, and effects on outcomes*. J Bone Joint Surg Am, 2015. **97**(11).
71. Herberts, P. and H. Malchau, *Long-term registration has improved the quality of hip replacement: A review of the Swedish THR Register comparing 160,000 cases*. Acta Orthopaedica Scandinavica, 2009. **71**(2): p. 111-121.
72. Bell, D. and Y. Weerakkody. *Aseptic loosening of hip joint replacements*. Available from: <https://radiopaedia.org/articles/aseptic-loosening-of-hip-joint-replacements>.
73. Skyrme, A., et al., *Polyethylene wear rates with Zirconia and cobalt chrome heads in the ABG hipPoly*. Hip International, 2005. **15**.
74. Green, T., et al., *Polyethylene particles of a 'critical size' are necessary for the induction of cytokines by macrophages in vitro*. Biomaterials Research, 1998. **19**(24): p. 2297-2302.
75. Cohen, D., *How safe are metal-on-metal hip implants?* BMJ, 2012. **344**: p. e1410.
76. Cuckler, J., *The Rationale for Metal-on-Metal Total Hip Arthroplasty*. Clinical Orthopaedics and Related Research, 2005. **441**: p. 132-136.
77. McKellop, H., et al., *In Vivo Wear of 3 Types of Metal on Metal Hip Prostheses During 2 Decades of Use*. Clinical Orthopaedics and Related Research, 1996. **329**: p. 128-140.
78. Wait, M., P. Walker, and G. Blunn, *Tissue reaction of CoCr wear debris from metal on metal total hip replacements.*, in *European Orthopaedic Research Society*. 1995. p. 462.
79. Soh, E.W., et al., *Size and shape of metal particles from metal on metal total hip replacements.*, in *42nd Annual Meeting of the Orthopaedic Research Society*. 1996. p. 462.
80. Shanbhag, A.S., et al., *Composition and morphology of wear debris in failed uncemented total hip replacements*. J.Bone Jt Surgery, 1994. **76**: p. 60–67.
81. Tipper, J.L., et al., *Quantitative comparison of polyethylene wear debris, wear rate and head damage in retrieved hip prostheses.* , in *43rd Annual Meeting of the Orthopaedic Research Society*,. 1997. p. 355.
82. Grammatopoulos, G., et al., *Hip resurfacings revised for inflammatory pseudotumour have a poor outcome*. J Bone Joint Surg Br, 2009. **91**(8): p. 1019-24.
83. Schewelov, T.v. and L. Sanzen, *Catastrophic failure due to aggressive metallosis 4 years after hip resurfacing in a woman in her forties—a case report*. Acta Orthopaedica, 2010. **81**(3): p. 2.
84. Schaffer, A.W., et al., *Increased blood cobalt and chromium after total hip replacement*. Clin. Toxic, 1999. **37**(7): p. 839–844.
85. Gray, M., et al., *Changes seen in lymph nodes draining sites of large joint prostheses*. Am. J. Surgery Pathology, 1989. **13**: p. 1050-1056.
86. Case, C.P., et al., *Widespread dissemination of metal debris from implants*. J Bone Joint Surg Br, 1994. **76**(5): p. 701-12.
87. Goodman, S.B., *The effects of micromotion and particulate materials on tissue differentiation. Bone chamber studies in rabbits*. Acta Orthop Scand, 1994. **65**: p. 1-43.
88. Zhang, H., et al., *Understanding initiation and propagation of fretting wear on the femoral stem in total hip replacement*. Wear, 2008. **266**(5-6): p. 566-569.
89. Engh, C.A. and J.D. Bobyn, *The influence of stem size and extent of porous coating on femoral bone resorption after primary cementless hip arthroplasty*. Clin Orthop, 1988. **231**: p. 7-28.
90. McCarthy, C.K., et al., *Quantifying bone loss from the proximal femur after total hip arthroplasty*. J Bone Joint Surg (Br) 1991; . **73**(5): p. 774–8.
91. Maloney, W.J., et al., *Skeletal response to well fixed femoral components inserted with and without cement*. Clin Orthop, 1996. **333**: p. 15–26.
92. Karachalios, T., G. Komnos, and A. Koutalos, *Total hip arthroplasty: Survival and modes of failure*. EFORT Open Rev., 2018. **3**(5): p. 232-239.
93. Seagrave, K., et al., *Acetabular cup position and risk of dislocation in primary total hip arthroplasty*. Gromov K Acta Orthop, 2017;. **88**.
94. Gullmark, G., *The unstable total hip arthroplasty*. EFORT Open Rev. , 2017. **1**: p. 83-88.

95. Sorrentino, S. *Joint dislocation after total hip replacement*. Available from: <https://radiopaedia.org/cases/joint-dislocation-after-total-hip-replacement>.
96. Foran, J. and W. Peace. *Joint Replacement Infection*. 2018; Available from: <https://orthoinfo.aaos.org/en/diseases--conditions/joint-replacement-infection/>.
97. National Institute for Health Research, *Joint infection after hip replacement is linked to some risk factors that could be modified*. 2018.
98. Karadsheh, M. *THA Periprosthetic Fracture*. 2020; Available from: <https://www.orthobullets.com/recon/5013/tha-periprosthetic-fracture>.
99. Miettinen, S., et al., *Risk factors for intraoperative calcar fracture in cementless total hip arthroplasty*. *Acta Orthop*, 2016. **87**(2): p. 113-9.
100. Sidler-Maier, C. and J. Waddell, *Incidence and predisposing factors of periprosthetic proximal femoral fractures: a literature review*. *Int Orthop*, 2015. **39**(9): p. 1673-82.
101. Sadoghi, P., et al., *The incidence of implant fractures after total hip arthroplasty*. *Int Orthop*, 2014. **38**(1): p. 39-46.
102. Dowson, D., et al., *A hip joint simulator study of the performance of metal-on-metal joints: Part II: Design*. *The Journal of Arthroplasty*, 2004. **19**(8): p. 124-130.
103. Richard J Underwood, A.Z., Ritchie S Sayles, Alister Hart, and Philippa Cann, *Edge loading in metal-on-metal hips: low clearance is a new risk factor*. *Proc Inst Mech Eng H*, 2012. **226**(3): p. 217–226.
104. Trevisan, C., et al., *Long-term results of the M2A-38-mm metal-on-metal articulation*. *J Orthop Traumatol*, 2018. **19**(1).
105. Leslie, I.J., Williams, S., Isaac, G. et al., *High Cup Angle and Microseparation Increase the Wear of Hip Surface Replacements*. *Clinical Orthopaedics and Related Research*, 2009. **467**(9): p. 2259–2265.
106. Harris, W.H., *Edge Loading Has a Paradoxical Effect on Wear in Metal-on-Polyethylene Total Hip Arthroplasties*. *Clinical Orthopaedics and Related Research*, 2012. **470**: p. 3077-3082.
107. Kovochich, M., et al., *Characterization of wear debris from metal-on-metal hip implants during normal wear versus edge-loading conditions*. *J Biomed Mater Res B Appl Biomater*, 2017.
108. Clarke, I., et al., *Risk of Impingement and Third-body Abrasion With 28-mm Metal-on-metal Bearings*. *Clinical Orthopaedics and Related Research*, 2013. **472**: p. 497-508.
109. Walker, P. and B. Gold, *The tribology (friction, lubrication and wear) of all-metal artificial hip joints*. *Wear*, 1971. **17**(4): p. 285-299.
110. Gascoyne, T., T. Turgeon, and C. Burnell, *Retrieval Analysis of Large-Head Modular Metal-on-Metal Hip Replacements of a Single Design*. *The Journal of Arthroplasty*, 2017. **33**: p. 1945-1952.
111. Lundberg, H., et al., *Problematic sites of third body embedment in polyethylene for total hip wear acceleration*. *Journal of Biomechanics*, 2006. **39**(7): p. 1208-1216.
112. Michael Shang Kung, J.M., Scott D. Nelson and Patricia Campbel, *The Synovial Lining and Synovial Fluid Properties after Joint Arthroplasty*. *lubricants*, 2015.
113. Dowson, D. and Z. Jin, *Metal-on-metal hip joint tribology*. *Proceedings of the Institution of Mechanical Engineers Part H Journal of Engineering in Medicine*, 2006. **220**(2): p. 107-18.
114. Hosseinzadeh, H.R.S., A. Eajazi, and A.S. Shahi, *Recent Advances in Arthroplasty*. 2012.
115. Brockett, C., *A comparison of friction in 28 mm conventional and 55 mm resurfacing metal-on-metal hip replacements*. *P I Mech Eng C-J Mec*, 2007. **221**: p. 391-398.
116. Brockett, C., et al., *Friction of total hip replacements with different bearings and loading conditions*. *J Biomed Mater Res B Appl Biomater*, 2007. **81**: p. 508-515.
117. Bragdon, C., et al., *Third-body wear of highly cross-linked polyethylene in a hip simulator*. *J Arthroplasty*, 2003. **18**(5): p. 553-61.
118. Halim, T., et al., *Third-body Wear Damage Produced in CoCr Surfaces by Hydroxyapatite and Alumina Ceramic Debris: A 10-cycle Metal-on-Metal Simulator Study*. *Reconstructive Review*, 2015. **5**.

119. BSI ISO, *Geometrical product specifications (GPS) — Surface texture: Areal. Part 3: Specification operators (ISO 25178-3:2012)*. 2012.
120. Calonijs, O. and V. Saikko, *Force track analysis of contemporary hip simulators*. *Biomechanics*, 2003. **36**(11): p. 1719-1726.
121. *ORTHOPEDIC WEAR TESTING*. NA; Available from: <https://www.amti.biz/owt.aspx>.
122. Science Photo Library. *Failed hip replacement surgery*. NA; Available from: <https://www.sciencephoto.com/media/120098/view/failed-hip-replacement-surgery>.
123. Flack, D., J. Claverley, and R. Leach, *Chapter 9: 'Coordinate Metrology' in Fundamental Principles of Engineering Nanometrology*. 2014.
124. Flack, D., *NPL - Good Practice Guide No. 43 - CMM Probing*. 2014.
125. HEXAGON. *Intro to Coordinate Metrology*. ND; Available from: [https://www.hexagonmi.com/solutions/technical-resources/metrology-101/intro-to-coordinate-metrology#:~:text=A%20coordinate%20measuring%20machine%20\(CMM,to%20the%20machine's%20coordinate%20system](https://www.hexagonmi.com/solutions/technical-resources/metrology-101/intro-to-coordinate-metrology#:~:text=A%20coordinate%20measuring%20machine%20(CMM,to%20the%20machine's%20coordinate%20system).
126. Zeiss. *Bridge Coordinate Measuring Machines*. 2020; Available from: <https://www.zeiss.com/metrology/products/systems/coordinate-measuring-machines/bridge-type-cmms.html>.
127. Flack, D., *Measurement Good Practice Guide No. 42 - CMM Verification*. 2011.
128. Flack, D., *NPL Good Practice Guide No. 41: CMM Measurement Strategies*. 2014.
129. BS ISO, *Geometrical Product Specifications (GPS) — Acceptance and reverification tests for coordinate measuring machines (CMM) — Part 1: Vocabulary*. 2001.
130. REDLUX. *REDLUX*. 2019; Available from: <https://www.redlux.net/>.
131. Bruker Alicona. *Optical CMM machine to measure tight tolerances*. 2020; Available from: <https://www.alicon.com/products/cmm/>.
132. Mike Tuke, A.T., Anne Roques, Christian Maul *3D linear and volumetric wear measurement on artificial hip joints—Validation of a new methodology*. *Precision Engineering*, 2010. **34**(4): p. 777-783.
133. Laboratory of Biomechanics and Implant Research. *Wear analysis*. ND; Available from: <http://www.arthroplasty-research.com/sites/forsch/cmm.html>.
134. Smith, S.L. and A. Unsworth, *A comparison between gravimetric and volumetric techniques of wear measurement of UHMWPE acetabular cups against zirconia and cobalt–chromium–molybdenum femoral heads in a hip simulator*. *Engineering in Medicine*, 1999. **213**(6).
135. Bills, P., L. Blunt, and X. Jiang, *Development of a technique for accurately determining clinical wear in explanted total hip replacements*. *Wear*, 2007. **263**(7-12): p. 1133-1137.
136. Bills, P.J., Underwood, R.J., Cann, P., Hart, A, Jiang, Xiangqian and Blunt, Liam, *What is required to measure the wear of explanted metal-on-metal hips?* British Orthopaedic Research Society Annual Meeting, 2010.
137. Goto, K., et al., *Clinical and radiological evaluation of revision hip arthroplasty using the cement-in-cement technique*. *J. Bone Joint Surg*, 2008: p. 1013–1018.
138. Livermore, J., D. Ilstrup, and B. Morrey, *Effect of femoral head size on wear of the polyethylene acetabular component*. *J. Bone Joint Surg*, 1990: p. 518–528.
139. Ebramzehl, E., et al., *Accuracy of measurement of polyethylene wear with use of radiographs of total hip replacements*. *J. Bone Joint Surg*, 2003: p. 2378–2384.
140. Geerdink, C., et al., *The determination of linear and angular penetration of the femoral head into the acetabular component as an assessment of wear in total hip replacement: a comparison of four computer-assisted methods*. *J. Bone Joint Surg.*, 2008: p. 839–846.
141. Chuter, G., et al., *Wear analysis of failed acetabular polyethylene: a comparison of analytical methods*. *J. Bone Joint Surg*, 2007: p. 273–279.
142. P. Bills, L.B., X. Jiang, L. Blunt, , *A metrology solution for the orthopaedic industry*. *J. Phys. Conf*, 2005: p. 316–319.

143. Kabo, J., et al., *In vivo wear of polyethylene acetabular components*. J. Bone Joint Surg., 1993: p. 254-258.
144. Reinisch, G., et al., *Retrieval study of uncemented metal-metal hip prostheses revised for early loosening*. Biomaterials 24 2003: p. 1081-1091.
145. Joyce, T., D. Langton, and A. Nargol, *A study of the wear of explanted metal-on-metal resurfacing hip prostheses*. Tribol. Int. , 2010.
146. Morlock, M., *Biomechanical, morphological, and histological analysis of early failures in hip resurfacing arthroplasty*. roc. Inst. Mech. Eng. Part H: J. Eng. Med, 2006. **220**: p. 333-344.
147. Blunt, L., et al., *Improvement in the assessment of wear of total knee replacements using coordinate-measuring machine techniques*. Proc. Inst. Mech. Eng. Part H: J. Eng. Med., 2008. **222**: p. 309-318.
148. BS ISO, *Geometrical product specifications (GPS) — Coordinate measuring machines (CMM): Technique for determining the uncertainty of measurement — Part 3: Use of calibrated workpieces or measurement standards*. 2011.
149. Bell, S. *NPL Good Practice Guide No.11: The Beginner's Guide to Uncertainty of Measurement*. 2001.
150. Carmignato, S., et al., *Uncertainty evaluation of volumetric wear assessment from coordinate measurements of ceramic hip joint prostheses*. Wear, 2011. **270**(9-10): p. 584-590.
151. L Russell Alberts, et al., *Comparison of metal-on-metal hip simulator wear measured by gravimetric, CMM and optical profiling methods*. Surface Topography: Metrology and Properties, 2018. **6**(1).
152. Rosén, S., T. Thomas, and B. Rosén, *The Stedman diagram revisited*. Surface Topography: Metrology and Properties, 2013. **2**.
153. Stedman, M., *Basis for comparing the performance of surface measuring machines*. Prec. Eng, 1987: p. p. 149-152.
154. BSI ISO, *Geometrical product specifications (GPS) — Surface texture: Areal. Part 2: Terms, definitions and surface texture parameters (ISO 25178-2:2012)*. 2012.
155. Walton, K., *Introduction to Surface Metrology*, in *The Future Metrology Hub, 2 Day Seminar*. 2017, University of Huddersfield.
156. Blunt, L., *Surface texture areal parameters; Principles and applications of areal surface parameters (ISO 25178)*, in *The Future Metrology Hub, 2 Day Seminar*. 2017: University of Huddersfield.
157. Renishaw. *Interferometry explained*. Available from: <https://www.renishaw.com/en/interferometry-explained--7854>.
158. Woodford, C. *Interferometers*. 2020; Available from: <https://www.explainthatstuff.com/howinterferometerswork.html>.
159. The Electropaedia Battery Knowledge Base. *Michelson Interferometer*. Available from: <https://www.mpoweruk.com/figs/Michelson-Interferometer.htm>.
160. Ling, S., J. Sanny, and W. Moebis, *BC Open Textbooks UNIVERSITY PHYSICS VOLUME 3*. 2019.
161. Leach, R., *Optical Measurement of Surface Topography*. 2011.
162. Groot, P., *Dimensional Optical Metrology and Inspection for Practical Applications: Progress in the specification of optical instruments for the measurement of surface form and texture*. 2014.
163. BS ISO, *Geometrical product specifications (GPS) — Surface texture: Areal - Part 604: Nominal characteristics of noncontact (coherence scanning interferometry) instruments*. 2013.
164. Bruker Alicona. *Contour GT-X*. 2020; Available from: <https://www.bruker.com/products/surface-and-dimensional-analysis/3d-optical-microscopes/contourg-t-x/overview.html>.
165. Olympus. *Roughness Evaluation Parameters*. Available from: <https://www.olympus-ims.com/en/metrology/surface-roughness-measurement-portal/evaluating-parameters/>.

166. Michigan Metrology. *3D S Parameters - Hybrid Parameters*. Available from: https://michmet.com/3d_s_hybrid_parameters_sdr.htm.
167. Michigan Metrology, *3D S Parameters - Spatial Parameters*.
168. McKellop, H., et al., *Lexicon for Wear of Metal-on-Metal Hip Prostheses*. Journal of Orthopaedic Research, 2014. **32**(9): p. 1221-1233.
169. Blunt, L. and T. Thomas, *Wear ranking of hard on hard bearings for prosthetic hip joints*. Wear, 2004. **257**(12): p. 1208-1212.
170. Niemczewska-Wójcik, M., *Wear mechanisms and surface topography of artificial hip joint components at the subsequent stages of tribological tests*. Measurement, 2017. **107**: p. 89-98.
171. Dowson, D., et al., *Influence of Counterface Topography on the Wear of Ultra High Molecular Weight Polyethylene Under Wet or Dry Conditions* ACS Symposium Series: Polymer Wear and Its Control 1985: p. 171-187.
172. Wang, A., et al., *Lubrication and wear of ultra-high molecular weight polyethylene in total joint replacements*. Tribology International, 1998. **31**(1-3): p. 17-33.
173. Weckenmann, A., et al., *Multisensor data fusion in dimensional metrology*. CIRP Annals - Manufacturing Technology, 2009. **58**: p. 701-721.
174. Wang, J., R. Leach, and X. Jiang, *Review of the mathematical foundations of data fusion techniques in surface metrology*. Surface Topography: Metrology and Properties, 2015. **3**(2).
175. Bruker Alicona. *Webinar: Form and roughness measurement with one system: practical reports from daily use*. 2020.
176. BS ISO, *Geometrical product specifications (GPS) — Acceptance and reverification tests for coordinate measuring systems (CMS) Part 8: CMMs with optical distance sensors*. 2013.
177. Synthes, D., *Pinnacle Hip Solutions, Polyethylene Surgical Technique*. 2014.
178. Alberts, L.R., et al., *Comparison of Simulator Wear Measured by Gravimetric vs Optical Surface Methods for Two Million Cycles*. 2016.
179. DASSAULT SYSTEMS. CATIA. Available from: https://www.3ds.com/products-services/catia/?wockw=card_content_cta_1_url%3A%22https%3A%2F%2Fblogs.3ds.com%2Fcatia%2F%22.
180. National Physical Laboratory. *Is there a difference between measurement 'accuracy' and 'uncertainty'?* ND; Available from: <https://www.npl.co.uk/resources/q-a/difference-accuracy-uncertainty>.
181. Potts, P., *Glossary of Analytical and Metrological Terms from the International Vocabulary of Metrology*. Geostandards and Geoanalytical Research, 2008. **36**: p. 231-246.
182. DASSAULT SYSTEMS. SOLIDWORKS. Available from: <https://www.solidworks.com/>.
183. Standa. *8MR174-11 - Motorized Rotation Stage*. 2020; Available from: http://www.standa.it/products/catalog/motorised_positioners?item=68&prod=motorized_rotation_stage.
184. Banner. *Q4X Series*. Available from: <https://www.bannerengineering.com/us/en/products/sensors/photoelectric-sensors/q4x-laser-distance-sensor.html?sort=4#all>.
185. The Engineering ToolBox. *Young's Modulus - Tensile and Yield Strength for common Materials*. 2003; Available from: https://www.engineeringtoolbox.com/young-modulus-d_417.html.
186. The Engineering ToolBox. *Metals and Alloys - Densities*. 2004; Available from: https://www.engineeringtoolbox.com/metal-alloys-densities-d_50.html.
187. MathWorks. *MATLAB*. 2020; Available from: <https://uk.mathworks.com/products/matlab.html>.
188. Orientalmotor. *Basics of Stepper Motors*. ND; Available from: <https://www.orientalmotor.com/stepper-motors/technology/stepper-motor-basics.html>.
189. MySecretMathTutor;. *Statistics - How to use the Empirical Rule*. 2020; Available from: https://www.youtube.com/watch?v=n7phemRMb98&ab_channel=MySecretMathTutor.

190. AMETEK TAYLOR HOBSON. *CCI system specifications*. 2012.
191. University of Huddersfield. *Surface measurement – improving products and boosting sales*. 2011; Available from: <https://research.hud.ac.uk/impact/case-studies/surface-measurement/>.
192. Digital Surf. *Digital Surf*. 2021; Available from: <https://www.digitalsurf.com/>.
193. Blunt, L. and X. Jiang, *Advanced Techniques for Assessment Surface Topography*. 2003.
194. BUEHLER. *Grinding and Polishing Guide*. Available from: <https://www.buehler.com/grinding-and-polishing-guide.php>.

Appendix

Metrology Definitions

Table 28: Metrology ISO definitions set by VIM:2008 [181].

Term	Definition
Metrology	- Science of measurement and its application.
Measurand	- Quantity intended to be measured.
Accuracy	- Closeness of agreement between a measured quantity value and a true quantity value of a measurand.
Trueness	- Closeness of agreement between the average of an infinite number of replicate measured quantity values and a reference quantity value.
Precision	- Closeness of agreement between indications or measured quantity values obtained by replicate measurements on the same or similar objects under specified conditions.
Error	- Measured quantity value minus a reference quantity value.
Systematic error	- Component of measurement error that in replicate measurements remains constant or varies in a predictable manner.
Bias	- Estimate of a systematic measurement error.
Correction	- Compensation for an estimated systematic effect.
Random error	- Component of measurement error that in replicate measurements varies in an unpredictable manner.
Repeatability	- Measurement precision under a set of repeatability conditions of measurement.
Reproducibility	- Measurement precision under a set of reproducibility conditions of measurement reproducibility (of results of measurements): closeness of the agreement between the results of measurements carried out under changed conditions of measurement.
Uncertainty	- Non-negative parameter characterising the dispersion of the quantity values being attributed to a measurand, based on the information used.
Standard measurement uncertainty	- Measurement uncertainty expressed as a standard deviation.
Uncertainty budget	- Statement of a measurement uncertainty, of the components of that uncertainty budget, and of their calculation and calibration.
Calibration	- Operation that, under specified conditions, in a first step, establishes a relation between the quantity values with measurement uncertainties provided by measurement standards and corresponding indications with associated measurement uncertainties and, in a second step, uses this information to establish a relation for obtaining a measurement result from an indication.
Metrological traceability	- Property of a measurement result whereby the result can be related to a reference through a documented unbroken chain of calibrations, each contributing to the measurement uncertainty.
Verification	- Provision of objective evidence that a given item fulfils specific requirements.
Validation	- Verification where the specific requirements are adequate for an intended use.
Resolution	- Smallest change in a quantity being measured that causes a perceptible change in the corresponding indication.
Detection limit	- Measured quantity value, obtained by a given measurement procedure, for which the probability of falsely claiming the absence of a component in a material is b , given a probability a of falsely claiming its presence. IUPAC recommends default values for a and b equal to 0.05.
Stability	- Property of a measuring instrument whereby its metrological properties remain constant in time.

RedLux and Zeiss Full CMM Measurement Results

Table 29: RedLux and Zeiss Full CMM Measurement Results.

Machine	Component	No.	Radius (mm)	Linear Wear (um)	CMM Vol. (mm ³)	Volumetric Wear (mm ³)
CMM	Poly Liner	1	18.45224	68.40	12193.20	-38.52
CMM	Poly Liner	2	18.44662	73.40	12177.50	-43.38
CMM	Poly Liner	3	18.44292	76.10	12212.95	-48.25
CMM	Poly Liner	4	18.44582	78.70	12191.51	-45.65
CMM	Poly Liner	5	18.44286	77.00	12198.14	-47.67
Median			18.44582	76.10	12193.20	-45.65
SD			0.00343	3.60	11.43	3.53
CMM	Metal Head	1	17.99935	-2.40	11195.92	0.81
CMM	Metal Head	2	17.99897	-2.30	11195.12	0.81
CMM	Metal Head	3	17.99898	-2.10	11196.16	0.91
CMM	Metal Head	4	17.99872	-2.20	11194.10	0.83
CMM	Metal Head	5	17.99936	-2.10	11196.73	0.78
Median			17.99898	-2.20	11195.92	0.81
SD			0.00025	0.12	0.91	0.04
CMM	Ceramic Liner	1	18.02573	6.20	8251.62	0.26
CMM	Ceramic Liner	2	18.02521	7.00	8249.58	0.19
CMM	Ceramic Liner	3	18.02530	6.10	8251.78	0.28
CMM	Ceramic Liner	4	18.02558	5.80	8252.57	0.36
CMM	Ceramic Liner	5	18.02565	6.30	8251.62	0.22
Median			18.02558	6.20	8251.62	0.26
SD			0.00020	0.40	0.99	0.06
RedLux	Poly Liner	1	18.43447	92.30	12155.69	-41.23
RedLux	Poly Liner	2	18.43932	92.20	12167.48	-42.06
RedLux	Poly Liner	3	18.44734	84.10	12165.57	-34.66
RedLux	Poly Liner	4	18.43298	59.00	12148.61	-40.41
RedLux	Poly Liner	5	18.43358	99.90	12148.36	-39.42
Median			18.43447	92.20	12155.69	-40.41
SD			0.00539	14.16	8.12	2.60
RedLux	Metal Head	1	17.99983	-4.30	11197.79	0.73
RedLux	Metal Head	2	18.00033	-7.90	11198.75	0.69
RedLux	Metal Head	3	18.00032	-7.90	11198.75	0.71
RedLux	Metal Head	4	18.00000	-6.70	11197.55	0.76
RedLux	Metal Head	5	17.99997	-6.80	11197.44	0.72
Median			18.00000	-6.80	11197.79	0.72
SD			0.00020	1.32	0.58	0.02
RedLux	Ceramic Liner	1	18.02464	6.90	8241.76	-0.14
RedLux	Ceramic Liner	2	18.02533	6.80	8233.89	-0.04
RedLux	Ceramic Liner	3	18.02566	7.00	8228.19	-0.16
RedLux	Ceramic Liner	4	18.02599	7.00	8247.24	-0.11
RedLux	Ceramic Liner	5	18.02637	6.50	8247.37	0.12
Median			18.02566	6.90	8241.76	-0.11
SD			0.00059	0.19	7.56	0.10

Phase 1 Measurement Testing of the Custom Fixture System

Repeatability Testing

Home Position (0 az., 0 el.)

Table 30: Repeatability test of the fixture at origin position results.

No.	Az. (deg.)	El. (deg.)
O1_01	0.00400	0.01990
O1_02	0.00370	0.02030
O1_03	0.00380	0.02010
O1 Median	0.00380	0.02010
O2_01	0.00400	0.01990
O2_02	0.00380	0.01980
O2_03	0.00370	0.01950
O2_04	0.00360	0.01970
O2_05	0.00390	0.01920
O2_06	0.00380	0.01970
O2_07	0.00380	0.02020
O2_08	0.00310	0.02060
O2_09	0.00390	0.02010
O2_10	0.00390	0.02010
O2 Median	0.00380	0.01985
Difference	0	0.00025

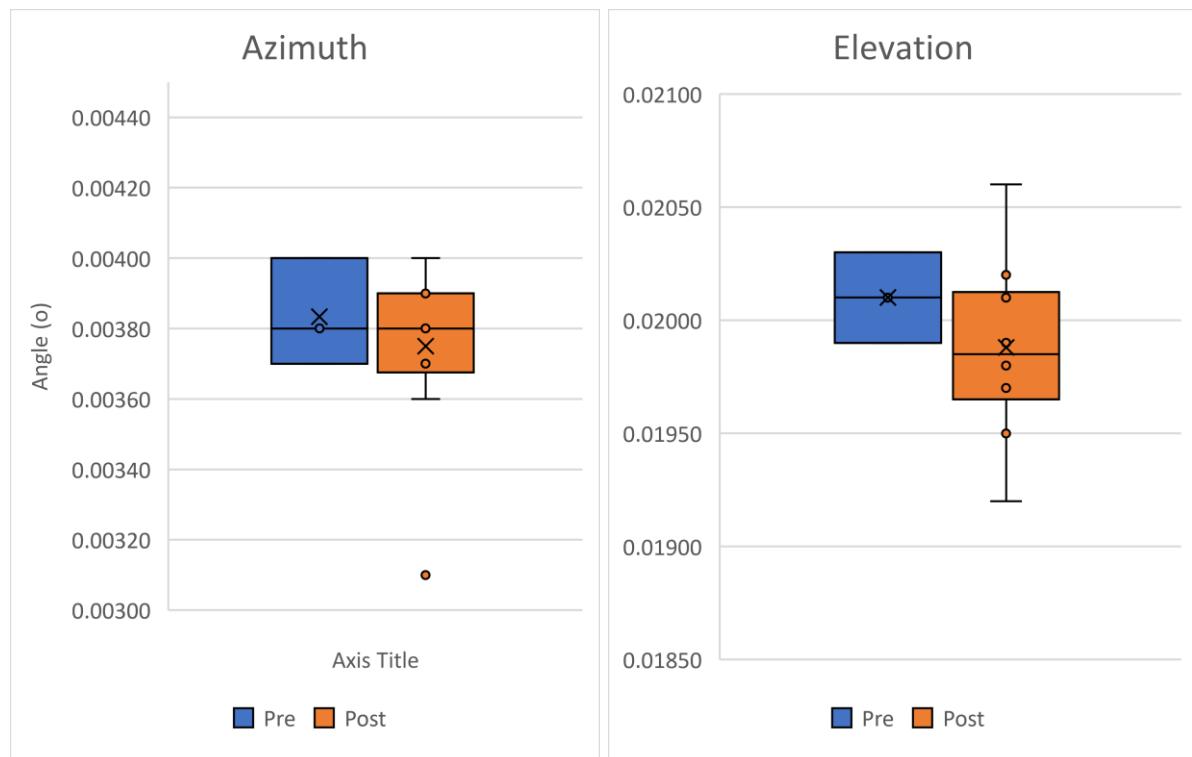


Figure 232: Box and whisker plots for the repeatability testing of the fixture at the home position.

Random Position (57 az., 73. el.)

Table 31: Repeatability test of the fixture at random position, spherical coordinates: 57 azimuth, 73 elevation.

No.	CA1 (deg.)	CA2 (deg.)
R1_01	53.5177	140.4692
R1_02	53.5178	140.4693
R1_03	53.5176	140.4692
R1 Median	53.5177	140.4692
R2_01	53.5156	140.4672
R2_02	53.5157	140.4674
R2_03	53.5157	140.4674
R2 Median	53.5157	140.4674
Difference	0.002	0.0018

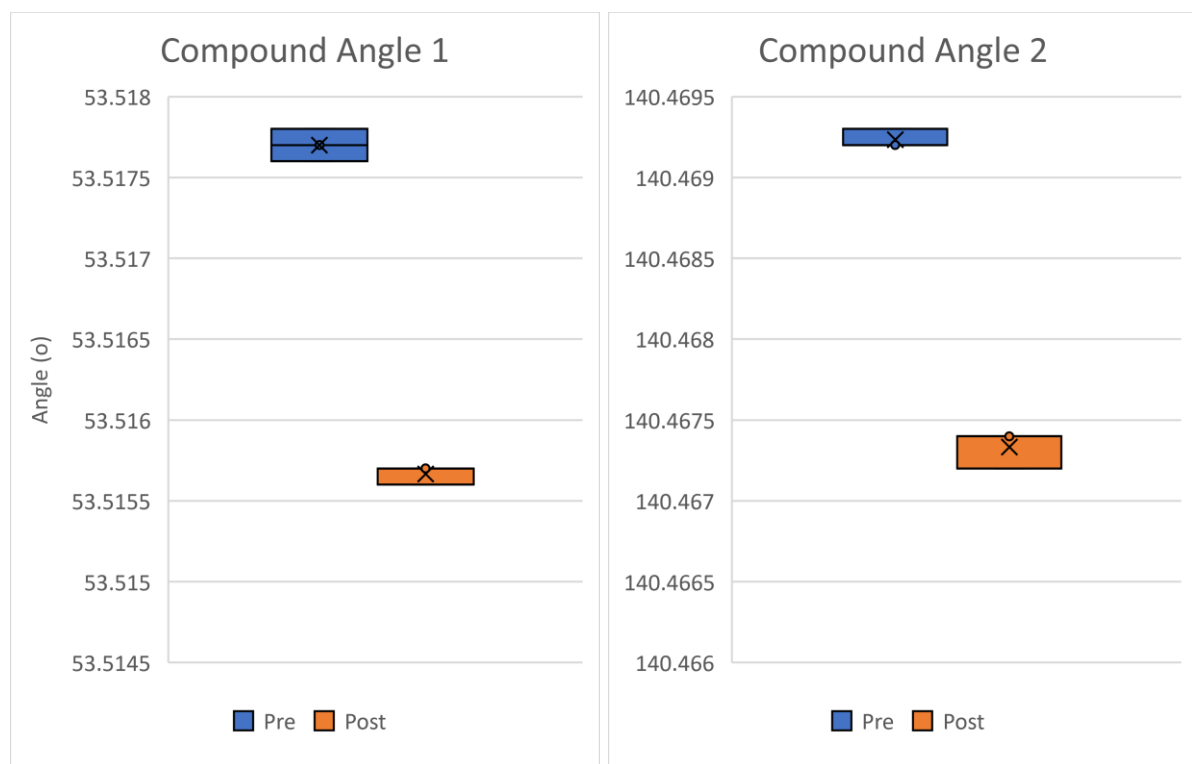


Figure 233: Box and whisker plots for the repeatability testing of the fixture at the random position.

Positional Uncertainty Testing

Azimuth adjustment only

Table 32: Angular positional error from varying azimuth rotary stage.

No.	Target Az. (o)	Az. (o)	Error (o)
A1_01	156	155.9727	-0.0273
A1_02	156	155.9723	-0.0277
A1_03	156	155.9722	-0.0278
A1_F	156	155.9723	-0.0277
A2_01	110	109.9796	-0.0204
A2_02	110	109.9797	-0.0203
A2_03	110	109.9799	-0.0201
A2_F	110	109.9797	-0.0203
A3_01	150	149.9711	-0.0289
A3_02	150	149.9714	-0.0286
A3_03	150	149.9715	-0.0285
A3_F	150	149.9714	-0.0286
A4_01	92	91.9751	-0.0249
A4_02	92	91.9751	-0.0249
A4_03	92	91.9752	-0.0248
A4_F	92	91.9751	-0.0249
A5_01	318	318.0064	0.0064
A5_02	318	318.0066	0.0066
A5_03	318	318.0067	0.0067
A5_F	318	318.0066	0.0066
A6_01	299	299.0015	0.0015
A6_02	299	299.0013	0.0013
A6_03	299	299.0014	0.0014
A6_F	299	299.0014	0.0014
A7_01	239	239.0063	0.0063
A7_02	239	239.0064	0.0064
A7_03	239	239.0067	0.0067
A7_F	239	239.0064	0.0064
A8_01	5	4.9876	-0.0124
A8_02	5	4.9872	-0.0128
A8_03	5	4.9883	-0.0117
A8_F	5	4.9876	-0.0124
A9_01	231	231.0308	0.0308
A9_02	231	231.098	0.098
A9_03	231	231.0308	0.0308
A9_F	231	231.0308	0.0308
A10_01	19	19.0107	0.0107
A10_02	19	19.0104	0.0104
A10_03	19	19.0106	0.0106
A10_F	19	19.0106	0.0106
Maximum			0.0308
Median			-0.0055
Standard Deviation			0.018924

2SD

0.037848

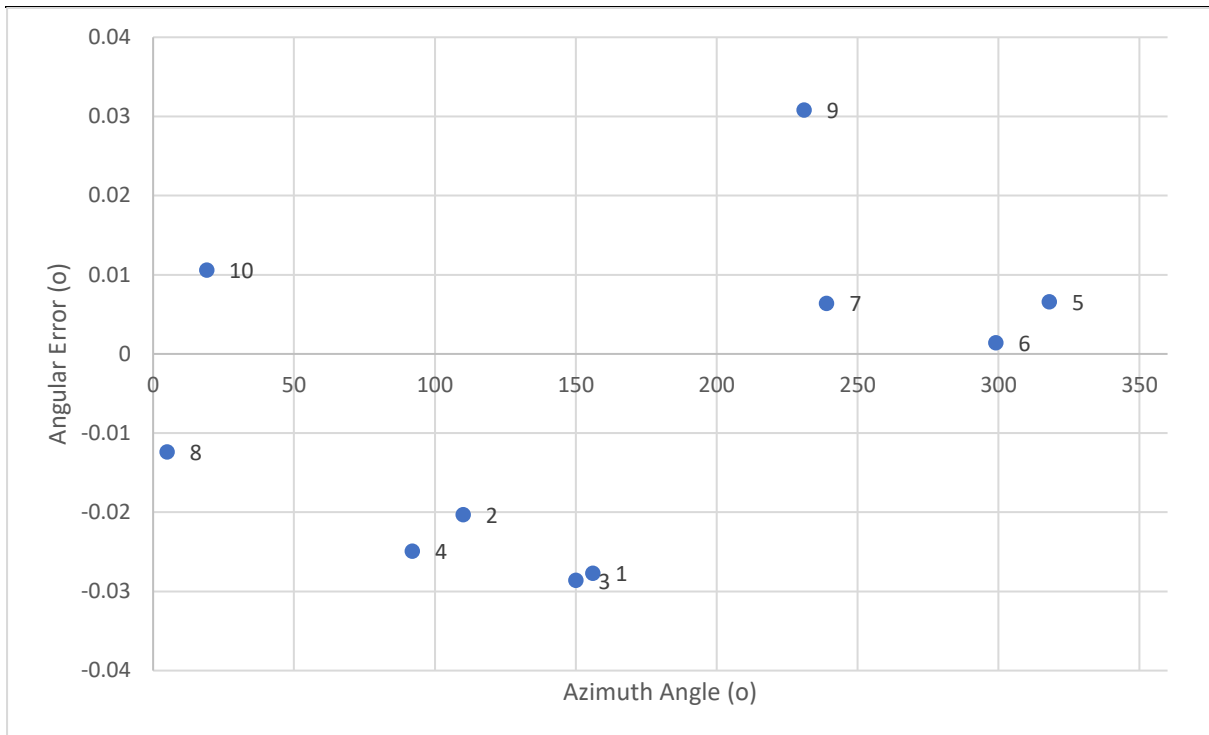


Figure 234: Scatter plot of the angular error at each azimuth position during uncertainty testing. Each point on the scatter plot is labelled with a number to show the chronological order in which the measurements were taken.

Elevation adjustment only

Table 33: Angular positional error from varying elevation rotary stage.

No.	Target El. (o)	Calc. El. (o)	Error El. (o)
E1_01	59	58.9258	-0.0742
E1_02	59	58.9266	-0.0734
E1_03	59	58.9268	-0.0732
E1_F	59	58.9266	-0.0734
E2_01	2	1.9846	-0.0154
E2_02	2	1.9846	-0.0154
E2_03	2	1.9847	-0.0153
E2_F	2	1.9846	-0.0154
E3_01	17	16.9703	-0.0297
E3_02	17	16.9707	-0.0293
E3_03	17	16.9706	-0.0294
E3_F	17	16.9706	-0.0294
E4_01	36	35.9612	-0.0388
E4_02	36	35.9619	-0.0381
E4_03	36	35.9618	-0.0382
E4_F	36	35.9618	-0.0382
E5_01	81	80.9612	-0.0388
E5_02	81	80.9613	-0.0387
E5_03	81	80.9615	-0.0385
E5_F	81	80.9613	-0.0387
E6_01	73	72.9251	-0.0749
E6_02	73	72.9254	-0.0746
E6_03	73	72.9255	-0.0745
E6_F	73	72.9254	-0.0746
E7_01	67	66.9329	-0.0671
E7_02	67	66.9327	-0.0673
E7_03	67	66.9328	-0.0672
E7_F	67	66.9328	-0.0672
E8_01	26	25.9574	-0.0426
E8_02	26	25.957	-0.043
E8_03	26	25.9567	-0.0433
E8_F	26	25.957	-0.043
E9_01	57	56.9488	-0.0512
E9_02	57	56.949	-0.051
E9_03	57	56.9492	-0.0508
E9_F	57	56.949	-0.051
E10_01	40	39.9384	-0.0616
E10_02	40	39.9383	-0.0617
E10_03	40	39.9385	-0.0615
E10_F	40	39.9384	-0.0616
Maximum			-0.0746
Median			-0.047
Standard Deviation			0.018751

2SD

0.037502

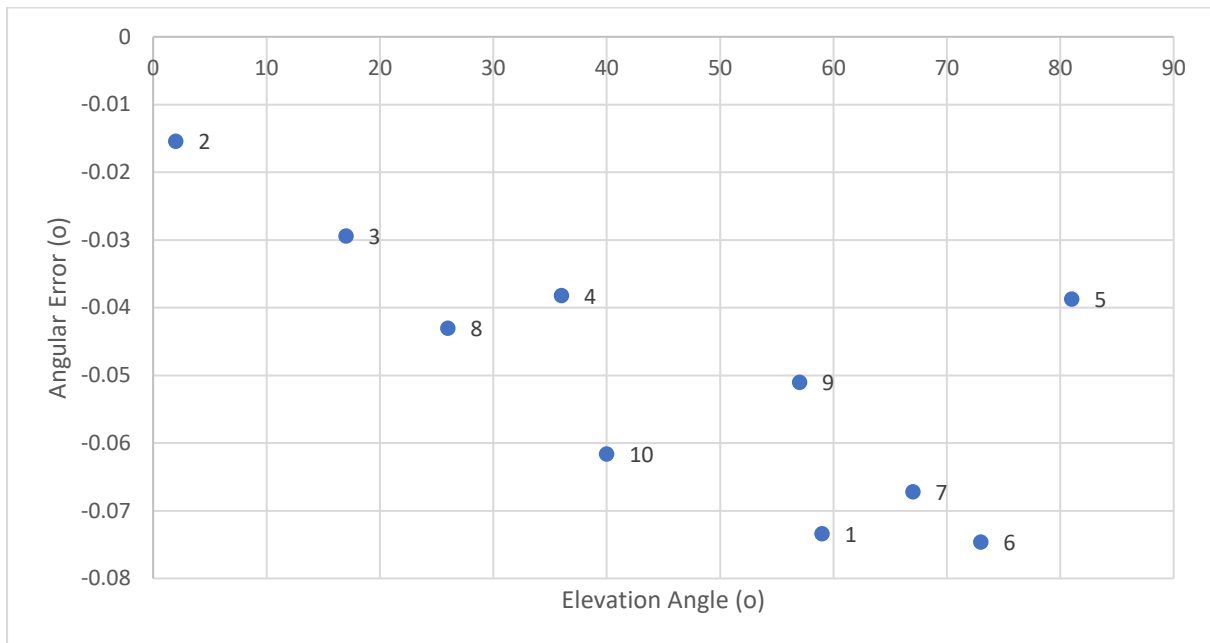


Figure 235: Scatter plot of the angular error at each elevation position during uncertainty testing. Each point on the scatter plot is labelled with a number to show the chronological order in which the measurements were taken.

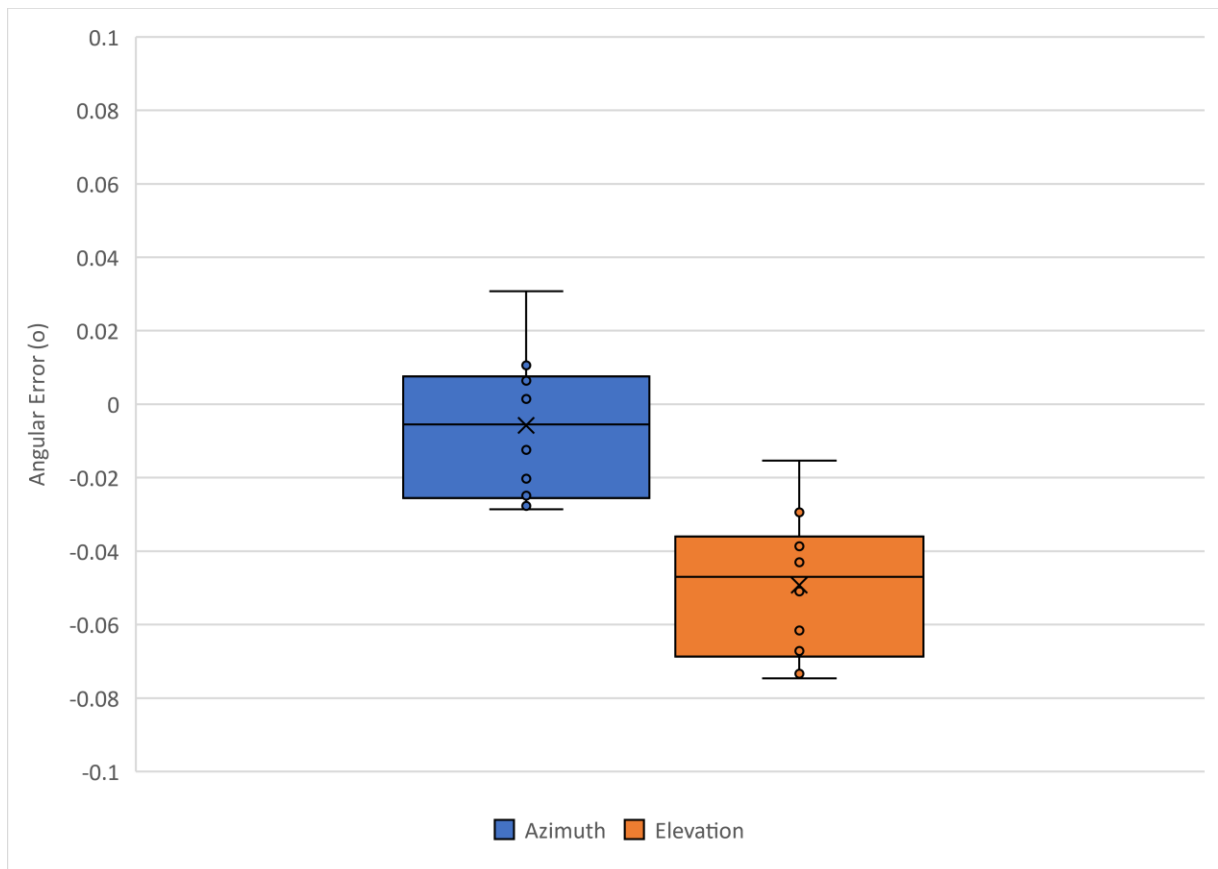


Figure 236: Box and whisker plot containing the angular error values from the azimuth and elevation testing. Target positional error of the fixture is shown on the plot with red lines.

Retrieved MoM Wear Maps

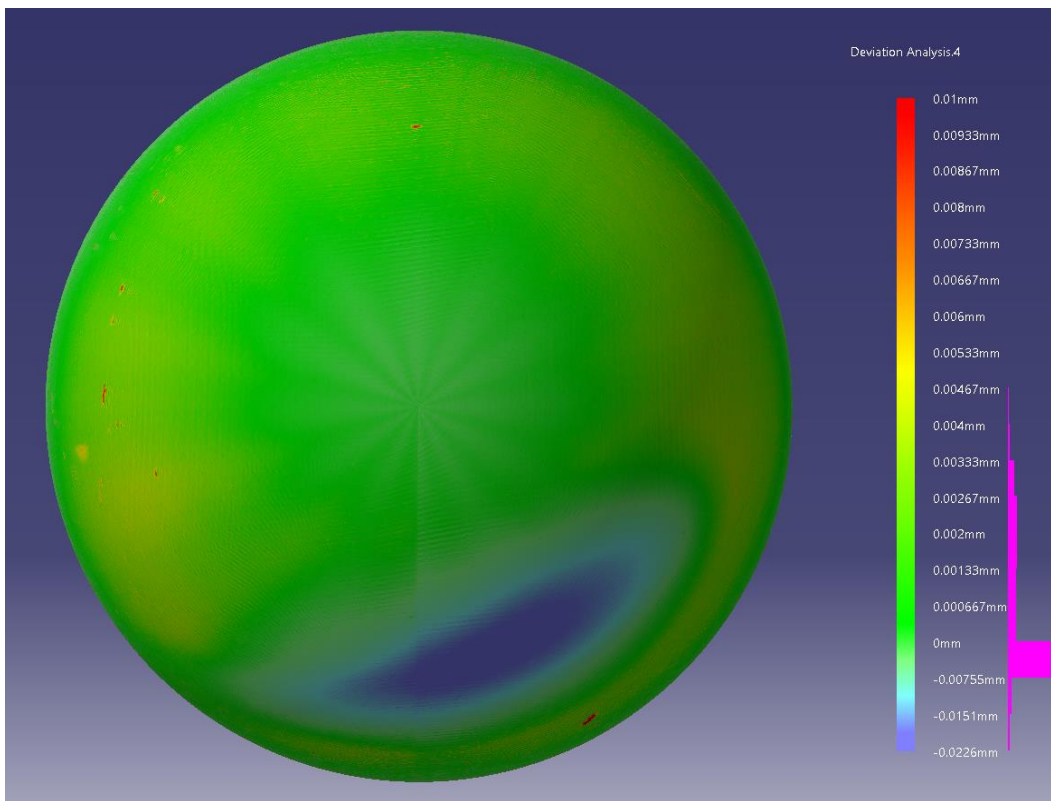


Figure 237: Femoral Head 135 Wear Map.

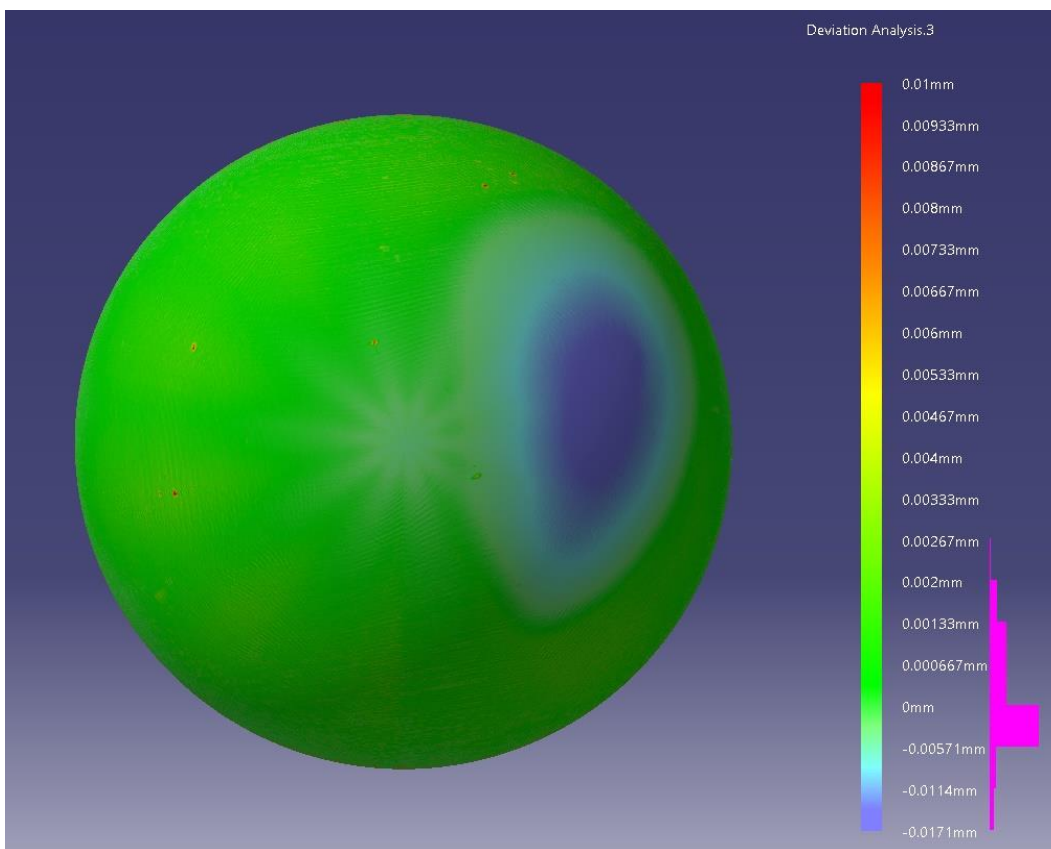


Figure 238: Femoral Head 294 Wear Map.

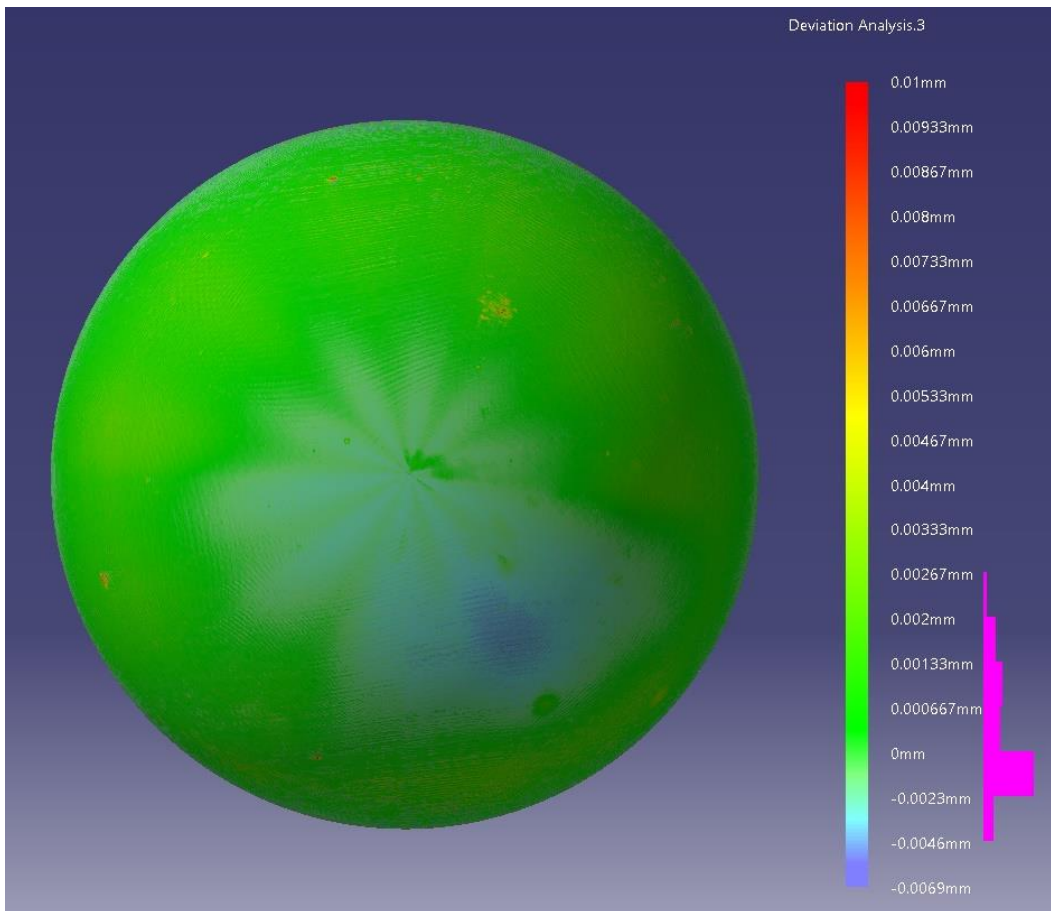


Figure 239: Femoral Head 213 Wear Map.

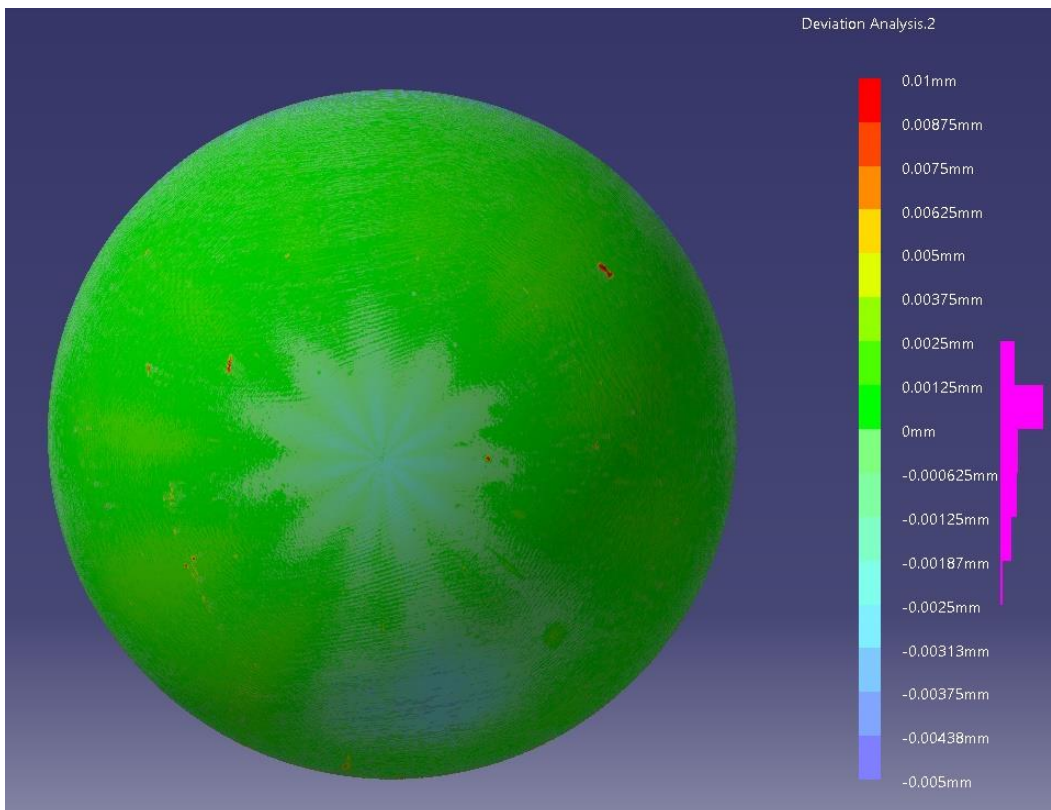


Figure 240: Femoral Head 608 Wear Map.

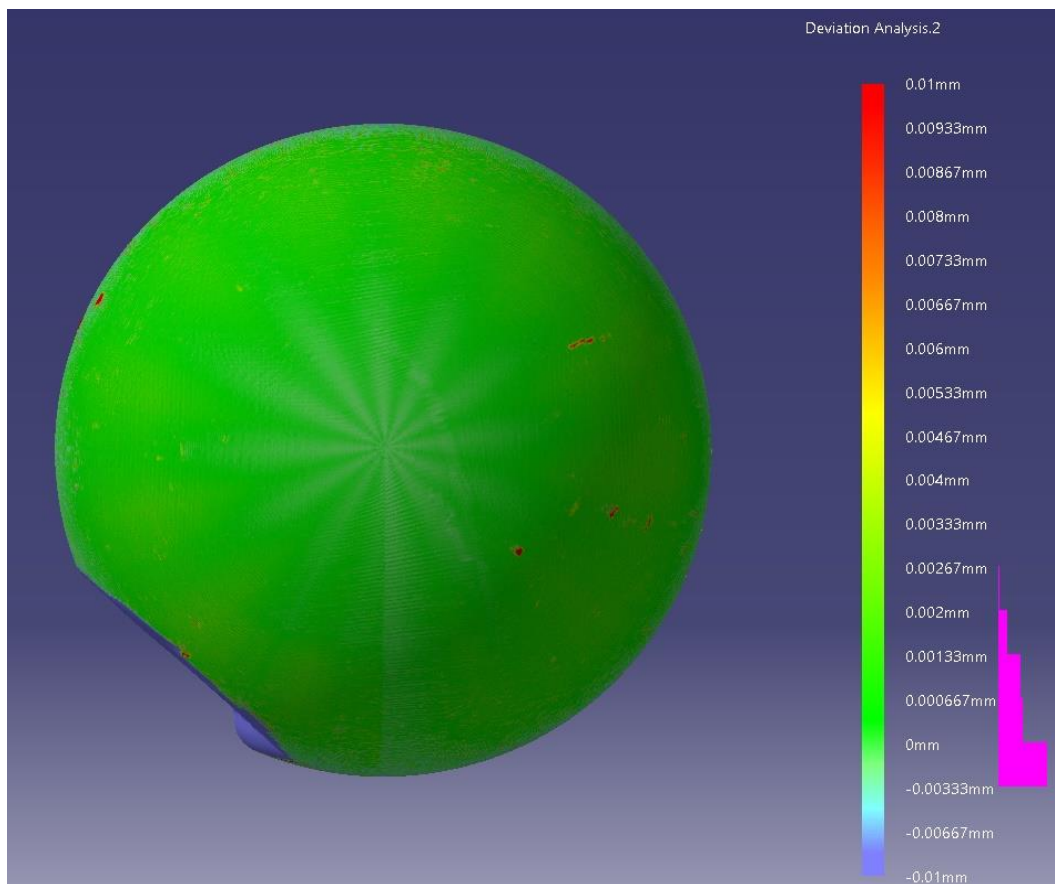


Figure 241: Femoral Head 082 Wear Map.

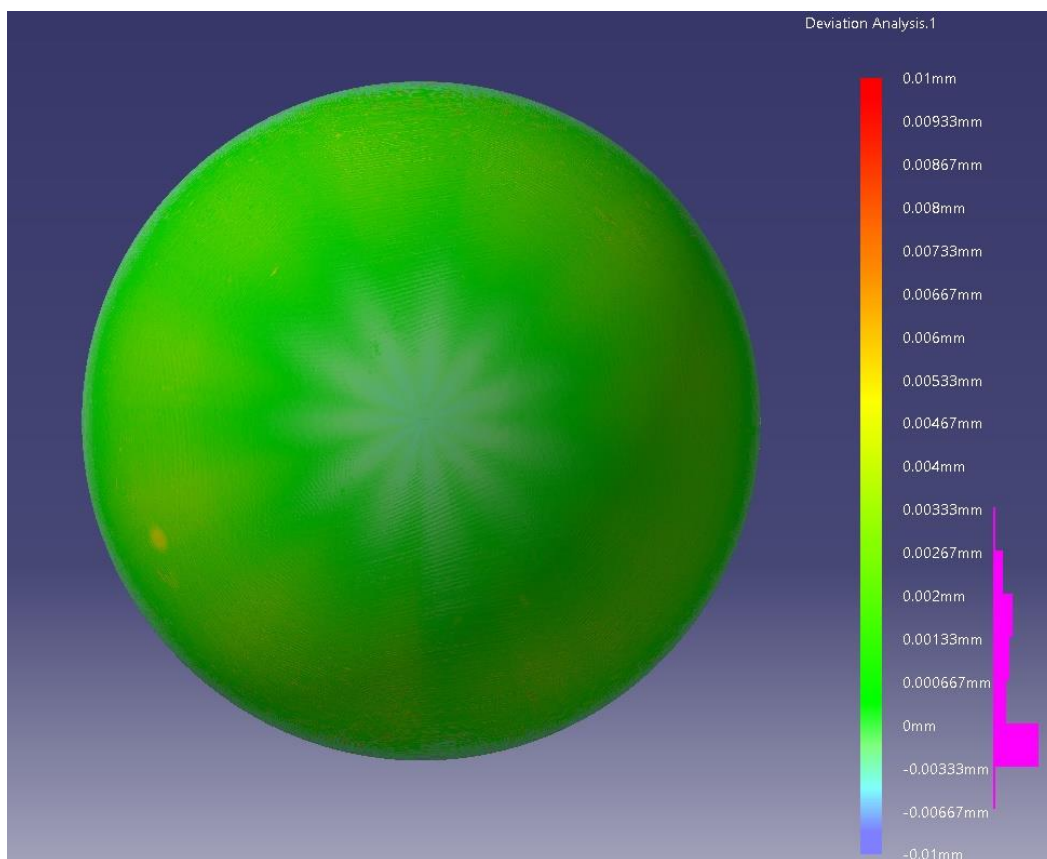


Figure 242: Femoral Head 109 Wear Map.

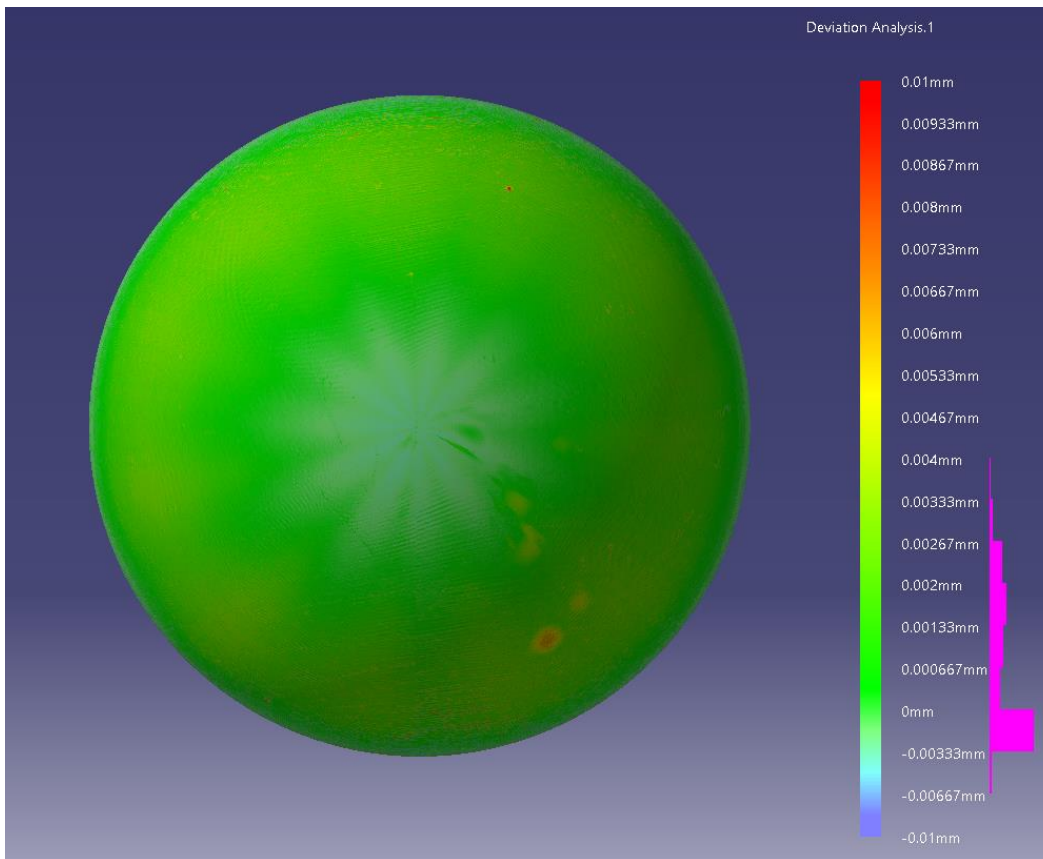


Figure 243: Femoral Head 131 Wear Map.

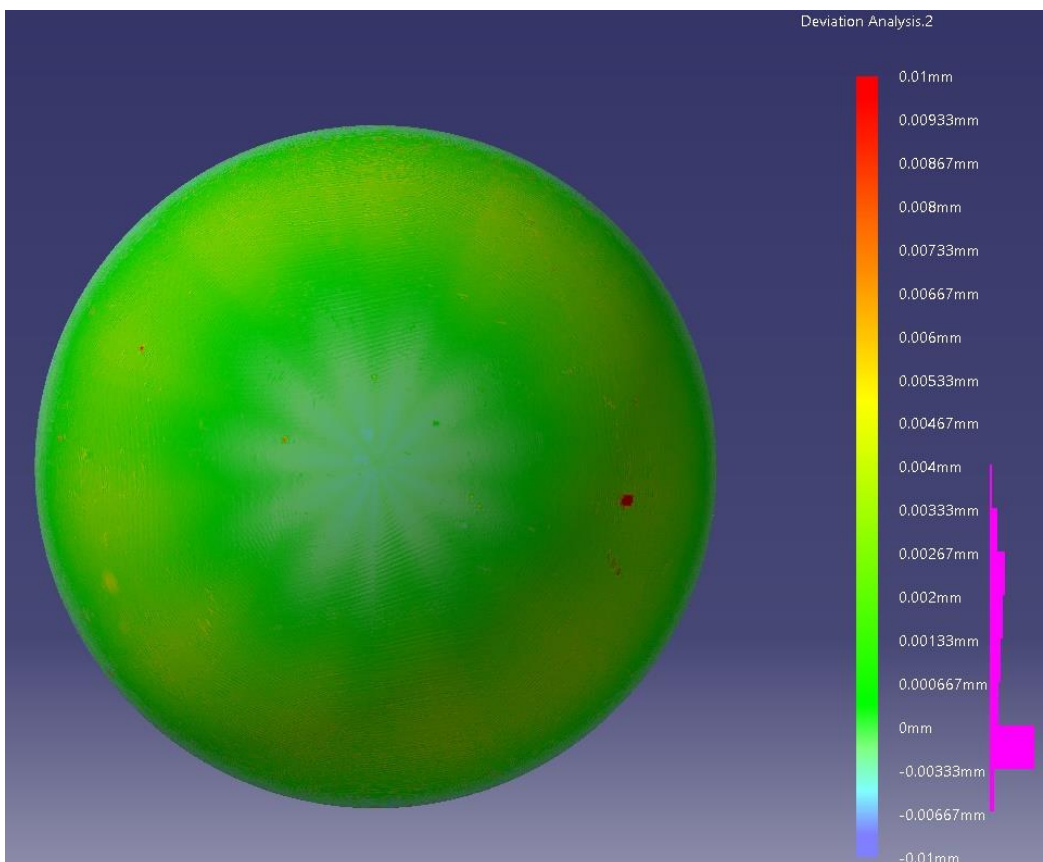


Figure 244: Femoral Head 162 Wear Map.

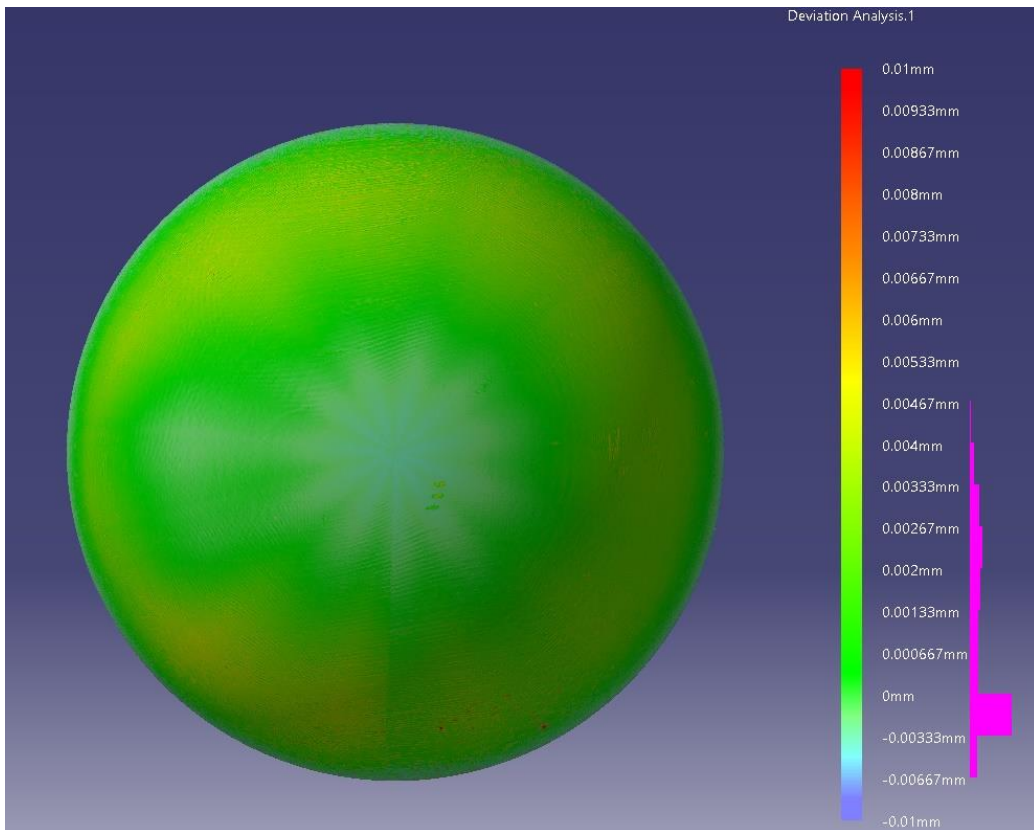


Figure 245: Femoral Head 550 Wear Map.

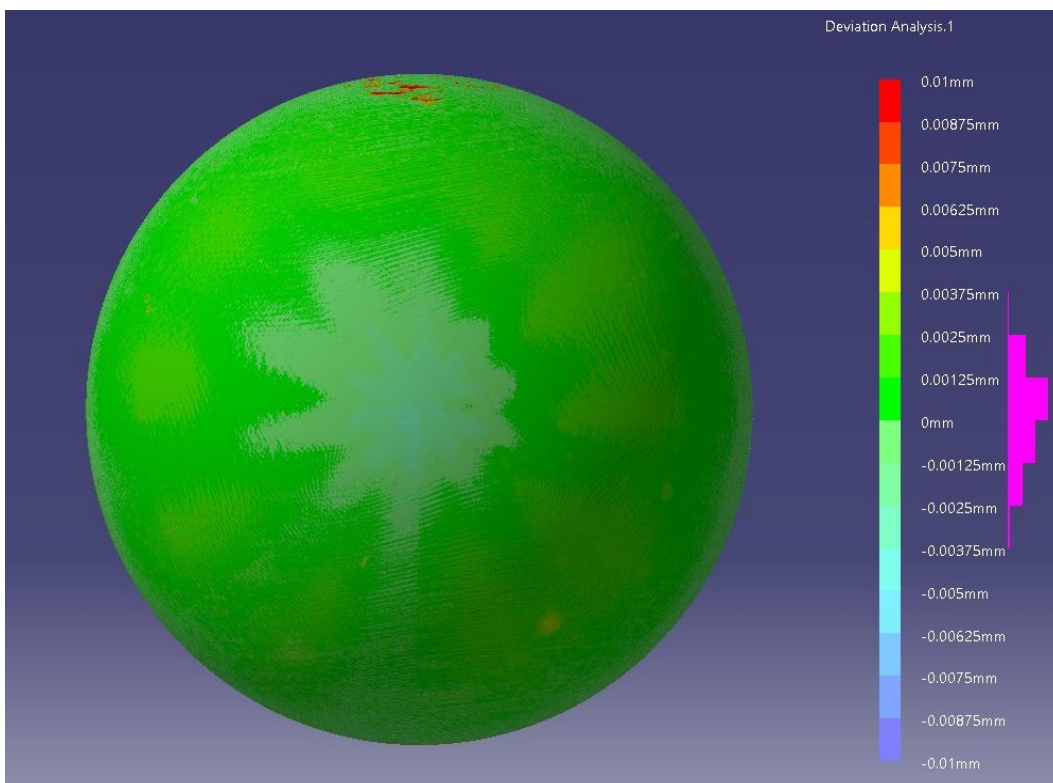


Figure 246: Femoral Head 618 Wear Map.

Unworn Area Surface Measurements

Table 34: Femoral Head 135, Unworn Area Surface Measurements.

No.	Az (o)	El (o)	Sa (nm)	Sdr (x10 ⁻³)	Ssk
UN01	89	63	35.09	2.000	-1.36
UN02	76	63	41.00	25.000	-3.09
UN03	53	70	28.00	16.000	-2.67
UN04	59	20	125.00	195.000	0.47
UN05	15	9	87.00	96.000	-0.73
UN06	137	26	57.00	56.000	2.08
UN07	136	58	33.00	28.000	3.94
UN08	162	29	45.00	38.000	2.67
UN09	146	4	68.00	63.000	1.06
UN10	166	8	53.69	35.000	1.75
UN11	197	65	32.00	25.000	3.82
UN12	213	28	36.00	17.000	2.50
UN13	237	55	20.34	3.000	-0.37
UN14	243	24	28.92	1.000	0.03
UN15	265	59	52.00	79.000	-1.23
UN16	-77	16	44.00	12.000	-3.35
UN17	-79	45	29.30	7.000	-0.75
UN18	-62	25	30.94	3.000	-1.40
UN19	-52	54	32.49	16.000	-0.07
UN20	-18	72	27.00	9.000	-0.46
RIM01	0	95	3.46	0.150	-12.20
RIM02	72	95	3.78	0.058	-2.55
RIM03	144	95	5.00	3.000	-32.83
RIM04	216	95	3.57	0.087	-3.34
RIM05	288	95	3.14	0.017	-0.15
Min	NA	NA	3.14	0.017	-32.83
Max	NA	NA	125.00	195.000	3.94
Median	NA	NA	32.49	16.000	-0.46
SD	NA	NA	27.16	42.483	7.04

Table 35: Femoral Head 294, Unworn Area Surface Measurements..

No.	Az.	El.	Sa (nm)	Sdr (x10 ⁻³)	Ssk
UN01	139	55	8.00	3.000	-34.47
UN02	146	31	11.10	8.000	-6.56
UN03	124	9	16.70	3.000	-0.35
UN04	181	51	45.00	37.000	-8.81
UN05	184	26	18.00	13.000	-5.65
UN06	210	10	11.52	2.000	-5.99
UN07	212	38	11.00	10.000	-8.14
UN08	227	56	7.11	2.000	6.37
UN09	258	54	14.89	5.000	-1.07
UN10	230	29	6.26	1.000	2.68
UN11	266	8	16.27	8.000	3.00
UN12	-88	33	10.11	0.765	-2.55
UN13	-76	60	18.41	10.000	-2.49
UN14	-61	19	25.97	24.000	-1.60
UN15	-52	55	6.54	0.195	-2.83
UN16	-18	14	20.89	6.000	-1.35
UN17	-44	32	8.27	0.958	7.58
UN18	-29	48	5.69	0.890	24.48
UN19	-4	57	16.00	7.000	4.37
UN20	15	60	50.00	38.000	-2.03
RIM01	0	95	4.88	0.095	0.89
RIM02	72	95	10.00	7.000	-23.13
RIM03	144	95	7.00	2.000	-11.15
RIM04	216	95	14.00	14.000	-13.74
RIM05	288	95	7.20	0.415	-0.98
Min	NA	NA	4.88	0.095	-34.47
Max	NA	NA	50.00	38.000	24.48
Median	NA	NA	11.10	5.000	-2.03
SD	NA	NA	10.99	10.239	10.54

Table 36: Femoral Head 213, Unworn Area Surface Measurements.

No.	Az (o)	El (o)	Sa (nm)	Sdr (x10 ⁻³)	Ssk
UN01	0	10	8.00	6.000	2.76
UN02	72	10	8.00	3.000	-13.80
UN03	144	10	15.00	11.000	-9.43
UN04	216	10	3.69	1.000	1.51
UN05	288	10	5.00	3.000	-9.14
UN06	0	30	7.00	3.000	-2.14
UN07	72	30	16.43	9.000	-2.23
UN08	144	30	19.00	13.000	-21.48
UN09	216	30	3.00	1.000	-28.02
UN10	288	30	3.34	0.854	-12.01
UN11	0	50	3.63	1.000	-14.17
UN12	72	50	16.99	6.000	1.94
UN13	144	50	14.00	4.000	4.32
UN14	216	50	9.00	6.000	-39.11
UN15	288	50	4.00	2.000	-33.46
UN16	0	70	11.96	4.000	6.94
UN17	72	70	20.00	3.000	-3.68
UN18	144	70	21.00	126.000	-7.94
UN19	216	70	13.00	2.000	-5.75
UN20	288	70	4.00	3.000	-49.14
RIM01	0	95	7.93	0.425	7.07
RIM02	72	95	13.00	7.000	-10.50
RIM03	144	95	9.18	0.509	0.85
RIM04	216	95	7.39	0.190	-0.97
RIM05	288	95	7.53	0.761	0.76
Min	NA	NA	3.00	0.190	-49.14
Max	NA	NA	21.00	126.000	7.07
Median	NA	NA	8.00	3.000	-5.75
SD	NA	NA	5.52	24.178	14.34

Table 37: Femoral Head 608, Unworn Area Surface Measurements.

No.	Az (o)	El (o)	Sa (nm)	Sdr (x10 ⁻³)	Ssk
UN01	0	10	2.41	0.015	-0.52
UN02	72	10	1.51	0.005	-0.55
UN03	144	10	4.00	3.000	11.18
UN04	216	10	3.93	0.190	17.12
UN05	288	10	2.96	0.015	-0.18
UN06	0	30	9.00	7.000	9.82
UN07	72	30	18.00	12.000	3.59
UN08	144	30	14.00	19.000	-15.67
UN09	216	30	7.00	2.000	12.59
UN10	288	30	10.00	6.000	6.43
UN11	0	50	3.16	0.083	-6.48
UN12	72	50	2.07	0.723	21.66
UN13	144	50	14.00	16.000	-17.40
UN14	216	50	5.52	0.813	-14.41
UN15	288	50	10.00	4.000	20.10
UN16	0	70	6.00	3.000	-13.01
UN17	72	70	13.00	11.000	5.92
UN18	144	70	6.00	2.000	1.67
UN19	216	70	10.00	8.000	31.57
UN20	288	70	5.73	0.505	-11.44
RIM01	0	95	16.00	9.000	-16.78
RIM02	72	95	8.00	0.997	-18.98
RIM03	144	95	8.65	0.939	-3.72
RIM04	216	95	17.00	14.000	-11.68
RIM05	288	95	16.00	10.000	-2.88
Min	NA	NA	1.51	0.005	-18.98
Max	NA	NA	18.00	19.000	31.57
Median	NA	NA	8.00	3.000	-0.52
SD	NA	NA	4.99	5.566	13.46

Table 38: Femoral Head 082, Unworn Area Surface Measurements.

No.	Az (o)	El (o)	Sa (nm)	Sdr (x10 ⁻³)	Ssk
UN01	0	10	31.00	34.000	-3.19
UN02	72	10	28.00	12.000	-1.30
UN03	144	10	17.30	9.000	-3.12
UN04	216	10	9.43	5.000	-2.59
UN05	288	10	31.00	27.000	-2.89
UN06	0	30	27.00	14.000	-10.60
UN07	72	30	30.00	27.000	-3.85
UN08	144	30	8.58	3.000	-3.49
UN09	216	30	16.00	14.000	-5.61
UN10	288	30	19.00	19.000	-5.20
UN11	0	50	9.87	5.000	-7.72
UN12	72	50	16.77	1.000	-1.44
UN13	144	50	16.00	9.000	-2.32
UN14	216	50	25.00	21.000	-10.22
UN15	288	50	35.00	48.000	16.79
UN16	0	70	45.00	40.000	-2.53
UN17	72	70	18.00	2.000	-3.81
UN18	144	70	18.00	9.000	-8.91
UN19	216	70	10.00	5.000	-13.13
UN20	288	70	23.00	12.000	-11.00
RIM01	0	95	16.00	9.000	-16.92
RIM02	72	95	33.00	46.000	-2.45
RIM03	144	95	11.00	5.000	-33.65
RIM04	216	95	18.00	7.000	-1.76
RIM05	288	95	23.00	12.000	-10.44
Min	NA	NA	8.58	1.000	-13.13
Max	NA	NA	45.00	48.000	16.79
Median	NA	NA	18.00	12.000	-3.81
SD	NA	NA	9.11	13.425	8.25

Table 39: Femoral Head 109, Unworn Area Surface Measurements.

No.	Az (o)	El (o)	Sa (nm)	Sdr (x10 ⁻³)	Ssk
UN01	0	10	4.08	1.000	-1.33
UN02	72	10	32.00	11.000	-1.19
UN03	144	10	18.00	11.000	-0.82
UN04	216	10	6.09	1.000	5.58
UN05	288	10	3.08	0.034	4.23
UN06	0	30	4.52	1.000	-2.74
UN07	72	30	4.63	4.000	3.45
UN08	144	30	3.83	2.000	7.12
UN09	216	30	3.81	0.286	-16.11
UN10	288	30	6.00	3.000	-5.38
UN11	0	50	3.65	0.025	0.06
UN12	72	50	6.08	4.000	-7.73
UN13	144	50	13.12	4.000	3.46
UN14	216	50	3.56	0.028	-0.54
UN15	288	50	8.00	3.000	-0.26
UN16	0	70	7.00	5.000	-22.37
UN17	72	70	5.00	0.600	-32.97
UN18	144	70	4.73	0.559	11.33
UN19	216	70	10.00	5.000	-15.92
UN20	288	70	12.28	12.000	-3.97
RIM01	0	95	4.50	0.298	-25.51
RIM02	72	95	4.71	0.331	-7.17
RIM03	144	95	14.00	0.398	-2.16
RIM04	216	95	10.00	11.000	3.39
RIM05	288	95	36.00	38.000	-14.43
Min	NA	NA	3.08	0.03	-32.97
Max	NA	NA	36.00	38.00	11.33
Median	NA	NA	6.00	2.000	-1.33
SD	NA	NA	8.26	7.779	10.58

Table 40: Femoral Head 131, Unworn Area Surface Measurements.

No.	Az (o)	El (o)	Sa (nm)	Sdr (x10 ⁻³)	Ssk
UN01	0	10	16.00	7.000	-2.69
UN02	72	10	12.53	1.000	-1.84
UN03	144	10	10.10	2.000	2.18
UN04	216	10	15.19	0.895	0.09
UN05	288	10	13.00	2.000	-1.15
UN06	0	30	17.57	3.000	2.49
UN07	72	30	172.00	41.000	-2.13
UN08	144	30	22.00	14.000	-6.28
UN09	216	30	17.00	4.000	-16.91
UN10	288	30	28.00	13.000	0.19
UN11	0	50	30.00	18.000	2.39
UN12	72	50	235.00	41.000	-0.63
UN13	144	50	11.00	7.000	-17.18
UN14	216	50	18.00	11.000	2.91
UN15	288	50	30.64	17.000	2.36
UN16	0	70	34.75	22.000	2.36
UN17	72	70	13.02	6.000	-5.94
UN18	144	70	9.66	0.553	-0.45
UN19	216	70	34.00	22.000	1.31
UN20	288	70	34.60	22.000	2.40
RIM01	0	95	38.00	24.000	2.05
RIM02	72	95	21.00	8.000	-7.62
RIM03	144	95	32.46	19.000	1.97
RIM04	216	95	40.00	33.000	-18.45
RIM05	288	95	43.00	30.000	-5.35
Min	NA	NA	9.66	0.55	-18.45
Max	NA	NA	235.00	41.00	2.91
Median	NA	NA	22.00	13.00	-0.45
SD	NA	NA	50.63	12.07	6.29

Table 41: Femoral Head 162, Unworn Area Surface Measurements.

No.	Az (o)	El (o)	Sa (nm)	Sdr (x10 ⁻³)	Ssk
UN01	0	10	20.00	23.000	0.63
UN02	72	10	11.66	10.000	-2.98
UN03	144	10	22.00	22.000	-1.54
UN04	216	10	6.00	3.000	-4.90
UN05	288	10	11.00	6.000	-11.24
UN06	0	30	25.00	29.000	-1.73
UN07	72	30	17.00	105.000	-2.91
UN08	144	30	5.93	2.000	9.25
UN09	216	30	215.00	209.000	-1.91
UN10	288	30	9.60	5.000	-3.53
UN11	0	50	12.00	7.000	5.62
UN12	72	50	5.00	1.000	-4.85
UN13	144	50	10.00	10.000	-11.91
UN14	216	50	5.94	2.000	-1.35
UN15	288	50	19.00	14.000	-2.21
UN16	0	70	93.00	106.000	-1.95
UN17	72	70	6.00	1.000	-16.27
UN18	144	70	10.00	4.000	-21.98
UN19	216	70	4.58	0.530	-17.93
UN20	288	70	14.00	10.000	5.20
RIM01	0	95	14.00	10.000	5.23
RIM02	72	95	44.00	20.000	-4.45
RIM03	144	95	14.00	13.000	1.22
RIM04	216	95	48.00	5.000	-2.74
RIM05	288	95	409.00	358.000	-0.24
Min	NA	NA	4.58	0.53	-21.98
Max	NA	NA	409.00	358.00	9.25
Median	NA	NA	14.00	10.000	-2.21
SD	NA	NA	86.20	79.807	7.25

Table 42: Femoral Head 550, Unworn Area Surface Measurements.

No.	Az (o)	El (o)	Sa (nm)	Sdr (x10 ⁻³)	Ssk
UN01	0	10	3.71	1.000	-11.75
UN02	72	10	3.00	1.000	-20.11
UN03	144	10	6.00	6.000	-5.59
UN04	216	10	33.00	19.000	-2.79
UN05	288	10	21.00	27.000	-6.51
UN06	0	30	19.51	19.000	-3.29
UN07	72	30	2.16	0.042	-5.76
UN08	144	30	3.96	0.128	-1.57
UN09	216	30	28.00	36.000	-4.61
UN10	288	30	16.00	12.000	-11.47
UN11	0	50	58.82	73.000	-2.28
UN12	72	50	5.01	0.615	-5.31
UN13	144	50	2.96	0.087	-14.40
UN14	216	50	4.16	1.000	-11.19
UN15	288	50	2.76	0.911	-15.08
UN16	0	70	39.00	48.000	-9.33
UN17	72	70	4.96	0.211	-2.18
UN18	144	70	18.00	9.000	-8.85
UN19	216	70	4.00	1.000	-6.64
UN20	288	70	3.58	0.408	-7.85
RIM01	0	95	3.59	0.026	-0.21
RIM02	72	95	8.22	4.000	-6.31
RIM03	144	95	10.00	4.000	-32.90
RIM04	216	95	6.67	0.187	-1.74
RIM05	288	95	4.78	0.030	-0.49
Min	NA	NA	2.16	0.026	-32.90
Max	NA	NA	58.82	73.000	-0.21
Median	NA	NA	5.01	1.000	-6.31
SD	NA	NA	13.83	17.774	7.06

Table 43: Femoral Head 618, Unworn Area Surface Measurements.

No.	Az (o)	El (o)	Sa (nm)	Sdr (x10 ⁻³)	Ssk
UN01	0	10	1.53	0.084	-23.38
UN02	72	10	1.23	0.012	-2.49
UN03	144	10	2.15	0.093	-4.39
UN04	216	10	5.68	0.207	0.33
UN05	288	10	3.23	0.140	-0.42
UN06	0	30	2.97	0.200	-2.55
UN07	72	30	4.18	0.013	-2.86
UN08	144	30	6.42	0.081	0.43
UN09	216	30	4.76	0.028	0.16
UN10	288	30	2.16	0.377	-13.27
UN11	0	50	2.86	0.011	0.02
UN12	72	50	3.00	0.022	3.22
UN13	144	50	3.00	0.110	-20.62
UN14	216	50	6.77	1.000	-0.93
UN15	288	50	6.00	6.000	2.34
UN16	0	70	3.28	0.014	-0.51
UN17	72	70	3.50	0.018	0.34
UN18	144	70	2.54	0.011	0.58
UN19	216	70	3.55	0.911	24.19
UN20	288	70	3.74	0.466	-18.40
RIM01	0	95	5.00	3.000	-23.37
RIM02	72	95	5.00	1.000	-13.40
RIM03	144	95	13.00	9.000	-6.91
RIM04	216	95	13.00	10.000	-7.14
RIM05	288	95	9.00	3.000	-17.52
Min	NA	NA	1.23	0.01	-23.38
Max	NA	NA	13.00	10.00	24.19
Median	NA	NA	3.55	0.14	-2.49
SD	NA	NA	3.01	2.74	10.24

Wear Surface Measurements – Femoral Head 135

Table 44: Component 135, Grouped Measurements, Full Surface Measurement Results.

No.	WSC (mm)	WSC (o)	Sa (nm)	Sdr	Ssk	Spk (nm)	Svk (nm)	Ssk mag
CWS01	-	-	116	0.082	-0.761	159	263	0.761
CWS02	6.579	15.078	90	0.09	-0.647	179	228	0.647
CWS03	5.251	12.035	150	0.122	-0.352	236	293	0.352
CWS04	3.680	8.434	85	0.054	-0.147	179	170	0.147
CWS05	3.465	7.941	124	0.122	-0.955	168	290	0.955
CWS06	2.455	5.627	122	0.098	-0.343	186	207	0.343
CWS07	1.430	3.278	132	0.104	-0.494	173	250	0.494
CWS08	1.120	2.566	131	0.143	1.553	375	235	1.553
CWS09	0.927	2.124	117	0.06	-0.183	158	178	0.183
CWS10	2.096	4.803	121	0.064	-0.235	185	207	0.235
OWS01	11.080	25.394	95	0.049	-1.114	111	249	1.114
OWS02	8.485	19.446	123	0.054	-1.537	143	365	1.537
OWS03	7.926	18.165	87	0.049	-1.405	159	314	1.405
OWS04	6.128	14.043	129	0.058	-0.955	60	254	0.955
OWS05	4.663	10.686	65	0.043	0.755	167	123	0.755
OWS06	2.674	6.128	129	0.057	-0.904	102	278	0.904
OWS07	3.170	7.264	53	0.025	1.245	148	78	1.245
OWS08	5.599	12.831	38.23	0.008	0.985	100.608	81.108	0.985
OWS09	6.317	14.478	43	0.014	-1.288	78	149	1.288
OWS10	6.287	14.408	48	0.009	0.42	116	107	0.42
UN01	24.062	55.145	35.088	0.002	-1.358	61.099	134.607	1.358
UN02	20.552	47.102	41	0.025	-3.089	84	213	3.089
UN03	16.715	38.309	28	0.016	-2.665	80	172	2.665
UN04	12.751	29.224	125	0.195	0.465	198	133	0.465
UN05	12.967	29.718	87	0.096	-0.729	147	219	0.729
UN06	23.299	53.398	57	0.056	2.078	217	99	2.078
UN07	32.813	75.201	33	0.028	3.935	173	47	3.935
UN08	26.049	59.699	45	0.038	2.665	187	73	2.665
UN09	17.290	39.626	68	0.063	1.06	202	123	1.06
UN10	19.013	43.574	53.691	0.035	1.746	182.835	61.703	1.746
UN11	39.720	91.032	32	0.025	3.817	196	46	3.817
UN12	25.978	59.536	36	0.017	2.5	138	45	2.5
UN13	32.175	73.739	20.344	0.003	-0.366	52.84	59.054	0.366
UN14	22.232	50.951	28.922	0.001	0.028	59.328	49.565	0.028
UN15	27.854	63.838	52	0.079	-1.233	285	277	1.233
UN16	16.575	37.988	44	0.012	-3.349	79	140	3.349
UN17	21.175	48.530	29.298	0.007	-0.751	56.916	71.404	0.751
UN18	15.116	34.643	30.942	0.003	-1.399	41.919	75.194	1.399
UN19	16.557	37.945	32.487	0.016	-0.07	79.315	77.919	0.07
UN20	12.804	29.346	27	0.009	-0.46	74	92	0.46
RIM01	-	-	3.464	0.0001503	-12.199	5.331	12.178	12.199
RIM02	-	-	3.78	0.00005828	-2.549	7.296	9.394	2.549
RIM03	-	-	5	0.003	-32.834	8	57	32.834
RIM04	-	-	3.572	0.00008718	-3.34	8.529	10.025	3.34
RIM05	-	-	3.138	0.00001701	-0.151	4.294	4.87	0.151

Table 45: Component 135, Stitched Measurements, Full Surface Measurement Results.

No.	Az.	El.	Sa (nm)	Sdr	Ssk	Spk (nm)	Svk (nm)
STI1_01	2	13.69655	109	0.125	-1.111	98	244
STI1_02	2	15.38463	133	0.094	-0.729	248	463
STI1_03	2	17.07272	114	0.143	-0.715	175	237
STI1_04	2	18.7608	102	0.117	-1.642	133	256
STI1_05	2	20.44889	101	0.14	-0.891	130	216
STI1_06	2	22.13697	103	0.135	-1.312	94	229
STI1_07	2	23.82506	110	0.153	-0.422	82	159
STI1_08	2	25.51315	81	0.102	-0.697	135	184
STI1_09	2	27.20123	76	0.059	-0.799	71	148
STI1_10	2	28.88932	108	0.154	-0.878	108	218
STI1_11	2	30.5774	107	0.148	-1.097	109	240
STI1_12	2	32.26549	67	0.047	-0.452	133	174
STI1_13	2	33.95357	102	0.159	0.973	265	208
STI1_14	2	35.64166	105	0.156	0.708	248	193
STI1_15	2	37.32975	100	0.145	1.43	302	196
STI1_16	2	39.01783	74	0.073	1.089	237	191
STI1_17	2	40.70592	88	0.061	0.775	222	194
STI1_18	2	42.394	134	0.094	-0.121	292	269
STI1_19	2	44.08209	118	0.062	-0.172	173	194
STI1_20	2	45.77017	126	0.081	-0.443	178	246
STI1_21	2	47.45826	160	0.135	-0.427	200	286
STI1_22	2	49.14634	164	0.136	-0.781	146	316
STI1_23	2	50.83443	140	0.086	-0.897	145	313
STI1_24	2	52.52252	113	0.073	-0.079	207	194
STI1_25	2	54.2106	144	0.112	-0.722	161	278
STI1_26	2	55.89869	148	0.11	-1.018	112	323
STI1_27	2	57.58677	71	0.046	-1.045	117	203
STI1_28	2	59.27486	41	0.019	-1.867	67	135
STI1_29	2	60.96294	25	0.008	-3.084	41	115
STI1_30	2	62.65103	22	0.005	-2.455	42	96
STI1_31	2	64.33912	16	0.009	-9.855	75	75
STI1_32	2	66.0272	14	0.007	-8.364	67	61
STI1_33	2	67.71529	12	0.004	-19.387	31	54
STI1_34	2	69.40337	15	0.007	-8.673	74	59
STI1_35	2	71.09146	14	0.004	4.025	44	42
STI2_01	7.2932	13.69655	91	0.119	-0.347	142	187
STI2_02	7.2932	15.38463	94	0.115	-1.13	97	210
STI2_03	7.2932	17.07272	104	0.127	-1.222	98	222
STI2_04	7.2932	18.7608	106	0.164	-0.701	120	193
STI2_05	7.2932	20.44889	100	0.139	-0.772	137	202
STI2_06	7.2932	22.13697	116	0.154	-1.686	155	286
STI2_07	7.2932	23.82506	96	0.107	-2.062	107	229
STI2_08	7.2932	25.51315	87	0.109	-0.785	100	187
STI2_09	7.2932	27.20123	90	0.112	-1.013	92	206
STI2_10	7.2932	28.88932	109	0.172	-0.887	113	215
STI2_11	7.2932	30.5774	88	0.133	-0.111	161	188
STI2_12	7.2932	32.26549	68	0.081	0.241	164	161
STI2_13	7.2932	33.95357	71	0.082	-0.032	175	207
STI2_14	7.2932	35.64166	82	0.105	1.13	213	110

STI2_15	7.2932	37.32975	63	0.059	1.351	204	119
STI2_16	7.2932	39.01783	85	0.053	-0.386	187	226
STI2_17	7.2932	40.70592	129	0.132	1.448	354	232
STI2_18	7.2932	42.394	114	0.098	0.065	233	222
STI2_19	7.2932	44.08209	120	0.085	-0.811	155	257
STI2_20	7.2932	45.77017	122	0.082	-0.31	177	210
STI2_21	7.2932	47.45826	131	0.108	-0.31	170	233
STI2_22	7.2932	49.14634	166	0.14	-0.859	143	353
STI2_23	7.2932	50.83443	165	0.115	-0.88	123	344
STI2_24	7.2932	52.52252	168	0.114	-0.873	122	334
STI2_25	7.2932	54.2106	132	0.097	-0.715	151	257
STI2_26	7.2932	55.89869	156	0.107	-1.039	84	332
STI2_27	7.2932	57.58677	104	0.059	-1.614	100	311
STI2_28	7.2932	59.27486	91	0.034	-1.815	77	311
STI2_29	7.2932	60.96294	17	0.005	-0.651	44	70
STI2_30	7.2932	62.65103	17	0.008	-7.814	84	65
STI2_31	7.2932	64.33912	19	0.006	-1.639	55	107
STI2_32	7.2932	66.0272	15	0.008	-1.005	60	58
STI2_33	7.2932	67.71529	13	0.009	-1.659	56	58
STI2_34	7.2932	69.40337	9.089	0.001	1.395	28.241	24.574
STI2_35	7.2932	71.09146	9	0.002	3.154	35	26
STI3_01	15	13.69655	89	0.123	-0.099	155	176
STI3_02	15	15.38463	92	0.123	-0.758	135	224
STI3_03	15	17.07272	111	0.165	-2.758	124	265
STI3_04	15	18.7608	115	0.194	-0.491	132	203
STI3_05	15	20.44889	107	0.15	-1.22	128	250
STI3_06	15	22.13697	93	0.143	-0.291	143	186
STI3_07	15	23.82506	94	0.127	-1.204	102	199
STI3_08	15	25.51315	103	0.134	-1.886	104	278
STI3_09	15	27.20123	114	0.178	-0.024	331	352
STI3_10	15	28.88932	80	0.113	-0.171	151	185
STI3_11	15	30.5774	79	0.107	-0.265	153	189
STI3_12	15	32.26549	69	0.08	0.316	175	172
STI3_13	15	33.95357	82	0.105	0.458	218	150
STI3_14	15	35.64166	57	0.053	1.546	187	96
STI3_15	15	37.32975	57	0.048	0.646	189	160
STI3_16	15	39.01783	110	0.065	0.012	187	169
STI3_17	15	40.70592	127	0.106	-0.39	199	237
STI3_18	15	42.394	128	0.105	-0.446	162	238
STI3_19	15	44.08209	162	0.153	-0.645	160	301
STI3_20	15	45.77017	129	0.115	-1.005	161	335
STI3_21	15	47.45826	137	0.101	-0.904	149	317
STI3_22	15	49.14634	147	0.114	-0.602	133	242
STI3_23	15	50.83443	138	0.109	-0.721	128	251
STI3_24	15	52.52252	142	0.108	-0.922	152	299
STI3_25	15	54.2106	142	0.098	-0.852	120	282
STI3_26	15	55.89869	140	0.09	-1.065	83	313
STI3_27	15	57.58677	143	0.084	-2.192	90	522
STI3_28	15	59.27486	117	0.062	-3.043	91	490
STI3_29	15	60.96294	51	0.029	-2.473	110	232
STI3_30	15	62.65103	14	0.006	4.004	63	36
STI3_31	15	64.33912	15	0.007	5.612	71	28
STI3_32	15	66.0272	21	0.015	-29.789	59	138

STI3_33	15	67.71529	12	0.004	5.611	60	27
STI3_34	15	69.40337	8.307	0.002	7.065	37.307	18.809
STI3_35	15	71.09146	14	0.01	2.853	68	45
STI4_01	25	13.69655	106	0.145	-0.211	147	181
STI4_02	25	15.38463	100	0.142	-0.726	150	202
STI4_03	25	17.07272	105	0.173	0.038	156	165
STI4_04	25	18.7608	115	0.207	-0.273	142	191
STI4_05	25	20.44889	110	0.186	-0.655	141	234
STI4_06	25	22.13697	92	0.136	-0.623	145	213
STI4_07	25	23.82506	96	0.129	-0.653	106	186
STI4_08	25	25.51315	99	0.13	-0.881	107	217
STI4_09	25	27.20123	82	0.115	-0.767	140	220
STI4_10	25	28.88932	82	0.116	-0.053	165	187
STI4_11	25	30.5774	78	0.097	0.628	188	152
STI4_12	25	32.26549	88	0.119	0.229	199	199
STI4_13	25	33.95357	87	0.096	0.193	211	225
STI4_14	25	35.64166	91	0.098	-0.815	204	291
STI4_15	25	37.32975	129	0.122	-0.381	227	281
STI4_16	25	39.01783	104	0.07	-0.18	190	202
STI4_17	25	40.70592	101	0.072	-0.059	154	154
STI4_18	25	42.394	115	0.097	-0.368	193	233
STI4_19	25	44.08209	148	0.137	-0.764	178	301
STI4_20	25	45.77017	154	0.145	-1.291	101	346
STI4_21	25	47.45826	159	0.144	-1.054	107	338
STI4_22	25	49.14634	142	0.1	-0.75	169	309
STI4_23	25	50.83443	177	0.127	-1.085	156	428
STI4_24	25	52.52252	178	0.11	-1.143	129	441
STI4_25	25	54.2106	172	0.111	-1.298	100	417
STI4_26	25	55.89869	150	0.089	-1.756	64	393
STI4_27	25	57.58677	111	0.055	-2.167	66	359
STI4_28	25	59.27486	111	0.053	-1.732	87	332
STI4_29	25	60.96294	48	0.015	-3.552	59	196
STI4_30	25	62.65103	31	0.01	-3.716	49	179
STI4_31	25	64.33912	14	0.004	2.005	55	62
STI4_32	25	66.0272	13.297	0.001	0.319	29.865	36.253
STI4_33	25	67.71529	15	0.002	-1.4	43	67
STI4_34	25	69.40337	15	0.003	-3.686	34	92
STI4_35	25	71.09146	11	0.004	-16.271	47	54
STI5_01	200	13.69655	37	0.017	1.903	146	56
STI5_02	200	15.38463	29	0.01	2.928	108	37
STI5_03	200	17.07272	51.479	0.014	0.967	140.568	88.106
STI5_04	200	18.7608	55	0.036	1.369	189	113
STI5_05	200	20.44889	59	0.046	1.522	199	117
STI5_06	200	22.13697	36	0.025	2.678	159	46
STI5_07	200	23.82506	63	0.055	1.768	238	84
STI5_08	200	25.51315	50	0.045	0.997	213	91
STI5_09	200	27.20123	64	0.068	1.804	244	97
STI5_10	200	28.88932	42	0.038	1.147	163	117
STI5_11	200	30.5774	50	0.047	2.984	206	87
STI5_12	200	32.26549	36	0.032	2.701	167	56
STI5_13	200	33.95357	41	0.034	3.814	190	35
STI5_14	200	35.64166	42	0.036	3.704	204	44
STI5_15	200	37.32975	24	0.011	0.593	94	65

STI5_16	200	39.01783	22.949	0.012	3.964	104.666	27.544
STI5_17	200	40.70592	20	0.01	3.591	100	46
STI5_18	200	42.394	32	0.027	2.726	150	63
STI5_19	200	44.08209	45	0.039	2.529	202	97
STI5_20	200	45.77017	40	0.034	3.954	210	71
STI5_21	200	47.45826	27	0.023	4.443	166	31
STI5_22	200	49.14634	29	0.022	4.251	164	30
STI5_23	200	50.83443	18	0.013	5.286	127	35
STI5_24	200	52.52252	10.336	0.005	7.949	63.594	19.053
STI5_25	200	54.2106	11	0.006	7.272	85	19
STI5_26	200	55.89869	43	0.029	6.092	250	46
STI5_27	200	57.58677	13	0.008	5.045	84	31
STI5_28	200	59.27486	15	0.01	7.316	94	37
STI5_29	200	60.96294	20	0.013	5.153	148	44
STI5_30	200	62.65103	29	0.009	1.655	139	76
STI5_31	200	64.33912	27	0.021	4.678	195	62
STI5_32	200	66.0272	14	0.009	7.932	110	23
STI5_33	200	67.71529	18	0.01	7.346	178	25
STI5_34	200	69.40337	18	0.014	5.674	143	24
STI5_35	200	71.09146	32	0.03	-0.708	149	157

Surface Measurements – Femoral Head 294

Table 46: Component 294, Full Surface Measurement Results, Grouped Measurements.

No.	Az.	El.	Sa (nm)	Sdr(x10 ⁻³)	Ssk
CWS01	72.97	38.71	82.00	99.000	-1.08
CWS02	82.95	37.27	80.97	67.000	0.52
CWS03	80.25	43.34	77.53	71.000	0.24
CWS04	76.66	35.38	84.87	82.000	0.56
CWS05	73.94	43.14	117.60	164.000	-0.23
CWS06	67.66	32.80	56.46	45.000	-0.27
CWS07	66.77	37.49	39.79	30.000	-0.62
CWS08	61.35	32.58	27.24	18.000	0.41
CWS09	63.13	36.52	29.41	21.000	-0.70
CWS10	57.71	35.82	23.02	17.000	-1.00
OWS01	100.06	43.38	14.00	5.000	-3.01
OWS02	89.23	55.26	12.33	6.000	-5.62
OWS03	95.64	29.63	6.33	5.000	-7.42
OWS04	83.96	26.33	57.00	69.000	0.11
OWS05	74.80	54.77	57.00	48.000	-2.24
OWS06	64.09	23.94	14.90	10.000	1.47
OWS07	61.28	49.84	16.00	8.000	-5.26
OWS08	36.07	25.06	4.37	0.676	-11.56
OWS09	46.87	44.68	49.13	36.000	-2.15
OWS10	29.69	34.89	11.68	6.000	-5.35
UN01	138.73	55.12	8.00	3.000	-34.47
UN02	146.01	30.90	11.10	8.000	-6.56
UN03	124.15	8.68	16.70	3.000	-0.35
UN04	180.94	50.78	45.00	37.000	-8.81
UN05	183.68	26.02	18.00	13.000	-5.65
UN06	209.55	10.20	11.52	2.000	-5.99
UN07	212.33	37.97	11.00	10.000	-8.14
UN08	226.71	56.37	7.11	2.000	6.37
UN09	258.14	53.73	14.89	5.000	-1.07
UN10	230.24	29.06	6.26	1.000	2.68
UN11	266.42	8.00	16.27	8.000	3.00
UN12	-88.48	33.19	10.11	0.765	-2.55
UN13	-75.79	59.75	18.41	10.000	-2.49
UN14	-60.74	19.11	25.97	24.000	-1.60
UN15	-52.38	54.56	6.54	0.195	-2.83
UN16	-18.41	14.15	20.89	6.000	-1.35
UN17	-44.37	32.18	8.27	0.958	7.58
UN18	-28.98	48.44	5.69	0.890	24.48
UN19	-3.69	57.26	16.00	7.000	4.37
UN20	15.26	60.32	50.00	38.000	-2.03
RIM01	0.00	95.00	4.93	0.122	1.77
RIM02	72.00	95.00	10.00	7.000	-22.31
RIM03	144.00	95.00	7.00	2.000	-11.67
RIM04	216.00	95.00	13.00	14.000	-13.59
RIM05	288.00	95.00	7.20	0.423	-0.83

Table 47: Component 294, Full Surface Measurement Results, Stitch Measurements

No.	Az.	El.	Sa (nm)	Sdr(x10 ⁻³)	Ssk
STI1_01	73.90	8.44	18.95	7.000	-1.59
STI1_02	73.90	10.45	15.38	4.000	-1.36
STI1_03	73.90	12.46	5.06	0.804	-8.50
STI1_04	73.90	14.47	3.91	0.363	-6.16
STI1_05	73.90	16.48	3.87	0.223	-2.44
STI1_06	73.90	18.49	0.01	6.000	-35.38
STI1_07	73.90	20.50	0.01	8.000	3.22
STI1_08	73.90	22.51	0.00	3.000	-5.00
STI1_09	73.90	24.52	0.02	24.000	-2.21
STI1_10	73.90	26.53	0.07	68.000	-1.24
STI1_11	73.90	28.54	0.10	104.000	9.33
STI1_12	73.90	30.55	0.13	132.000	-0.46
STI1_13	73.90	32.56	0.10	104.000	0.16
STI1_14	73.90	34.57	0.09	87.000	0.15
STI1_15	73.90	36.58	0.09	87.000	0.46
STI1_16	73.90	38.59	0.11	113.000	0.35
STI1_17	73.90	40.60	0.12	117.000	0.15
STI1_18	73.90	42.61	0.16	158.000	-0.25
STI1_19	73.90	44.62	0.18	184.000	0.00
STI1_20	73.90	46.63	0.22	219.000	0.09
STI1_21	73.90	48.64	0.21	213.000	-0.05
STI1_22	73.90	50.65	0.18	178.000	-0.51
STI1_23	73.90	52.66	0.08	84.000	-1.55
STI1_24	73.90	54.67	0.04	43.000	-2.16
STI1_25	73.90	56.68	0.03	31.000	-2.56
STI1_26	73.90	58.69	0.01	9.000	-2.69
STI1_27	73.90	60.70	0.00	4.000	-4.59
STI1_28	73.90	62.71	0.00	0.764	-10.25
STI1_29	73.90	64.72	0.00	0.141	-3.36
STI1_30	73.90	66.73	0.00	0.760	9.02
STI1_31	73.90	68.74	0.00	2.000	-7.01
STI1_32	73.90	70.75	0.01	10.000	2.39
STI1_33	73.90	72.76	0.00	3.000	-7.26
STI1_34	73.90	74.77	0.00	1.000	-1.38
STI2_1	85.00	8.44	0.00	3.000	-1.19
STI2_2	85.00	10.45	0.00	2.000	-1.09
STI2_3	85.00	12.46	0.00	0.568	-5.23
STI2_4	85.00	14.47	0.00	0.449	-8.77
STI2_5	85.00	16.48	0.00	0.151	-9.24
STI2_6	85.00	18.49	0.00	3.000	-4.48

STI2_7	85.00	20.50	0.01	14.000	-0.92
STI2_8	85.00	22.51	0.02	22.000	-0.75
STI2_9	85.00	24.52	0.03	25.000	0.13
STI2_10	85.00	26.53	0.04	44.000	0.25
STI2_11	85.00	28.54	0.05	46.000	0.32
STI2_12	85.00	30.55	0.04	41.000	-0.31
STI2_13	85.00	32.56	0.04	37.000	-0.45
STI2_14	85.00	34.57	0.04	35.000	-0.79
STI2_15	85.00	36.58	0.03	26.000	0.16
STI2_16	85.00	38.59	0.05	49.000	0.19
STI2_17	85.00	40.60	0.04	43.000	0.70
STI2_18	85.00	42.61	0.07	73.000	-3.20
STI2_19	85.00	44.62	0.10	96.000	0.32
STI2_20	85.00	46.63	0.06	62.000	0.18
STI2_21	85.00	48.64	0.03	32.000	0.25
STI2_22	85.00	50.65	0.04	35.000	0.77
STI2_23	85.00	52.66	0.03	32.000	-0.51
STI2_24	85.00	54.67	0.01	9.000	-3.31
STI2_25	85.00	56.68	0.01	5.000	-5.49
STI2_26	85.00	58.69	0.01	5.000	-8.00
STI2_27	85.00	60.70	0.00	1.000	-5.39
STI2_28	85.00	62.71	0.00	2.000	-8.90
STI2_29	85.00	64.72	0.00	2.000	-9.19
STI2_30	85.00	66.73	0.00	3.000	-8.08
STI2_31	85.00	68.74	0.00	0.315	-4.94
STI2_32	85.00	70.75	0.01	7.000	0.13
STI2_33	85.00	72.76	0.01	5.000	-11.24
STI2_34	85.00	74.77	0.00	0.781	3.40
STI3_1	65.00	8.44	0.01	7.000	-4.11
STI3_2	65.00	10.45	0.00	1.000	-3.60
STI3_3	65.00	12.46	0.00	2.000	-5.06
STI3_4	65.00	14.47	0.00	2.000	2.83
STI3_5	65.00	16.48	0.00	3.000	1.57
STI3_6	65.00	18.49	0.01	5.000	4.63
STI3_7	65.00	20.50	0.00	3.000	-5.23
STI3_8	65.00	22.51	0.00	4.000	4.61
STI3_9	65.00	24.52	0.01	8.000	-1.75
STI3_10	65.00	26.53	0.03	29.000	-2.01
STI3_11	65.00	28.54	0.02	17.000	-1.16
STI3_12	65.00	30.55	0.03	33.000	-2.26
STI3_13	65.00	32.56	0.04	36.000	-0.02
STI3_14	65.00	34.57	0.03	29.000	0.05
STI3_15	65.00	36.58	0.03	29.000	-0.64
STI3_16	65.00	38.59	0.02	21.000	-1.28
STI3_17	65.00	40.60	0.01	11.000	-1.88

STI3_18	65.00	42.61	0.03	31.000	-2.26
STI3_19	65.00	44.62	0.04	41.000	-2.05
STI3_20	65.00	46.63	0.06	62.000	-1.95
STI3_21	65.00	48.64	0.07	73.000	-1.46
STI3_22	65.00	50.65	0.05	48.000	-1.56
STI3_23	65.00	52.66	0.01	12.000	-0.28
STI3_24	65.00	54.67	0.04	40.000	-2.36
STI3_25	65.00	56.68	0.07	71.000	-1.55
STI3_26	65.00	58.69	0.05	54.000	-2.04
STI3_27	65.00	60.70	0.01	10.000	-6.49
STI3_28	65.00	62.71	0.00	0.164	-14.61
STI3_29	65.00	64.72	0.00	2.000	-9.61
STI3_30	65.00	66.73	0.01	6.000	-0.62
STI3_31	65.00	68.74	0.00	2.000	-13.56
STI3_32	65.00	70.75	0.00	2.000	-16.87
STI3_33	65.00	72.76	0.00	0.784	1.84
STI3_34	65.00	74.77	0.00	2.000	-24.92
STI4_1	55.00	8.44	0.01	6.000	-2.05
STI4_2	55.00	10.45	0.00	1.000	-2.40
STI4_3	55.00	12.46	0.00	4.000	-3.31
STI4_4	55.00	14.47	0.00	3.000	-6.48
STI4_5	55.00	16.48	0.00	0.639	-4.55
STI4_6	55.00	18.49	0.00	1.000	-19.09
STI4_7	55.00	20.50	ME	ME	ME
STI4_8	55.00	22.51	0.00	0.778	1.59
STI4_9	55.00	24.52	0.01	5.000	-2.35
STI4_10	55.00	26.53	0.00	2.000	-1.82
STI4_11	55.00	28.54	0.00	3.000	0.45
STI4_12	55.00	30.55	0.00	4.000	-2.89
STI4_13	55.00	32.56	ME	ME	ME
STI4_14	55.00	34.57	0.03	26.000	-1.89
STI4_15	55.00	36.58	0.03	30.000	-2.17
STI4_16	55.00	38.59	0.03	26.000	-2.02
STI4_17	55.00	40.60	0.01	5.000	-1.47
STI4_18	55.00	42.61	0.00	4.000	-1.90
STI4_19	55.00	44.62	ME	ME	ME
STI4_20	55.00	46.63	0.01	10.000	-5.83
STI4_21	55.00	48.64	0.01	13.000	-3.13
STI4_22	55.00	50.65	0.02	20.000	-3.72
STI4_23	55.00	52.66	0.06	58.000	-1.80
STI4_24	55.00	54.67	0.07	72.000	-1.65
STI4_25	55.00	56.68	0.04	41.000	-2.28
STI4_26	55.00	58.69	0.02	21.000	-3.73
STI4_27	55.00	60.70	0.02	21.000	-3.40
STI4_28	55.00	62.71	0.02	21.000	-1.78

STI4_29	55.00	64.72	0.01	8.000	-5.04
STI4_30	55.00	66.73	0.00	4.000	-7.19
STI4_31	55.00	68.74	0.00	0.078	-1.97
STI4_32	55.00	70.75	0.00	0.043	-0.39
STI4_33	55.00	72.76	0.00	0.106	0.60
STI4_34	55.00	74.77	0.00	0.198	2.02
STI5_1	200.00	8.44	0.00	2.000	6.24
STI5_2	200.00	10.45	0.00	3.000	-3.14
STI5_3	200.00	12.46	ME	ME	ME
STI5_4	200.00	14.47	0.01	7.000	1.74
STI5_5	200.00	16.48	0.01	6.000	-0.27
STI5_6	200.00	18.49	ME	ME	ME
STI5_7	200.00	20.50	0.00	3.000	-0.32
STI5_8	200.00	22.51	0.00	4.000	-0.63
STI5_9	200.00	24.52	0.01	8.000	-5.16
STI5_10	200.00	26.53	0.02	22.000	-0.62
STI5_11	200.00	28.54	0.01	8.000	-2.90
STI5_12	200.00	30.55	0.01	5.000	-8.46
STI5_13	200.00	32.56	0.00	3.000	-8.41
STI5_14	200.00	34.57	0.00	0.907	-25.45
STI5_15	200.00	36.58	0.00	0.283	2.09
STI5_16	200.00	38.59	0.01	9.000	0.03
STI5_17	200.00	40.60	0.00	4.000	-15.30
STI5_18	200.00	42.61	0.00	1.000	5.88
STI5_19	200.00	44.62	0.00	2.000	6.87
STI5_20	200.00	46.63	0.00	0.840	2.69
STI5_21	200.00	48.64	0.00	4.000	5.74
STI5_22	200.00	50.65	0.00	1.000	1.21
STI5_23	200.00	52.66	0.00	0.612	8.23
STI5_24	200.00	54.67	0.00	1.000	-3.13
STI5_25	200.00	56.68	0.00	0.532	3.13
STI5_26	200.00	58.69	0.00	0.434	-0.91
STI5_27	200.00	60.70	0.00	0.524	8.45
STI5_28	200.00	62.71	0.00	0.960	5.18
STI5_29	200.00	64.72	0.00	0.319	-0.30
STI5_30	200.00	66.73	0.00	0.526	5.40
STI5_31	200.00	68.74	0.00	1.000	1.98
STI5_32	200.00	70.75	0.01	5.000	-28.26
STI5_33	200.00	72.76	0.00	0.367	-10.68
STI5_34	200.00	74.77	0.00	0.702	0.22